FOSSIL ENERGY

DOE/MC/21136-21

(DE89000756)

IMPROVEMENT OF CO_2 FLOOD PERFORMANCE

Fourth Annual Report for the Period

October 1, 1987--September 30, 1988

By

J. P. Heller

F. S. Kovarik

July 1989

Performed Under Contract No. FC21-84MC21136

New Mexico Institute of Mining and Technology

New Mexico Petroleum Recovery Research Center

Socorro, New Mexico

Bartlesville Project Office
U. S. DEPARTMENT OF ENERGY
Bartlesville, Oklahoma

This report has been reproduced directly from the best available copy.

Available to DOE and DOE contractors from the Office Of Scientific and Technical Information, P.O. Box 62, Oak Ridge, TN 37831; prices available from (615)576-8401, FTS 626-8401.

Available to the public from the National Technical Information Service, U.S. Department of Commerce, 5285 Port Royal Rd., Springfield, VA 22161

Price: Printed **A14**
Microfiche A01

DOE/MC/21136-21
Distribution Category UC-122

IMPROVEMENT OF CO_2 FLOOD PERFORMANCE

Fourth Annual Report for the Period October 1, 1987--September 30, 1988

By
J. P. Heller
F. S. Kovarik

July 1989

Work Performed Under Contract No. FC21-84MC21136

Prepared for
U. S. Department of Energy
Assistant Secretary for Fossil Energy

Royal J. Watts, Project Manager
Morgantown Energy Technology Center
P. O. Box 880
Morgantown, WV 26505

Prepared by
New Mexico Institute of Mining and Technology
New Mexico Petroleum Recovery Research Center
Socorro, New Mexico

ABSTRACT

In Task Area I, an oscillating quartz viscometer was developed to measure viscosities of CO_2/hydrocarbon systems over a range of conditions. Viscosity dependency on density, composition, and temperature is examined and the functional form of a modified Lohrenz, Bray, and Clark correlation for CO_2-oil systems is presented. Also, the effect of free gas on displacement efficiency and that of multiple hydrocarbon phase flow on sweep efficiency are being investigated. With two-dimensional glass micromodels at reservoir conditions, we studied the effects of different scales of microscopic heterogeneity on flow behavior and blocking mechanisms using both in-situ foaming and pregenerated foam. Additionally, the initial formulation of a two-dimensional simulator which models high-pressure gas-foam flow is presented. A simulation of the processes of high-permeability zone blockage with foam, fluid diversion, and increased trapped oil recovery is included. Also, an NMR imaging study on fluid flow through porous media addressing the nonlinear stability analysis of miscible displacements and matrix-fracture fluid transport functions has been initiated.

In Task Area 2, work commenced on a new subarea, the non-uniformity of flow which results from rock heterogeneity. Emphasis was placed on the effect of this non-uniformity on displacement efficiency, in both field and laboratory situations. In addition to this new work, more such measurements were made of the steady-state mobility of foam-like dispersions of dense CO_2 in surfactant solutions. Most striking of the results of these experiments was the delineation of the range over which rock permeability has a significant effect on relative mobility. This promises additional utility from reservoir use of CO_2-foam. Additionally, new direct thickeners were synthesized and tested with the goal of increasing the viscosity of dense CO_2.

TABLE OF CONTENTS

ABSTRACT iii

LIST OF FIGURES viii

LIST OF TABLES xv

ACKNOWLEDGEMENTS xvi

EXECUTIVE SUMMARY xvii

I. DISPLACEMENTS WITH PURE AND IMPURE CO_2 1

A. PHASE BEHAVIOR AND FLUID PROPERTY STUDIES 1
1. Continuous Phase Equilibrium Runs 234, 235, and 236 1
2. CPE 237 - Gas Data Averaging Investigation 1
3. Building of Fluids Lab 10
4. Modifying the PVT System 13
5. Composition, Viscosity, and Density Correlation with Asphaltene Precipitation 13

B. PHASE BEHAVIOR AND FLUID PROPERTY STUDIES: DEVELOPMENT OF AN IMPROVED VISCOSITY CORRELATION 19
1. Introduction 19
2. Theoretical Background 28
3. The Lorenz, Bray, and Clark Correlation 31
4. Results and Discussion 36
5. Nomenclature 41

C. EFFECT OF PHASE BEHAVIOR ON DISPLACEMENT EFFICIENCY 43
1. Solution and Free Gas Effect on the Development of Miscibility 43
2. The Effect of Multiple Hydrocarbon Phases on Displacement Efficiency 46
a. Introduction 46
b. Experimental Aspects 47
c. Results and Discussion 50
1) CO_2-Synthetic Oil Displacements 50
2) CO_2-Wasson Oil Displacements 56

D. MECHANISTIC STUDIES ON HIGH PRESSURE GAS/FOAM FLOW: EXPERIMENTAL 58
1. Introduction 58
2. Experimental Results and Discussion 67
a. Mechanisms Associated with In-situ Foam Generation and Propagation 67
b. Parametric Studies 73
1) Effect of Microscopic Heterogeneity 73
a) Injection of Pure CO_2 into a Surfactant-Solution-Saturated Model 73
b) Simultaneous Injection of CO_2 and Surfactant Solution in the Presence of Crude Oil 75
2) Comparison of In-Situ Foam and Pregenerated Foam 88
3) Presence of Oil Phase 88
4) Surfactant Concentration 91

5) Effect of Flow Rate 94
3. Conclusions 94

E. MECHANISTIC STUDIES ON HIGH PRESSURE GAS/FOAM FLOW: THEORETICAL 97

F. CONCLUSIONS--TASK AREA I 110

II CO_2 MOBILITY CONTROL AND FLOW HETEROGENEITIES 134

A. INTRODUCTION—ORIGINS OF NON-UNIFORM DISPLACEMENT 134

B. HETEROGENEITIES OF THE RESERVOIR ROCK 136
1. Base Case For Well-To-Well Tracer Studies 136
a. Classification and Practice of Tracer Tests 136
b. Information Obtained from a Tracer Test 137
c. Outline of The Numerical Method 139
d. The Flow Field in a Five-Spot 140
e. Derivation of Equation of Motion 141
f. Time Stability of the Calculations 142
g. Computation of Tracer Peaks and Widths 143
h. Presentation and Discussion of Results 143
1) Tracer Movements 145
2) Output Concentration 150
3) Effect of Transverse Dispersion 150
i. Conclusions 155
2. Displacement in a Heterogeneous Five-Spot 157
a. Introduction 157
b. History and Background Literature 158
c. Method of the Numerical Experiment 163
d. Results of the Calculations 165
1) The Permeability Distribution 165
2) The Pressure Distribution and the Streamlines 172
3) Tracking of the Front 172
4) Recovery Computation 184
e. Conclusions 195
f. Plans for Continuation of the Work 196
3. Flow Heterogeneity In Porous Media At Small-Scale 196
a. Laboratory Observation of Flow Non-Uniformity 197
b. Preliminary Results 197
c. Data Analysis 200
d. Flow Visualization Data Using a CT Scanner 200
e. Rock Porosity Measurements 201
f. Miscible Displacement Data 201
g. Conclusions 203

C. THE DEVELOPMENT OF DIRECT THICKENERS 203
1. Summary 203
2. Method II Molecules 204
3. Method III Molecules 205

D. CO_2-FOAM MOBILITY CONTROL 218
1. Overview 218
2. Introduction 220
3. CO_2-Foam Mobility Measurements 220
a. Experimental 220

b. The Effect of Surfactant Concentration 222
c. Effect of CO_2-Foam Fraction 224
d. Effect of Rock Permeability 224
4. Dynamic Surfactant Adsorption Experiment 230
a. Description of the Experiment and Apparatus 232
b. Results and Discussion on Dynamic Adsorption Measurements 234
5. High Temperature CO_2-Foam Mobility Measurement 239
a. Schematic of the Apparatus 239
b. Modification of the CO_2-Foam Mobility Apparatus 241
c. Operating Procedure for the High Temperature CO_2-Foam Mobility Apparatus 243
d. Calibration of the Capillary Tube Flowmeter 243
6. Future Studies 243

E. INTEGRATION WITH RESERVOIR SIMULATION 244

F. PROJECT PROSPECTS AND CONCLUSION 246

REFERENCES 248

APPENDIX A ..... A

APPENDIX B ..... B

APPENDIX C C

APPENDIX D ..... D

APPENDIX E ..... E

APPENDIX F ..... F

APPENDIX G ..... G

APPENDIX H ..... H

LIST OF FIGURES

Figure 1 Viscosity/pseudoternary diagram for Wasson stock tank oil at 109°F and 1200 psia 2

Figure 2 Viscosity/density/time plot for Wasson stock tank oil at 109°F and 1200 psia, lower sample 3

Figure 3 Viscosity/density/time plot for Wasson stock tank oil at 109°F and 1500 psia, upper sample 4

Figure 4 Viscosity/density/time plot for Wasson stock tank oil at 109°F and 1500 psia, lower sample 5

Figure 5 Viscosity/density/time plot for Oil A at 155°F and 2100 psia, upper sample 6

Figure 6 Viscosity/pseudoternary diagram for Oil A at 155°F and 2100 psia 7

Figure 7 Viscosity/density/time plot for synthetic oil (C_3, C_4, C_5, C_{10}) at 100°F and 1500 psia, upper sample 8

Figure 8 Viscosity/density/time plot for synthetic oil (C_3, C_4, C_5, C_{10}) at 100°F and 1500 psia, lower sample 9

Figure 9 Change in CO_2 concentration over first sample period 11

Figure 10 Gas production over first sample period 11

Figure 11 Change in CO_2 concentration over second sample period 12

Figure 12 Gas production over second sample period 12

Figure 13 Viscosities of binary systems with CO_2 and hydrocarbons from C_5 to C_8 14

Figure 14 Comparison of Maljamar and Oil A compositional analyses 21

Figure 15 Pressure/composition diagram for Oil A/CO_2 system CPE experiment conditions indicated at 2100 psia and 1500 psia 22

Figure 16 Viscosity/pseudoternary diagram for Oil A/CO_2 system P = 2100 psia, T = 145°F 23

Figure 17 Viscosity/pseudoternary diagram for Oil A/CO_2 system P = 1500 psia, T = 145°F 24

Figure 18	Viscosity/density/time plot from Oil A/CO_2 CPE experiment P = 2100 psia, T = 145°F, lower phase	25
Figure 19	Viscosity/density/time plot from Oil A/CO_2 CPE experiment P = 2100 psia, T = 145°F, upper phase	26
Figure 20	90% CO_2 - 10% N_2/Wasson Oil Viscosity-Density-Time Plot at 109°F and 1500 psia	27
Figure 21	Comparison between Lohrenz-Bray-Clark calculated and experimentally observed viscosities for equilibrium liquid mixtures of CO_2 and Maljamar stock tank oil at 1200 psia and 90°F	39
Figure 22	Comparison between Lohrenz-Bray-Clark calculated and experimentally observed viscosities for equilibrium liquid mixtures of CO_2 and Wasson stock tank oil at 1500 psia and 109°F	40
Figure 23	Schematic diagram of the CO_2/crude oil displacement apparatus	48
Figure 24	Schematic diagram of the back pressure regulator system	49
Figure 25	Recovery versus pressure plot for CO_2-synthetic oil displacements	53
Figure 26	Critical injection flow rate versus pressure for gravity stabilized displacement for the CO_2-synthetic oil system at 93°F	55
Figure 27	Pressure-composition phase diagrams for mixtures of CO_2 with Wasson stock tank oil	57
Figure 28	Schematic diagram of high-pressure glass micromodel apparatus	60
Figure 29(a)	Micromodel patterns and pore size distribution of homogeneous model (HOM)	61
Figure 29(b)	Micromodel patterns and pore size distribution of heterogeneous model (HET)	62
Figure 29(c)	Micromodel patterns and pore size distribution of modified heterogeneous model (MDH)	63
Figure 29(d)	Micromodel patterns and pore distribution of layered model (LAY)	64
Figure 30	Downstream snap-off mechanism	69
Figure 31	Upstream snap-off mechanism	70
Figure 32	Upstream bubble subdivision mechanism	71
Figure 33	Downstream bubble subdivision mechanism	72

Figure 34 Lamellae and bubble propagation methods 74

Figure 35 Surfactant solution saturation vs. pore volumes of CO_2 injected for displacement model HOM-4: a) 0.42 PVI, b) 3.0 PVI 76

Figure 36 Surfactant solution saturation vs. pore volumes of CO_2 injected for displacement model HET-4: a) 0.5 PVI, b) 3.0 PVI 77

Figure 37 Surfactant solution saturation vs. pore volumes of CO_2 injected for displacement model MDH-4: a) 0.5 PVI, b) 3.0 PVI 78

Figure 38 Surfactant solution saturation vs. pore volumes of CO_2 injected for displacement model LAY-4: a) 0.5 PVI, b) 3.0 PVI 79

Figure 39 Oil saturation vs. pore volumes of CO_2 injected for displacement model HOM-8: a) 0.43 PVI, b) 0.92 PVI, c) 1.93 PVI, d) 3.0 PVI 80

Figure 40 Oil saturation vs. pore volumes of CO_2 injected for displacement model HET-8: a) 0.0 PVI, b) 0.63 PVI, c) 0.91 PVI, d) 3.0 PVI 81

Figure 41 Oil saturation vs. pore volumes of CO_2 injected for displacement model MDH-8: a) 0.00 PVI, b) 0.6 PVI, c) 1.0 PVI, d) 3.0 PVI 82

Figure 42 Oil saturation vs. pore volumes of CO_2 injected for displacement model LAY-8: a) 0.52 PVI, b) 1.0 PVI, c) 3.0 PVI 83

Figure 43 Recovery efficiency as a function of heterogeneity coefficient, aspect ratio, and injection mode. PV_R/PV_0 = pore volumes recovered/initial pore volume 85

Figure 44 Recovery efficiency as a function of injection ratio. PV_R/PV_0 = pore volumes recovered/initial pore volume 86

Figure 45 Recovery efficiency as a function of upstream aspect ratio. PV_R/PV_0 = pore volumes recovered/initial pore volume 87

Figure 46 Comparison of in-situ and pregenerated foam recovery efficiency. (BT means breakthrough) 89

Figure 47 Effect of oil type on foam mobility, pressure drop vs. pore volumes of CO_2 injected 90

Figure 48 Comparison of foam mobility in secondary and tertiary floods (simultaneous injection) 92

Figure 49 Effect of surfactant concentration on foam mobility, pressure drop vs. pore volumes of CO_2 injected 93

Figure 50 Effect of CO_2 flow rate on sweep efficiency 95

Figure 51 Critical capillary number 96

Figure 52 Flow diagram of foam model 102
Figure 53 Layout of system 103
Figure 54 Capillary pressure curve for water-oil system 105
Figure 55 Capillary pressure curve for gas-oil system 106
Figure 56 Relative permeability curves for water-oil system (Case No. 1) 107
Figure 57 Relative permeability curves for water-oil system (Case No. 2) 108
Figure 58 Relative permeability curves for gas-oil system 109
Figure 59 Effect of relative permeability on pressure drop across the system 111
Figure 60 Effect of leave-behind lamellae on pressure drop across the system 112
Figure 61 Effect of foam on pressure drop across the system 113
Figure 62 Gas velocity field with foam at time 600 sec 114
Figure 63 Gas velocity field with foam at time 1080 sec 115
Figure 64 Gas velocity field with foam at time 1800 sec 116
Figure 65 Gas velocity field with foam at time 2760 sec 117
Figure 66 Gas velocity field with foam at time 5880 sec 118
Figure 67 Gas velocity field without foam at time 600 sec 119
Figure 68 Gas velocity field without foam at time 1800 sec 120
Figure 69 Gas velocity field without foam at time 5880 sec 121
Figure 70 Oil saturation profile with foam at time 600 sec 122
Figure 71 Oil saturation profile with foam at time 1080 sec 123
Figure 72 Oil saturation profile with foam at time 1800 sec 124
Figure 73 Oil saturation profile with foam at time 2760 sec 125
Figure 74 Oil saturation profile with foam at time 5880 sec 126
Figure 75 Gas saturation profile with foam at time 600 sec 127
Figure 76 Gas saturation profile with foam at time 1800 sec 128
Figure 77 Gas saturation profile with foam at time 2760 sec 129

Figure 78	Gas saturation profile with foam at time 5880 sec	130
Figure 79	Stream paths in a five-spot pattern	144
Figure 80	Front locations (first and last isoconcentration lines) of tracer slug at different values of the pore volume injected	146
Figure 81	Plot of tracer concentration distributions, near injection well for a single streamline	147
Figure 82	Behavior of tracer bandwidth on a single streamline	148
Figure 83	Behavior of tracer peak concentration on a single streamline	149
Figure 84	Plot of tracer concentration distribution on different streamlines at breakthrough	151
Figure 85	Plot of integrated output concentration vs. pore volume injected for different peclet numbers	152
Figure 86	Front location of the first and last isoconcentration lines with no dispersion. (Note that in all cases but the first, trailing and leading edges of tracer band are the same line)	153
Figure 87	Plot of integrated output concentration vs. Pore volume injected, no dispersion	154
Figure 88	Plot of integrated output concentration vs. Pore volume injected to show the effect of transverse dispersion	156
Figure 89	Potentiometric model study of the five-spot network, showing the isopotential lines, streamlines, and flood fronts. (After Wyckoff, 1933)	160
Figure 90	Histogram of log permeability values, $N_{sp} = 40$	166
Figure 91	Histogram of log permeability values, $N_{sp} = 100$	167
Figure 92	Contour map of log permeability values, $N_{sp} = 40$	168
Figure 93	Contour map of log permeability values, $N_{sp} = 100$	169
Figure 94	Variograms of permeability distributions, in five cases with different numbers of source points	171
Figure 95	Dykstra-Parsons coefficient vs. α	173
Figure 96	Pressure distribution, $\alpha = 0$, uniform permeability	174
Figure 97	Pressure distribution, $\alpha = 1$, $N_{sp} = 40$	175

Figure 98 Pressure distribution, $\alpha = 2$, $N_{sp} = 40$ 176

Figure 99 Pressure distribution, $\alpha = 3$, $N_{sp} = 40$ 177

Figure 100 Pressure distribution, $\alpha = 1$, $N_{sp} = 100$ 178

Figure 101 Pressure distribution, $\alpha = 3$, $N_{sp} = 100$ 179

Figure 102 Map of fluid particle streamlines on a five-spot, $\alpha = 0$, uniform permeability field 180

Figure 103 Fluid particle streamlines, $\alpha = 1$, $N_{sp} = 40$ 181

Figure 104 Fluid particle streamlines, $\alpha = 3$ $N_{sp} = 100$ 182

Figure 105 Front locations, $\alpha = 0$, uniform permeability field 183

Figure 106 Front locations vs. Time, $\alpha = 1$, $N_{sp} = 40$ 185

Figure 107 Front locations vs. Time, $\alpha = 1$, $N_{sp} = 100$ 186

Figure 108 Recovery curve, $\alpha = 0$, uniform permeability field 187

Figure 109 Recovery curve, $\alpha = 1$, $N_{sp} = 40$ 188

Figure 110 Recovery curve, $\alpha = 2$, $N_{sp} = 40$ 189

Figure 111 Recovery curve, $\alpha = 3$, $N_{sp} = 40$ 190

Figure 112 Recovery curve, $\alpha = 1$, $N_{sp} = 100$ 191

Figure 113 Recovery curve, $\alpha = 3$, $N_{sp} = 100$ 192

Figure 114 Recovery curve, $\alpha = 1$, $N_{sp} = 200$ 193

Figure 115 Recovery curve, $\alpha = 2$, $N_{sp} = 200$ 194

Figure 116 Apparatus for measurements of flow heterogeneity 198

Figure 117 Brightness vs. Time, Berea SS #6: Indicating dye concentration at 20 locations on output face of core 199

Figure 118 Porosity variation of Antolini SS 202

Figure 119 IR spectrum of 1-hexene, 1-decene, and 5-ethylidene-2-norbornene terpolymer 208

Figure 120 Viscosity of P119*n in hexane 209

Figure 121 High pressure capillary viscometer 210

Figure 122 Synthesis of silylated organotin fluorides 212

Figure 123 Viscosity as a function of concentration for tris(trimethylsilylpropyl)tin fluoride and dibutyltrimethylsilylpropyltin fluoride. Solvent n-hexane, temperature 25°C. (Number near each data point indicates approximate shear rate at the wall) 215

Figure 124 Viscosity vs. concentration curves for tris(trimethylsilylpropyl)tin fluoride in various solvents at 25°C. Number near each data point indicates approximate shear rate at the wall 216

Figure 125 Viscosity of solutions of PTF in carbon dioxide 217

Figure 126a Viscosity vs. shear rate plot of PTF 219

Figure 126b Viscosity vs. shear rate plot of BTF 219

Figure 127 Schematic of foam mobility measurement apparatus 221

Figure 128 Effect of surfactant concentration on CO_2-foam mobility 223

Figure 129 Effect of foam volume fraction on mobility - Baker Dolomite 225

Figure 130 Effect of foam volume fraction on mobility - Berea sandstone 226

Figure 131 Foam Fraction effect at constant velocity 227

Figure 132 Relative mobility variations with velocity for different rocks 228

Figure 133 Effect of rock permeability or relative foam 229

Figure 134 Effect of flow velocity at different surfactant concentrations 231

Figure 135 Dynamic adsorption apparatus 233

Figure 136 Irreversibile adsorption, as function of flow rate 235

Figure 137 High temperature foam mobility apparatus 240

Figure 138 New end-plate for high-pressure core holder 242

LIST OF TABLES

Table 1	CPE 232 Binary System CO_2 and C_7	15
Table 2	CPE 233 Binary System CO_2 and C_8	17
Table 3	Compositions of Oil A and Maljamar Oil January 22, 1988	20
Table 4	Comparison of Lohrenz, Bray, and Clark Viscosity Correlation Prediction to the CO_2-Maljamar Stock Tank Oil Run (CPE 210) at 1200 psia and 90°F	37
Table 5	Comparison of Lohrenz, Bray, and Clark Viscosity Correlation Prediction to the CO_2-Wasson Stock Tank Oil Run (CPE 234) at 1500 psia and 109°F	38
Table 6	Fluid Properties of Synthetic Oil	44
Table 7	Critical Velocities for Stable Displacements	45
Table 8	Properties of Core B7	51
Table 9	Summary of Vertical CO_2-Synthetic Oil Displacements	52
Table 10	Schedule of Coreflood and Microcore Experiments for the Multiphase Flow Effect on Sweep Efficiency Project	59
Table 11	Properties of Pore Networks	65
Table 12	Summary of Flow Visualization Experiments	66
Table 13	Properties of the Fluids	68
Table 14	Conditions and Parameters Used in the "Process-Demonstration" Simulations	104
Table 15	Nomenclature	131
Table 16	Comparison of Intrinsic Viscosity and Solubility of Method I and Method II Polymers	206
Table 17	Method II Polymer Synthesis	207
Table 18	Solubilities of Silcon-Containing Triorganotin Fluorides at 25°C	214
Table 19	Adsorption Measurement—Baker Dolomite	236
Table 20	Adsorption Measurement—Rock Creek Sandstone	237
Table 21	Adsorption Measurements. Effects of Concentrations on M and Chromatographic Time Delay Factor at 10cc/hr	238

ACKNOWLEDGEMENTS

The research work described herein was made possible by the cooperation and assistance of several groups and individuals, to whom we express our great appreciation.

First among these are the sponsoring agencies and companies who contributed financially to support our work during this year. These are the Morgantown Energy Technology Center, representing the United States Department of Energy, the New Mexico Research and Development Institute, representing the State of New Mexico, and the following oil companies: the Abu Dhabi National Reservoir Research Foundation, Amoco Production Company, the Arco Oil and Gas Company, BP America, the Chevron Oil Field Research Company, Marathon Oil Company, Oxy USA, Inc, and Texaco USA.

In addition to these groups, there are a number of individuals associated with the New Mexico Petroleum Recovery Research Center who deserve special mention. The Principal Investigators, and those listed as Contributors, are greatly indebted to those who have helped us to perform our research and to report it. The reader can easily detect that they have done their jobs extremely well. They are listed below under one of two headings that identify their specialties:

Editing, Typing, Illustrating	Undergraduate Laboratory Assistants
Toni Johnson	Glenn McColpin
K. Allbritton	Mustafa Sadeq
Stephanie Dalem	Bob Sumpter
Carol Dotson	Bob Svec
Janet Golding	Eric Jacobson
Llewellyn Landavazo	Dean Zipse
Jody Baze	Wendy Weiss
Kevin Clower	

We wish to acknowledge most gratefully the assistance offered by all of those listed above, and to others at New Mexico Tech who have assisted us.

EXECUTIVE SUMMARY

TASK AREA I

At the end of year one of our new three-year contract on CO_2 flooding, progress has been made in several key areas which are summarized below.

An oscillating quartz crystal viscometer was recently developed to measure viscosities of CO_2/hydrocarbon systems over a range of conditions from 90°F to 250°F and from 1000 psi to 4000 psi. This is the range of interest in carbon dioxide-enhanced oil recovery processes, and published viscosity data on these systems are rare.

This crystal viscometer has been integrated into the continuous phase equilibrium apparatus (CPE), a continuous flow experiment which measures compositions and densities simultaneously and rapidly for two phases in near equilibrium. Because this system operates continuously, phase equilibrium data can be generated faster than with a static equilibrium cell. Thus, the system can now simultaneously measure viscosity, density, and composition of flowing phases. An accurate viscosity database can be generated in a fraction of the time that would be necessary with conventional equipment.

The experimental error in viscosity measurement is estimated to be less than 5% over a range of 0.04 cp to 4.0 cp, the range of interest in light oil/CO_2 reservoir modeling. Recent data are compared to the well-known Lohrenz, Bray, and Clark reservoir fluid viscosity correlation that is commonly used for predicting CO_2/oil mixture viscosities in reservoir simulation studies. Viscosity dependency on density, composition, and temperature is also examined. The need for a new correlation for CO_2/oil systems is demonstrated. The functional form of a modified Lohrenz, Bray, and Clark correlation for CO_2-oil systems is presented.

Coreflood experiments are currently being run to investigate the effect of solution gas and free gas on displacement efficiency. Preliminary results suggest that high recoveries may be able to be achieved below the original bubble point pressure of the oil.

A series of gravity-stabilized CO_2-oil corefloods have been performed investigating the effect of multiple hydrocarbon phase flow on sweep efficiency. Early results indicate that higher-than-miscible oil recoveries could be possible at a pressure range demonstrating complex multiple hydrocarbon phase behavior.

The heterogeneity of oil-bearing reservoirs and the high mobility of displacing fluids are the most serious problems in miscible gas flooding. These problems cause early breakthrough of injection gas at production wells and also lower the oil recovery efficiency, resulting in a high residual oil saturation. Both high-pressure gas-foams and chemical gels are good candidates for the blocking of high-permeability zones or fractures.

The mechanisms associated with foam generation and propagation were studied in two-dimensional glass micromodels at standard CO_2 flooding reservoir conditions. In this study we investigated the effects of different scales of microscopic heterogeneity on flow behavior and blocking mechanisms using both in-situ foaming and pregenerated foam. Pregenerated foams were obtained by simultaneously injecting CO_2 and surfactant solution into a foam generator (Berea

sandstone). The effects of oil phase, surfactant concentration, injection mode, and initial water saturation on the foam flow behavior were also investigated.

Results show that bubble density and foam texture depend upon pore structure of the micromodel and foam generation methods. Upstream snap-off was recognized as a dominant mechanism of foam generation when liquid and gas phases were simultaneously injected into a liquid-saturated model, while downstream snap-off was dominant when a gas phase was injected into a liquid-saturated model. Excellent near-miscible fluid diversion into the oil matrix was obtained by a multiphase foam because of the foam's ability to block high-permeability zones.

A two-dimensional numerical simulator is currently being developed which models high-pressure gas-foam flow. The initial formulation of the model is presented here. "Foam" is presently generated by the mechanisms of snap-off, or travelling lamellae division, and static lamellae that are assumed to affect gas relative permeability are generated at this time by the "leave-behind" mechanism. In addition, foam coalescence and trapping mechanisms are incorporated into the simulator. Many of the assumptions used in this initial formulation have been presented elsewhere in the literature. A simulation of the processes of high-permeability zone blockage with foam, fluid diversion (e.g., crossflow), and increased trapped oil recovery is presented. Modifications to the foam simulator are underway, including (1) separation of bubble and lamellae generation mechanisms, (2) separation of bubble and lamellae propagation mechanisms, (3) definition of a critical capillary number for upstream snap-off, and (4) addition of new correlations (from micromodel and coreflood experiments) for foam generation, coalescence, trapping, and adsorption terms. Also, micromodel results are being scaled to berea coreflood data generated with short and long cores.

An NMR imaging study on fluid flow through porous media has been initiated. So far, water-oil dolomite corefloods have been imaged. Initial studies are addressing the nonlinear stability analysis of miscible displacements and matrix-fracture fluid transport functions.

TASK AREA II

Task II of the research project, "Improvement of CO_2 Flood Performance," is devoted to the study of three major subareas and to the search for practical applications related to them. Each of these subareas is concerned with the reduced recovery efficiency and profitability that occurs as a result of non-uniform displacement in CO_2 flooding and in related processes of secondary or tertiary oil production. The first of the three subareas pertains to the effect of rock heterogeneity on displacement efficiency, while in the second and third areas, we are involved in the development of mobility control additives (and the techniques for their use) to minimize the non-uniformity of displacement that arises from frontal instability. The two types of mobility control additives sought in the two subareas are, respectively, direct thickeners (chemicals that form a viscous, polymeric solution in dense CO_2) and foams (which are dispersions of surfactant solutions in the dense CO_2).

In this first year of the continuation and extension of the project, we have made significant progress in all three subareas of the research. In the first subarea, two computer simulation studies have been completed, and one laboratory flow experiment is being performed, in which the effects of reservoir heterogeneity on displacement are considered. The simulations are of quarter five-spot patterns, and are directed at two different questions. The first simulation investigates the effect of dispersion on the tracer production profile in a single-layer homogeneous formation. The full tensor form of dispersion is considered in the calculation, permitting the importance of the longitudinal and

transverse components to be examined separately. The general result is that the largest effect on the spreading of an injected spike of tracer is caused by the great disparity in total well-to-well travel time between those parts of the tracer slug that travel along the different streamlines. Next in importance, and capable of producing very noticeable effects, is the magnitude of the longitudinal dispersion coefficient. Last in importance, and barely noticeable, is the change made by the transverse dispersion coefficient. Some of the details of the calculation, as well as a graphic compilation of the results, are presented in the body of the report.

The second simulation calculation is also in a five-spot geometry, but here the effects of reservoir heterogeneity are considered. For simplicity in this first treatment, the computation is two-dimensional, ignores dispersion, and assumes both a perpetually sharp front and a mobility ratio of one. The heterogeneity of the reservoir segment is introduced by use of the source-point method first utilized in 1972, which provides some facility for the variation of the two dominant geostatistical parameters—the correlation length and the width of the log normal permeability distribution (i.e., as indexed, for example, by the Dykstra-Parsons coefficient). The results of this study indicate how breakthrough time and the subsequent production curves vary as these two parameters are changed. In brief, the displacement efficiency is considerably degraded as the width of the permeability distribution is increased (as the Dykstra-Parsons coefficient is increased towards one). The effect is more pronounced if the correlation length is large. Indeed, for a small correlation length, the effect of the heterogeneity is simply approximated by an increased dispersion coefficient. The next step in this series of simulations will be to combine the two studies in various ways, with the aim of obtaining for the reservoir engineer a catalog of the effects of heterogeneity on the production curves of both tracers and oil. The purpose here is to enable these field measurements to be used diagnostically to determine the character and intensity of reservoir variability.

A third activity in support of our studies of heterogeneity is experimental. Miscible floods are conducted in laboratory samples. These differ from conventional displacement experiments in that the coreflood is not regarded as one-dimensional. Instead, the concentration history over the entire output face is observed as a function of time. In our laboratory at New Mexico Tech, this data is obtained by use of an optical method involving fluorescent dyes, video recording, and computer image analysis. In addition, and with the kind cooperation of Drs. Gary Pope and Bruce Rouse and their colleagues at the University of Texas, we have obtained some data taken with their computerized tomography (CT) scanner during a miscible displacement in a layered sandstone. These data also are being used to assess the smaller-scale heterogeneity of samples of both quarried and reservoir rock. Our conclusions in these experiments will be of interest relative to the gathering of meaningful information about the reservoir from laboratory corefloods.

A final facet of our efforts in this subarea devoted to reservoir structure consists of an overall review and assessment, from our special viewpoint, of the current status of the recent mathematical and geological investigations of reservoir irregularity. This is in the form of a report on the literature and the concepts that are important in shaping current work on the characterization of reservoirs. This PRRC report, which will be distributed to our supporters when completed, will describe both geological and mathematical features of current research work, and will attempt to place this current research in perspective relative to the conduct of CO_2 or other dense gas floods for maximum displacement efficiency.

The second subarea of our research is a program of chemical synthesis and testing, in search of direct thickeners for CO_2 and dense hydrocarbon gas mixtures. As far as we are aware, there has been only one other open research project with this goal. Our own research has explored the variety of polymers and other organic compounds that are soluble in condensed gases, defining the features and placing limits on the molecular types, pendent groups, and polymer chain lengths of possible

candidates for such materials. We have written the definitive papers on these polymers, and hold one patent for a special type of direct thickener that is able to thicken propane or butane to the hundreds-of-centipoise range. In this past year, we have done exploratory work on two different kinds of associative polymeric viscosifiers. In such solutions the polymeric chains responsible for the viscosity increase are based on associative chemical bonds between similar molecules or oligomers. These transient bonds are formed at a rate that increases faster than linearly with concentration. The two classes of thickeners include both the organotin fluorides and low-molecular-weight, hydrocarbon-based oligomers with one sulfonated and neutralized ionic group. A number of the compounds of both classes have been synthesized and tested during this past year, yielding new results that are presented in this report. In addition, we have recently been able to add a polymer chemist to our staff, as a postdoctoral Research Associate, to once again bring specialized chemical knowledge to our direct thickeners project. Dr. Pratap Gullapalli came to us from the Hyderabad Research Institute where he was engaged in research on polymeric paraffin inhibitors designed to assist in the handling of waxy crudes.

The third subarea also is concerned with the development of a mobility control additive for CO_2 and similar floods. Although this additive, CO_2-foam, takes its name from the well-known dispersion of soap bubbles at atmospheric pressure, the analogy is deceiving if carried very far. Mobility control foam exists at high pressure and with compressed CO_2 or a light hydrocarbon, rather than air, as the high-volume-fraction component. This non-aqueous phase itself thus has liquid-like density. Secondly, this foam exists and flows within the pores of the rock, so that its rheology differs profoundly from that of free foam in pipes or containers that are large compared to the bubble size. In fact, the mobility of foam in reservoir rock is unique, and we believe that its patterns of variation provide opportunities that can be used to advantage in EOR. In this subarea of the project, we perform high-pressure, steady-state measurements of the pressure drop across core samples of reservoir or quarried rock. These experiments are performed with different rock samples, at different gas volume fractions, with different surfactants, with different surfactant concentrations, and at different rates.

In our results this year, we have added greatly to the total available information, and can now report with greater certainty on the effects of these variables. Especially significant is the effect of the rock's intrinsic permeability, which now appears to be quite similar in sandstone and in carbonates. The effect is such that foam is a more effective thickening agent in higher permeability rock. This property offers the hope that, in addition to its ordinary mobility-control uses, foam will greatly assist in smoothing displacement fronts that are otherwise badly contorted by non-uniform permeability of the reservoir. To benefit from that potential, more information is needed on the parameter limits within which the effect occurs and on how these limits can be reliably determined for a particular reservoir. One of these parameters is the extent of adsorption of surfactant onto the rock. Our program includes laboratory measurements of this parameter. These experiments also are described in this report. They are designed not only to provide assurance of the economic viability of a surfactant, but also to give the reservoir engineer the data needed to compute optimum concentrations and slug size of a surfactant "pad" pre-flush.

To conclude this summary, Task II of the project includes three active subareas in which we perform research both to evaluate and to alleviate the recovery inefficiencies caused by non-uniform displacements in CO_2 and other dense-gas floods.

I. DISPLACEMENTS WITH PURE AND IMPURE CO_2

A. PHASE BEHAVIOR AND FLUID PROPERTY STUDIES

Considerable time has been spent on modifications to the phase behavior equipment during the past year. A second circulation pump has been added to the system. The viscometer pressure vessels have been improved and are now easier to clean and safer for the quartz crystals. The back pressure regulators have been replaced with better, easier to use, bi-valve regulators. Also, such modifications as gas composition averaging using error analysis have been made to the gas sampling system (CPE software). Methods of dealing with asphaltene precipitation, knowing what causes it, and how and when to clean it, have been improved. Running pressure and temperature limits have been increased and have been tested by running an experiment at 5000 psi and 250°F (CPE 229).

Companies have begun sending requested samples of oil for our data base and viscosity correlation project. As these oils are received they are being recombined and stored in floating pistons cells. (Enough recombined fluid will be mixed and stored to supply up to three continuous phase equilibrium (CPE) runs from each oil.)

1. Continuous Phase Equilibrium Runs 234, 235, and 236

CPE 235 (Fig. 1) was run with Wasson stock tank oil (STO) and CO_2 at 109°F and 1200 psia. CPE 235 was processed to the best of our ability given the small amount of liquid sample produced. CPE 234 used the same fluid as CPE 235 and was run at 109°F and 1500 psia. Since CPE 235 was run at a lower pressure than CPE 234, the phase split came slightly earlier, and the stripping process was greatly reduced. These effects occurred because the density of CO_2 is reduced at the lower pressure, making the upper phase less prone to extracting and dissolving heavier hydrocarbons. This is evident from the viscosity/density/time plots shown in Figs. 2, 3, and 4.

CPE 236 was run with Oil A (from northwest New Mexico) and CO_2 at 155°F and 2100 psia. This run was done primarily because we wanted to measure the amount of asphaltene dropout as it relates to increased measured viscosity caused by asphaltene coating of the crystal surface (Figs. 5 and 6).

2. CPE 237 - Gas Data Averaging Investigation

CPE 237 was a synthetic oil run (C_{10}, C_5, C_4, and C_3), which we performed in order to implement the new fluids lab. An additional purpose for this run was to characterize the trend of compositional change vs. time for the initial three sample periods. CPE processing is pending. Viscosity/density/time plots are included (Figs. 7 and 8).

Past investigations were conducted to determine at exactly what time during a sample period the composition of evolved gas represented the average values over the whole sample period. This information is important in obtaining accurate composition analyses for correlating fluid properties. A scheme was devised whereby consecutive gas chromatograph (GC) analyses and gas volume data were plotted against time to graphically determine the total amount of a particular gas evolved over a sample period. From this information, the volume percent of a specific gas could be determined with respect to the total gas volume and then referenced back to the gas composition/time plot to find

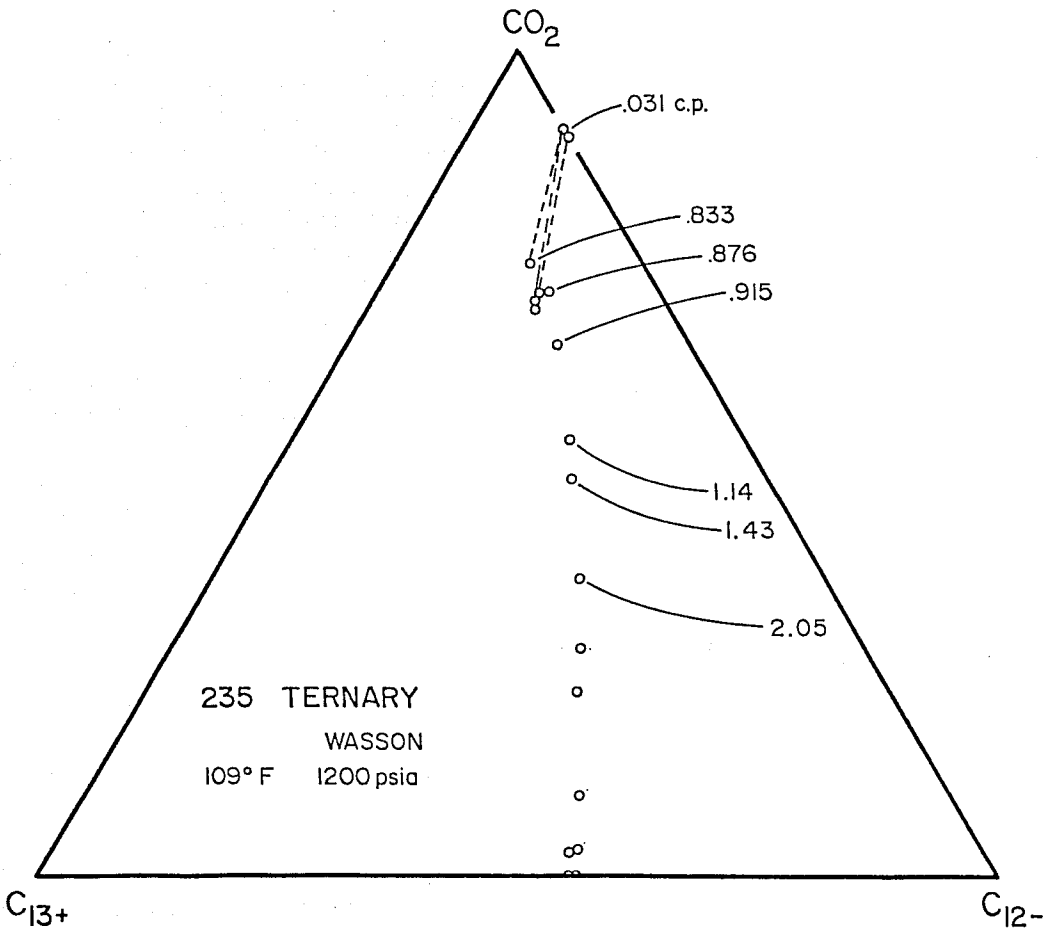

Figure 1. Viscosity/pseudoternary diagram for Wasson stock tank oil at 109°F and 1200 psia.

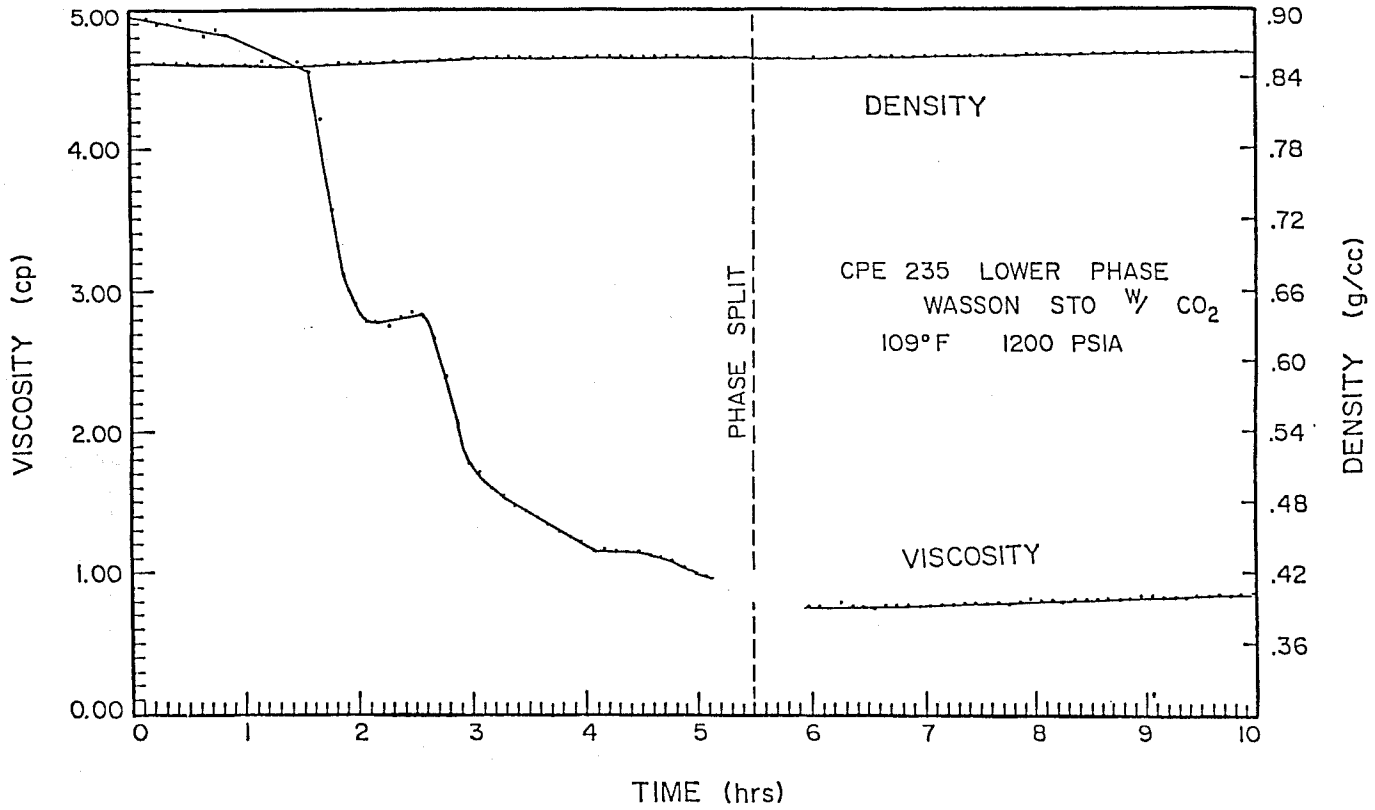

Figure 2. Viscosity/density/time plot for Wasson stock tank oil at 109°F and 1200 psia, lower sample.

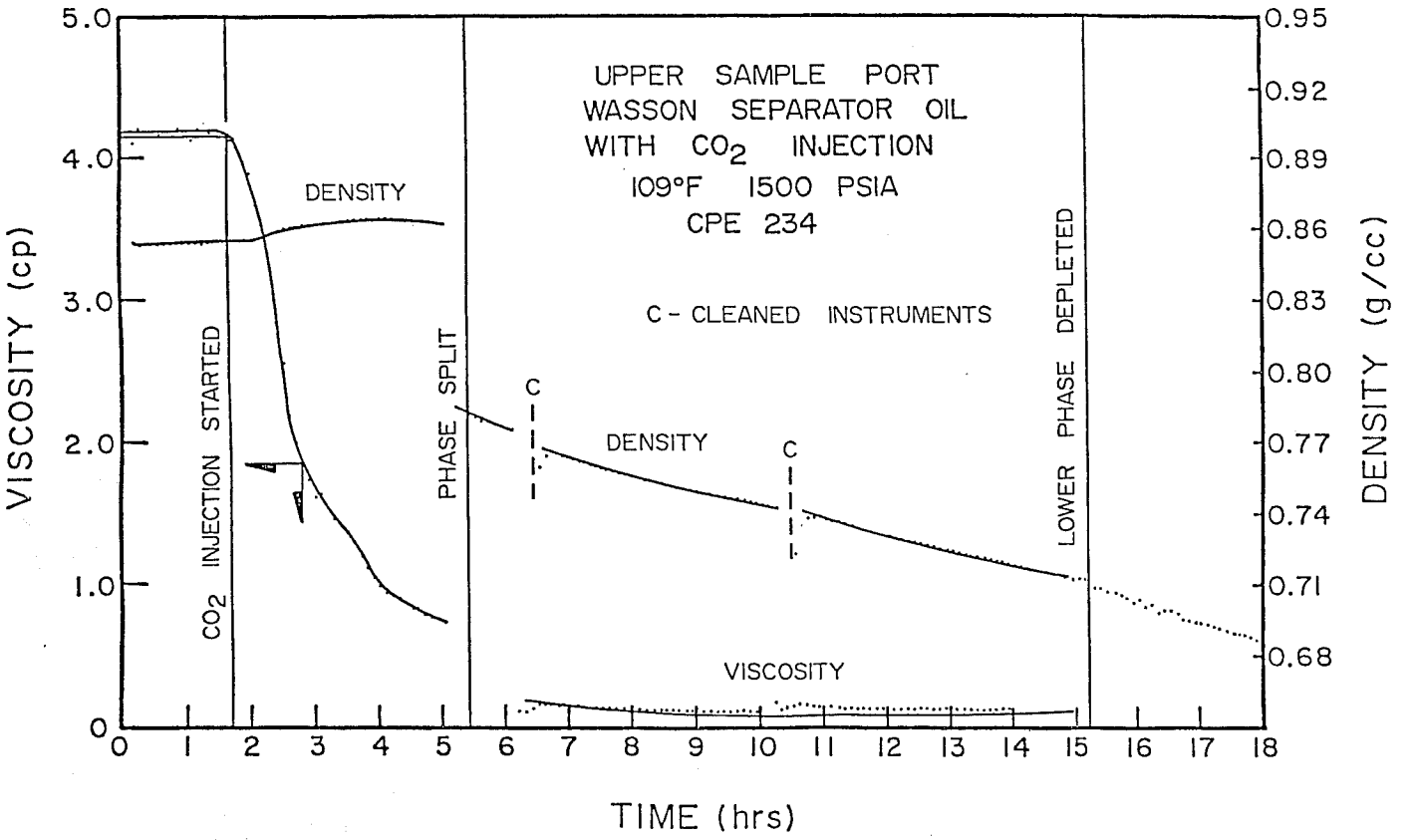

Figure 3. Viscosity/density/time plot for Wasson stock tank oil at 109°F and 1500 psia, upper sample.

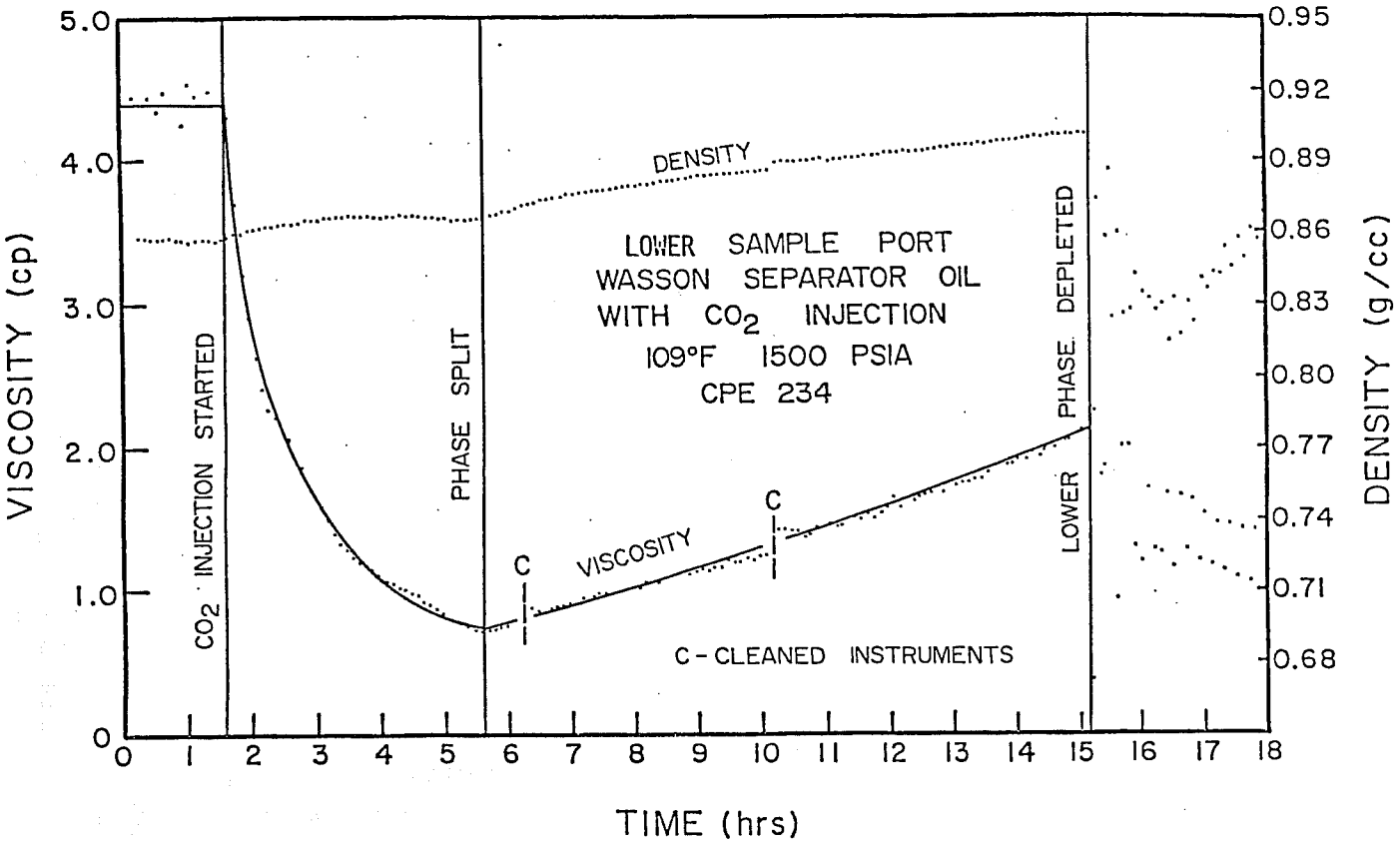

Figure 4. Viscosity/density/time plot for Wasson stock tank at 109°F and 1500 psia, lower sample.

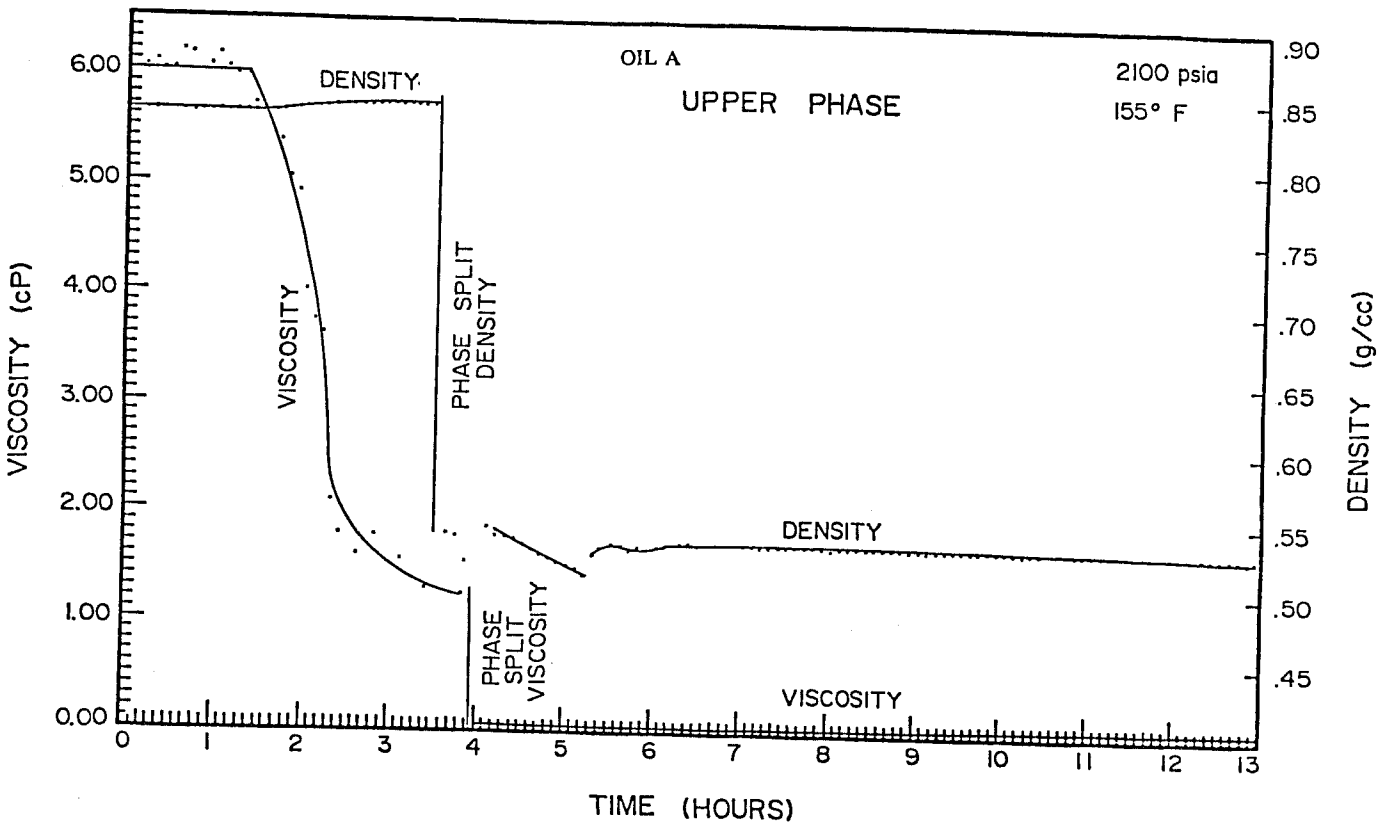

Figure 5. Viscosity/density/time plot for Oil A at 155°F and 2100 psia, upper sample.

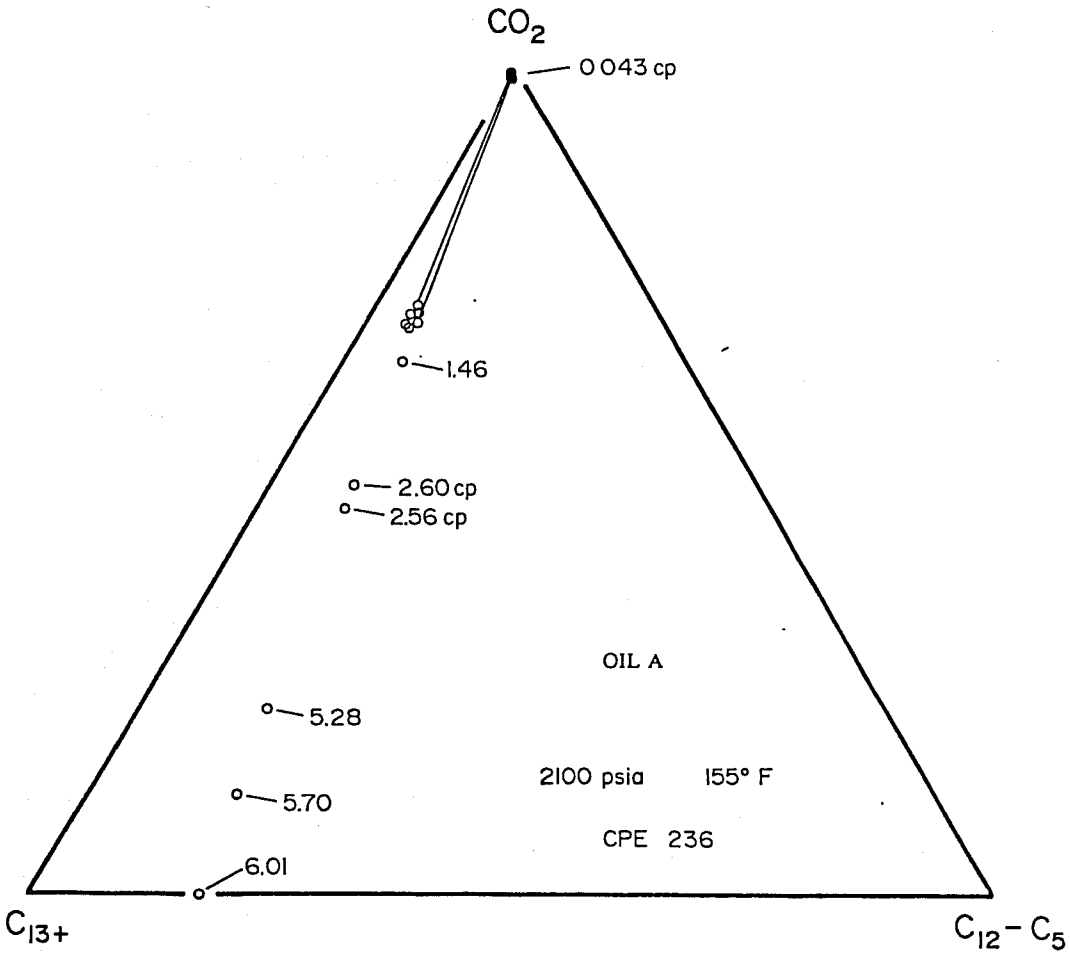

Figure 6. Viscosity/pseudoternary diagram for Oil A at 155°F and 2100 psia.

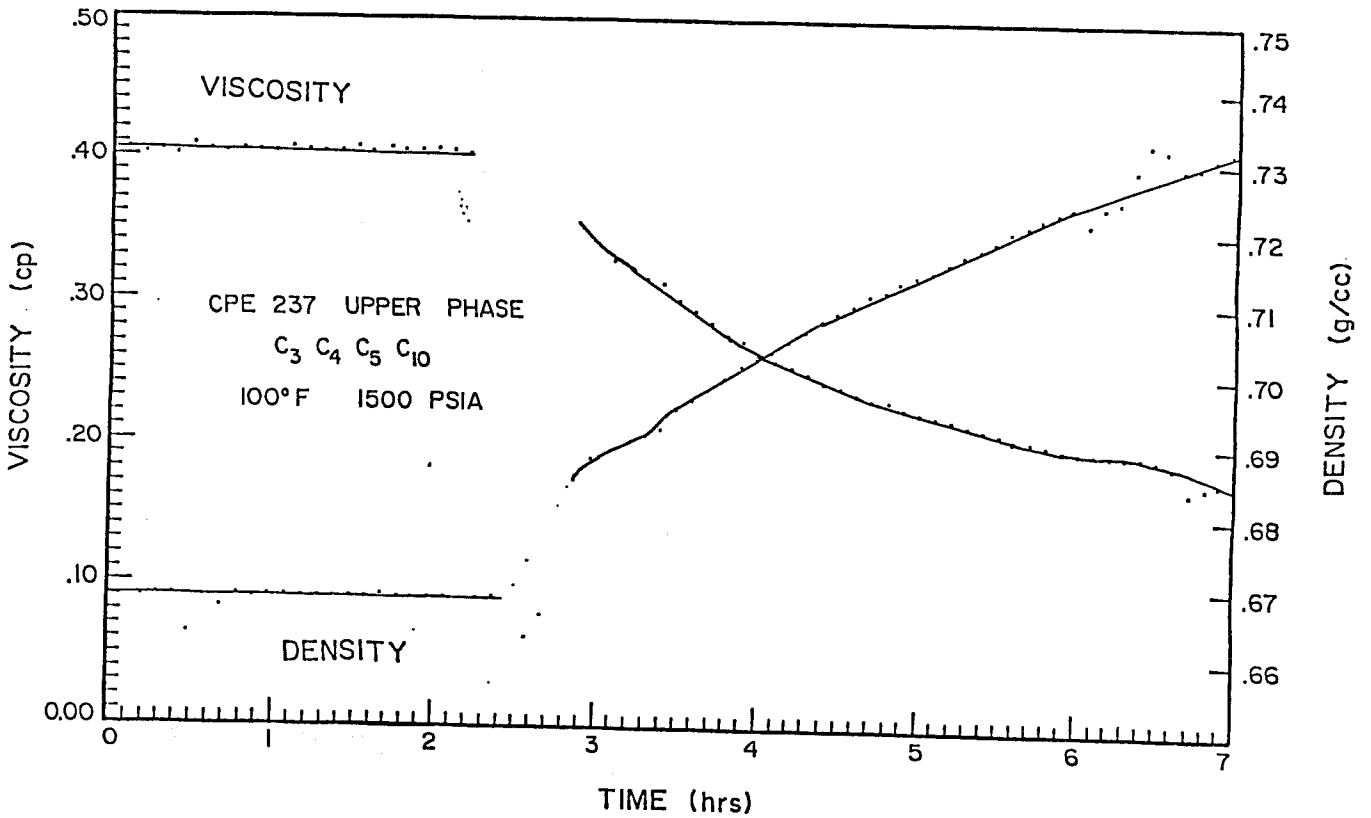

Figure 7. Viscosity/density/time plot for synthetic oil (C_3, C_4, C_5, C_{10}) at 100°F and 1500 psia, upper sample.

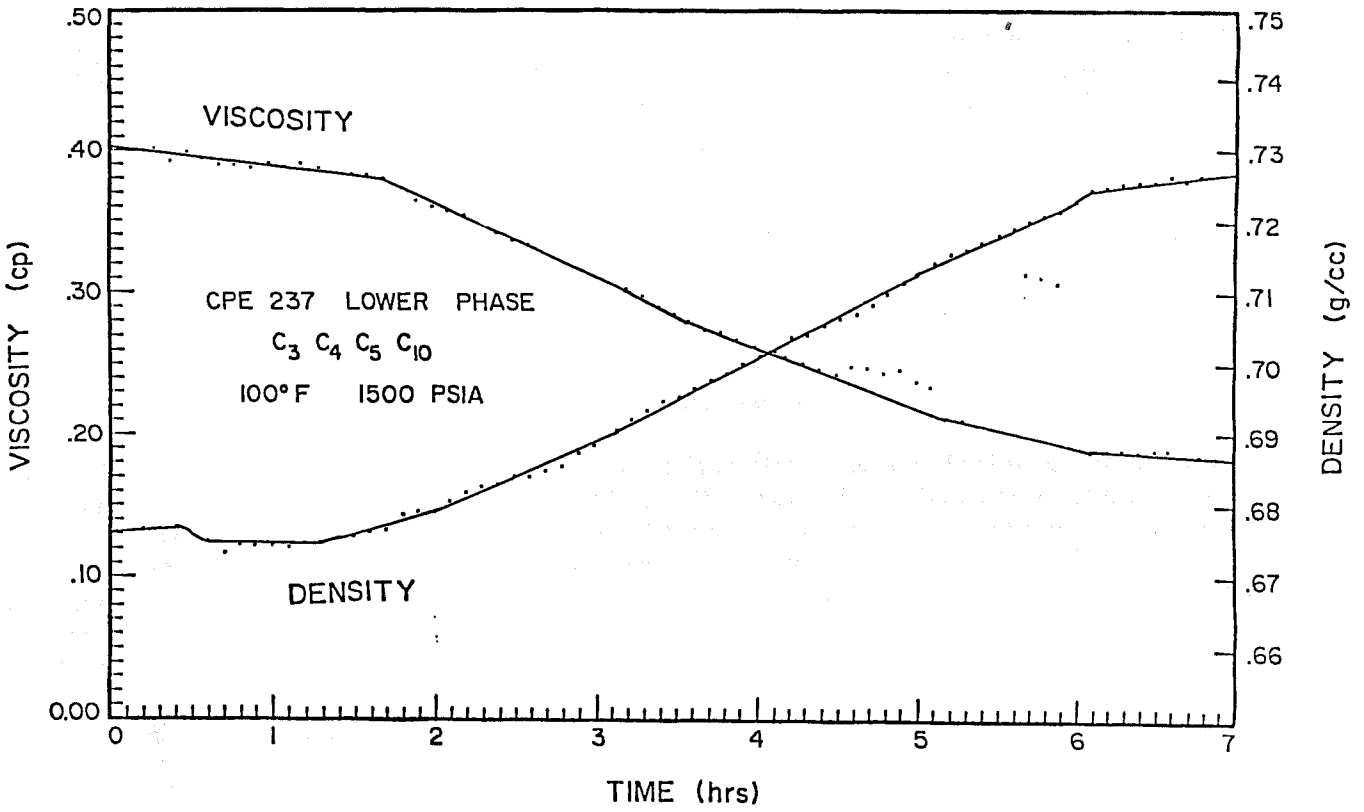

Figure 8. Viscosity/density/time plot for synthetic oil (C_3, C_4, C_5, C_{10}) at 100°F and 1500 psia, lower sample.

the time at which the produced gas composition was equal to the computed average composition. This representative time is used in the CPE process control program to decide when, within a sample period, the GC should sample the flowing gas stream to produce an analysis most characteristic of the sample period. Because the previous investigation and the vast majority of CPE experiments have been performed on dead oils, it was decided to redo the gas timing experiment to see if previous conclusions held true when light hydrocarbons were present.

A synthetic oil consisting of C_{10}, C_5, C_4 and C_3 was used in CPE 237 with pure CO_2 as the injection gas. The first two sample periods (one hour each) were conducted with the GC operating as rapidly as possible (every 13 minutes) to add resolution to the gas composition profile. CO_2 concentration plots for sample periods 1 and 2 are shown in Figs. 9 and 11 respectively. Gas volume profiles are shown below the concentration profiles in Figs. 10 and 12.

The appropriate sample time, read from Figs. 9 and 11 using the computed average CO_2 volume percent, is 43 minutes into the sample period for the first hour and 37 minutes for the second hour. It should be noted that the change in CO_2 concentration with respect to time becomes more constant after the first sample period; however, the appropriate sample time should always be greater than the midpoint of the sample period (30 min.) because total gas production increases with respect to time, thus giving more weight to the latter gas analyses.

From these results, it is clear that the appropriate GC sample time is not constant but starts late in the first sample period and trends toward the middle of a sample period as an experiment progresses. It is likely that the range is between 43 and 35 minutes; however, the possibility of sampling time causing a significant error is far greater during the first two sample periods when gas composition is changing rapidly. As an experiment progresses toward mid-stage, gas composition may only change by a few percent per sample period. For this reason, it is recommended that the 40-minute sample position be used until there is time to modify the scheduling program so that the sample-time position can be made variable. Until such time, the uncertainty caused by sample-time position should not be greater than ± 1.5 mole %.

3. Building of Fluids Lab

It was decided that the data base would be generated using live oils so that the proposed viscosity correlation would not be dependent on other correlations to correct for depleted C_5-C_1 in dead oils. Our recombining equipment left much to be desired. Two or more days were typically required to restore a dead oil to the original reservoir composition.

The first problem was deciding what equipment to order and how to set it up. Since price was our most important factor, we first thought of building pure component reservoirs with floating pistons. However, we found that Welker Engineering made acceptable floating piston cells (with gauges and piston position indicator) and sold them for less than they would cost us to build them. We spent quite a bit of time building the air bath to contain the piston cells, mounting valves, and installing fittings and tubing. Next we installed temperature control devices, pressure transducers, and readouts.

Extensive time was spent calibrating and pressure testing the new equipment and fittings. However, the real test of the equipment was actually combining a fluid. For this first test, we chose a C_3, C_4, C_5, and C_{10} mixture. This fluid also was used in CPE 237. The biggest problem encountered during the test was the blowing of rupture discs on the Welker cylinders (these cylinders are set at 2200 psi and rupture anywhere between 2000-2100 psia). Because of this, and for

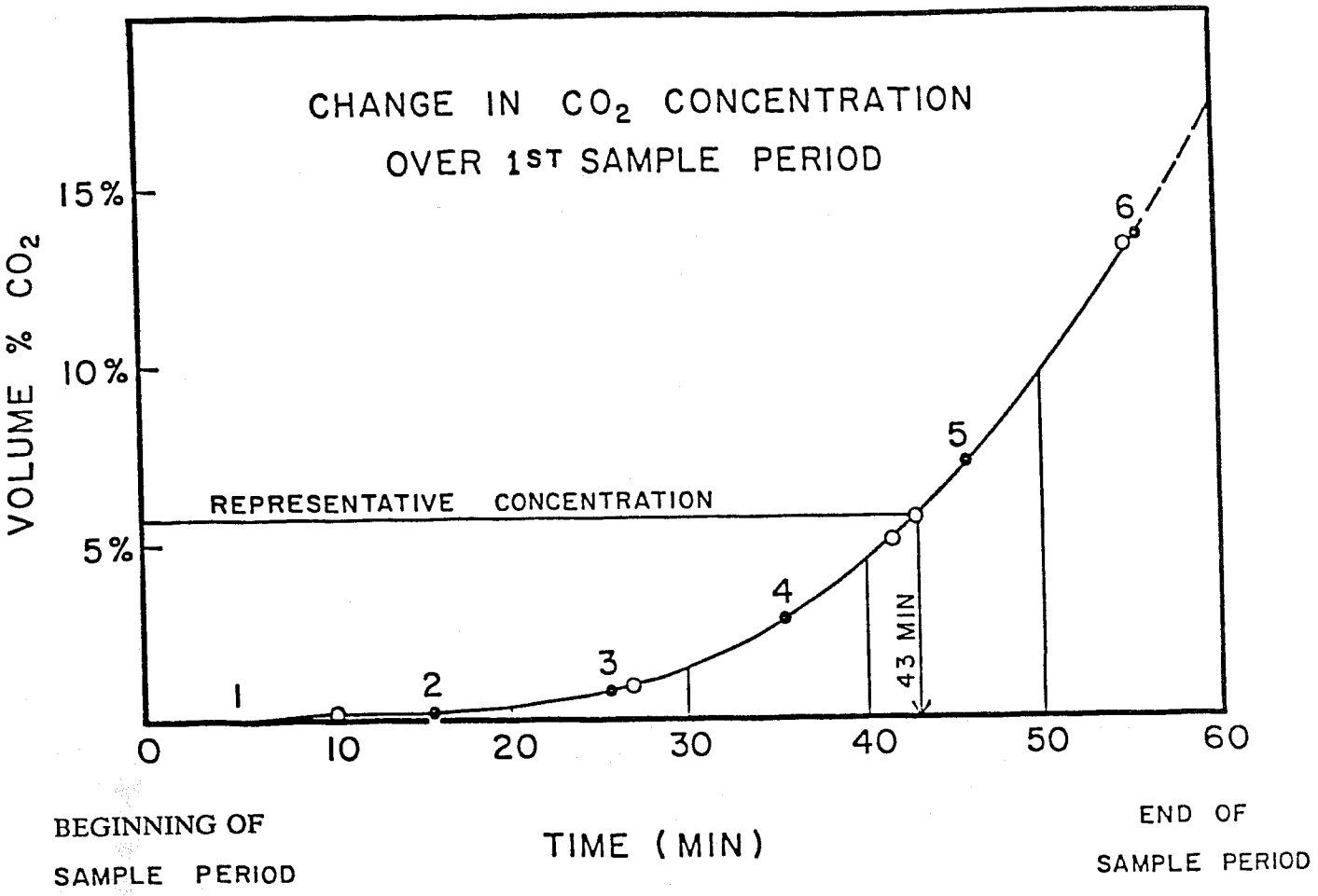

Figure 9. Change in CO_2 concentration over first sample period.

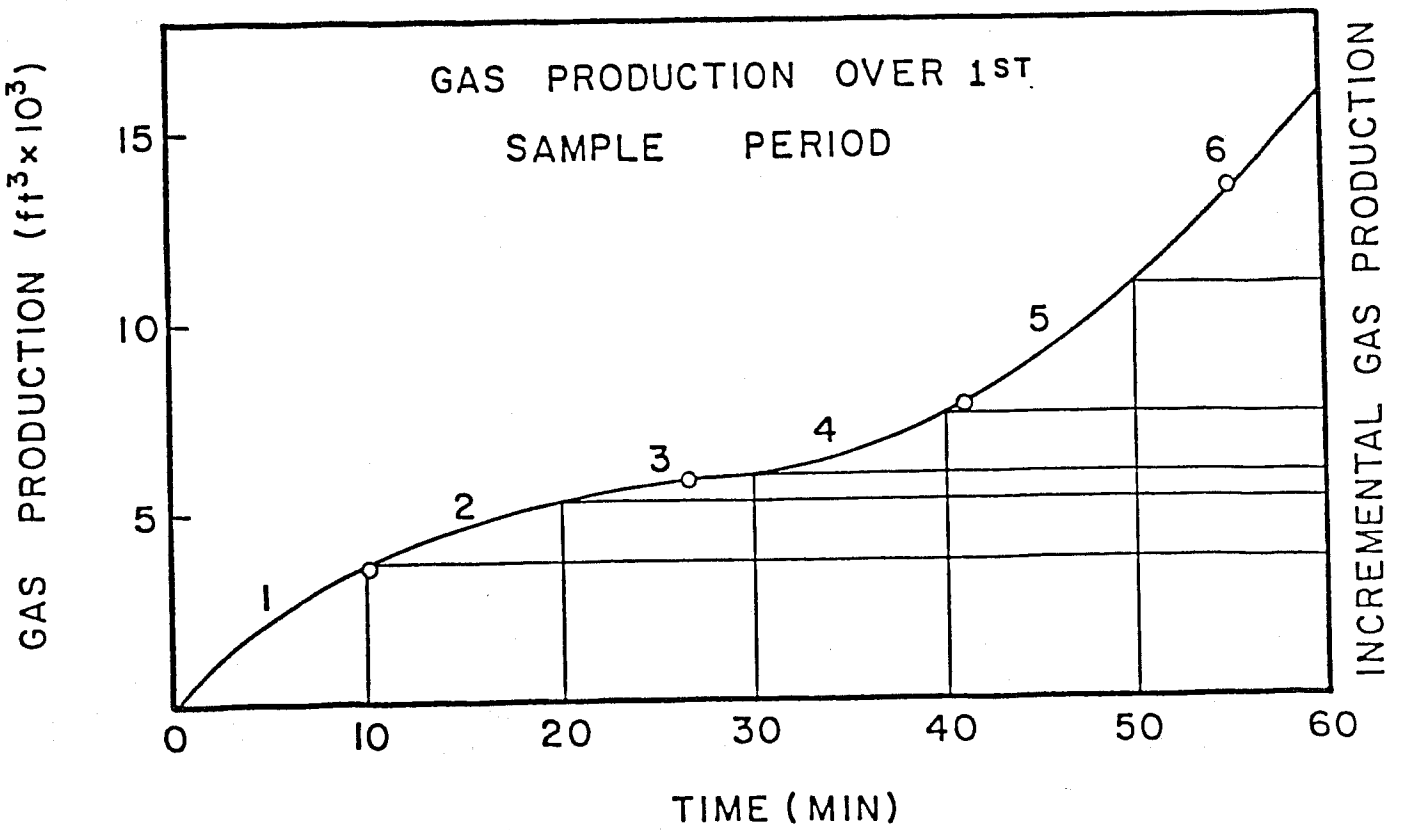

Figure 10. Gas production over first sample period.

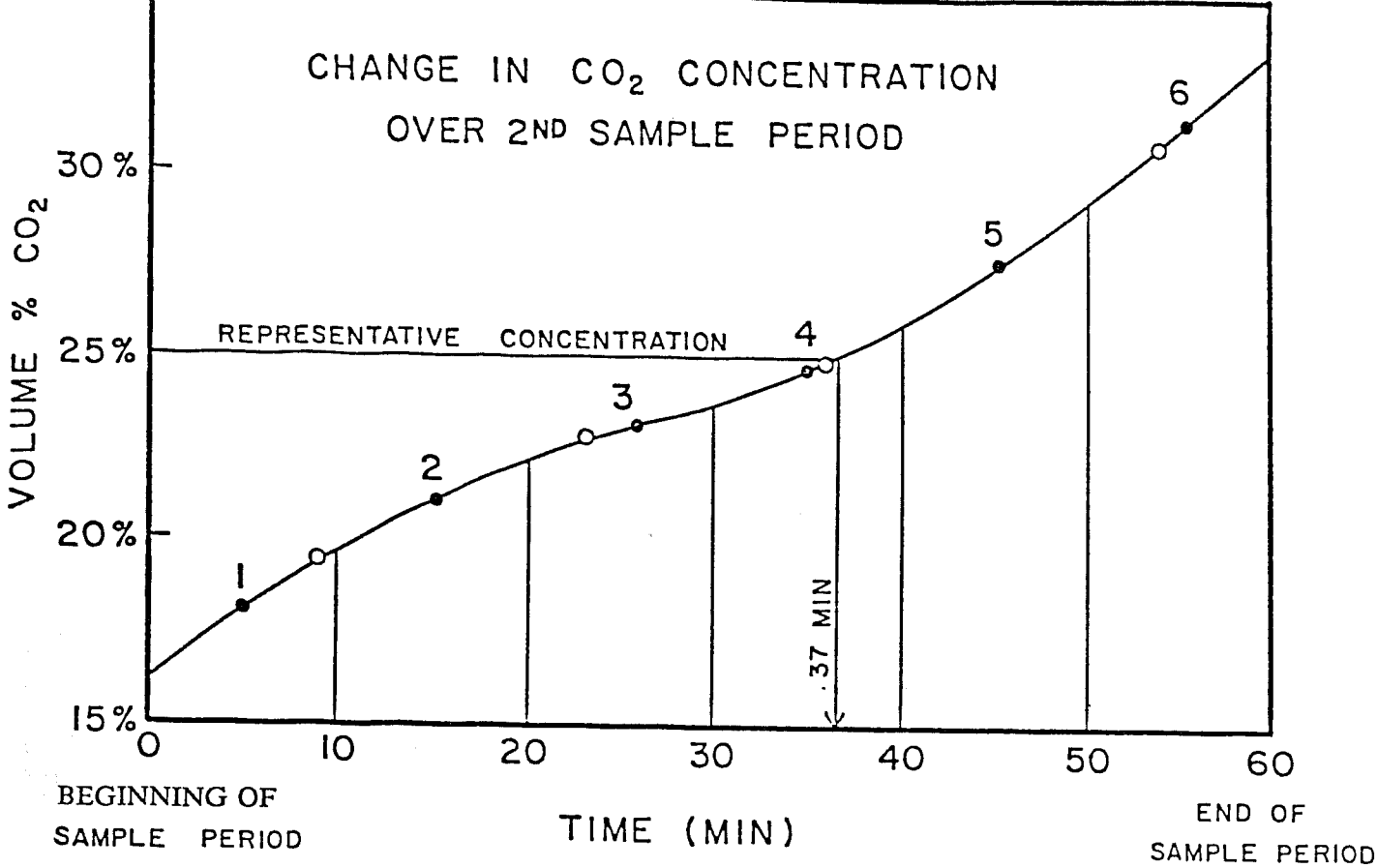

Figure 11. Change in CO_2 concentration over second sample period.

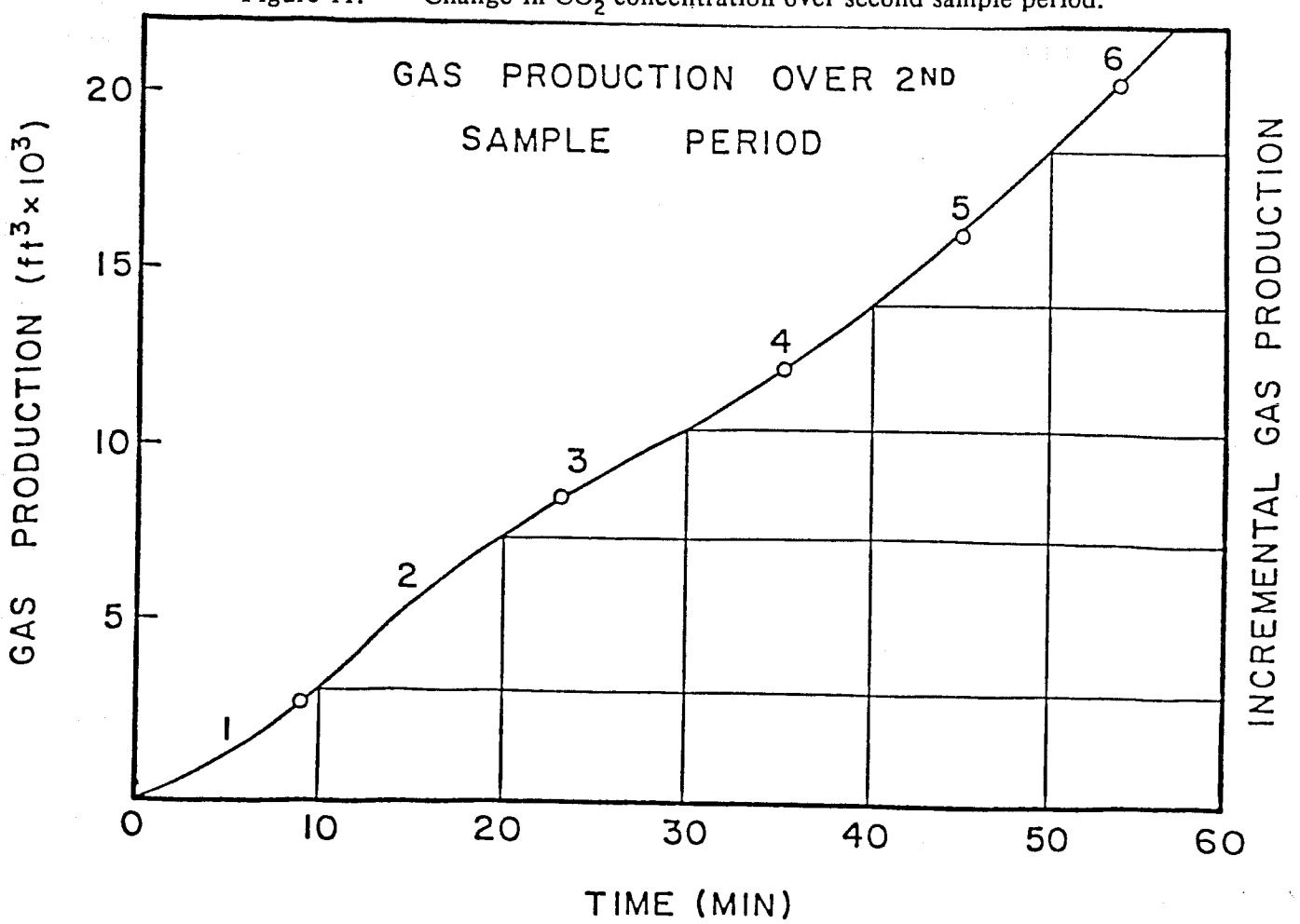

Figure 12. Gas production over second sample period.

simplicity, we decided to always transfer fluids at 100°F and 1500 psia. This was decided partially because of the rupture disc problem, but primarily because, at fixed temperature and pressure, it is a simple matter to obtain and keep on hand accurate density information.

We found that extreme care had to be taken when transferring liquid fractions; this is definitely a two-person operation. While one person is pumping water into one side of the floating piston accumulator, the other must carefully release the fluid from the other side into an external accumulator. Caution must be taken to maintain a pressure of 1500 ±100 psia in the Welker cylinder while transferring the fluid. If the pressure gets too high, the rupture disc will blow. If the pressure gets too low, the certainty of ending at 1500 psia is questionable, risking incorrect mixing.

4. Modifying the PVT System

Decisions had to be made concerning how to install a densitometer along with the viscometer and what type of flow system to use. At this time a Mettler-Paar densitometer is being installed in the system. Now we can compare viscosity, density, and composition data on the PVT system to data on the CPE system.

An extensive search to find viscosity-composition data suitable for testing the modified CPE software was unsuccessful. We decided to use a system designed especially for our purposes and to confirm the results by spot checking CPE data with the capillary tube viscometer in the PVT cell. A special requirement was that the test mixture had to produce a liquid and evolve at least two gases when reduced to atmospheric pressure.

Our first attempt to use this system was made with a synthetic oil composed of normal pentane and hexadecane; the C_{16} was to provide the liquid portion and the two gases were to be C_5 and CO_2. Unfortunately, after the C_{16}-C_5 mixture became saturated with CO_2, the upper sample port instruments began reading erratically. Since both the densitometer and viscometer were showing the erratic behavior, it was concluded that there was some kind of liquid entrainment at the upper sample port causing the problem. The erratic measurement behavior made the CO_2-C_5-C_{16} system unsuitable for validating the new software, and rather than experimenting with the C_5-C_{16} ratio, it was decided to scrap that approach and try another.

The binary systems with CO_2 and hydrocarbons from C_5 to C_8 were used to produce the one liquid-two gas requirement. The results of these CPE runs are shown in Fig. 13 and Tables 1 and 2. All experiments were done at 100°F and 1500 psia except for the CO_2-C_6 experiment (not shown here), which was run at 220°F and 1500 psia. The higher temperature was chosen because a reference viscosity for C_6 could not be found at lower temperatures. The unexpected result was that the C_6 system at about 70% CO_2 formed two phases at 220°F. The data from these binary experiments should prove to be useful to the viscosity correlation effort. For the purpose of software validation, however, only the CO_2-C_5 and CO_2-C_6 experiments can be used.

5. Composition, Viscosity, and Density Correlation with Asphaltene Precipitation

Comparisons of different oils are extremely useful for the viscosity, density, and composition data base. Experiments with various crude oils show that studying asphaltene precipitation is another way of understanding oil properties.

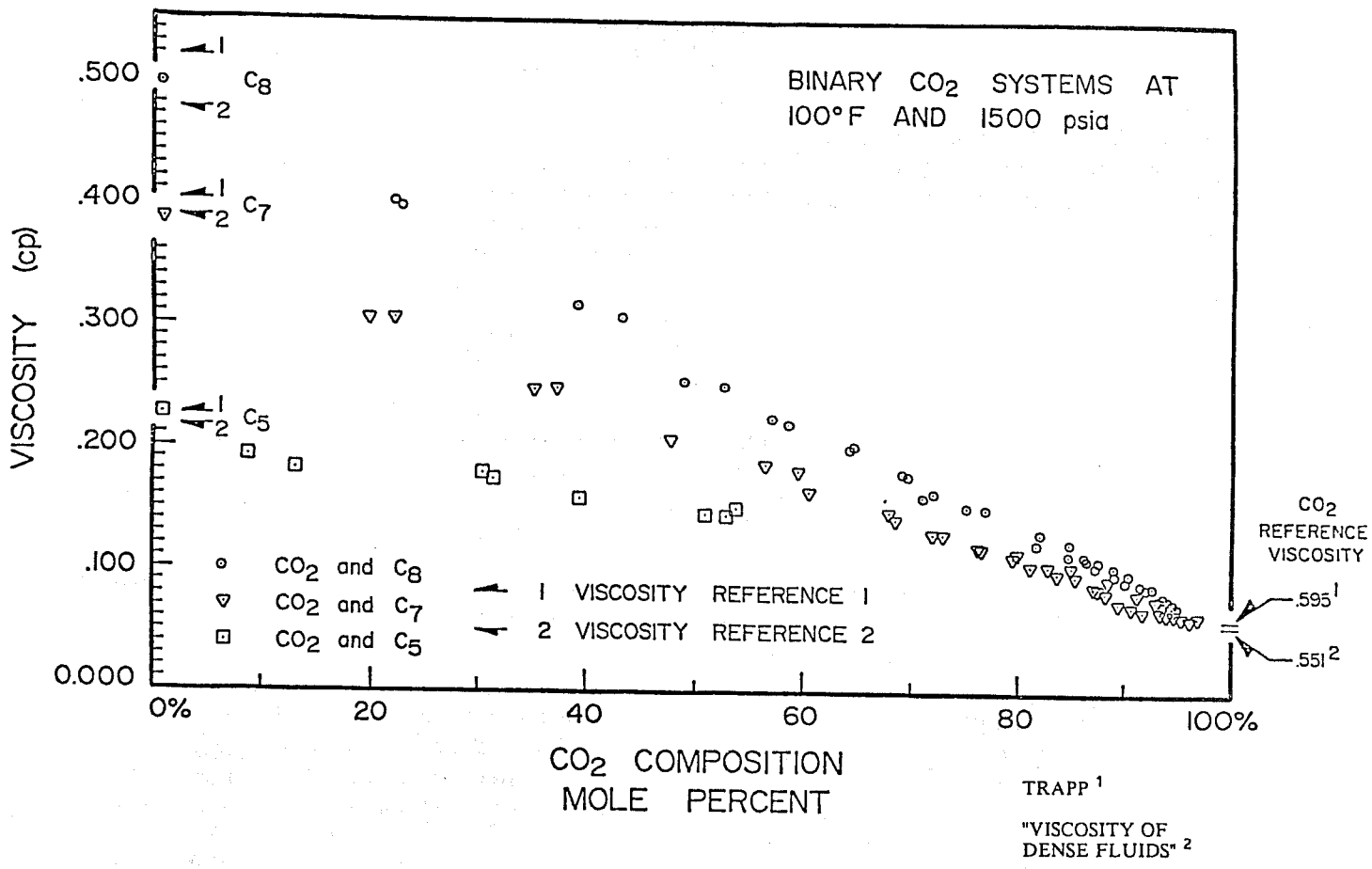

Figure 13. Viscosities of binary systems with CO_2 and hydrocarbons from C_5 to C_8.

TABLE 1

CPE 232
Binary System
CO_2 and C_7

100°F 1500 psia

Sample	CO_2 mole%	Density (g/cc)	Viscosity (cp)
1 U	0.00	.683	.391
1 L	0.00	.684	.383
2 U	0.00	.684	.381
2 L	0.00	.684	.379
3 U	21.95	.700	.305
3 L	19.72	.697	.305
4 U	36.89	.715	.249
4 L	34.83	.712	.247
5 U	54.27	.727	.209
5 L	47.53	.724	.207
6 U	56.15	.735	.187
6 L	59.31	.736	.181
7 U	67.15	.744	.160
7 L	60.30	.743	.164
8 U	68.16	.749	.141
8 L	67.57	.751	.148
9 U	72.69	.755	.130
9 L	71.78	.756	.129
10 U	76.52	.759	.119
10 L	76.16	.759	.119
11 U	79.38	.761	.111
11 L	79.60	.760	.112
12 U	82.71	.762	.104
12 L	80.98	.761	.105
13 U	83.51	.762	.098
13 L	84.78	.762	.103
14 U	88.45	.762	.093
14 L	85.27	.762	.096

TABLE 1
(continued)

15 U	86.97	.761	.088
15 L	87.45	.760	.088
16 U	83.79	.759	.079
16 L	87.99	.759	.084
17 U	89.29	.757	.076
17 L	91.08	.756	.083
18 U	90.43	.753	.073
18 L	92.75	.751	.077
19 U	91.48	.747	.070
19 L	93.76	.745	.069
20 U	93.21	.741	.069
20 L	93.84	.739	.070
21 U	94.50	.735	.068
21 L	93.78	.733	.070
22 U	95.50	.730	.066
22 L	93.44	.729	.072
23 U	96.71	.724	.065
23 L	96.01	.723	.065

TABLE 2

CPE 233
Binary System
CO_2 and C_8

100°F 1500 psia

Sample	CO_2 mole%	Density (g/cc)	Viscosity (cp)
1 U	0.00	.702	.501
1 L	0.00	.702	.500
2 U	0.00	.702	.504
2 L	0.00	.702	.501
3 U	0.00	.702	.503
3 L	0.00	.702	.499
4 U	22.82	.718	.397
4 L	22.13	.717	.401
5 U	43.12	.728	.307
5 L	38.97	.730	.317
6 U	52.57	.743	.250
6 L	48.78	.741	.254
7 U	58.52	.751	.221
7 L	57.01	.750	.224
8 U	64.42	.757	.202
8 L	64.27	.756	.201
9 U	69.43	.763	.179
9 L	69.26	.762	.179
10 U	71.12	.766	.161
10 L	71.98	.766	.164
11 U	76.89	.770	.151
11 L	75.06	.770	.152
12 U	81.72	.774	.122
12 L	82.05	.774	.131
13 U	84.91	.774	.113
13 L	84.90	.774	.123
14 U	87.66	.774	.109
14 L	86.34	.774	.113

TABLE 2
(Continued)

15 U	87.35	.773	.105
15 L	86.45	.774	.110
16 U	89.14	.772	.098
16 L	89.11	.773	.103
17 U	90.04	.769	.092
17 L	90.41	.770	.098
18 U	92.16	.765	.087
18 L	91.59	.767	.090
19 U	93.30	.760	.081
19 L	92.87	.762	.088
20 U	94.17	.755	.078
20 L	94.02	.756	.081
21 U	93.90	.749	.075
21 L	94.84	.749	.075
22 U	94.60	.743	.072
22 L	95.02	.744	.072

Table 3 and Fig. 14 compare the compositional analyses of Oil A (from northern New Mexico) and Maljamar oil. Note the much higher C_5+ molecular weight for Oil A (311 vs. 207 g/mole). Figure 15 shows the approximate bubble point curve where the critical point is probably somewhere above 3000 psia. Also shown are the conditions for the two CPE experiments run at 1500 psia and 2100 psia.

Figures 16 and 17 are the viscosity/pseudoternary diagrams at 2100 psia and 1500 psia, respectively. The phase envelope at 1500 psia is slightly larger than at 2100 psia, as expected. The CPE dilution path from crude oil to near 100% CO_2 is indicated on these figures. The lower and upper phase viscosity/density/time plots (Figs. 18 and 19 indicate phase separation at approximately 6 hours into the experiment ($\approx$ 73 mole% CO_2). At these conditions (2100 psia, 145°F), a substantial amount of asphaltene precipitate was observed. There is insufficient data, at this point, to determine whether these asphaltenes would cause injectivity problems. Some engineers believe that this precipitate could actually help improve sweep efficiency. This is an area we are currently investigating. Notice also in Fig. 18 the rapid drop in viscosity (from over 6 cp down to almost 1 cp) which began with CO_2 injection. The asphaltenes began to precipitate out at phase split ($\approx$ 73 mole% CO_2). Even at 1500 psia the oil viscosity rapidly dropped to near 1 cp, although no asphaltene precipitation was observed at these conditions (1500 psia, 145°F). After phase separation, the lower-phase viscosity increased very little because CO_2 stripped out the intermediate hydrocarbon components both at 2100 psia and 1500 psia. Figure 20 presents some of our first results in the phase behavior of impure CO_2 (nitrogen contaminants)-crude oil systems.

B. PHASE BEHAVIOR AND FLUID PROPERTY STUDIES: DEVELOPMENT OF AN IMPROVED VISCOSITY CORRELATION

1. Introduction

Accurate simulation and performance prediction of multiple-contact miscibility processes requires, among other information, the thermophysical properties of the injected solvent, the in-situ reservoir fluid, and their mixtures. In the absence of extensive experimental data within the range of temperature and pressure of interest, one has to rely on available correlations to estimate these properties. Viscosity is one of the important physical parameters needed to perform a consistent compositional material balance. The literature abounds with correlations for the prediction of viscosities of hydrocarbon mixtures in both the gaseous (low pressure) and dense fluid (high pressure) phases. For the prediction of CO_2-reservoir oil mixture viscosities, however, an accurate and consistent correlation covering a wide range of conditions is highly desired.

The objective of this work is to create a data base relating the composition of mixtures of CO_2 and reservoir oils to the viscosity and density of these mixtures. The data base then will be employed to develop a mathematical correlation of viscosity of both vapor and liquid CO_2-hydrocarbon mixtures as a function of pressure, temperature, and composition that can be incorporated easily in digital process simulations. An extensive study of existing viscosity correlations found in theliterature for both vapor and liquid mixtures has been performed for the purpose of developing a correlation that can accurately predict and/or interpolate viscosities of CO_2 and reservoir oil mixtures.

A correlation that has enjoyed popularity in the petroleum industry is the Lohrenz, Bray, and Clark (LBC)[3] correlation. It has been used extensively in reservoir simulators because of the relative

TABLE 3

COMPOSITIONS OF OIL A AND MALJAMAR OIL

January 22, 1988

C#	Oil A Mol Fr	Maljamar Mol Fr
5	0.0008	0.0440
6	0.0012	0.0713
7	0.0054	0.1241
8	0.0167	0.1164
9	0.0302	0.0633
10	0.0359	0.0550
11	0.0406	0.0481
12	0.0515	0.0441
13	0.0600	0.0363
14	0.0535	0.0429
15	0.0494	0.0315
16	0.0492	0.0291
17	0.0447	0.0278
18	0.0584	0.0200
19	0.0333	0.0225
20	0.0299	0.0164
21	0.0276	0.0151
22	0.0265	1.0148
23	0.0248	0.0130
24	0.0229	0.0086
25	0.0158	0.0117
26	0.0158	0.0116
27	0.0151	0.0074
28	0.0214	0.0074
29	0.0217	0.0109
30	0.0154	0.0068
31	0.0142	0.0067
32	0.0075	0.0058
33	0.0112	0.0056
34	0.0107	0.0053
35	0.0092	0.0052
36	0.0082	0.0051
37+	0.1713	0.0664
Average Mole Weights:	311.315	207.797

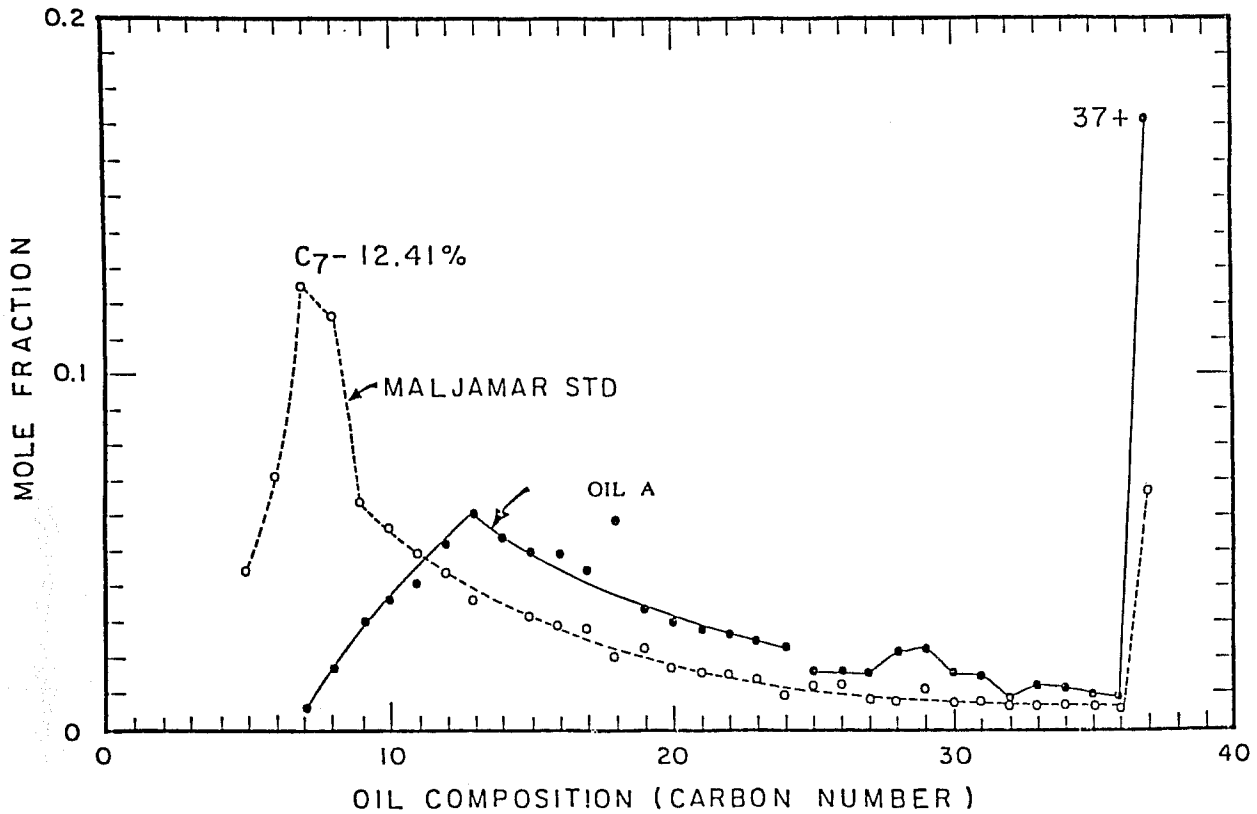

Figure 14. Comparison of Maljamar and Oil A compositional analyses.

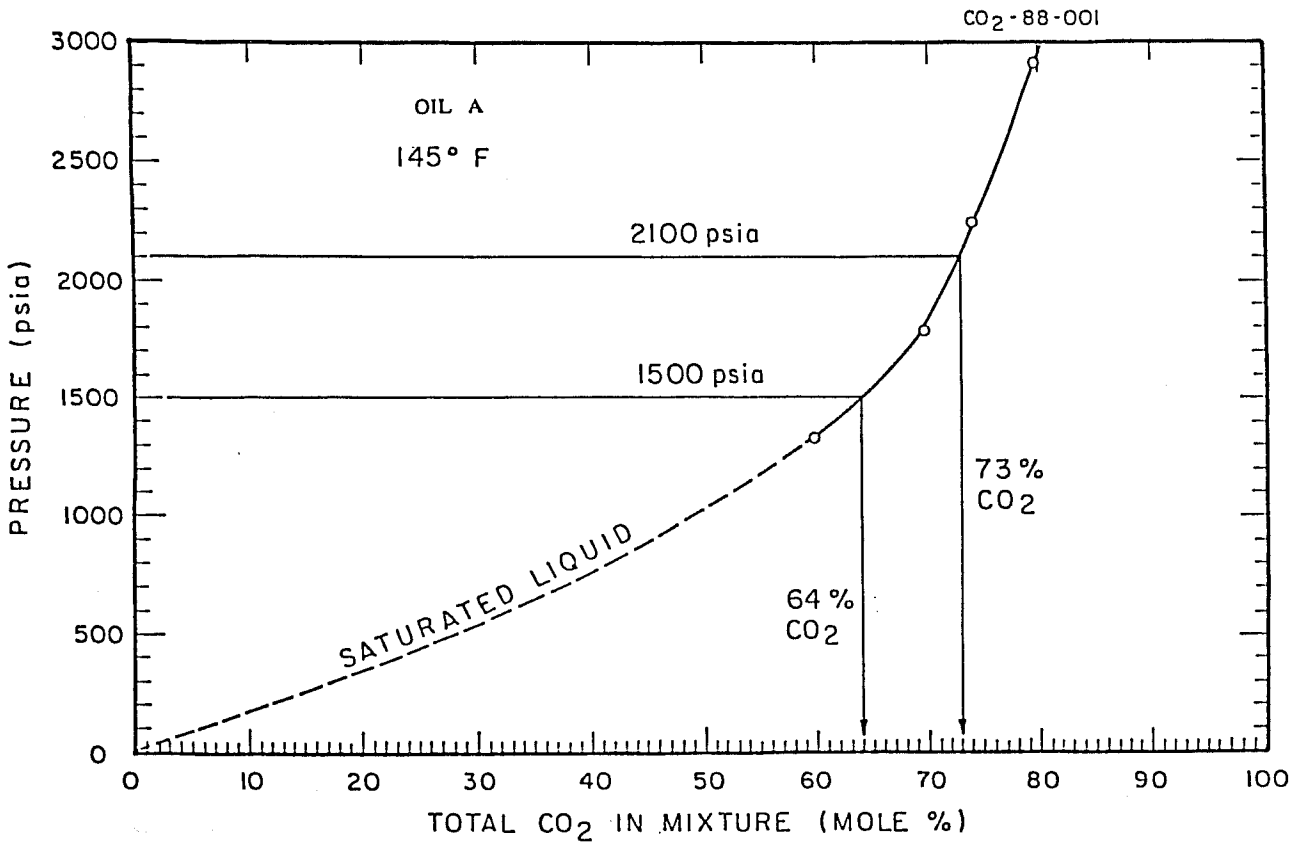

Figure 15. Pressure/composition diagram for Oil A/CO_2 system CPE experiment conditions indicated at 2100 psia and 1500 psia.

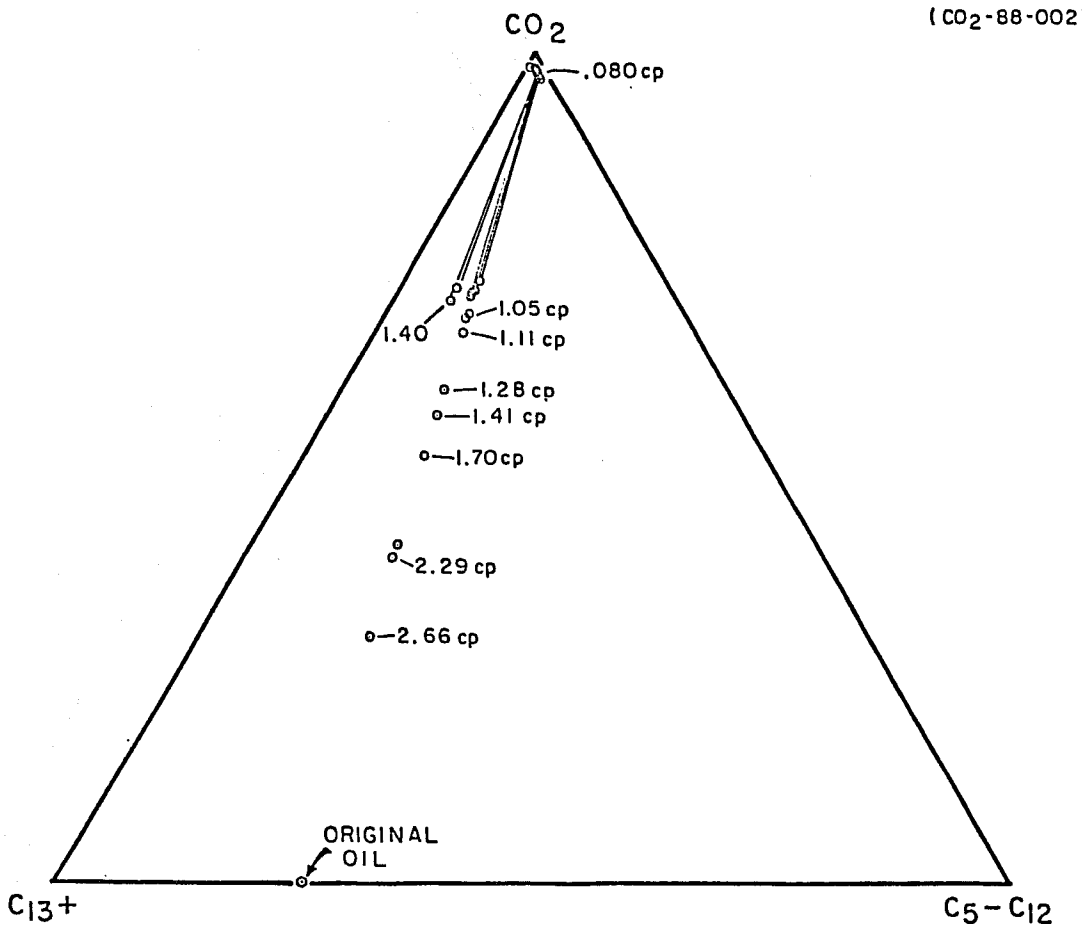

Figure 16. Viscosity/pseudoternary diagram for Oil A/CO_2 system
P = 2100 psia, T = 145°F.

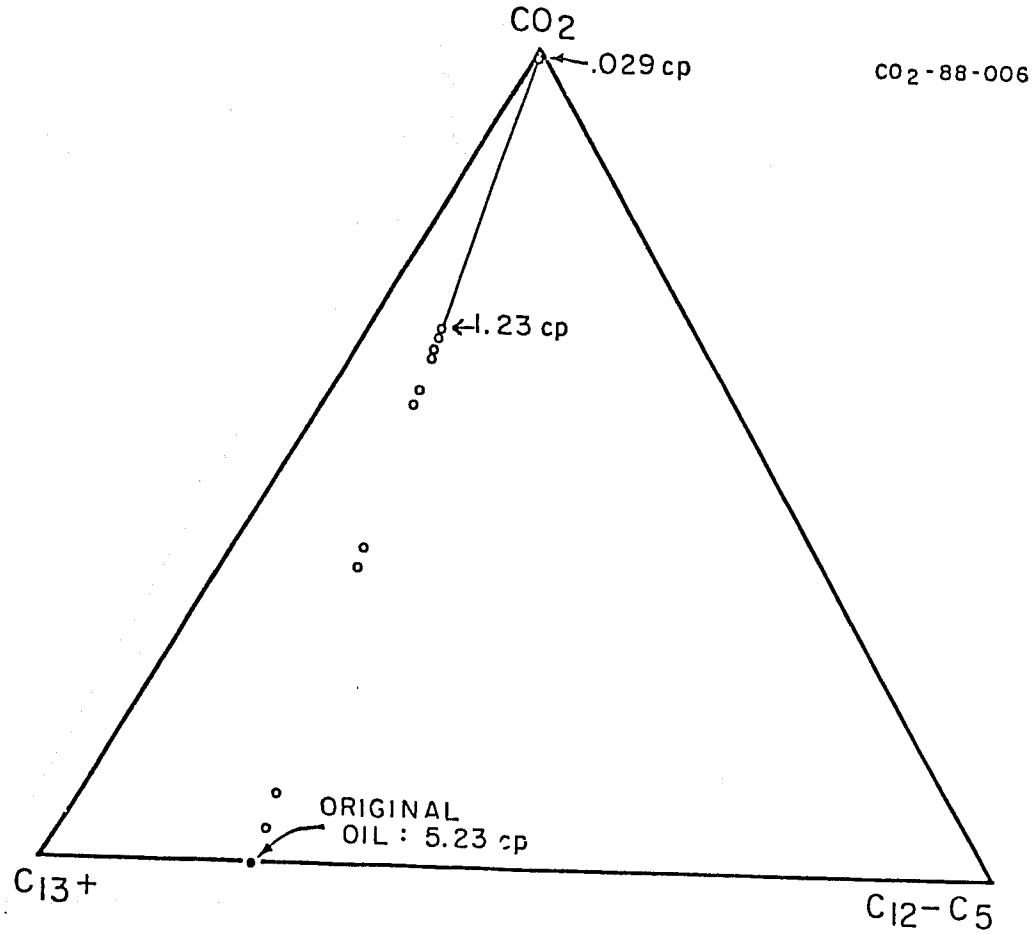

Figure 17. Viscosity/pseudoternary diagram for Oil A/CO_2 system P = 1500 psia, T = 145°F.

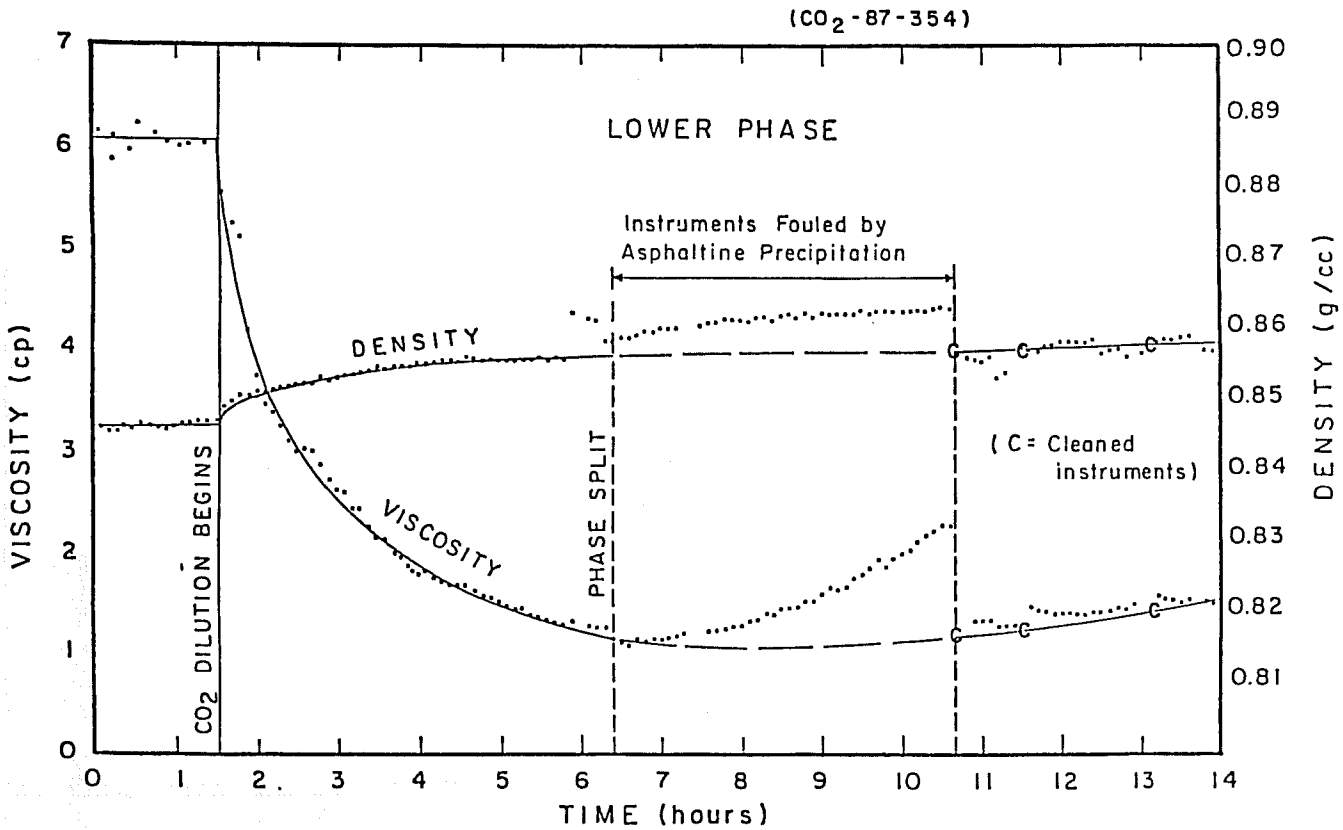

Figure 18. Viscosity/density/time plot from Oil A/CO_2 CPE experiment
P = 2100 psia, T = 145°F, lower phase.

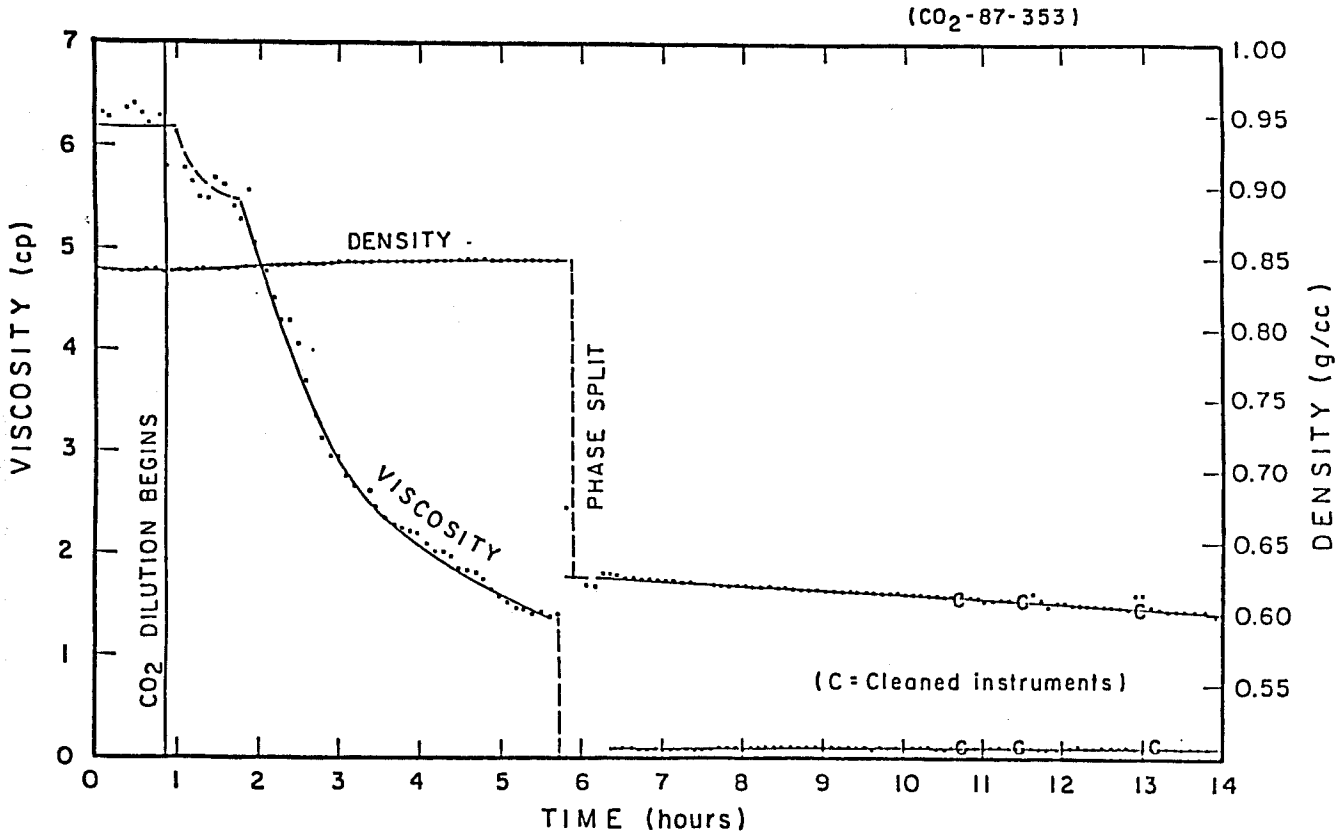

Figure 19. Viscosity/density/time plot from Oil A/CO_2 CPE experiment P = 2100 psia, T = 145°F, upper phase.

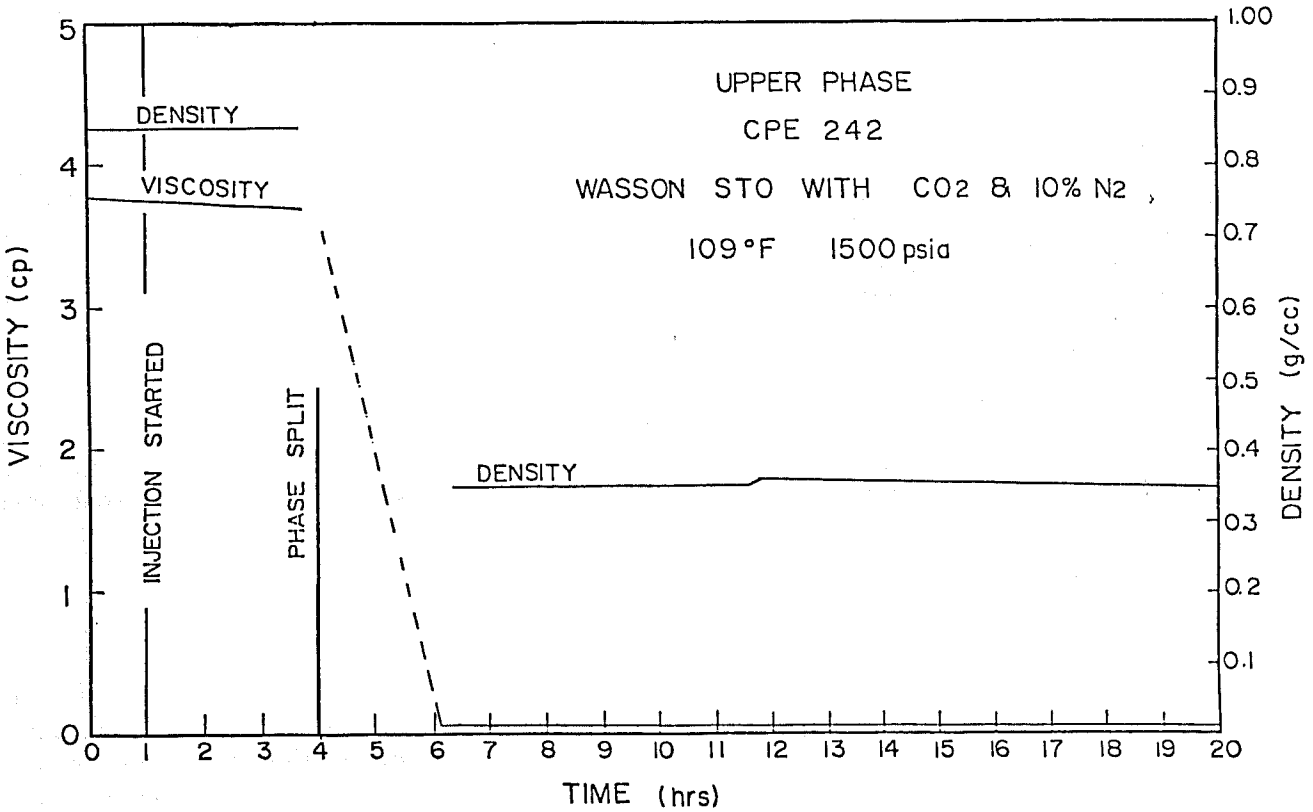

Figure 20. 90% CO_2 - 10% N_2/Wasson Oil Viscosity-Density-Time Plot at 109°F and 1500 psia.

ease to which it can be tuned to fit experimental data in comparison to other methods available. However, certain restrictions are required in the use of the LBC correlation. The compositional dependence of mixture viscosity is implicitly defined in the LBC method, i.e., the composition appears in the mixing rules for the correlating parameters. The reduced mixture density is, instead, employed as one of the state variables and thus requies accurate volumetric data. Pedersen et al.[4] reported that the accuracy of the viscosity predictions of the LBC correlation is heavily dependent on the density correlation used. This finding is corroborated by the results of Kovarik and Taylor.[5] Their calculations revealed that for heavy pure components, the critical molar volume correlation given by Lohrenz et al. resulted in a lower average absolute deviation (AAD) than the calculations where the real critical molar volume of the pure component was used. They also reported the inability of the LBC method to accurately predict the viscosity even for simple, well-defined, CO_2-synthetic oil mixtures.

Another shortcoming associated with the LBC correlation is the lack of smooth convergence as the critical point is approached. Saeedi and Rowe[6] reported inaccurate vapor viscosity prediction and the nonconvergence of viscosity at the critical point for a wide variety of reservoir fluid mixtures. Lawal[7] showed that the lack of continuous transition of viscosity from the liquid state to the gaseous state or vice versa results in the nonconvergence of equilibrium gas and liquid phase viscosities at the critical point.

As a first step in developing a new correlation, several existing methods will be tested for relative accuracy in predicting viscosities of well-defined CO_2-hydrocarbon and CO_2-crude oil mixtures. The viscosity data previously generated in our laboratory using the continuous phase equilibrium (CPE) apparatus on CO_2-synthetic oil and certain CO_2-crude oil mixtures as well as new experiments currently being performed will be used as the data base.

2. Theoretical Background

Essentially all gas and gas-mixture viscosity-estimation procedures are modifications of the theoretical expressions based on either the Chapman-Enskog (CE) kinetic theory or the law of corresponding states. The CE theory is rigorous, and the class of equations derived from it involve the collision integral, Ω_v, which accounts for the effects of intermolecular forces. The mathematical formalism of the CE theory is well known, but the complexities involved often preclude an alalytical solution. Moreover, the form of Ω_v will depend on the choice of the intermolecular potential function, $\psi(r)$, incorporated in the theory to characterize the interaction of molecules. Several investigators have introduced simplifications to the rigorous theoretical expressions resulting in methods that are essentially interpolative in nature.

In contrast to the CE theory, the corresponding-states approach employs pure component viscosity data (either experimental or estimated). These data are coupled with combinatorial rules to relate critical and other properties of the mixture to pure component properties in order to estimate the mixture viscosity, μ_m. The combinatorial rules are essentially empirical in nature, each investigator proposing a set of rules.

Several new approaches based on the Enskog dense-gas theory someday may lead to accurate predictive methods for gas and gas mixture viscosities. At present, however, techniques based on the corresponding-states principle provide more reliable methods.

Even though the theoretical understanding of gas viscosity is well founded, there is presently no comparable theoretical basis for the estimation of liquid viscosities. Current liquid mixture viscosity

correlations are essentially mixing rules applied to pure component viscosities to account for composition dependence.

In the present study, a preliminary investigation is underway to assess the relative success of three exisiting correlations and a modified version of one of the above correlations in predicting CO_2-hydrocarbon mixture viscosities for the case of a pure CO_2 stream. The correlations that will be tested are as follows: 1) Lohrenz, Bray, and Clark,[3] 2) Pedersen et al. method,[4] 3) Ely and Hanley method,[8] and 4) a modified Jossi et al. approach.[9]

Jossi, Stiel, and Thodos[9] developed a correlation for the viscosity of pure substances applicable in the dense gaseous and liquid states. Their correlation forms the backbone of the LBC correlation. In the Jossi et al. method, temperature and density are employed as state variables. Thus, one must have accurate volumetric data or an equation of state whose parameters are tuned to fit available PVT data for accurate dense gas and liquid viscosity estimates.

The approach of Jossi et al. will be used to develop the procedure for the fourth correlation mentioned above. The formalism is based on the residual viscosity concept coupled with the corresponding-states theory to obtain the desired parameters. Using dimensional analysis and the Abas-Zade[9] relationship, Jossi et al. present an analytical expression relating the residual viscosity, critical compressibility factor, and the reduced density given by

$$(\mu - \mu^*)\,\zeta = \beta Z_c^m \rho_r^n \qquad (1)$$

where

μ^* is the low-pressure gas viscosity,

ζ is the inverse viscosity parameter

$$= \frac{T_c^{1/6}}{M^{1/2} P_c^{2/3}} \quad , \text{and}$$

β, m, and n are the constants.

Data tables generated by the CPE apparatus will be used to define the constants in Eq. (1). The composition dependence of the mixture viscosities will be incorporated via mixing rules to obtain μ^* and ζ.

Lohrenz et al. tested several mixing rules for μ^* and ζ. Their choice of the proper set employed in the LBC correlation was based on the lowest AAD between calculated and experimental results for each mixing rule set employed. The mixing rules investigated by Lohrenz et al., and perhaps others, will be tested to find the best fit with the experimental data. In the Jossi et al. correlation, m is zero (i.e., for the substances studied, the residual viscosity was found to be independent of Z_c). A fourth-degree polynomial in the reduced density ρ_r, gave the best fit over the entire range of reduced densities used in their study. The inclusion of Z_c in Eq. (1) was intended to account for differences in molecular size and may prove important for CO_2-hyrocarbon systems.

The correlation of Pedersen et al.[4,10] is an extension of the model proposed by Tham and Gubbins[11] for prediction of thermal conductivities and viscosities of both gaseous and liquid mixtures. The Tham and Gubbins model introduces a parameter called rotation coupling coefficient,

α_{TG}, to account for the deviation of nonpolar polyatomic fluids from the simple classical correspondence principle where a reduced viscosity in the latter is given by:

$$\mu_r(\rho, T) = \frac{\mu(\rho, T)}{T_c^{1/2} V_c^{-2/3} M^{1/2}} \tag{2}$$

A group of substances obey the corresponding-states principle if a universal functional dependence of μ_r on the reduced density, ρ_r, and reduced temperature, T_r, can be found, i.e.,

$$\mu_r(\rho, T) = \mathcal{F}(\rho_r, T_r) \tag{3}$$

If the functional dependence, F, is indeed obeyed by all the substances in the group at a given state when compared from its departure relative to the respective critical points of each component, then comprehensive viscosity data is needed only for a representative component in the group. That component is then used as the reference substance, o, from which the viscosity of another substance in the group, x, can be calculated via the following expression:

$$\mu_x(\rho, T) = \left(\frac{T_{cx}}{T_{co}}\right)^{1/2} \left(\frac{V_{cx}}{V_{co}}\right)^{-2/3} \left(\frac{M_x}{M_o}\right)^{1/2} \times \mu_o \left[\frac{\rho \bullet \rho_{co}}{\rho_{cx}}, \frac{T \bullet T_{co}}{T_{cx}}\right] \tag{4}$$

where the subscript, cx, refers to the critical properties of substance, x, and
the subscript, co, refers to the critical properties of the reference substance, o.

The model proposed by Tham and Gubbins[11] is based on the theory that free molecular rotation is not possible in the liquid state. The new parameters, α_{TG}, accounts for the hindered molecular rotation and appears in the expression for the viscosity correlation based on a modified simple correspondence principle as follows:

$$\mu_m(P, T) = \left(\frac{T_{cm}}{T_{co}}\right)^{-1/6} \left(\frac{P_{cm}}{P_{co}}\right)^{2/3} \left(\frac{M_m}{M_o}\right)^{1/2} \times \mu_o \left[\frac{P \bullet P_{co}\alpha_{TG,o}}{P_{cm}\alpha_{TG,m}}, \frac{T \bullet T_{co}\alpha_{TG,o}}{T_{cm}\alpha_{TG,m}}\right] \tag{5}$$

where pressure replaces density as a state variable. The coefficient, α_{TG}, is treated as an adjustable parameter, and it is determined by a fit to experimental liquid viscosities.

In Ely and Hanley's model,[8] the deviation from the simple correspondence principle is expressed in terms of two shape factors, $\Theta(T_r, V_r, \omega)$ and $\Phi(T_r, V_r, \omega)$, which enter the viscosity correlation as follows:

$$\mu_m(\rho, T) = \left(\frac{\Theta T_{cm}}{T_{co}}\right)^{1/2} \left(\frac{\Phi V_{cm}}{V_{co}}\right)^{-2/3} \left(\frac{M_m}{M_o}\right)^{1/2} \times \mu_o \left[\frac{\rho_m \bullet \rho_{co}\Phi}{\rho_{cm}}, \frac{T \bullet T_{co}}{T_{cm}\Theta}\right] \tag{6}$$

The above equation also is based on the corresponding-states principle and the conformal-solution, one-fluid model. The basic idea of the theory is the assumption that the configurational properties of a single-phase mixture can be equated to those of a hypothetical pure fluid (conformal

solution) whose properties are then evaluated via corresponding states with respect to a given reference fluid (one-fluid model).

Both the Pedersen et al.[4,10] and the Ely and Hanley[8] methods employ the mixing rules of Mo and Gubbins[12] to obtain the critical properties of the mixture. Pedersen et al.[4,10] proposed a mixing rule for the molecular weight of the mixture which is employed directly in the mixture rotation coupling coefficient, thus circumventing the need for a mixing rule for this parameter.

3. The Lorenz, Bray, and Clark Correlation

Work during the past year has been devoted to the coding and debugging of the Lohrenz, Bray, and Clark (LBC) correlation and the characterization of the CO_2-crude oil mixtures obtained from the CPE experiments. Of particular interest are the CPE runs performed on the Maljamar stock tank oil at 1200 psia and 90°F and the Wasson stock tank oil at 1500 psia and 109°F (CPE 210, PRRC Report 87-8[13]; CPE 234, PRRC Report 88-8[14]) to which the initial comparisons with the LBC prediction, reported herein, were made.

The LBC method appeared in the literature in 1964 and thereafter became a routine method for calculating the viscosity of crude oils and natural gas-crude oil mixtures. Part of the reason for the popularity of the correlation is that it requires input data that are readily available. A conventional PVT analysis of a given crude oil sample would include the bubble point pressure at the conditions of the reservoir, the breakdown of the nonhydrocarbon and hydrocarbon components up to the hexanes, the heptanes-plus (C_{7+}) fraction and its molecular weight and specific gravity, and the overall molecular weight of the crude oil. All the pertinent information is then available for the straightforward, noniterative LBC correlation to calculate the viscosity of the crude oil.

There are, however, a number of shortcomings associated with the LBC correlation that can result in deviations between the calculated and the corresponding experimental viscosity value. These deviations can be on the order of 100% or more even for well-defined synthetic oil systems as well as for mixtures containing a sizeable amount of CO_2. The latter is not surprising considering that the data base used by Lohrenz et al. has CO_2 concentrations of 5% by mole or less.

The following are highlights of the LBC method. The viscosity of a liquid mixture is given by

$$[(\mu - \mu^*)\zeta + 10^{-4}]^{1/4} = 0.1023 + 0.023364\rho_r + 0.058533\rho_r^2 - 0.040758\rho_r^3 + 0.0093324\rho_r^4 \tag{7}$$

where

$$\mu^* = \frac{\sum_{i=1}^{n} x_i \mu_i^* M_i^{1/2}}{\sum_{i=1}^{n} x_i M_i^{1/2}} \tag{8}$$

$$\zeta = \frac{\left(\sum_{i=1}^{n} x_i T_{c_i}\right)^{1/6}}{\left(\sum_{i=1}^{n} x_i M_i\right)^{1/2} \left(\sum_{i=1}^{n} x_i P_{c_i}\right)^{2/3}} \tag{9}$$

x_i is the mole fraction of component i,
M_i is the molecular weight of component i,
T_{ci} is the pure-component critical temperature,
P_{ci} is the pure-component critical pressure, and
μ_i^* is the low-pressure, pure-component gas viscosity.

The low-pressure, pure-component gas viscosity is given by

$$\mu_i^* \zeta_i = \begin{cases} 34.0 \times 10^{-5} T_{r_i}^{0.94}, & T_{r_i} < 1.5 \\ 17.78 \times 10^{-5} (4.58 T_{r_i} - 1.67)^{5/8}, & T_{r_i} > 1.5 \end{cases} \tag{10}$$

where

$$T_{r_i} = \frac{T}{T_{c_i}} \tag{11}$$

and

$$\zeta_i = \frac{T_{c_i}^{1/6}}{M_i^{1/2} P_{c_i}^{2/3}} \tag{12}$$

The pseudocritical mixture density is calculated from

$$\rho_c' = \frac{1}{V_c'} \tag{13}$$

$$V_c' = \sum_{i=1}^{n-1} x_i V_{c_i} + x_{C7+} V_{c_{C7+}}$$

where

V_{ci} is the critical molar volume of component i, and

V_{cC7+} is the pseudocritical molar volume of the C7+ fraction.

Lohrenz et al. presented a correlation to estimate the C7+ pseudocritical molar volume as follows:

$$V_{cC7+} = 21.573 + 0.015122M_{C7+} - 27.656\gamma_{C7+} + 0.070615M_{C7+}\gamma_{C7+} \tag{14}$$

where

γ_{C7+} is the specific gravity of the C7+ fraction, and

M_{C7+} is the average molecular weight of the C7+ fraction.

The reduced mixture density is then obtained as

$$\rho_r = \frac{\rho}{\rho_c'} \tag{15}$$

where

ρ is the mixture density.

The input data required to perform the calculations are the pure component critical properties and molecular weights (T_{ci}, P_{ci}, V_{ci}, M_i), the mixture composition and density ($\{x_i\}$, ρ), and the molecular weight and specific gravity of the C7+ fraction (M_{c7+}, $\gamma c7+$).

Kovarik and Taylor[5] compared the viscosity predictions of LBC with experimental values for a well-defined CO_2-synthetic oil mixture. Their results show maximum absolute percentage deviations of around 40%. It is interesting to note the authors' observation that for the heavy pure components in the mixture, the critical molar volume correlation given by Eq. (14) resulted in lower absolute deviations than the calculations where the experimental critical molar volume of the pure component was used. They concluded that Eq. (14) must always be used in conjunction with the LBC correlation.

To perform the computations for the comparison of experimental and predicted viscosities for the CO_2-Maljamar and CO_2-Wasson stock tank oil runs, one has to characterize the C7+ fractions in terms of their average molecular weights, specific gravities, and pseudocritical properties. The gas-liquid chromatographic analyses of the produced fluid samples from the CPE experiment detail the composition of each sample in terms of nonhydrocarbon and hydrocarbon components up to $nC_{36}H_{74}$, the balance being lumped into a C37+ group. The analyses, however, and the present experimental setup are incapable of reporting the specific gravity of the C7+ fraction of the liquid phase samples. The average molecular weights are readily obtained as a linear combination of the pure component molecular weights weighted by their respective mole fractions, but as alluded to earlier, the other parameters characterizing the C7+ fraction have to be obtained or estimated by some other appropriate means.

The critical properties of the heptanes-plus were estimated via the correlations of Lin and Chao,[15] where T_c and P_c are given in terms of the average molecular weight as follows:

$$T_c = 272.697 + 3.91999M_{C7+} - 1.17706 \times 10^{-2}M_{C7+}^2 + 1.48679 \times 10^{-5}M_{C7+}^3 - 2.27789 \times 10^3/M_{C7+} \tag{16}$$

$$\ln P_c = 1.77645 - 1.01820 \times 10^{-2}M_{C7+} + 2.51106 \times 10^{-5}M_{C7+}^2 - 3.73775 \times 10^{-8}M_{C7+}^3 + 3.50737/M_{C7+} \tag{17}$$

The specific gravities of the heptanes-plus were estimated from the Hankinson-Brobst-Thomson[16,17] (HBT) technique. The HBT method is a generalization of the Tait equation for compressed liquid and liquid mixture densities. The saturated liquid density in the generalized Tait equation is obtained via the corresponding-states theory. The main features of the HBT method are presented below.

The compressed liquid mixture molar volume is obtained from

$$V = V_s\left[1 - c\ln\left(\frac{\beta + P}{\beta + P_{vp_m}}\right)\right] \tag{18}$$

where V_s is the saturated molar volume at the mixture vapor pressure, P_{vp_m}.

The parameter β is a function of temperature and is given by

$$\beta/P_{c_m} = -1 + a(1 - T_{r_m})^{1/3} + b(1 - T_{r_m})^{2/3} + d(1 - T_{r_m}) + e(1 - T_{r_m})^{4/3} \tag{19}$$

where

$$e = \exp\left(f + g\omega_{SRK_m} + h\omega_{SRK_m}^2\right) \tag{20}$$

and

$$c = j + k\omega_{SRK_m} \tag{21}$$

The constants a through k for Eqs. 19-21 are:

a	-9.070217	b	62.45326
d	-135.1102	f	4.79594
g	0.250047	h	1.14188
j	0.0861488	k	0.0344483

The saturated liquid mixture molar volume is given by

$$\frac{V_s}{V_m^*} = V_R^{(0)} \left[1 - \omega_{SRK_m} V_R^{(\delta)}\right] \tag{22}$$

where

$$V_R^{(0)} = 1 + c_1(1 - T_{r_m})^{1/3} + c_2(1 - T_{r_m})^{2/3} + c_3(1 - T_{r_m}) + c_4(1 - T_{r_m})^{4/3} \quad 0.25 < T_{r_m} < 0.95 \tag{23}$$

and

$$V_R^{(\delta)} = \left(c_5 + c_6 T_{r_m} + c_7 T_{r_m}^2 + c_8 T_{r_m}^3\right) / (T_{r_m} - 1.00001) \qquad 0.25 < T_{r_m} < 1.0 \tag{24}$$

The constants c_1 through c_8 for Eqs. 23 and 24 are:

c_1	-1.52816	c_2	1.43907
c_3	-0.81446	c_4	0.190454
c_5	-0.296123	c_6	0.386914
c_7	-0.0427258	c_8	-0.0480645

V_m^* = mixture characteristic molar volume.

Mixing rules used with the HBT equations are

$$T_{c_m} = \frac{\sum_i \sum_j x_i x_j V_{ij}^* T_{c_{ij}}}{V_m^*} \tag{25}$$

$$V_m^* = \frac{1}{4}\left[\sum_i x_i V_i^* + 3\left(\sum_i x_i V_i^{*2/3}\right)\left(\sum_i x_i V_i^{*1/3}\right)\right] \tag{26}$$

$$V_{ij}^* T_{c_{ij}} = \left(V_i^* T_{c_i} V_j^* T_{c_j}\right)^{1/2} \tag{27}$$

$$\omega_{SRK_m} = \sum_i x_i \omega_{SRK_i} \tag{28}$$

$$P_{c_m} = \frac{(0.291 - 0.080\omega_{SRK_m})\, RT_{c_m}}{V_m^*} \tag{29}$$

The mixture vapor pressure, P_{vp_m}, is calculated by

$$P_{vp_m} = P_{c_m} P_{r_m} \tag{30}$$

where P_{c_m} is given by Eq. 29 and P_{r_m} is calculated from the generalized Riedel vapor pressure equation.

$$\log_{10} P_{r_m} = P_{r_m}^{(0)} + \omega_{SRK_m} P_{r_m}^{(1)} \tag{31}$$

$$P_{r_m}^{(0)} = 5.8031817 \log_{10} T_{r_m} + 0.07608141\alpha \tag{32}$$

$$P_{r_m}^{(1)} = 4.86601 \log_{10} T_{r_m} + 0.03721754\alpha \tag{33}$$

$$\alpha = 35.0 - \frac{36.0}{T_{r_m}} - 96.736 \log_{10} T_{r_m} + T_{r_m}^6 \tag{34}$$

and

$$T_{r_m} = \frac{T}{T_{c_m}} \tag{35}$$

The input data and pure component parameters required to perform the calculations are critical temperatures and pressures (T_{c_i}, P_{c_i}), Soave-Redlich-Kwong acentric factors (ω_{srk_i}), molecular weights (M_i), characteristic molar volumes (V_i^*), and the mixture composition, temperature, and pressure ($\{x_i\}$, T, P).

4. Results and Discussion

The calculations were performed for the CO_2-Maljamar stock tank oil (CPE 210) and the CO_2-Wasson stock tank oil run (CPE 234), and the results are presented in Tables 4 and 5. The agreement between the calculated and observed viscosities are shown in Figs. 21 and 22. Noteworthy is that the LBC correlation consistently predicts a higher viscosity value for the CO_2-crude oil mixtures. This is not surprising considering the well known viscosity-reduction effect CO_2 has on hydrocarbon mixtures which the correlation apparently cannot account for. Examples of the detailed compositional analyses of the samples to which the comparisons were made are given in Appendices A and B. The characterization of the C7+ fractions for each sample using the Lin-Chao and HBT correlations are presented in Appendices C and D, respectively.

TABLE 4. COMPARISON OF LOHRENZ, BRAY, AND CLARK[3] VISCOSITY CORRELATION PREDICTION TO THE CO_2-MALJAMAR STOCK TANK OIL RUN (CPE 210) AT 1200 PSIA AND 90°F.

CO_2	nC_3	nC_4	nC_5	nC_6	C7+	ρ	μ^{exp}	μ^{calc}	Dev.*
		mole		frac.		(g/cm^3)	(cP)	(cP)	%
.0000	.0000	.0000	.0440	.0713	.8847	.8359	4.300	4.553	5.9
.2279	.0069	.0236	.0442	.0600	.6374	.8416	2.780	4.539	62.9
.2584	.0258	.0631	.0502	.0416	.5609	.8431	2.270	4.780	110.6
.4177	.0039	.0064	.0235	.0559	.4926	.8481	1.486	3.246	118.4
.5408	.0017	.0093	.0209	.0349	.3924	.8495	1.278	2.300	80.0
.6389	.0011	.0068	.0114	.0253	.3165	.8524	0.914	1.390	52.0
.6230	.0012	.0068	.0175	.0306	.3209	.8535	0.933	1.654	77.3
.6791	.0004	.0026	.0087	.0227	.2865	.8592	0.838	1.398	66.9
.7152	.0003	.0021	.0064	.0166	.2594	.8624	0.911	1.221	34.0
.6522	.0002	.0014	.0065	.0178	.3219	.8651	1.009	1.887	87.0
.7037	.0002	.0012	.0055	.0132	.2762	.8678	1.113	1.582	42.1
.7050	.0002	.0013	.0051	.0134	.2750	.8702	1.231	1.601	30.1
.7071	.0002	.0012	.0052	.0142	.2721	.8727	1.334	1.668	25.0
.6940	.0003	.0020	.0061	.0146	.2830	.8751	1.499	1.961	30.8
.6997	.0002	.0009	.0043	.0118	.2831	.8771	1.639	2.199	34.2
.6715	.0001	.0008	.0042	.0131	.3103	.8792	1.846	2.561	38.7
.6705	.0001	.0007	.0041	.0128	.3118	.8820	1.984	2.658	34.0

*Dev.$= \frac{\mu^{calc} - \mu^{exp}}{\mu^{exp}} \times 100\%$

TABLE 5. COMPARISON OF LOHRENZ, BRAY, AND CLARK[3] VISCOSITY CORRELATION PREDICTION TO THE CO_2-WASSON STOCK TANK OIL RUN (CPE 234) AT 1500 PSIA AND 109°F.

CO_2	nC_4	nC_5	nC_6	C7+	ρ	μ^{exp}	μ^{calc}	Dev.*
	mole		frac.		(g/cm^3)	(cP)	(cP)	%
.0000	.0000	.0480	.0581	.8939	.856	4.200	5.938	41.4
.2650	.0098	.0408	.0484	.6360	.859	2.869	5.629	96.2
.2910	.0134	.0406	.0477	.6073	.863	2.204	5.748	160.8
.4962	.0084	.0328	.0387	.4239	.865	1.479	3.450	133.2
.5376	.0127	.0288	.0375	.3834	.866	1.271	2.950	132.1
.6489	.0079	.0233	.0313	.2886	.867	0.998	1.720	72.4
.6099	.0100	.0267	.0333	.3201	.866	0.922	2.095	127.2
.7051	.0049	.0165	.0284	.2451	.865	0.720	1.159	61.0
.7199	.0045	.0097	.0163	.2496	.872	0.820	1.567	91.1
.6993	.0054	.0108	.0194	.2651	.877	0.968	1.698	75.4
.6914	.0059	.0100	.0197	.2730	.881	1.078	1.935	79.5
.6810	.0030	.0089	.0171	.2900	.885	1.154	2.282	97.7
.6814	.0054	.0087	.0205	.2813	.890	1.310	1.859	41.9
.6424	.0027	.0087	.0200	.3262	.892	1.507	2.660	76.5
.5869	.0070	.0128	.0264	.3669	.894	1.650	3.739	126.6
.6040	.0033	.0095	.0241	.3591	.897	1.753	3.722	112.3
.5676	.0037	.0088	.0246	.3953	.900	1.962	4.769	143.1

$$*\text{Dev.} = \frac{\mu^{calc} - \mu^{exp}}{\mu^{exp}} \times 100\%$$

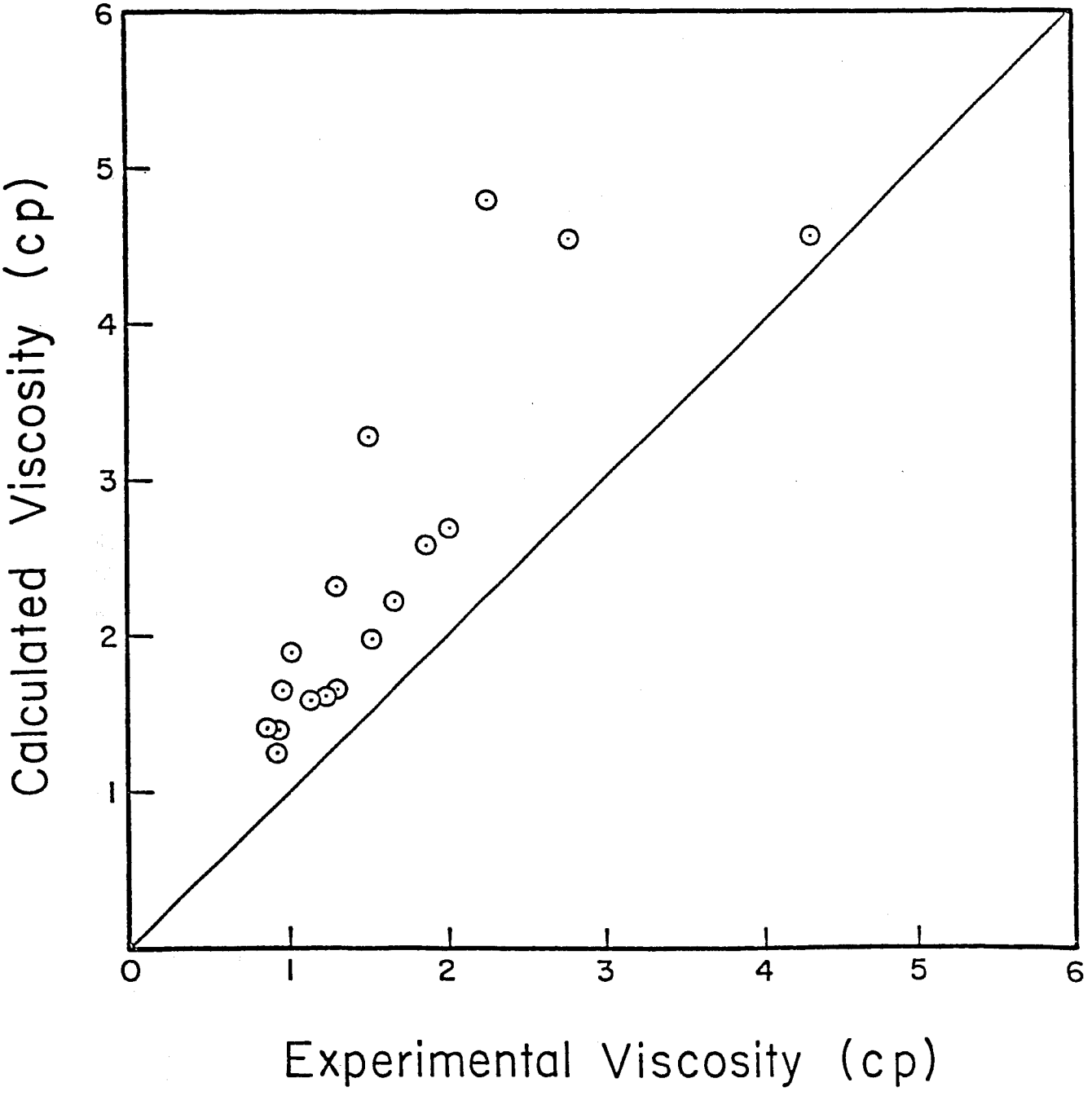

Figure 21. Comparison between Lohrenz-Bray-Clark calculated and experimentally observed viscosities for equilibrium liquid mixtures of CO_2 and Maljamar stock tank oil at 1200 psia and 90°F.

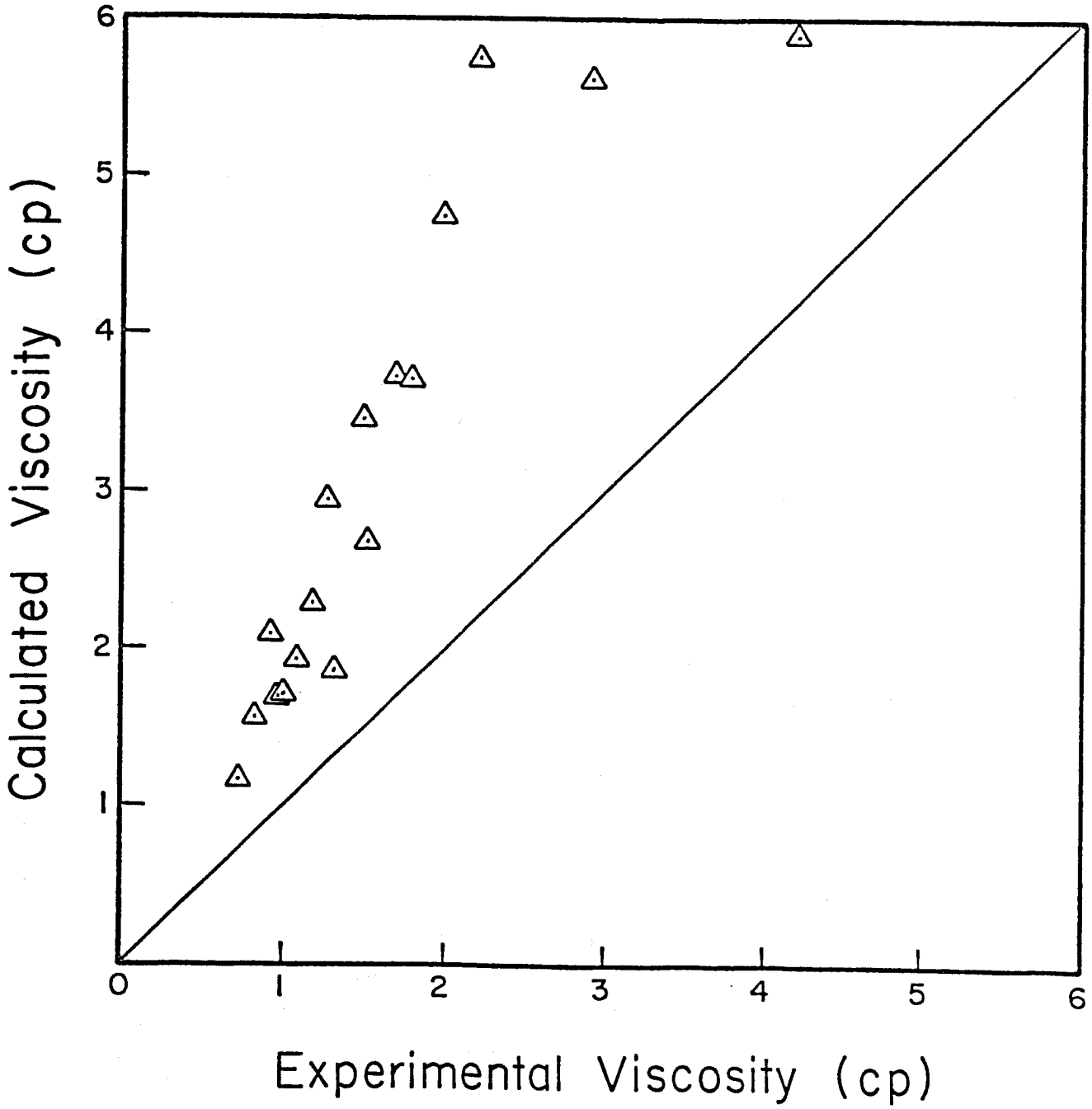

Figure 22. Comparison between Lohrenz-Bray-Clark calculated and experimentally observed viscosities for equilibrium liquid mixtures of CO_2 and Wasson stock tank oil at 1500 psia and 109°F.

It is evident from Tables 4 and 5 that deviations on the order of 100% can be expected between the LBC predicted and experimental viscosities for hydrocarbon mixtures containing CO_2.

A mathematical model of what we call a first-generation viscosity correlation is currently being developed in our laboratory. The model has the form

$$\log_{10}\mu = \log_{10}\mu^{(LBC)} + \Im(T, P, x_{CO_2}, \ldots) \tag{36}$$

The functional form of $\Im$ will be determined as more data become available.

5. Nomenclature

$a, b, d, e, f, g, h, j, k$ = parameters defined in Eqs. (19)–(21)
c = parameter in the Tait equation, Eqs. (18) and (21)
$c_1 - c_8$ = constants in Eqs. (23) and (24)
M_i = molecular weight of component i
M_{C7+} = molecular weight of the C7+ fraction
n = number of components in the mixture
P = pressure
P_c = critical pressure
P_{c_i} = critical pressure of component i
P_{c_m} = mixture pseudocritical pressure
P_{r_m} = pseudoreduced pressure of the mixture
P_{vp_m} = vapor pressure of the liquid mixture at temperature T
$P_R^{(0)}, P_R^{(1)}$ = terms in Eq. (31), defined in Eqs. (32) and (33)
R = universal gas constant
T = temperature
T_c = absolute critical temperature
T_{c_i} = absolute critical temperature of component i
T_{c_m} = mixture pseudocritical absolute temperature
T_{r_m} = pseudoreduced temperature of the mixture
T_{r_i} = reduced temperature of component i
V = liquid mixture molar volume
V_s = saturated liquid mixture molar volume
V_c' = pseudocritical molar volume of a mixture

$V_{c_{C7+}}$ = critical molar volume of the C7+ fraction given by Eq. (13)
V_i^* = characteristic molar volume of component i
V_m^* = mixture characteristic molar volume
$V_R^{(0)}$ = corresponding states function for normal fluids, defined in Eq. (23)
$V_R^{(\delta)}$ = corresponding states deviation function
x_{C7+} = mole fraction of the C7+ fraction
x_i = mole fraction of component i
$\Im$ = general function

Greek Letters

α = generalized Riedel parameter, defined in Eq. (34)
β = parameter in the Tait equation, defined in Eq. (19)
μ = mixture viscosity
μ^* = viscosity of a gas mixture at low pressure, defined in Eq.(8)
μ_i^* = viscosity of component i as a gas at low pressure
ζ = viscosity parameter of a mixture, defined in Eq. (7)
ζ_i = viscosity parameter of component i, defined in Eq. (9)
ρ = mixture density
ρ_c' = pseudocritical density of a mixture
ρ_r = reduced density
γ_{C7+} = specific gravity of the C7+ fraction
ω_{SRK_i} = Soave-Redlich-Kwong acentric factor of component i
ω_{SRK_m} = Soave-Redlich-Kwong acentric factor for a mixture

Subscripts

c = critical state
i, j = component i or j
m = mixture
R, r = reduced property
s = saturation
SRK = obtained using Soave-Redlich-Kwong equation of state

C. EFFECT OF PHASE BEHAVIOR ON DISPLACEMENT EFFICIENCY

1. Solution and Free Gas Effect on the Development of Miscibility

After the successful completion of the slim-tube experiment that was run above the bubble point pressure (BPP) last year, the slim-tube apparatus was modified into a core displacement unit. This unit was used to investigate the effect of free gas as well as solution gas on displacement efficiency. Building the core unit initially caused a leak from the annulus between the core and potting alloy. After trying several bonding materials, ceramic cement was used successfully for coating the core.

In this study two oil systems are being used: synthetic oil ($C_1 + C_4 + C_{10}$) and crude oil (Wasson crude oil). To have the same displacement efficiency that can be obtained in slim-tube experiments, vertically downward gravity-assisted displacements are being used. Tiffin and Kremsee[18] reported that the critical rate expression developed by Hill[19] was found to predict the correct stability criteria for a CO_2-reservoir oil system in which miscibility develops in a liquid-liquid phase region. The critical rate is

$$q_c = \frac{3.481 \Delta\rho k A \sin\theta}{\Delta\mu} \quad \text{(cc/hr)}$$

where

q_c is the critical rate (cc/hr),
$\Delta\rho$ is the density difference (gm/cc),
k is the permeability (Darcies),
θ is the dip angle (from horizontal),
$\Delta\mu$ is the viscosity difference (cp), and
A is the cross sectional area (cm^2).

For the synthetic oil system, densities and viscosities of CO_2 and oils are calculated by the TRAPP program (Table 6), a transport properties prediction program. This TRAPP program is based on the corresponding-state principle, using methane as a reference fluid. The first oil mixture has no methane in it (40% C_4 + 60% C_{10}), and the second oil mixture contains 45% methane (45% C_1 + 22% C_4 + 33% C_{10}) in order to raise the bubble point pressure above the MMP of the first oil mixture (MMP of 40% C_4 + 60% C_{10} is around 1600 psia at 160°F). The bubble point pressure of the second oil mixture is 1897.9 psia.

For these two oil mixtures, critical injection rates were calculated and are shown in Table 7. Berea sandstone with 20% porosity and 400-md permeability was used in the calculation. All of these critical velocities were higher than the injection rate of 10 cc/hr so that stable displacements could be obtained.

One-dimensional simulation (CRSIM ID) is currently being performed using the Peng-Robinson equation of state (PREOS). This one-dimensional simulation will be matched with phase behavior and core displacement data.

TABLE 6. FLUID PROPERTIES OF SYNTHETIC OIL

T = 160°F

Pressure (psia)	CO_2 Density (gm/cc)	CO_2 Viscosity (cp)	Mixture A* Density (gm/cc)	Mixture A* Viscosity (cp)	Mixture B* Density (gm/cc)	Mixture B* Viscosity (cp)
1400	0.2285	0.0235	0.6732	0.3718	-----	------
1500	0.2571	0.0248	0.6741	0.3747	-----	------
1600	0.2890	0.0263	0.6749	0.3777	-----	------
1700	0.3244	0.0281	0.6757	0.3806	-----	------
1800	0.3627	0.0302	0.6766	0.3836	-----	------
1950	0.4222	0.0339	0.6778	0.3880	0.5955	0.1824
2050	0.4601	0.0365	0.6786	0.3910	0.5968	0.1840

* Mixture A: 40% C_4 + 60% C_{10}

* Mixture B: 45% C_1 + 22% C_4 + 33% C_{10}

TABLE 7. CRITICAL VELOCITIES FOR STABLE DISPLACEMENTS

$T = 160°F$, $\phi = 20\%$, $k = 400$ md

$A = 11.4\ cm^2$, $L = 25.4$ cm

Pressure (psia)	Mixture A (40% C_4 + 60% C_{10})	Mixture B (45% C_1 + 22% C_4 + 33% C_{10})
1400	101 cc/hr	------
1500	95 "	------
1600	87 "	------
1700	79 "	------
1800	70 "	------
1950	57 "	93 cc/hr
2050	49 "	74 "

2. The Effect of Multiple Hydrocarbon Phases on Displacement Efficiency

a. Introduction

The mechanism of oil entrapment during waterflooding and the residual oil mobilization by an aqueous, low-tension displacing fluid certainly are well understood.[20,21,22] In contrast, the mechanisms by which carbon dioxide floods operate are not fully understood.

Experimental evidence exists to verify that the so-called "miscible" displacement of oil by CO_2 actually operates, for the most part, in the immiscible or "near" miscible regimes. Several circumstances allow for the possibility of these regimes to occur. These include the following: (a) displacements operated close to but below the slim-tube measured minimum miscibility pressure, (b) conditions where the CO_2-oil mixtures exhibit liquid-liquid and liquid-liquid-vapor immiscibility, and (c) the subsequent degradation of the transition zone due to dispersion causing a miscible front to revert to an immiscible displacement process. The multiple hydrocarbon phases and the interfacial tension (IFT) between these fluids, which are present during the displacement, can affect the process recovery efficiency through the influence of IFT on the capillary pressure gradient and the influence of multiple hydrocarbon phases on relative permeabilities.[23,24]

Vaporization appears to be the dominant mechanism for systems exhibiting a liquid-vapor (L_1V) type of phase behavior, while condensation is the controlling mechanism when two liquid phases (L_1L_2) are present. Huang and Tracht[25] showed that liquid-liquid extraction may be viable under certain conditions of pressure and temperature.

Several naturally occurring crude oils, when mixed with CO_2, exhibit multiple-phase separation, i.e., the formation of a hydrocarbon-rich liquid phase (L_1), a CO_2-rich liquid phase (L_2), and a vapor phase (V), accompanied in some cases by the precipitation of asphaltenes. Metcalfe and Yarborough[26] commented that the case where an L_1L_2V type of phase behavior is encountered maybe the most significant of all due to the reduced mobility effect of multiple phases flowing in the rock matrix. The principal controlling mechanism of this condition is not yet well understood.

Shelton and Yarborough,[27] on the other hand, published results which seem to indicate that a higher residual oil saturation occurs after a CO_2 flood when the multiple-phase region is traversed by the CO-crude oil composition path. Furthermore, they stated that the presence of multiple flowing phases reduces the relative permeability to water during the water-alternating-gas injection process. This results in the reduction of the oil production rate. Pontius and Tham[28] reported the injectivity problems encountered in Shell Oil Co.'s North Cross Devonian unit upon conversion to a CO_2 flood. Injection wells with a low average pressure at the time of conversion resulted in a high degree of injectivity impairment compared to wells with higher initial average pressures. This phenomenon was attributed to the formation of multiple phases that resulted in a zone of reduced mobility. The wells with lower pressure probably lie deep within the L_1L_2V region in the P-T space for the CO_2-North Cross crude oil system, thus allowing the phase separation to occur more extensively as CO_2 is injected.

Henry and Metcalfe[29] conducted CO_2 displacements with reservoir oils that exhibit multiple phases. The authors observed what they termed a "hump" in the otherwise monotonically decreasing pressure drop across the core that corresponded to the visual observation of three flowing phases. The authors also conducted phase equilibria measurements on the same crude oil sample used in the displacements. Their results show that the multiphase region projected on the pressure-temperature space is slightly larger, extending towards higher temperature and pressure, when determined by multiple-contact experiments (which can be argued to more closely simulate the resulting phase

behavior in a dynamic flow process) as compared to static PVT measurements. Thus it is probable that the multiple-phase region might not be confined to a very small section of the transition zone but might, in fact, be interspersed locally, the aggregate of which can be a significant portion of the zone. The multiple-phase generation could result in a zone of reduced mobility which could lead to improved sweep efficiency of the CO_2 flood. The authors, however, did not correlate the reduced-mobility-effect theory with the improvement of oil recovery.

The principal goal of the proposed study is to assess the impact of the multiple-phase generation on sweep efficiency by attempting to quantify the effect on mobility. An "overall effective mobility" will be defined for the transition zone as opposed to individual phase mobilities which would introduce intractable complexities. An a priori assumption is that a transition zone which contains three phases (two liquid and one vapor phase) will have a lower effective mobility compared to one with only two phases (either two liquid or a liquid and a vapor phase), i.e.,

$$M_{TZ}^{LLV} < M_{TZ}^{LL} < M_{TZ}^{LV}$$

b. Experimental Aspects

The design of the experiments in this study was such that the run temperatures were close to the CO_2 critical point temperature. A stable temperature is essential at this condition because of the sensitivity of the CO_2 density to slight thermal fluctuations in the vicinity of the critical point.

The airbath has been insulated with 1-inch-thick polystyrene material with reflecting aluminum sheets covering both sides. Heat is provided by four 100-watt light bulbs connected in parallel to a variable transformer. Finer temperature control is achieved through a 60-watt light bulb connected to an automatic temperature controller (YSI Model 63RC). A shaded pole blower has been installed to provide air circulation. Resistance temperature devices (RTD), reliable to within ±0.1 K, are used to monitor the temperature in several locations within the entire apparatus. The RTD's have been calibrated at ice-point and at various temperatures. Two RTD's, which gave a reading of 32°F at the ice point and consistently had identical readings for the range of temperatures measured, were used as the reference standard.

The system pressure is monitored via pressure transducers, housed in the airbath, to minimize pressure calibration drift caused by temperature fluctuations. The transducers are frequently calibrated against a dead weight gauge on site in the laboratory. A differential pressure transducer has been installed to monitor the pressure drop across the core in the course of a run.

Changes also have been made in the plumbing to facilitate the operation of the apparatus. A core bypass loop has been installed to stabilize the flow of CO_2 prior to injection into the core. Figure 23 is a schematic of the modified apparatus, and Fig. 24 shows the details of the back pressure regulator system. The following is an outline of the procedure for conducting the displacement experiments.

To start the displacement:

- bring the back pressure regulator (BPR) to the run pressure,
- saturate the core with the synthetic oil mixture at the run displacement rate,
- switch core bypass valves to "bypass" mode,

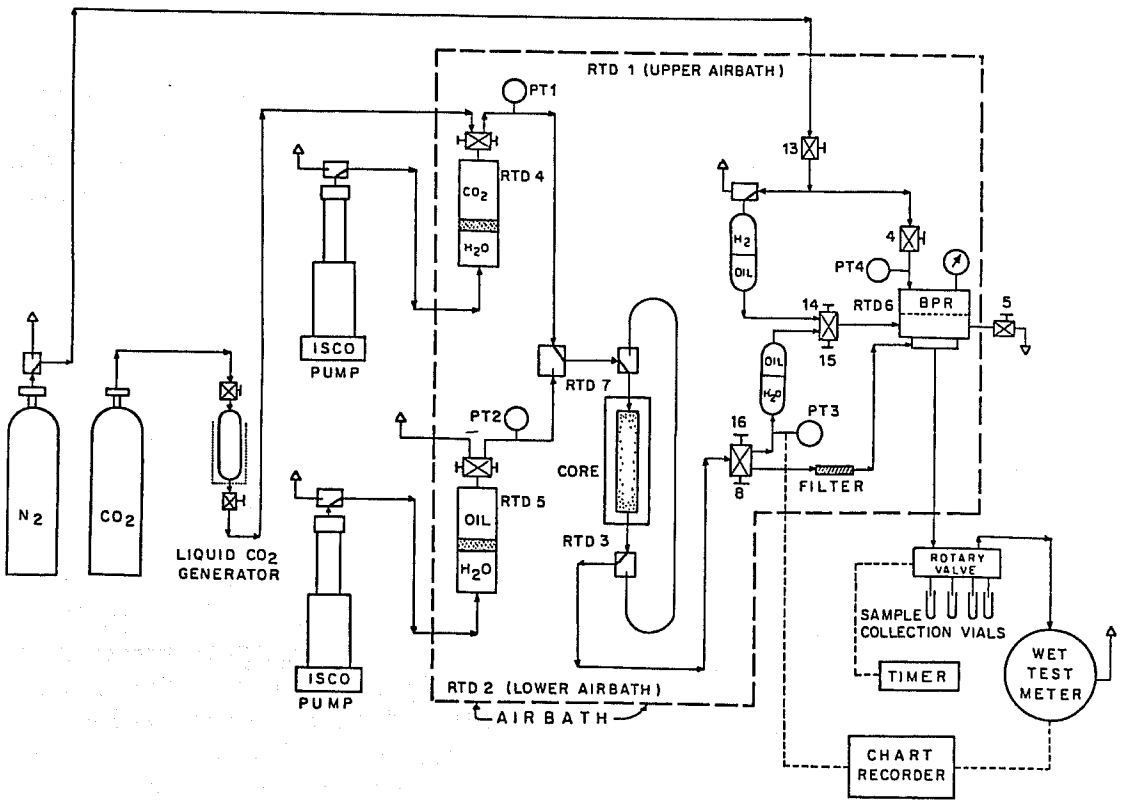

Figure 23. Schematic diagram of the CO_2/crude oil displacement apparatus.

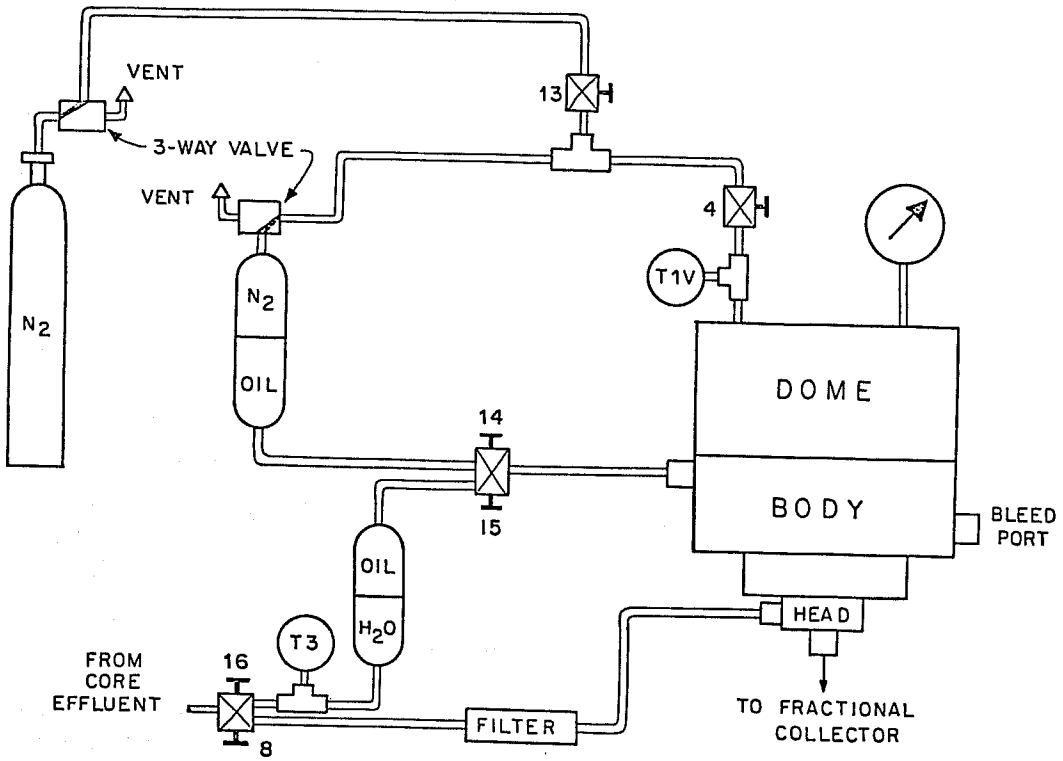

Figure 24. Schematic diagram of the back pressure regulator system.

- turn the strip-chart recorder on to record the volume of CO_2 produced,
- turn the CO_2 pump to "run" mode and allow flow stabilization to proceed until two or three stable cycles have been recorded on the chart recorder,
- switch core bypass valves to "inject" mode,
- turn the rotary valve timer on,
- make an event mark on the strip-chart paper and record the time of the start of the run.

To end the displacement:

- close valves 8, 15, and 16 (see Fig. 24),
- turn off the switching valve (valve 10),
- turn off the strip-chart recorder, again making an event mark recording the time of the end of the run,
- bring BPR down to atmospheric pressure and collect the blow down oil,
- remove core and measure the final weight.

The amount of oil recovered was determined by weight rather than by less accurate volumetric measurements. The dead volume from the core effluent to the collection tubes was carefully measured by saturating the line with water, then displacing the water by nitrogen. This procedure was repeated several times, and the volume of water collected in each run was averaged to give the desired value.

c. Results and Discussion

A series of gravity-assisted vertical CO_2 core floods was conducted with a synthetic oil (nC_{10} + nC_{16}) and a naturally occurring crude oil (Wasson stock tank oil) system. All the displacements were carried out using a fired Berea sandstone core with the less dense CO_2 solvent injected from the top. A summary of the properties of the Berea core used is presented in Table 8. The displacements with the synthetic oil were conducted at, above, and below the two-liquid phase region, while the Wasson stock tank oil runs focused on the three-phase region.

1) CO_2-Synthetic Oil Displacements

Fifteen experiments have been performed on the CO_2-synthetic oil system. A summary of the experimental results is presented in Table 9. The experiments were conducted in the pressure range of 1000-1550 psia at roughly 100-psia intervals. The temperature was set at 93°F (slightly supercritical to CO_2) and the injection flow rate of CO_2 was fixed at 4 cc/hr for all the runs. At least one replicate run was performed for each pressure level to check the reproducibility of the results. Figure 25 is a plot of the recovery at 1.2 PVI versus the run pressure.

TABLE 8

PROPERTIES OF CORE B7

Core Description:	Outcrop Berea Sandstone
Length:	14.94 cm
Diameter:	3.790 cm
Area:	11.28 cm^2
Pore Volume:	32 cm^3
Porosity:	19%
Absolute Permeability:	216.5 md

TABLE 9

SUMMARY OF VERTICAL CO_2-SYNTHETIC OIL DISPLACEMENTS

T = 93°F q = 4 cc/hr

Run No.	P (psia)	Recovery @ 1.2 PVI
1	998	0.509
2	998	0.545
3	998	0.499
4	1122	0.631
5	1112	0.606
6	1116	0.601
7	1124	0.612
8	1220	0.689
9	1220	0.689
10	1318	0.741
11	1318	0.733
12	1458	0.751
13	1458	0.740
14	1532	0.722
15	1532	0.717

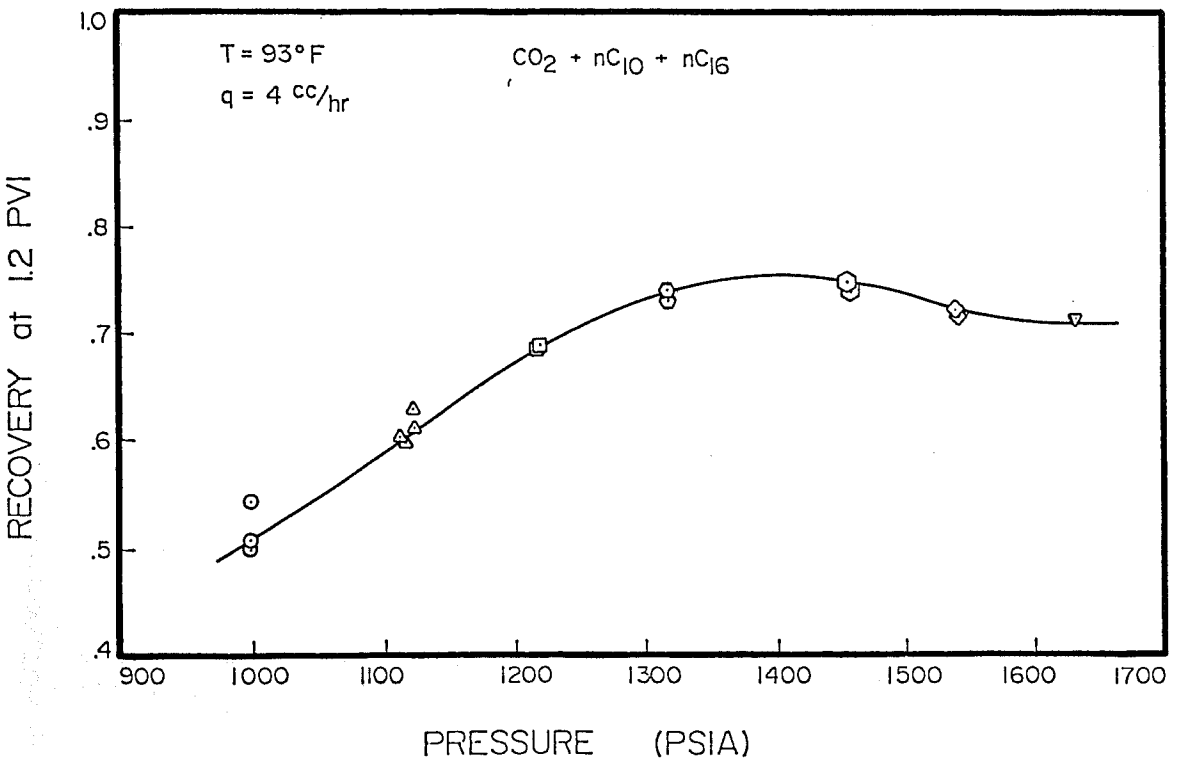

Figure 25. Recovery versus pressure plot for CO_2-synthetic oil displacements.

The critical velocity, above which viscous forces dominate and frontal instabilities occur, was calculated from the equation derived by Hill.[19]

$$v_c = \frac{3.481 \Delta\rho k \sin\theta}{\phi \Delta\mu} \tag{37}$$

where

v_c is the critical average intersticial velocity (cm/hr),
$\Delta\rho$ is the density difference (oil minus solvent),
k is the permeability (darcies),
θ is the dip angle measured from the horizontal,
ϕ is the core porosity, and
$\Delta\mu$ is the viscosity difference (oil minus solvent, cp).

The critical or gravity stable injection flowrate is then obtained from

$$q_c = \phi A v_c \tag{38}$$

where

q_c is the critical injection flowrate (cm^3/hr), and
A is the core cross-sectional area (cm^2).

A plot of q_c as a function of pressure for the CO_2-synthetic oil system is shown in Fig. 26. Note that the critical rate decreases with pressure because the density contrast decreases faster than the viscosity difference. All of the displacements in Fig. 25 were performed at 4 cc/hr, somewhat above the critical velocities calculated for the pressure in Fig. 26.

As can be seen in Fig. 25, the recovery at 1.2 PV CO_2-injected increases with pressure even at flowrates above the gravity-stable value (critical velocity) at the run pressure. Although this result is not itself especially exciting, it is noteworthy to see the trend of the recovery curve in the pressure interval of 1200-1600 psia. The calculated minimum miscibility pressure for this system is about 1550 psia at 93°F. Thus, one would expect the recovery to approach the 95% range at 1500 psia if the displacements were carried out in a slim tube. For the porous medium used, the recovery at this pressure should probably be in the 80-85% range considering scaling effects. The experimental results, however, show that recovery reaches a maximum of 74% at about 1400 psia and then drops off slightly at the higher pressures.

The recovery curve shown in Fig. 25 at pressures below 1300 psia represents the immiscible displacement regime where by passing can be dominated by capillary forces due to high liquid-vapor interfacial tension. At pressures above 1300 psia but below the minimum miscibility pressure, the recovery curve flattens out, exhibiting a maximum. Although one expects the recovery to increase as the MMP is approached, this result is not surprising if one considers the fact that the displacements were conducted at flowrates well above the critical value for gravity to stabilize the displacement front. Thus, the displacements were dominated by viscous instabilities resulting in poor recoveries caused by the gross bypassing of oil by the solvent. The 1200-1500-psia pressure interval corresponds to the formation of two equilibrium liquid phases in a static PVT cell for the CO_2-

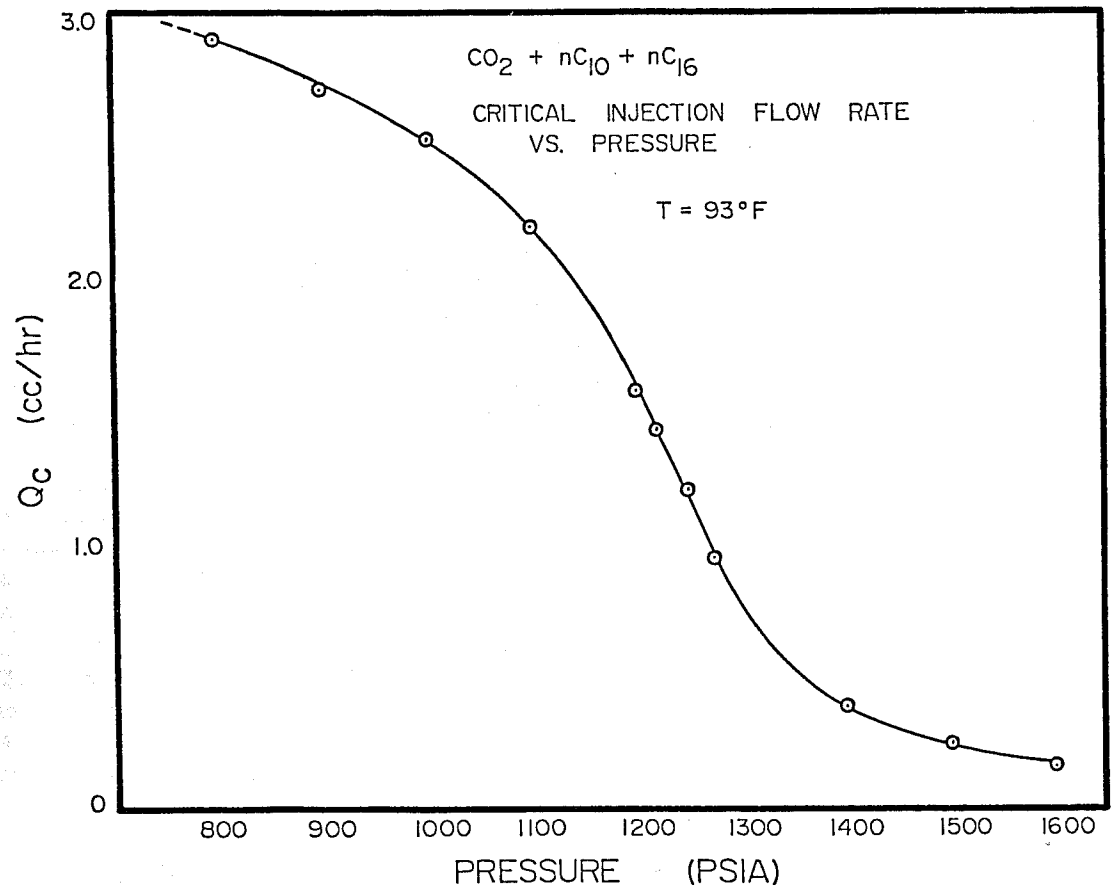

Figure 26. Critical injection flow rate versus pressure for gravity stabilized displacement for the CO_2-synthetic oil system at 93°F.

synthetic oil system. The two liquid phases, i.e., L_1, the hydrocarbon-rich lower phase, and L_2, the CO_2-rich upper phase, are characterized by interfacial tension values that are on the order of 10^{-1} dyne/cm. Also plotted in Fig. 25 is a data point that was taken from a series of displacements that was reported in the 1987 Annual Report (PRRC Report 87-9).[30] The run (also at a flow rate of 4 cc/hr) was performed at 1634 psia, which is well above the minimum miscibility pressure.

Thus, the recovery curve appears to exhibit a maximum at around 1400 psia for the displacements here performed at a flow rate well above the gravity-stable value. The 1634-psia displacement is characterized by the absence of capillary forces resulting from the miscible nature of the displacement. The lower recovery, however, is characteristic of an immiscible displacement because of the viscous instabilities. The flow rate of 4 cc/hr, which is equivalent to about 1.5 ft/day, is slightly high compared to typical field rates of 1 ft/day. The next set of runs will address the question of whether the recovery curve behavior reported here will persist to flow rates approaching the gravity-stable values.

The capillary number, which is the product of Darcy velocity and oil viscosity divided by the interfacial tension between the in-place and displacing fluid, gives an approximate measure of the relative importance of viscous and capillary forces. Capillary forces which arise because of interfacial tension can have a dampening effect on viscous instabilities and would tend to stabilize the displacement front. On the other hand, capillary forces are responsible for trapping oil during immiscible displacements. In a traditional waterflooding process, a plot of residual oil saturation, S_{or}, as a function of the capillary number, N_{Ca}, shows the curve to start out flat at around 40% S_{or} (for Berea sandstone) for low values of N_{Ca}. However, when a critical value of N_{Ca} is reached (this value will vary with different porous media), the S_{or} steadily approaches zero for increasing values of N_{Ca}, i.e., for higher flooding rates.

It would be interesting to determine the dependence of "residual oil saturation" (bypassed oil caused by viscous fingering after some reasonable pore volume of solvent has been injected) on the capillary number for a gasflooding process such as CO_2, from the immiscible to the first-contact miscible pressure range.

2) CO_2-Wasson Oil Displacements

A series of experiments are scheduled to be conducted on a 6-in.-long Berea sandstone core with a 1/2-in. O.D. Upstream of the core will be a 5-ft.-long slim tube that will be used to pregenerate a transition zone. The pressure drop across the core will be recorded throughout the course of the experiment to determine if the passage of a three-phase transition zone will indeed leave a "fingerprint" in the pressure drop history curve. These runs are essentially a replication of the experiments performed by Henry and Metcalfe[29] and will be repeated to confirm the mobility-reduction-effect theory.

To accomodate the above experiments on the present coreflood apparatus, a differential pressure transducer (Sensotec Model TJE) has been added to the setup. The core holder assembly and the slim tube currently are being assembled. These modifications are expected to be completed by the end of the first quarter of 1989.

Presented in Fig. 27 are P-X (pressure composition) diagrams for the Wasson stock tank oil at three temperatures. The above-mentioned experiments will be conducted at 105°F (which, incidentally, is also the reservoir temperature) since the three-phase region at that temperature appears to be larger than the one at 90°F. There also is an apparent sloping of the region, i.e., increasing in pressure with increasing CO_2 concentration. This feature will allow a wider pressure

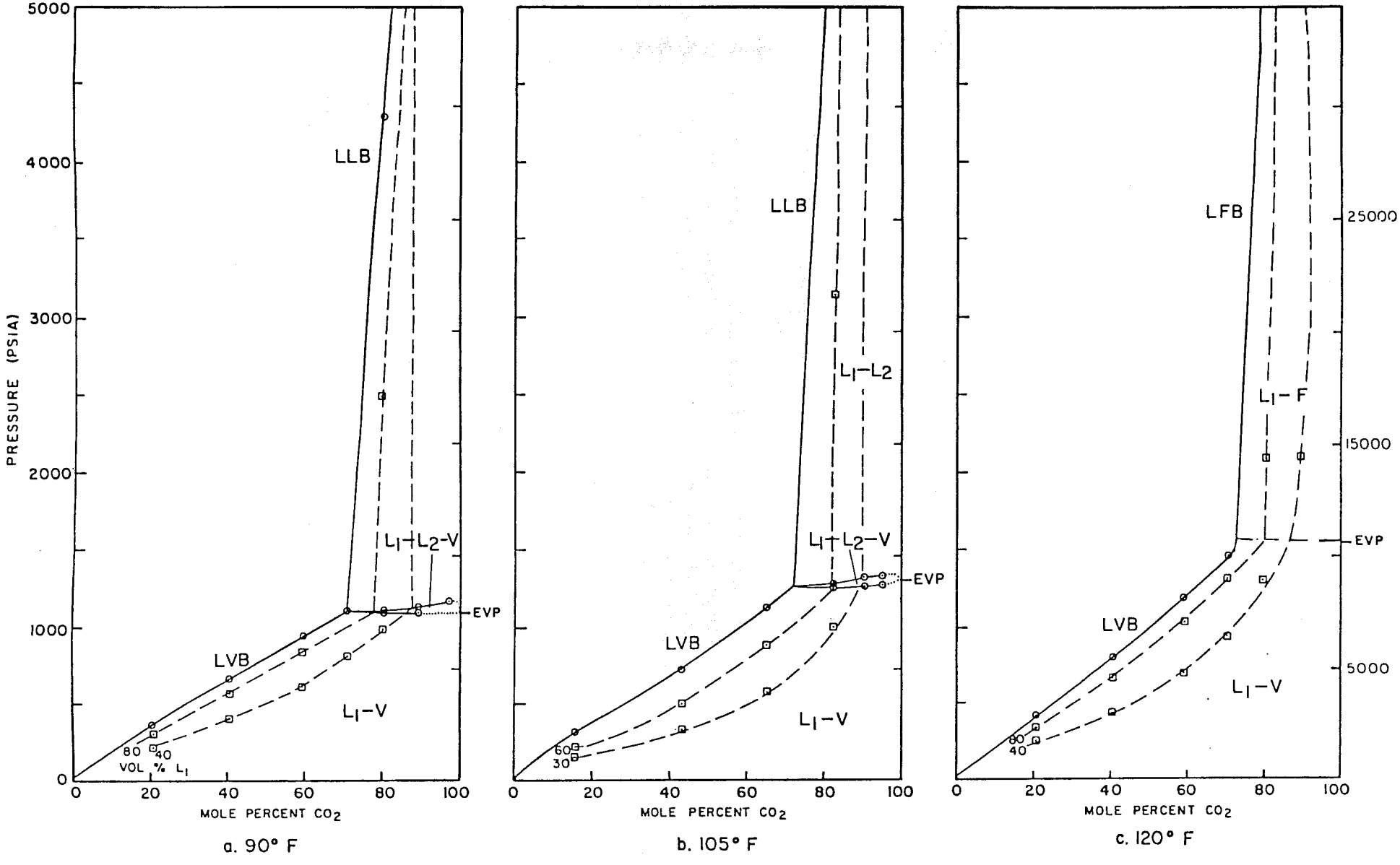

Figure 27. Pressure-composition phase diagrams for mixtures of CO_2 with Wasson stock tank oil.[31]

range to be scanned for the multiphase flow effect on sweep efficiency that is anticipated. The pressures were chosen to be above, below, and at the three-phase region. The Wasson stock tank oil has a minimum miscibility pressure of 1350 psia at the reservoir temperature of 105°F.

There are fifteen scheduled experiments listed in Table 10. Each experiment will be repeated to verify the reproducibility of the results. Additional experiments will be performed at the gravity-table injection rate based on the Hill[19] criteria.

D. MECHANISTIC STUDIES ON HIGH PRESSURE GAS/FOAM FLOW: EXPERIMENTAL

1. Introduction

After the preliminary experiments as detailed in the report by Heller, Kovarik, and Taber[32] were finished successfully, a new set of experiments was performed. In this study, the mechanisms associated with CO_2 permeability reduction were investigated in terms of microscopic heterogeneity, presence of an oil phase, surfactant concentration, injection method, and flow rate in secondary and tertiary miscible CO_2 floods.

The previous high-pressure micromodel apparatus was modified by installing a foam generator (2-in. diameter and 4-in. length, Berea sandstone). Figure 28 shows the schematic of the new high-pressure micromodel apparatus.

Four different pore structures, each with a different scale of heterogeneity, were used. The pore structures and pore-size distributions are shown in Figs. 29 a-d. The first two pore patterns were designed by Bahralolom[33] who also measured the pore-size distributions. The homogeneous model (HOM) is a patio-stone pattern with a low aspect ratio. The heterogeneous model (HET) was developed from a San Andreas carbonate thin section that has a preferential flow path at the center. Figure 29(b). Micromodel patterns and pore size distribution of heterogeneous model (HET).[33]

The HET model was modified to make model MDH (modified heterogeneous model). In this model the wide pores near the inlets to two preferential flow paths have been blocked. This higher aspect ratio at the inlet of model MDH promotes foam generation. The layered model (LAY) was developed in order to study both aspect ratio and layer effect with crossflow. The widest pore body layer has the highest permeability and the least resistance to flow. Table 11 shows the properties of these four pore networks.

A total of 34 displacements were performed at the conditions given in Table 12. Throughout the experiment, Alipal CD-128 was used as a foaming agent in a 1.0% NaCl brine solution. Foam was generated by three methods. First, a CO_2 phase was injected into a surfactant-saturated model. Second, CO_2 and surfactant were injected simultaneously into a brine or surfactant-saturated model. Foam was generated in-situ at the upstream side by these two methods. Finally, foams were pregenerated with a foam generator (2-in. diameter and 4-in. length, Berea sandstone) before injection into a micromodel. CO_2 flow rates between 10 ft/day to 120 ft/day were used in all displacements. In the displacements with oil, both secondary and tertiary floods were performed. In preparation for a secondary flood, the micromodel first was saturated with distilled water. This 100% water saturation was displaced by an oil phase until immobile saturation was reached (connate water saturation). The connate water saturation was around 10% for all runs. For a tertiary flood, the secondary flood fluid saturation initial condition ($\approx$ 10% connate water, $\approx$ 90% oil) was flooded by a water phase to achieve residual oil saturation ($\approx$ 30%-40% oil). Then the experiment commenced

TABLE 10

SCHEDULE OF COREFLOOD AND MICROCORE EXPERIMENTS FOR THE MULTIPHASE FLOW EFFECT ON SWEEP EFFICIENCY PROJECT

Run No.*	P (psia)	Flow Rate (cc/hr)
1	1100	1.5
2	1200	1.5
3	1250	1.5
4	1290	1.5
5	1350	1.5
6	1100	4.0
7	1200	4.0
8	1250	4.0
9	1290	4.0
10	1350	4.0
11	1100	10.0
12	1200	10.0
13	1250	10.0
14	1290	10.0
15	1350	10.0

*All runs will be conducted at 105°F.

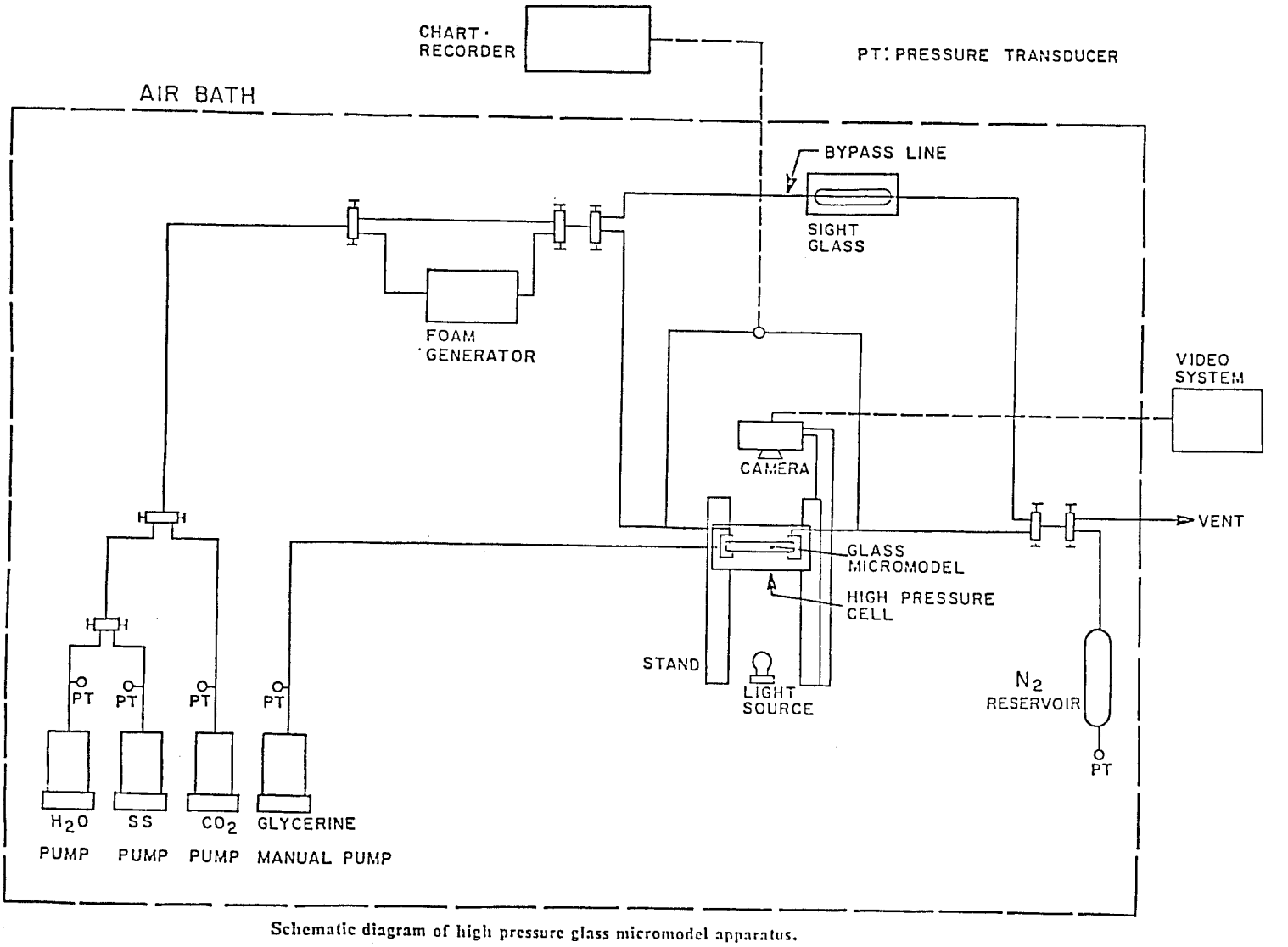

Schematic diagram of high pressure glass micromodel apparatus.

Figure 28. Schematic diagram of high-pressure glass micromodel apparatus

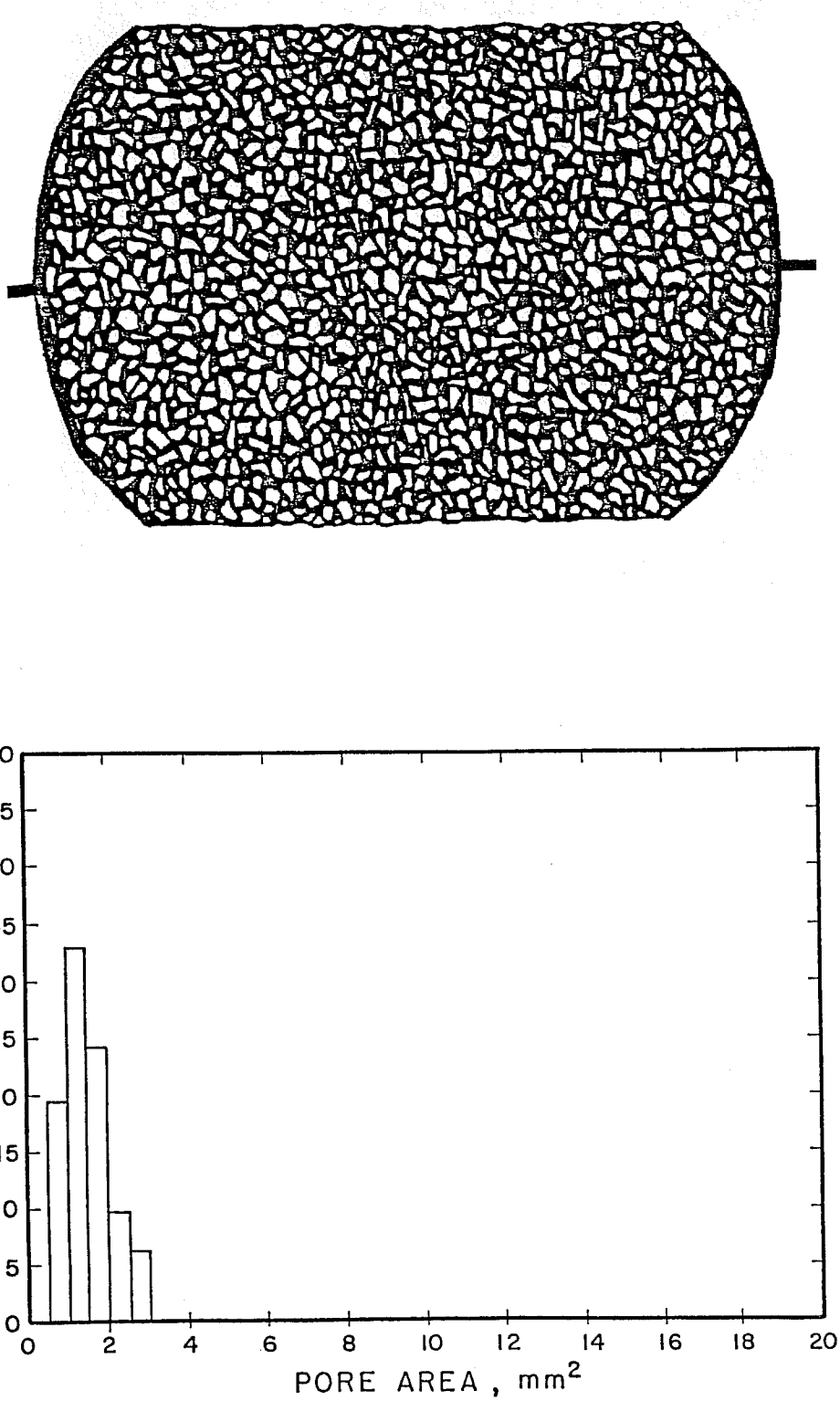

Figure 29(a). Micromodel patterns and pore size distribution of homogeneous model (HOM).[33]

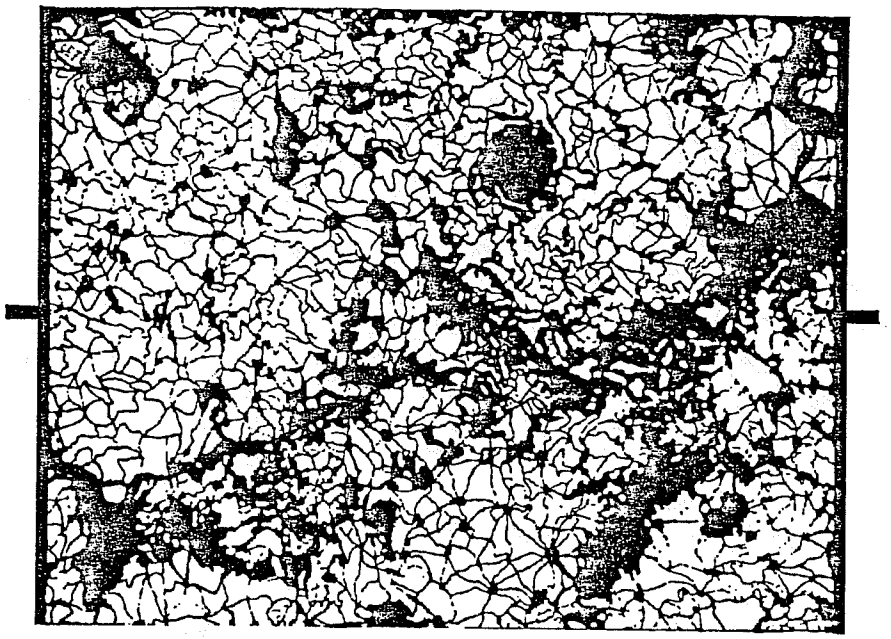

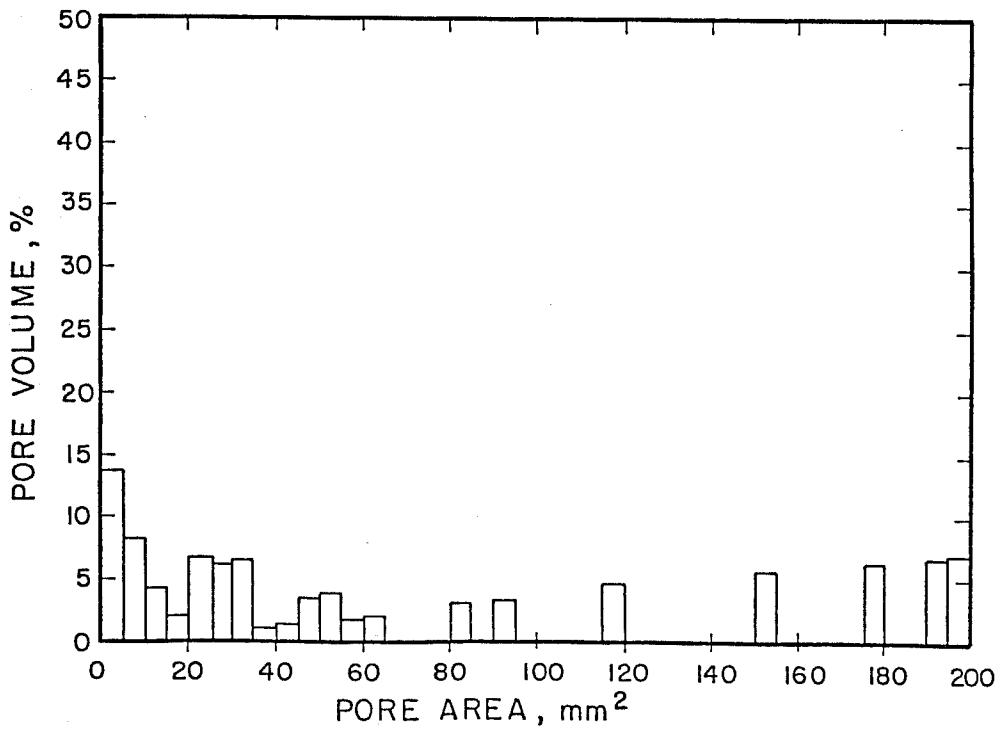

Figure 29(b). Micromodel patterns and pore size distribution of heterogeneous model (HET).[33]

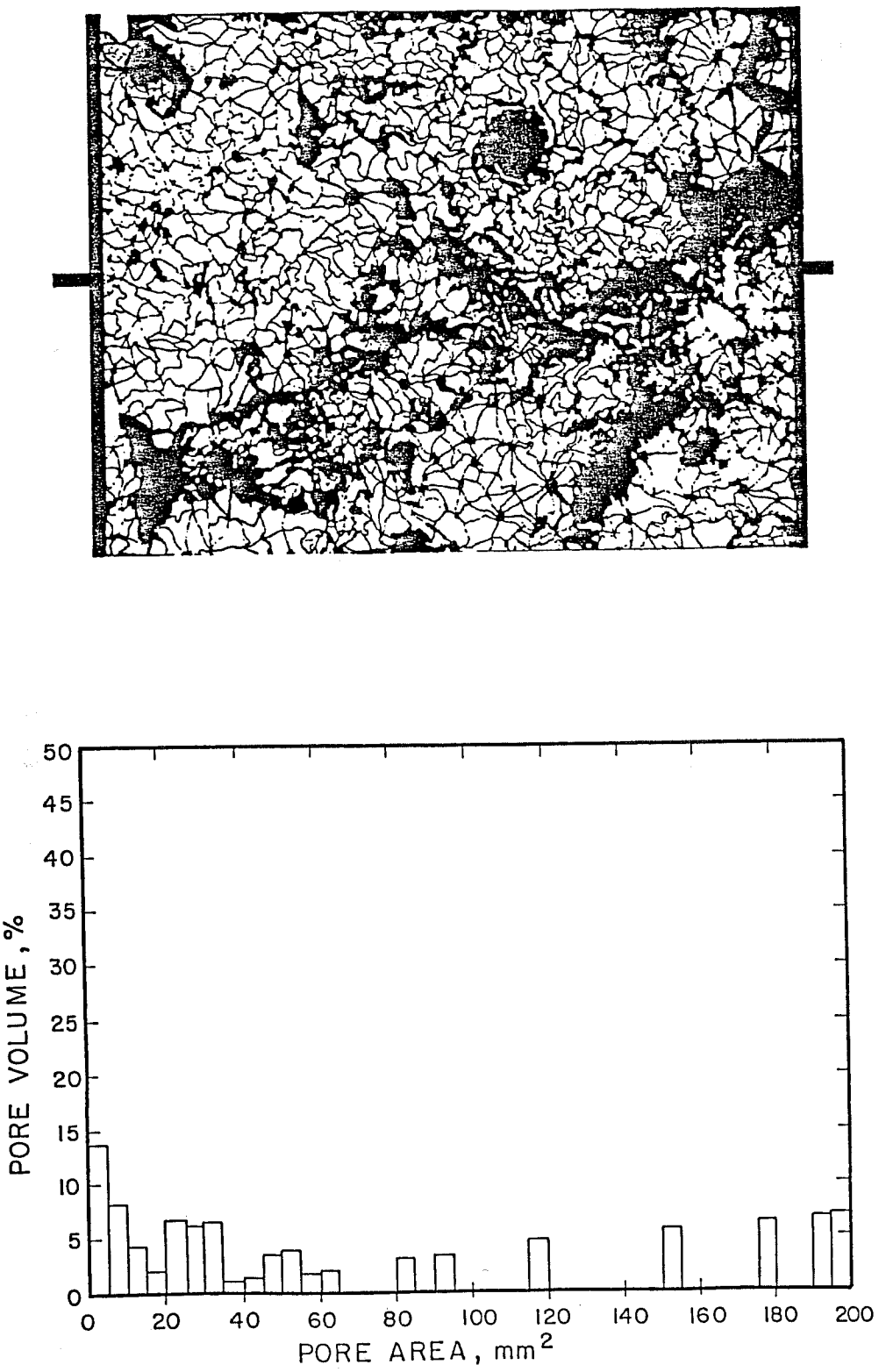

Figure 29(c). Micromodel patterns and pore size distribution of modified heterogeneous model (MDH).[34]

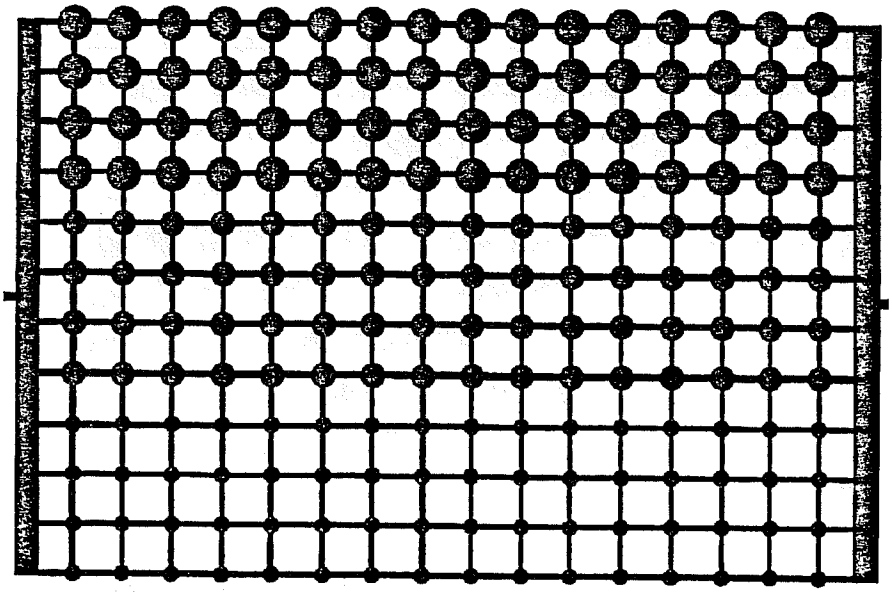

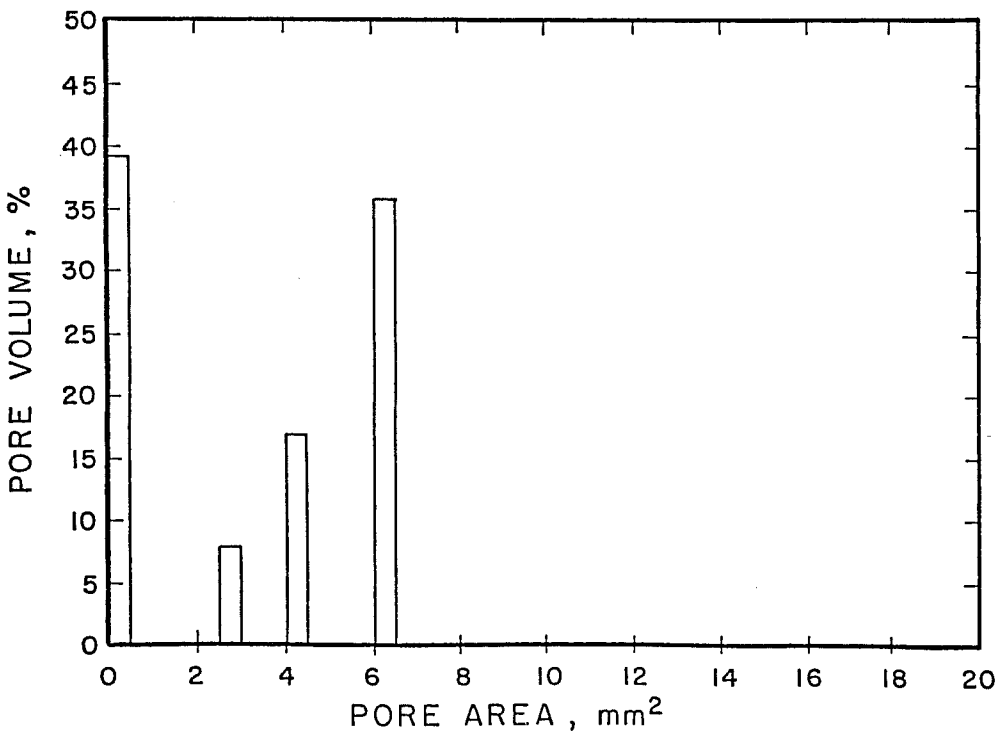

Figure 29(d). Micromodel patterns and pore distribution of layered model (LAY).[34]

TABLE 11. PROPERTIES OF PORE NETWORKS

Micromodel	Length (cm)	Width cm	Pore Volume (cc)
Homogeneous model (HOM)	5.7	4.3	0.12
Heterogeneous model (HET)	6.8	5.0	0.15
Modified Heterogeneous model (MDH)	6.8	5.0	0.23
Layered model (LAY)	6.4	4.1	0.12

TABLE 12. SUMMARY OF FLOW VISUALIZATION EXPERIMENTS

Run # (model-)	Injection mode	Surf. Conc. (wt%)	Q_{CO_2} (ft/D)	Initial Saturation
HOM-1	P	0.0	10	Brine
HOM-2	P	0.1	10	SS
HOM-3	P	1.0	10	SS
HOM-4	P	5.0	10	SS
HOM-5	P	1.0	60	SS
HOM-6	P	1.0	120	SS
HOM-8	S	1.0	10	M@Swc
HOM-9	S	1.0	10	M@Sor
HOM-10	S	1.0	10	R@Swc
HET-1	P	0.0	10	Brine
HET-2	P	0.1	10	SS
HET-3	P	1.0	10	SS
HET-4	P	5.0	10	SS
HET-5	P	1.0	50	SS
HET-7	S	1.0	10	SS
HET-8	S	1.0	10	R@Swc
MDH-1	P	0.0	10	Brine
MDH-4	P	5.0	10	SS
MDH-5	P	1.0	60	SS
MDH-7	S	1.0	10	SS
MDH-8	S	1.0	10	M@Swc
MDH-9	S	1.0	10	M@Swc
MDH-10	S	1.0	10	R@Swc
LAY-1	P	0.0	10	Brine
LAY-2	P	1.0	10	SS
LAY-3	P	5.0	10	SS
LAY-4	P	0.1	10	SS
LAY-5	P	1.0	60	SS
LAY-6	P	1.0	120	SS
LAY-7	S	1.0	10	SS
LAY-8	S	1.0	10	M@Swc
LAY-9	S	1.0	10	M@Sor
LAY-10	S	1.0	10	R@Swc
LAY-11	F	1.0	10	M@Swc

P = Single phase pure CO_2 injection
S = Simultaneous injection of CO_2 and surfactant solution
SS = Surfactant solution
M = Maljamar crude oil
R = Refined oil (Soltrol)
F = Pregenerated foam
Swc = Connate water saturation
Sor = Residual oil saturation

P = 1320 psia
T = 90°F
Surfactant: Alipal-CD128

and CO_2 and surfactant solution were injected simultaneously into the micromodel. Fluid properties are given in Table 13. The pressure drop was measured with a Honeywell STD120 pressure transducer, which has an accuracy of 0.005 psia. Temperature was maintained at 90° ± 0.1°F to give an accurate flow rate. The displacements were videotaped, which enabled us to review the results extensively and to identify the physical mechanisms associated with foam flow.

2. Experimental Results and Discussion

a. Mechanisms Associated with In-situ Foam Generation and Propagation

In our flow visualization study, two primary mechanisms were shown to be main causes of foam generation: snap-off and bubble subdivision. Previous investigators[35,36] have observed bubble generation by snap-off at the bubble generation site and bubble subdivision at branching pores. The foam generation sites here refer to a pore structure which has a certain aspect ratio (pore-body to pore-throat ratio). Roof[35] calculated the minimum distance that a non-wetting phase must advance before snap-off can occur in a toroidal constriction. This minimum distance is 7.07 times the pore-throat radius at static conditions. For dynamic conditions, this distance is expected to be smaller. This type of snap-off mechanism is called downstream snap-off because bubbles are generated only at the exit of the constriction. Downstream snap-off is illustrated in Fig. 30.

For bubble generation by downstream snap-off to occur, the following requirements must be satisfied.[37] First, the porous medium must be a water-wet system, and sufficient surfactant solution must be available at the bubble generation site. Second, the wetting phase should backflow to generate a collar at the pore constriction. Third, a high pressure drop must be present so that the non-wetting phase can invade the bubble generation site.

A different type of snap-off mechanism also was observed in our study. When a slug of surfactant solution is injected into a CO_2 swept zone, the surfactant solution flows along the wall of the pore body. Then this wetting phase (surfactant solution) pinches off the nonwetting phase (gas) at the leading edge of the surfactant solution. This type of snap-off mechanism is called upstream snap-off. Bubbles generated by upstream snap-off are usually larger than bubbles generated by downstream snap-off. A minimum aspect ratio is not a necessary condition for the upstream snap-off mechanism. The majority of upstream snap-off occurrences took place in the preferential flow path in the heterogeneous model. Figure 31 shows the upstream snap-off mechanism through an open channel.

It should be noted that when the nonwetting phase (CO_2) is injected into the wetting-phase-saturated (surfactant solution) porous medium, most snap-off occurs by the downstream snap-off mechanism. Simultaneous injection of CO_2 and surfactant solution results in upstream snap-off.

Bubble subdivision at branching pores is another generation mechanism we observed in this investigation. Large bubbles are subdivided into smaller bubbles at both the inlet and outlet of branching pores (see Figs. 32 and 33). Bubble division at the inlet of the branching pores occurs when the flow velocity in one channel is much lower than that in the other channel. When a large bubble approaches the branching pores, it stretches into both channels, and is then pinched off by the following bubble at the branch point. Smaller bubbles continue to be generated as this process is repeated until the channel is completely blocked. For bubble subdivision to occur at the outlet of branching pores, both channels should be flowing at a similar velocity. The bubbles in one channel pinch off the bubbles in the other channel. This is illustrated in Fig. 33. Bubble subdivision is a less frequent and less effective foam generation mechanism than snap-off.

TABLE 13. PROPERTIES OF THE FLUIDS

Fluid	Density (gm/cc)	Viscosity (cp)
CO_2 (1320 psia, 90°F)	0.743	0.064
Maljamar crude oil	0.813	3.3
Soltrol™ + Red Dye	0.748	1.45
Alipal CD-128 (1.0%)	≈1.0	≈1.0

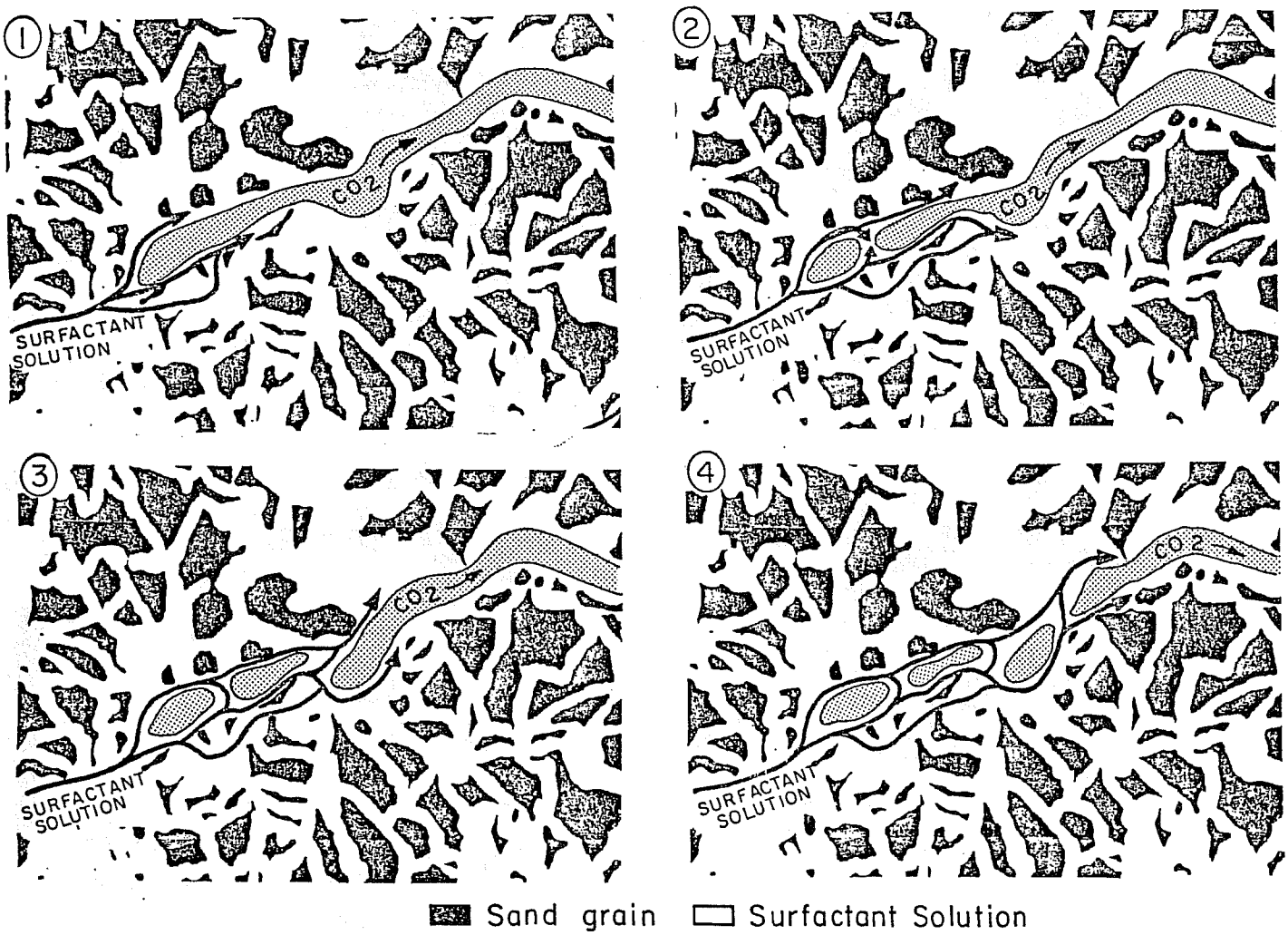

Figure 30. Downstream snap-off mechanism.

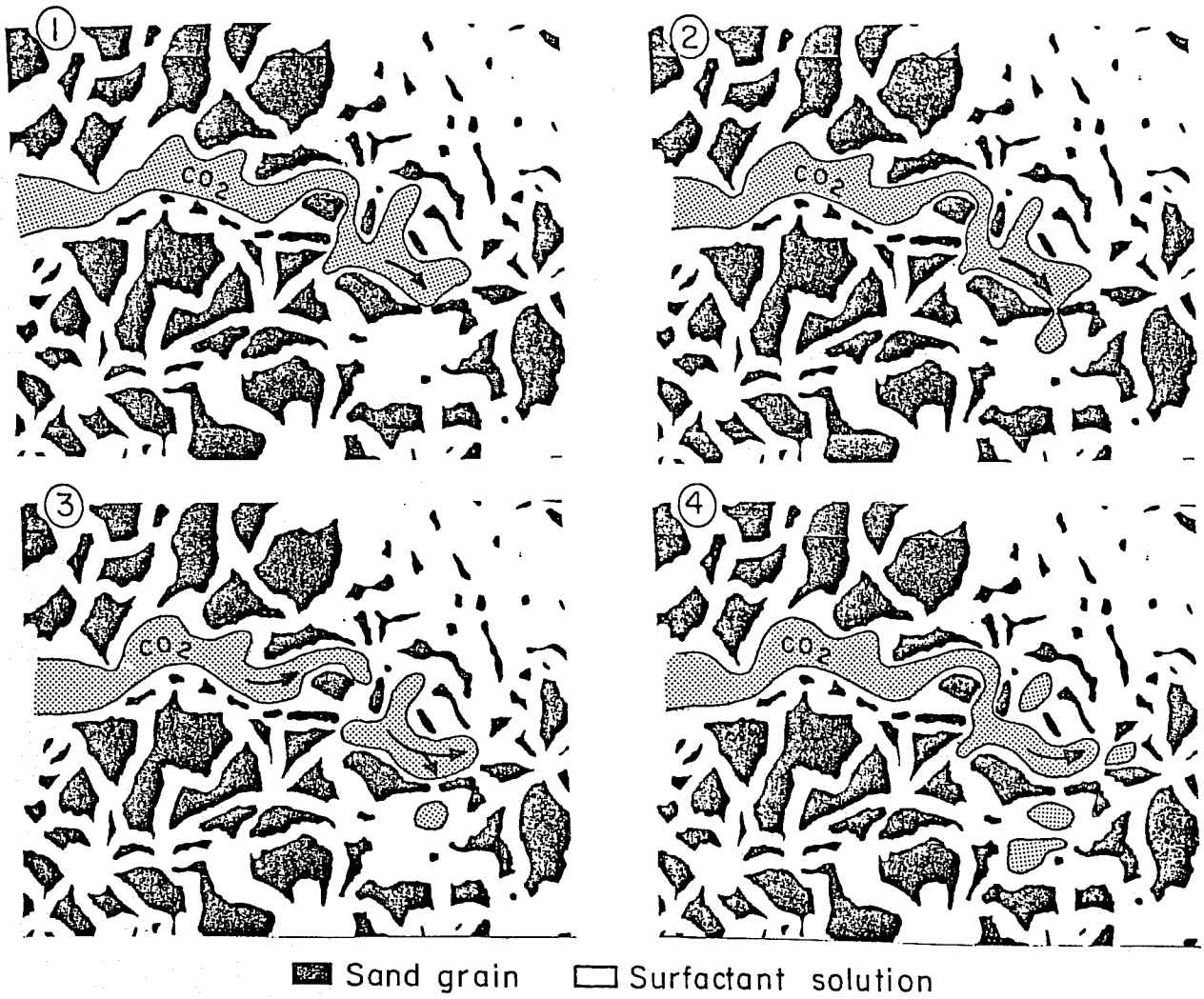

Figure 31. Upstream snap-off mechanism.

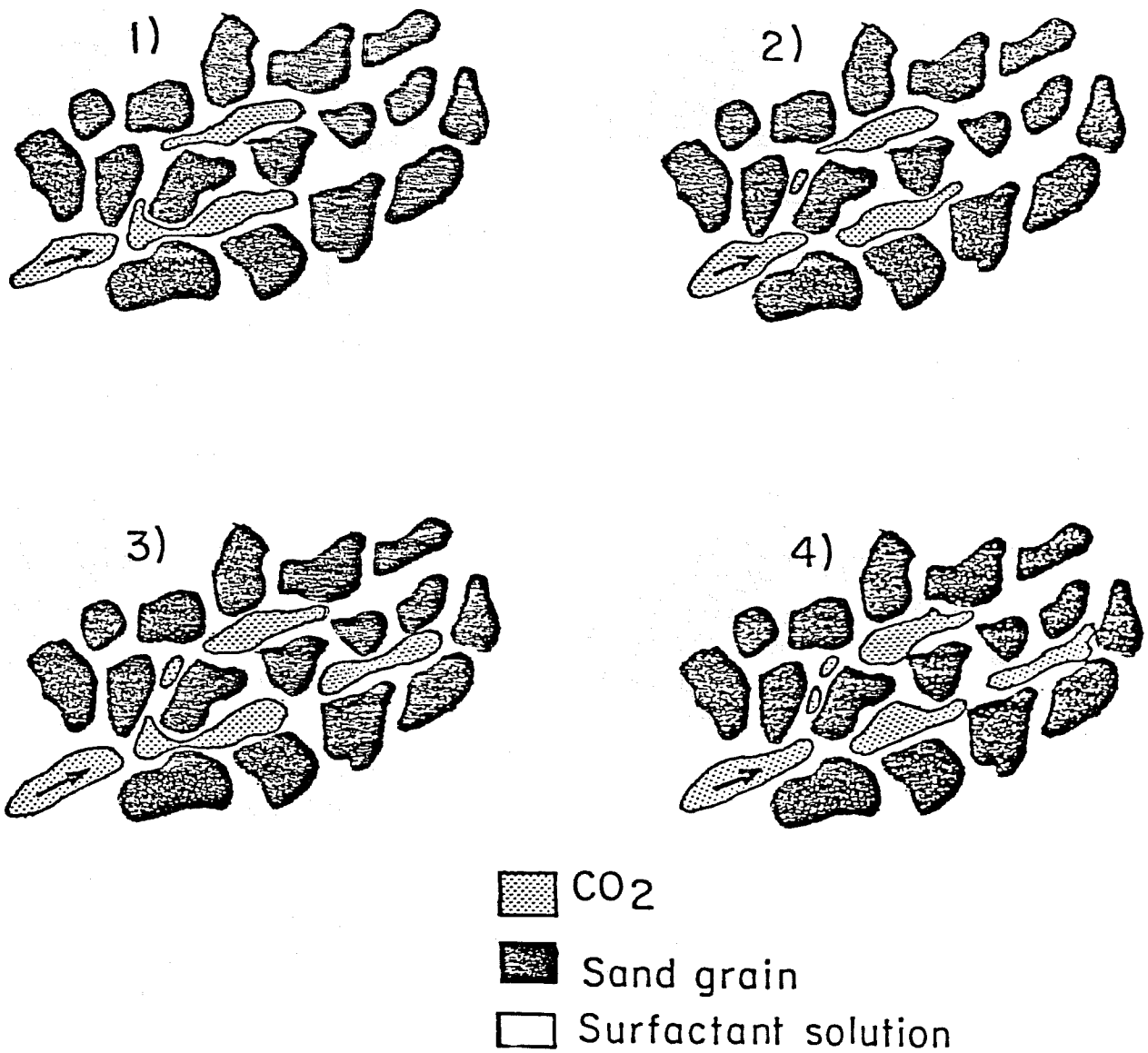

Figure 32. Upstream bubble subdivision mechanism.

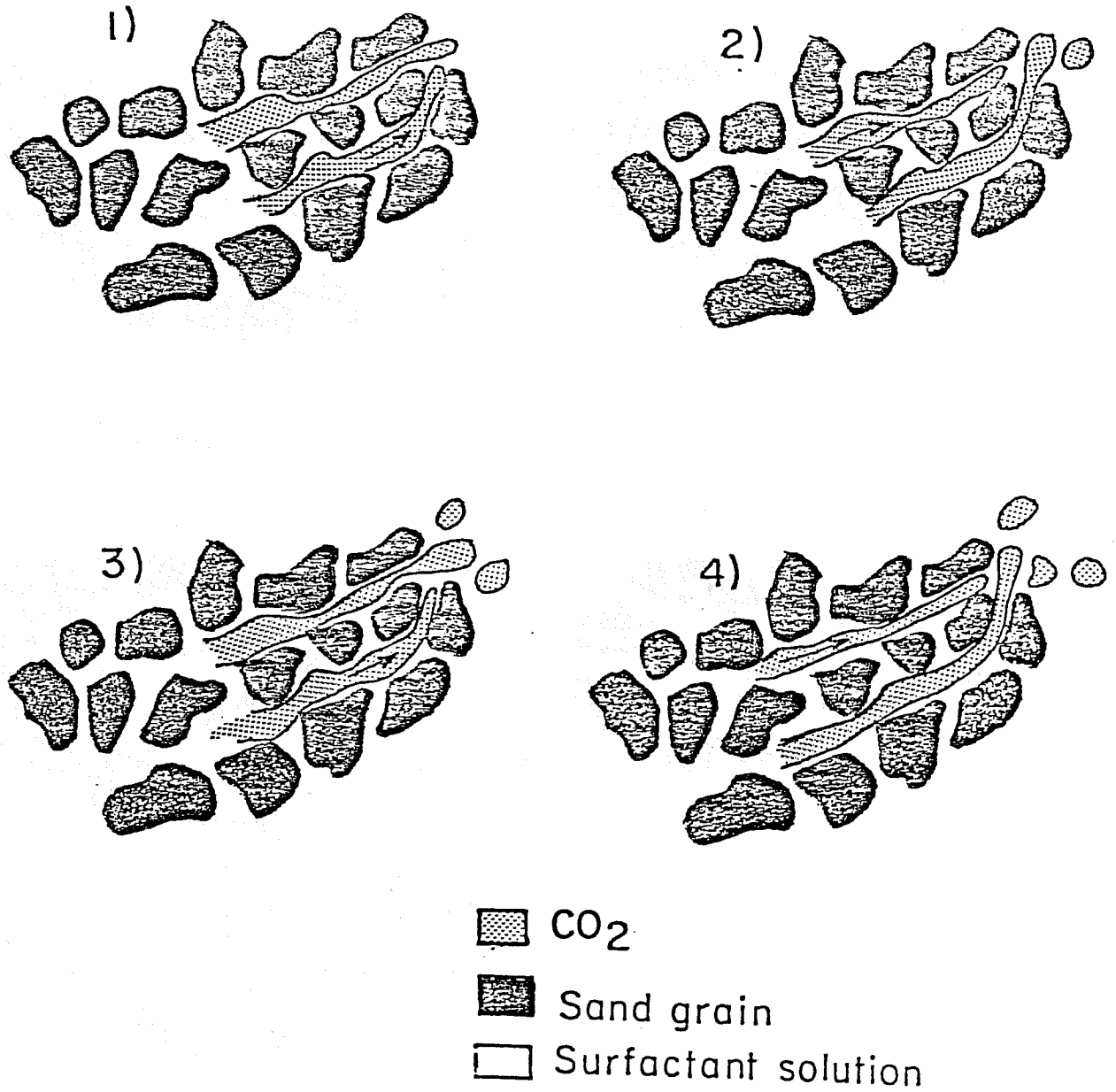

Figure 33. Downstream bubble subdivision mechanism.

Foam generation is a function of pore structure. In the homogeneous model, downstream snap-off was not present because of the pore network's low aspect ratio. Only liquid-phase lamellae were generated and propagated by upstream snap-off or crossflow (Fig. 34). Both foam bubbles and lamellae were generated and propagated (Fig. 34) in the heterogeneous models, more so in the modified heterogeneous model (MHE).

In the layered model, small stable bubbles were generated in the pore space with the higher aspect ratio, while lamellae were generated in the layer with the lowest aspect ratio. In any micromodel, continued collapse of small bubbles into larger bubbles can make lamellae. The density of lamellae per unit length generally is much smaller than the density of bubbles. Foam generation increases when CO_2 and surfactant solution are injected simultaneously, as compared to single-phase, pure CO_2 injection. The mixing of pore space fluids and the pore body/pore throat aspect ratio are the most important factors in foam generation. The degree of heterogeneity determines, to a large degree, the mixing among CO_2, surfactant solution, and oil phases.

Pregenerated foam, on the other hand, is quite different from in-situ foam. The size of pregenerated foam bubbles generally is quite small, and the bubble density, which depends on the type of foam generator, is great. Bubbles created at the exit of the foam generator, which in our case is Berea sandstone, are on the order of 10 microns, the average pore size of the rock.

When bubbles are stable, they can be propagated for long distances without breaking, and they coalescence in high-permeability channels. Unstable bubbles collapse easily and become continuous phase. However, at the next foam generation site, new bubbles can be formed if sufficient wetting phase is available (breaking and reforming process).

Lamellae present in the homogeneous model appeared to be more stable than those present in the heterogeneous model (HET). The surfactant-solution films which are propagated in the heterogeneous model are stretched because of the constantly changing pore radius; thus they burst easily over short distances. While in the homogeneous model, a uniform pore radius enables the lamellae to travel over much longer distances. As the lamellae or bubbles continue to accumulate in the model, flow of CO_2 eventually will be diverted into alternate flow paths.

b. Parametric Studies

1) Effect of Microscopic Heterogeneity

The mixing and flow behavior of CO_2/foam in porous medium depends on the heterogeneity of the pore structure. It has been reported that gas-phase mobility reduction in the presence of foam is a strong function of the absolute permeability of the porous medium. In this section, recovery efficiencies at three pore volumes injected CO_2 (PVI CO_2) were compared in different pore structures. Two injection methods were used to observe the differences between single-phase CO_2 injection into the surfactant-solution-saturated model and simultaneous injection of CO_2 and surfactant solution into the oil-saturated model.

a) Injection of Pure CO_2 into a Surfactant-Solution-Saturated Model

In these experiments, single-phase CO_2 injection into four different models saturated with surfactant solution will be compared (Displacement models-4 as shown in Table 12).

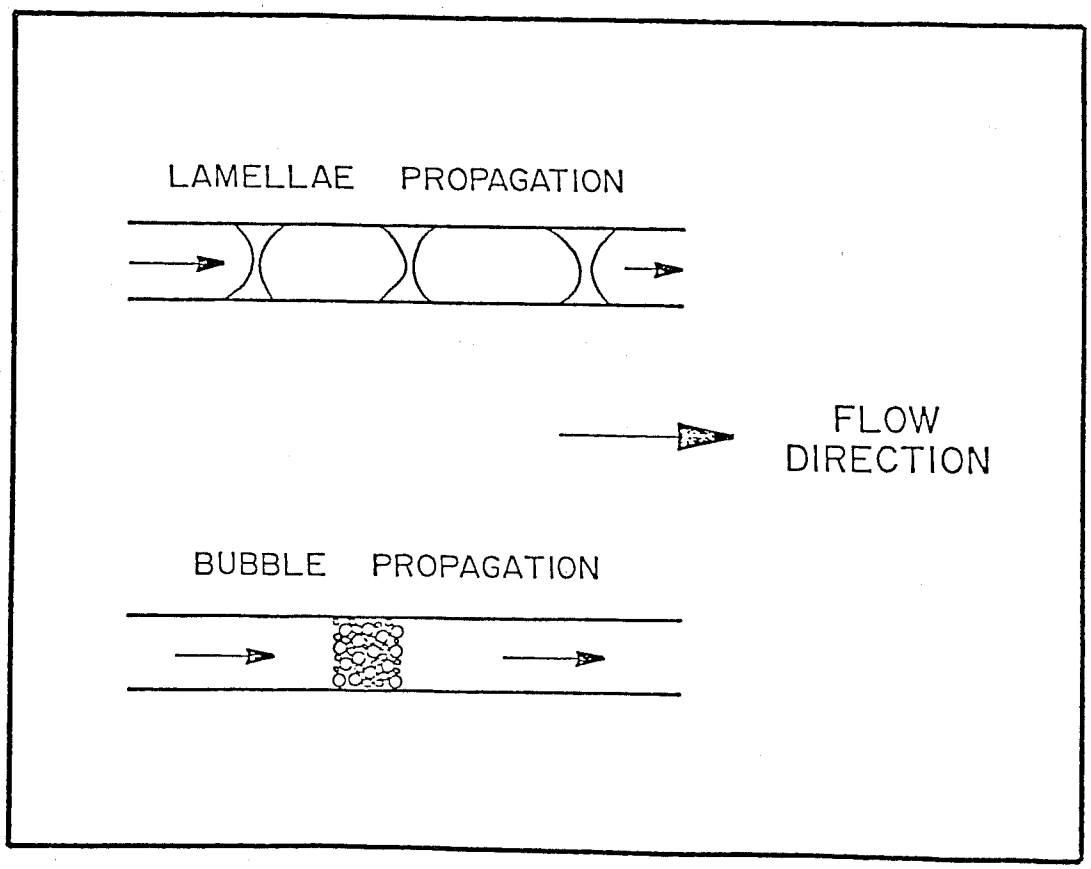

Figure 34. Lamellae and bubble propagation methods.

Single-phase CO_2 injection in the homogeneous model (HOM) exhibited the lowest recovery. In the homogeneous model, each edge of the model is more permeable than the rest of the area because of the slight difference in etching depth. When the CO_2 was first injected, the two edges of the model were swept immediately, leaving the large middle region unswept (see Fig. 35). However, when CO_2 injection was continued, lamellae were generated and a portion of the flow was diverted into the center region. Because the aspect ratio was near unity and most of the wetting phase was already displaced in the swept zone, no foam was generated.

The heterogeneous model (HET) has a large preferential flow channel, so CO_2 moved preferentially through this zone. Although a few bubbles and lamellae were generated, they were not sufficient for zone blocking. Continued injection of CO_2 slightly improved the sweep efficiency (Fig. 36); however, in general, foam generation in this heterogeneous model was disappointing. Either wetting-phase saturation or tighter pore constrictions upstream in the model was needed for better performance.

The highest recovery efficiency was obtained in the modified heterogeneous model (MDH). As shown in Fig. 37, foam generation and fluid diversion both worked very well in this model. Even very small pores were swept at 0.5 PV of CO_2 injected. A wide distribution of pore sizes and a high-aspect ratio promote a better mixing between CO_2 and surfactant solution, hence the generation of more bubbles. One small change, i.e., pore constriction at the inlet, makes a dramatic difference. This foam generation site with a high-aspect ratio is necessary for the downstream snap-off mechanism to occur.

It may be possible to apply these results to the reservoir. For example, if the reservoir has a large fracture similar to the HET model, either surfactant solution and CO_2 should be injected simultaneously or else pregenerated foam should be injected in order to obtain blockage and fluid diversion. When continuous CO_2 is injected into a small slug of surfactant solution, most of the wetting phase is displaced in the fracture and little or no foam is generated. Hence no formation plugging will be obtained, at least at these laboratory-length scales.

The final model that we used in this investigation was a layered model consisting of three communicating zones, each with a different permeability. The recovery efficiency in this model was better than that observed in the homogeneous model but not as good as that observed in the modified heterogeneous model. As CO_2 flowed into the most permeable zone, several bubbles (lamellae) were generated in the first few pores (Fig. 38). Immediately thereafter, CO_2 flow was diverted to the middle layer of that model, with gas breakthrough occurring through this flow channel. With continued injection of CO_2, several pore necks perpendicular to the flow direction were blocked by small bubbles (lamellae). Crossflow between layers was seldom observed. The layered model is a homogeneous model with a higher aspect ratio than the model HOM. Consequently, good bubble and lamellae generation was observed, and most of the model was swept rather uniformly.

b) Simultaneous Injection of CO_2 and Surfactant Solution in the Presence of Crude Oil

In these experiments, CO_2 and 1.0% surfactant solution were injected simultaneously at a ratio of 4/1 into the crude-oil-saturated model (Displacement models-8 as shown in Table 12). Although the surfactant concentration was lower here than in the case with single-phase CO_2 injection (where it was 5.0%), better foam generation and sweep efficiency were obtained in all four micromodels. This improved performance with simultaneous injection is caused by the increased mixing of phases and the continuous supply of the wetting phase. The oil displacements are shown in Figs. 39-42 for the four different micromodels.

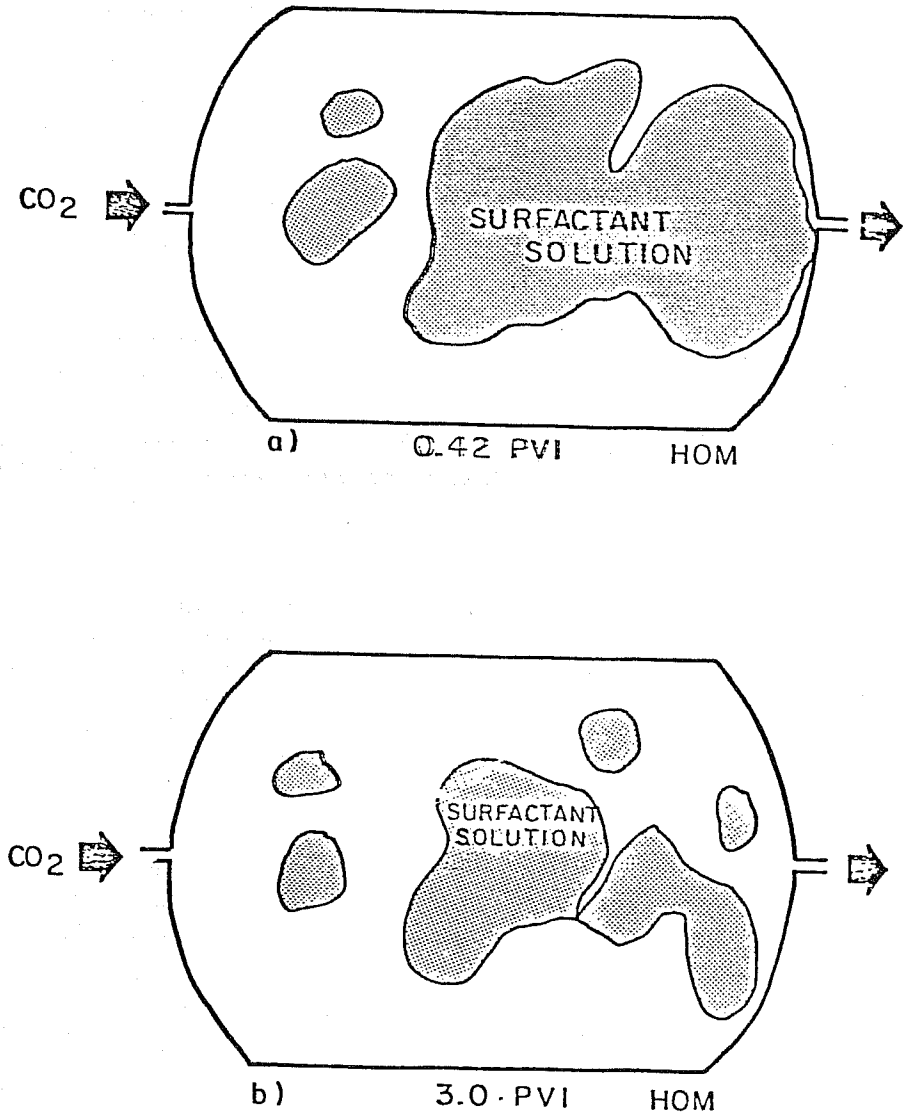

Figure 35. Surfactant solution saturation vs. pore volumes of CO_2 injected for displacement model HOM-4: a) 0.42 PVI, b) 3.0 PVI.

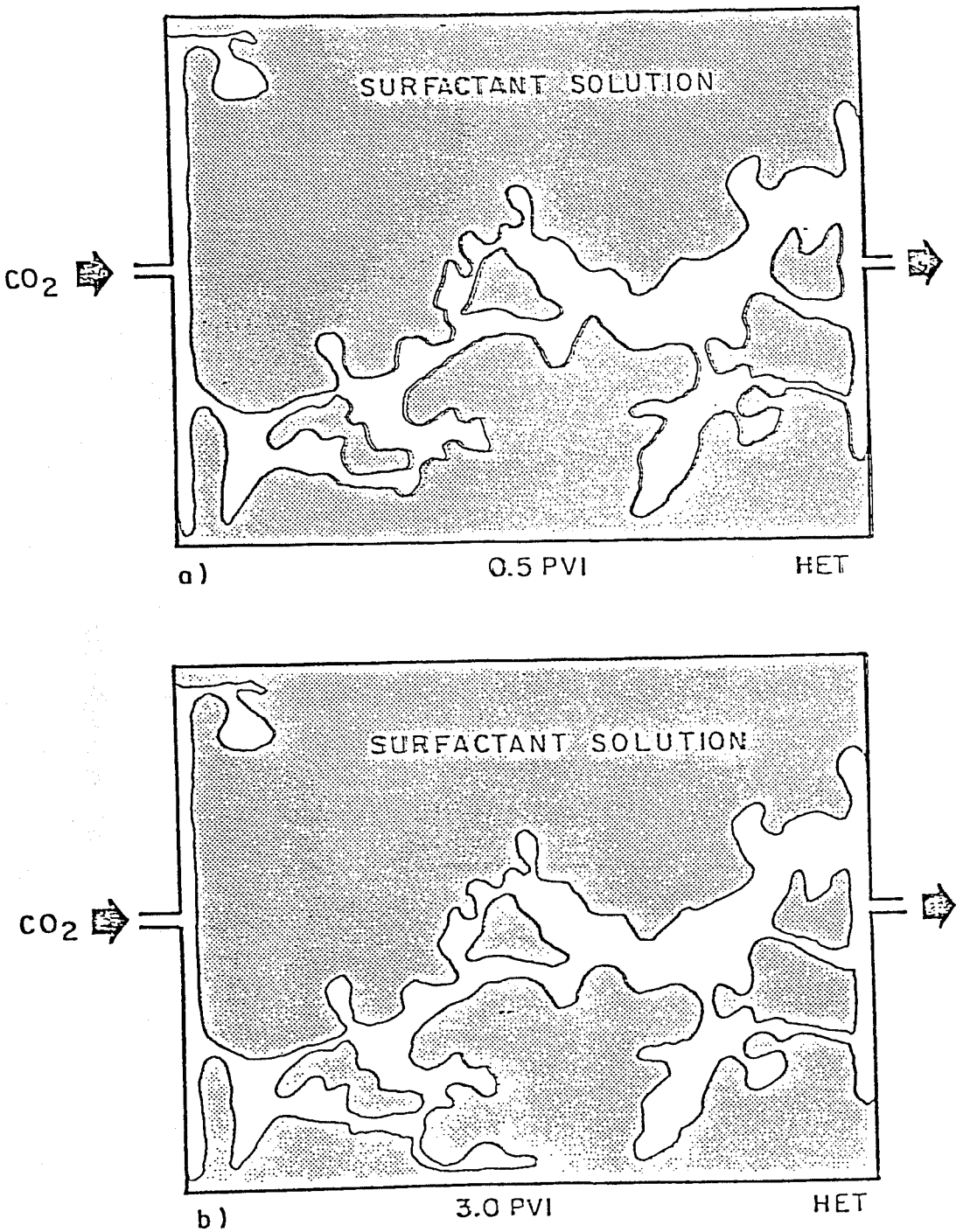

Figure 36. Surfactant solution saturation vs. pore volumes of CO_2 injected for displacement model HET-4: a) 0.5 PVI, b) 3.0 PVI.

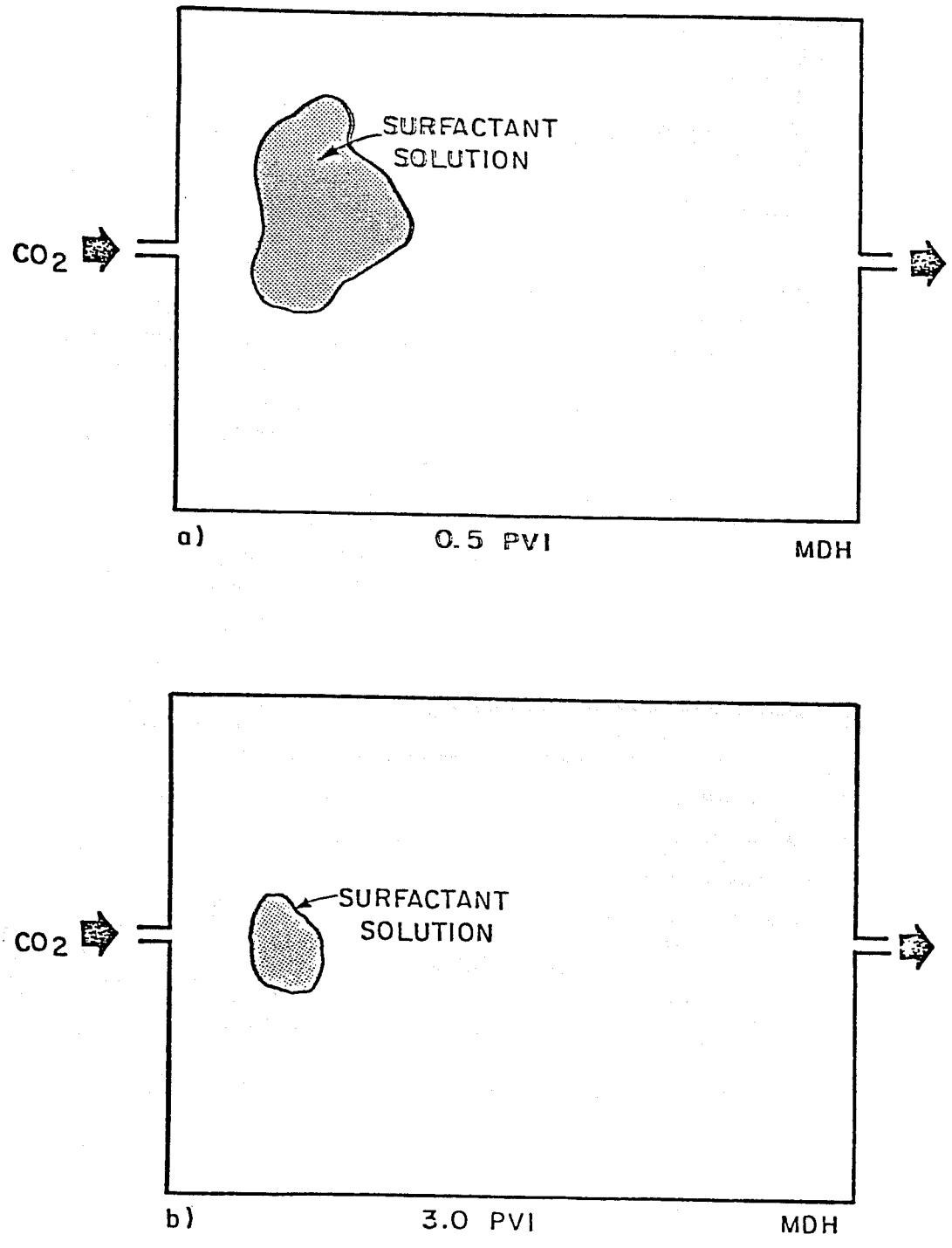

Figure 37. Surfactant solution saturation vs. pore volumes of CO_2 injected for displacement model MDH-4: a) 0.5 PVI, b) 3.0 PVI.

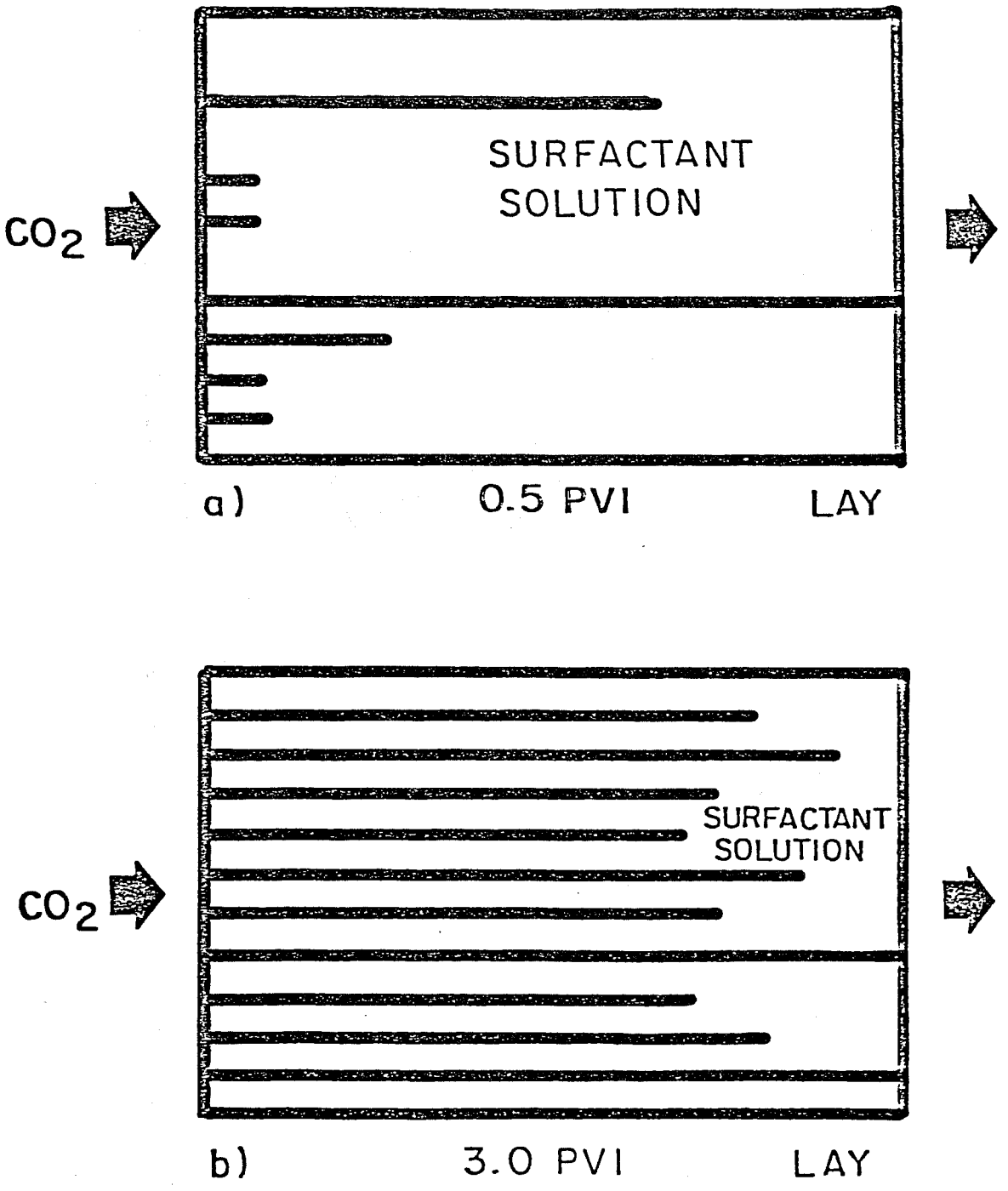

Figure 38. Surfactant solution saturation vs. pore volumes of CO_2 injected for displacement model LAY-4: a) 0.5 PVI, b) 3.0 PVI.

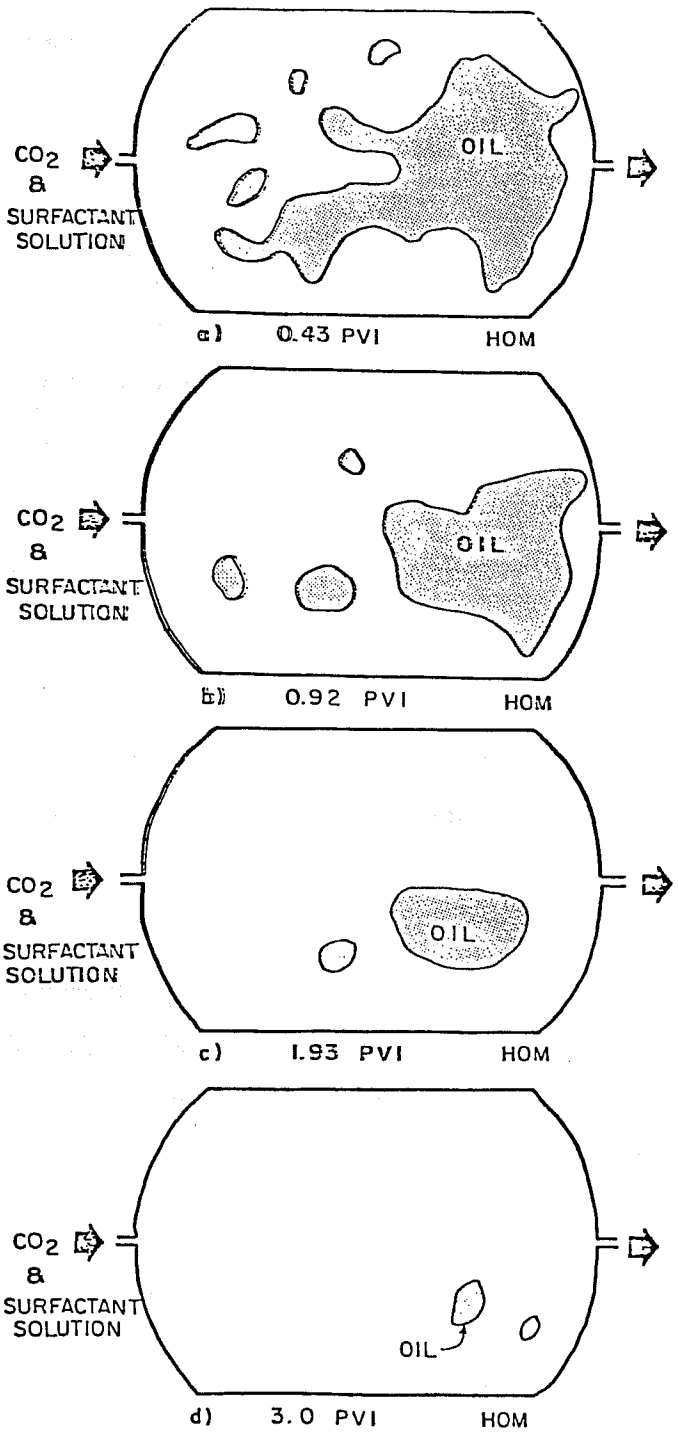

Figure 39. Oil saturation vs. pore volumes of CO_2 injected for displacement model HOM-8: a) 0.43 PVI, b) 0.92 PVI, c) 1.93 PVI, d) 3.0 PVI.

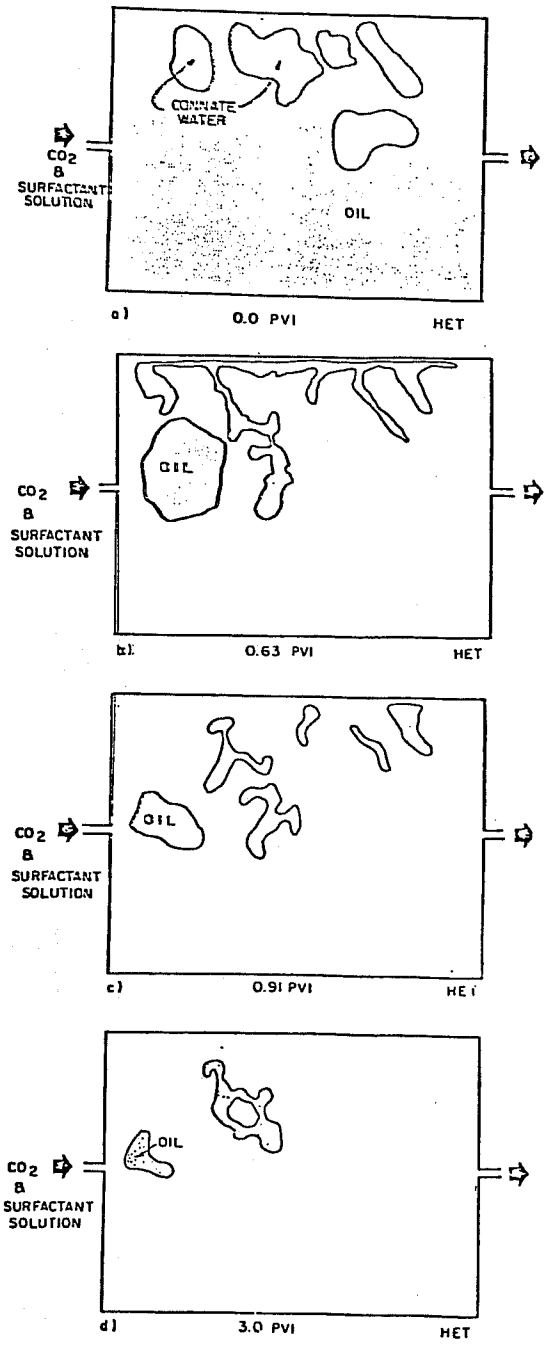

Figure 40. Oil saturation vs. pore volumes of CO_2 injected for displacement model HET-8: a) 0.0 PVI, b) 0.63 PVI, c) 0.91 PVI, d) 3.0 PVI.

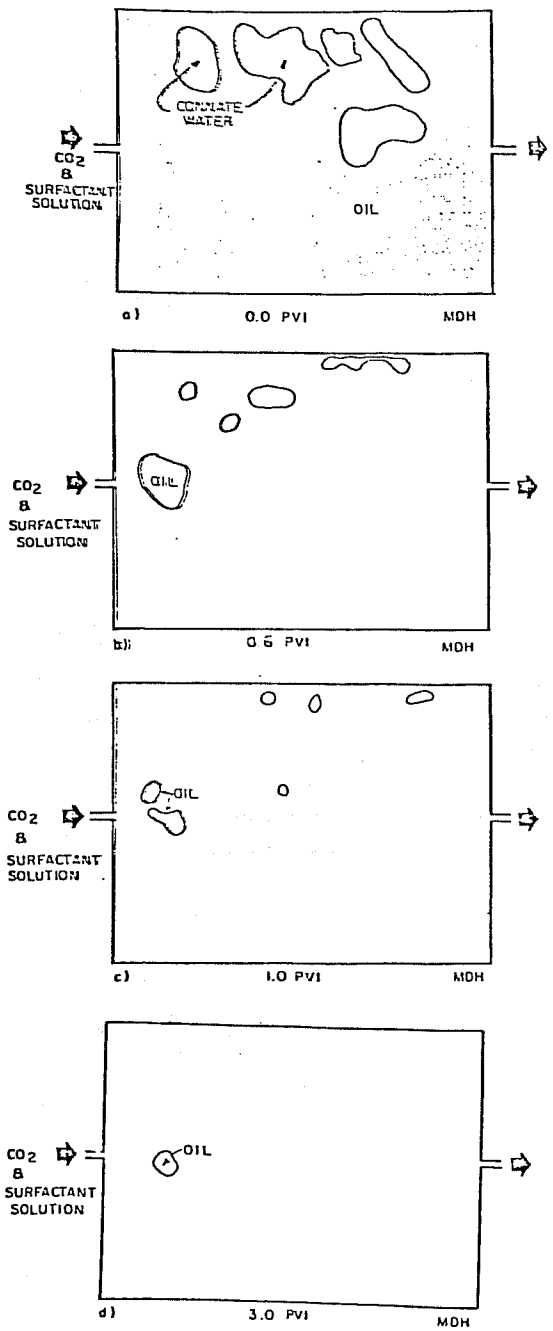

Figure 41. Oil saturation vs. pore volumes of CO_2 injected for displacement model MDH-8: a) 0.00 PVI, b) 0.6 PVI, c) 1.0 PVI, d) 3.0 PVI.

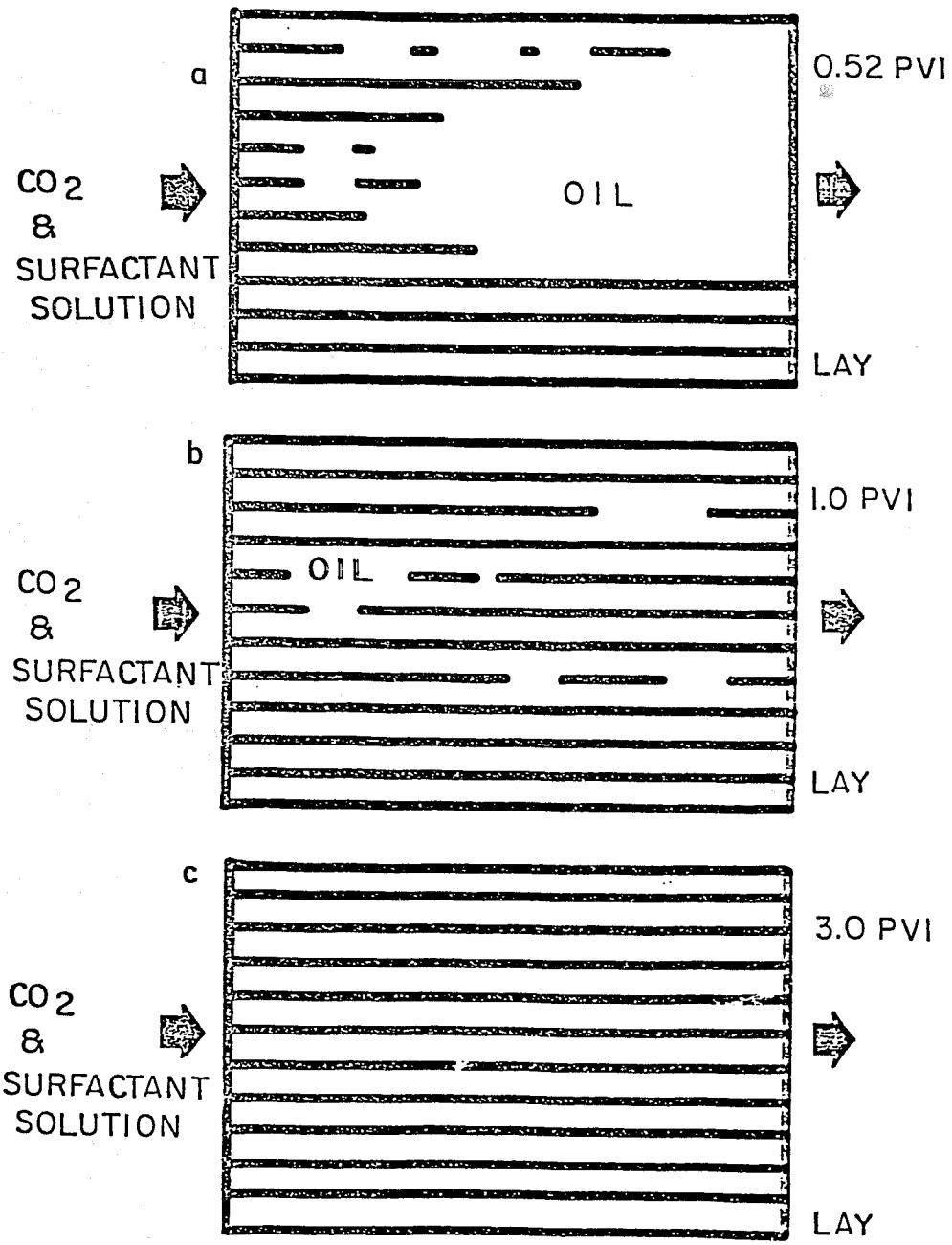

Figure 42. Oil saturation vs. pore volumes of CO_2 injected for displacement model LAY-8: a) 0.52 PVI, b) 1.0 PVI, c) 3.0 PVI.

When CO_2 and surfactant solution were injected into the homogeneous model, the increased mixing and continuous supply of surfactant solution produced a low density of bubbles by upstream snap-off and additional lamellae. As a result, recovery efficiency was increased around 18% over the single-phase injection case (Fig. 39).

In the heterogeneous model (HET), a much greater sweep efficiency was obtained with simultaneous injection into an oil saturation (Fig. 40) than in the case of single-phase CO_2 injection into a surfactant-solution saturation (Fig. 36). This is primarily caused by two-phase flow (increased mixing) with CO_2 and surfactant solution in the preferential flow paths. The smallest difference between single phase and simultaneous injection was observed in the modified heterogeneous model because simultaneous injection is not necessary where there is a wide range of pore sizes and high upstream aspect ratio (Fig. 41).

In the layered model (LAY), the two highest permeability layers were blocked because of increased bubble density. The least permeable layer was then swept and CO_2 breakthrough occurred through this tightest zone. With continued injection of CO_2 and surfactant solution, fluids would start flowing through tortuous paths with repeated flow direction reversal caused by localized foam blockage. Crossflow between layers was a typical mechanism for fluid diversion.

Figure 43 shows the recovery efficiencies as a function of heterogeneity coefficient. This heterogeneity coefficient is the coefficient of variation (CV) of the pore size distribution. $CV = s/\bar{x}$ where s is the standard deviation and $\bar{x}$ is the mean of the pore area. The coefficient of variation for the homogeneous model is 0.381, for the modified heterogeneous model it is 0.954, and for the layered model it is 0.800.

As shown in Fig. 43, increasing variation coefficient and aspect ratio result in higher sweep efficiency because of better mixing and more foam generation. Also shown is the effect of injection mode. The sweep efficiencies in simultaneous injections are always higher than those in single-phase injections. The effect of heterogeneity in simultaneous injections is less pronounced than in single-phase injections.

The effect of different injection methods is indicated in Fig. 44. Upstream snap-off is the primary mechanism for bubble or lamellae generation in the heterogeneous model. In this model, there is a preferential flow path (microfracture). When single-phase CO_2 was injected into a surfactant-solution-saturated model, a very low density of bubbles and lamellae was generated, not enough for preferential flow path blockage. On the other hand, simultaneous injection increased the mixing of CO_2 and surfactant solution, hence recovery efficiency was greatly improved because of the high-permeability channel blockage.

Figure 45 illustrates the importance of the upstream aspect ratio (flow inlet to preferential flow path). This figure compares the recovery efficiency of single-phase CO_2 injection into the surfactant-solution-saturated heterogeneous and modified heterogeneous models. The upstream aspect ratio in the heterogeneous model is approximately unity, which precludes downstream snap-off. But the modified heterogeneous model has an upstream aspect ratio of around 14, which enables the generation of a high density of small bubbles. Differences in upstream aspect ratio have a great impact on the overall recovery efficiency. The high density of bubbles generated at the inlet portion of the modified heterogeneous model was mainly responsible for the blockage of the preferential flow path. As a result, the gas (CO_2) phase was diverted into the tight matrix and even very small pores were swept.

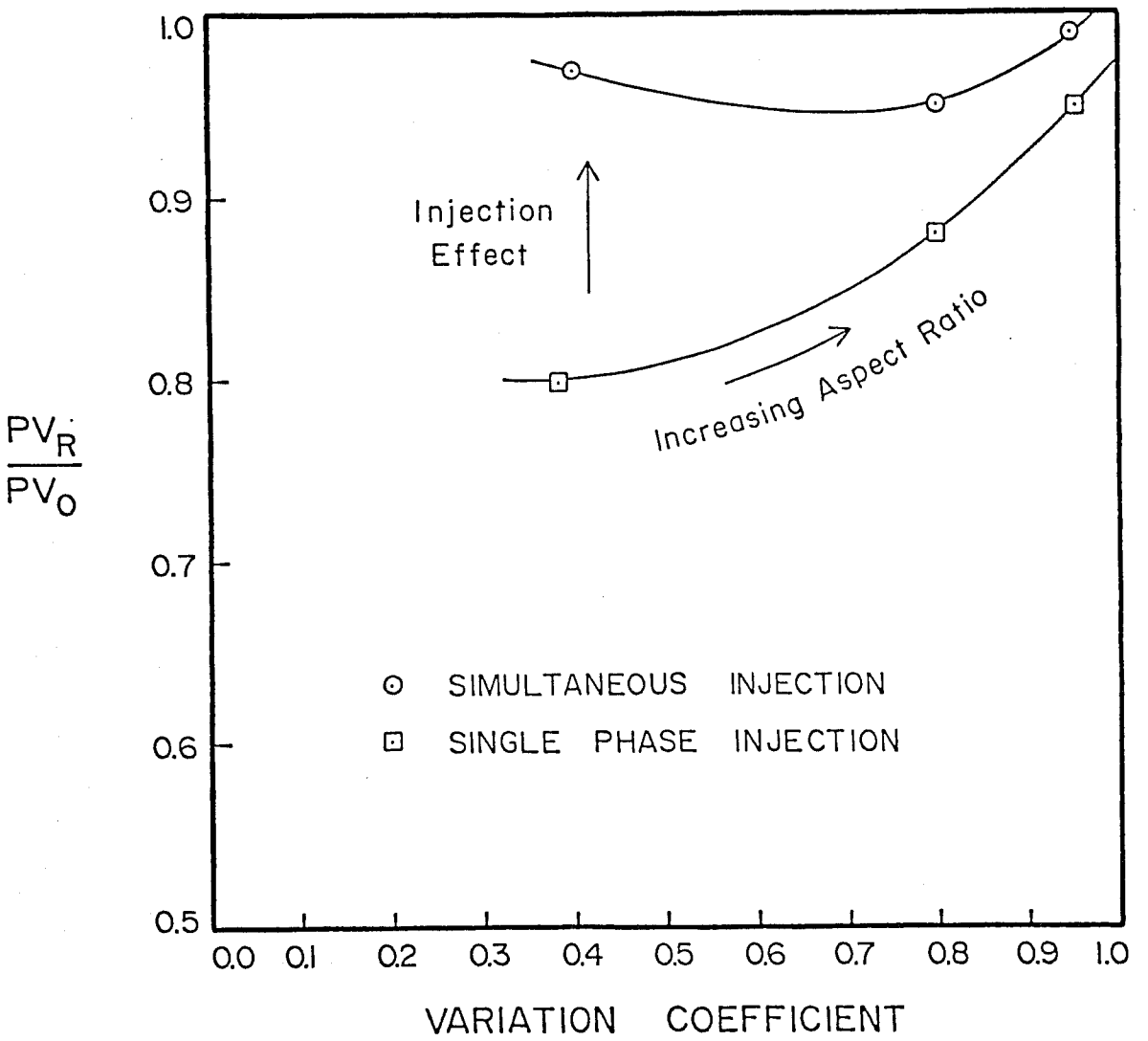

Figure 43. Recovery efficiency as a function of heterogeneity coefficient, aspect ratio, and injection mode. PV_R/PV_0 = pore volumes recovered/initial pore volume.

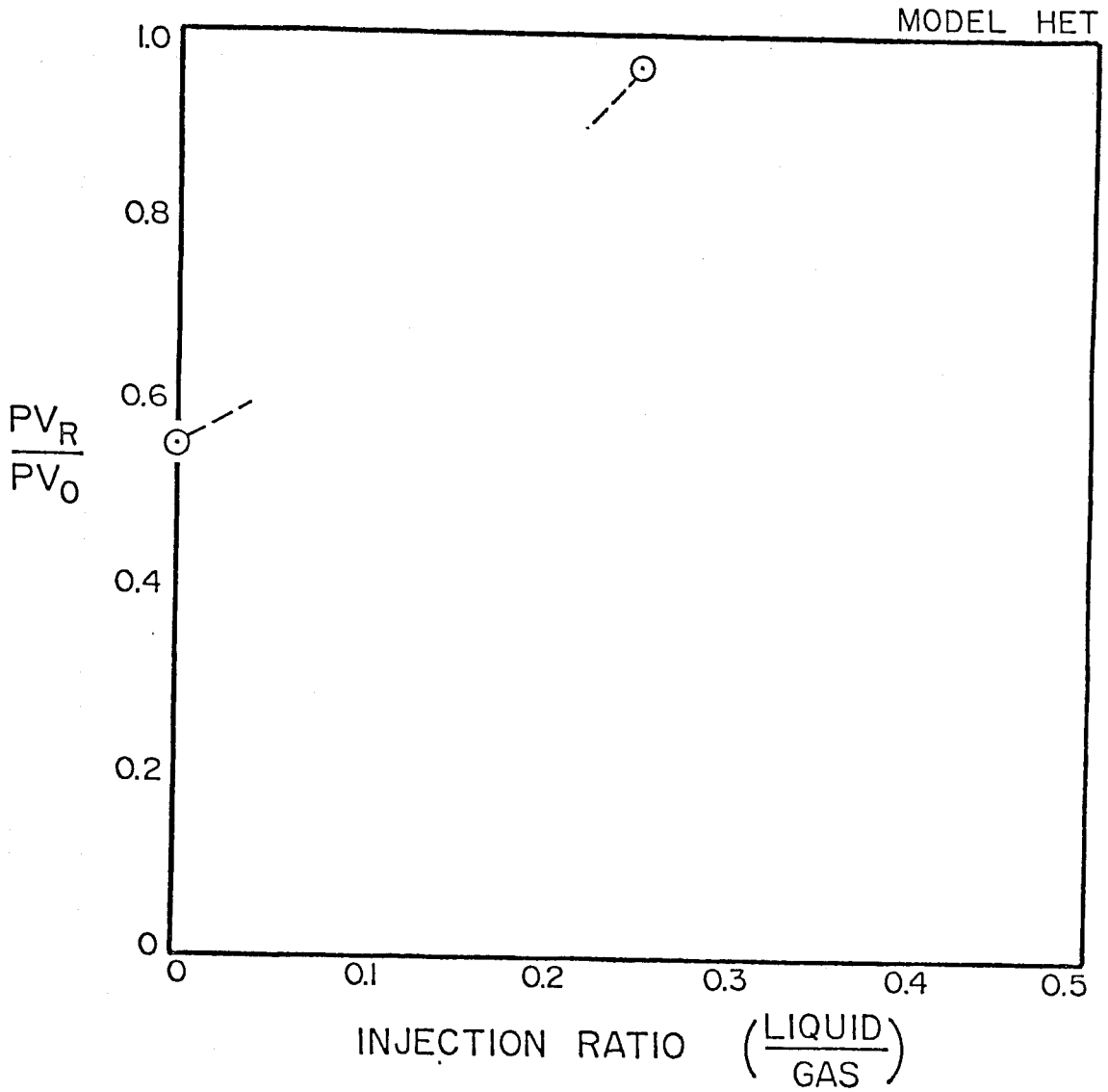

Figure 44. Recovery efficiency as a function of injection ratio. PV_R/PV_0 = pore volumes recovered/initial pore volume.

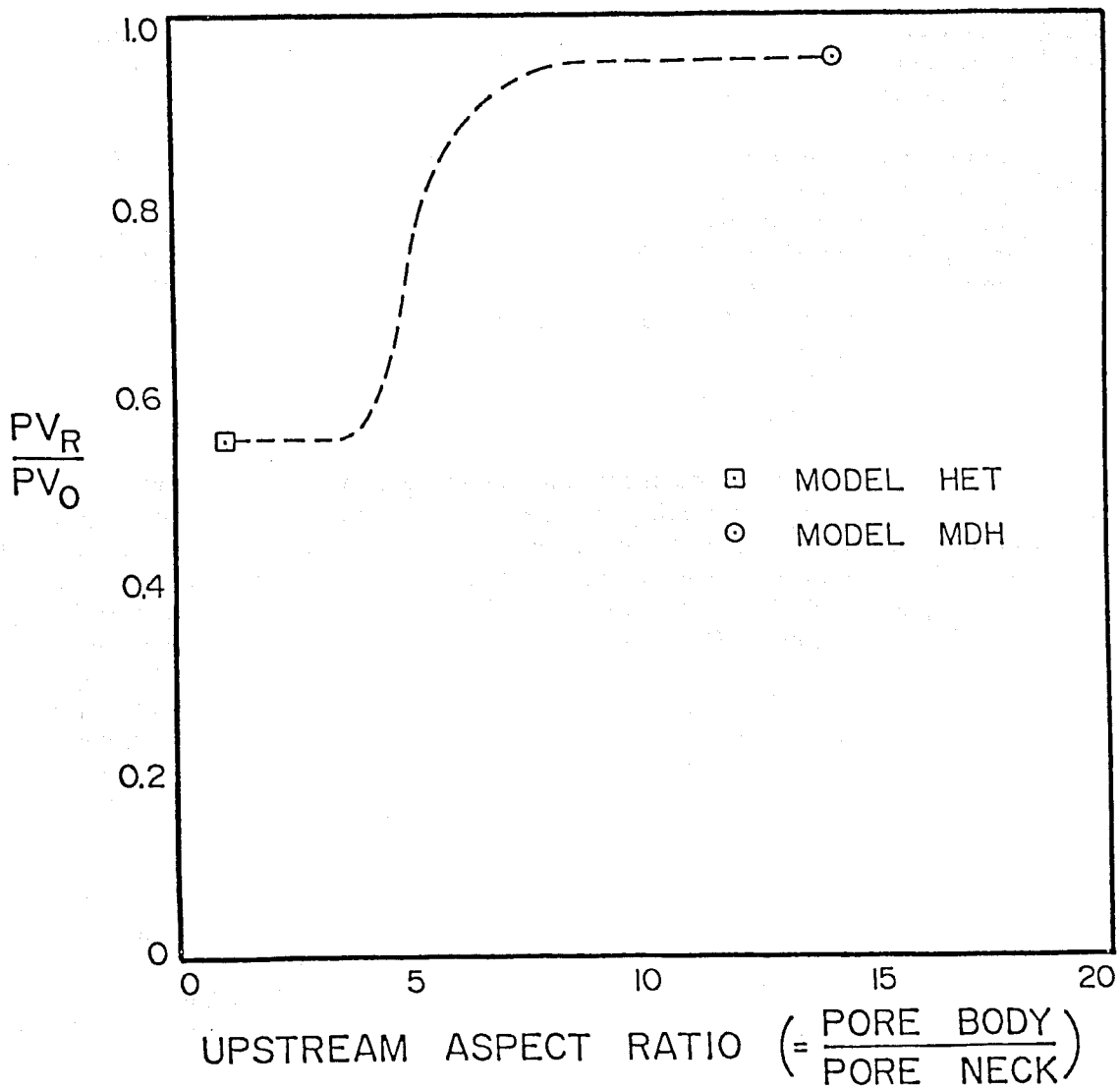

Figure 45. Recovery efficiency as a function of upstream aspect ratio. PV_R/PV_0 = pore volumes recovered/initial pore volume.

2) Comparison of In-Situ Foam and Pregenerated Foam

Generation of foam bubbles depends mainly on the mixing between gas and surfactant solution caused by the pore structure and injection mode. In this study, foams are pregenerated through a 2-in. x 4-in. Berea sandstone foam generator. Berea sandstone provides excellent foam generation sites. Most of the foam probably is generated at the exit of the core because the end face serves as an infinite aspect ratio pore structure. The major difference between in-situ foam and pregenerated foam is the number and size of the bubbles. Pregenerated foam bubbles are on the order of the rock pore size. The in-situ generated macro emulsion of CO_2, surfactant solution, and oil, which will be explained in the next section, contains bubbles similar in size to the pregenerated foam and has a flow behavior much like pregenerated foam.

The pressure drop in a pregenerated foam experiment is much higher than that in an in-situ foam generation experiment, and it shows a plateau after about two pore volumes of foam are injected. A comparison of pressure drop data obtained in experiments using in-situ and pregenerated foam is shown in Fig. 46. This figure also shows the recovery efficiency. The displacement by pregenerated foam is a piston-like displacement caused by the high bubble density. Only about one pore volume of foam was required to displace all the original fluid in the model.

3) Presence of Oil Phase

The presence of an oil phase in a porous medium affects the foam flow in two ways: it causes surfactant loss because of partitioning into the oil phase, and it changes the properties of foam that comes in contact with the oil. As expected, we observed that foam generation and stability are adversely affected by an oil phase. Foam bubbles coalesced or ruptured and foam generation was inhibited when foaming agents flowed into an oil zone. This could be beneficial for systems with a preferential flow channel, i.e., under flow conditions that could occur in some open fractures.

When CO_2 bubbles enter a preferential flow path that already has been swept of oil, a high pressure drop is generated and the zone is blocked. Fluid flow is diverted toward the less permeable oil-saturated region. Here CO_2 bubbles contact the oil phase in the less permeable zone and collapse, and the CO_2 becomes the continuous phase with the oil recovery process now being dictated, to a large degree, by CO_2/oil phase behavior.

The effect of the oil phase, however, is complicated by the generation of micro- and macroemulsions of CO_2-saturated oil and surfactant solution. Refined oil (Soltrol) generated more microemulsion than crude oil; microemulsions were not observed in the absence of the oil phase. Whenever a microemulsion existed in the glass micromodel, CO_2-foam generation was enhanced, probably because the emulsion prevents contact between CO_2 and the oil phase. With the simultaneous injection of CO_2 and surfactant solution into Maljamar crude oil, very fine black particles were observed. These were considered asphaltene precipitates caused by the CO_2/crude oil interaction. Excellent fluid diversion was obtained in the presence of microemulsions of CO_2-saturated oil and surfactant solution.

Simultaneous injection of surfactant solution and CO_2 into the micromodel saturated with Soltrol generated substantially more foam than the same injection into the Maljamar crude-oil-saturated model. The better foam generation with Soltrol is verified by the higher pressure drop as shown in Fig. 47 using the modified heterogeneous model.

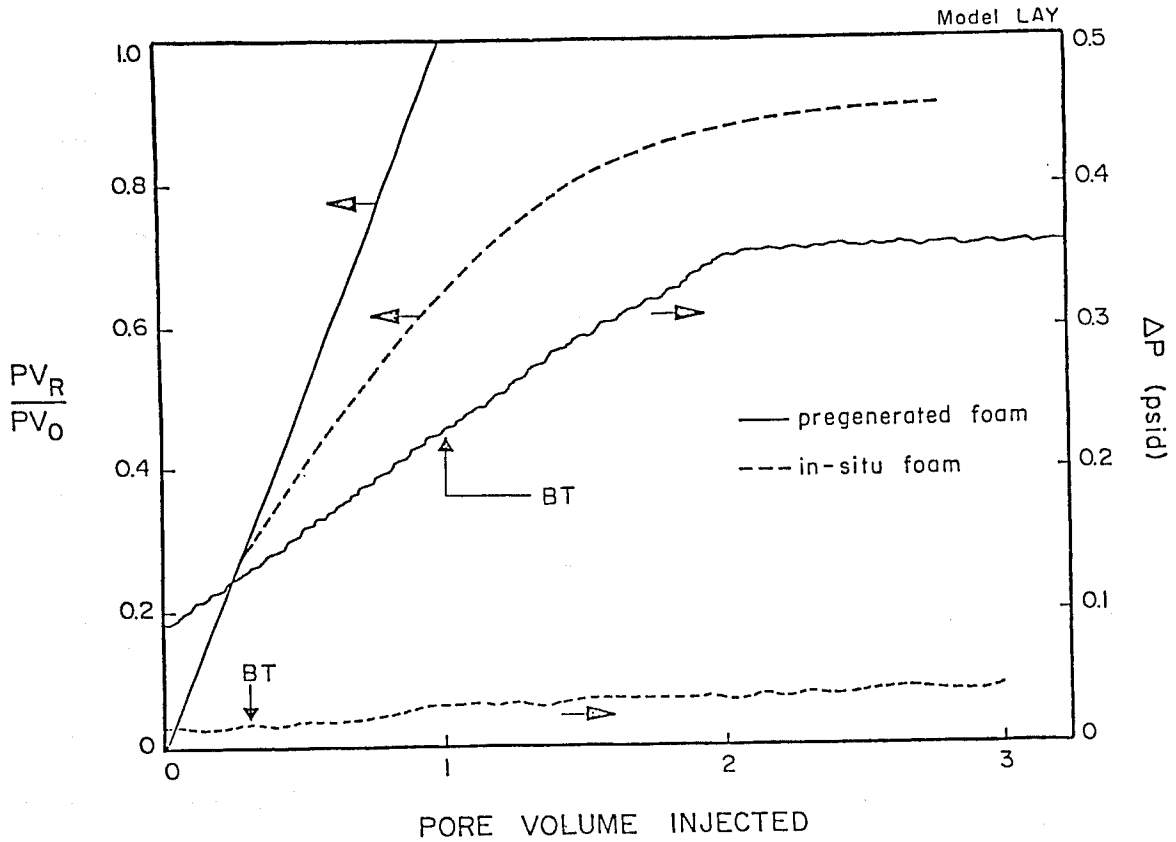

Figure 46. Comparison of in-situ and pregenerated foam recovery efficiency. (BT means breakthrough)

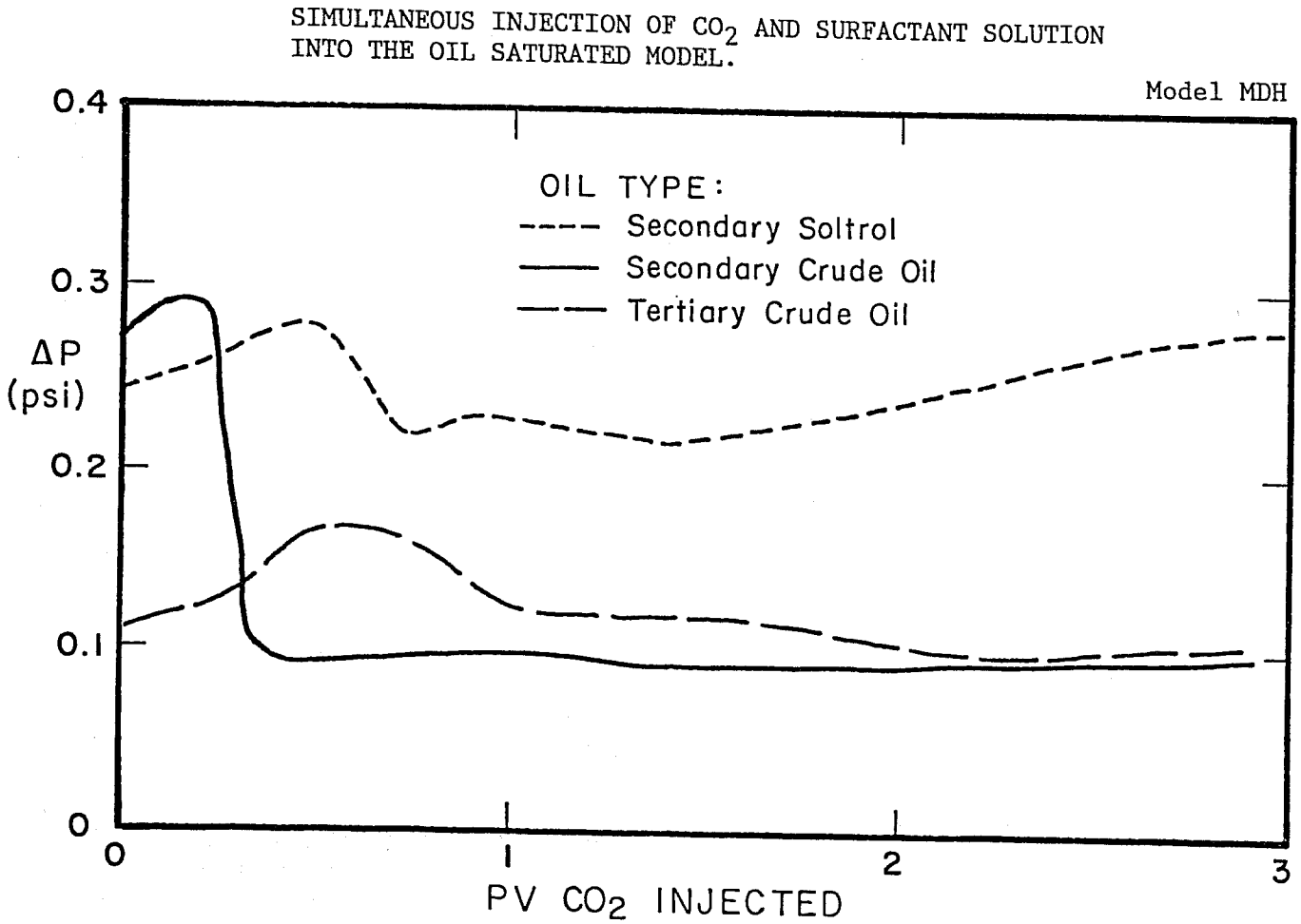

Figure 47. Effect of oil type on foam mobility, pressure drop vs. pore volumes of CO_2 injected.

Figure 48 shows a comparison of pressure drops in secondary and tertiary floods. During a secondary flood, foam was generated by simultaneous injection of surfactant and CO_2 into an oil-saturated model with immobile water. In a tertiary flood, surfactant and CO_2 were injected at residual oil saturation after waterflooding. In general, a higher pressure drop and lower foam mobility were obtained during the tertiary flood than during the secondary flood.

A higher initial oil saturation in the secondary flood probably caused greater coalescence and/or collapse of bubbles. The higher water saturation in the tertiary flood could have provided a barrier between the oil phase and foam bubbles, therefore inhibiting bubble coalescence. Both high water saturation and low oil saturation tend to promote increased bubble generation and increased foam stability, therefore resulting in lower CO_2 mobility.

The oil phase also is detrimental to foam stability when the spreading coefficient[38] is positive. With a positive spreading coefficient, the oil phase moves into the interface between CO_2 and surfactant solution, decreasing the foam generation rate and increasing the bubble coalescence rate. The spreading coefficient is defined as:

$$S_{oil} = \sigma_{surfactant\ solution/CO2} - \sigma_{oil/CO2} - \sigma_{surfactant\ solution/oil}$$

Manlowe and Radke,[39] however, concluded that the spreading coefficient is not related to foam stability and that the overall foam stability is controlled by the stability of a "pseudoemulsion film" between individual foam bubbles and trapped oil drops. If the "pseudoemulsion films" are stable, the foam does not rupture or coalesce, even in contact with the oil phase.

The change in the micromodel wettability caused by contact with the oil phase was another important factor in these displacements. When Soltrol was used as the oil phase, the micromodel remained water-wet. When Maljamar crude oil was injected into the model, however, the wettability changed to intermediate or oil wet, with foam generation being greatly reduced because of the lack of surfactant solution at the foam generation sites.

4) Surfactant Concentration

Three different surfactant concentrations were studied: 0.1%, 1.0%, and 5.0%. From surface tension measurements of the Alipal CD-128, the critical micellar concentration (CMC) was estimated as 0.1% in 1.0% NaCl solution. Previous investigators indicated that foaming action is a strong function of surfactant concentration. Indeed, in this study, higher surfactant concentrations promoted more foam generation and improved sweep efficiency. No significant differences in bubble size were observed with increasing surfactant concentration. However, foam bubbles at higher surfactant concentrations exhibited greater stability and were displaced over long distances through the micromodel without rupturing and coalescence.

As shown in Fig. 49, a higher pressure drop and increased sweep efficiency were obtained with higher surfactant concentrations. In these runs, single-phase injection of CO_2 into a 100% water-saturated, layered micromodel was performed. The highest pressure drop was obtained before CO_2 breakthrough with the system containing no surfactant because the capillary pressure of a CO_2-brine solution is higher than the capillary pressure of a CO_2-surfactant solution. Before CO_2 breakthrough, upstream pressure represents the non-wetting-phase pressure (CO_2 pressure), and downstream pressure is the wetting-phase pressure (water pressure). However, after CO_2 breakthrough, both pressures are nonwetting-phase pressures.

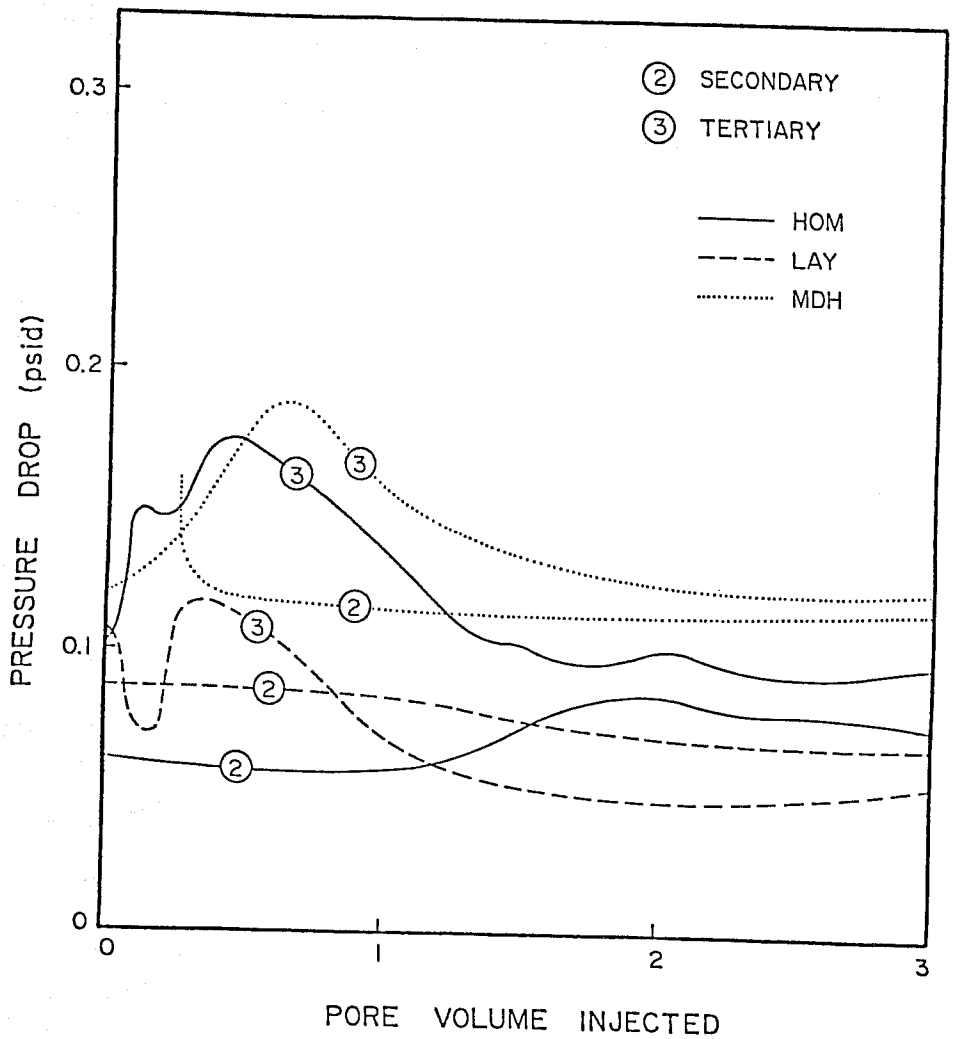

Figure 48. Comparison of foam mobility in secondary and tertiary floods (simultaneous injection).

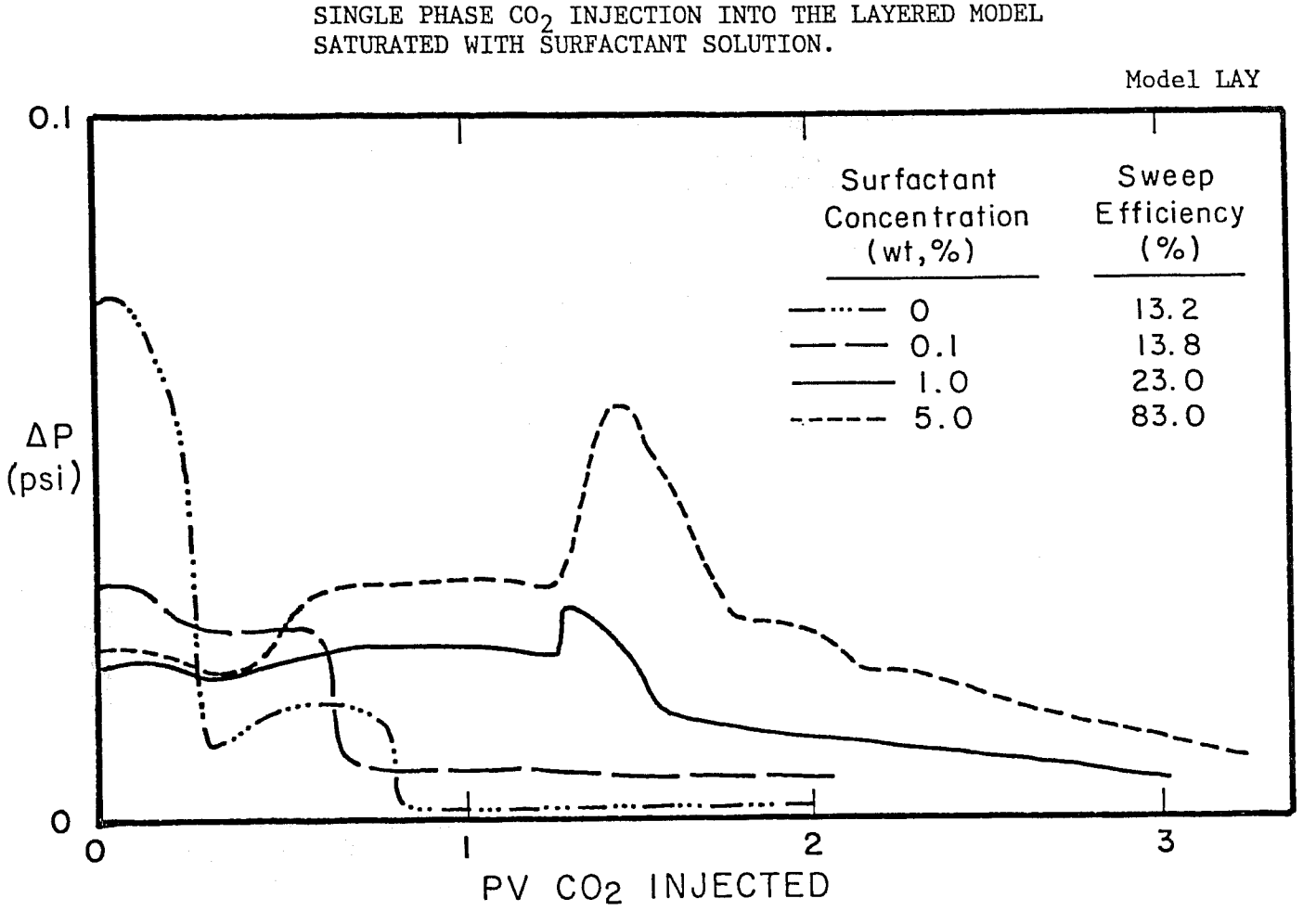

Figure 49. Effect of surfactant concentration on foam mobility, pressure drop vs. pore volumes of CO_2 injected.

But what is the optimum surfactant concentration for minimum CO_2 mobility? Chiang et al.[40] reported that in-situ foaming increased with concentration until the critical micellar concentration was attained. Above the CMC, additional surfactant had very little effect on the foam performance because surface tension remained constant or even increased.

In our study, better foam generation and reduced mobility still were observed with increasing surfactant concentration above the CMC: from 0.1% (CMC) to 1.0% to 5.0%. This probably occurs because the formation of micelles above the critical micelle concentration accelerates the movement of surfactant molecules into the interface where the lamellae experience stretching and thinning.[41]

5) Effect of Flow Rate

The effect of flow rate on CO_2/foam performance has been a controversial subject. In the Darcy flow regime, the permeability of fluids is independent of the flow rate. In the case of foam (or bubble/lamella) flow, the permeability is the function of flow rate. With increasing gas or liquid flow rate, both reduced and increased mobility have been reported. In this study, we use three CO_2 flow rates: 0.24 cc/hr, 1.44 cc/hr, and 2.88 cc/hr. These correspond to interstitial velocities of 10 ft/D, 60 ft/D, and 120 ft/D.

When injecting CO_2 into a surfactant-solution-saturated model, higher CO_2 flow rates increase phase mixing and destabilize the CO_2/surfactant solution interfaces. As a result, more foam is generated, corresponding to increased pressure drops and improved sweep efficiencies. Figure 50 shows the sweep efficiency at three CO_2 flow rates into the layered model (LAY). This layered model has higher permeability zones adjacent to the edges. At a flow rate of 10 ft/D, these two channels were displaced first. However, when a low density of stable bubbles was generated, one middle channel was then displaced because previously flowing channels became blocked. Shortly thereafter, all flow took place only through the preferential flow channel. No additional sweep improvement was obtained until 3PV of CO_2 was injected. If the flow rate was increased to 60 ft/D, bubble density increased and flow was diverted into neighboring channels. With a flow rate of 120 ft/D, smaller bubbles were generated by snap-off and bubble subdivision; almost all channels were displaced with the swept area being approximately 82%. A critical capillary number,[37] above which a strong foam is generated, was calculated to be on the order of 10^{-5}. In our experiments, the critical capillary number was estimated to be on the order of 10^{-6} as shown in Fig. 51. The critical capillary number should be a strong function of the porous medium.

3. Conclusions

1. Foam was generated by upstream snap-off as well as downstream snap-off and bubble division. Upstream snap-off can be the dominant generation mechanism in preferential flow path systems at reservoir temperature and pressure conditions for CO_2 flooding.

2. In the homogeneous model, only liquid lamellae were generated and propagated. Both bubbles and lamellae were formed in the heterogeneous models. The mixing of fluids and the aspect ratio of the porous media are the most important factors in foam generation.

3. A wider distribution of pore sizes can promote better mixing between fluids, hence it can enhance the generation of foam.

4. In preferential flow path systems, the upstream aspect ratio (flow inlet to the preferential flow path) can have a large effect on zone blockage.

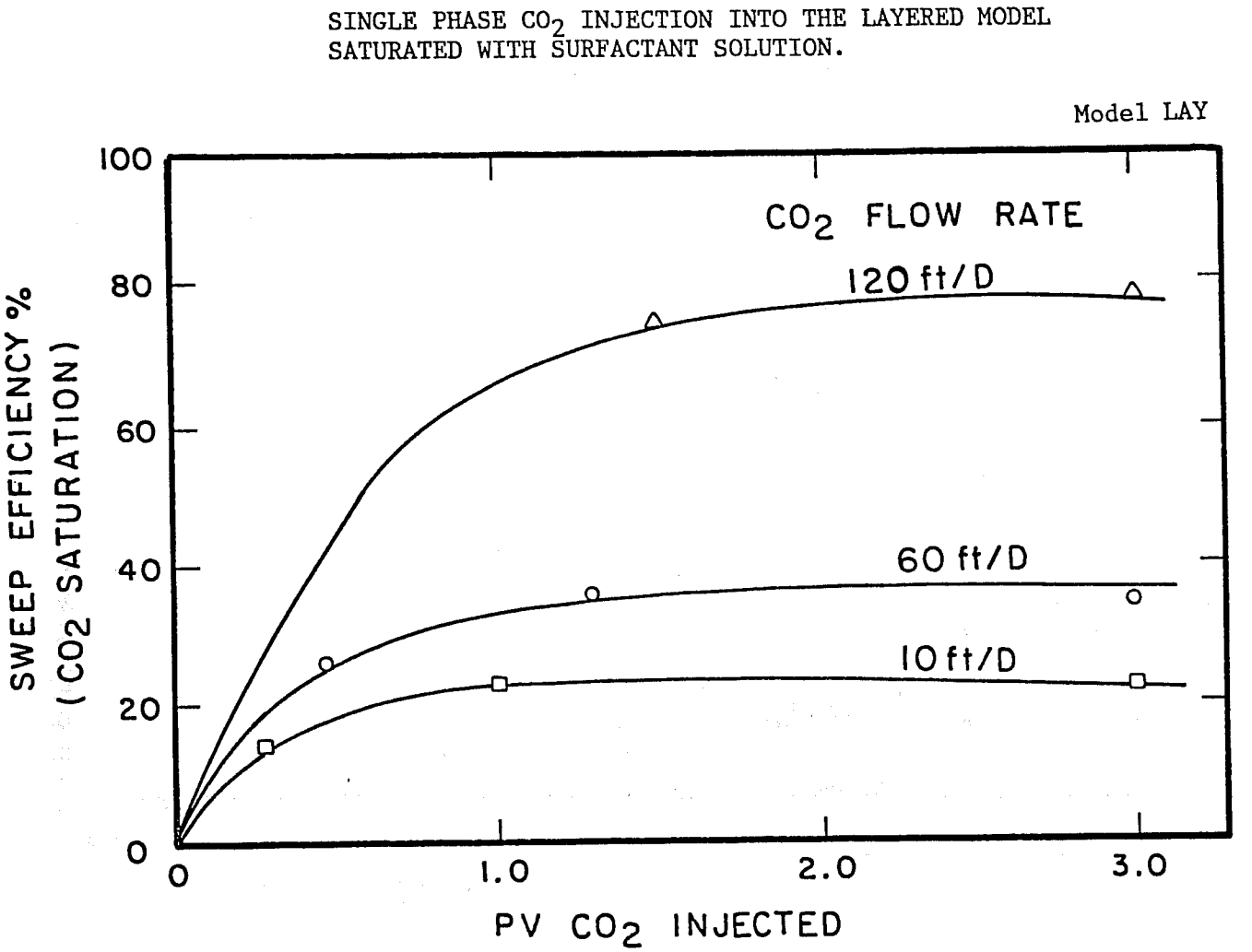

Figure 50. Effect of CO_2 flow rate on sweep efficiency.

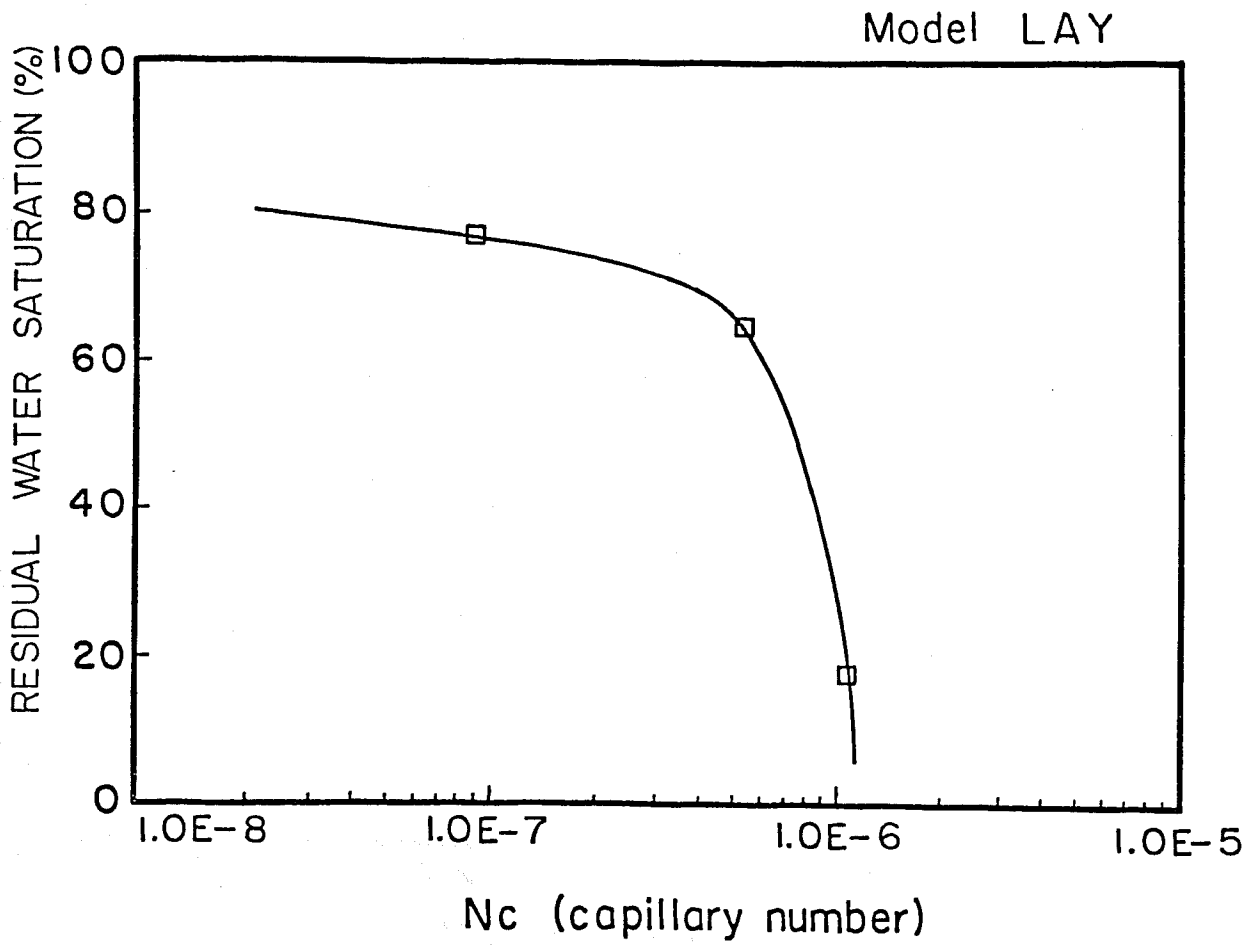

Figure 51. Critical capillary number.

5. Simultaneous injection of CO_2 and surfactant solution is more effective in achieving high-permeability channel blockage than single-phase CO_2 injection into a surfactant solution.

6. The bubble size of Berea sandstone-pregenerated foam was much smaller than that of the micromodel-generated, in-situ foam. As a result, the displacement by pregenerated foam was piston-like.

7. The mobility of foam generated in a tertiary flood is lower than that of foam generated in a secondary flood. A tertiary flood has lower oil saturation; high water saturation provides a barrier between the oil phase and foam bubbles. The oil phase can destabilize the foam.

8. Saturating the micromodel with crude oil changes the wettability to intermediate or oil wet. As a result, foam generation is greatly reduced because of the lack of surfactant solution at the foam generation site.

9. With all the micromodels, better sweep efficiency was obtained with higher surfactant concentrations and higher flow rates.

E. MECHANISTIC STUDIES ON HIGH PRESSURE GAS/FOAM FLOW: THEORETICAL

A two-dimensional numerical simulator is currently being developed which models high pressure gas/foam flow. At this time, foam is generated by the following mechanisms: snap-off, or lamella division, and leave-behind, all of which are included in the model. In addition, foam coalescence and trapping mechanisms are incorporated in the simulator. Some of the assumptions used in this preliminary model have been defined by others.[42,43]

The assumptions used in the model are as follows:

1) There are four components: oil, gas, water, and surfactant; and three phases: oil, gas, and water.

2) The amount of surfactant in the oil and gas phases is negligible.

3) Loss of surfactant by foam formation is negligible.

4) Surfactant concentration adsorbed on the rock (Γ) is in equilibrium with the surfactant concentration in the water phase (C_s).

5) Surfactant does not affect the mobility of the water phase.

6) Foam affects only the gas-phase mobility.

7) Darcy's law applies for the gas phase in the presence of foam.

8) Foam can not exist if the oil saturation (S_o) is larger than a limiting oil saturation (S_o^{lim}) or if the surfactant concentration (C_s) is less than a limiting surfactant concentration (C_s^{lim}).

9) Snap-off or division and mobilization of stranded lamellae only occurs above a critical gas velocity (V_c).

10) The flowing and trapped foams do not discriminate between pores of different size.

11) The process of foam trapping is instantaneous, and the bubble density of trapped foam (n_s) is in equilibrium with the bubble density of flowing foam (n_f).

12) The mass transfer among the bubbles has a negligible effect on the average bubble density.

13) Mechanical dispersion is negligible.

The mass balance equation for each phase is

$$-\nabla \cdot (\rho_l \mathbf{U}_l) = \frac{\partial}{\partial t}(\rho_l \phi S_l) - q_l \tag{39}$$

where

$$\mathbf{U}_l = -\frac{k k_{rl}}{\mu_l}(\nabla P_l - \rho_l \mathrm{g}) \tag{40}$$

Here g is the gravitational acceleration vector and the subscript l refers to the phases, with l = o for oil phase, l = w for water phase, and l = g for gas phase.

To track the surfactant concentration in the water phase, the following mass balance is included:

$$-\nabla \cdot (C_s \rho_w \mathbf{U}_w) = \frac{\partial}{\partial t}[C_s \rho_w \phi S_w + \rho_r (1-\phi)\delta\Gamma] - \hat{C}_s q_w \tag{41}$$

where

$$\hat{C}_s = \begin{cases} C_{sI} & \text{at injection} \\ C_s & \text{at production} \end{cases} \tag{42}$$

and Γ, the surfactant concentration adsorbed on the rock, is modeled with a Langmuir-type model:

$$\Gamma = \frac{K_s A_s C_s}{1 + K_s C_s} \tag{43}$$

Foam texture is one of the most important variables governing foam mobility. To account for changes in foam texture, the balances on the bubble density in flowing and trapped foams are used. In view of the above assumptions, the bubble population balances can be combined as follows:

$$-\nabla \cdot (n_f \mathbf{U}_g) + G_f - C_f = \frac{\partial}{\partial t}[X_f n_f \phi S_g + (1 - X_f) n_s \phi S_g] - \hat{n}_f \hat{q}_g \tag{44}$$

where

$$\hat{q}_g = \frac{q_g}{\rho_g} \tag{45}$$

$$\hat{n}_f = \begin{cases} n_{fI} & \text{at injection} \\ n_f & \text{at production} \end{cases} \tag{46}$$

The equilibrium relationship between n_s and n_f is described by

$$n_s = \frac{K_f A_f n_f}{1 + K_f n_f} \tag{47}$$

Here, A_f and K_f are the bubble trapping parameters. The following function is used to model the rate of bubble generation:

$$G_f = \begin{cases} \left[\dfrac{K_1}{1 + (\dfrac{n_f}{n_c})^{e_1}}\right] \left[\dfrac{c_1(\dfrac{|\mathbf{U}_g|}{V_c} - 1)}{1 + c_1(\dfrac{|\mathbf{U}_g|}{V_c} - 1)}\right] & |\mathbf{U}_g| > V_c \\ 0 & |\mathbf{U}_g| \leq V_c \end{cases} \tag{48}$$

where

$$V_c = \frac{d}{w^e} \tag{49}$$

and $|U_g|$ is the magnitude of U_g. The rate of bubble consumption by coalescence is modeled as follows:

$$C_f = \begin{cases} K_2 n_f (\frac{C_{sref}}{C_s})^{e_2} & C_s > C_s^{lim} \\ K_2 n_f (\frac{C_{sref}}{C_s^{lim}})^{e_2} & C_s \leq C_s^{lim} \end{cases} \tag{50}$$

This viscosity of the flowing foam is calculated with the following expression:

$$\mu_{gf} = \mu_g K_3 n_f k^{1.5} (\frac{U_{ref}}{|U_g|})^{e_3} \tag{51}$$

If the calculated value is greater than μ_g, set $\mu_g = \mu_{gf}$. The relative permeability of the gas phase is modified according to the effective foam relative permeability:

$$k_{rgf} = X_f k_{rg} \tag{52}$$

that is, set $k_{rg} = k_{rgf}$. Equation (52) is based on the assumption that the flowing and trapped foams do not discriminate between pores of different size. For the case of leave-behind lamellae, only the permeability of the gas phase needs to be modified. In this case,

$$k_{rgf} = \frac{k_{rg}}{a} \tag{53}$$

where a is a reduction factor which is modeled as

$$a = 1 + bS_g \tag{54}$$

The gas-phase mobility is modified in the simulator according to the flow diagram shown in Fig. 52. The basic idea is outlined below.

The first decision is whether or not foam exists. If foam exists, the gas-phase mobility is modified according to Eqs. (51) and (52). The next decision is whether or not foam can occur. In order for foam to occur, the following conditions must be satisfied: $S_g > 0$, $S_o < S_o^{lim}$, and $C_s > C_s^{lim}$. If any of these conditions are not met, the gas-phase mobility is not modified. Next, the gas velocity is checked to see if it is above a critical value at which moving foam occurs. No distinction between the mechanisms of snap-off and lamella division is made here. If the gas velocity is above the critical value, the gas-phase mobility is modified according to Eqs. (51) and (52). The last decision determines whether or not leave-behind lamellae can be generated. For leave-behind lamellae to occur, surfactant must be present in the water phase before gas invades that location in the porous medium. If this case occurs, the gas-phase relative permeability is modified according to Eq. (53). Otherwise, no modification is made.

To solve the multiphase equations, the following constraints are used:

$$S_o + S_g + S_w = 1 \tag{55}$$

$$P_{cgo} = P_g - P_o \tag{56}$$

$$P_{cow} = P_o - P_w \tag{57}$$

The implicit pressure explicit saturation (IMPES) method is used to solve the multiphase equations. The basic idea is to obtain a single pressure equation by combining the multiphase equations. After the pressure has been advanced in time implicitly, the saturations are updated explicitly. The iterative alternating direction implicit (ADI) scheme is used to find the pressure solution. Surfactant concentration and foam bubble density from the previous time step are used to modify the gas-phase mobility. After the solution converges, the surfactant and population balance equations are solved for the current time.

Figure 53 is the layout of a hypothetical system that we considered initially. This system is 6.8 cm in length, 5 cm in width, and 0.0221 cm in thickness. A high-permeability zone which has been labeled as PFP, preferential flow path, is located at the center portion of the system. When foam occurs in the PFP, the blockage and diversion of flow can be observed.

The initial conditions for this system are uniform pressure and uniform oil saturation at connate water. The boundary conditions are no flow at boundary, constant production pressure, and constant injection rate for both water and gas phases. The water and gas phases are being injected into the system simultaneously. The conditions and parameters used in the simulations are listed in Table 14. In addition, the capillary pressure and relative permeability data are plotted in Figs. 54-58. Stone's method is used to estimate the three-phase relative permeability. Some of the conditions and parameters are chosen from the study by Friedmann et al.[43] because experimental results are lacking.

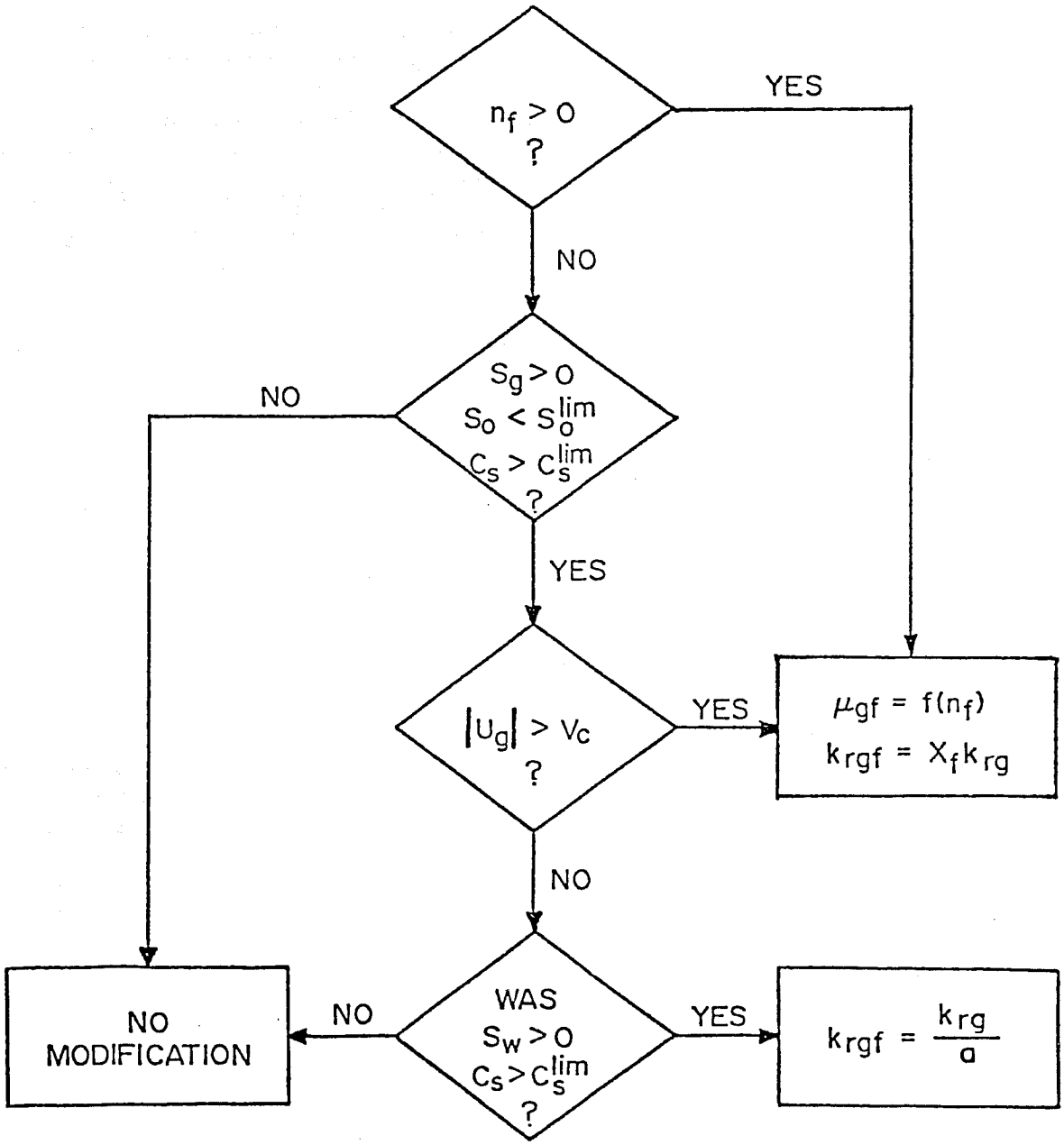

Figure 52. Flow diagram of foam model.

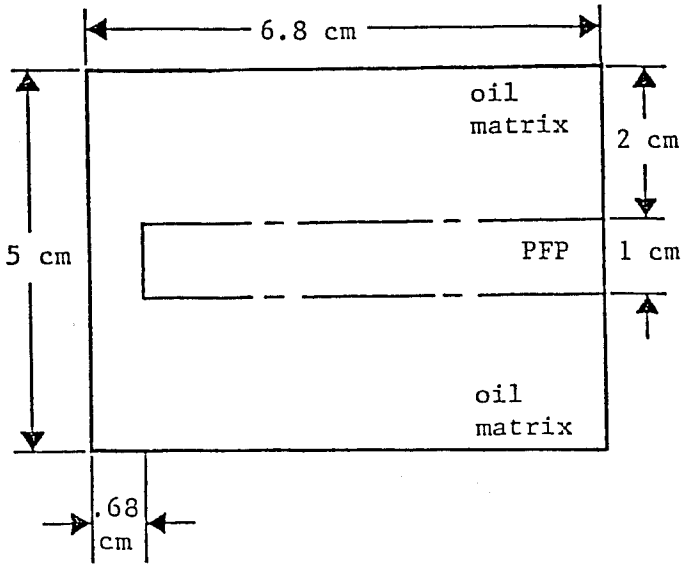

Figure 53. Layout of system.

TABLE 14. CONDITIONS AND PARAMETERS USED IN THE "PROCESS-DEMONSTRATION" SIUMULATIONS.

Oil matrix:	0.01 darcy
PFP:	0.5 darcy
Production pressure:	89.82 atm
Gas flow rate:	1.667×10^{-5} g/sec
Water flow rate:	1.667×10^{-5} g/sec
Initial conditions:	$S_o = 0.74, S_w = 0.26$
Mass density:	$\rho_o = 0.834, \rho_w = 1.0, \rho_g = 0.743$ g/cm^3
Viscosity:	$\mu_o = 2.8, \mu_w = 1.0, \mu_g = 0.064$ cp
PV:	0.15028 cm^3
A_f:	7.5×10^7 #/cm^3
A_s:	1.68×10^{-8} g/cm^2
b:	25.345
C_{sI}:	0.01 g/g
C_s^{lim}:	0.0001 g/g
C_{sref}:	0.01 g/g
c_1:	10
d:	5.5×10^{-5} cm/sec
e:	1.54
e_1:	5
e_2:	1.4
e_3:	0.29
K_f:	1.0×10^{-5} cm^3/#
K_s:	793.0 g/g
K_1:	1.0218×10^7 #/sec/cm^3
K_2:	2.0436×10^{-3} cm^3/cm^3/sec
K_3:	1.9×10^7
n_c:	2.0×10^7 #/cm^3
n_{fI}:	0.0 #/cm^3
S_o^{lim}:	0.6
U_{ref}:	0.03916 cm/sec
X_f:	0.15
δ:	3000 cm^2/g
ρ_r:	2.66 g/cm^3
ϕ:	0.2

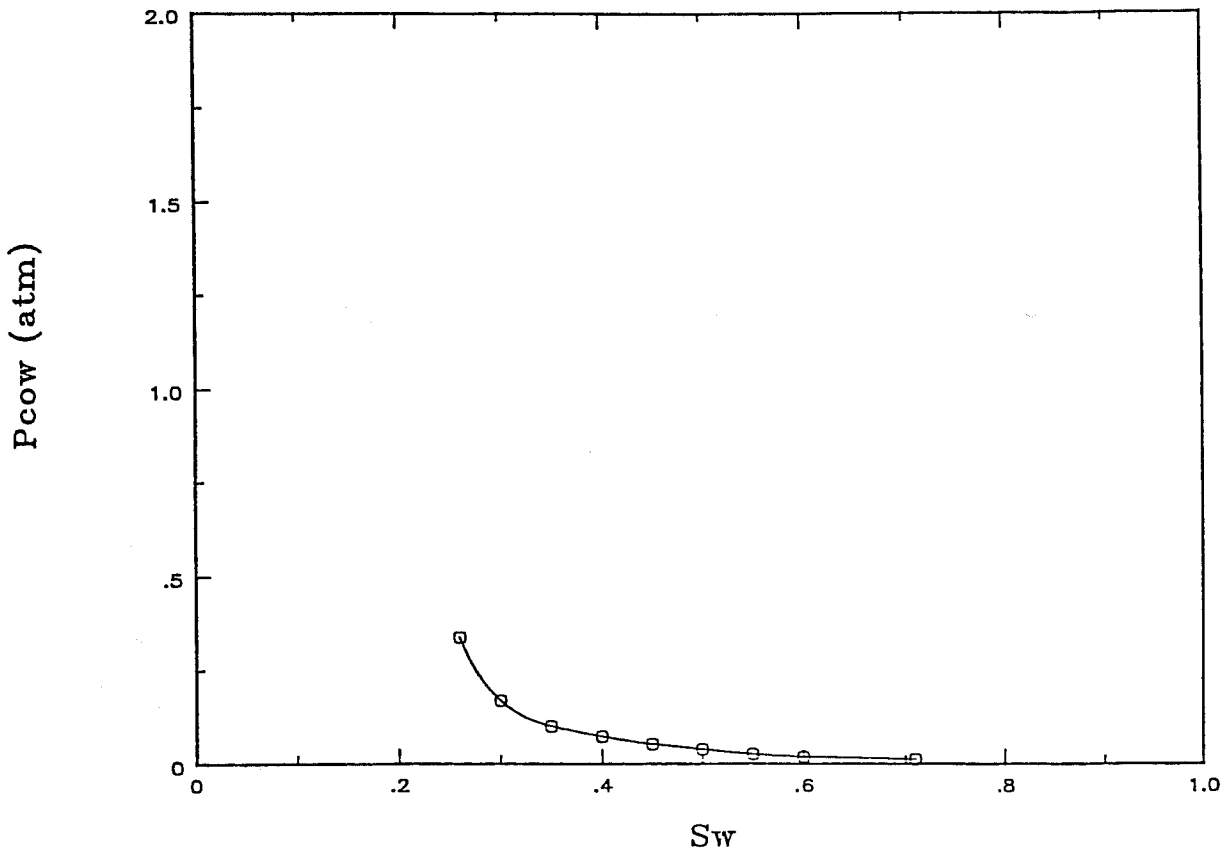

Figure 54. Capillary pressure curve for water-oil system.

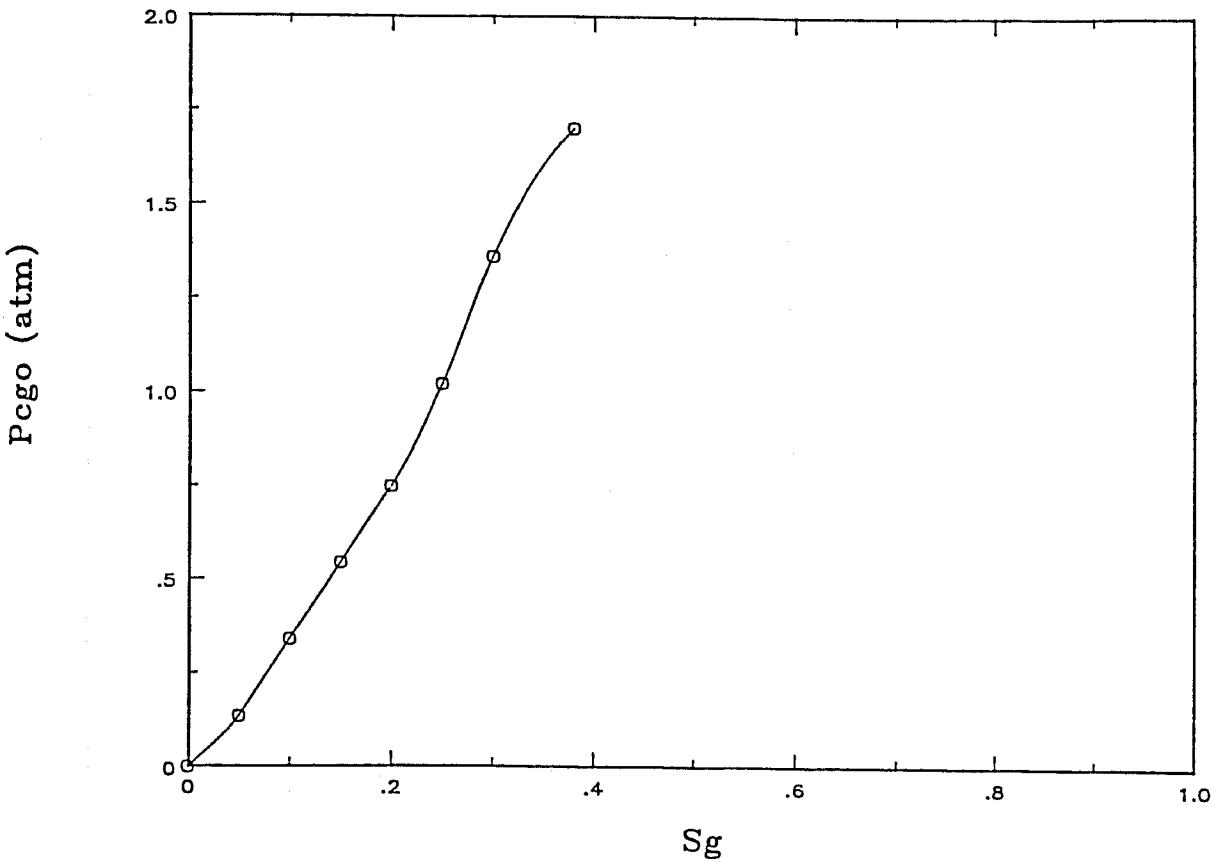

Figure 55. Capillary pressure curve for gas-oil system.

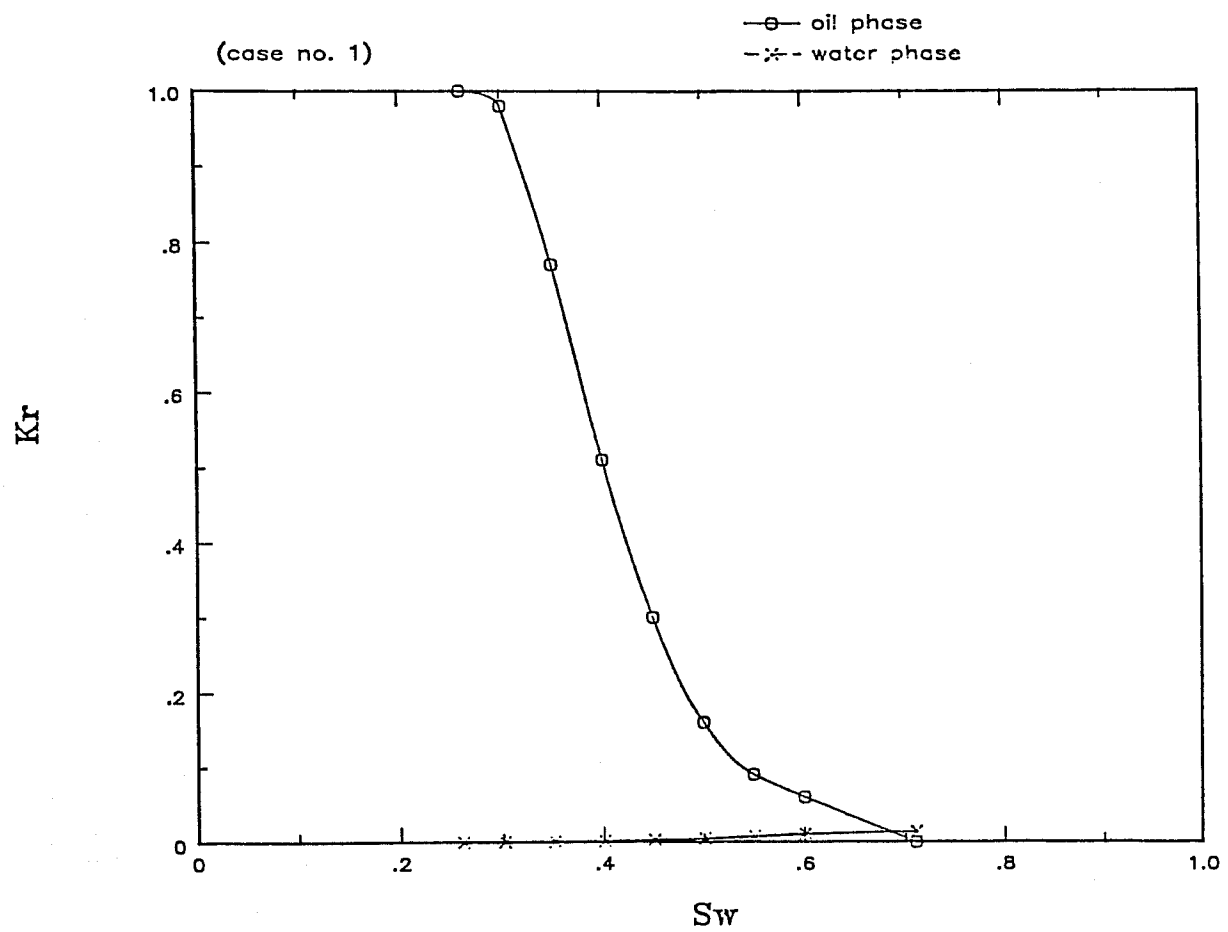

Figure 56. Relative permeability curves for water-oil system (Case No. 1).

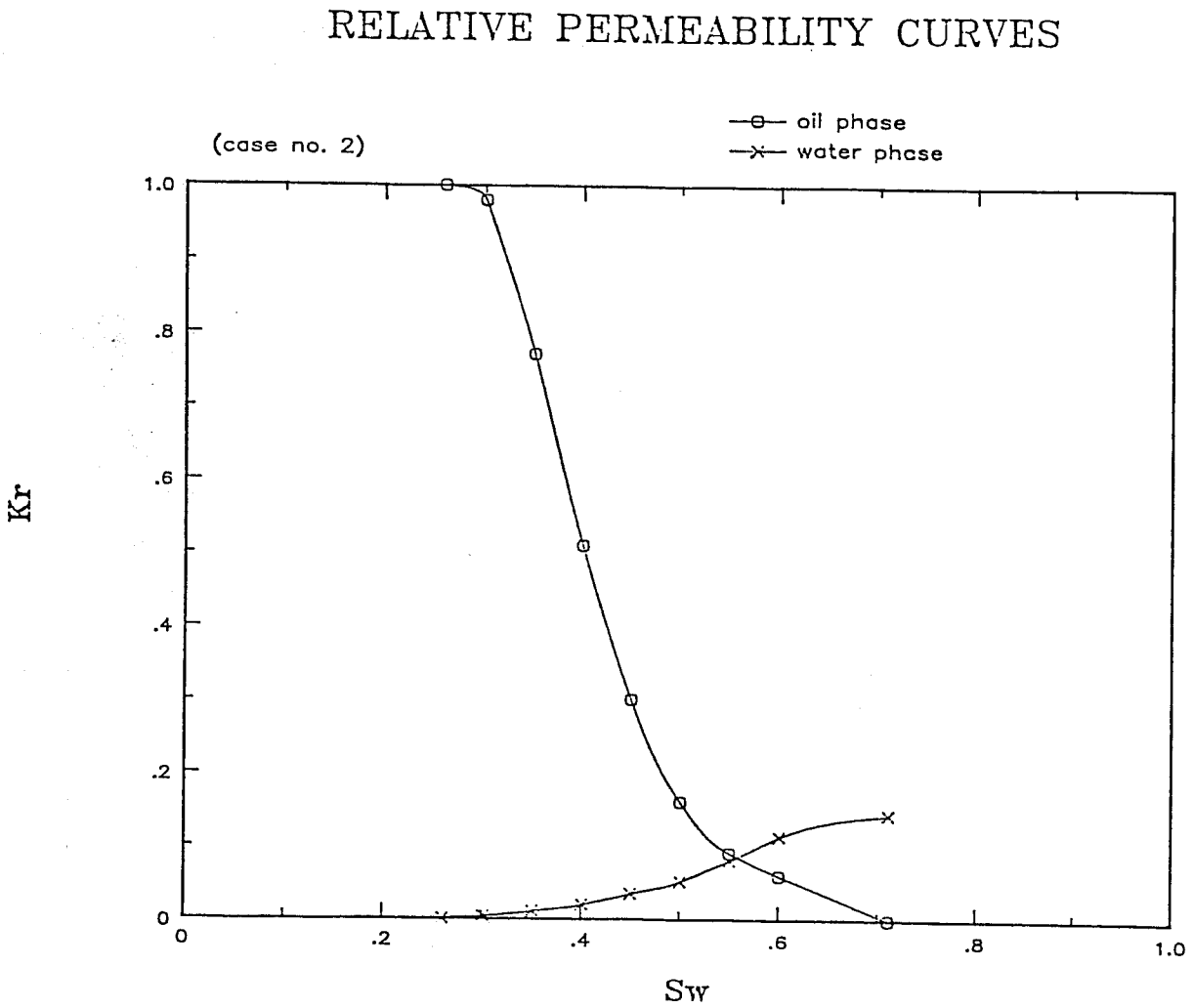

Figure 57. Relative permeability curves for water-oil system (Case No. 2).

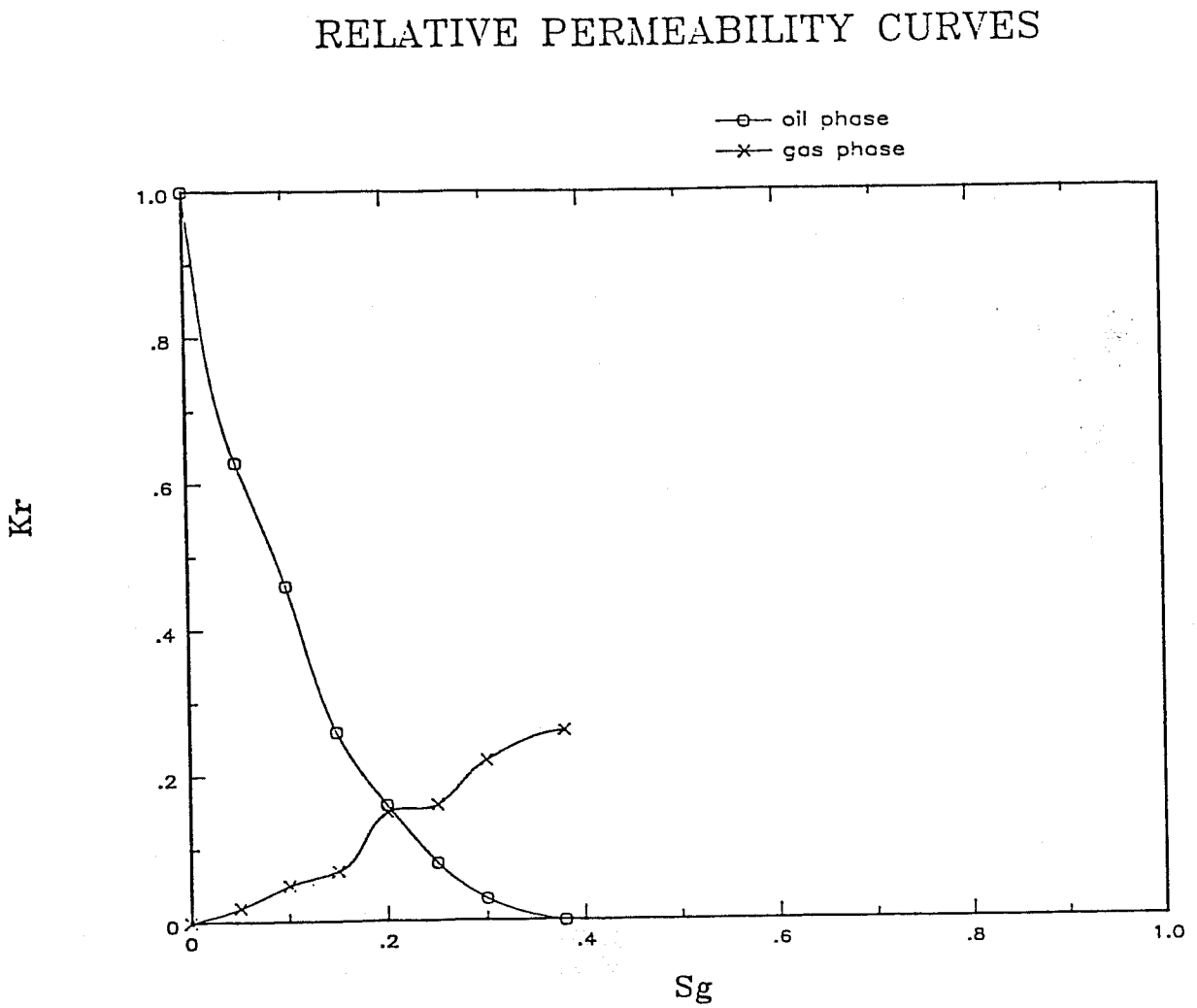

Figure 58. Relative permeability curves for gas-oil system.

Two sets of relative permeability data for oil and water phases, shown in Figs. 56 and 57, are used in the simulations. The effect of relative permeability upon the pressure drop across the system can be significant, as shown in Fig. 59.

To show how foam affects the pressure drop across the system, the pressure drop histories for the case where leave-behind lamellae occurred in-situ and for the case without lamellae are plotted in Fig. 60. The pressure drop is higher when leave-behind lamellae exist. A comparison of pressure drop histories between the case where foam was generated in-situ and the case without foam is shown in Fig. 61. The pressure drop is higher when flowing foam exists.

To demonstrate the blockage and diversion of flow by foam, the gas velocity fields for different times are shown in Figs. 62-66 for the case where foam occurred in the PFP. The gas velocity fields for different times are shown in Figs. 67-69 for the case without foam. The region enclosed by the dotted line is the PFP. The length of the arrow represents the magnitude of the gas velocity and the direction the arrow is pointed in is the flow direction. It is clear that the flow was blocked and diverted and that trapped oil was recovered. Figures 70-74 are the corresponding oil saturation profiles for the case with foam. The oil saturation in the region of the trapped oil matrix in Fig. 74 (on the wings) is less than that present if foam did not block the PFP and divert gas and water. This indicates that the sweep efficiency in the region of the oil matrix is improved when foam exists. However, a bump which occurred near the beginning of the PFP also can be seen for the case with foam. By examining the gas saturation profiles as shown in Figs. 75-78, it is concluded that trapped foam is the cause of the bump. As the amount of trapped foam in the PFP increases, the gas saturation in the PFP also increases; therefore, the relative permeability of the oil phase decreases correspondingly. When the relative permeability of the oil phase becomes zero, the oil phase becomes immobile at that location.

In summary, this two-dimensional simulator is currently under development and will be able to simulate many of the processes associated with blockage and diversion of flow by foam. This simulator makes no distinction between generation mechanisms (snap-off and lamella division) or propagation mechanisms (bubbles and lamellae). Currently, an effort to separate these mechanisms is underway. Sensitivity analyses for the parameters used in the simulator are being performed. In addition, the experimental results from the coreflood studies are being matched.

The nomenclature for this section is given in Table 15.

F. CONCLUSIONS--TASK AREA I

A comprehensive, simultaneous viscosity, density, and composition database covering a wide range of pure and impure CO_2/synthetic and crude oil mixtures is currently under development. New CO_2/crude oil viscosity correlations, utilizing this new database, are being generated. The functional form of a modified Lohrenz, Bray, and Clark correlation is presented. A paper entitled, "Viscosity Measurements of High-Pressure CO_2/Hydrocarbon Mixtures" was presented at the 1987 AIChE annual meeting in November.

The slim tube apparatus was modified to incorporate a core displacement unit. Coreflood experiments are being run to investigate the effect of solution and free gas on displacement efficiency. Coreflood results will be reported in the next quarterly. A one-dimensional compositional simulation is being performed utiizing the Peng-Robinson equation of state.

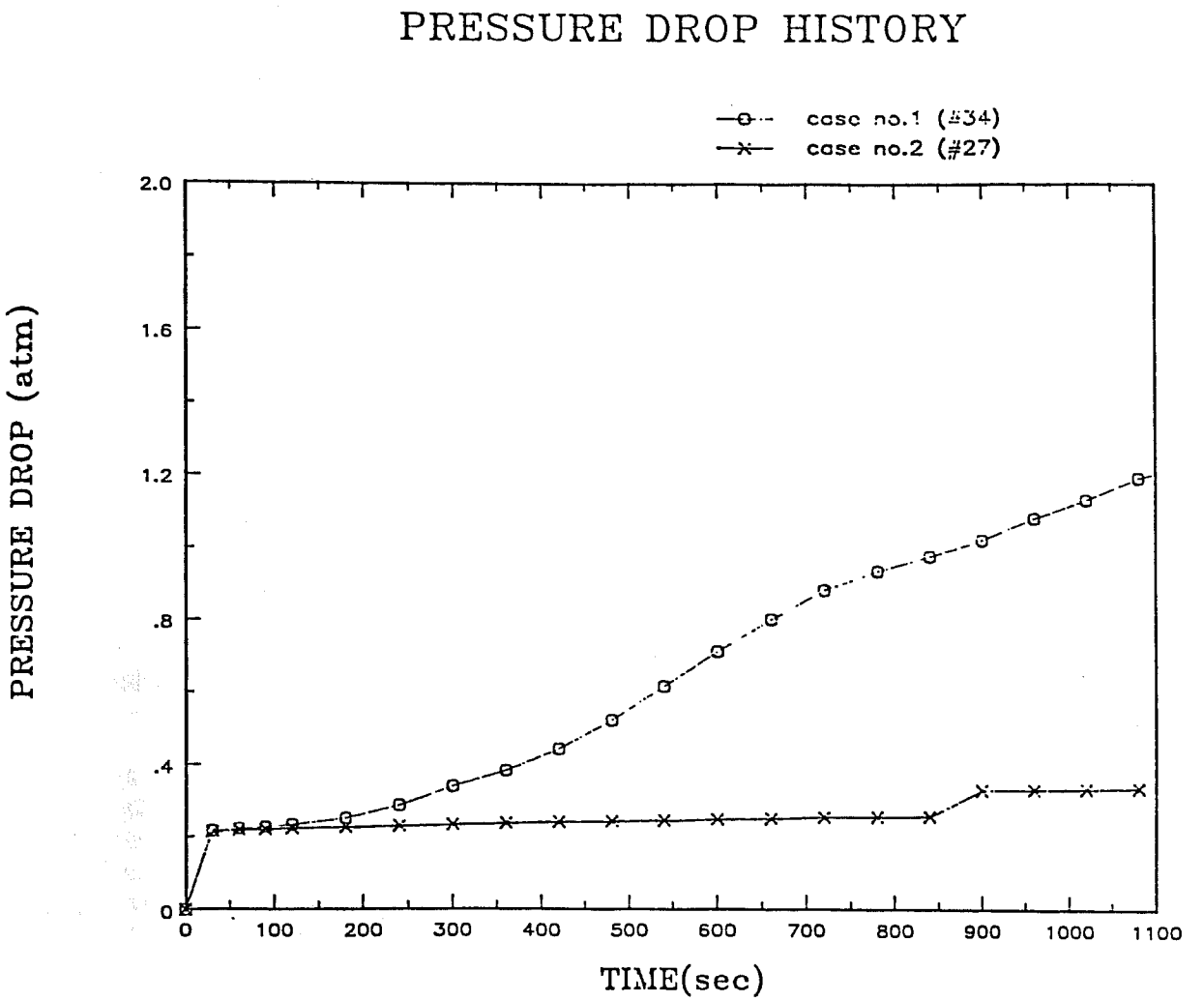

Figure 59. Effect of relative permeability on pressure drop across the system.

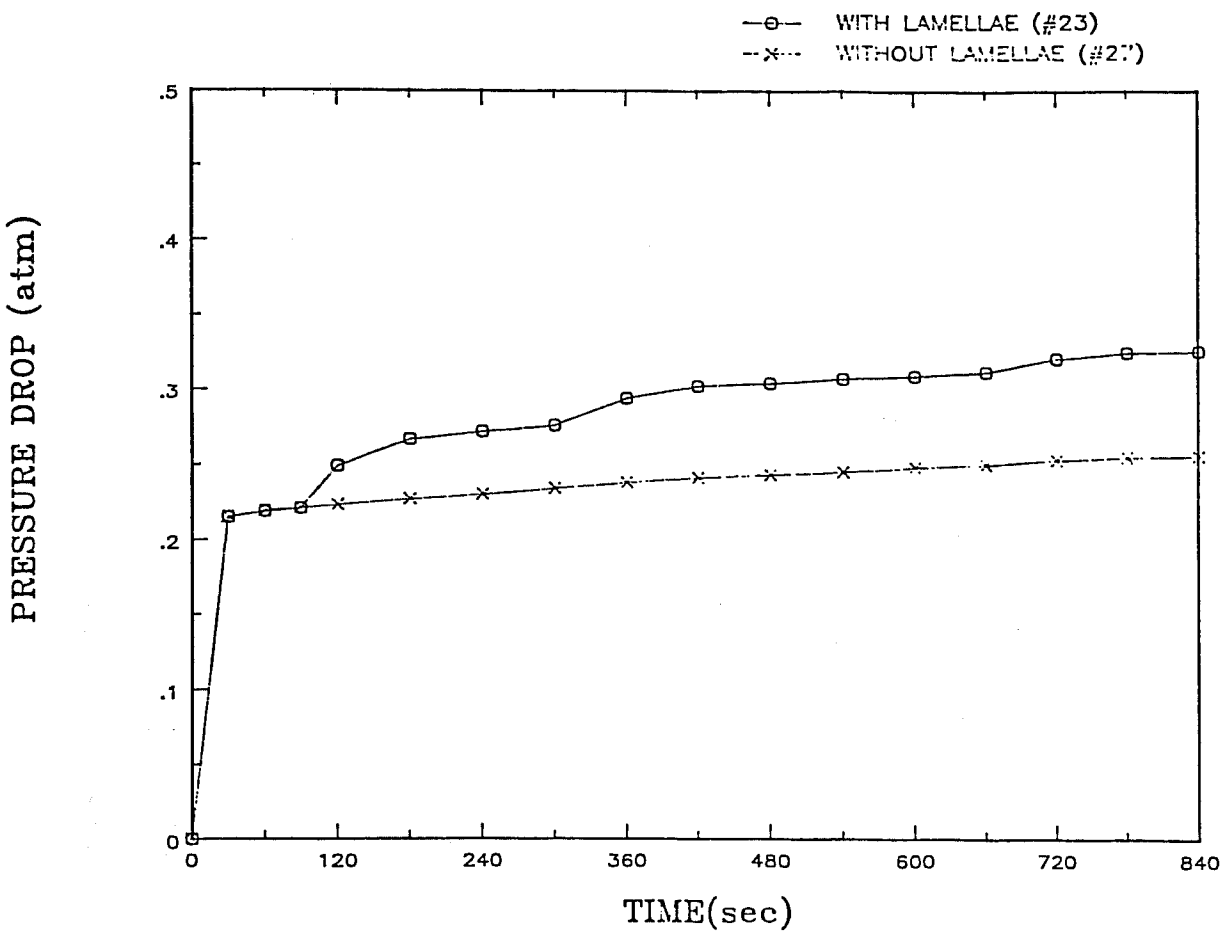

Figure 60. Effect of leave-behind lamellae on pressure drop across the system.

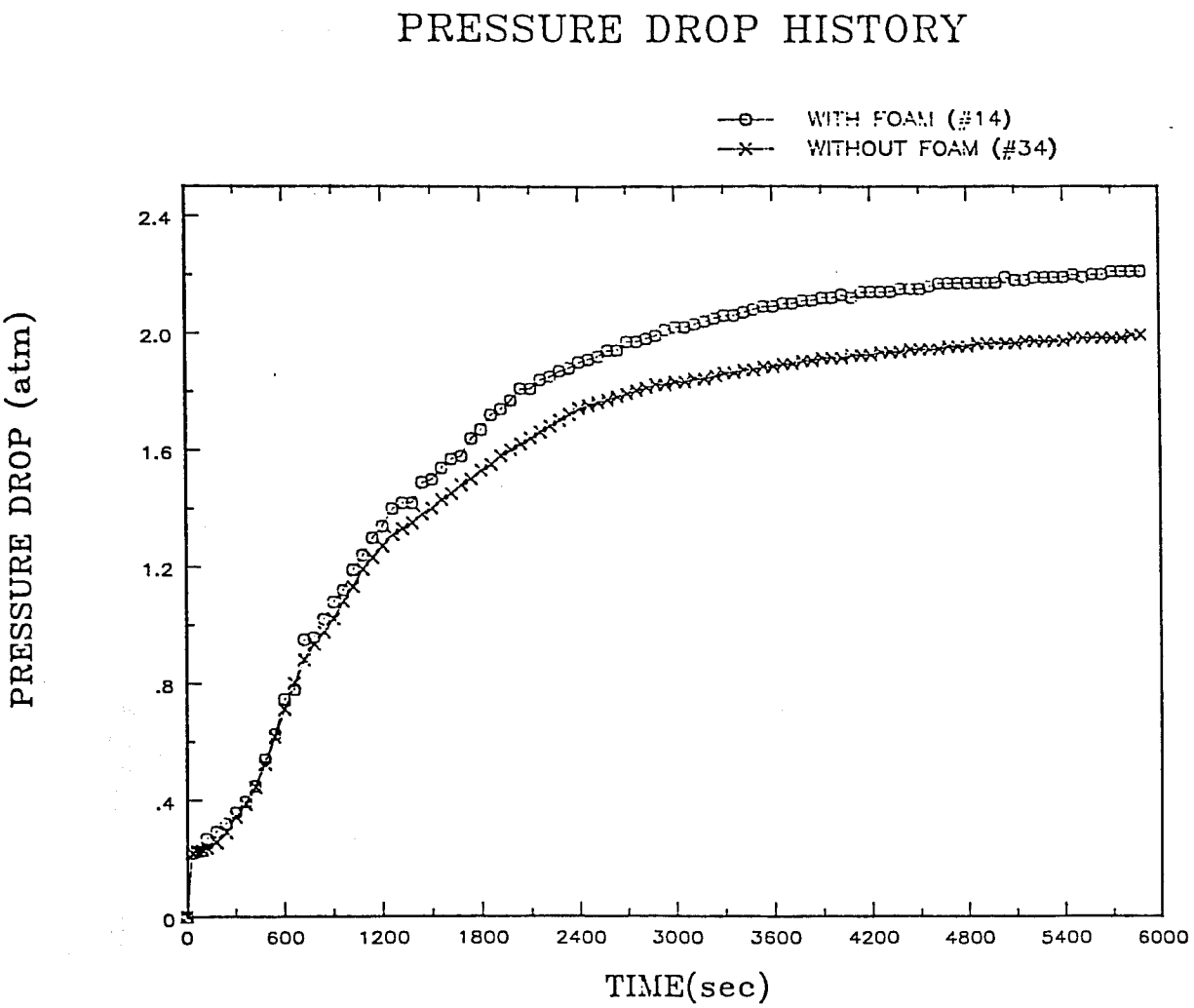

Figure 61. Effect of foam on pressure drop across the system.

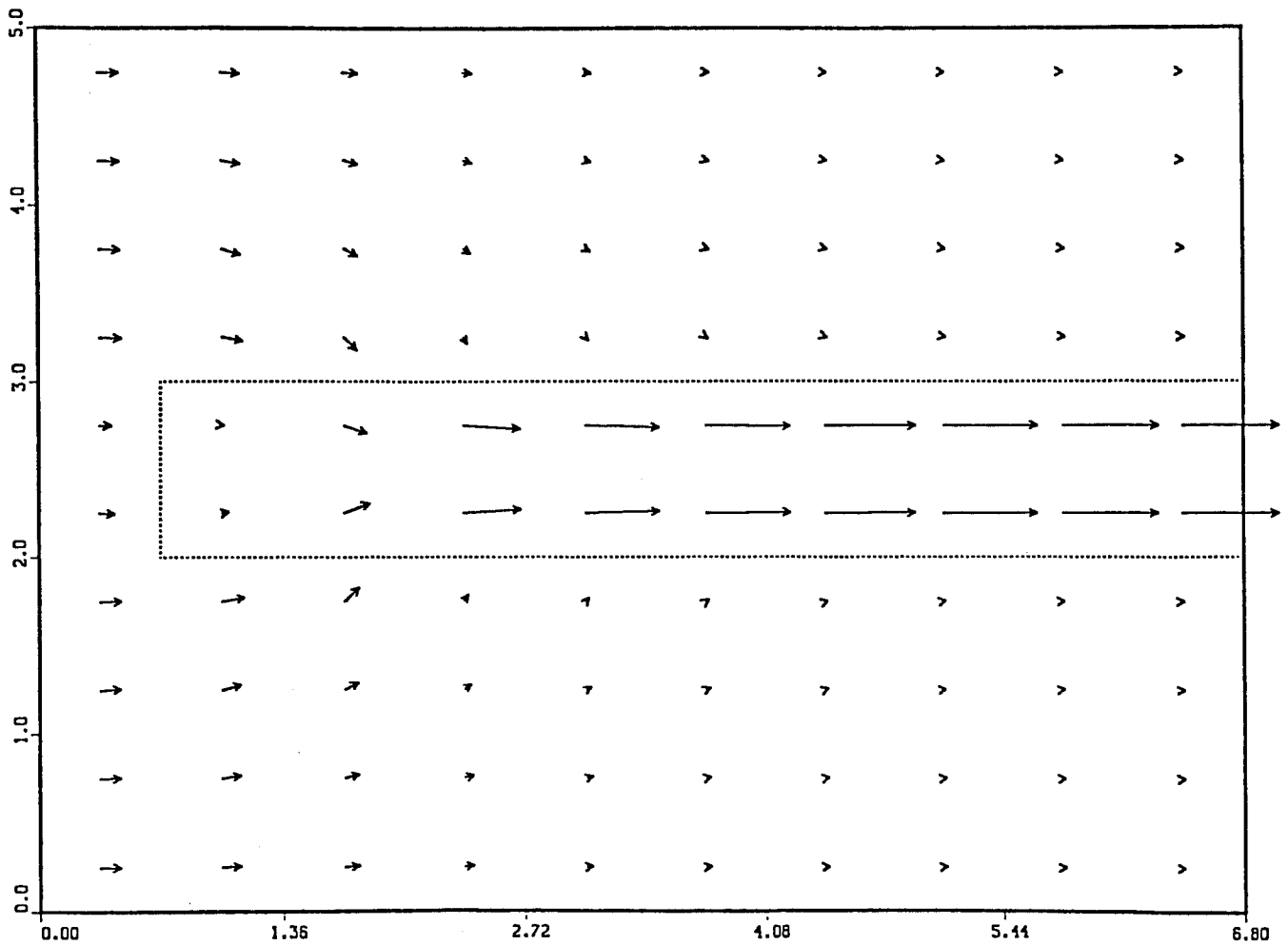

Figure 62. Gas velocity field with foam at time 600 sec.

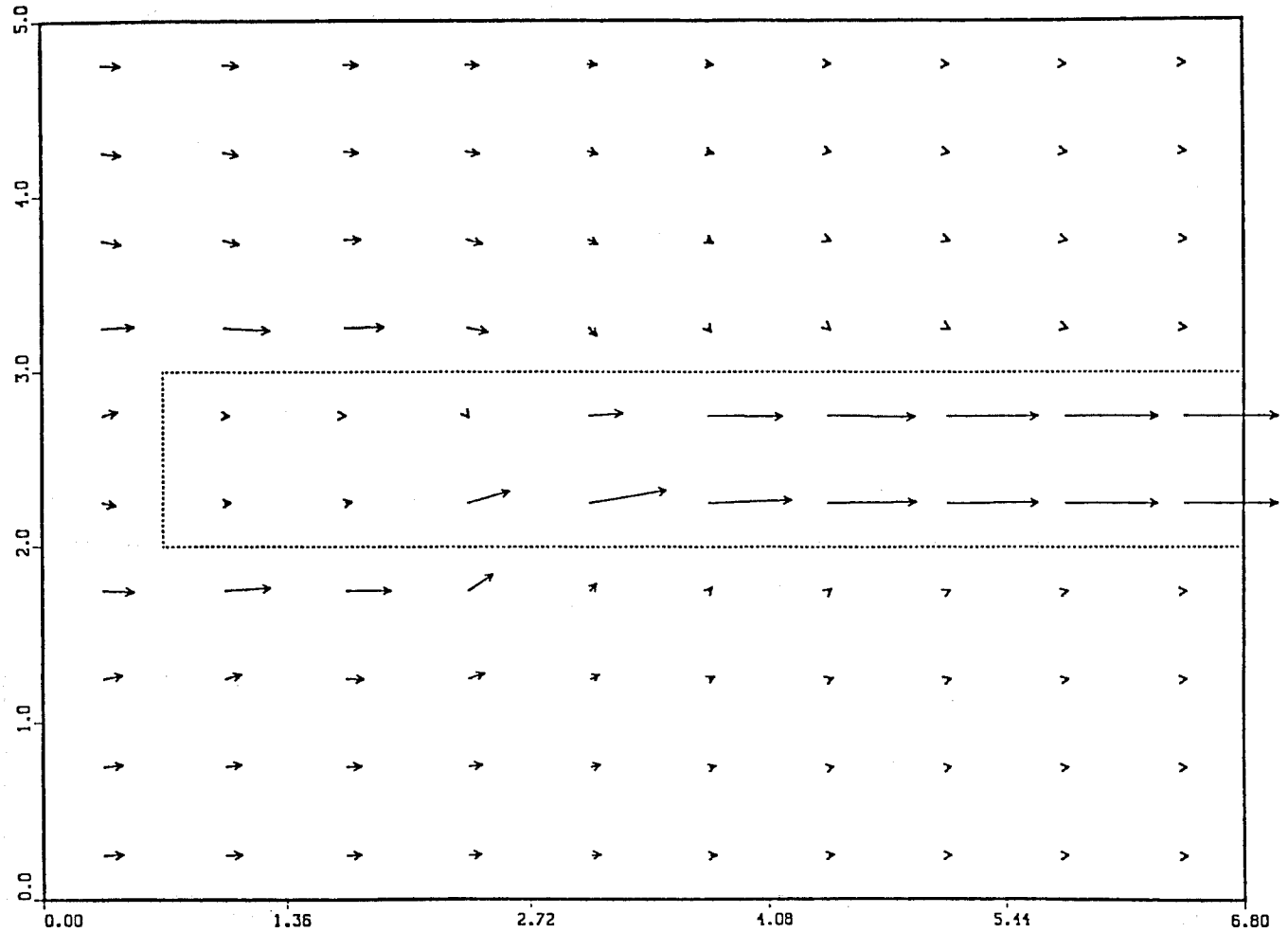

Figure 63. Gas velocity field with foam at time 1080 sec.

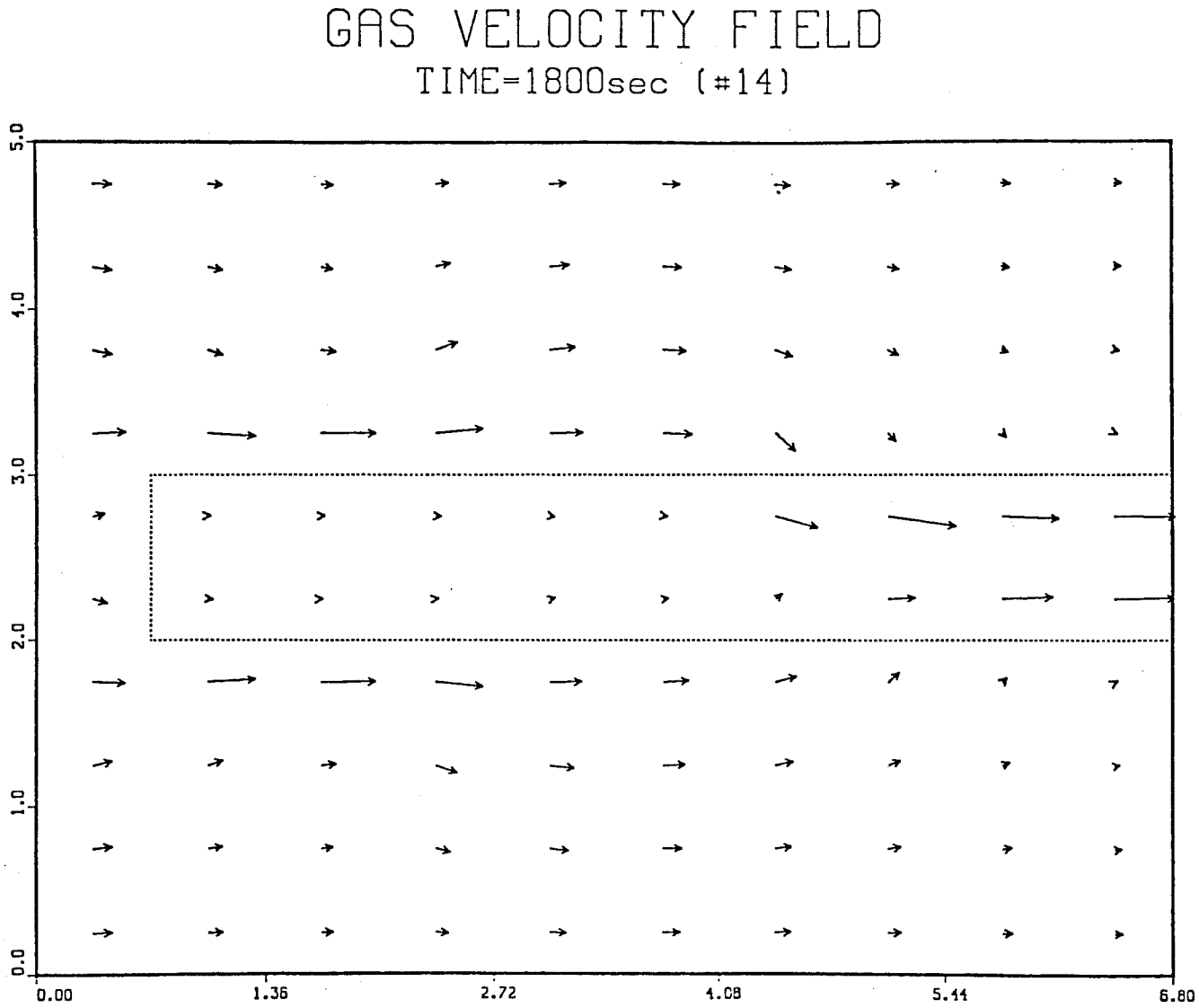

Figure 64. Gas velocity field with foam at time 1800 sec.

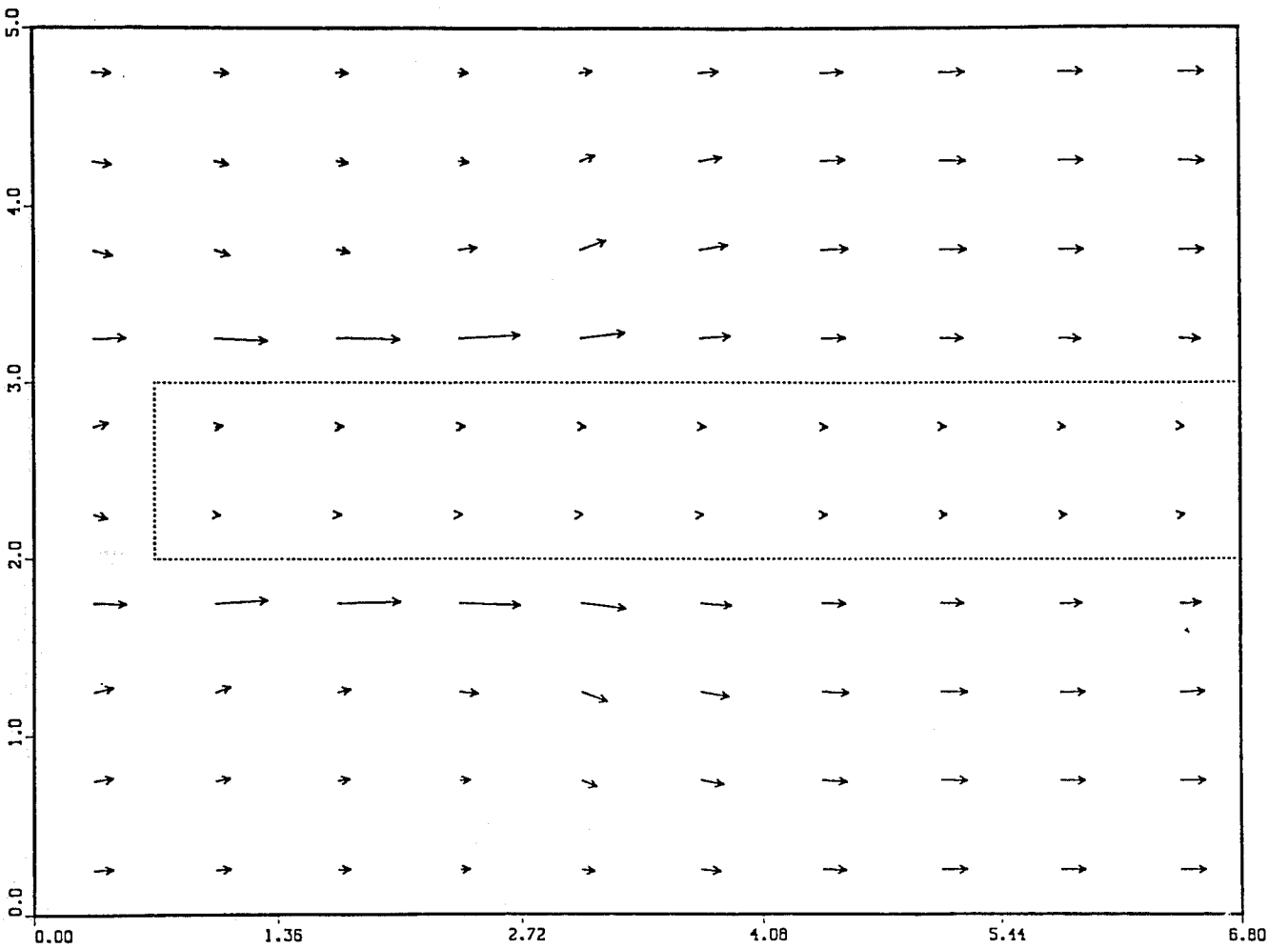

Figure 65. Gas velocity field with foam at time 2760 sec.

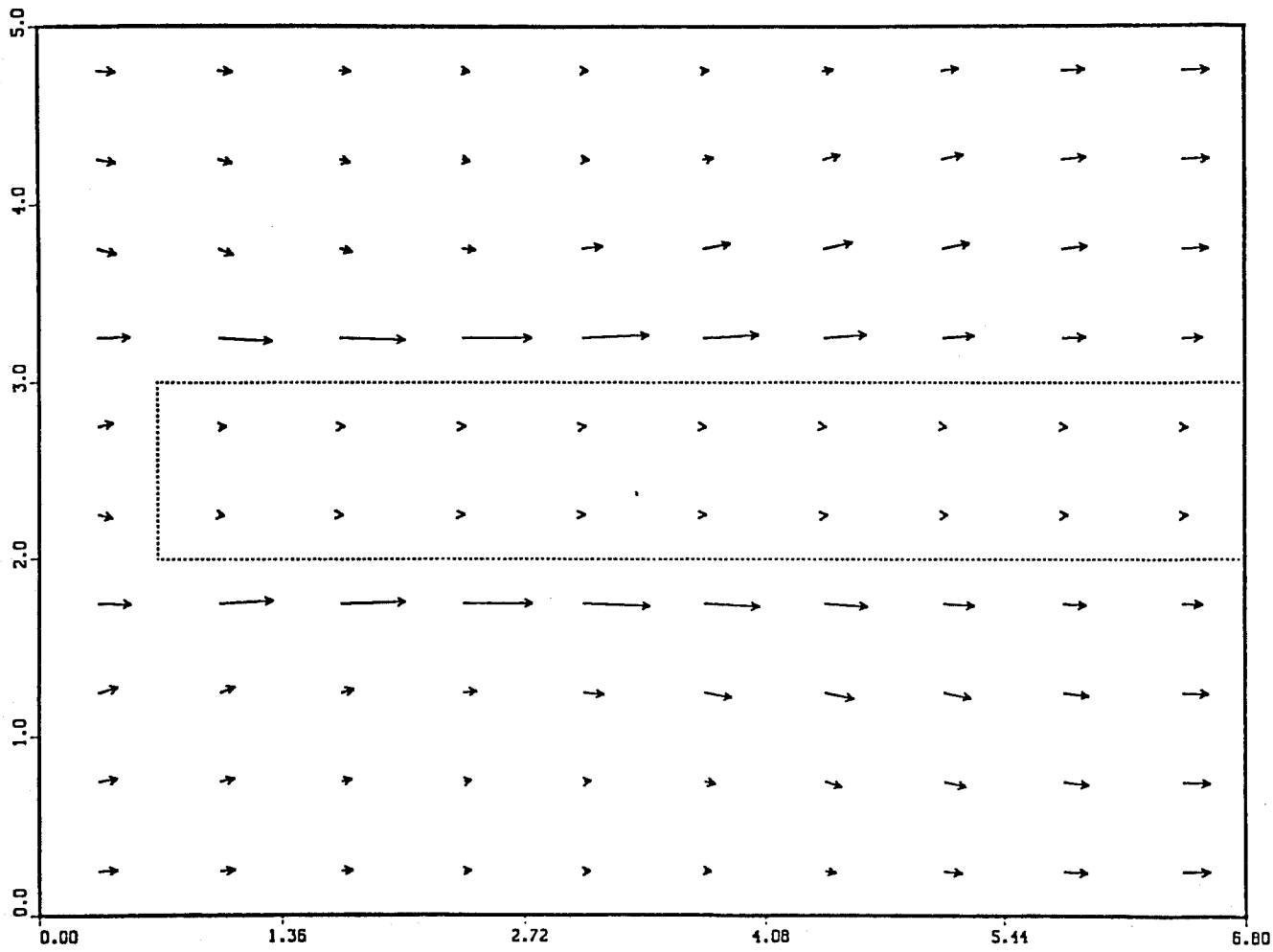

Figure 66. Gas velocity field with foam at time 5880 sec.

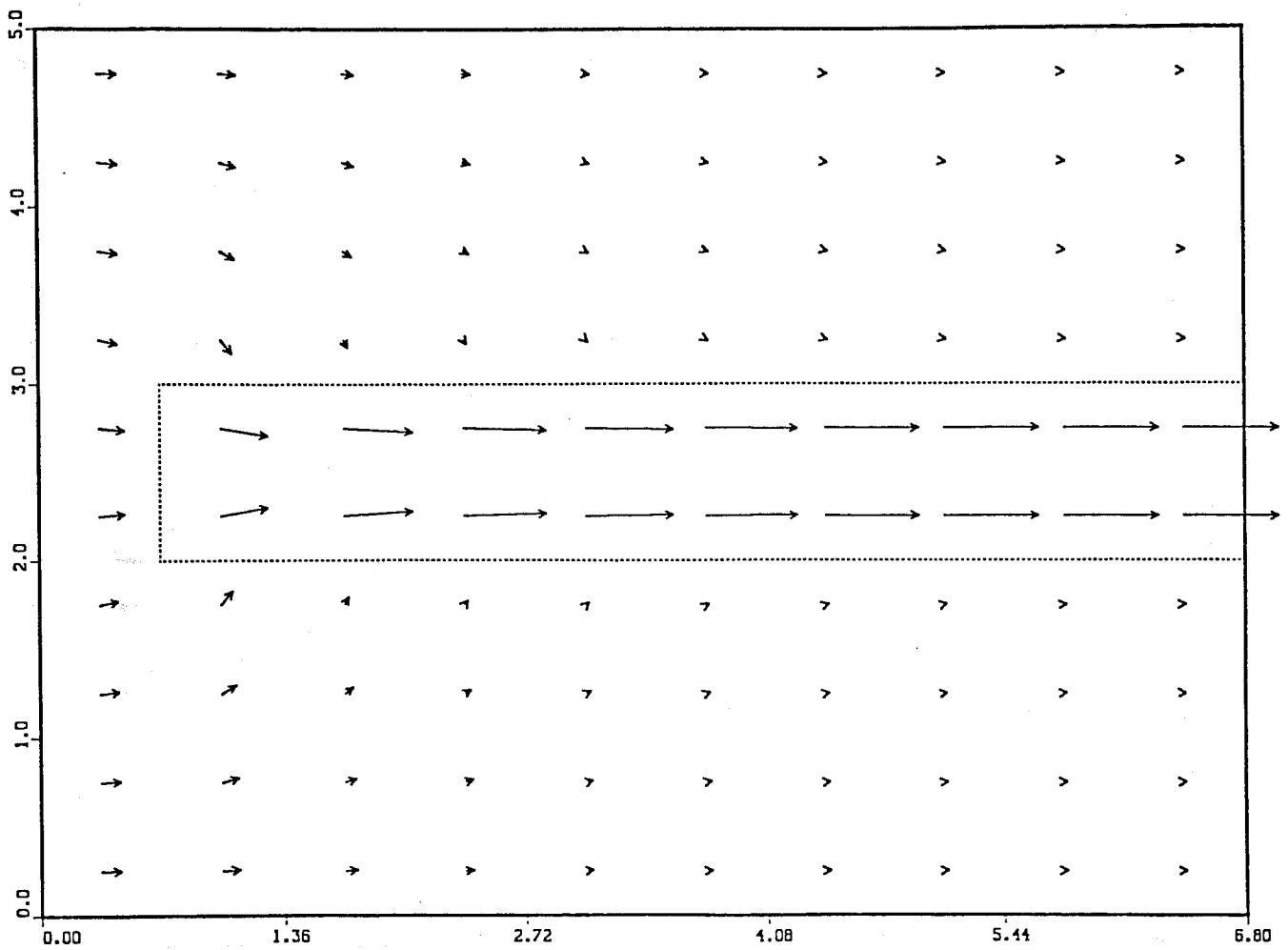

Figure 67. Gas velocity field without foam at time 600 sec.

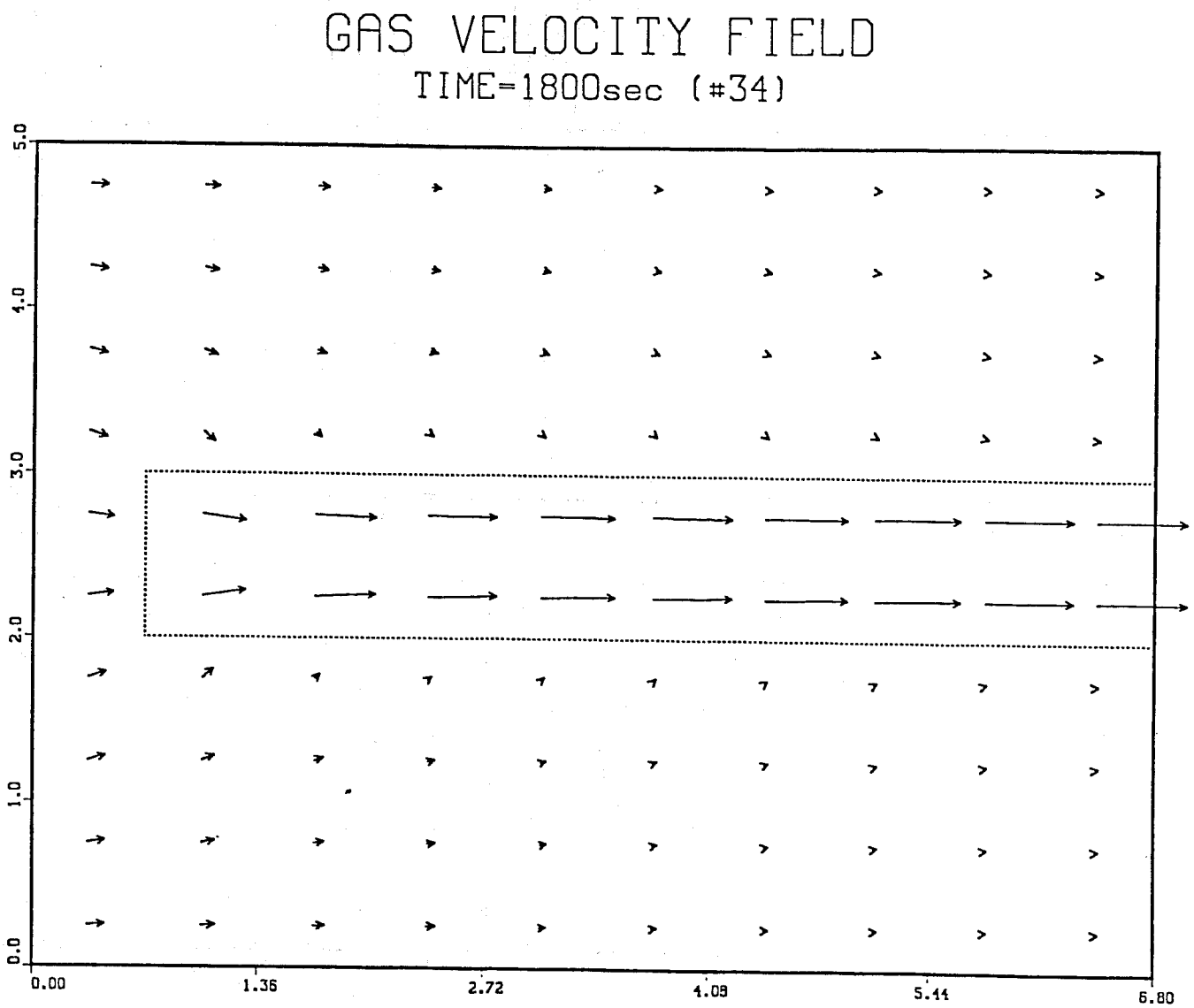

Figure 68. Gas velocity field without foam at time 1800 sec.

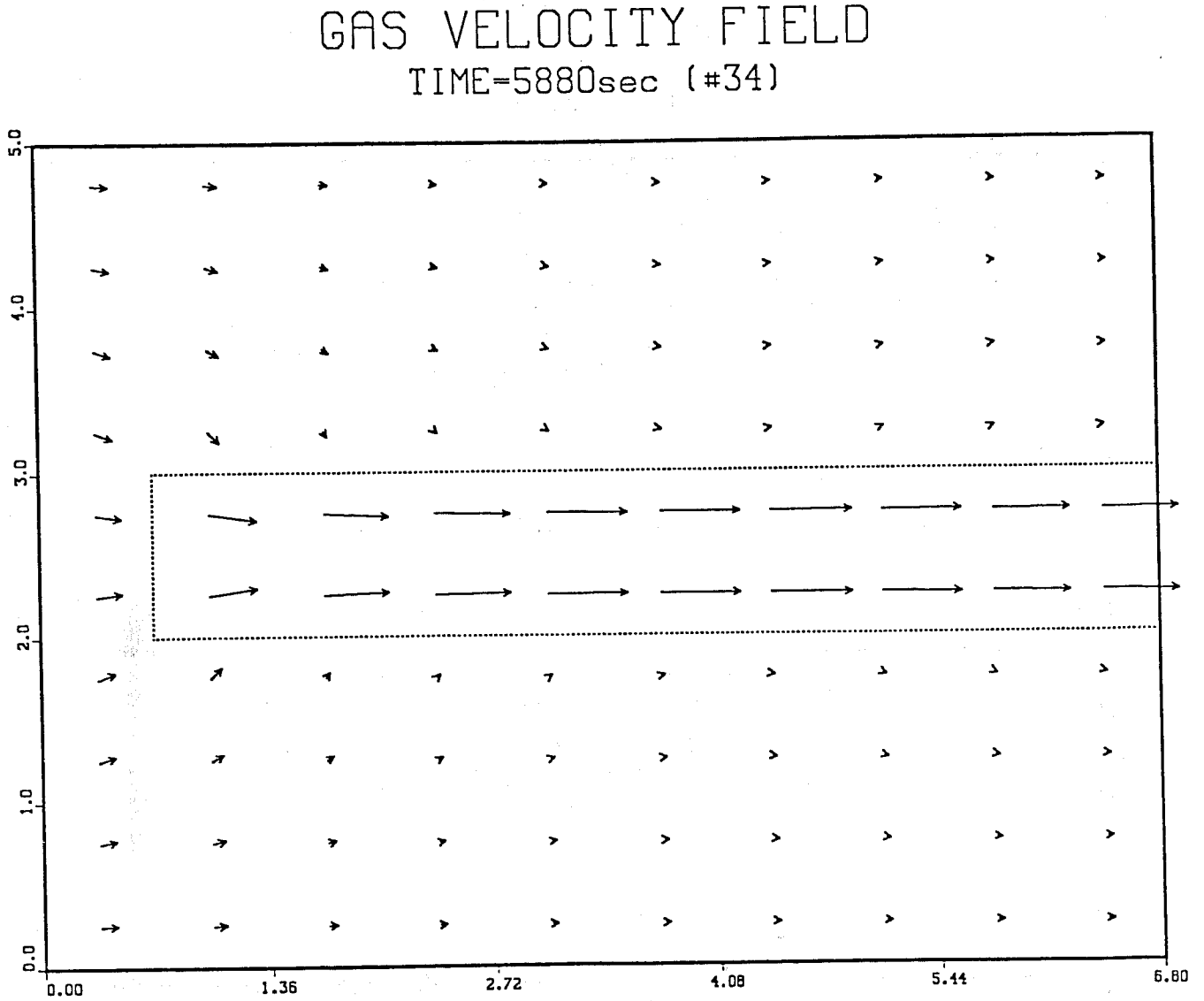

Figure 69. Gas velocity field without foam at time 5880 sec.

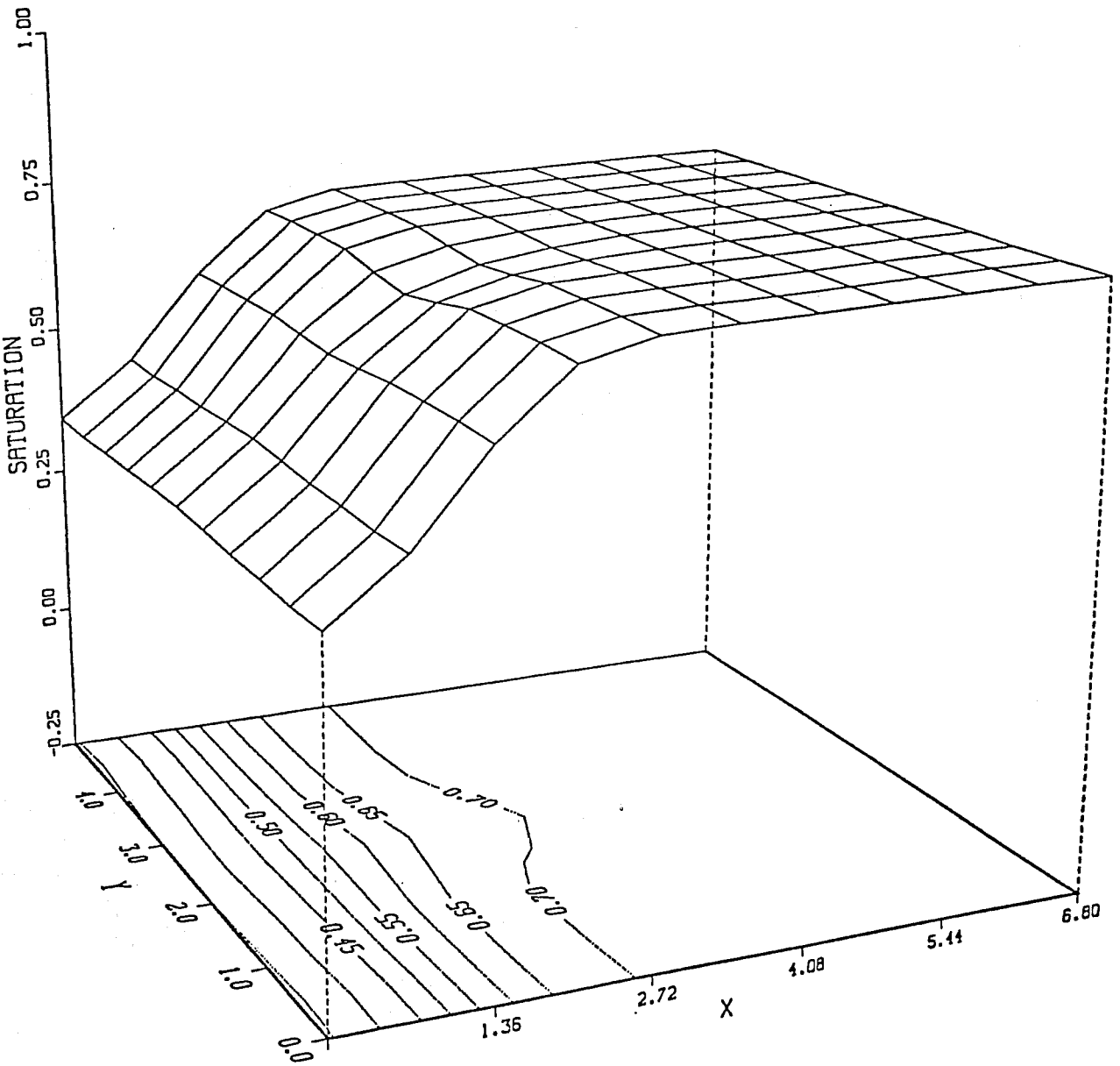

Figure 70. Oil saturation profile with foam at time 600 sec.

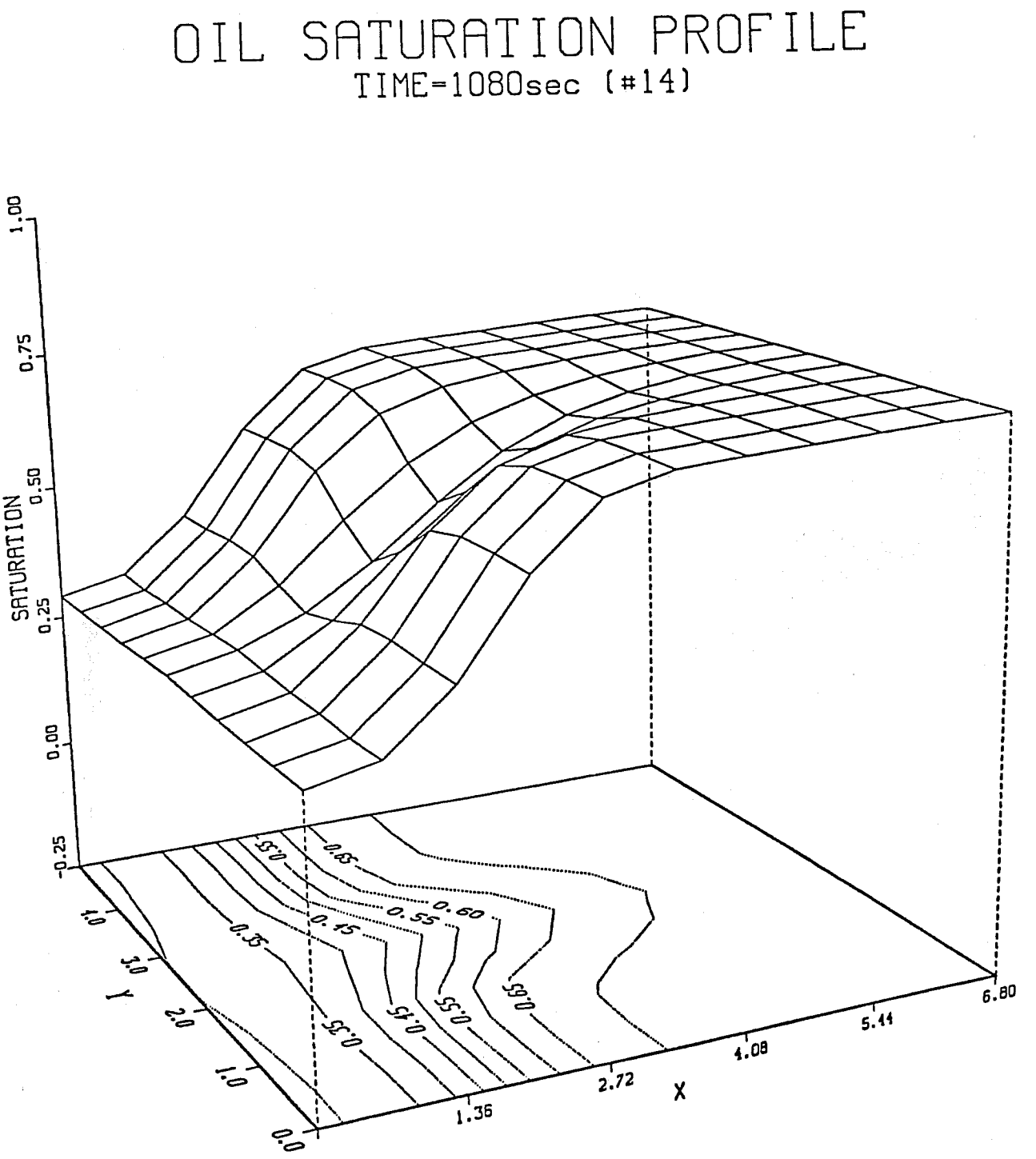

Figure 71. Oil saturation profile with foam at time 1080 sec.

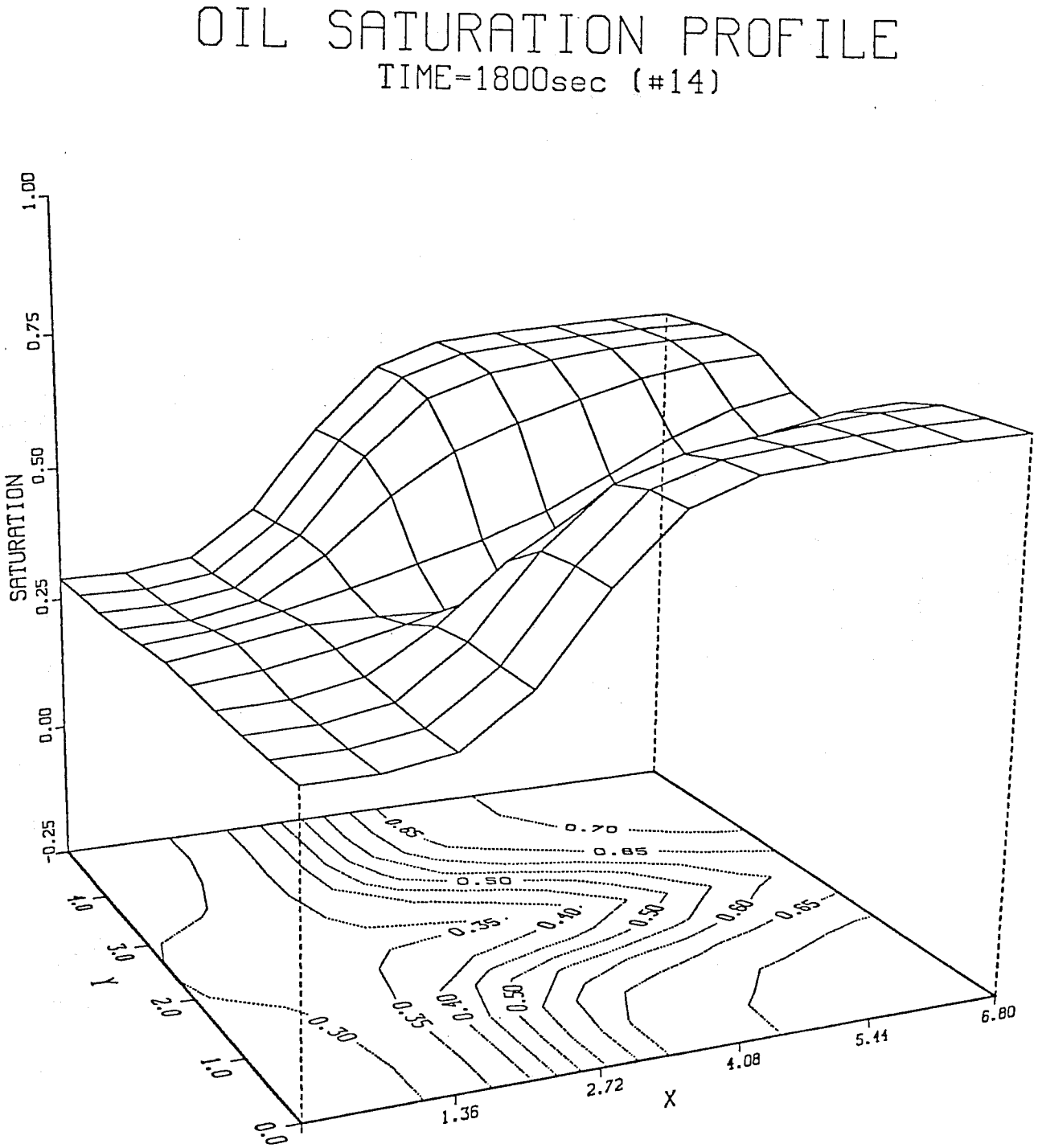

Figure 72. Oil saturation profile with foam at time 1800 sec.

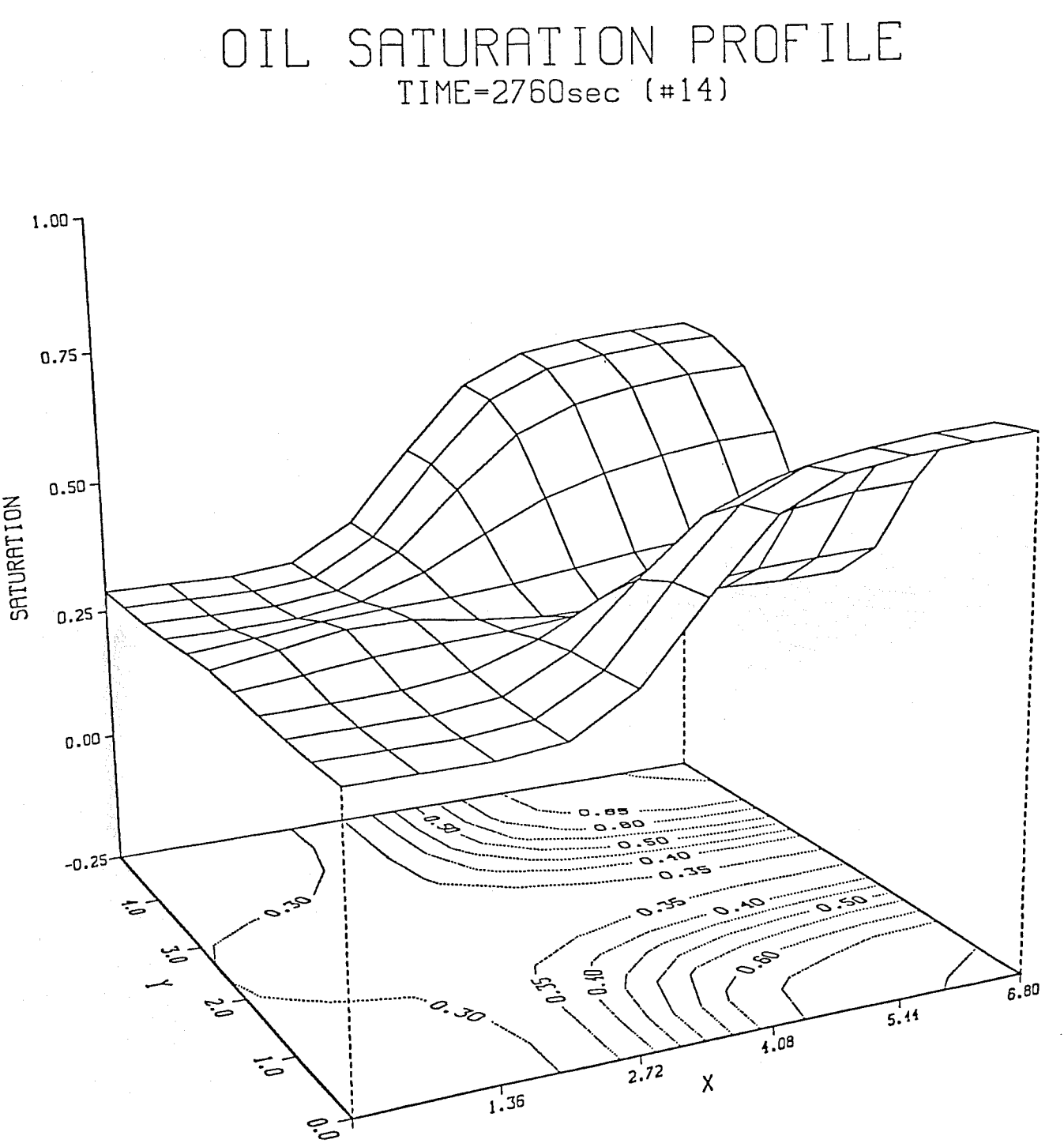

Figure 73. Oil saturation profile with foam at time 2760 sec.

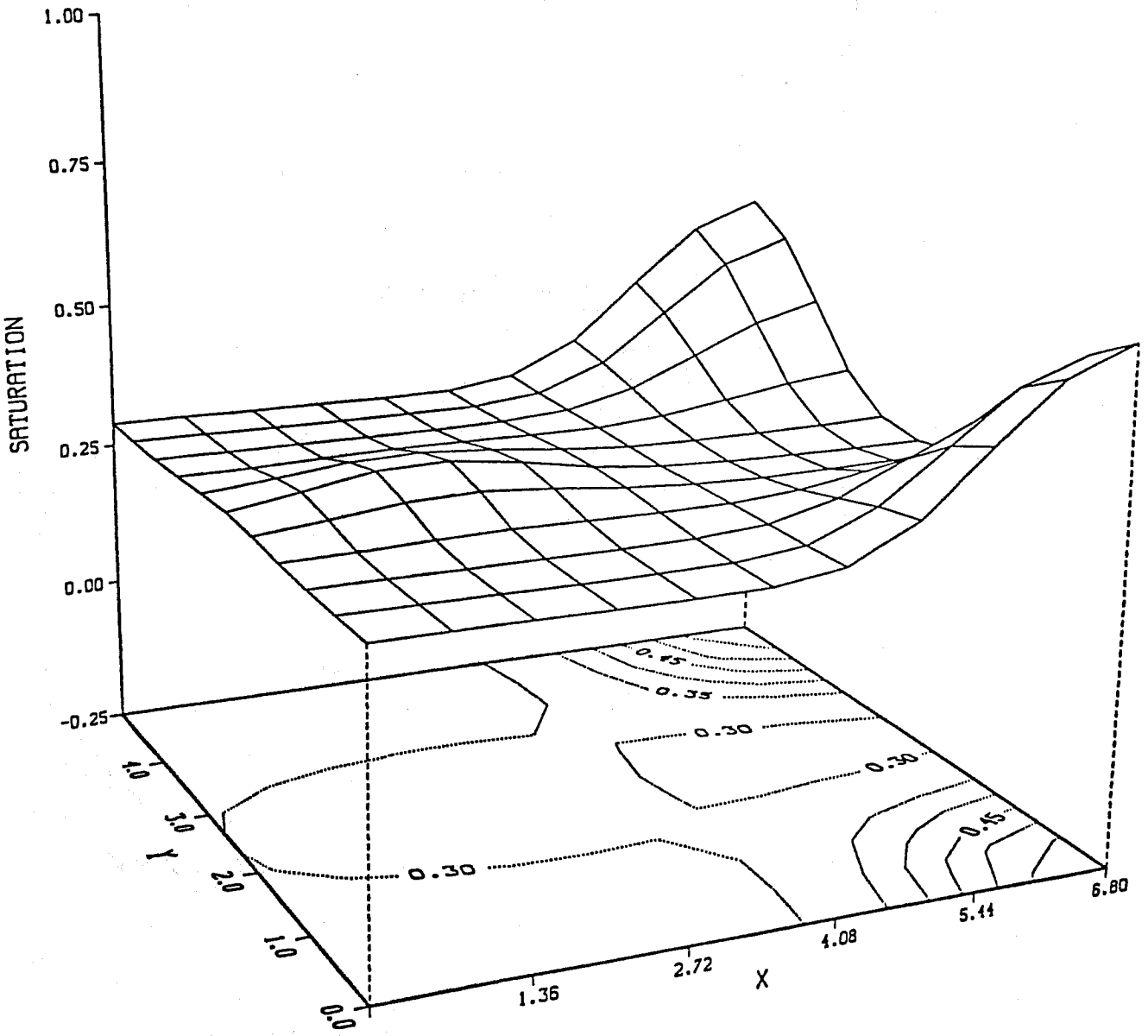

Figure 74. Oil saturation profile with foam at time 5880 sec.

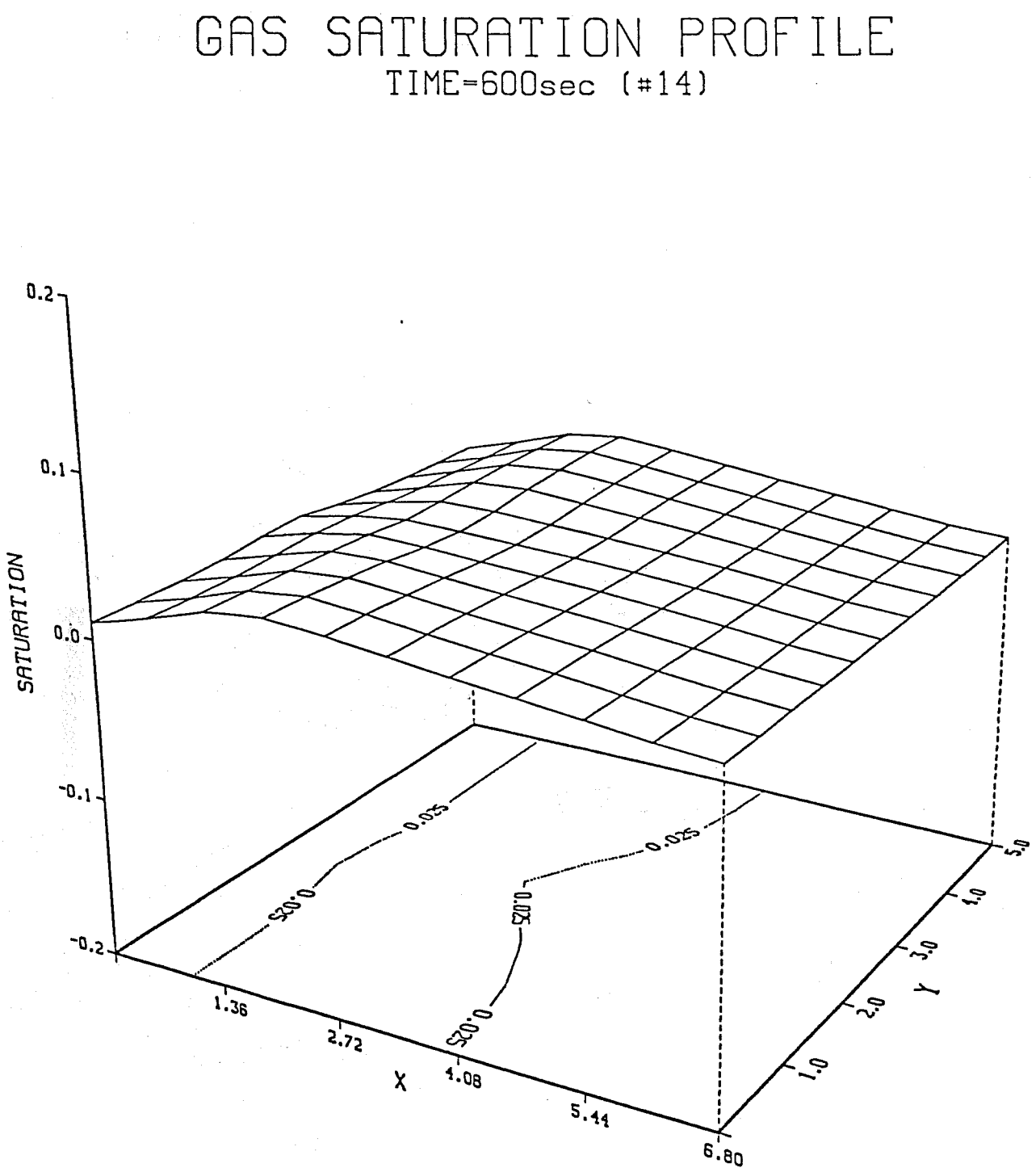

Figure 75. Gas saturation profile with foam at time 600 sec.

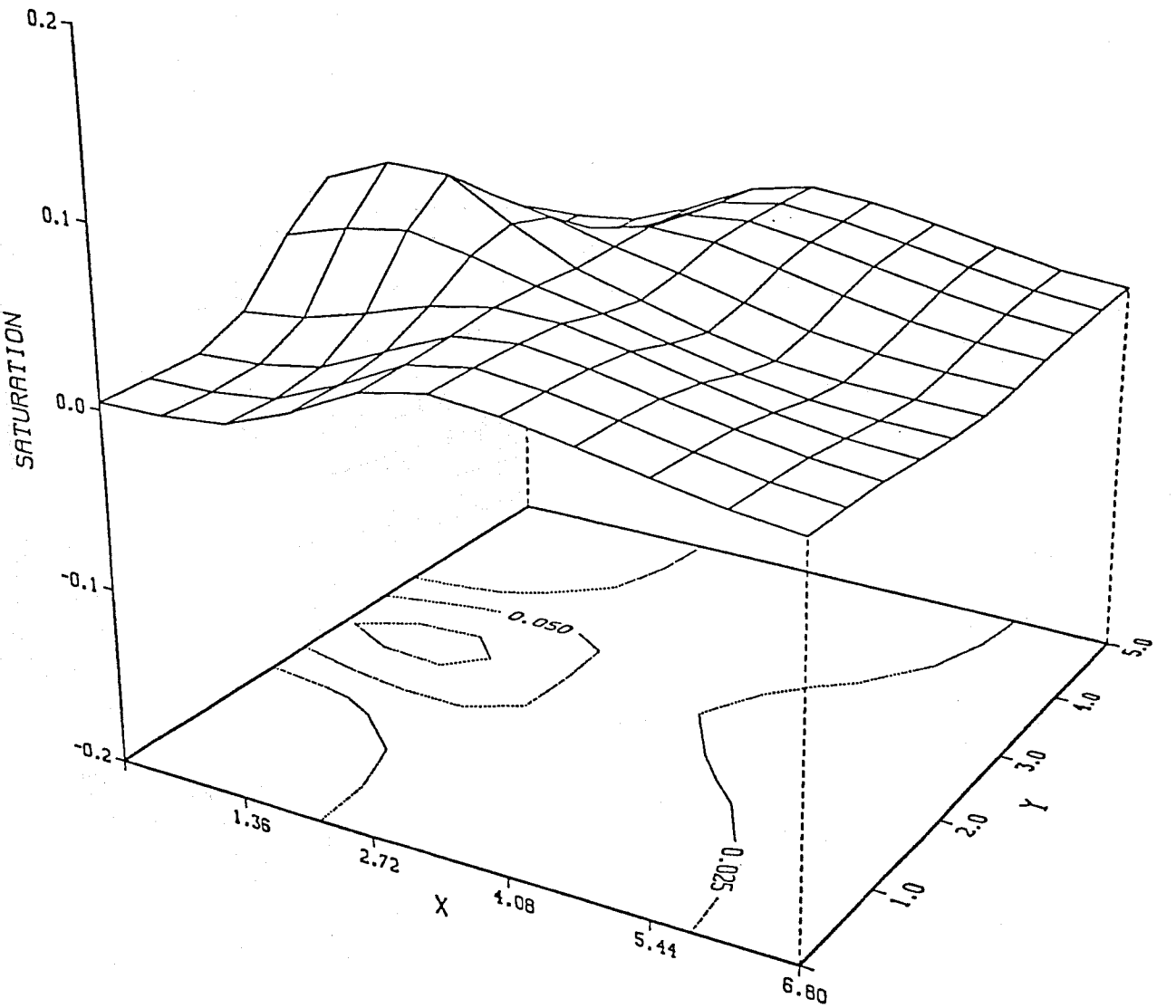

Figure 76. Gas saturation profile with foam at time 1800 sec.

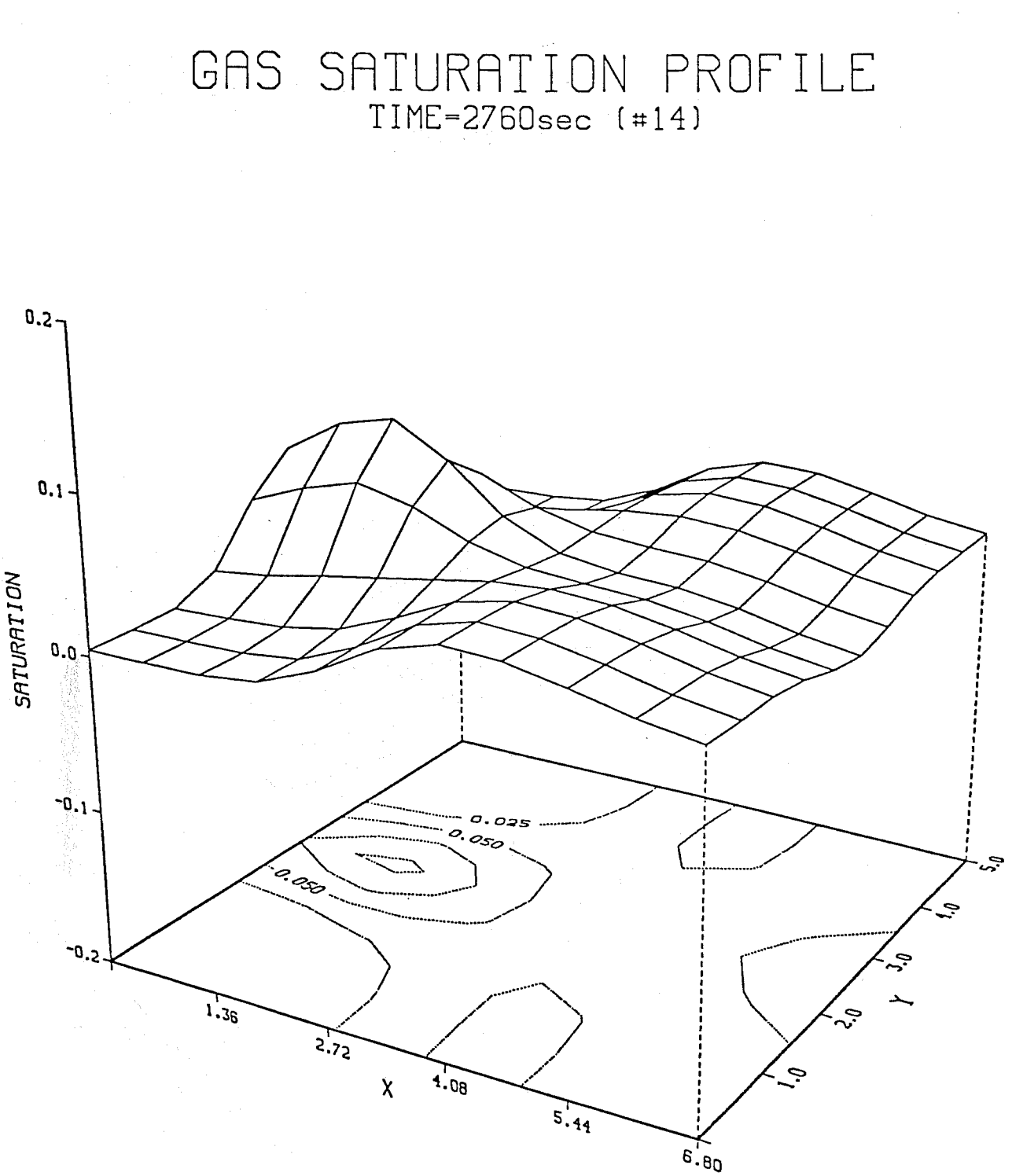

Figure 77. Gas saturation profile with foam at time 2760 sec.

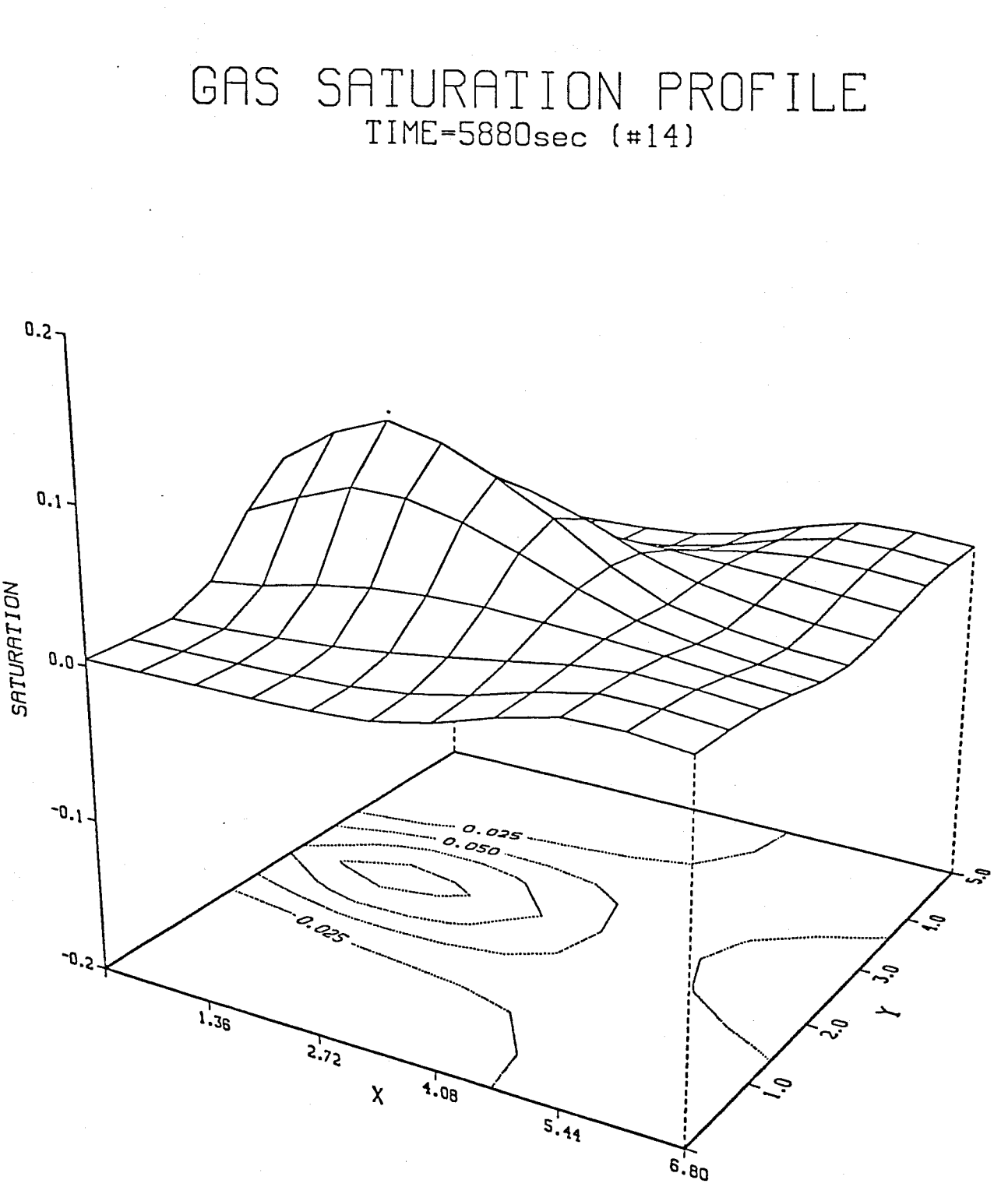

Figure 78. Gas saturation profile with foam at time 5880 sec.

TABLE 15. NOMENCLATURE

A_f = bubble trapping parameter, #/cm^3.

A_s = constant in the Langmuir model, g/cm^2.

a = reduction factor.

b = parameter in Equation 15.

C_f = bubble coalescence rate per unit reservoir volume, #/sec/cm^3.

C_s = surfactant concentration, g/g.

C_{sI} = injection surfactant concentration, g/g.

C_s^{lim} = minimum surfactant concentration for which foam can exist, g/g.

C_{sref} = reference surfactant concentration, g/g.

c_1 = parameter in Equation 10.

d = constant in Equation 11, cm/sec.

e = exponent in Equation 11.

e_1 = exponent in Equation 10.

e_2 = exponent in Equation 12.

e_3 = exponent in Equation 13.

G_f = bubble generation rate per unit reservoir volume, #/sec/cm^3.

g = gravitational acceleration vector.

K_f = bubble trapping parameter, cm^3/#.

K_s = equilibrium constant in the Langmuir model, g/g.

K_1 = generation rate constant, #/sec/cm^3.

K_2 = coalescence rate constant, cm^3/cm^3/sec.

K_3 = geometric factor.

k = absolute permeability, darcy.

k_{rgf} = effective relative permeability of the gas phase when foam exists.

$k_{r\ell}$ = relative permeability of phase ℓ.

n_c = critical bubble density above which the generation rate approaches

zero, #/cm^3.

n_f = bubble density of the flowing foam, #/cm^3.

n_{fI} = injection bubble density, #/cm^3.

n_s = bubble density of the trapped foam, #/cm^3.

P_{cgo} = gas-oil capillary pressure, atm.

P_{cow} = oil-water capillary pressure, atm.

P_ℓ = pressure of phase ℓ, atm.

q_ℓ = injection/production rate of phase ℓ per unit reservoir volume, g/sec/cm^3.

S_ℓ = saturation of phase ℓ.

S_o^{lim} = maximum oil saturation for which foam can exist.

t = time, sec.

$\mathbf{U}_\ell$ = velocity of phase ℓ, cm/sec.

U_{ref} = reference gas velocity, cm/sec.

V_c = critical gas velocity above which moving foam can be generated, cm/sec.

w = injected liquid fraction.

X_f = fraction of gas that is flowing.

Greek

Γ = surfactant adsorbed concentration, g/cm^2.

δ = rock surface area per unit mass, cm^2/g.

μ_{gf} = effective viscosity of gas phase when foam exists, cp.

μ_ℓ = viscosity of phase ℓ, cp.

ρ_ℓ = mass density of phase ℓ, g/cm^3.

ρ_r = mass density of rock, g/cm^3.

ϕ = porosity.

A series of gravity-stabilized, CO_2-synthetic oil corefloods were performed over a pressure range from immiscible through fully miscible. The oil recovery/pressure curve appears to exhibit a small increase in recovery over a pressure range where complex multiple hydrocarbon phase behavior is present, a few percent higher than fully miscible recovery. Additional experiments, e.g., berea corefloods, micromodel displacements, and micro-core tests, are being conducted to determine if there is a significant and meaningful multiple hydrocarbon phase flow effect on sweep efficiency. Early micromodel results appear to demonstrate the L_2 (hydrocarbon-rich) phase sticking to the walls, decreasing the effective permeability.

The mechanisms associated with foam generation and propagation were studied in two-dimensional glass micromodels at CO_2 flooding reservoir conditions. We investigated the effects of different scales of microscopic heterogeneity on flow behavior and blocking mechanisms using both in-situ and pregenerated foam. Also investigated were the effects of oil phase, surfactant concentration, injection mode, and initial water saturation on foam flow behavior. Two papers on foam flow have been presented,: "The Effect of Microscopic Heterogeneity on CO_2-Foam Mobility: Part 1-A Mechanistic Study," was presented at the 1988 SPE/DOE Enhanced Oil Recovery Symposium held in Tulsa, OK, and "Effect of Pore-Level Heterogeneity on High Pressure Gas/Foam Flow Through an Oil Saturated Porous Media" was presented at the 1988 AIChE Annual Meeting held in Washington, D.C. Also presented at the 1988 SPE/DOE Enhanced Oil Recovery Symposium was the paper "Gels for CO_2 Profile Modification."

A two-dimensional numerical simulator is currently being developed which models high pressure gas/foam flow. The initial formulation of the model is presented here. "Foam" is presently generated by the mechanisms of snap-off or travelling lamella division, and static lamellae that are assumed to affect gas relative permeability are generated at this time by the "leave-behind" mechanism. A simulation of the processes associated with high-permeability zone blockage by foam, fluid diversion (crossflow), and increased trapped oil recovery is demonstrated with this initial version of the simulator. A paper entitled, "Modeling Multiphase Flow in Oil Reservoirs," is being presented at the 1989 Eastern Simulation Multiconference in March.

An NMR Imaging Study on fluid flow through porous media was initiated. Water-oil dolomite corefloods have been imaged. Nonlinear growth rates of frontal displacement instabilities and matrix-fracture transport functions are currently being investigated.

II. CO_2 MOBILITY CONTROL AND FLOW HETEROGENEITIES

Our primary research emphasis still conforms to the project title, and is still directed towards the use of relatively pure CO_2 as a displacement fluid. Although our results are still being given in terms of this more restricted aim, we anticipate that there will be applications of these results beyond the immediate needs of CO_2 flooding. Consequently, we will discuss, or at least mention, the possible uses of our work in other gas displacement projects wherever it seems appropriate in this report.

A. INTRODUCTION—ORIGINS OF NON-UNIFORM DISPLACEMENT

In Task II of the CO_2 project, our aim is to find procedures that the operator can use in order to minimize the lost production resulting from non-uniform displacement. Our research addresses two distinct but interacting causes of this common deficiency that is experienced in both secondary and tertiary oil recovery projects. Non-uniform displacement of crude oil from the reservoir, which is responsible for early breakthrough of the displacing fluid and premature abandonment of the oil field, is itself a consequence of several natural (and difficult-to-change) factors.* In this section of the project, as noted, we concentrate our efforts on two of these factors or causes.

The first of the two major causes to be discussed is the non-uniform displacement caused by heterogeneities of the reservoir rock. Although the presence of extreme variability of properties in natural sedimentary rock is obvious, its effects on flow and displacement and the mathematical methods by which to deal with this situation have not been so clear. This portion of the PRRC project has been stimulated by the significant progress made recently in the characterization of reservoirs. Our special interest in this work has been to adapt it to the study of displacement efficiency and timing. We have become involved both with techniques to diagnose and describe heterogeneity in reservoirs, and with the interpretation of laboratory corefloods performed in cores or in quarried samples. Most of this work has been performed by graduate students in the Petroleum Engineering Department of New Mexico Tech as part of their thesis research. In this first year of our project continuation, we have made, and report here, significant progress in three related directions concerned with reservoir heterogeneity as follows:

1. To enable the heterogeneity of the reservoir to be judged from the results of conventional tracer tests. The material presented under the title "Base Case for Well-to-Well Tracer Studies" is a condensation of the master's thesis of Saleem Ghori.

---

*Some causes of non-uniform displacement at present lie outside the scope of this project. One of these is simply that access to most oil fields is by approximately vertical wells. Because the shape of the oil-bearing formation is generally such that its vertical dimension is much smaller than the horizontal extent, large areas of the "swept zone" are traversed by streamlines of appreciably lower velocity than those on more direct well-to-well paths. Consequently, much of the oil in these areas is left unrecovered when the pattern is abandoned. A common answer to this problem, the drilling of properly timed and located infill wells, involves important and interesting technical problems. Although this strategy often can be justified economically, it will not be discussed further here.

2. To establish simple rules by which the operator can judge the effect of the heterogeneity of a particular reservoir on the displacement efficiency. The material entitled "Displacement in a Heterogeneous Five Spot" is adapted from the master's thesis of Naser Heravi.

3. The effects of smaller scale heterogeneity, both on laboratory results and on reservoir performance are the subject matter of doctoral research by Ibrahim Bahralolom, whose recent work is presented under the heading "Flow Heterogeneity In Porous Media At Small-Scale."

The second cause of non-uniform displacement of interest here is the growth of frontal instability brought about by the differences in properties of displacing and displaced fluids. In predominately horizontal miscible or developed miscibility floods, this frontal instability occurs when a more viscous fluid is displaced by less viscous one. As a result of this instability, irregularities in the frontal region between displaced and displacing fluids grow into "viscous fingers" that move faster than the average front. The industry has been aware of this problem for almost four decades in connection with waterfloods.[44] The fingers bring some of the displacing fluid towards the production wells more rapidly than the average rate, and they can cause early breakthrough even in apparently one-dimensional flow systems. Although the use of a more gradual change (a "grading") of the initial displacement front can postpone the formation of these fingers and retard the growth of the more closely spaced ones, the only known means to suppress the more widely-spaced fingers (which, in the reservoir, are the more serious ones) is to somehow thicken the displacing fluid so that it is effectively as viscous as the crude oil itself. To this end, we have been seeking ways to thicken CO_2, and in particular we have been simultaneously following two different and promising paths.

The first type of additive that we are developing to increase the pressure gradient behind the front is called a "direct thickener." Direct thickeners are chemicals which form polymeric solutions in the CO_2, or in other dense gas displacing fluid, to increase its viscosity significantly. Our work is a continuation of research that had to a large extent been planned and directed by Dr. Dileep Dandge, who is now working on different scientific problems in a private company in California. The section headed "The Development of Direct Thickeners" is a report of work by him and by Kirk Hollis. Several others who have contributed, but who also have left the project, are Pradeep Singh, Rita Singh, and Ann Westerberg. The direct thickeners research already is showing the influence of Dr. Pratap Gullapalli, who has recently joined us to take over direct supervision of this work. Our report details progress in synthesis and testing of several compounds that achieve the viscosity increase in nonpolar solvents by what is known as "association" between the molecules of the dissolved additive.

The second type of additive is called "foam" and consists of surfactant-stabilized, aqueous bubble-films or lamellae in the pore space of the rock. These lamellae separate the CO_2 or other dense-gas displacing fluid so that it cannot flow as easily. The pressure gradient behind the front is thus increased, and the growth of viscous instabilities can be slowed or suppressed. Progress during this year, reported below under the heading "CO_2-Foam Mobility Control," has been centered on two aspects of our laboratory work. The first of these is the effect of surfactant concentration on measured foam mobility, in order to enable operators to design for the desired mobility reduction. The second is the acquisition of new data, on a variety of core material, to verify and explore the dependence of relative mobility on rock permeability. In connection with the latter portion of the work, it appears even more likely, on the basis of the work this year, that CO_2-foam will be effective in many circumstances in counteracting some of the flow non-uniformities caused by the natural reservoir heterogeneity. The research reported was performed by, or under the direction of, Dr. Hae Ok Lee. Assisting her in the work this year have been a Chemistry graduate student, Sandy Svec, an undergraduate Petroleum Engineering student, Mustafa Sadeq, and a Physics undergraduate student, Bob Svec. Also assisting in some of the foam work have been Jim McLemore and Kirk

Hollis. Our goal is to acquire the capability to specify surfactant type and concentration, injection volume ratio of dense CO_2 to total fluid, and other design parameters, to support a field test of CO_2-foam as a mobility control additive.

For each of these research areas, the necessity of integrating the results into the current procedures of reservoir engineering must be taken into account. These procedures generally involve the use of numerical analysis or computer simulation, and it is therefore a goal of this project to format our results in ways such that they can be of immediate use within the existing simulation programs. Progress towards this goal also was made during an extended visit by the Principal Investigator to the Petroleum Department of the University of Texas at Austin, in which the testing and possible adaptation of their well-known simulation packages were explored.

Final sections of the Report discuss one of the problems of this integration and summarize the research performed under Task II.

B. HETEROGENEITIES OF THE RESERVOIR ROCK

1. Base Case For Well-To-Well Tracer Studies

Radioactive or chemical tracers have long been used in reservoir floods to give operating engineers information about reservoir and flow characteristics. All of the details of these studies are important in the design and operation of enhanced oil recovery projects. The topic for this work, however, is not that inclusive. It does not discuss the kind of tracer to use, or give detailed instruction on how to characterize reservoir heterogeneity by tracer tests. Although this study is primarily concerned with the numerical analysis of miscible displacement, some introductory material on these other topics is warranted.

a. Classification and Practice of Tracer Tests

Tracer tests are usually either (1) well-to-well, in which a tracer is injected in an injection well and detected at a production or observation well, or (2) single well tests, in which the tracer is injected into a well and is allowed to react with the formation fluids before being detected in samples produced from the same well. The considerations of this work have as yet been applied only to the first type. Two kinds of tracers have been used to evaluate underground oil and water formations. The test materials can be radioactive or chemical, depending upon the type of formation, the fluid, and availability of tracers. The detection of chemical tracers requires the taking of samples at the wellhead, whereas radioactive tracers also can be detected by logging—even without producing the well. The present study, however, concerns tracers detected at a producing well.

Wagner[45] gave a list of information that can be attained by tracer tests, concerning volumetric sweep, the identification of offending injectors, directional flow trends or flow barriers, the relative velocities of injected fluids, and the evaluation of sweep-improvement treatments.

Necessary characteristics of a good tracer material were described by Carpenter et al.[46] Their list included a discussion of the detectability of a good tracer relative to materials naturally present in formation fluids as well as solubility. In addition, and ideally, the tracer material should not be adsorbed onto the rocks, should not react with reservoir materials, and should be as inexpensive as possible. In consideration of these requirements, Carpenter used boron in the form of borax

($Na_2B_4O_7 \cdot 10H_2O$) and boric acid (H_3BO_3) as tracers to determine water channelling in three different formations.

Strum and Johnson[47] determined qualitatively the applicability of certain chemicals in tracing the progress of flood waters through the underground oil reservoirs. Brine, fluorescein, and a surface-active compound were used in this work. The tracers were first tested on the laboratory cores, then applied to the Pennsylvanian Bradford Third Sand Formation. They showed that many adverse conditions such as crevices, fissures, or directional permeability can be detected by these tests. Such anomalies can be determined from a study of time elapsing between the injection of the tracer and its appearance in the surrounding producing wells.

b. Information Obtained from a Tracer Test

The data from tracer tests often are put into the form of the tracer breakthrough profile at the production well, where the tracer output concentration is the summation of tracer responses from the many streamlines that comprise the flow geometry inside the reservoir. In addition, the tracer flow is affected by dispersion, which is mainly caused by the interaction of the tortuosity of the flow paths and molecular diffusion. The object of this study is to compute a "base case" tracer breakthrough profile for the simple case where the formation is a single layer of the ideal but mythical homogeneous and isotropic porous medium.

With the assumption of uniform permeability, the mathematical solution of Darcy's equation in five-spot geometry, as in most regular two-dimensional domains, is available in the literature. These solutions or solution methods give only the pressure distributions, however, and problems remain concerning their use in computing tracer displacement and in determining the output concentrations that would be observed at the output well(s) of the system.

Mathematically the flow of a miscible tracer in the x-direction in a homogeneous, isotropic, porous medium is described by the well known convective dispersion equation as

$$\frac{\partial C}{\partial t} = -\frac{U}{\phi}\frac{\partial C}{\partial x} + D_L\frac{\partial^2 C}{\partial x^2} + D_T\frac{\partial^2 C}{\partial y^2} \tag{58}$$

where

U is the Darcy velocity,
ϕ is the porosity,
D_L is the longitudinal dispersion coefficient, and
D_T is the transverse dispersion coefficient.

Numerous experiments on laboratory cores have shown that D_T is usually much smaller than D_L, and deJong[48] and Bear[49] have shown that dispersion can be represented by a second-order tensor with a characteristic direction parallel to the flow. Thus, the transverse dispersion plays an important role in any flow pattern where the concentration gradient is not in the direction of flow velocity.

Hydrodynamic dispersion incorporates two mechanisms, mechanical dispersion and molecular diffusion. Mechanical dispersion consists of the mixing due to the variations in local velocity. Whereas the Darcy velocity is an average over a portion of the rock containing many pores and varies rather smoothly from place to place, the actual fluid velocities within the porespace vary over a wide range in both magnitude and direction, along the tortuous flow paths. This velocity distribution causes any initial tracer mass within the flow domain to spread at a rate proportional to the flow

velocities and to the gradient of tracer concentration. It also can be seen that this spreading has at least two components, one in the direction of Darcy velocity and the other in the directions perpendicular to the mean flow, and that this is the reason for the existence of at least two components of the tensor described above.

Molecular diffusion results from the continual random motions of the molecules of the liquid and of the tracer dissolved in it. As a result of this diffusion, the tracer concentration tends toward uniformity within the liquid phase. This diffusive flux occurs independently of the bulk motion of the fluid, and it is proportional to a diffusion coefficient and to the concentration gradient. Inside a porous medium, the rate of diffusion is slowed because of the tortuosity of the internal geometry. In a way, this is analogous to the decreased electrical conductivity of a brine-saturated, nonconductive rock of similar geometry. Because molecular diffusion depends on time, its effects on the overall dispersion will be greater when more time is available—that is, at low flow velocities.

The variation of the dispersion coefficients with velocity has been measured by many investigators (mostly for unconsolidated packs, which are usually more uniform macroscopically). Their results have been summarized by both Blackwell[50] and by Perkins and Johnston[51] by the equation:

$$D_c = \frac{D}{\phi F} + \frac{\lambda_c d_p U}{\phi} \tag{59}$$

where

the subscript c is either L or T,
D (unsubscripted) is the molecular diffusion coefficient,
ϕ is the porosity of the rock or other matrix,
F is the electrical formation resistivity factor,
λ_c has the dimensions of length,
d_p is the particle size of the rock grains, and
U is the Darcy velocity.

The constant λ_L is somehow descriptive of the geometry of the porous matrix, and is often called the dispersion distance. The ratio λ_L/λ_T is large, and for unconsolidated packs is on the order of 30.

For flow along a column, or in some other geometry of constant cross section, the solution of the Darcy equation specifies a constant value of velocity. Thus the dispersion is also constant inside the boundaries of the porous media, and Eq. (58) is appropriate. But for other geometries, e.g., radial flow or flow in a five-spot pattern, the velocity is a function of position, and consequently the dispersion coefficient is a variable. For these more complex geometries, the convective-dispersion equation becomes a second-order partial differential equation with variable coefficients. This makes it very difficult, if not impossible, to derive an analytical solution to describe the mixing in non-uniform flow fields. An added difficulty that springs from the two-dimensional flow system is that in order for the solution to be correct, transverse dispersion must be included along with longitudinal dispersion. In consequence, exact and general analytical solutions for this type of equation are not available.

Nevertheless, there have been several approximate or numerical solutions proposed to this problem. Some of these describe mixing in restricted regions of radial flow systems with good accuracy. The five-spot pattern (or variations of it), however, is the most commonly used flood pattern for the recovery of oil. A considerable amount of work already has been done to simulate the pattern numerically or analytically for immiscible displacements.

For a miscible case, though the complexity of the flow is less, the literature is more sparse. Brigham and Smith[52] performed a quantitative analysis on tracer dilution curves for developed five-spot patterns. They approximated the flow as radial in the pattern, and devised an equation for the tracer breakthrough curve by combining the tracer dispersion (longitudinal) effects with the areal sweep effects. Equations also were developed to predict the time of tracer breakthrough and peak concentration of the tracer. This approximation, however, introduced errors in the computation of arrival times for the different streamlines.

Baldwin[53] approximated a quadrant of a five-spot pattern by diverging-converging radial elements. These elements allowed the consideration of only longitudinal dispersion in the media. Baldwin matched his results to both experimental and field data, and achieved a better match.

Abbaszadeh and Brigham[54] produced useful approximate analytical solutions for different developed patterns with a mobility ratio of one. The derivation of his equations was accomplished by combining the tracer dispersion (longitudinal) effects with the areal sweep effects for many types of flood patterns. For tracer dispersion effects, he used the same concept as given by Lau et al.,[55] Baldwin,[53] and Brigham.[56] By integrating individual stream tube tracer concentrations, analytical expressions were obtained which define the tracer breakthrough curves for several developed patterns. For areal-sweep effects, exact analytical equations were obtained in the form of elliptic integrals which describe several pattern breakthrough curves. Abbaszadeh's study shows that the tracer breakthrough curves from a homogeneous system depend upon the geometry, pattern size, and dispersion constant of the formation rock. The work by Abbaszadeh did not include either transverse dispersion or the velocity-independent component of dispersion that is due to molecular diffusion.

This study by the PRRC was initiated to develop a numerical model for the tracer analysis which could be used for comparison in a five-spot pattern within the limitations of a homogeneous formation. To do this, a stable numerical scheme is required, one which should not be affected by numerical dispersion. Proper inclusion of the transverse dispersion component along with the longitudinal component can increase the accuracy of the numerical solution and provide information on its relative importance in this situation. With these points in mind, a new numerical technique has been developed to analyze tracer flow in a homogeneous five-spot pattern. The method takes into account the effects of both convection and dispersion.

c. Outline of the Numerical Method

In this method of numerical analysis, the solution is approached differently than in the conventional finite difference methods of solving the convective dispersion equation. Instead, the problem is rephrased in terms of the equation of motion of the isoconcentration lines, and the numerical computation is directed toward keeping track of their positions. Both the convective and dispersive contributions to isoconcentration line velocity are explicitly considered in the calculation. It turns out that this scheme is numerically stable and avoids numerical dispersion. In addition, this method eliminates the need to make any detailed assumption about the outer boundary conditions. The initial concentration distribution near the well is a 'ramp up ramp down' input profile instead of a step input profile. This type of input profile is physically more realistic than a discontinuous change in concentration, and it also eases the computation near the input well.

This method is an extension of a technique published by Heller,[57] who solved the radial flow problem in terms of equations of motion of the isoconcentration lines with the above initial form for the concentration distribution. The tracer slug was divided into some number of points lying on isoconcentration surfaces. Each isoconcentration point was subjected to the influence of convection

and dispersion, and the numerical technique was directed towards following their positions. Only a one-dimensional radial flow problem with longitudinal dispersion and molecular diffusion at low flow velocities was considered. The results were not compared with any of the analytical solutions, although an analysis of the behavior of displacement fronts in radial geometry was given.

The additional complexity of the present problem stems from the presence of the production well at the opposite corner of the five-spot and the consequent need to deal with a more complex flow pattern and situations in which the concentration gradient and the flow velocity are no longer parallel. Even in radial flow, the modifications of the slug's concentration distribution by hydrodynamic dispersion are not simple. In the five-spot case, the continuous changes that occur as the slug is swept towards the production well are different along different streamlines.

First, the equation of motion of isoconcentration lines is stated in Cartesian coordinates. A general equation in tensorial form then is derived for non-uniform flow in any coordinate system. Finally, the equation of motion of isoconcentration lines is expressed in a simplified form in a curvilinear orthogonal coordinate system. One family of the coordinate curves, the (Φ,Ψ), coincides with the family of streamlines and isopotentials. Because the flow direction is everywhere parallel to the streamlines, this change of coordinates reduces the dispersion tensor to the two components used in the two-dimensional flow system of Eq. (58).

d. The Flow Field in a Five-Spot

It is assumed that the injection rates are equal to the production rates, and that the formation is uniform. Therefore, flow is symmetrical around each injector, with one quarter of the injection rate directed towards each producer. Because of the assumed symmetry, the pattern can be further simplified to one-eighth of the full five-spot pattern.

The convective part of the equation of motion of isoconcentration lines includes the Darcy velocity. Following Prats,[58] Morel-Seytoux,[59] and Abbaszadeh and Brigham,[54] the Darcy equation is solved in the geometry of the five-spot. Analytical expressions for the Darcy velocity in the (Φ,Ψ) coordinates are rederived, using complex variable theory. In the derivation of these equations, it is assumed that no capillary or gravity effects are included and that the velocity as derived is a function of space only, and not of time. Analytical expressions for the breakthrough time in a "piston-like" displacement and distances along streamlines also are calculated. These analytical solutions are various forms of the elliptic integral. Use of the analytic expression of Darcy velocity in the equation of motion of isoconcentration lines has made the problem more analytical than numerical.

In this gravity-free system, the Darcy velocity in differential form can be written as

$$U = -(k/\mu)\nabla P \tag{60}$$

where ∇P is the pressure gradient and k is the permeability.

Additionally, if the fluid viscosity, μ, and permeability, k, are independent of position, and if the fluid is incompressible, then this equation can be reduced by taking the divergence, which produces Laplace's partial differential equation in pressure:

$$\nabla^2 P = 0 \tag{61}$$

Analytic solutions to this equation can be obtained easily if the function P or normal component of its gradient is given on the boundary. For this case, the solutions have been obtained in a complex plane, and an expression has been derived for the complex potential of the flow field in this geometry. The real part is the equation for the pressure distribution, and the imaginary part is the stream function.[59] The complex potential is:

$$\Omega(z) = \Phi(x,y) + i\Psi(x,y) \tag{62}$$

where i is the base of the imaginary number system, and $z = x+iy$.

The mathematical expressions for Φ and Ψ, and of the components of Darcy velocity as derived from these expressions, can be written in terms of elliptic functions. The formulas for the distances along streamlines and the time of breakthrough for a five-spot are presented in Appendix A of Ghori's thesis.[60]

e. Derivation of Equation of Motion

In the development of equations to describe the flow of the tracer slug through the homogeneous five-spot pattern, it is assumed that the following are true:

1. There is only one mobile, fluid phase in the system;
2. The tracer material is miscible with fluids both ahead of and behind the slug;
3. The tracer does not adsorb onto the formation rock, or become adsorbed into any immobile fluid phase;
4. The tracer does not react with either the formation fluid or the formation matrix;
5. If the tracer is radioactive, its half-life is long enough that it does not decay appreciably during flow and prior to breakthrough; and
6. The tracer slug has the same viscosity as the displaced and displacing fluids.

The displacement of miscible fluids with the same viscosity and density through a porous medium proceeds along the same streamlines as those established for single-phase flow in the same geometry. The streamlines and isopotential lines for the system are unaffected by the location of the displacement fronts. Because of this, the state of the displacement of such a miscible fluid tracer in a porous medium can be specified completely by two macroscopic variables—a vector, U, which represents the Darcy velocity, and a scalar, C, representing the concentration of displacing fluid. The latter often is normalized to range from 0 to 1.

The concentration distribution can be described by a moving family of isoconcentration lines. In a rectangular coordinate system, the variation with time and position of the concentration of a displacing fluid is defined by the partial differential equation (58) as given earlier. By simple manipulation, and writing D for the tensor dispersion coefficient, the equation yields a formula by which V, the velocity of points on the isoconcentration curves, can be computed.

$$V \bullet \nabla C = U \bullet \nabla C/\phi - \nabla \bullet D \bullet \nabla C \tag{63}$$

In the five-spot geometry, the situation is complicated by the curved streamlines and by the fact that the gradient of concentration is parallel to the Darcy velocity only in the immediate neighborhood of the injection wellbore. Because of this, the tensor characteristic of the dispersion must be taken into account. It turns out that if the equation is written in terms of the same (Φ,Ψ) coordinate system used earlier to describe the streamlines and isopotential lines, the velocity of points on the isoconcentration line can be computed.

The analytic expression in the (Φ,Ψ) coordinate system, which is the equation of motion of the isoconcentration lines, is used directly for computing the two-dimensional miscible displacement of the tracer slug in the five-spot pattern. The computation has been coded in Fortran 77. The program calculates the velocity of the isoconcentration surfaces, following the motion of an injected tracer slug under the joint influence of convection and dispersion.

The numerical technique employed here has eliminated the use of any type of outer boundary conditions, since they are represented automatically by the symmetry. Nevertheless, an initial condition is required to start the computations of tracer band movements. It is presumed that the actual tracer band is initially introduced as a flat-topped slug with inner and outer edges, in which the concentration varies linearly, ramp-fashion, from 0 to 1 and from 1 to 0, respectively. These ramps can be quite steep; the thickness of the flat-top portion then determines the amount of tracer injected into the pattern. This concentration profile is divided into seventeen isoconcentration lines or points. The outward or front velocities of each of these isoconcentration points on a streamline of a five-spot pattern are calculated. This type of input profile was first introduced by Heller in 1986 to calculate dispersion in a radial pattern. The "ramp up ramp down" input profile is more realistic than a step-input profile, and it eliminates the difficulties that might be caused by an infinite value of concentration gradient.

There are two distinct effects on the shape of the concentration profile of the slug as it moves outward from the injection well. The first influence on the slug shape is that of dispersion due to the mixing at the front and rear edges of the tracer. Dispersion rapidly smooths the corners of the initial ramp, and tends to increase the thickness of the slug—especially after it has decreased the central concentration from the value of one.

The second influence on the shape of the concentration profile of the slug is from the geometry of the five-spot pattern. On each streamline, the flow velocity reaches a minimum where that streamline crosses the diagonal that stretches between those corners of the square without wells. The decreasing velocity (and increasing perimeter of the region occupied by the tracer) as the slug is first carried outward from the injector causes the slug to decrease rapidly in thickness along the streamline direction. The flow velocities are symmetrical across this diagonal also, and they increase beyond the crossing point as the producing well is approached.

f. Time Stability of the Calculations

Once the velocities of isoconcentration lines have been computed, their new positions are obtained by using a suitable time step. The time step criterion is important in terms of the stability of the numerical scheme. By definition, a numerical algorithm is considered stable if any errors introduced at some stage of computation do not amplify during subsequent computations. Two kinds of errors may be amplified if the numerical scheme is unstable. These are round-off errors, caused by the finite accuracy of the computer performing the operations, and truncation errors which result from the lack of accuracy of the finite difference scheme used in approximating the needed derivatives.

Because the convection part of the equation of motion of isoconcentration lines has been replaced by an exact solution of the Laplace's equation, and because the dispersive part represents a physical process that smooths out local inaccuracies, the present numerical scheme can be made unconditionally stable. A small inaccuracy (a bump on the concentration profile), caused by a previous error in the calculation of velocity will damp out in the next iteration if a suitable time step is used. The magnitude of the optimum time step varies with position, and several criteria are utilized for its choice. For instance, in the near vicinity of the wellbore, there are large concentration gradients and high-flow velocities. Tracer flow is dominated by convection, and dispersive effects are less—it is thus desirable in this region to use a smaller time-step. More details on the calculation of the time step criteria, as well as on the overall checks made on the convergence of the calculation method, may be found in the thesis.

g. Computation of Tracer Peaks and Widths

Only a short time after injection of the flat-topped slug of tracer, the combination of the narrowing geometric peak and dispersion causes the leading and following edges of the slug to approach each other. The result of continued dispersion is that the peak concentration decreases from its initial value of unity and, in fact, continues to decrease. Our calculation scheme, however, only enables isoconcentration points themselves to be followed. To calculate the peak concentration at any particular time, it is first recognized that, as the radial distance from the injection well increases, the shape of the peak approaches that of a normal distribution because of the influence of the dispersive term in the velocity equation. In the near neighborhood of the maximum concentration, this curve is well fitted by a parabola, from which the peak concentration can be calculated easily.

As the flow proceeds, the isoconcentration lines on each side of the slug approach each other, and the peak concentration decreases. A moment will come when the two isoconcentration lines nearest the peak come together and then disappear. When half of the isoconcentration lines have been lost in this way, their number is doubled by putting new ones between each of the remaining lines. In addition to the calculation of peak concentration at different times, the thickness of the tracer band also is calculated at 50% isoconcentration lines.

h. Presentation and Discussion of Results

In the present study, the Darcy flow in one-eighth of a five-spot pattern was divided into eleven streamlines. Figure 79 describes the paths followed by these streamlines. These paths were measured by calculating the components of Darcy velocity.

The numerical results confirm that in the diverging flow near the injection well, the tracer concentration decreases rapidly, caused by both geometric and dispersive effects. On the other hand, the converging flow near the production well causes the peak tracer concentration to decrease much more slowly as the flow traverses that region.

The output concentration profile is obtained as an integral over all of the streamlines entering the production well. The variation in well-to-well travel time amongst these streamlines is responsible for a minimum width of the produced tracer concentration peak. The results of simulation runs with different parameters demonstrate that the peak is modified strongly by longitudinal dispersion. For a larger value of the dispersion coefficient, or for a lower Peclet number, the peak becomes broader, and earlier breakthrough occurs. Comparison between the two

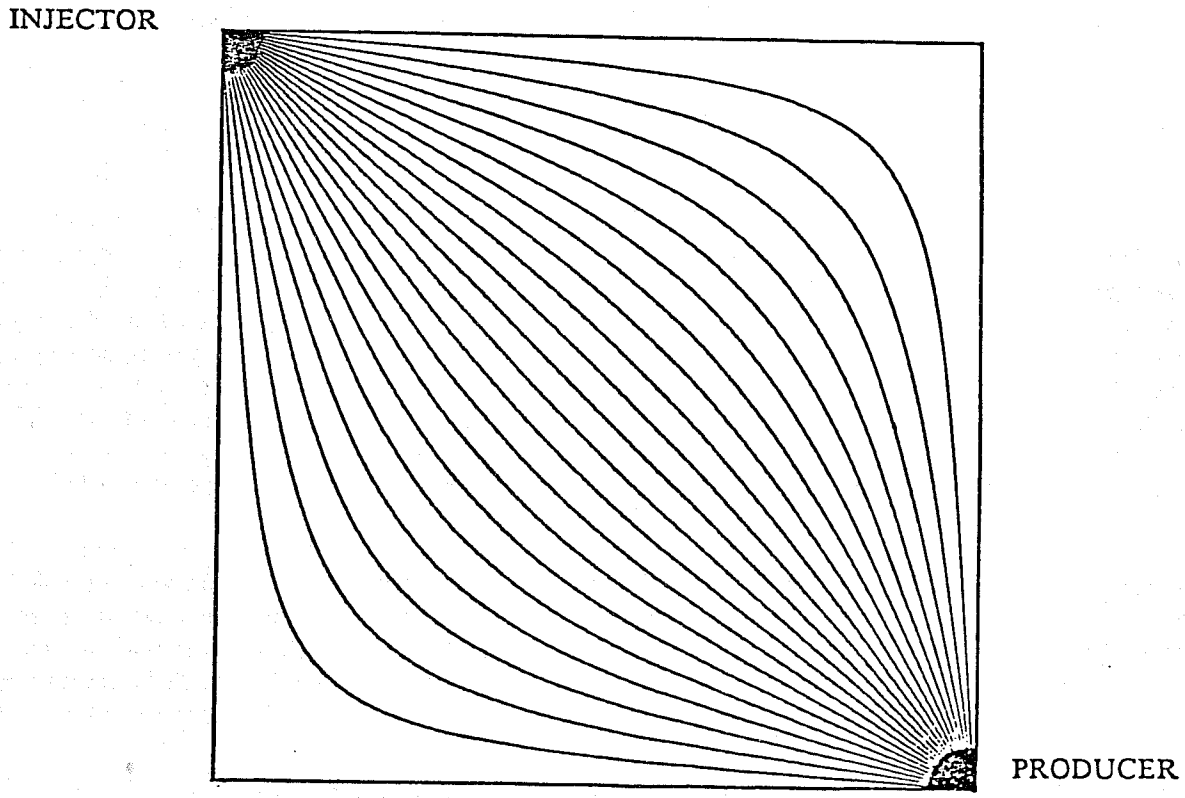

Figure 79. Stream paths in a five-spot pattern.

components of the dispersion coefficient shows that the effect of longitudinal dispersion is much greater than that of transverse dispersion.

1) Tracer Movements

The simulation follows the injection of a small slug of tracer into the injection well. (In the calculation, the slug volume was about 2.5×10^{-6} of the mobile reservoir volume.) It was assumed that the only mobile fluid is water and that the aqueous tracer slug is followed by the water injection again. Successive locations of the tracer slug are shown in Fig. 80. On each streamline, the distance occupied by the concentration profile is divided into seventeen intervals. The points between them mark the intersections of isoconcentration lines with the streamline. The velocities of these isoconcentration points on the streamlines are calculated in the manner discussed, and the updated positions of the isoconcentration lines are then obtained by multiplying the frontal velocity of each of them by a suitable time step.

Near the injection well, the flow velocity is high, so that convection is dominant. In addition, geometric effects are such, initially, that the flow velocity decreases with distance from the injection well. As a result, the spacing of the isoconcentration points on a concentration profile decreases during this initial period. This phenomenon is demonstrated in Fig. 81, in which it can be seen that near the injection well the concentration profile becomes narrower as the slug moves outward. As the front of the tracer slug proceeds further away from the injection well, dispersion finally becomes dominant. This then makes the concentration profile grow broader again, while the peak concentration continues to decrease.

The narrowing of the concentration profile also is shown by the tracer bandwidth or transition-zone calculations. The length of the transition zone can be visualized easily—and measured—in a linear unidirectional flow along a homogeneous core. But the bandwidth or transition-zone length varies from one streamline to another, as well as along the individual streamlines, in a flow regime where flow direction changes from point to point. In the calculated results of the simulations performed in this work, the tracer bandwidth is measured along a streamline as the distance between the 50% isoconcentration points on each side of the concentration profile. Figure 82 shows the plot of tracer bandwidth against distance along a single streamline. In this figure, the initial decline of tracer bandwidth shows that convection is more dominant near the injection well. The subsequent increase in the bandwidth, further from the injector, shows the dominance of dispersion effects throughout most of the flow region.

In the second flow regime, which starts from the midpoint between the wells on the streamline, the flow velocity increases toward the production well. In contrast to the diverging flow of the first flow regime, the flow is converging in the second flow regime. In the converging flow regime, the effects of both convection and dispersion on the tracer bandwidth produce effects that are in the same direction. Consequently, tracer bandwidth increases more rapidly in this region.

The two stages or regimes also are distinguished by the different behavior of the tracer peak concentration. The peak height decreases most rapidly early in the displacement during the first stage, while the change in the second stage is insignificant. Figure 83 is a plot of peak concentration against distance along a single streamline.

In a five-spot pattern, the middle streamline (joining the injector and producer diagonally) has the highest flow velocities, and the velocities on the extreme streamline (that which stays closest to the no-flow boundaries) are the lowest. The velocity distribution in the pattern affects the

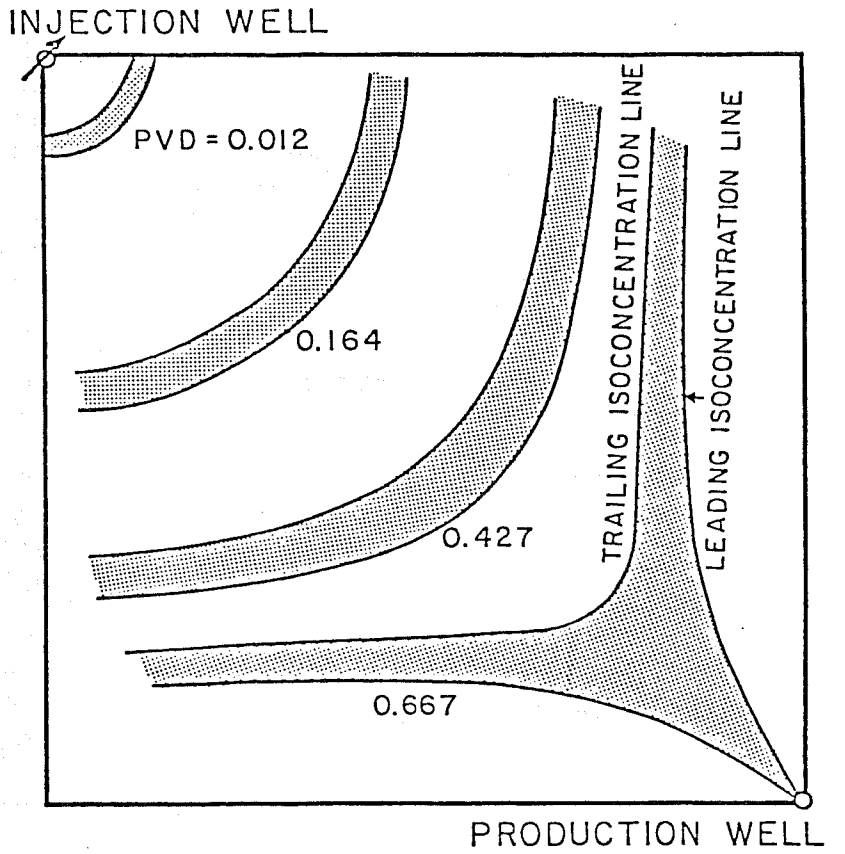

Figure 80. Front locations (first and last isocentration lines) of tracer slug at different values of the pore volume injected.

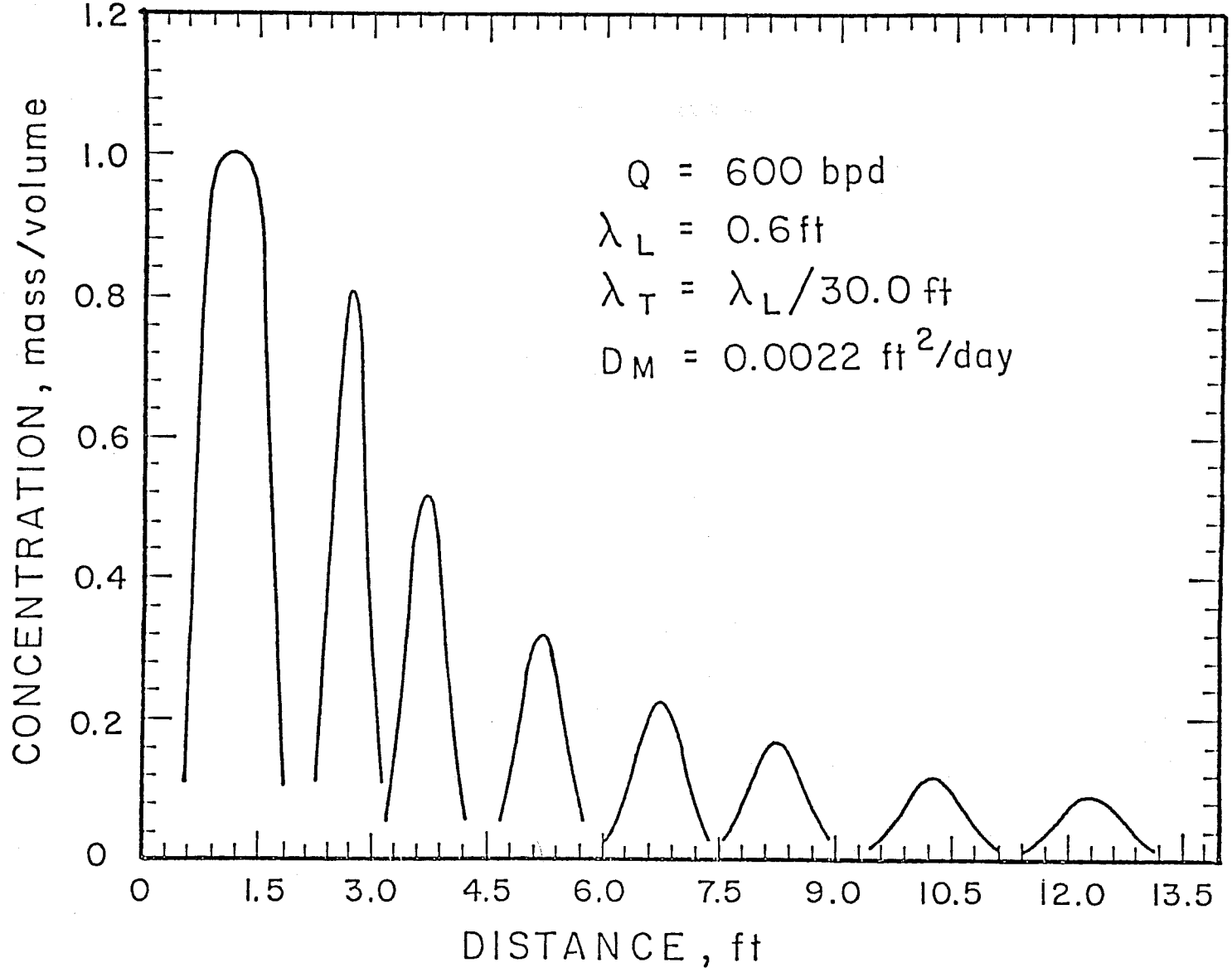

Figure 81. Plot of tracer concentration distributions, near injection well for a single streamline.

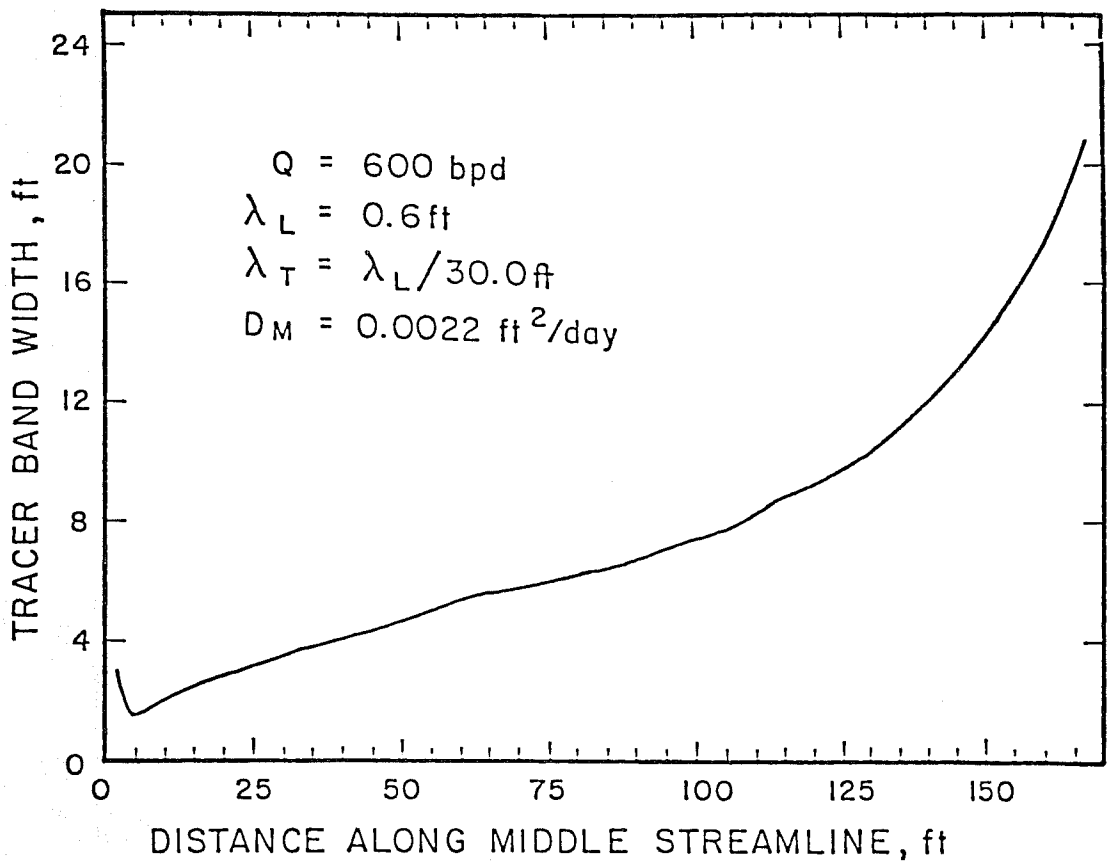

Figure 82. Behavior of tracer bandwidth on a single streamline.

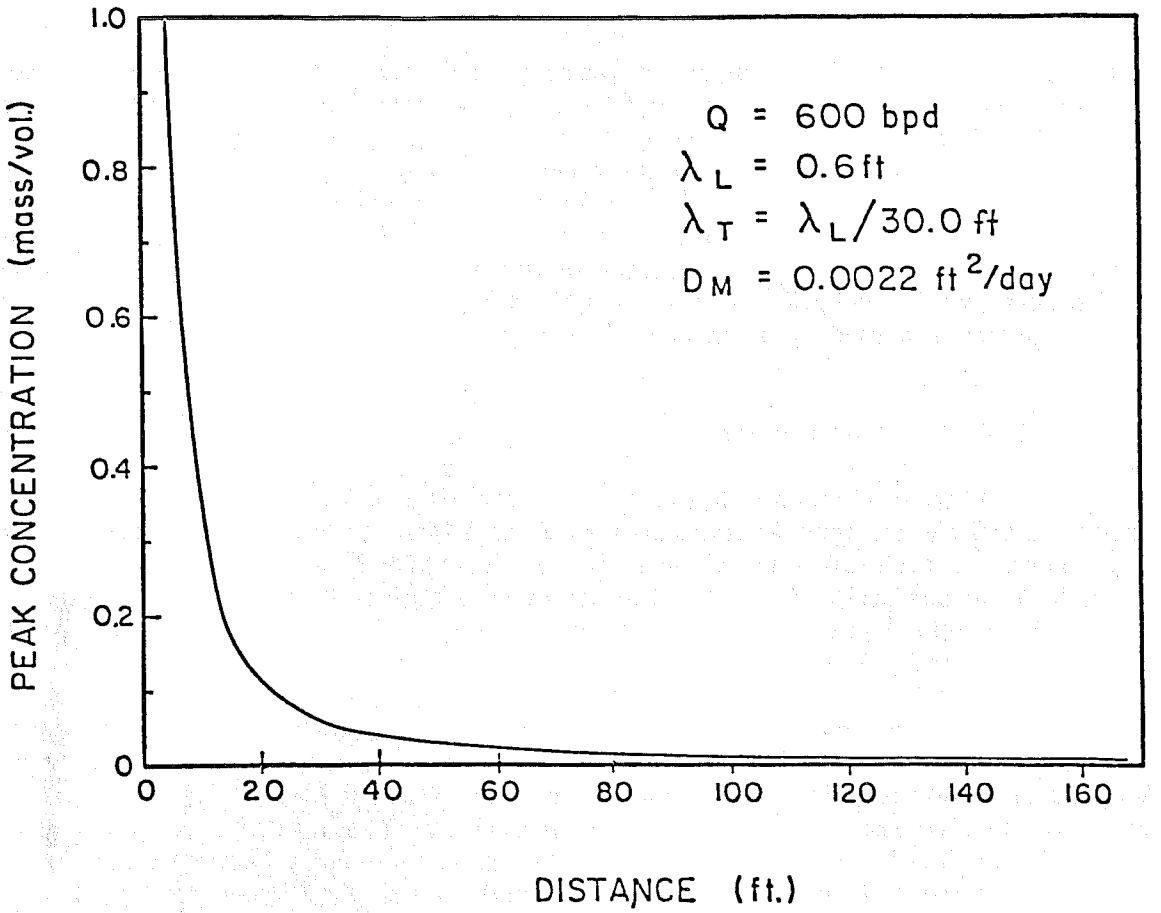

Figure 83. Behavior of tracer peak concentration on a single streamline.

concentration distribution along each streamline. Figure 84 shows the concentration distribution along different streamlines at the time of breakthrough on the fastest streamline. The middle streamline (Number 11) has the highest peak and the largest bandwidth because it has the least cross-sectional area available for flow (Fig. 79). On the other side, the extreme streamline (Number 1) has the lowest peak and smallest bandwidth because this streamline has the largest cross-sectional area available for flow.

Convection, as well as dispersion, affects the shape of the tracer-slug front. Figure 80 shows the successive front locations for the first and last isoconcentration lines of the tracer slug at four different periods as denoted by the values of the pore volume injection. Because flow is essentially radial near the injection well, the front in this region is almost exactly circular in shape. Away from the injection well the flow is noticeably different, and the higher velocities along the middle streamline make the shape of the front more nearly square as shown in Fig. 80. The breakthrough pore volume in a five-spot pattern, for a dispersionless idealized case, is about 0.717;[58] whereas, in the present case, where the Peclet number is 500, the breakthrough pore volume is 0.667. The earlier breakthrough time is caused by the mixing of the tracer slug in the direction of flow.

2) Output Concentration

At the production well, the output concentration can be obtained by integrating, over the octant of a circle, the concentrations arriving along different streamlines. Figure 85 shows the integrated output concentration against pore volume injected for different values of Peclet numbers. For a high Peclet number of 500, a late breakthrough, a high peak, and a narrow profile can be observed. On the other hand, for the lower Peclet number of 50, an earlier breakthrough is obtained, the peak is lower, and profile is broader.

In the absence of dispersion, the influence of the geometric or convective effects on the peak of the effluent concentration profile should be evident. A special version of the code was written, lacking the dispersion term in the equation, to check this phenomenon. Figure 86 shows the front locations of the first and last isoconcentration lines at six different values of the pore volume injected. Except for the first pair, they are so close as to be indistinguishable on the computer-drawn plot. The first pair are far enough apart to make the single line appreciably thicker. It is interesting to note that in the complete (and clearly impossible) absence of dispersion, the peak concentration level along any streamline remains at one as the front propagates toward the production well. At the same time, the area covered by the entire tracer slug remains constant, and this makes the location of the first and last isoconcentration lines approach each other quite closely. The breakthrough pore volume in this case is 0.717, which is in agreement with the theoretical result.[58]

As before, the output concentration at the production well can be obtained by integrating the concentration levels on different streamlines at that time. Figure 87 shows the output concentration curve for zero dispersion (that is, for infinite Peclet number). Because the tracer slug arrives at different times along the different streamlines, the integrated output concentration does not approach the input peak concentration of one. But to preserve material balance, the areas under the input and the output concentration profiles remain the same.

3) Effect of Transverse Dispersion

This study also includes the effects of transverse dispersion. As mentioned earlier, the effect of transverse dispersion is much smaller than the effect of longitudinal dispersion. An

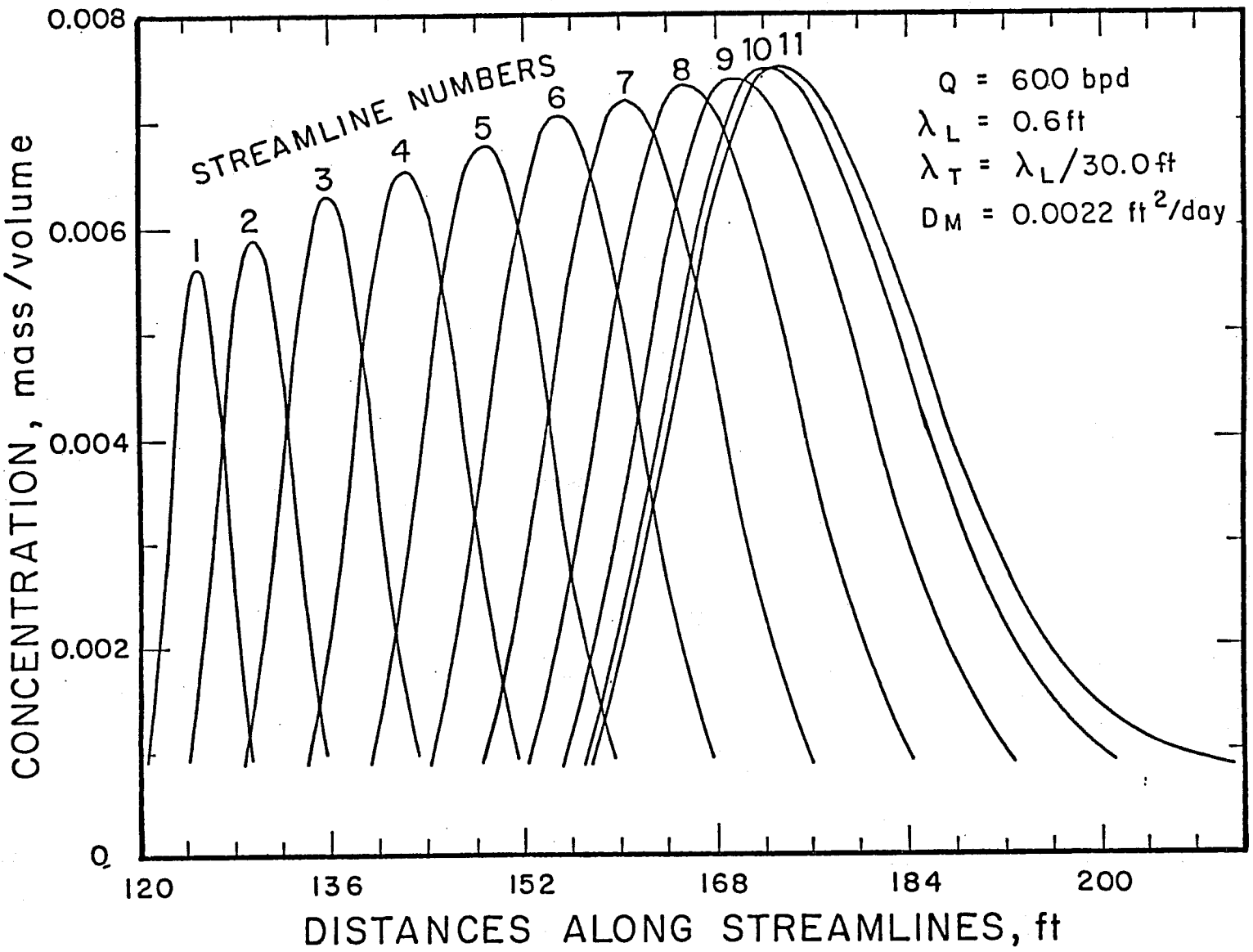

Figure 84. Plot of tracer concentration distribution on different streamlines at breakthrough.

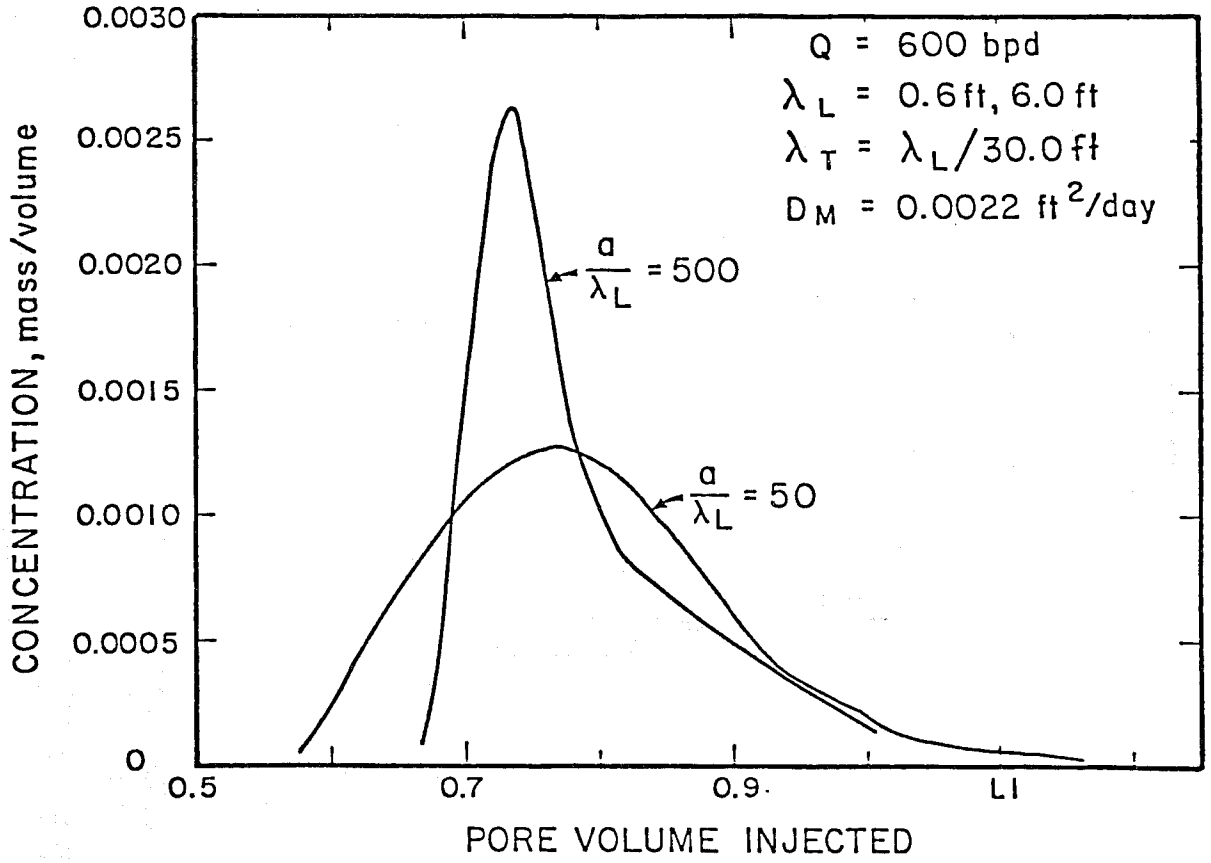

Figure 85. Plot of integrated output concentration vs. pore volume injected for different peclet numbers.

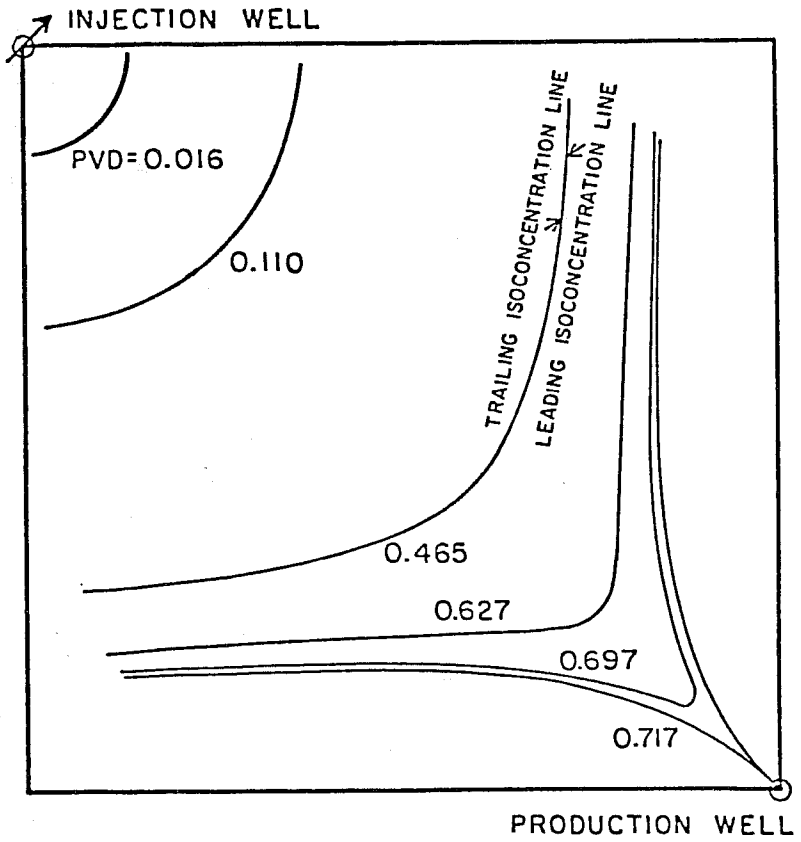

Figure 86. Front location of the first and last isoconcentration lines with no dispersion. (Note that in all cases but the first, trailing and leading edges of tracer band are the same line.)

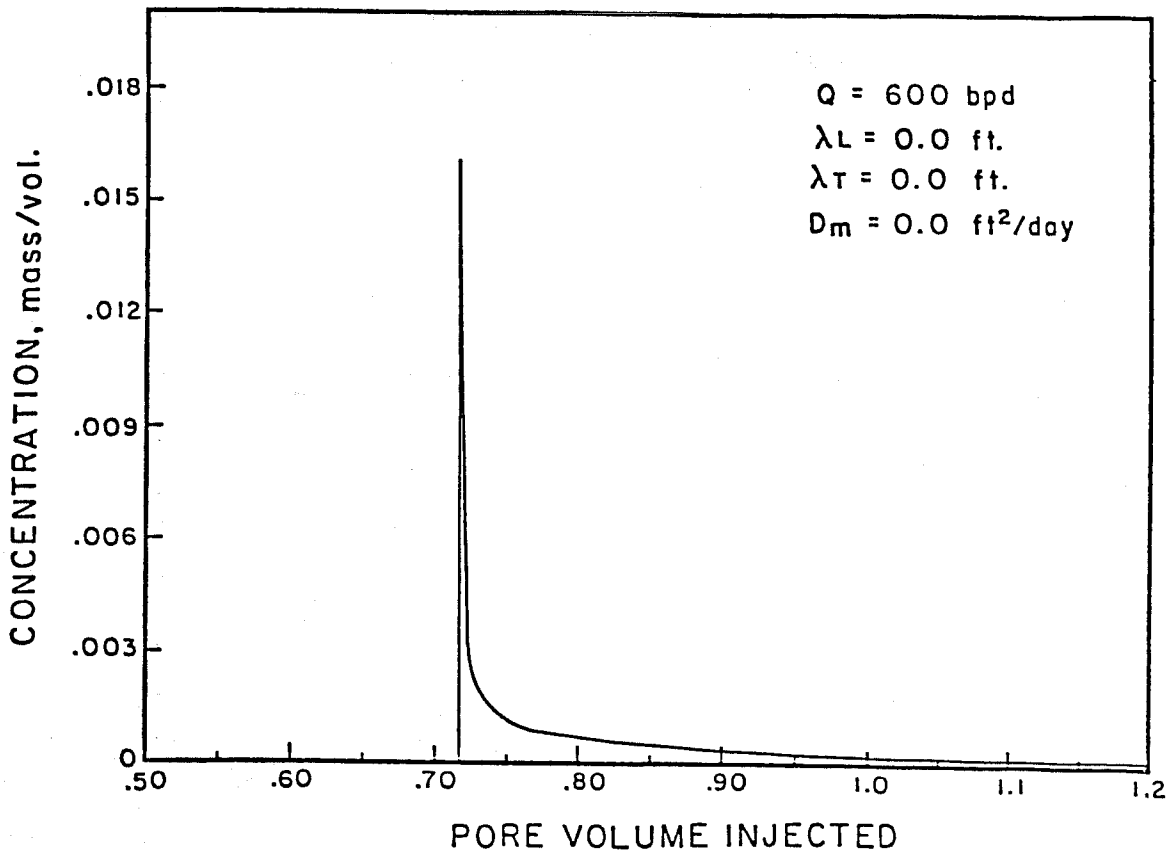

Figure 87. Plot of integrated output concentration vs. Pore volume injected, no dispersion.

attempt was made to quantify these effects. To accomplish this, the computer program simulating the displacement of the tracer was run twice. In the first run, both longitudinal and transverse dispersion were included, with the ratio λ_L/λ_T set equal to 30. In the second run, the transverse dispersion was set equal to zero. The integrated output tracer concentrations for both cases then were plotted against pore volume injected as shown in Fig. 88. A difference between the two curves is only evident at times near breakthrough, where peak values of tracer concentration for the case of $\lambda_T = 0$ were lower than those for the case of $\lambda_T > 0$. This was expected because the effect of transverse dispersion is to homogenize the concentration of the tracer slug.

i. Conclusions

A new numerical technique was presented for solving the convective-dispersion equation for a unit-mobility case in a homogeneous five-spot pattern. The convective-dispersion equation was recast into the equation of motion of isoconcentration lines. By using tensor analysis, this equation then was transformed into an orthogonal curvilinear (Φ,Ψ) coordinate system. In this equation, the dispersion coefficient was assumed to be a linear function of the fluid velocity, which was a function of position in the stream tube. Transverse dispersion and molecular diffusion also were included in the equation of motion.

The computation scheme proved to be stable and does not introduce any numerical dispersion. The technique does not require any type of outer boundary conditions. The use of a "ramp up ramp down" input concentration distribution eliminates the computational difficulties near the input well.

Simulation of the miscible displacement of a tracer slug in a five-spot pattern through a constant-permeability formation has led to the following conclusions:

1. A new method of numerical simulation was developed that makes it possible to follow the motion of isoconcentration lines when these are influenced by both convection and dispersion.

2. Near the injection well the tracer bandwidth decreases for a short distance and then starts to increase again. This occurs because the effect of convection is initially dominant over the effect of dispersion. Near the production well, however, the convective and dispersive effects are in the same direction. Therefore, in that region the tracer bandwidth increases more rapidly.

3. During a diverging flow the decrease in tracer peak concentration is much more rapid than during a converging flow situation.

4. The presence of both dispersive and geometric effects changes the shape of the tracer breakthrough curve. The change caused by longitudinal dispersion is much greater than that caused by transverse dispersion. The output concentration curve is broader and earlier breakthrough is observed for larger values of the longitudinal dispersion coefficient.

5. Even without the presence of dispersion, and with geometric effects alone, the output concentration is considerably less than 100%, and is of appreciable magnitude over relatively long times because of the large variations in the travel times along different streamlines.

6. The study has given "base case" curves of what the tracer production curve would be like from a five-spot pattern if the formation were homogeneous.

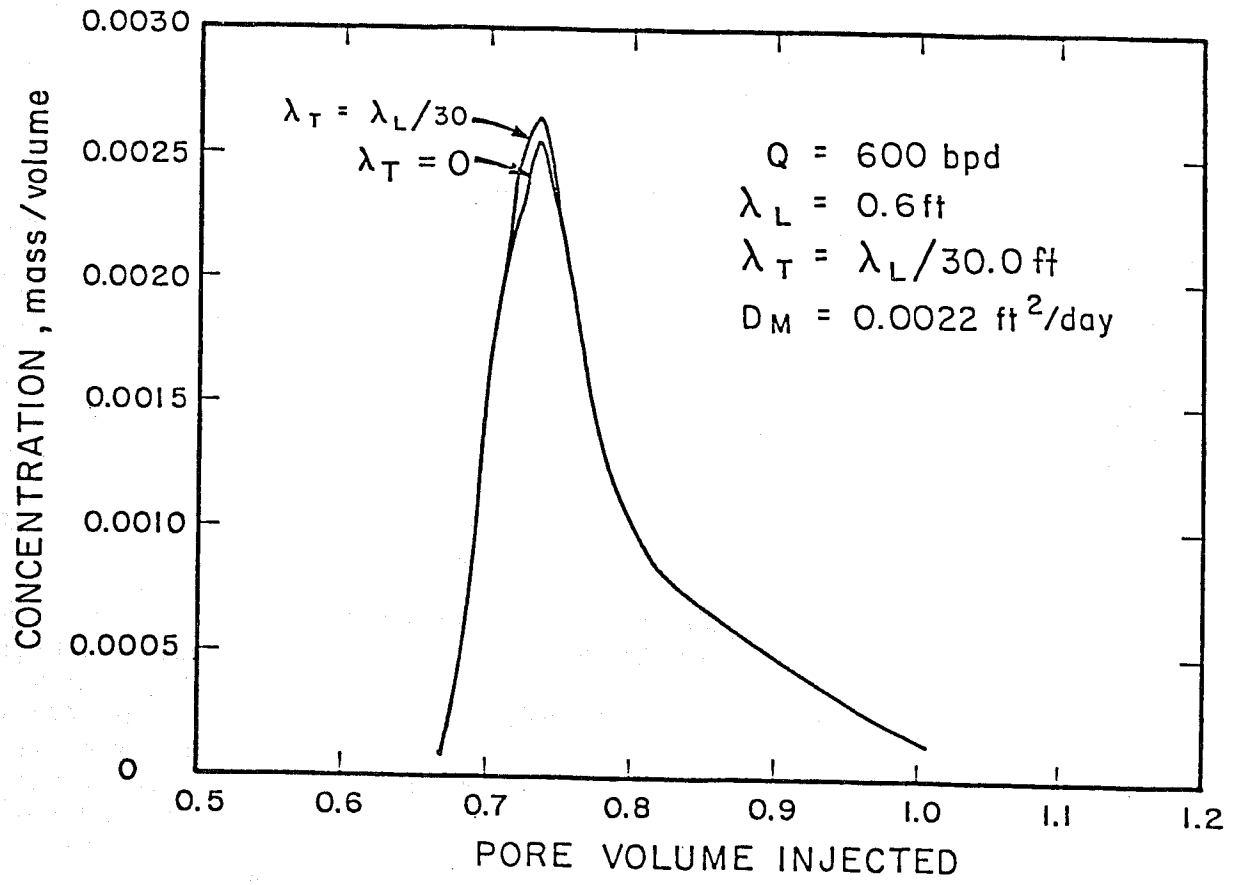

Figure 88. Plot of integrated output concentration vs. Pore volume injected to show the effect of transverse dispersion.

The numerical method presented in this study has been used to consider only a very idealized case—a developed five-spot pattern. Because the streamlines can be computed for systems with any well arrangements for unit-mobility ratio, the method can be extended to other developed or irregular patterns.

It is intended in the near future to extend this work to compute the tracer breakthrough curves from a heterogeneous reservoir. To consider heterogeneity, two approaches are most common. In the first approach the reservoir is considered to consist of a number of noncommunicating layers in parallel. Each layer is assumed homogeneous in its properties, but may differ from the other layers. This is the approach which has been taken by Abbaszadeh and Brigham.[54] Of course, the present numerical scheme also could be extended easily to such a three-dimensional flow system to compute tracer production curves from a layered system with no variation of permeability in horizontal directions.

The second approach assumes that heterogeneity also may be present in each of the layers. This would require generation of the variations of the permeability by using some stochastic approach. Together with the well locations and pumping rates, this permeability can be used to define the locations of streamlines. Once the pattern of the streamlines is known, the same equation of motion of the isoconcentration lines, as was used in the simulation which has been presented here, can be used to produce the tracer production curves.

2. Displacement in a Heterogeneous Five-Spot

a. Introduction

Most natural sedimentary rock is highly variable in permeability, at scales ranging from pore size up to the dimensions of the largest formations. This situation is very different from that which usually has been assumed in the prediction of oil recovery, and it may reasonably be expected to cause errors in those predictions. The general purpose of our research is to explore the occurrence and magnitude of such errors and to seek ways in which to minimize them.

In this study, and in search of these errors, we generate a variety of random permeability distributions such as might be found in an oil-bearing formation. We then calculate recovery curves from these single-layer, heterogeneous reservoirs. The flow domain for the calculation is a quadrant of a five-spot pattern. It is assumed that the mobility ratio is unity, so that the location of the front does not influence the pressure or flow fields. Further, it is assumed that the displacement front remains sharp. This amounts to the assumption that dispersion is negligible even though the oil is displaced miscibly.

Inhomogeneities are introduced by using the source-point method, which permits the magnitude of heterogeneity and its distribution in space to be varied independently. The permeability field also is characterized by the correlation distance, which may be varied as well. Within the limitations imposed by the flow simplifications noted above and certain others to be discussed, the results enable the reservoir engineer to evaluate the effects of permeability heterogeneities on production efficiency.

The formation heterogeneity is achieved by introducing a set of random numbers to describe the location and log of permeability of a number of source points. A simple algorithm permits these source points and the values associated with them to be used for the calculation of a mathematically

continuous permeability field that is log-normally distributed. In this work, the flow region was divided into a grid of 40 x 40 points (1600 mesh points), and permeabilities were calculated for each mesh point. A major geostatistical descriptor of such distributions, the variogram, is computed and plotted for each of the distributions that have been generated. From these curves, it is possible to estimate the values of the overall variance and of the correlation lengths that characterize each of the distributions.

The Darcy equation for the flow of an incompressible fluid through a formation in which permeability is a continuous function of the position gives rise to the linear partial differential equation shown below.

$$\nabla\bullet(K\nabla P) = 0 \tag{64a}$$

$$\text{or } \nabla^2 P + \nabla(ln K)\bullet\nabla P = 0 \tag{64b}$$

This equation, which resembles Laplace's (and reduces to it if the permeability is constant), can be used to calculate the pressure distribution field for a quadrant of a five-spot well pattern. Because the equation cannot be solved analytically for a general permeability distribution, the governing equation is discretized in space and solved numerically using a finite difference approximation.

Once the pressure distribution for the grid system is known, the velocity vectors at each grid point may be calculated, and the flood front location may then be traced in successive stages as it moves from the injection to the producing well. The method used here is to track the front to breakthrough into the producing well and beyond. This makes it possible to compute the recovery curve, which is the graph of the total area swept versus the total area invaded by the injected fluid, for different permeability distributions.

b. History and Background Literature

The patterns of fluid displacement and recovery in different well-to-well arrangements have been explored extensively and reported by Muskat.[61] Various other authors also have studied fluid flow in secondary recovery for many different geometries and under diverse conditions. Much of the effort in the analysis of the secondary recovery process has been expended in the study of five-spot geometry, as this has been the most widely used form of pattern flooding.

In the early days of reservoir engineering, electrolytic models were used to represent the history of the advance of the injection fluid among groups of wells in both regular and irregular networks. These 'potentiometric' models were introduced by Swearingen[62] for studying the sweep efficiency of gas-cycling operations. The economic justification for such model experiments was simply that analytical treatments of the flow equations in such geometries were impossibly complex, and that no means existed by which to perform the large amount of computation needed for practical numerical approximations.

The basic principle of potentiometric analog models is that the flow of electrical charge in an extended conductor under an imposed potential gradient is analogous to the flow of the "Darcy fluid" in a porous medium under an imposed pressure gradient. Distributions of the electrical potential in a tray of electrolyte and of the steady-state pressure distribution in a uniform rock formation of geometrically similar shape with similar boundary conditions and carrying homogeneous fluids are proportional to each other. Ohm's law, representing the current density as the product of specific conductivity and the gradient of the electrical potential, is an exact analog of Darcy's law, which

expresses the velocity of the Darcy fluid as the product of mobility (i.e., k/μ) and the gradient of pressure. Electrodes placed at correct positions correspond to the injection and production wells, and the potential distribution simulates the pressure distribution in a horizontal reservoir in which the influence of gravity can be ignored.

The advance of an injection fluid front towards the producing well was simulated, in models based on this electrical analogy, by locating the streamlines and measuring the voltage gradients along them. The position of the displacement front then was found by calculating and summing the incremental distances that the fluid would travel along the streamlines in each of a series of small time increments. Odeh et al.[63] dealt with the problem of variable permeability thickness product in their potentiometric model. Some fairly sophisticated systems of conductive media and electric field probing devices were developed for this task, such as the system by Bradley et al.[64]

A somewhat different scheme that also was based on the electrical analogy was able to give the successive front positions directly. In this method, the electrolyte was contained in a saturated piece of blotting paper (cut to the reservoir shape), and it contained ions which marked their presence by their color or by their effect on a colored indicator. A complete description of these model studies was presented first by Wyckoff.[65] He used copper and zinc ions in this early work. Muskat[61] shows photographs of models using phenolphthalein to track the transport of hydroxyl ions from the cathode of such a model. Complex ammonium ions later were used by Burton and Crawford[66] in an attempt to model mobility ratios.

Figure 89 shows the isopotential lines, streamlines, and two flood fronts obtained from such potentiometric studies for one quadrant of a five-spot network of constant thickness during displacement at unit mobility ratio.[65] A serious disadvantage of these electrolytic models is that when a large number of wells are involved, and where large-scale models are required, their operation becomes tedious and many instrumentation problems arise.

Although electrolytic models permit relatively accurate measurements of the behavior of the flooding networks, they are analog systems, limited in precision by measuring techniques and by the dimensions of the models used. It was shown quite early by Muskat[61] that a five-spot displacement can be simulated mathematically by the consideration of an infinite array of point sources and sinks. These should be staggered in such a way as to reproduce the required spacing in the flood, namely four producing wells at each corner with an injection well at the center or vice versa. As in the case of the model experiments, it is assumed that the flooding systems consist of infinite networks of injection and production wells. Each infinite line of wells may be represented by a contribution to the pressure distribution of the complete network, and the pressure distribution then is obtained by summing the terms due to the individual lines.

Muskat[61] gave pressure distribution functions for various flooding configurations. From the pressure distribution, isopotential lines (lines of constant pressure) may be constructed. Also, streamlines (the paths traveled by the injected solvent between the injecting and producing wells) may be obtained by drawing lines perpendicular to the isopotential lines. Isochrons, or successive positions of the front, are drawn by connecting those points on each streamline which the front has reached at given times. When the particular isochron on which the shortest travel-time streamline has just broken through to the production well is drawn, the sweep efficiency at that particular time may be calculated. The sweep efficiency at breakthrough for a five-spot well network in a homogeneous reservoir according to this analytical but approximate treatment was calculated by Muskat[61] to be 71.6%.

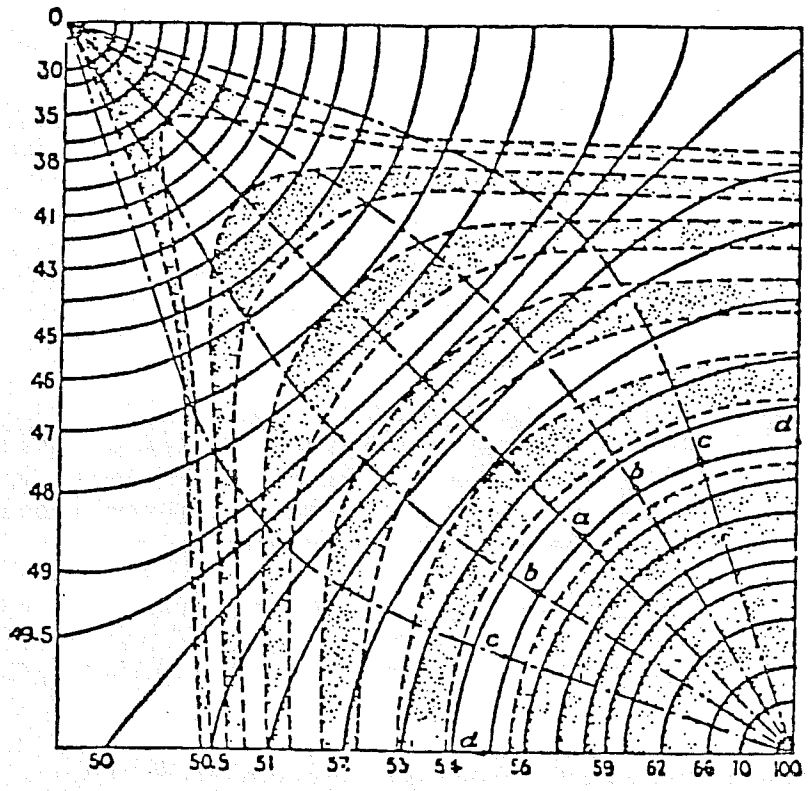

Figure 89. Potentiometric model study of the five-spot network, showing the isopotential lines, streamlines, and flood fronts. (After Wyckoff, 1933.)

Hurst[67] derived formulas for streamline distribution for a five-spot flood, and his application for a typical five-spot pattern gave the same distribution as shown by potentiometric studies and Muskat's approximation results. Prats et al.[68] gave exact analytical solutions to the Laplace equation using the complex potential theory. The assumptions made by Prats were that the fluids is incompressible, that the mobility of the displacing and the displaced fluids is the same, and that the formation is homogeneous with a constant permeability. He found that the sweep efficiency at breakthrough for a five-spot pattern flooding network would be 71.8%.

These and other methods for predicting breakthrough efficiency involved the assumption of a constant value for permeability throughout the entire formation. Studies of fluid flow through porous media often have assumed that the reservoir formations are isotropic and homogeneous. This has been done to ease the complexity of the flow problems. The fact that this is not an accurate picture of the reservoir has of course been recognized in the literature, and various attempts have been made to make due allowance for the large-scale random variations in permeability which are actually distributed throughout the formation.

In the earliest days of the use of digital computers in reservoir problems, McCarty and Barfield[69] attempted to take into account the variations in permeability. They constructed isopachous and isopermeability contour maps from well logs, laboratory core analyses, and well-testing information. By superimposing these maps onto their integration nets, they tried to assign the most appropriate values of permeability and thickness to each grid point in the field. But in obtaining such data from core analyses, errors related to sampling methods and testing techniques are sure to arise. Warren and Price[70] discussed these errors and concluded (with perhaps unwarranted optimism) that the most probable errors are the result either of coring an insufficient number of wells or of choosing test samples from irregular limestones or fractured sandstones that are macroscopically heterogeneous.

The permeability of rocks is the rock property which is most variable, far exceeding that of the variability of porosity values within a formation. Permeability in the same oil reservoir may vary by a factor of 10^3. This high degree of variability leads to severe difficulties, both in prediction of the appropriate overall average value of permeability, and of the effect of the variability on displacement. The first of these two problems apparently was considered in the early literature to be of major importance.

It has been widely held that the permeability values of samples from a formation belong to a log-normal probability distribution. This was proposed by Law,[71] based on core analysis data taken from typical fields. Later works by Bulens[72] and Warren and Price[73] also led to a log-normal observation for permeability data. Warren and Price[70] used a technique for comparing core-analysis permeabilities to those determined from pressure buildup tests. Their main result was to demonstrate the relationship of the permeability measurements to the nature of the heterogeneity that exists in the reservoir. They found an averaging method that reconciled the core and buildup permeabilities, and they also found that a log-normal distribution of permeabilities existed in the reservoir.

Warren and Price[73] also generated a random spatial distribution by reading in N values of permeability from a specified distribution function and by assigning a random number to each of the permeabilities. They then ordered the permeabilities according to the magnitude of the assigned random numbers and established a one-to-one correspondence between the ordered permeabilities and the mesh points of their physical model. They concluded that the most probable behavior of a heterogeneous system approaches that of a uniform system that has a permeability equal to the geometric mean. This method contains the limiting assumption that the permeabilities at adjacent grid points are statistically independent. The spatial structure of the medium is ignored in analyses

such as these, where the spacing of the grid points takes on major importance even though this dimension is not related to the actual distribution in space.

An algorithm for the generation of a random but continuous permeability field was proposed by Heller.[74] This method calls first for the generation of three sets of random numbers in order to locate a number of source points in the space of interest and to assign a field strength for each of these points. These 'field strengths' define extrema in the continuous field to be generated, and they are taken as proportional to the logarithm of permeability. The permeability logarithm at any other point is then calculable from a simple sum of terms that are linear in the values of the field at the known source points. This method has the advantages that the permeability is given analytically (it is differentiable) and can be calculated at any point without singularities. In addition, the proportionality constant can be chosen to fix the value of the overall variance of the permeability.

Smith and Freeze[75] used a method in which a correlation exists between the values of the hydraulic conductivity (which is proportional to permeability) in neighboring blocks. This was done by assuming the spatial variations in conductivity to be represented by a first-order, nearest-neighbor, stochastic process model. They studied steady-state groundwater flow in one dimension using stochastic analysis. They stated that stochastic simulation is justified because hydrogeological environments are exceedingly heterogeneous. They have shown that the ratio of the correlation distance for conductivity to the distance between boundary points is a fundamental parameter in modeling the stochastic behavior of the medium. In this method, conductivity is taken to be log-normally distributed, and conductivity realizations are generated from a first-order, nearest-neighbor model. The method provides a technique for generating spatially autocorrelated conductivity realizations, and it is used to give a more realistic representation of spatial variations in hydraulic conductivity in a solution of the stochastic flow equation. In a second contribution, Smith and Freeze[76] generated the conductivities for a two-dimensional flow model using the nearest-neighbor model.

Stochastic analyses of groundwater flow regimes have been approached by the spectral techniques given by Gelhar,[77] Bakr,[78] and Bakr et al.[79] Bakr[78] gave solutions to the governing flow equations that result in spectral expressions. These expressions relate fluctuations in the hydraulic conductivity (or input) to those of hydraulic head (or output). These input-output spectral relationships then are used to establish forms of covariance functions that describe the spatial variations of both input and output.

Monte Carlo simulation studies by McMillan[80] and Freeze[81] involve the repetitive solution of the governing equation by using a discretized representation of the flow domain. Hydraulic conductivity or permeability values were assigned to each grid point by random selection of values from the probabilistic model that describes the spatial variability.

Smith and Schwartz[82] analyzed the macroscopic dispersion phenomena in conventional modeling of mass transport in groundwater systems using stochastic approaches. They described a modeling concept which accounts for macroscopic dispersion, not as a large-scale diffusion process, but as mixing caused by spatial heterogeneities in hydraulic conductivity. Their method of generation of the conductivity field was the first-order, nearest-neighbor stochastic process.

Another method of generating random fields that preserves the spatial correlation of the generated process is the method of turning bands. This method was originally proposed by Matheron.[83] Montoglou and Wilson[84] used the turning bands method (TBM) to simulate random fields using line generation by a spectral method. Montoglou and Wilson show that this method is superior to the nearest-neighbor methods in computer cost and accuracy. The TBM basically involves

performing simulations along lines in space, rather than synthesizing the multidimensional field directly. The TBM transforms a multidimensional simulation into the sum of a series of equivalent unidimensional simulations while maintaining the statistics of the true field. Bras and Rodriguez-Iturbe[85] give a more detailed analysis of the TBM presented by Montoglou and Wilson.

Hewett[86] used random fractals to model the spatial structure. According to Hewett, measurements of permeability distribution in sedimentary environments show fractal character with long-range correlation. Fractal geometry was first described by Mandelbrot.[87] Ideal fractals exhibit variations at all scales of observation, and have partial correlations over all scales. Therefore, every attempt to divide such a geometry into smaller and more uniform regions results in the resolution of even more roughness or variability. The most useful fractals for describing property distributions are stochastic functions that possess a statistical rather than exact self-similar variability. Fractal application to the oil reservoirs and conditional simulation of the influence of reservoir heterogeneity on oil recovery process performance have been studied by Hewett, and future stages of work in this area are still being developed.

c. Method of the Numerical Experiment

In order to solve the governing equation for the pressure, the permeability values at each mesh point must be known. The extent of permeability variation in real formations, and the impossibility of measuring this parameter at every point in the reservoir, makes the exact solution of the flow equation just as difficult to achieve as exact knowledge of the permeability.

However, a reasonable substitute for detailed, exact knowledge of the actual oil-bearing formation might be the same kind of knowledge about a suitable, imaginary formation. This imaginary formation should be constructed to have the same statistical structure as the real one. If the substitute formation were sufficiently similar—that is, if all of the proper geostatistical choices had been made—we might expect that the displacement characteristics of prototype and model would be close enough that the model could safely be used to predict the behavior of the real oilfield.

It is on the basis of the above supposition that the following work is presented. A suitable permeability distribution is generated, and Eq. (64a) or (64b) is solved numerically in it. Given this known pressure distribution, it is possible to calculate the streamlines, the successive isochrons, and finally the production curves. This process is repeated, with different choices of parameters, during the original generation of the permeability field.

In this research the source point method is used to construct the permeability field. If the field is to be characterized by N_s randomly placed source points within the confines of the space to be studied, the first numerical task is to choose three sets of random numbers, each composed of N_s numbers. The first and second sets are used to fix the x and y coordinates of the points. Consequently, these two sets of random numbers should be chosen from populations that are distributed uniformly within the space. The third set of random numbers, which will determine the permeability extrema, can be distributed according to any convenient, predetermined rule. In this case, a normally distributed population with zero mean and unit variance is chosen, since it will lead to permeabilities that are log-normally distributed.

If the coordinates of the N_s source points are (x_i,y_i) and the log permeability values there are S_i, then the log permeability function is defined at a location (x,y) by the formula:

$$S_{(x,y)} = \frac{\sum_{i=1}^{N_s} \frac{S_i}{(x-x_i)^2+(y-y_i)^2}}{\sum_{i=1}^{N_s} \frac{1}{(x-x_i)^2+(y-y_i)^2}} \tag{65}$$

where

N_s is the number of source points,
S_i is the value of the extremum at the ith source point, and
x_i, y_i is the location of the ith source point.

The permeability function defined by this equation is taken as proportional to the logarithm of permeability. Thus, to calculate the permeability itself at the point (x,y), the appropriate formula is:

$$K_{(x,y)} = K_o \exp\{\alpha S_{(x,y)}\} \tag{66}$$

where K_o is the average permeability and α is a constant.

The value of α regulates the width of the permeability distribution; if α were equal to zero, the field would become uniform, with the permeability value of K_o everywhere. This property was used to obtain test cases for checking the front-tracking procedures.

To obtain an approximate solution for the pressure distribution, Eq. (64a) rather than Eq. (64b) is transformed into a set of finite difference equations. The values of permeability itself are then required at the grid points of the network used for the calculations. The discretized equations form a large sparse matrix, and they are solved for the values of P at the grid points by the method of Successive OverRelaxation (SOR). This finite difference method has been described by Burden and Faires.[88] Once the pressure distribution is found for the pattern flood, the components of the pressure gradient at any point can be calculated, and Darcy's equation is used to obtain the flow velocity there.

The flood simulation is started by computing the velocities at a number of points spaced along the perimeter of a small quarter-circle centered on the injection well. The velocity at which the fluid at any point is moving is determined by interpolating among the Darcy velocities at the surrounding grid-line intersections, then dividing by the (here-assumed-to-be-constant) porosity. The points are then moved by multiplying the component velocities of each point by a time increment to obtain a vector incremental distance. This is added to the previous location to compute the new point position.

In this way the originally selected points are expected to trace out the streamlines of the flow field which, along with the set of isopotential lines, form the same orthogonal network that was used (in the α=0 case) as the "natural coordinate system" of the previous study. Here, as well as in the analog methods discussed previously, this method of construction of the streamlines gives an added benefit.

With each successive point on each streamline, a time is associated. This is the time at which the fluid arrived at that point. By joining together the points on different streamlines which represent the same time, an isochron or trace of the fluid front can be obtained. Except for the various numerical errors inherent in the calculations, these points represent the intersection of the streamline with the C=50% isoconcentration line between a pair of miscible fluids of the same viscosity. Thus the "sharp front" assumption, made in this representation of the reservoir, becomes a more convincing approximation.

Each time a point is moved, its location is checked against the location of the production well. If any point falls within a specified radius of the producer, the well is considered to have been reached by the flood front. This breakthrough condition occurs first for the part of the isochrons that intersect the fastest streamline, the central streamline in the α=0 case. At breakthrough, the value of areal sweep efficiency is then determined by measuring the area under the flood front curve at the time breakthrough first occurs. In this work, 67 points initially are arrayed radially around the injection well. Their movement is tracked up to the first breakthrough of the displacing fluid into the producing well and beyond.

For the homogeneous case, in which the value of $\alpha = 0$, an areal sweep efficiency of 71.7% was obtained by these procedures. This value agrees closely with the values obtained by other methods that have been reported in the literature, and it lends some credence to results that were obtained in other cases computed in this work.

d. Results of the Calculations

1) The Permeability Distribution

Two variable parameters are available by which to modify the statistical character of the random field produced by the source point method—the number of source points, N_s, and the value of the intensity variable, α. The variation of these numbers produces different, although not entirely independent, results. In parts of this first study, N_s assumed the values 40, 100, 200, 300, and 1000, and computer runs were made with α having the values of 0, 1, 2, and 3.

Figures 90 and 91 show histograms for two cases when the number of source points is 40 and 100, respectively. The histograms show the distribution of the logarithm of permeability to be approximately normal. Figures 92 and 93 show contour maps of these permeability functions for 40 and 100 source points. For each map, a new set of random numbers was generated using a different seed for the random number generator routine. This caused each realization to be completely different from the others. The amount of spatial correlation shown in these distributions of log-permeability depends on the number of source points utilized in their generation. In fact, one can immediately estimate that the average distance between source points is given by

$$\bar{L} = \sqrt{\frac{Area\ of\ region}{N_s}} \tag{67}$$

Unless the number of source points is considerably smaller than the number of grid points, one would expect that there would be little spatial correlation of the values. Similarly, one would expect a large correlation in the permeability field if the number of source points is small compared to the number of grid points.

The accepted geostatistical measure of the correlation between functional values at different points is the semi-variogram, which is a function of a "lag distance," and is defined as:

$$\gamma(h) = \frac{1}{2N_h}\sum(S_{(\vec{x}+h)} - S_{(\vec{x})})^2 \tag{68}$$

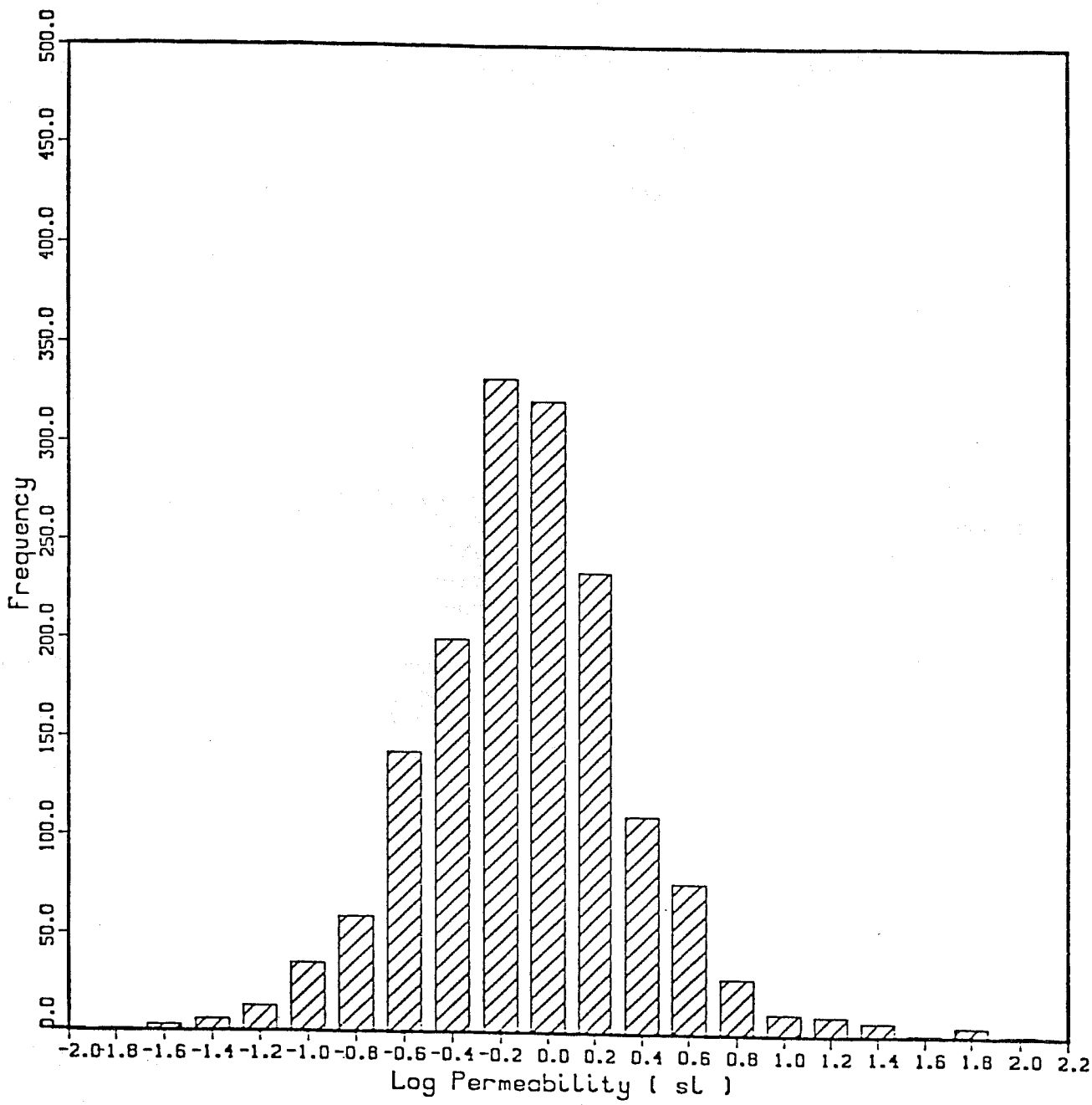

Figure 90.. Histogram of log permeability values, $N_{sp} = 40$.

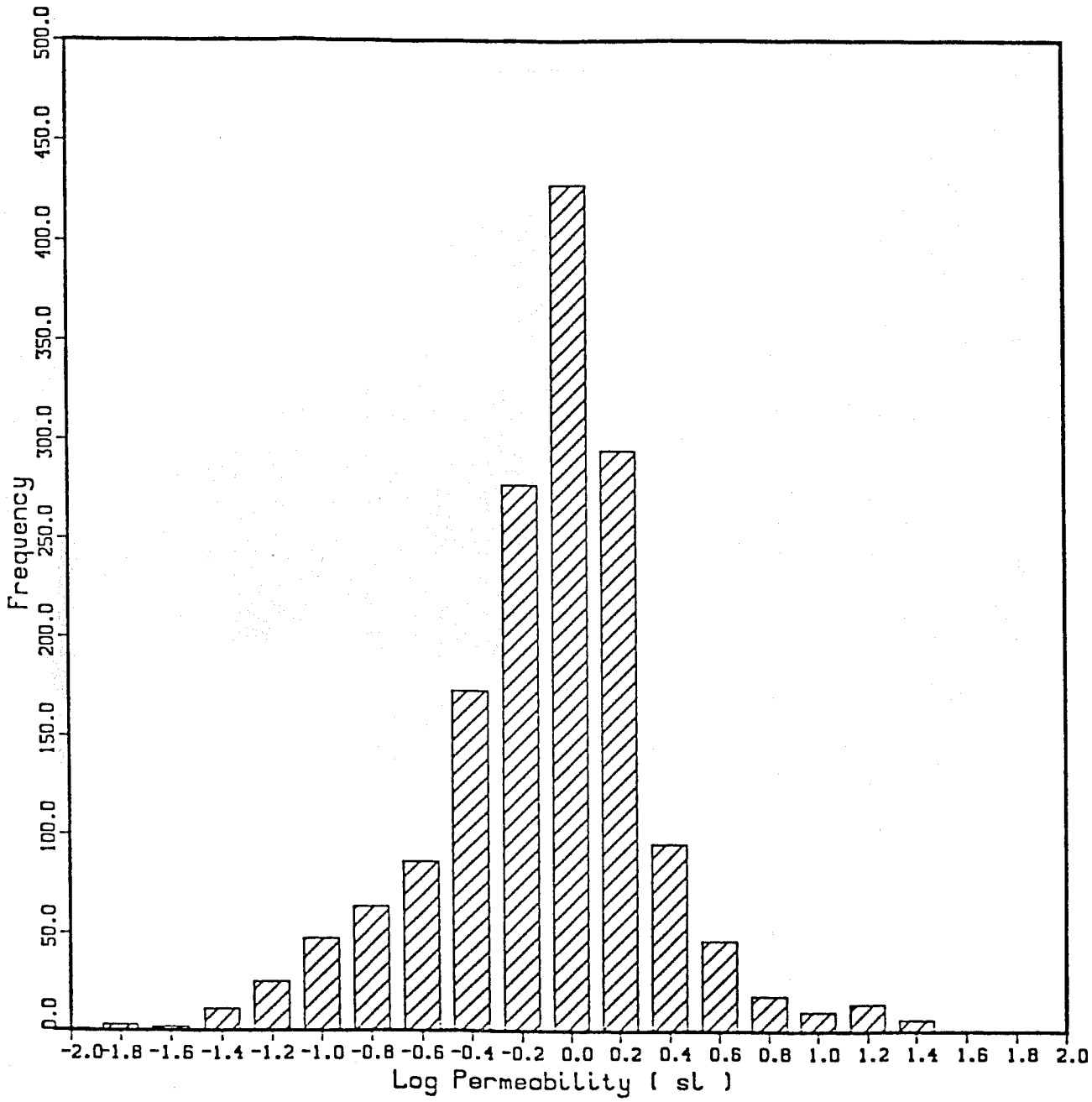

Figure 91. Histogram of log permeability values, N_{sp} = 100.

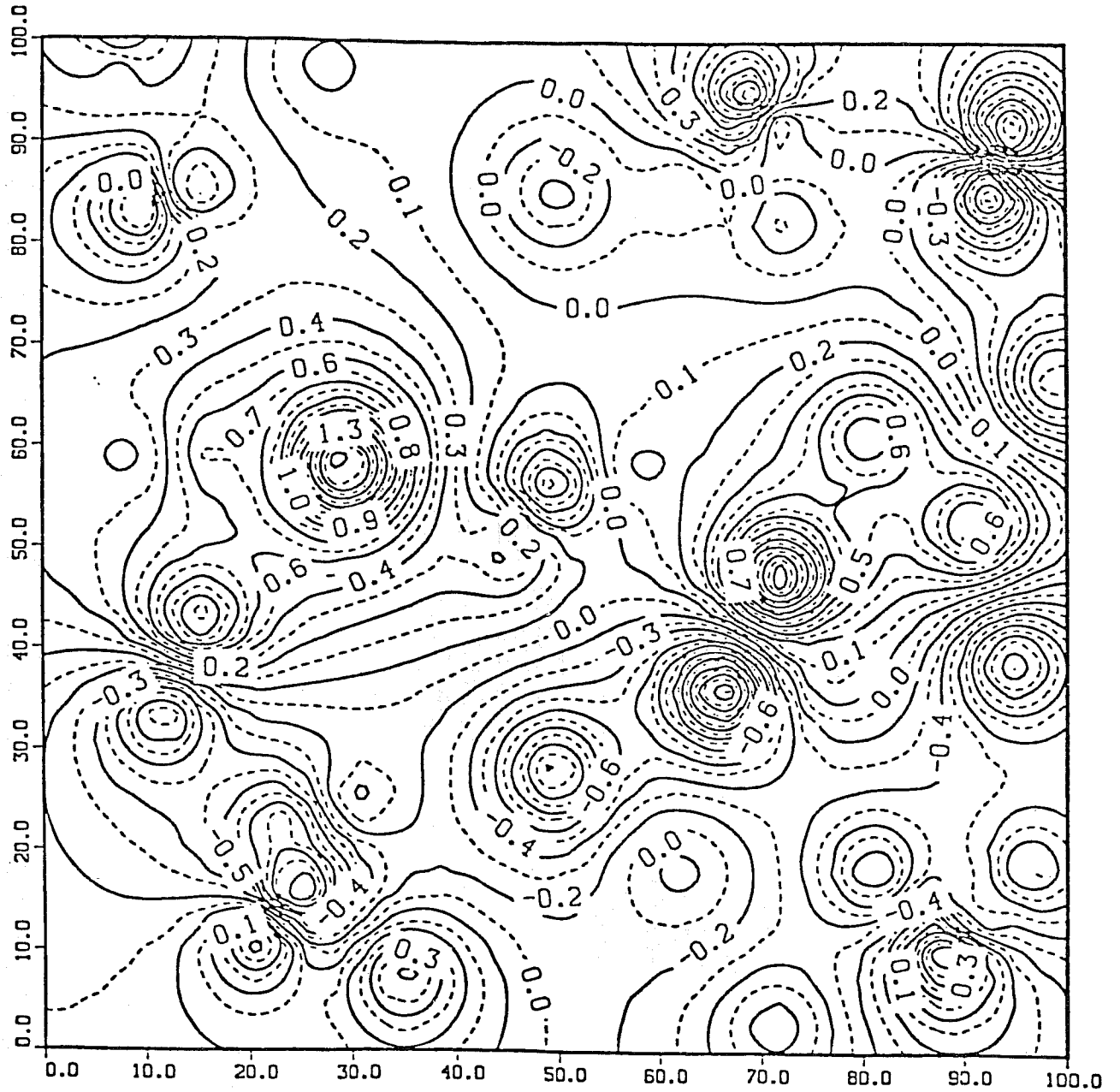

Figure 92. Contour map of log permeability values, N_{sp} = 40.

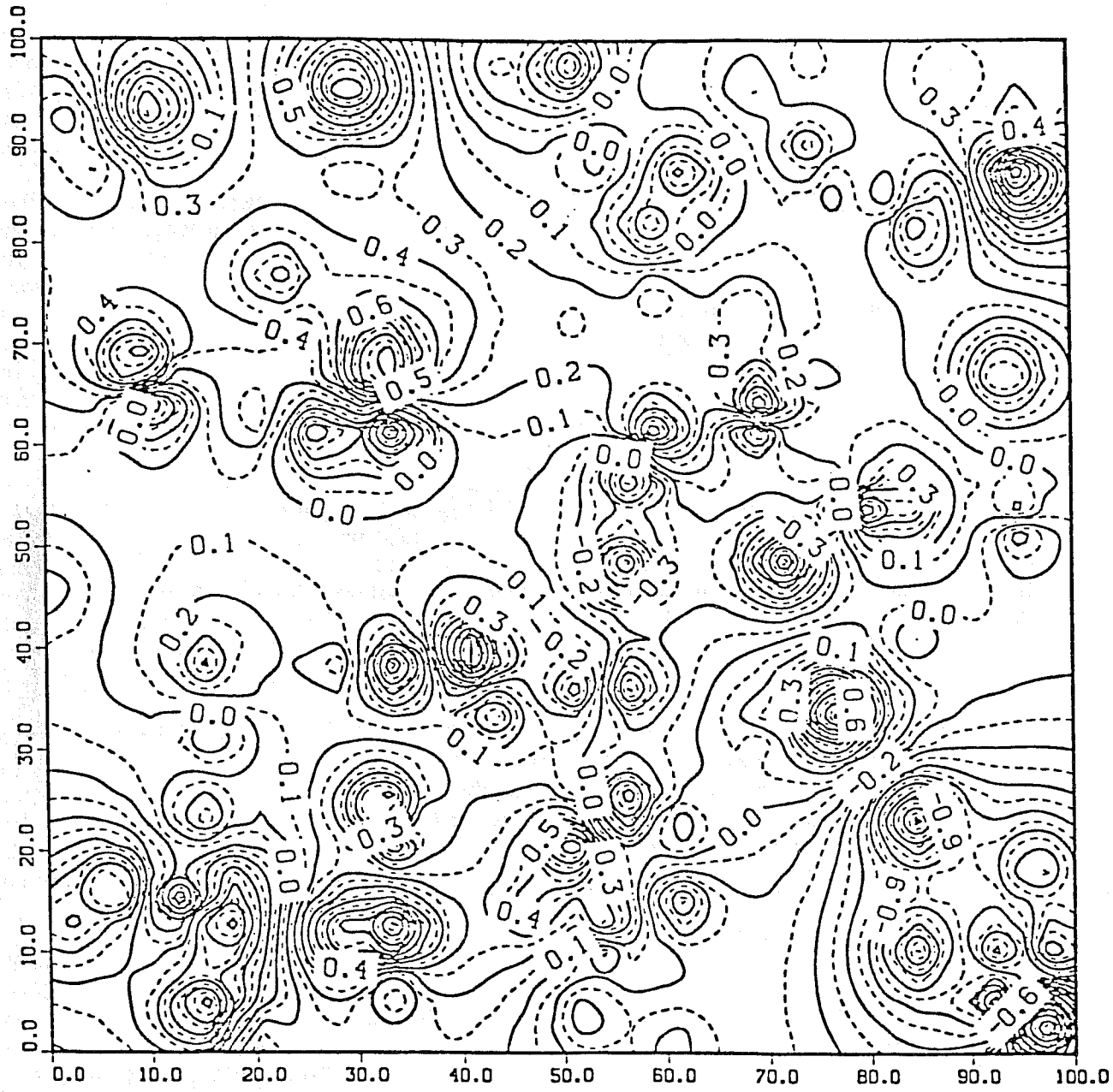

Figure 93. Contour map of log permeability values, N_{sp} = 100.

where the sum is over N_h, the number of pairs that are separated by a distance greater than $h-\delta/2$ and less than $h+\delta/2$. The distance, δ, is then the interval between the closest values of h at which $\gamma_{(h)}$ is evaluated.

If S is a continuous function, as in this case, $\gamma_{(0)}=0$. In this as in many other natural distributions, the value of $\gamma_{(h)}$ tends toward a maximum, which is approximately equal to the overall variance of the distribution. The lag distance within which this occurs is called the correlation length of the distribution, and it is a multiple of $\overline{L}$ as defined above. It is to be noted that for any value of h, the experimental value of $\gamma_{(h)}$ can only be an estimate, since it is based on a statistical sample of finite size, N_h. As with any such average, the probable relative error in the estimate is about $1/\sqrt{N_h}$.

Figure 94 is a composite graph showing the variograms of the permeability function for the five cases where N_s = 40, 100, 200, 300, and 1000. The decrease of correlation length with increasing N_s is quite apparent. If the variograms are fitted to the so-called spherical model, a more precise value of the "correlation length" can be calculated. This value proves to be about 7.1 times the average distance between points defined by Eq. (67). It should also be noted that for each larger value of N_s, the limiting value of the variogram or "overall variance" becomes less. This interaction between the two is a side effect of the source point method. If the number of source points is increased without changing the grid size on which samples are computed, the fraction of the samples which are close to the extrema is decreased. This decreases the variance of samples of the field taken at the grid points.

The previous paragraph discusses the variability of the "permeability function," which is important in its own right, since it is apparent from Eq. (64a) that the logarithm of the permeability determines the heterogeneity of the governing pressure field. But the log of permeability is obtained in the source point method as the product of the permeability function S and the constant α. Although the function $S_{(x,y)}$ carries the spatial variability part of K, the value of α determines the intensity, or amplitude of the variability. Because of the side effect discussed in the previous paragraph, the overall variance of the log permeability field depends on N_s as well as on α.

A measure of the overall variance in a permeability distribution, defined without reference to its spatial aspects, already exists in the field of petroleum engineering. This is a coefficient which was introduced by Dykstra and Parsons[89] in the analysis of data from core analyses. The purpose of the coefficient is to measure the effect of permeability stratification on the prediction of waterflooding performance. Assuming that permeability has a log-normal probability distribution in actual field conditions, Dykstra and Parsons proposed a method by which a useful quantitative measure of rock heterogeneity may be obtained.

Based on the symmetrical properties of the normal distribution of a variable, X, about its mean value, $\overline{x}$, the value of the standard deviation, σ, is such that 15.9% of the samples have values less than $(\overline{x} - \sigma)$ and 84.1% have values less than $(\overline{x} + \sigma)$. If the graph of the permeability vs. cumulative frequency distribution on log-normal probability paper can be approximated by a straight line, then the permeability data is log-normally distributed. Dykstra and Parsons recognized this important feature and introduced a way to characterize a particular distribution. The Dykstra-Parsons coefficient is defined by the following equation.

$$V_{DP} = (K_{50} - K_{84.1})/(K_{50}) \tag{69}$$

where

K_{50} is the log permeability with 50 percent probability, and
$K_{84.1}$ is the log permeability at 84.1 percent of the cumulative sample.

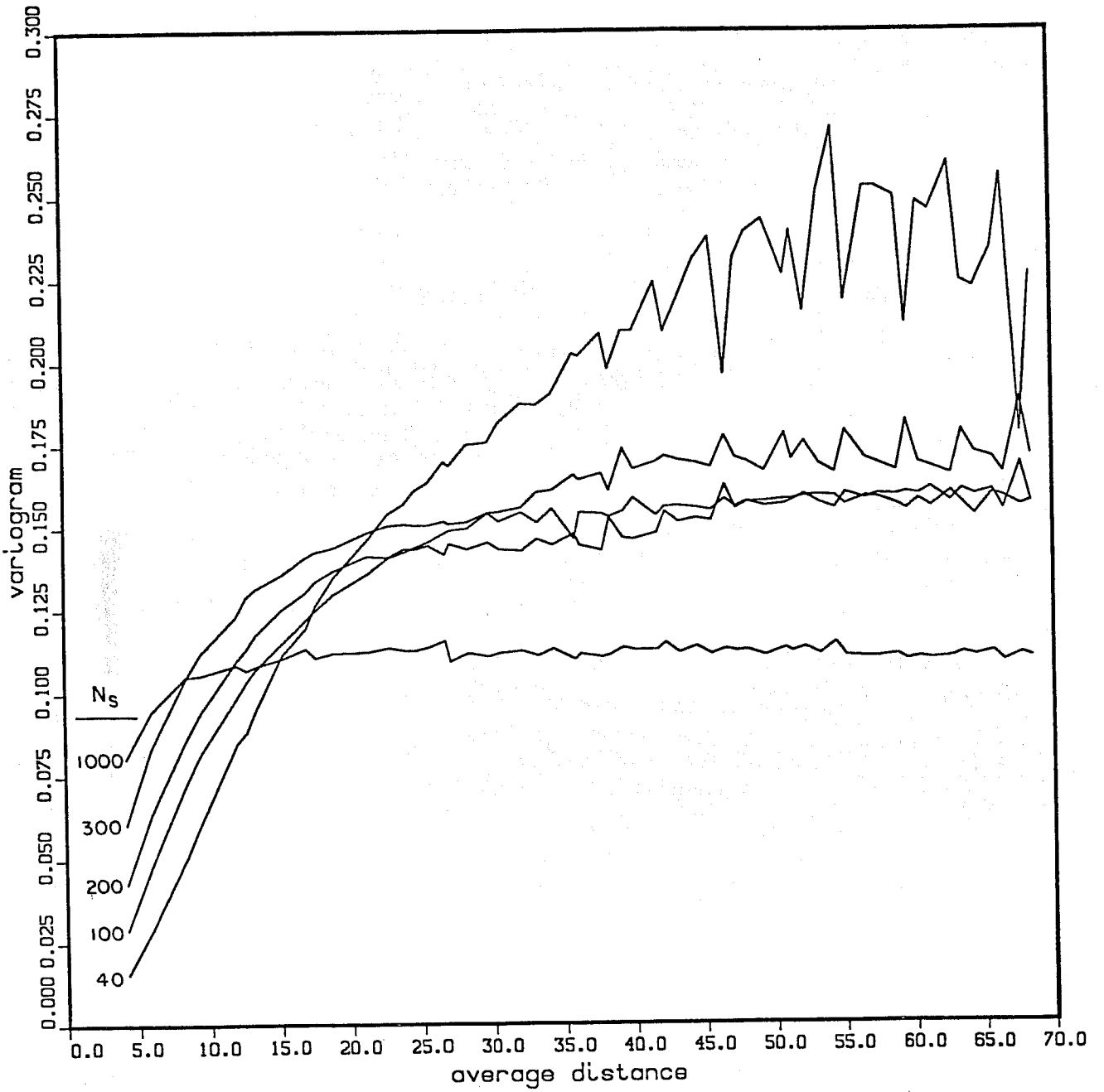

Figure 94. Variograms of permeability distributions, in five cases with different numbers of source points.

A very heterogeneous reservoir has a Dykstra-Parsons permeability variation coefficient that approaches 1.0, while a nearly homogeneous reservoir would have a permeability variation coefficient approaching zero. This coefficient is believed to be an excellent descriptor of reservoir heterogeneity,[90] and it has often been used to describe the variations encountered in stratified reservoirs.

Figure 95 shows a graph of the Dykstra-Parsons coefficient vs. α as used here for three different values of the number of source points. The graph shows that as the value of the Dykstra-Parsons coefficient increases, the magnitude of α also increases, indicating the major effect of α on the magnitude of heterogeneity as measured by the Dykstra-Parsons coefficient. The differences between the curves drawn for different values of N_s indicate, again, the operation of the side effect noted earlier.

2) The Pressure Distribution and the Streamlines

The finite difference calculation for the pressure distribution was made on a 40x40 mesh, using the different realizations of the pressure distributions characteristic of the values given above for N_s and α. First, for comparison with the ideal uniform case, Fig. 96 shows a map of the isopotentials when α=0. Some indication of the small size of the errors in the calculation can be noted from the deviation of the central isobar, labelled P=50, from a straight diagonal between the corners, and from the closeness to a right angle of the intersections of most of the isobars with the no-flow boundaries.

Figures 97 through 99 exhibit isopotential lines of the fields in the cases where the value of α was 1, 2, and 3—all computed for the same distribution of the log permeability function in the N_s=40 realization. Figures 100 and 101 show the pressure fields for N_s=100, for the two cases where α=1 and 3.

These figures were computed and plotted from the pressure and permeability fields, using the component form of Darcy's equation as described above. Figure 102 shows the streamlines for the uniform permeability case, α=0, for comparison to the well known analytical solution of Prats.[68] As could be expected, and as demonstrated by comparison to Figs. 103 and 104, the effect of permeability heterogeneities on the course of the streamlines is very evident.

3) Tracking of the Front

As noted above, the procedure for tracking the movement of the flood front is based on computing the particle velocity of each point on the flood front. The two velocity components of each point are multiplied by a specified time interval, and these products are added to the coordinates of the point to determine its new location. The process is repeated for each streamline until the point on that streamline reaches the production well.

Again for comparison with the known case, Fig. 105 shows the front location at six different time levels for the homogeneous case (α=0). Due to the radial nature of the pressure distribution field for the homogeneous case, close to the injection and the production wells, the initial flood advance is also nearly radial. The low pressure gradients near the well-free corners of the quadrant (actually reaching zero at the intersection of the no-flow boundaries) are responsible for the extreme retardation of the flood front advance along the edges. At the same time, the fluid along the other diagonal continues to advance rapidly, finally forming a sharp cusp on the front as it enters the

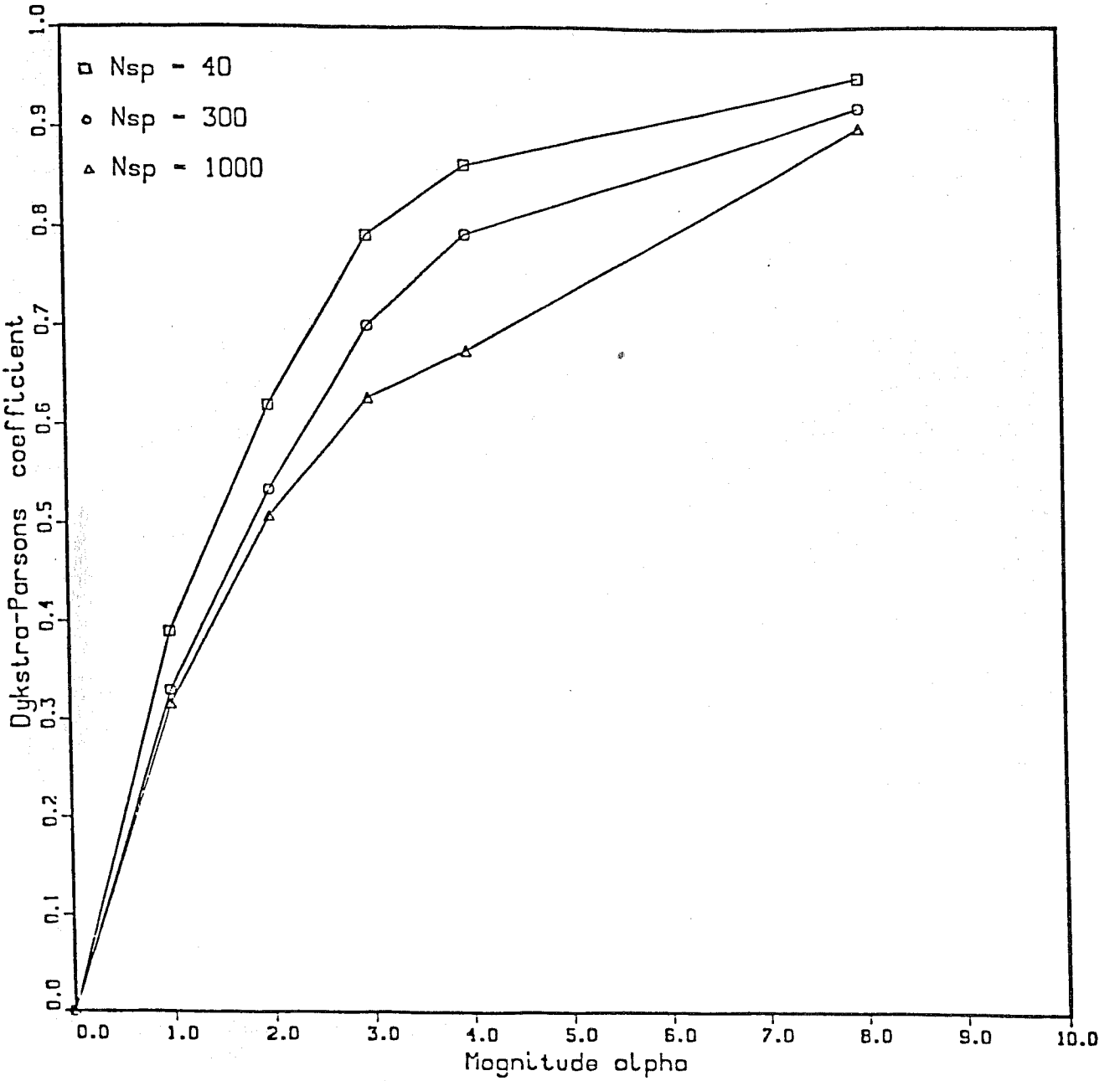

Figure 95. Dykstra-Parsons coefficient vs. α.

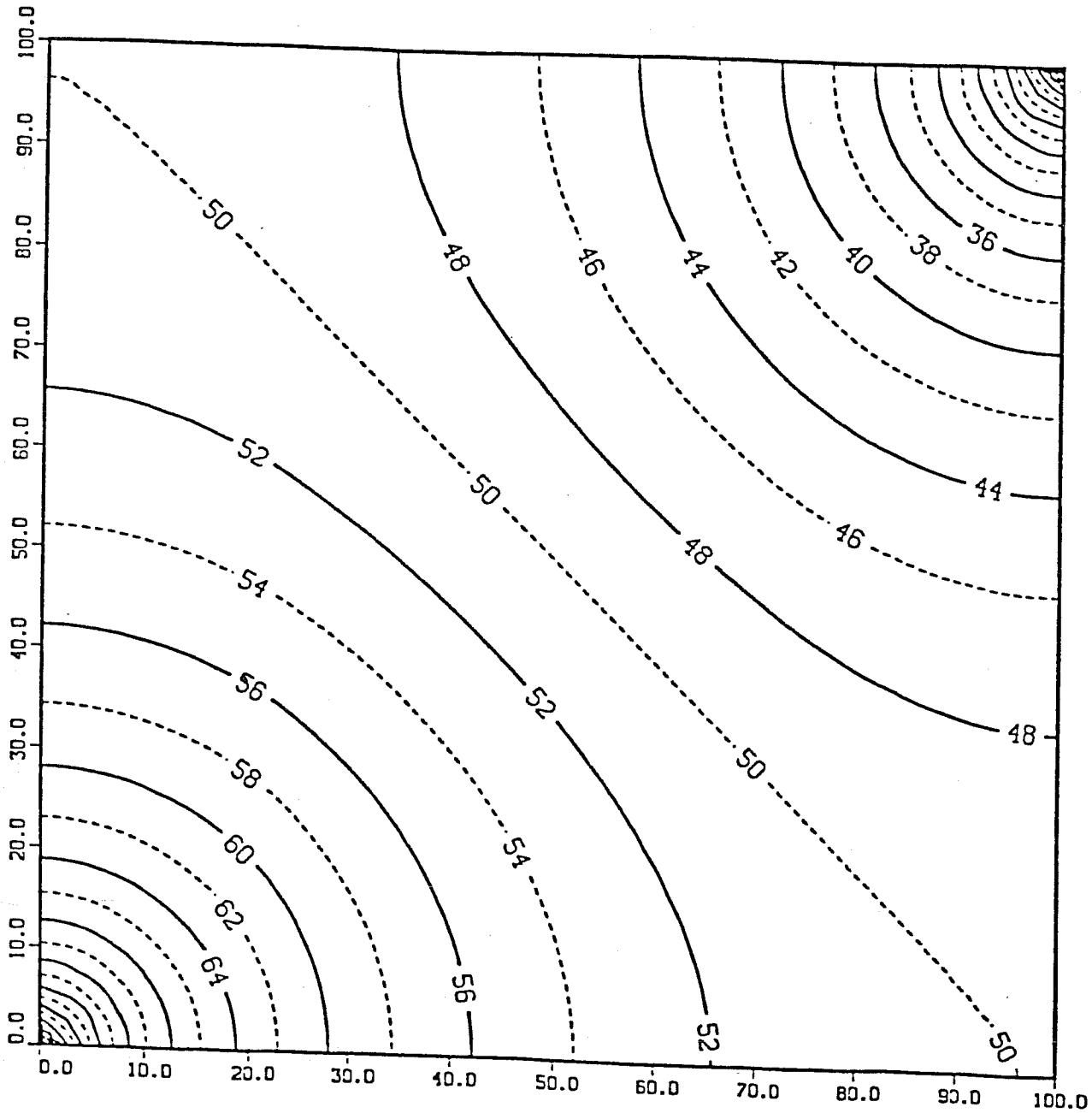

Figure 96. Pressure distribution, $\alpha = 0$, uniform permeability.

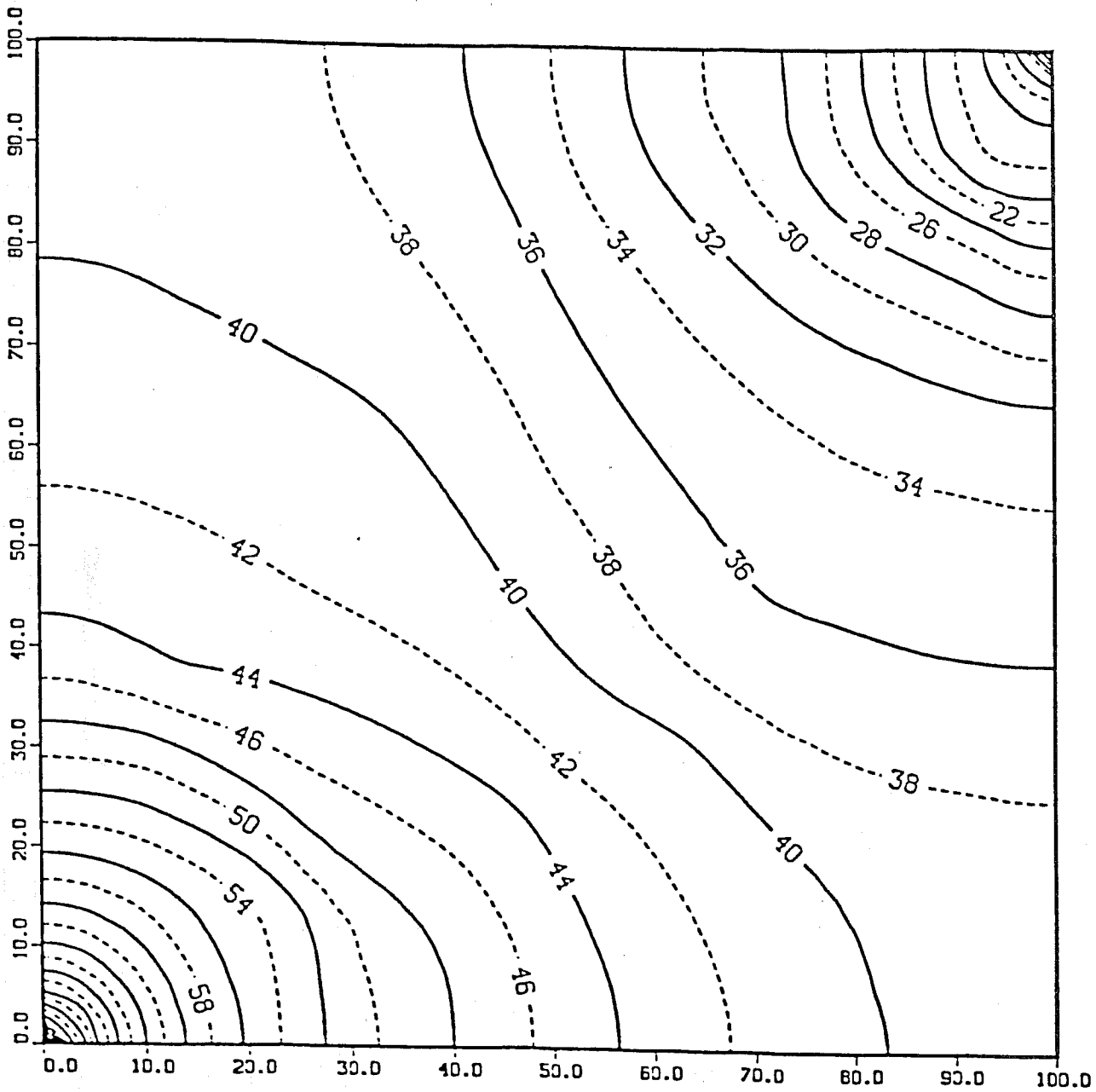

Figure 97. Pressure distribution, $\alpha = 1$, $N_{sp} = 40$.

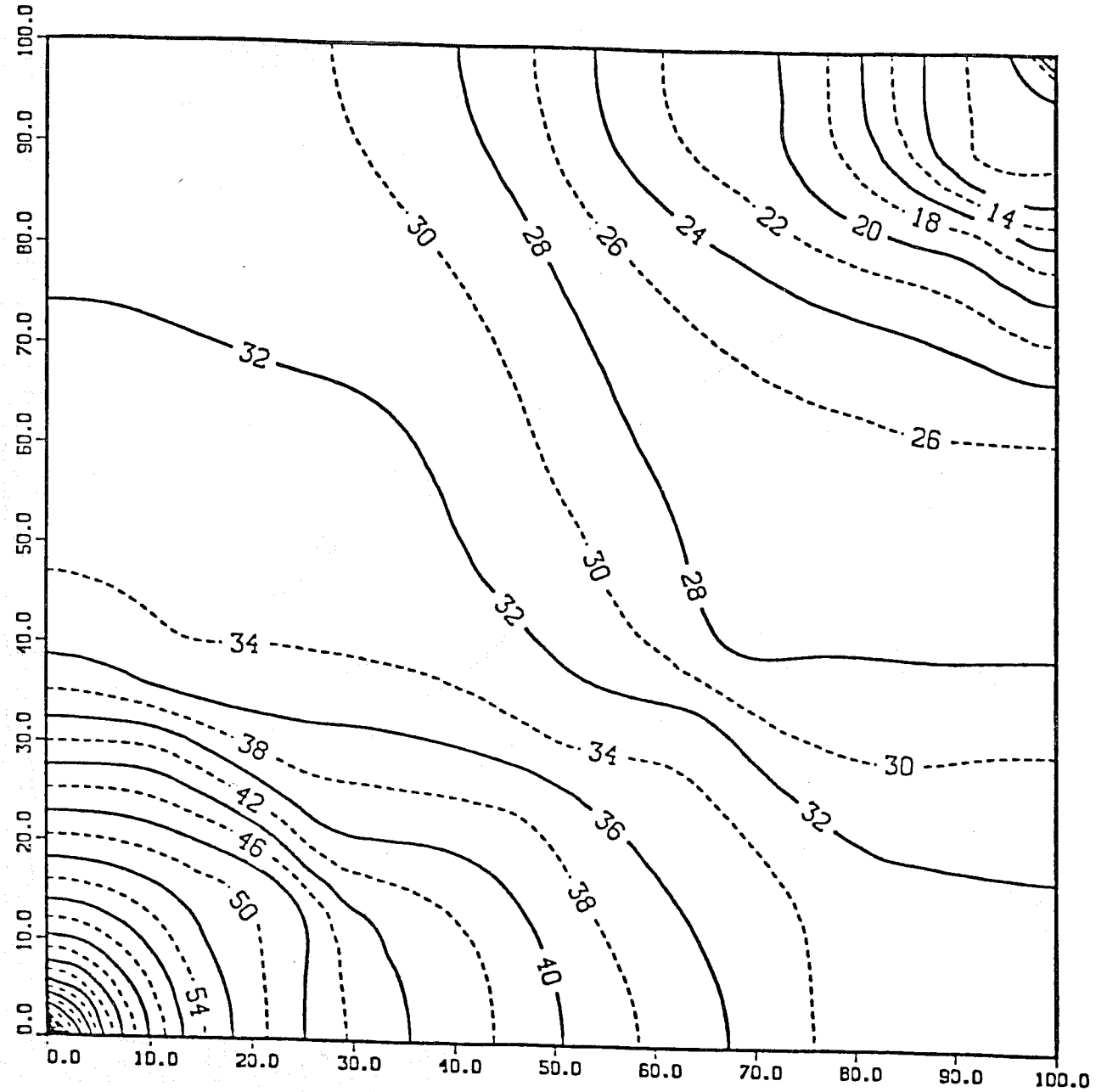

Figure 98. Pressure distribution, $\alpha = 2$, $N_{sp} = 40$.

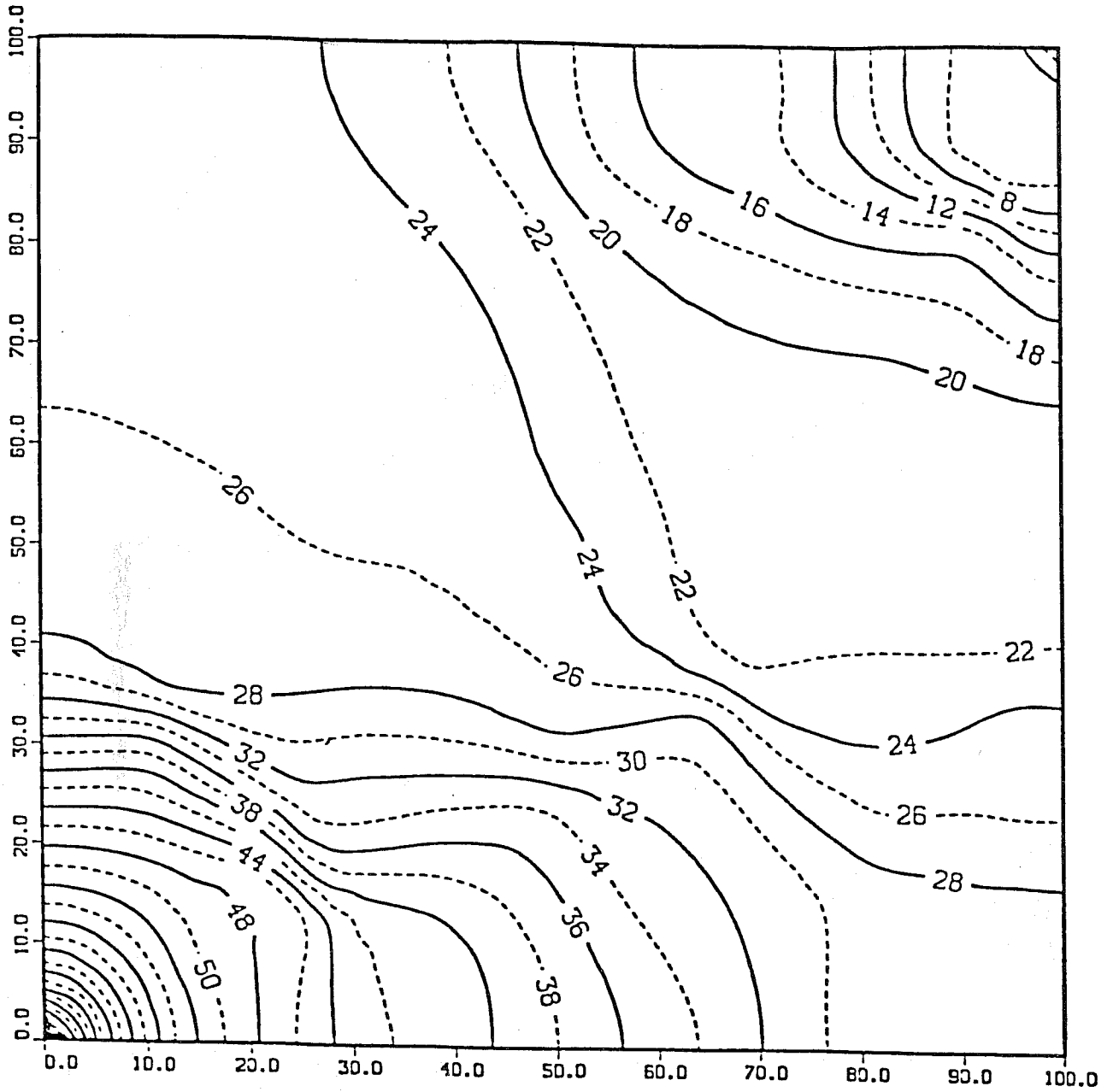

Figure 99. Pressure distribution, $\alpha = 3$, $N_{sp} = 40$.

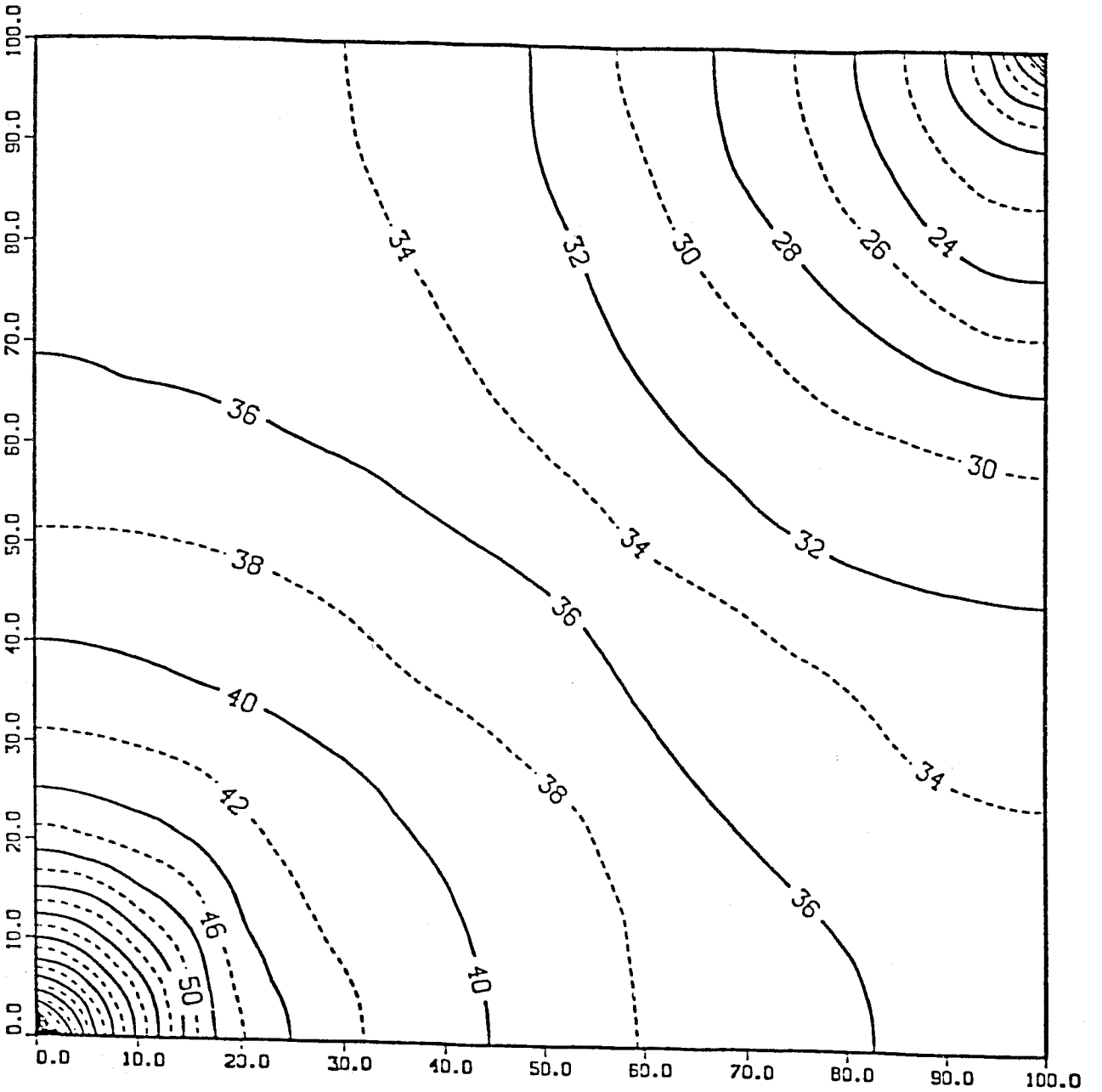

Figure 100. Pressure distribution, $\alpha = 1$, $N_{sp} = 100$.

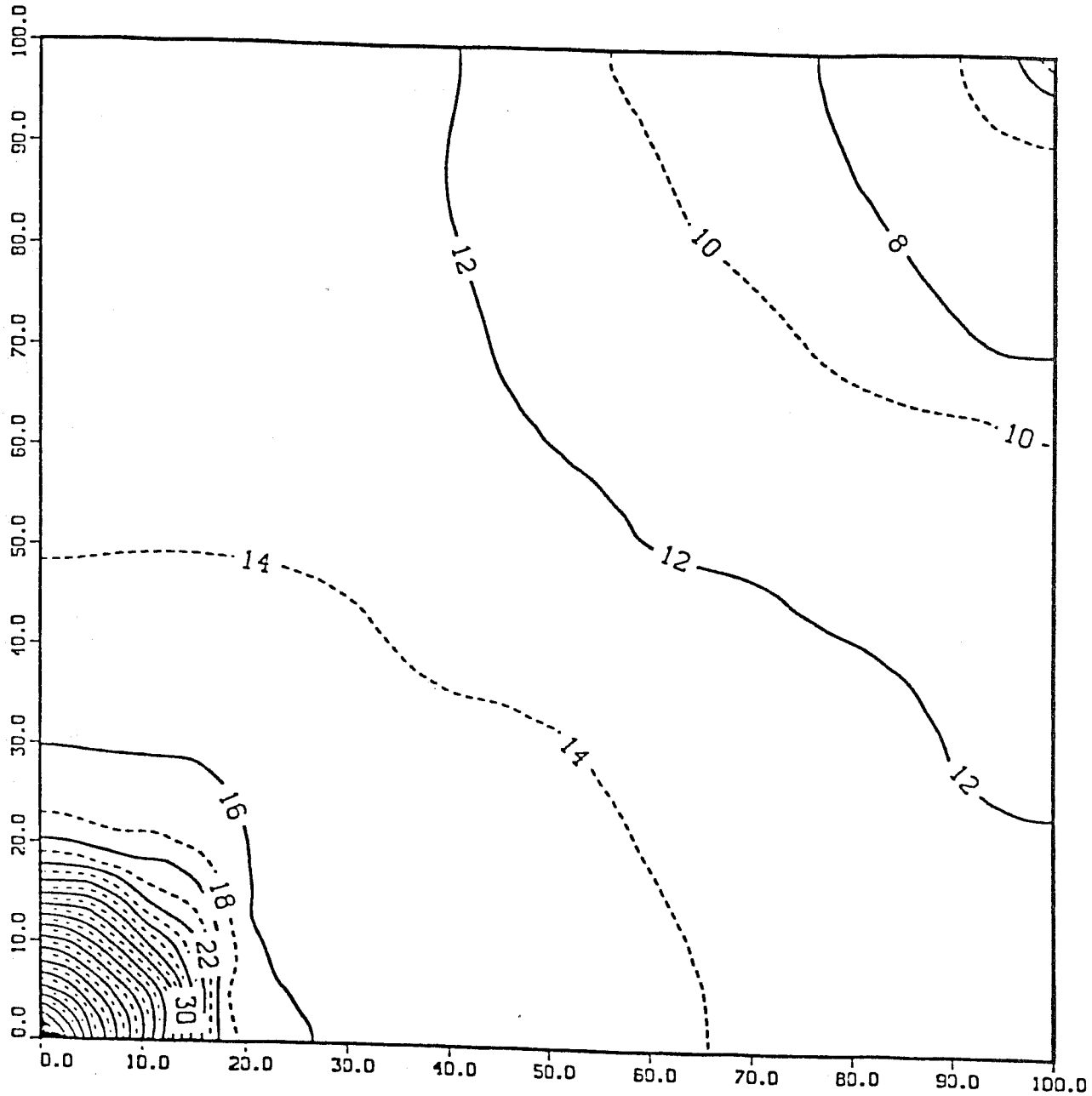

Figure 101. Pressure distribution, $\alpha = 3$, $N_{sp} = 100$.

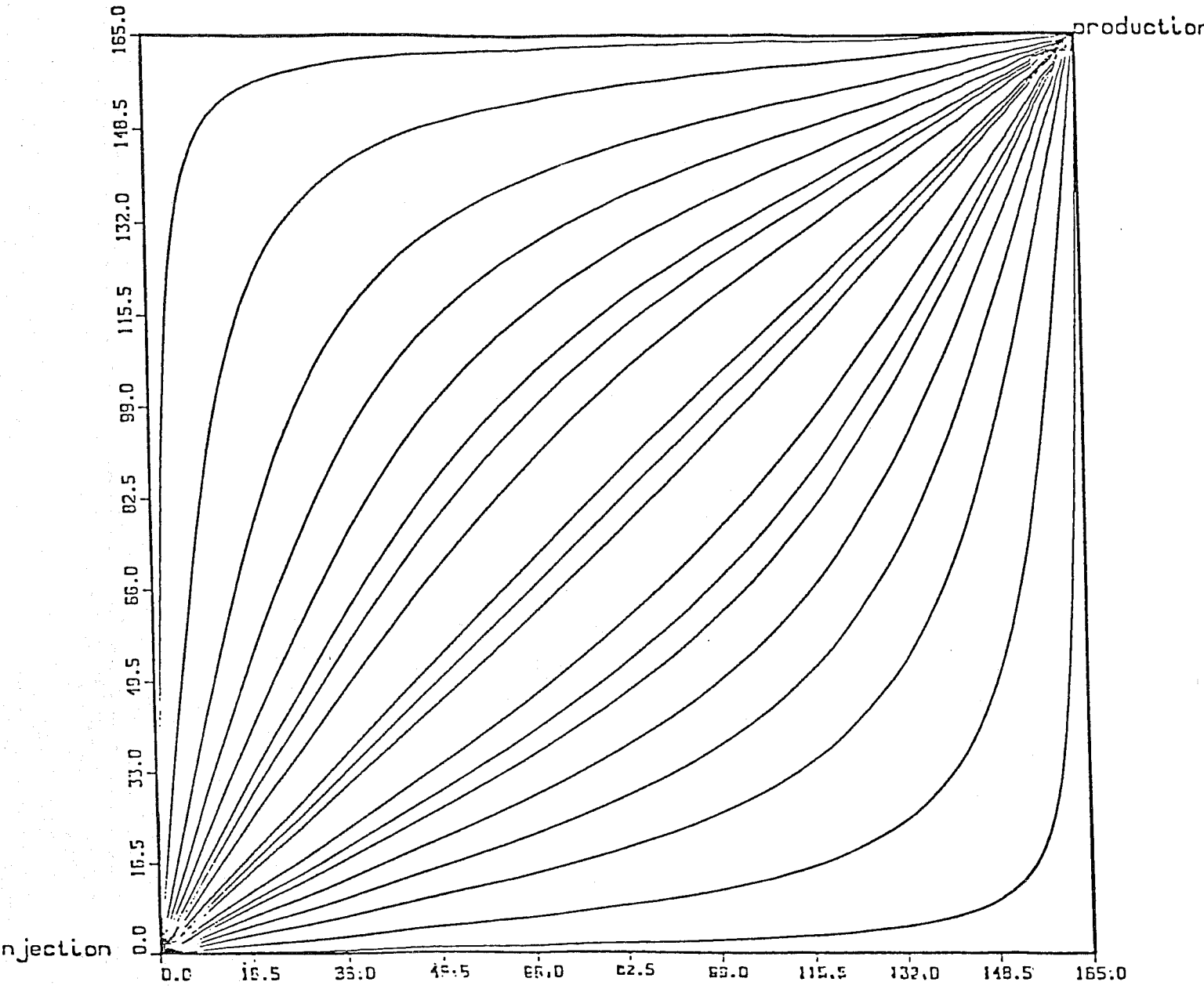

Figure 102. Map of fluid particle streamlines on a five-spot, $\alpha = 0$, uniform permeability field.

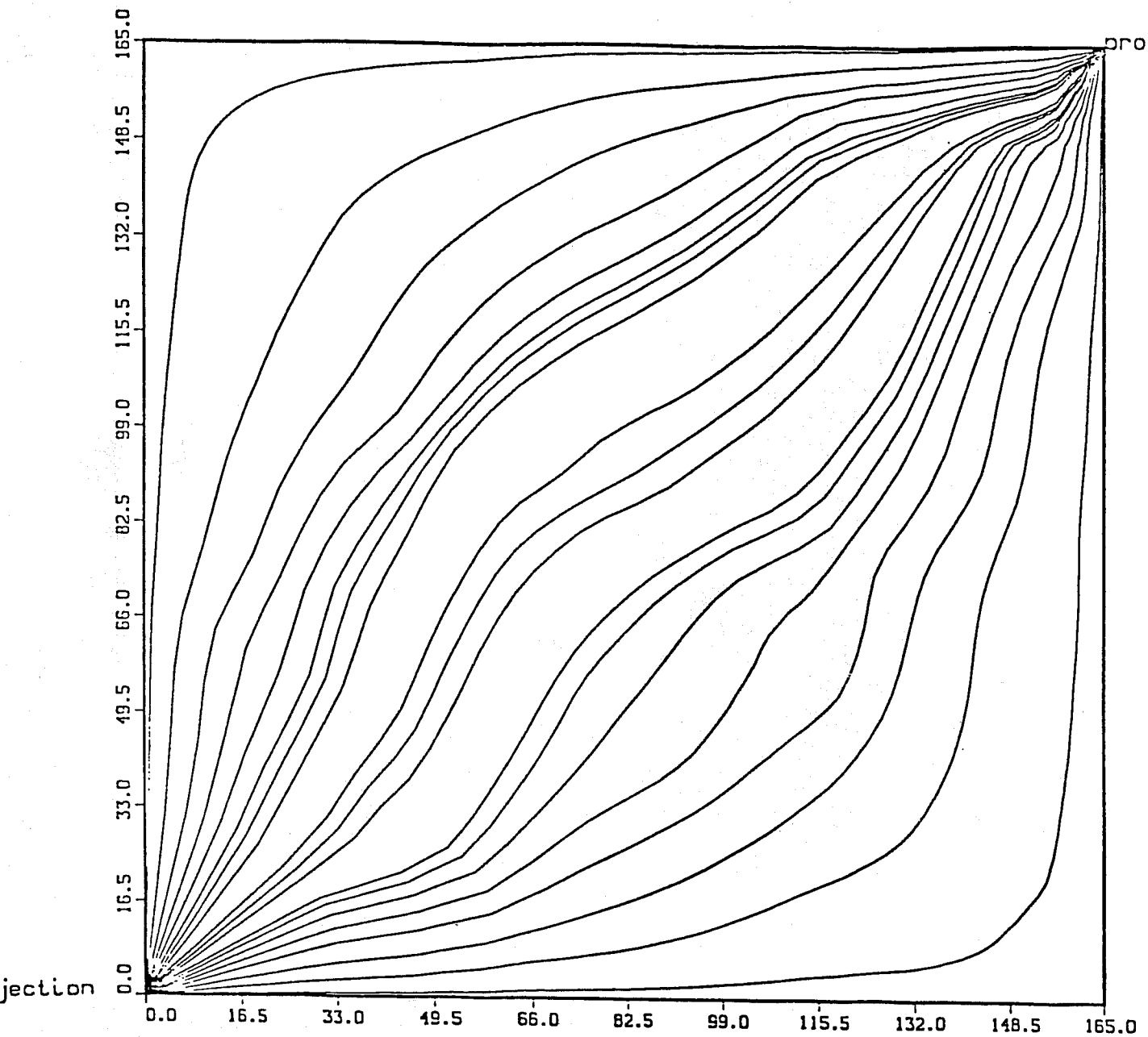

Figure 103. Fluid particle streamlines, $\alpha = 1$, $N_{sp} = 40$.

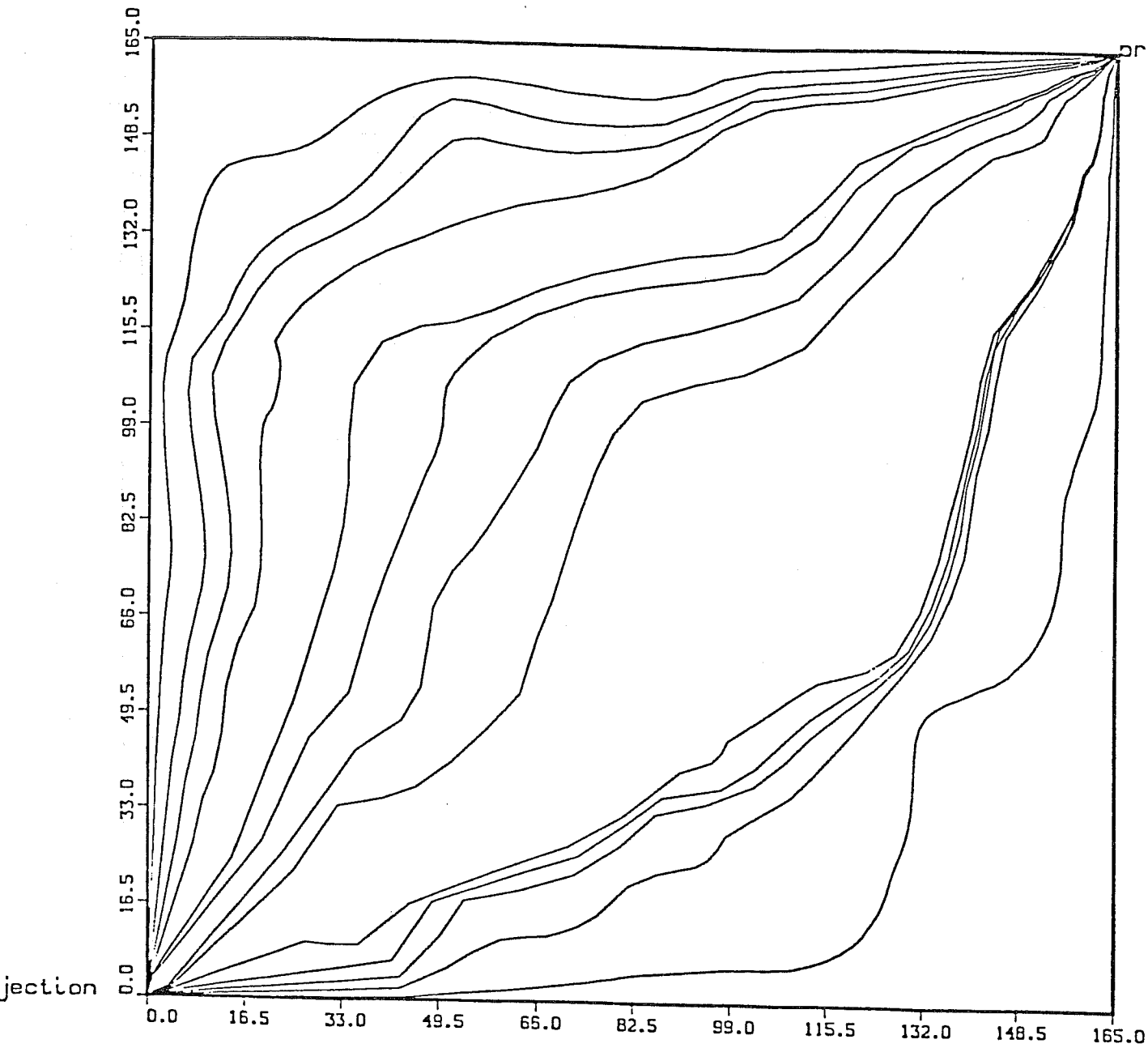

Figure 104. Fluid particle streamlines, $\alpha = 3$ $N_{sp} = 100$.

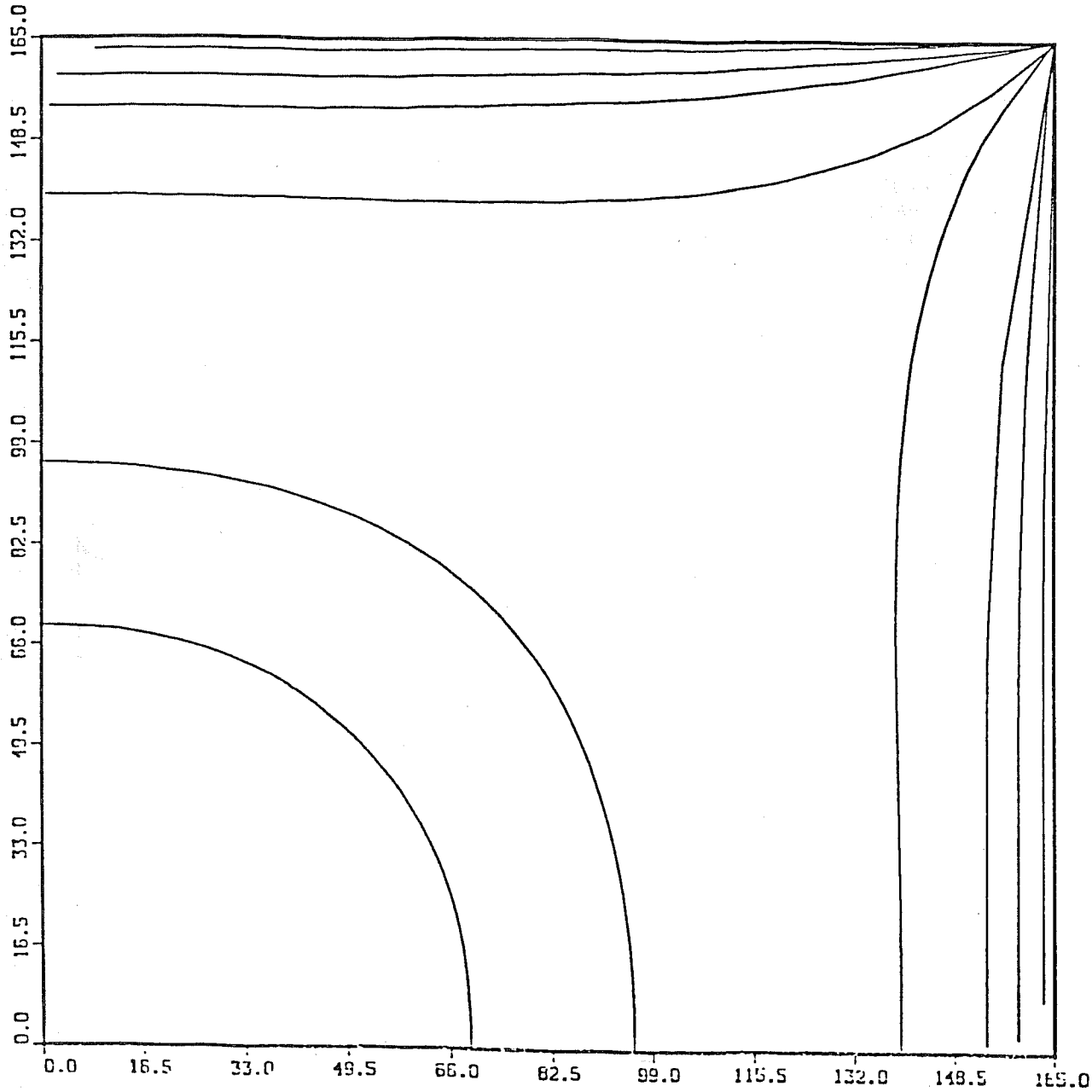

Figure 105. Front locations, $\alpha = 0$, uniform permeability field.

production well. The position of the front also is shown for two time levels after the first breakthrough of the displacing fluid. These were calculated by continuing to advance the other parts of the isochron after the time of breakthrough.

Permeability heterogeneity modifies the shapes of the isochrons, and generally hastens breakthrough, but does not invalidate the pattern described above. Figure 106 shows the front location at five different time levels for the heterogeneous field with $\alpha = 1$ and $N_s = 40$. For a case in which there are more source points, Fig. 107 shows the front location in a field in which $\alpha = 1$ and $N_{sp} = 100$. The front is not radial around the wells because the magnitude of heterogeneity involved tends to distort the shape of the flood fronts from those of the ideal case. The deep indentations in the breakthrough curve record the earlier passage of the front through recognizable low-permeability regions (see the contour map of the same realization in Fig. 97). Similarly, the part of the front on which the prebreakthrough cusp developed is determined by the position of the higher permeability areas of the quadrant. Part of the jagged nature of these curves is probably an artifact resulting from the use in the calculations of too few streamlines, or perhaps from excessively large steps between determinations of front position.

4) Recovery Computation

Analysis of the advance of the flood front from the time of injection to the first breakthrough into the production well and beyond leads to construction of a recovery curve which gives important information about the history of the flooding project. This curve is basically a plot of the percent of total area processed by the injected fluid versus the percent of the total fluid injected. Until the first breakthrough of the injected solvent into the producing well, the displaced fluid is the only fluid produced from the production well. After the breakthrough, some of the displacing fluid also begins to be produced. Once the position of the flood front at any time after breakthrough is established in this study, the area under the curve gives the amount of oil produced per unit thickness at that particular time. Division of this amount by the bulk area then gives the fraction of the total area swept by the injected fluid. The percentage of the total area processed by the injected solvent is obtained by dividing the amount of fluid injected, Qt, by the bulk volume of the element under study.

Figure 108 shows the recovery curve for the homogeneous case of uniform permeability. The curve again shows, in agreement with other studies performed in different ways, that first breakthrough of the displacing fluid occurs after .717 pore volumes of the displacing fluid have been injected. The amount of fluid recovered after the first breakthrough depends on the width of the cusp at which the injected fluid enters the production well. The computed results shown in this figure for the $\alpha=0$ case indicate that after two pore volumes, the residual of the original fluid would be down to about 2.5 percent.

Our first results for the effect of heterogeneity on the production curves are shown in Figs. 109 to 115. These curves also are affected to some unknown extent by the same difficulties noted previously, caused by the large steps between the computation of streamline positions. Despite this, it seems significant that the worst cases—the earliest breakthroughs, and the lowest values of recovery after breakthrough—are observed for the longest correlation length (the lowest values of N_s). A cautionary note is that it is in realizations with large correlation distances that the outcome is most dependent on the particular pattern of permeability heterogeneity.

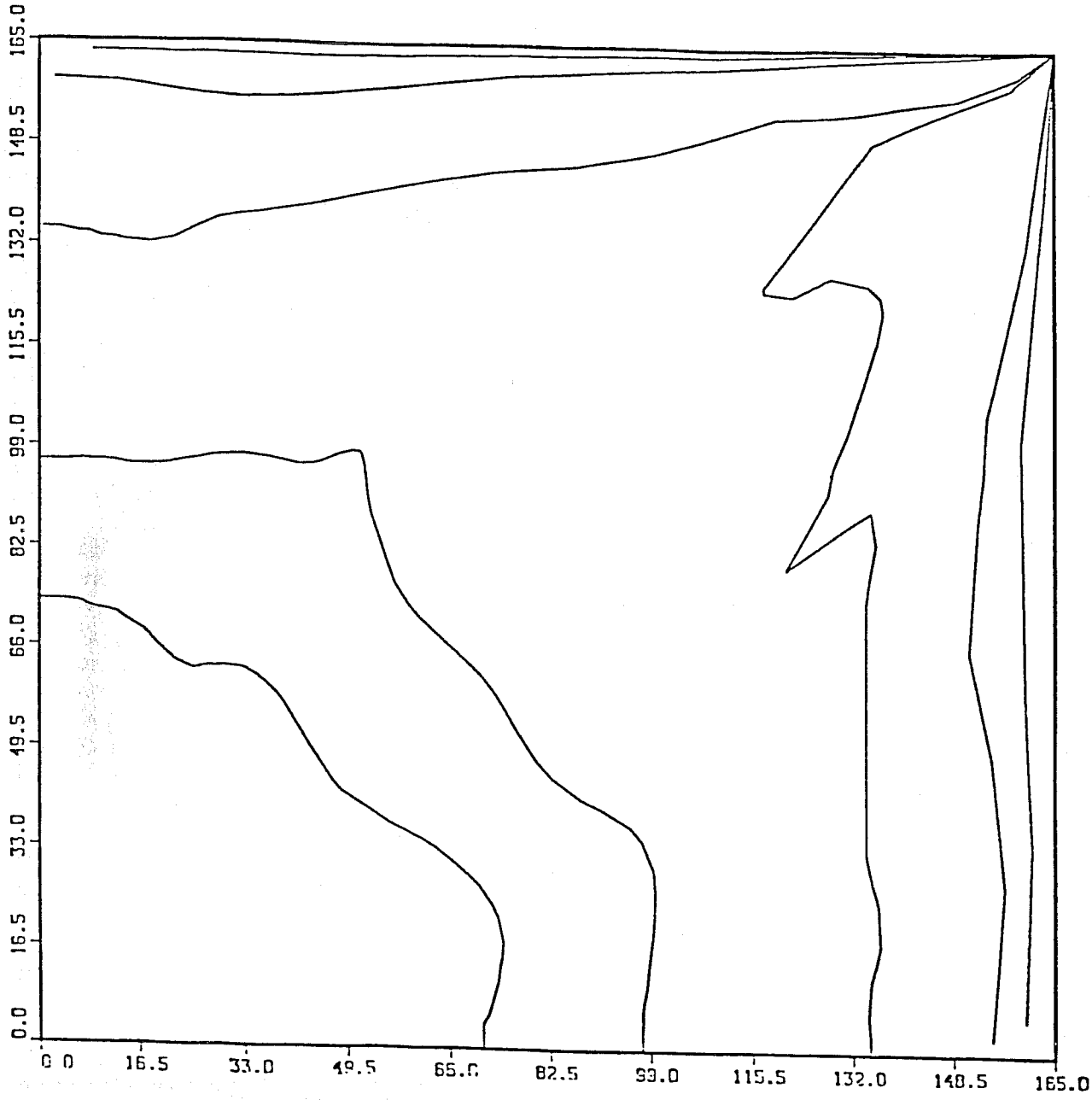

Figure 106. Front locations vs. Time, $\alpha = 1$, $N_{sp} = 40$.

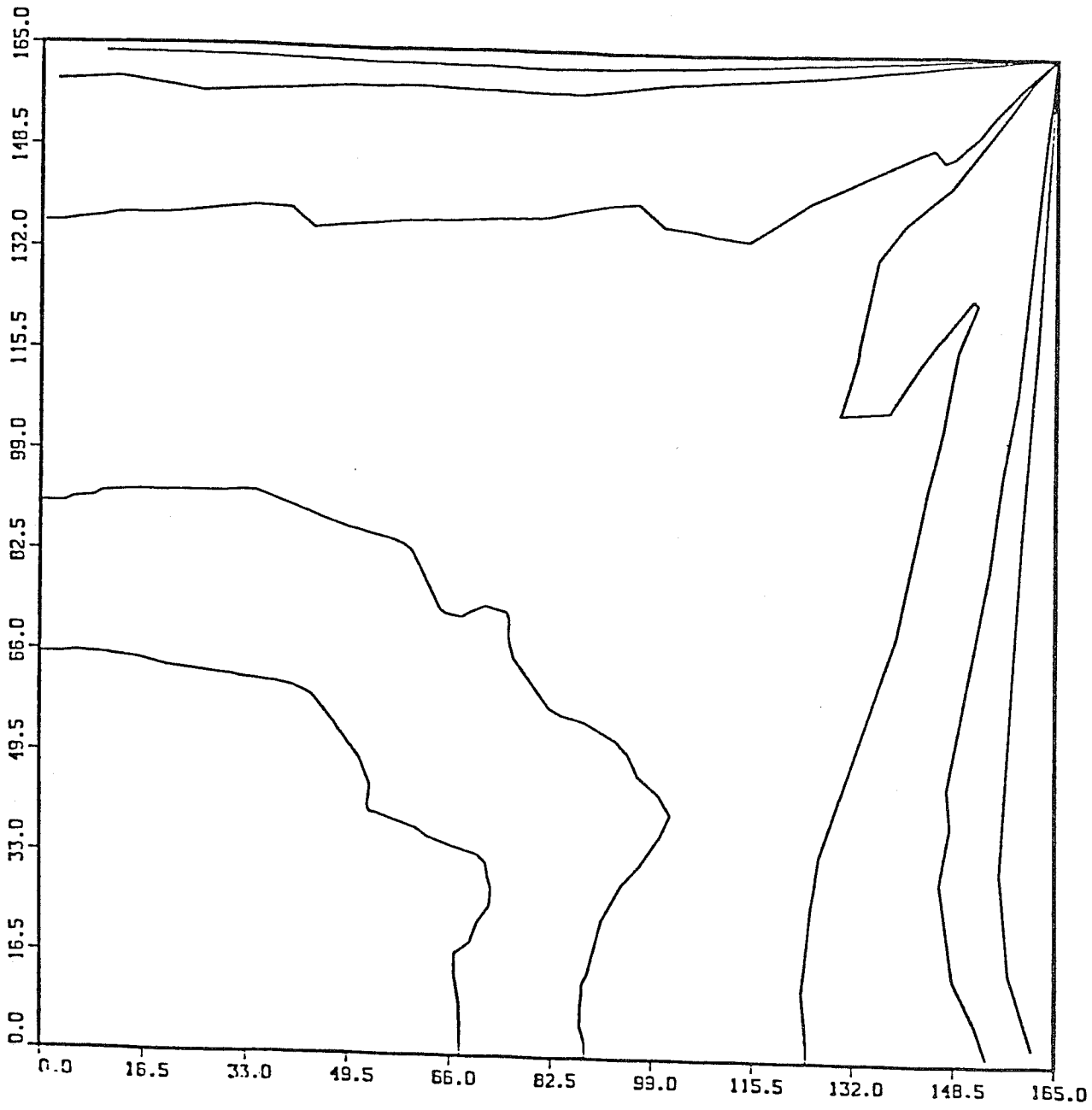

Figure 107. Front locations vs. Time, $\alpha = 1$, $N_{sp} = 100$.

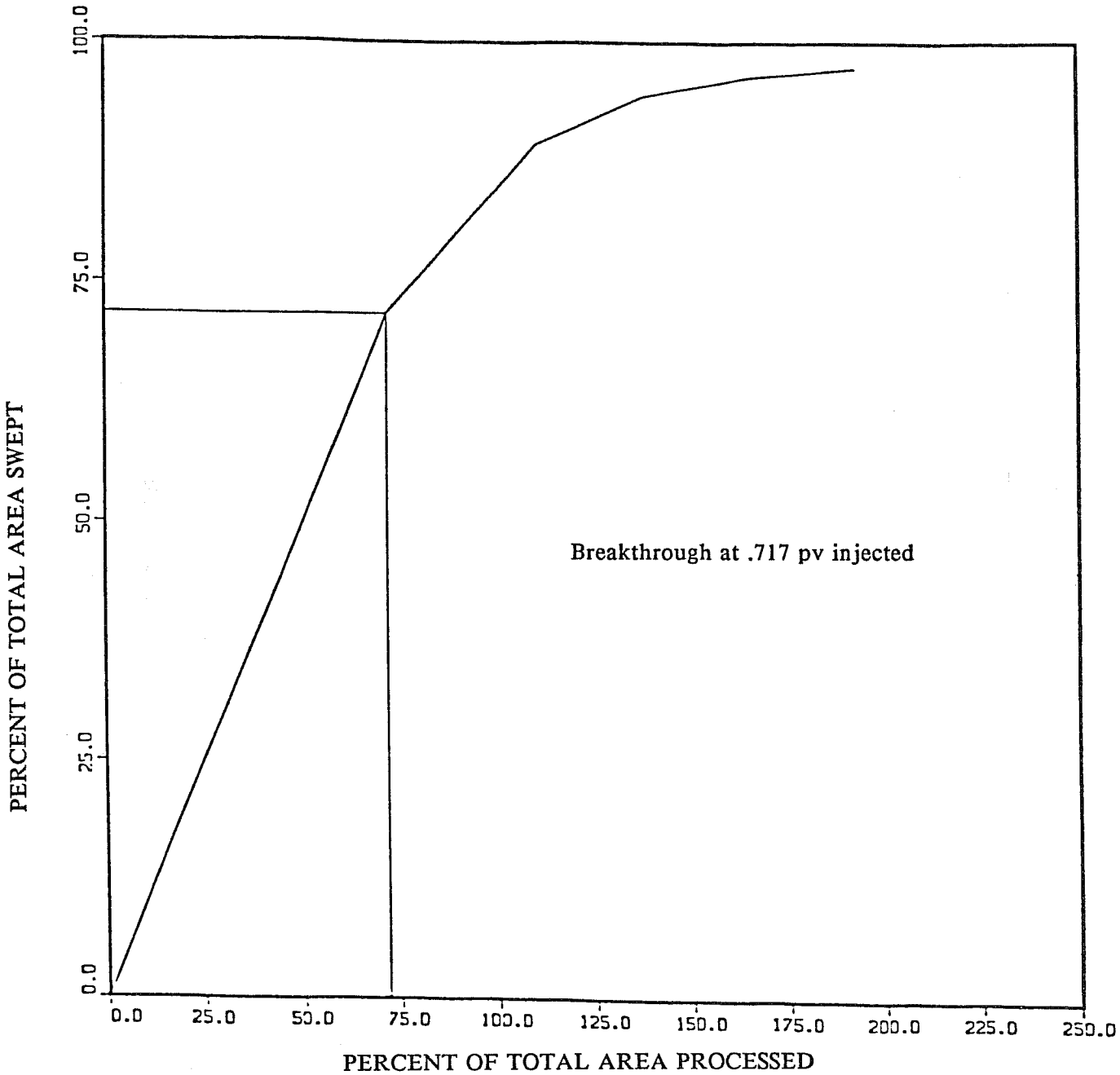

Figure 108. Recovery curve, $\alpha = 0$, uniform permeability field.

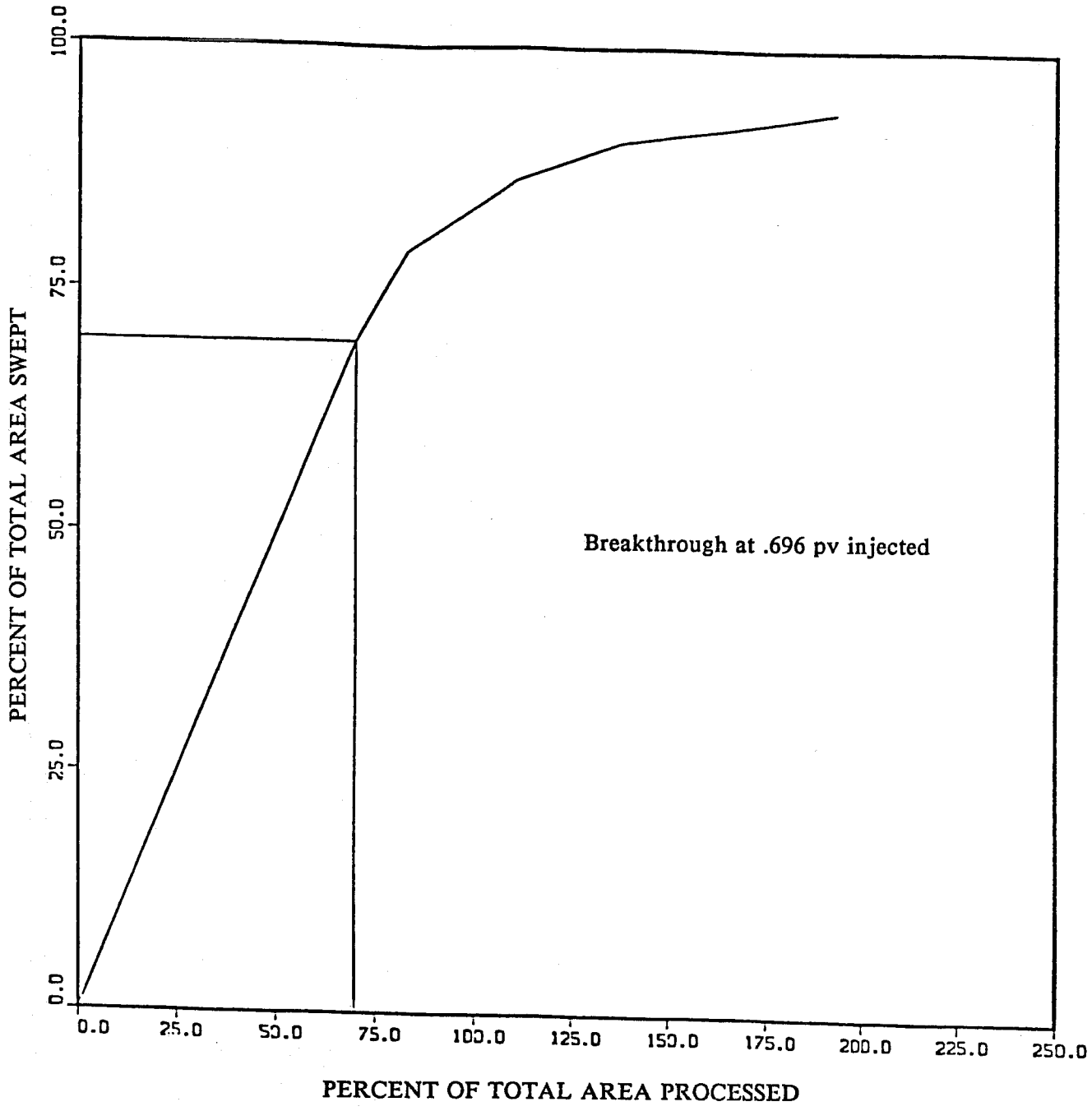

Figure 109. Recovery curve, $\alpha = 1$, $N_{sp} = 40$.

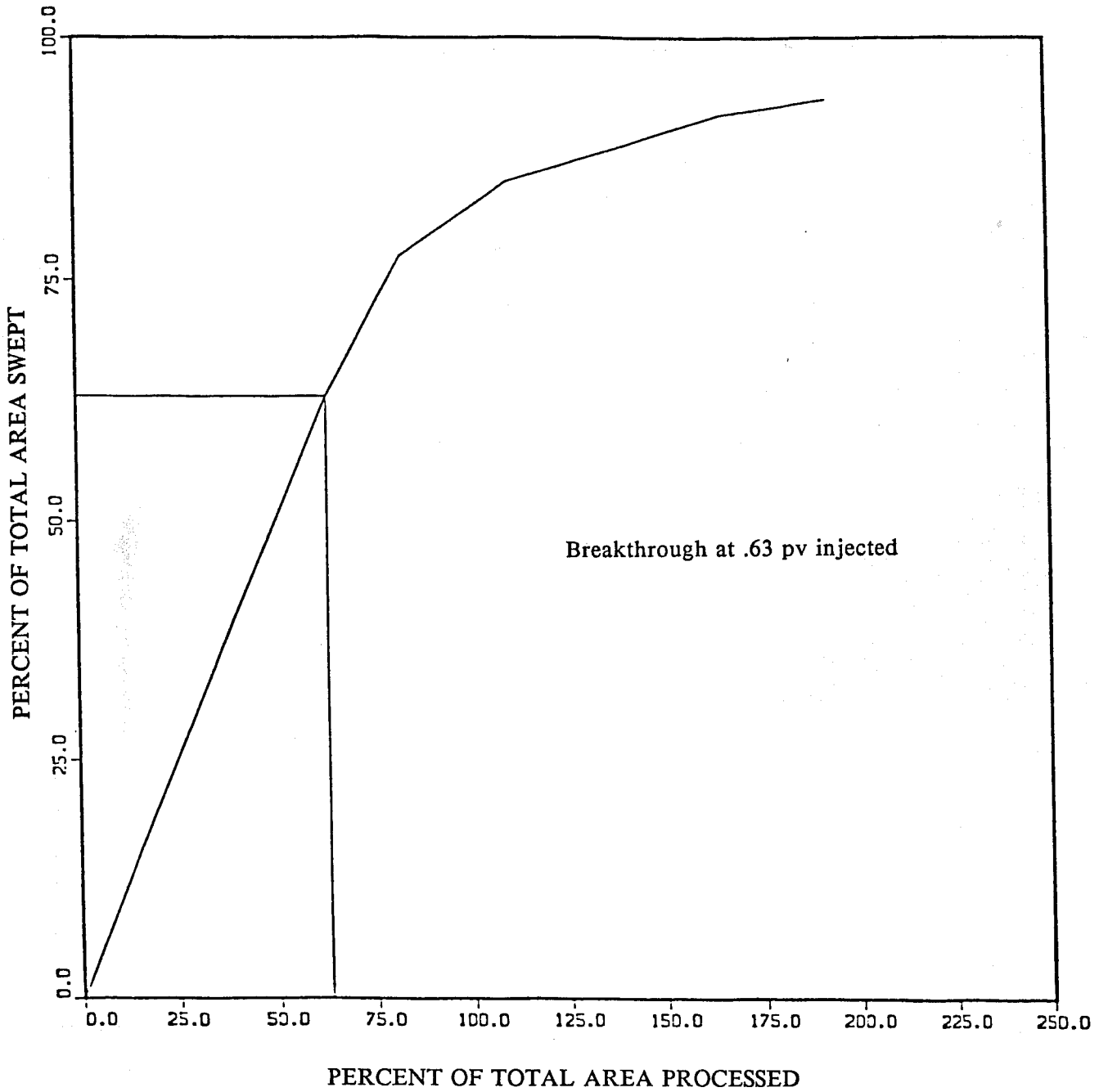

Figure 110. Recovery curve, $\alpha = 2$, $N_{sp} = 40$.

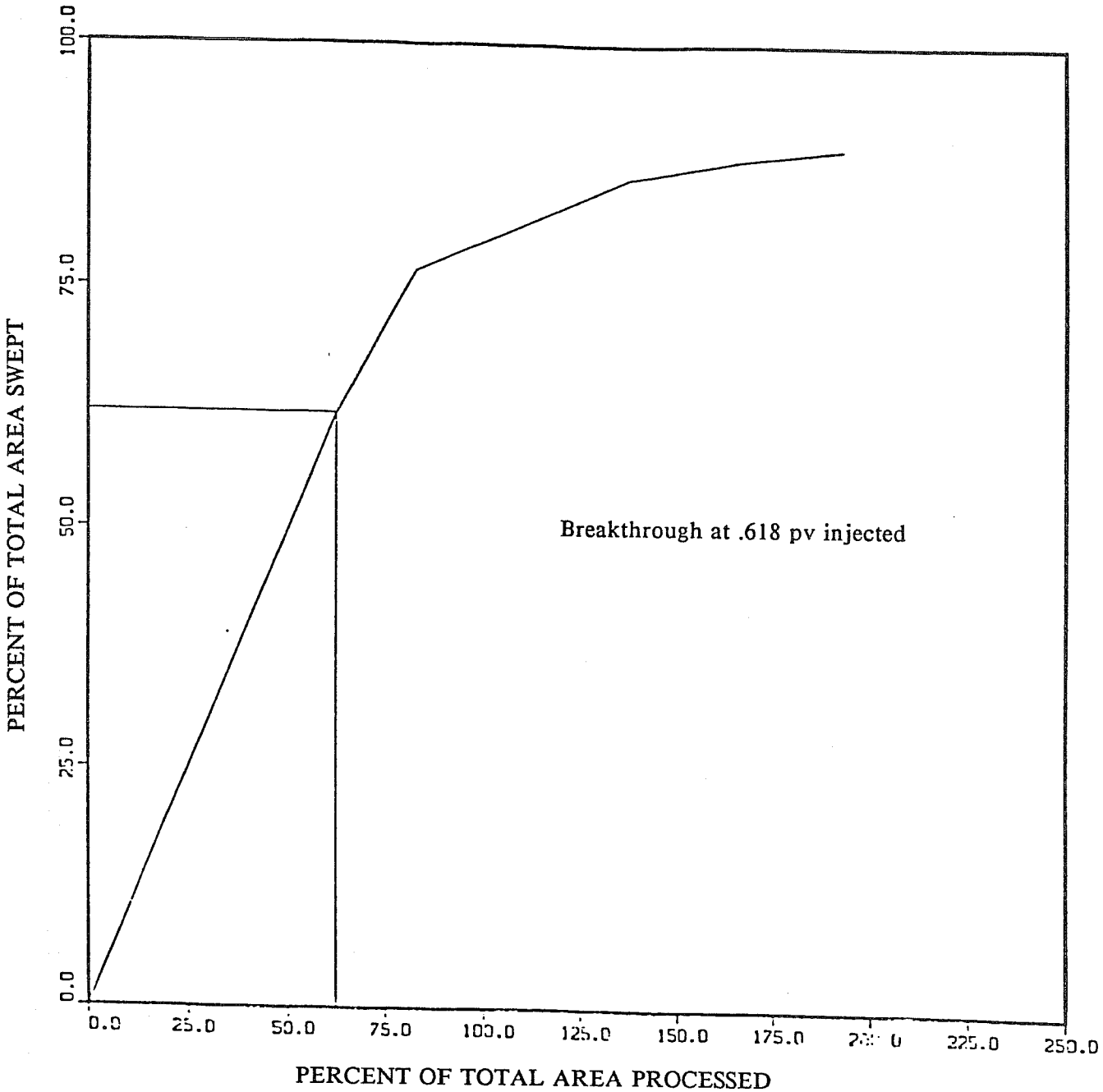

Figure 111. Recovery curve, $\alpha = 3$, $N_{sp} = 40$.

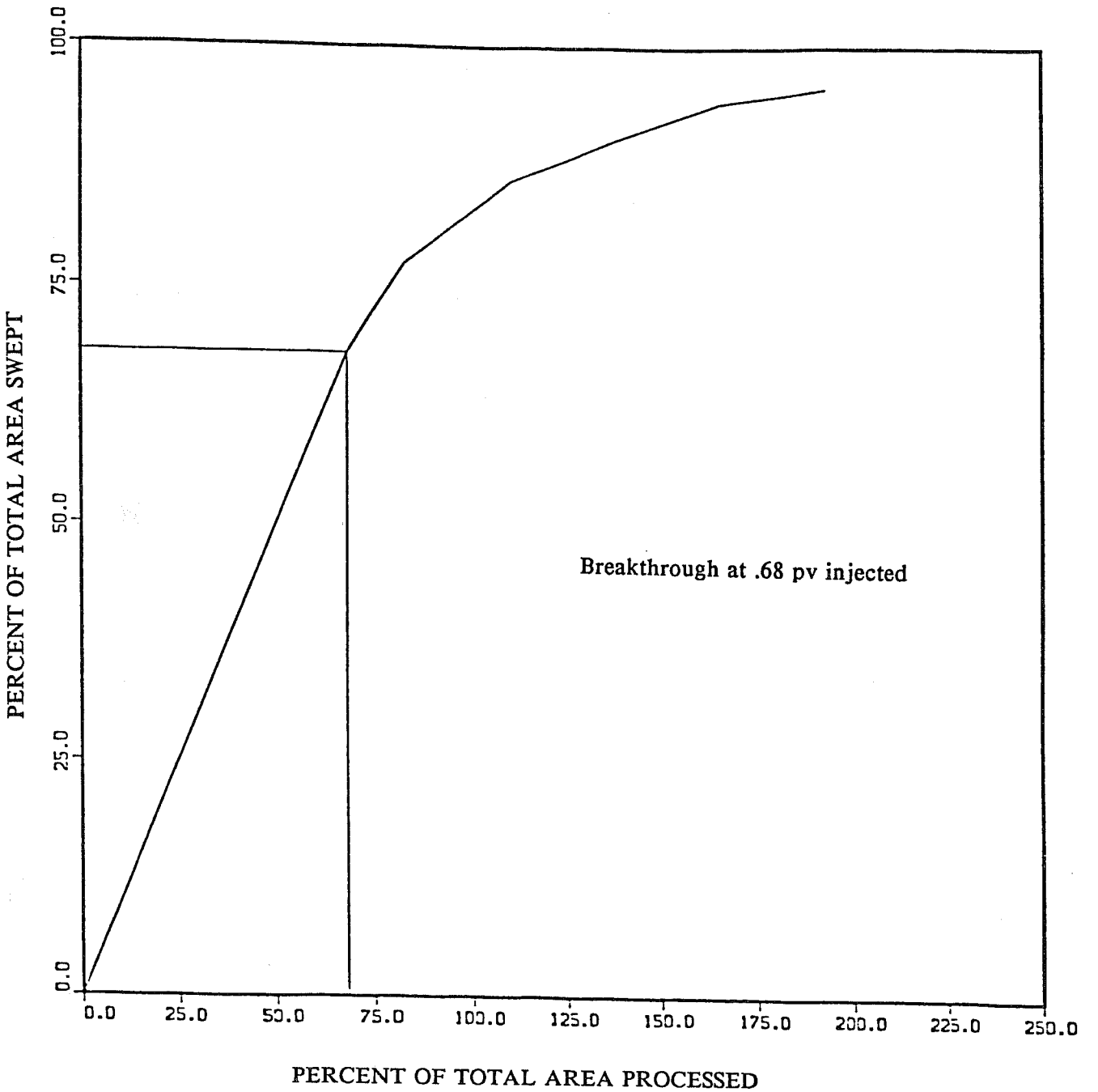

Figure 112. Recovery curve, $\alpha = 1$, $N_{sp} = 100$.

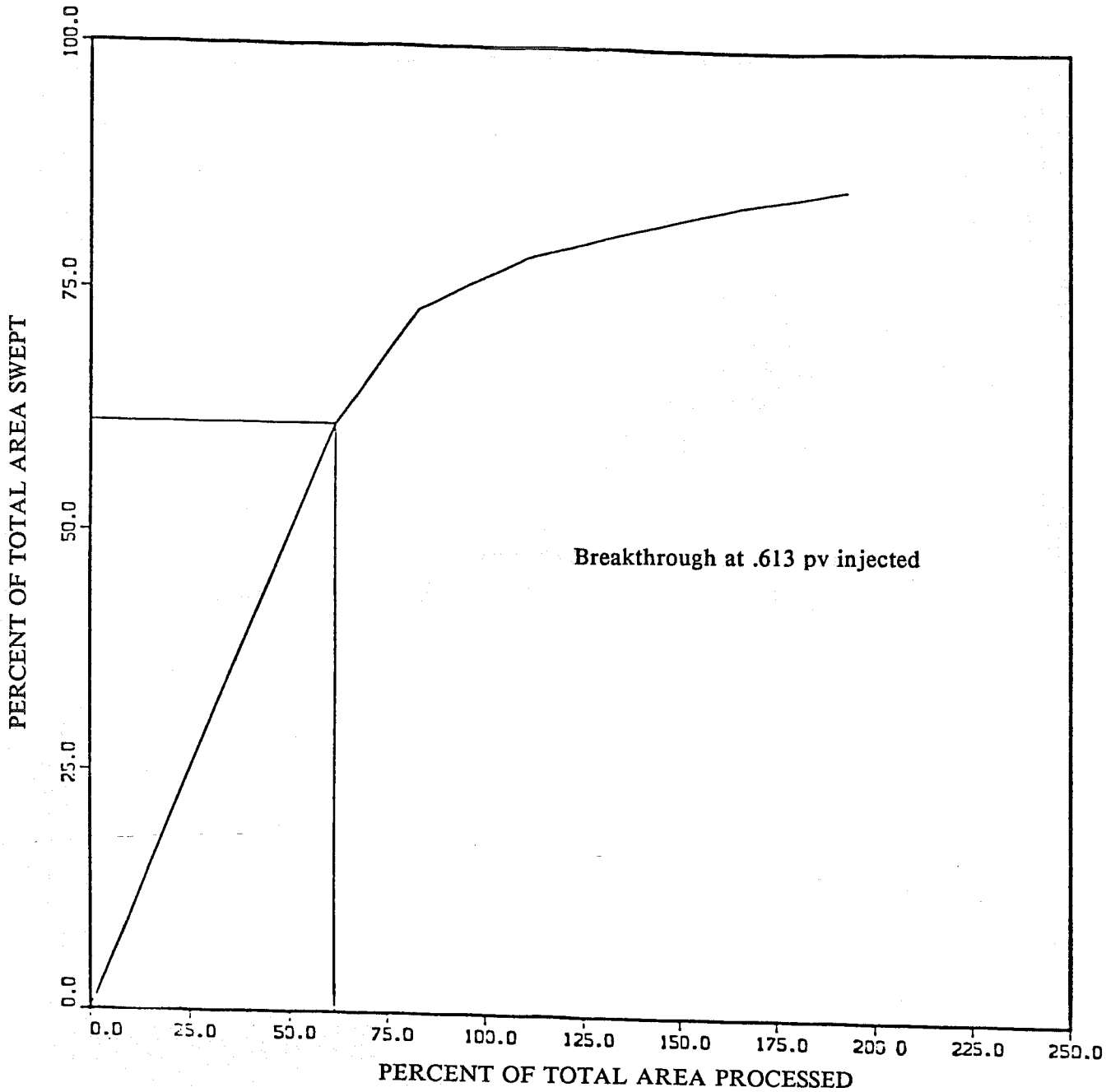

Figure 113. Recovery curve, $\alpha = 3$, $N_{sp} = 100$.

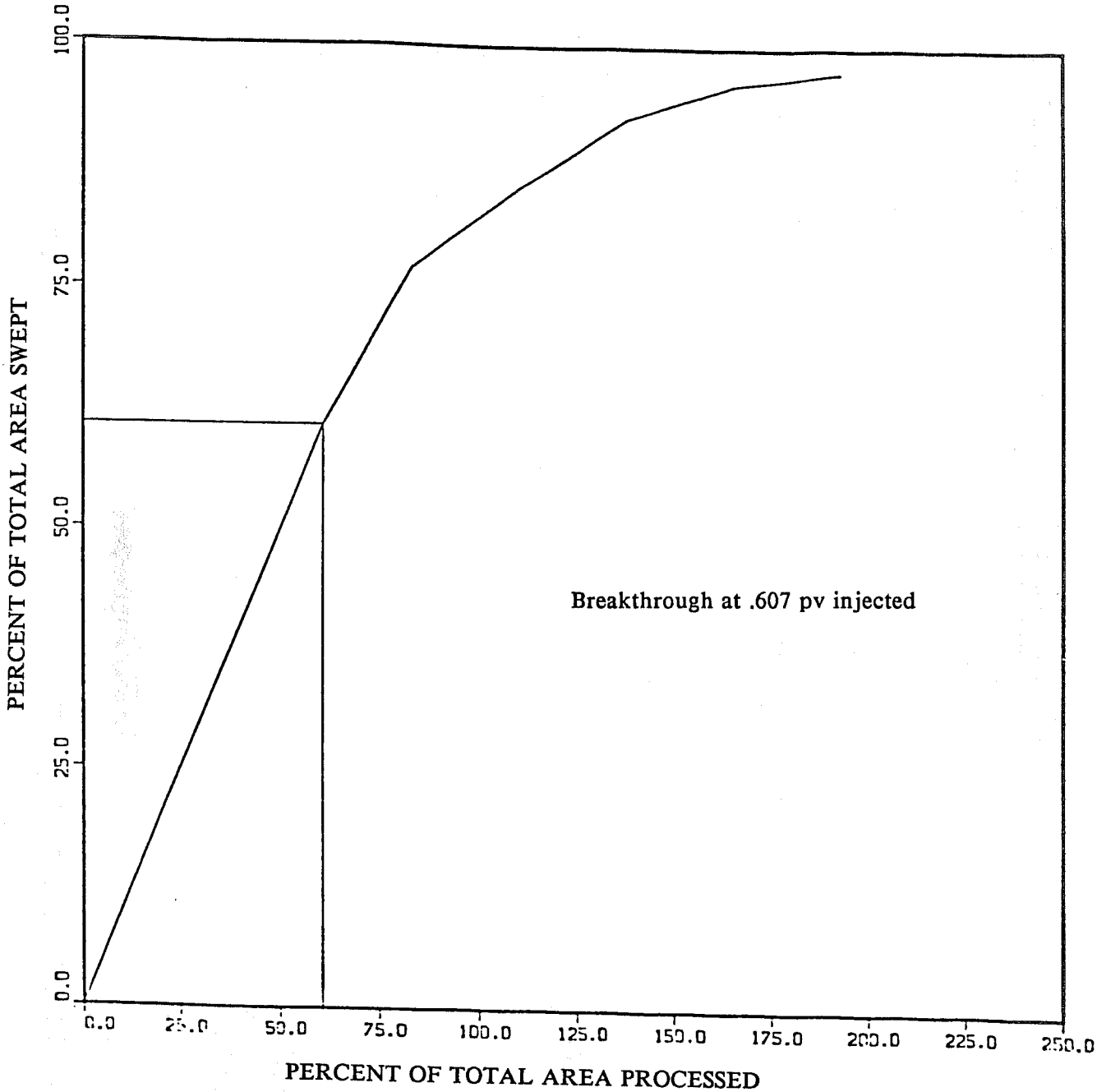

Figure 114. Recovery curve, $\alpha = 1$, $N_{sp} = 200$.

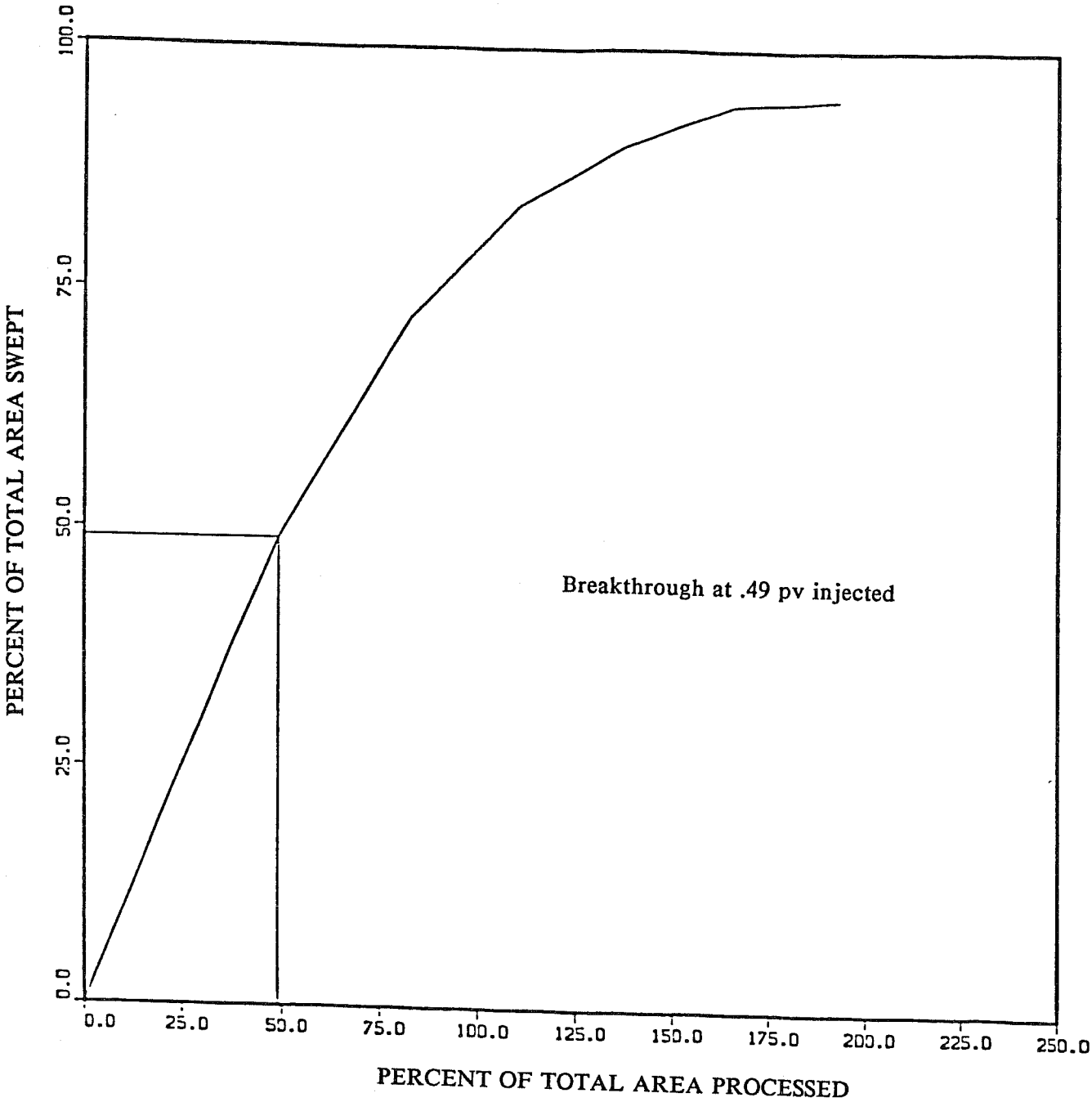

Figure 115. Recovery curve, $\alpha = 2$, $N_{sp} = 200$.

e. Conclusions

The purpose of this study was to investigate some effects of rock heterogeneity on single-phase displacement at unity mobility ratio in a five-spot pattern flood. Although the basic assumptions restrict their direct applicability, the results are expected to be useful as an initial delineation of the problem, demonstrating and evaluating on at least a semi-quantitative basis the effects of both the correlation length and the limiting value of the variance of the permeability field.

Objections can certainly be made about some of the details of this calculation, but it is believed that the force of these objections is not such as to decrease the generality of the results. Some of the evident artifacts of the streamline and frontal representations, for instance, can probably be eliminated by increasing the detail of the computations.

Another objection is that the study was performed in a square field, as if the symmetry of the α=0 case persisted when the permeability heterogeneities became important. The objection is that in a heterogeneous field, a square "symmetry unit" is no longer appropriate. This is answered by pointing out that in any pattern flood there will be no-flow boundaries in the pressure field, across which no fluid flows, and which therefore serve to separate each "quadrant" from its neighbor. In the case where the permeability heterogeneities are randomly placed, these boundaries will no longer be straight, but still will be locally perpendicular to the isobars that intersect them. Furthermore, in a five-spot pattern, even one in which the flow rates are not equal in all wells, there will be "corners" marking the intersections of the no-flow boundaries, at which even flow parallel to the boundaries is zero. Thus, the principal features of the square-sided approximation used here would still be present in a more accurate representation of the overall five-spot.

It is possible, in fact, to imagine a heterogeneous permeability distribution over a field developed in five-spots, with any specified geostatistical parameters, that would have straight line no-flow boundaries. It would only be necessary for the heterogeneities in the adjoining quadrants to have mirror symmetry across the quadrant boundaries. This would certainly be an unlikely configuration, but if the geostatistical parameters are sufficient to determine the flooding efficiencies, then investigation of these "unlikely configurations" should be sufficient to determine the precise effect of the parameters.

At any rate, one must remember that the production curves show only the averaged results of the non-uniformities in the front that are caused by the permeability heterogeneities. This initial study has demonstrated several important points about the displacement from heterogeneous formations:

1. The spatial distribution of the permeability field has a great influence on the flow process.

2. As the ratio of the number of source points to the total grid points of the system is increased, the correlation length of the spatial distribution is reduced, and the variability of the log(k) field is reduced to a lesser extent.

3. The flooding sweep efficiency tends to decrease as the permeability field becomes more heterogeneous. A more heterogeneous system is generated as the value of α (or the Dykstra-Parsons coefficient) is increased.

4. The magnitude of α, which determines the width of the permeability distribution, strongly affects the flow behavior. As its value is increased, a heterogeneous field with a higher contrast in the magnitude of the permeability is obtained, even though the spatial distribution structure of the field remains the same.

f. Plans for Continuation of the Work

As pointed out previously, this report is primarily a summary of the master's thesis work of Mr. Naser E. Heravi. More details of the work can be found in that thesis,[91] which is of course available to our supporters. The areas of investigation opened up by this work are large, however, and we expect to continue to refine the procedures and the results. We also intend to publish more complete and detailed accounts of that work as it becomes available.

3. Flow Heterogeneity In Porous Media At Small-Scale

Flow non-uniformity in porous media can be caused by the non-uniformity of fluid and rock properties. This section of our report is concerned mainly with the study of the flow heterogeneity which may arise from variation of rock properties at the scale of laboratory core samples. In real porous media, properties such as permeability and porosity vary from point to point. Such variations have been recognized on different scales, from pore level to interwell distance. It has been pointed out that the permeability variation is large as compared to the porosity variation. It also has been noted that variation of rock properties is not completely disordered, that there is some spatial structure which should be accounted for when the effect of rock properties is considered.[79] But the question is, how important is small-scale heterogeneity on displacement performance.

Morineau et al.[92] constructed and utilized a micropermeameter which operated on principles similar to the one described by Dykstra and Parsons.[89] They measured the local permeabilities at the ends of core samples, then performed miscible and immiscible displacements in the same cores to relate permeability heterogeneity to flow behavior. They found that permeability heterogeneity is an important factor in any flow experiment. They also derived a scale parameter, a distance at which some dependence exists between neighbouring points, to characterize the spatial heterogeneity using the autocorrelation function of micropermeability. The other experiment which was conducted to demonstrate the effect of rock heterogeneity on mixing behavior was the measurement of local tracer concentrations at several locations on the output face of a rock sample. Morineau et al. found that the mean velocity and the length of the transition zone were different from one area to another. Their conclusion was that proper interpretation for miscible displacements in short cores must take into account some description of the core heterogeneity.

Heller[93] demonstrated experimentally the impact of local heterogeneity on displacement patterns. He performed a miscible flood in which dyed styrene monomer displaced clear styrene in a relatively uniform porous media, Berea sandstone of 3/4-in. diameter. After about half a pore volume had been injected, the styrene polymerized and the core sectioned. In that experiment, evidence of channeling was clear as shown in Fig. 1 of his paper. He concluded that velocity variations exist even in relatively uniform porous media. Withjack[94] confirmed these observations by using a computerized tomography (CT) scanner to observe the front flood movement. Heller[95] studied the effect of dispersion in slim tubes (uniform, packed column with glass beads). He concluded that the possibility of permeability variations exists even in unconsolidated porous media.

These observations simply suggest that the assumption of rock uniformity is not a realistic description of the mixing behavior in porous media unless the correlation length of heterogeneity is small compared to the scale of displacement.[93] In addition, the rock non-uniformity produces variations of concentration in the direction perpendicular to the average flow direction. In many interpretations of experimental work on miscible floods, the produced concentration curves are matched to theories which are based on one-dimensional models. These models totally ignore the effects of transverse variations of the flow. The main objective of this study is to investigate the

importance of the interaction of transverse dispersion with permeability variations on flow behavior at the laboratory-core scale. In the following section, a brief summary is given about the experimental technique through which the impact of relatively small-scale heterogeneity can be observed and measured in miscible floods in which the mobility ratio is unity.

a. Laboratory Observation of Flow Non-Uniformity

In experiments currently being performed, the breakthrough curves are observed at different points on the output face of the core during miscible floods. The experimental technique by which this is done involves the use of a fluorescent dye tracer and illumination by collimated light from a mercury vapor lamp, defined by a slit, parallel to and almost grazing the output face of the sample. The illuminated plane of the fluid emerging from the output face of the rock sample is observed by a video camera and recorded. Periodically, image frames are digitized and stored by a computer. Figure 116 is a schematic of the apparatus used to measure flow heterogeneity. From the successive images, independent records can be constructed of the light brightness versus time at different locations on the face. The concentration of tracer has been found to have a linear relation with brightness of light in the range above 20% concentration. Calibration should be performed to take into account light absorption in the direction of the light path, before data can be used for calculation.

b. Preliminary Results

Berea sandstone core has been selected to validate the experimental technique. However, preliminary results showed clear indications of interaction of the fluorescent dye with the rock. A firing process has been applied to the rock to reduce the extent of the adsorption. Several fluorescent dyes have been tested for use as tracers, to select one with minimum adsorption. The results showed that Nil Red fluorescent dye (Kodak Laboratory Company) was relatively less adsorptive than the other tested dyes. Another experimental problem which needs to be mentioned here concerns the variation of local apparent concentration with time. The real reasons behind such fluctuations are not yet clear. Part of the problem is quantization error, which is expected in the output of the 6-bit A/D converter that digitizes the 256X256 pixel image. Another part of the problem could be caused by the heat convection produced by the mercury vapor light which may cause some of the fluid motion inside the plastic container. To alleviate this latter problem by controlling the fluid motion inside the container, an "egg crate" grid, made of micro cover glass of 0.20-mm thickness with 6.4mm square openings, has been installed on the output face of the rock.

Preliminary results are shown in Fig. 117 of a number of light output curves taken with a fired Berea sandstone core sample. The sample was 12 cm long with an almost square cross section of 14.8 cm^2 (3.8X3.9 cm). The experiment was conducted at the relatively slow flow rate of 105 cc/hr, which was equivalent to approximately 6 ft/day. Although the breakthrough curves shown are not yet corrected to light absorption, it is possible to notice the existence of velocity variations along different paths. These production curves have been taken at different pixel locations at the output face of the core. Each of the breakthrough curves is smoothed by averaging the chosen pixel with the other four pixels around it. One other point that needs to be mentioned is that some of the breakthrough times of flow paths do not represent the real times. This is caused by the poor sensitivity of the video camera to very low tracer concentrations. However, quantitative analysis of the calibrated results is in progress, and an intuitive outline of the analysis that is planned is given in the following paragraph.

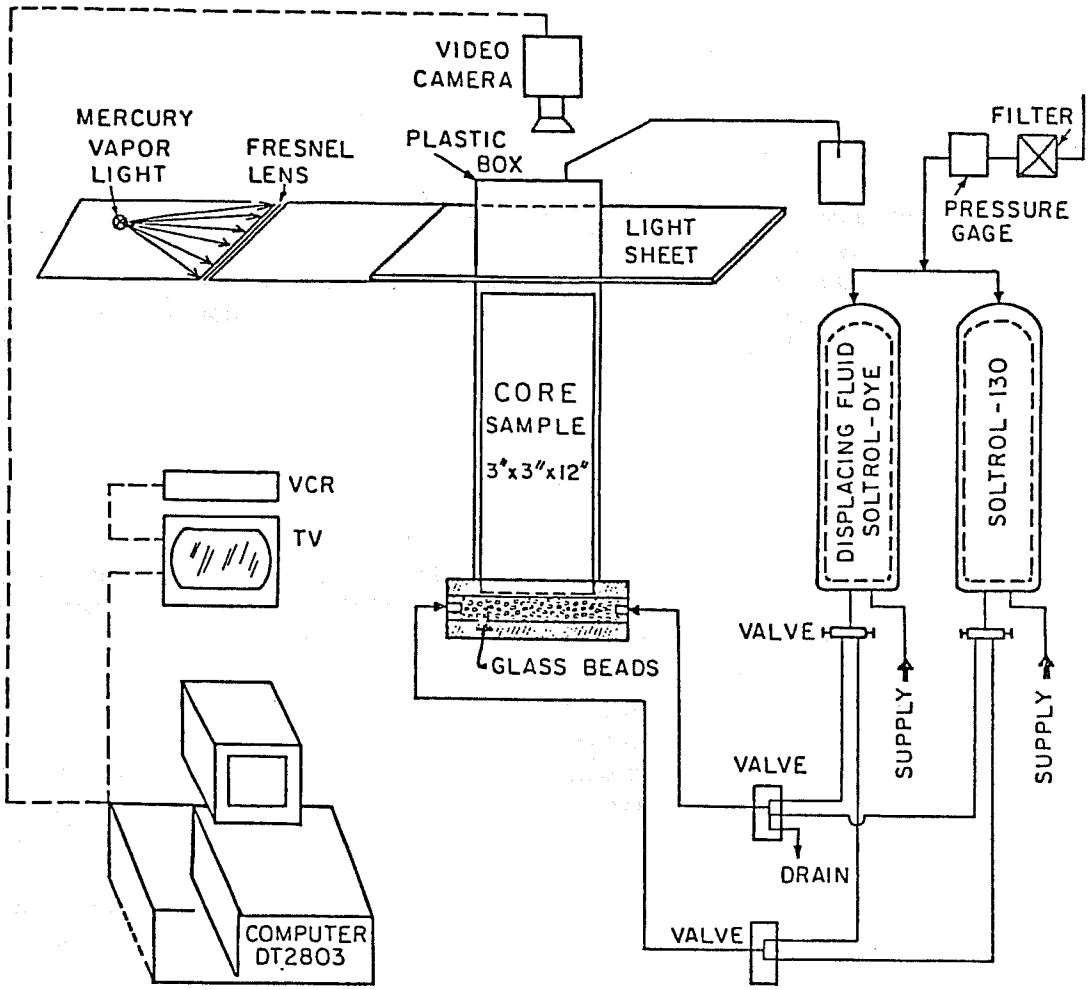

Apparatus for Measurements of Flow Heterogeneity

Figure 116. Apparatus for measurements of flow heterogeneity.

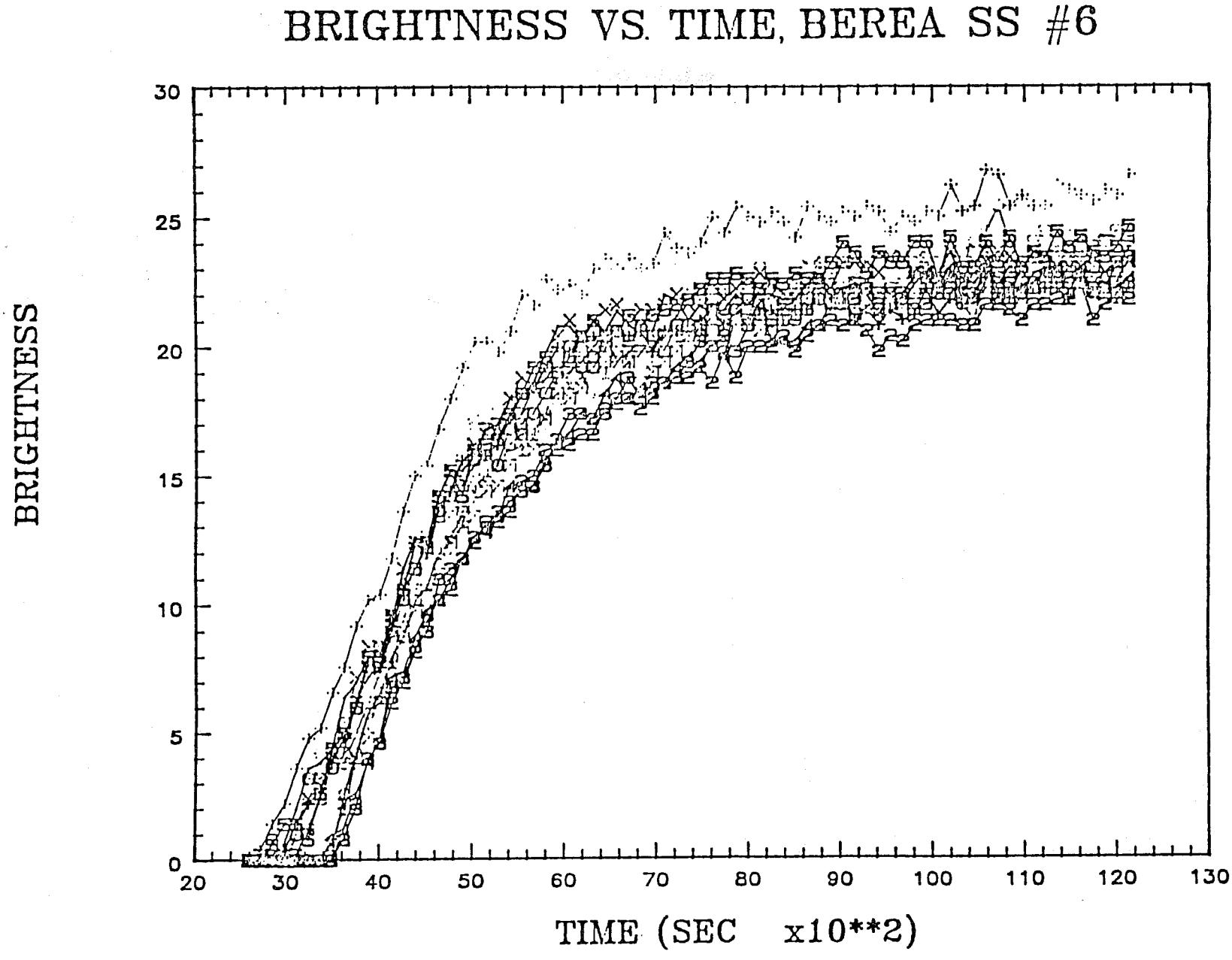

Figure 117. Brightness vs. Time, Berea SS #6: Indicating dye concentration at 20 locations on output face of core.

c. Data Analysis

Local concentration measurements at the output face of a core sample, at a scale larger than the pore level, provide the key to this experimental approach. From the sequence of video images, breakthrough curves for any point within the image frame can be constructed. Distribution of arrival time, average fluid velocity, and estimates of local permeability near the output face are the main results which can be obtained from breakthrough curves at the point of 50% concentration. Stochastic methods could be applied for studying permeability variation in different directions. Mean, variance, and the covariance and variogram of permeability can be estimated to characterize the permeability variation. Autocorrelation functions are very useful for studying spatial distribution of permeability. These functions can be used to derive correlation lengths that characterize the average distance over which neighboring data values are positively correlated. How these parameters can be related to the longitudial dispersion coefficient should be investigated.

The other goal of this project is to study how variability of different stochastic parameters may be related at different scales. This objective might be achieved by conducting another displacement in the same porous media with shorter flow-sample length than in the original experiment. One other aspect that could be studied is the effect of permeability variation in other directions. The experimental technique used here allows examination of the effect of anisotropy on displacement patterns by conducting similar displacement in the other directions on the same porous media.

One of the main objectives of the project is to develop a physical model that takes into account the spatial variation of rock properties. The common problem with most available models of mixing behavior in porous media is that the mixing is described as a function of only one dimension in space. The use of such a model disregards the importance of velocity and concentration variations perpendicular to the average flow direction. Ignoring such variations, however, can hardly be justified by the difficulty of measuring them. We hope that results of the displacement experiments described here will allow the interplay of transverse dispersion with the variation of rock properties to be studied in real rock. Hence, the project goal could be summarized as a challenge to describe the mixing behavior at the laboratory scale by representing rock variability stochastically.

d. Flow Visualization Data Using a CT Scanner

In addition to the results that can be provided by the experimental technique described above, another high-quality source of data was used as input for this study—the results of similar floods observed by CT scanner. Analysis of some of these data will be helpful for comparison and evaluation purposes. Along this direction, one valuable set of data recently was obtained. The scanned image files of an experiment in a sample of Antolini sandstone were graciously provided by the University of Texas at Austin. We are very grateful to Dr. Gary Pope and Dr. Bruce Rouse of the Petroleum Engineering Department for their permission to use this data and for their help in making it available to us for use in this project. The data provided consist of two sets of scanned image files. One set consists of images or "slices" taken at regular intervals along the core, first while the rock was dry, and then after it was saturated with $CaCl_2$ solution. This set provides data for porosity determination. The other set of images were all taken at a single location, and they record a miscible displacement performed in the same core. The following paragraphs concern the details of this data and a preliminary analysis.

In these experiments, a specially designed CT scanner was used to study fluid flow and rock characteristics in the sandstone core sample. The porous medium was an Antolini outcrop sandstone core, 14.1-cm long with a rectangular cross sectional area of 27.44 cm^2 (5.6 x 4.9 cm). The core

permeabilities with air and brine were reported as 357 md and 470 md, respectively. The measured porosity by a material balance method was 11.79%.

The data file of scanned images of the sandstone core sample was provided in a matrix of 256 x 256 picture elements (pixels). The size of the image of the rock is 158 x 138 pixels, which contains the entire cross section of the core (5.6 x 4.9 cm). The individual pixel size is approximately 0.35 x 0.35 mm on the cross section, with a thickness in the longitudial direction of 1.0 mm (slice thickness). Each pixel thus represents a volume containing many pores. The data is considered at a scale larger than the pore scale level.

e. Rock Porosity Measurements

Two sets of scanned images were taken to provide quantitative measurements of porosity. Each set has 12 scan images, which were equally spaced along the core (10 mm apart) beginning 20 mm from the inlet. If they were without error, they could be used to calculate sample porosity at each pixel. The first set consists of the images when the core sample was air-saturated. The other set of images was taken when the core was completely saturated with $CaCl_2$ solution. The images of the cross sections clearly show alternating light and dark regions. The latter (low density) regions indicate higher porosity than other zones of the sample. Preliminary analysis shows that the cross-sectional view of the core sample can be delineated into eight distinct strata. Utilizing apparent boundaries of the individual layers, the arithmetic-averaged porosity of each layer was calculated over the entire length of the system. Figure 118 shows porosity distribution across and over the core length. The average porosity of the cross-sectional slices showed small variability in general except for the first and last sections (labeled #9 in the figure). The first section, which is close to the inlet, showed the lowest porosity while the last section showed the highest porosity value. The average porosity variation of any individual layer is small. The higher porosity layer is about 13% with standard deviation of 2%. The lowest porosity layer is about 11.6% with slightly higher standard deviation. Further studies will be made to study the variation of local porosity within the layers themselves and to correlate it over the entire length.

f. Miscible Displacement Data

Images of the fluid flow pattern also were obtained in the same core during a miscible flood. A single-phase miscible displacement with unit mobility ratio was conducted to study the transport phenomena. Because the CT scanner usually is most sensitive to differences in density, in these experiments $BaCl_2$ (barium chloride) solution was used as the displacing fluid because its density is higher than that of the displaced fluid of $CaCl_2$ (calcium choride) solution. Because of the length of the transition zone, it was supposed that the difference in fluid density would not have a great effect on displacement stability if displacement was performed horizontally, the flow rate was high, and the concentration gradients were fairly low. The flow rate was reported to be 1 cc/min, which is equivalent to a flow velocity of 14 ft/day. A set of 17 scan images, at a fixed position, was taken during the experiment. The observation station was 120 mm from the inlet. The images were taken at different times during the $BaCl_2$-$CaCl_2$ miscible experiment.

Comparison of the images at different times indicates clearly the existence of velocity variations among differnt layers. The flow velocity appeared to be high along the most porous regions, which also were expected to be the most permeable, while the slow flow was along the lowest porosity region. However, this core sample is a good example of stratified flow where clear, stratified permeability layers exist. To quantify the results, local concentrations of the displacing fluid can be

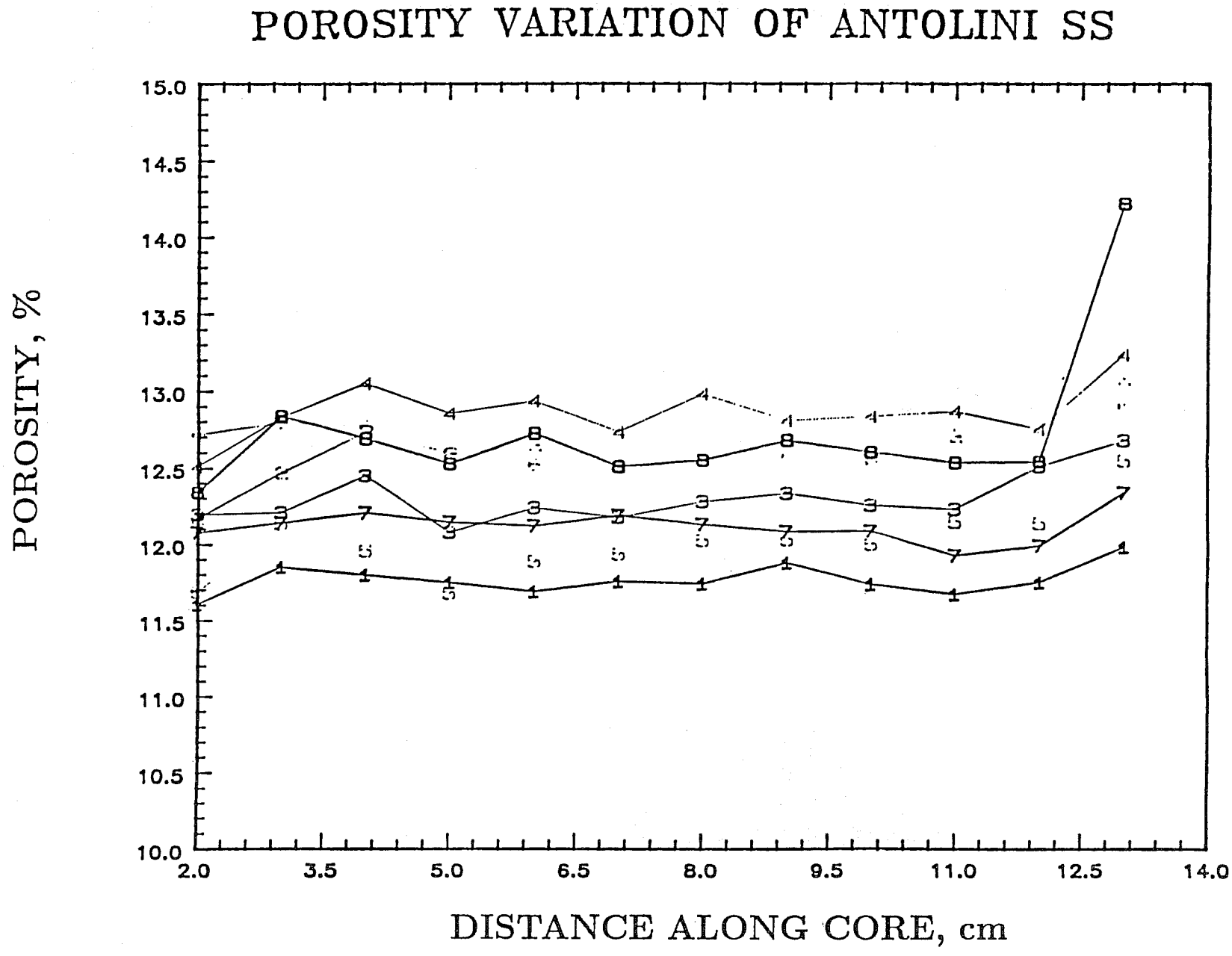

Figure 118. Porosity variation of Antolini SS.

studied in detail, because the arrival time distribution will reflect how the average permeability varies from layer to layer. Estimation of the permeability pattern, along with measurements of the porosity distribution, definitely will give information about the effect of heterogeneity on the displacement performance. The analysis that is being performed at the present time should also demonstrate the influence of transverse dispersion in such a stratified porous system. Details will be given in a subsequent report.

g. Conclusions

The preceding three sections, "Base Case for Well-to-Well Tracers," "Displacement in a Heterogeneous Five-Spot," and "Flow Heterogeneity in Porous Media at Small Scale," describe three subprojects of our work that are concerned with the contribution of rock structure to non-uniform displacement. In some unreported but parallel work on this topic, we also are investigating the applicability of recent geostatistical theories to reservoir problems. A supplementary report on this subject currently is being prepared. In this report we attempt to describe the latest mathematical techniques by which full advantage can be taken of known data, while at the same time avoiding unwarranted over-specification of the reservoir.

As may be discerned from the work that is reported in the sections above, our immediate objectives are three. The first of these is to build up a data base of known cases by which the degree of reservoir heterogeneity can be assessed from the results of conventional tracer tests. In this we have taken only the first step—the next being to perform the same simulations in heterogeneous fields.

Our second immediate objective is to obtain simulation results that are informative of the seriousness of reservoir heterogeneity in terms of production efficiency and scheduling. Our next work on this objective will be to collect more data and to determine through numerical experiments whether the two accepted geostatistical descriptors are sufficient to characterize fully the economic consequences of reservoir heterogeneity.

The third objective of the work above has been to assess the effect of the scale of rock heterogeneity on displacement during miscible or partially miscible floods. This question involves the interaction of diffusion and dispersion with the non-uniformity of the porous medium. It will also, eventually, include the effects of viscous and gravitational forces, and of phase behavior. Our first step is to examine the three-dimensional aspects of first-contact miscible displacement in samples with relatively simple patterns of heterogeneity.

It is hoped that these reports of our research on the above topics may be both useful in the relatively immediate future in the operation of dense-gas floods, and also of general interest in long-term design of reservoir exploitation methods.

C. THE DEVELOPMENT OF DIRECT THICKENERS

1. Summary

In past reports, as in this one, descriptions of this work have been classified into three groups. In brief summary, Method I has dealt with our initial attempts to find conventional polymers which are soluble in CO_2 and which might increase its viscosity sufficiently that frontal instabilities would

be suppressed or greatly reduced during use of this (predominately CO_2) solution as a displacement fluid for oil recovery. Our earlier experimental measurements,[96] on the commercially available polymers had indicated that atactic hydrocarbon polymers would make good candidates for achieving higher solubility in CO_2. Accordingly, we synthesized numerous homo- and copolymers of different α-olefins and obtained their solubility in CO_2 and other nonpolar solvents such as n-butane, n-pentane, etc.[97] Most of these polymers showed some solubility in CO_2 but not enough to considerably increase the viscosity of CO_2. It is well known that the solubility of a polymer in a given solvent decreases with increase in molecular weight. This phenomenon, however, was more pronounced in the case of the polymer-CO_2 system despite the high density of the solvent. We had anticipated that introduction of branching and atacticity in α-olefinic polymers would increase their entropy and result in higher solubility. While our choice of the polymer molecular structure may have helped to achieve entropy increase of the polymer and thus keep its solubility parameter (cohesive energy density)[98] low, the increase in polymer molecular weight certainly would have contributed to raising that parameter, causing lower solubility in CO_2.

According to Hildebrand and Scott,[98] the rule of thumb is that a solution results when the solubility parameters of solute and solvent are matched. In the liquid or liquid-like state, the solubility parameter of CO_2 has a value of approximately 6 δ $(cal/cm^3)^{1/2}$. α-olefinic polymers synthesized in Method I were soluble in solvents such as n-butane (δ = 6.8) and n-pentane (δ = 7.2) but showed no significant solubility in n-propane (δ = 6.3) at comparable solvent densities.[99]

It has become evident that Method I will not succeed in CO_2 viscosification unless polymers of very high molecular weight and very low solubility parameter (δ = 6) are used. Examples of such polymers are polysiloxanes and polytetrafluoroethylenes, the latter being notorious for their insolubility in most solvents. As for polysiloxanes (especially polydimethylsiloxanes), the higher limit on molecular weight for achieving significant CO_2 solubilities remains to be seen. In summary, although Method I polymers did not significantly improve CO_2 viscosity, much has been learned that can be applied to the other methods being pursued.

Rather than seek polymers which will viscosify the solvent in the conventional way, i.e., by virtue of strong interactions between the solute and solvent molecules yielding coil expansions of polymer chains, a second approach has become our principal goal. This new approach is associative viscosification, which occurs as a result of associations between the solute molecules themselves. These interactions could either be ionic or electrostatic, and they would create polymer clusters or transient chains, which can thicken the solution markedly. Furthermore, it is expected that the number of such clusters or chains existing at any given moment should depend on the solute concentration to some power higher than one. We have been synthesizing two types of molecules which we expect to show associative viscosification of dense CO_2 under the general designations, Method II and Method III.

2. Method II Molecules

Method II, in the development of direct thickeners, is the study of Coulombic interactions between relatively low molecular weight polymers, each of which contains only one polar group (or only a very small number of them**). Our work on the synthesis of ion-containing polymers has proceeded well. Initially, synthesized non-ion-containing polymers (α-olefins with a diene monomer component) have shown an increase in solubility over the polymers produced in Method I synthesis

** By test, each polymer contains ten mole percent or less of the polar groups.

(Table 16). This can be attributed to the low molecular weight of the polymers produced by the use of the Friedel-Craft catalyst system $AlCl_3$-2 butanone that has produced polymers with lower molecular weights. The unsaturated polymers produced by this method have been sulfonated and neutralized by the procedure outlined by Makowski et al.[100] to produce the ionomers.

A variety of copolymers and terpolymers, each containing a diene monomer component, were synthesized and are listed in Table 17. The presence of unsaturation in the polymers was confirmed by the presence of a peak at 1640 cm^{-1} in the infrared spectra of Makowski et al., as shown in Fig. 119. This unsaturation was used as a reaction site for sulfonation, followed by neutralization of the sulfonated polymer to yield the desired ionomer. Unfortunately, the extraction yields of the ionomer were not as high as expected. The problem was attributed to the thermal and oxidative degradation of the ionomer. Also, solubility preference of the ionomer with the reaction solvents may contribute to the low yields. New separation techniques (to remove the ionomer more completely and rapidly from the reaction solvents) are being tested now to overcome this problem. Initial viscosity tests have been completed with polymer sample P119*N, and these tests are shown in Fig. 120. The increase in CO_2 viscosity was minimal and has not reached the critical concentration at which a rapid thickening effect can be seen, as in the case of Method III polymers. Our current hypothesis is that this feature of the graph is related to the difficulty in extracting the ionomer cited earlier. The deficiency of neutralized polymers would result in a low degree of the association that is responsible for the thickening characteristic. When the ionomer extraction technique has been corrected, it is expected that viscosity effects will be achieved that are similar to those seen in the Method III polymers.

Further insight for maximizing solubility and viscosity properties of these polymers in CO_2 will be studied. Reaction kinetics will be investigated with the aid of a new HP 5890A Gas Chromatograph. Optimal conditions for ionomer synthesis will be found, and the polymer composition will be determined.

Also completed this year was the design and construction of a high-pressure capillary tube viscometer for dense gases and solutions. A schematic of this device is shown in Fig. 121. We expect that it will be easier to operate and calibrate than is the falling cylinder method. Once calibrated for capillary tube dimensions, this new instrument will provide absolute viscosity data rather than the relative viscosity values. As before, both CO_2 and light hydrocarbons can be used as solvents at a variety of pressures and temperatures. The apparatus is being calibrated now and data for the thickeners will be available soon.

3. Method III Molecules

In Method III, the work of the last year has been concerned with several new organotin fluoride compounds. This work, and some of that done previously, has been documented by three papers, "Associative Organotin Polymers-1," "Associative Organotin Polymers-2" (the material in these two papers report some of the findings that appeared in Craig Taylor's 1987 master's thesis),[101] and "Associative Organotin Polymers-5," (which includes some of the results being published in Pradeep Singh's master's thesis).[102] These papers, Dandge et al.,[103,104,105] have been accepted for publication in various chemical journals and are expected to appear in 1989. Most of the latter work was described in the three previous quarterly reports and is summarized below.

Certain triorganotin fluorides are known to be effective viscosifiers for nonpolar solvents. Dunn and Oldfield[106] studied the solution properties of tri-n-butyltin fluoride (BUF) in various organic solvents. They reported that, among n-alkanes, BUF dissolves only in n-hexane and not in n-

TABLE 16

COMPARISON OF INTRINSIC VISCOSITY AND SOLUBILITY OF METHOD I AND METHOD II POLYMERS

Polymer No.	Method	Intrinsic Viscosity [n] dl/g	Solubility in CO_2 2500 psi, g/l
94Ia	I	3.62	.38
87Ia	I	2.74	.88
94Ib	I	1.24	1.12
111	II	.138	5.12
120	II	.0450	10.63
112	II	.190	14.50

Intrinsic viscosities used n-hexane as solvent.
Method I polymer solubilities were measured at 32°C.
Method II polymer solubilities were measured at 25°C.

TABLE 17

METHOD II POLYMER SYNTHESIS

Polymer No.	Monomers	Initial Monomer Mole Percentage	Intrinsic Viscosities [n], 25°C, dl/g
111	H, D, ENB	47.5, 47.5, 5	.1379
119	D, ENB	90, 10	.0599
119S	D, ENB	90, 10	.0384
119*N	D, ENB	90, 10	.1191
120	H, ENB	90, 10	.0450
120N	H, ENB	90, 10	.0633
155	H, D, ENB	45, 45, 10	.0366
158	H, D, ENB	25, 25, 50	.0424

H: 1-hexene
D: 1-decene
ENB: 5-ethylidene-2-norbornene
S: sulfonated polymer
N: neutralized polymer, ionomer

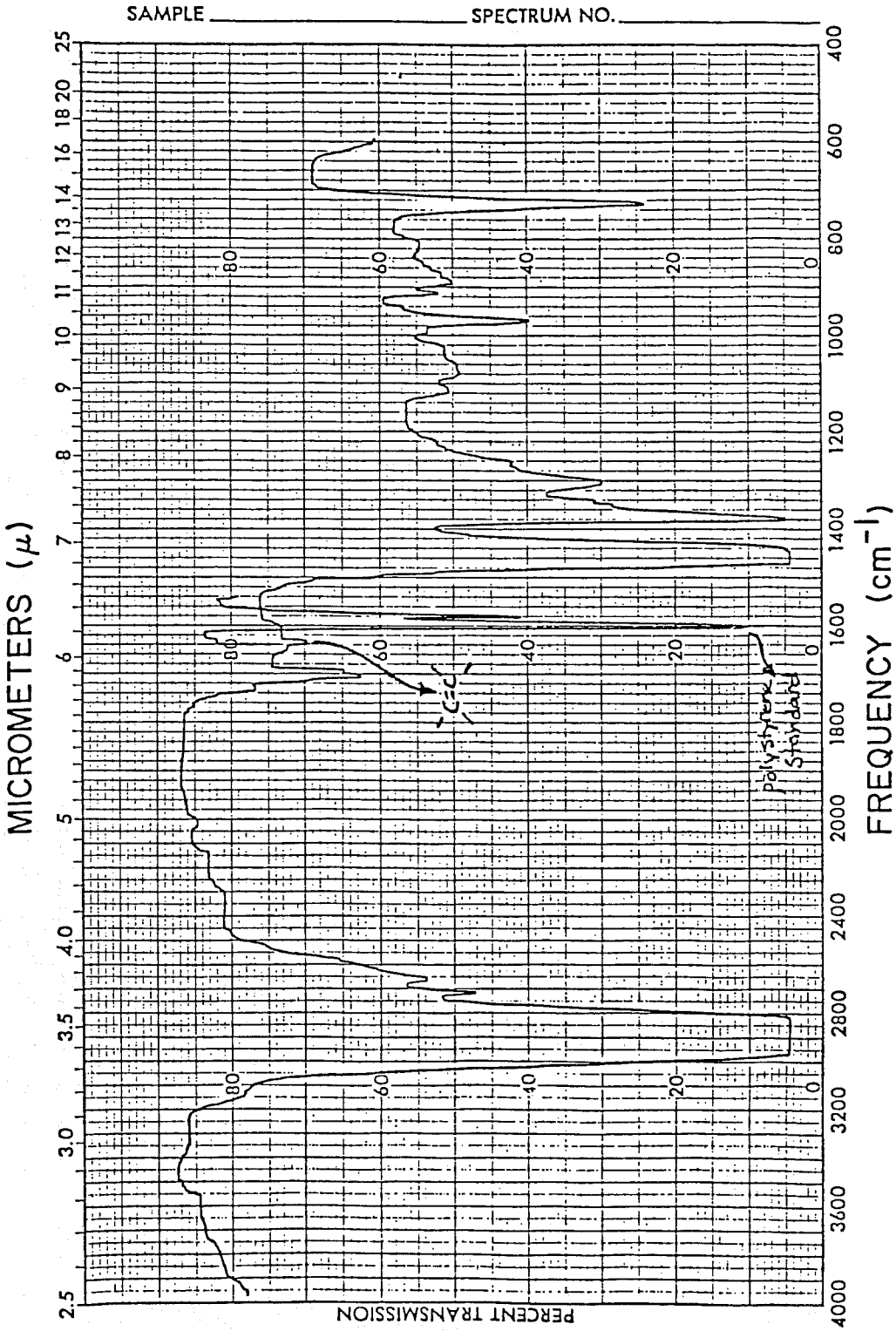

Figure 119. IR spectrum of 1-hexene, 1-decene, and 5-ethylidene-2-norbornene terpolymer.

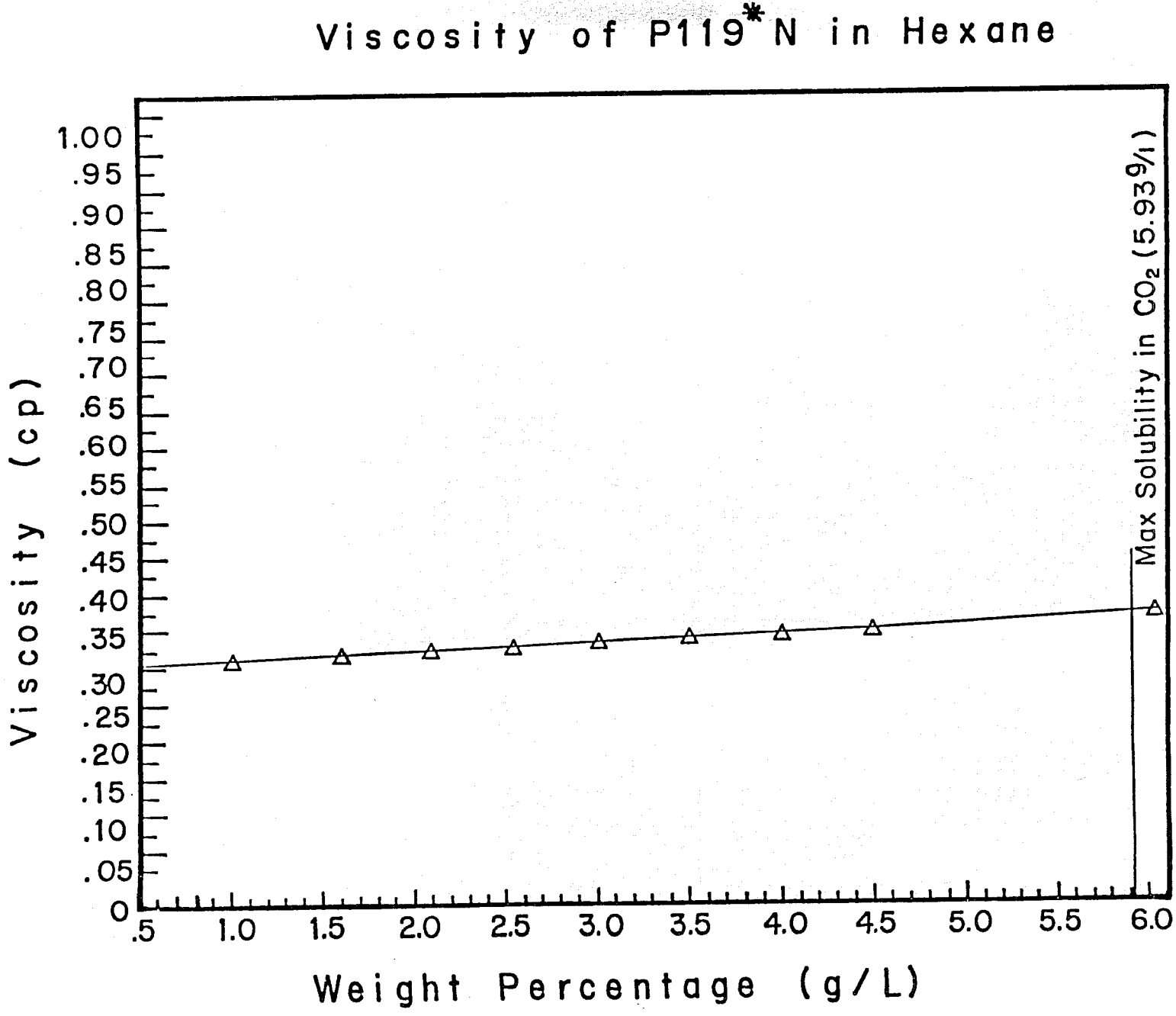

Figure 120. Viscosity of P119*n in hexane.

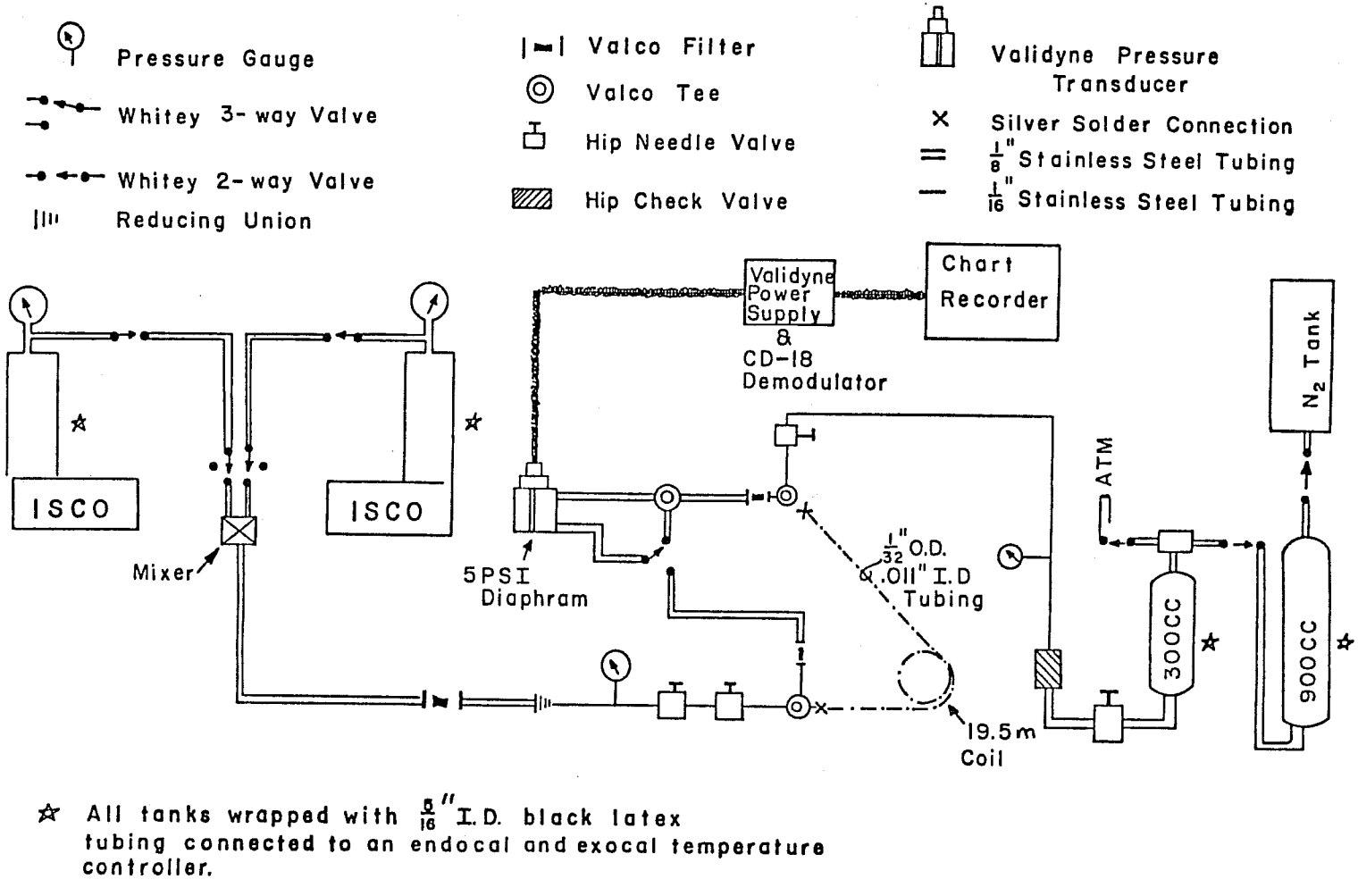

Figure 121. High pressure capillary viscometer.

heptane. This intriguing solubility behavior was attributed to the matching size of solvent molecules with those of the solute. Dandge et al.[104] and Taylor,[101] however, found that increasing the alkyl chain beyond C_4 in alkyltin fluorides (R_3SnF) substantially increases their solubility in most organic solvents. Furthermore, viscosification of nonpolar solvents by these trialkyltin fluorides (which ranged from triamyl to tridecyltin fluoride) was as effective as that by BUF or even better. Due to the large difference in the electronegativity of Sn and F atoms, R_3SnF-type compounds form polymeric chains[106] by association wherein Sn assumes a penta-coordinate structure:

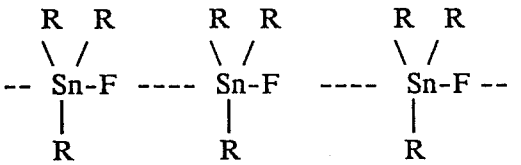

These transient polymeric chains resulting from dipole-dipole interactions are responsible for the increase in solvent viscosity which is asymptotic above a certain concentration. The structure dependence of both solubility and viscosity in triorganotin compounds is known. For example, trimethyl and tripropyltin fluorides are insoluble in most organic solvents while the bulky trineophyltin fluoride[107] dissolves in many solvents but does not increase their viscosity.

Our previous work showed that while increasing the alkyl chain in R_3SnF-type compounds increases both their solubility and viscosity in hydrocarbons such as propane (d = 0.5 g/cc) and butane (d = 0.5 g/cc),[108] their solubility in CO_2 did not show a considerable increase. Also, in a separate study,[96] it had been observed that silicon-containing polymers are more soluble in dense CO_2 than any other polymer of similar molecular weight. Taking these observations into consideration, we decided to synthesize silicon-substituted trialkyltin fluorides in order to increase the solubility of these associative compounds in CO_2. The field applicability of such viscosifiers, it is found, would depend on the price of oil. R_3SnF compounds with long-chain R groups are nontoxic and offer little risk to the environment.

Tris(trimethylsilylpropyl)tin fluoride (PTF) and tris(trimethylsilylmethyl)tin fluoride (MTF) were synthesized according to scheme A (Fig. 122), while scheme B was followed in the synthesis of dibutyl-(trimethylsilylpropyl)tin fluoride (BTF). MTF has been reported by Seyferth;[109] however, it was synthesized so that its solution properties could be compared with those of the other two novel compounds. The steps involved in these syntheses were straight forward and thus need no elaboration. In the synthesis of BTF, the unsymmetrical triorganotin fluoride, bromination of tetraorganotin compound resulted in the preferential displacement of the trimethylsilylpropyl group. Similar observations were reported by Seyferth.

The X-ray diffraction patterns for MTF, PTF, and BTF display an important difference in their structures. The unsymmetrical BTF shows broad dispersed peaks indicating an increase in amorphousness compared to MTF, its symmetrical analogue. The peaks in the pattern for PTF, on the other hand, are broader and less sharp than those for MTF, which may be the result of an increase in the alkyl chain length by two carbon atoms. (See Dandge[105] for x-ray diffraction spectra.)

Fourier transform infrared spectra of the three fluorides also were examined. Typical frequencies of the peaks found in the region of 450 cm^{-1} to 1300 cm^{-1} and their assignments are as follows:

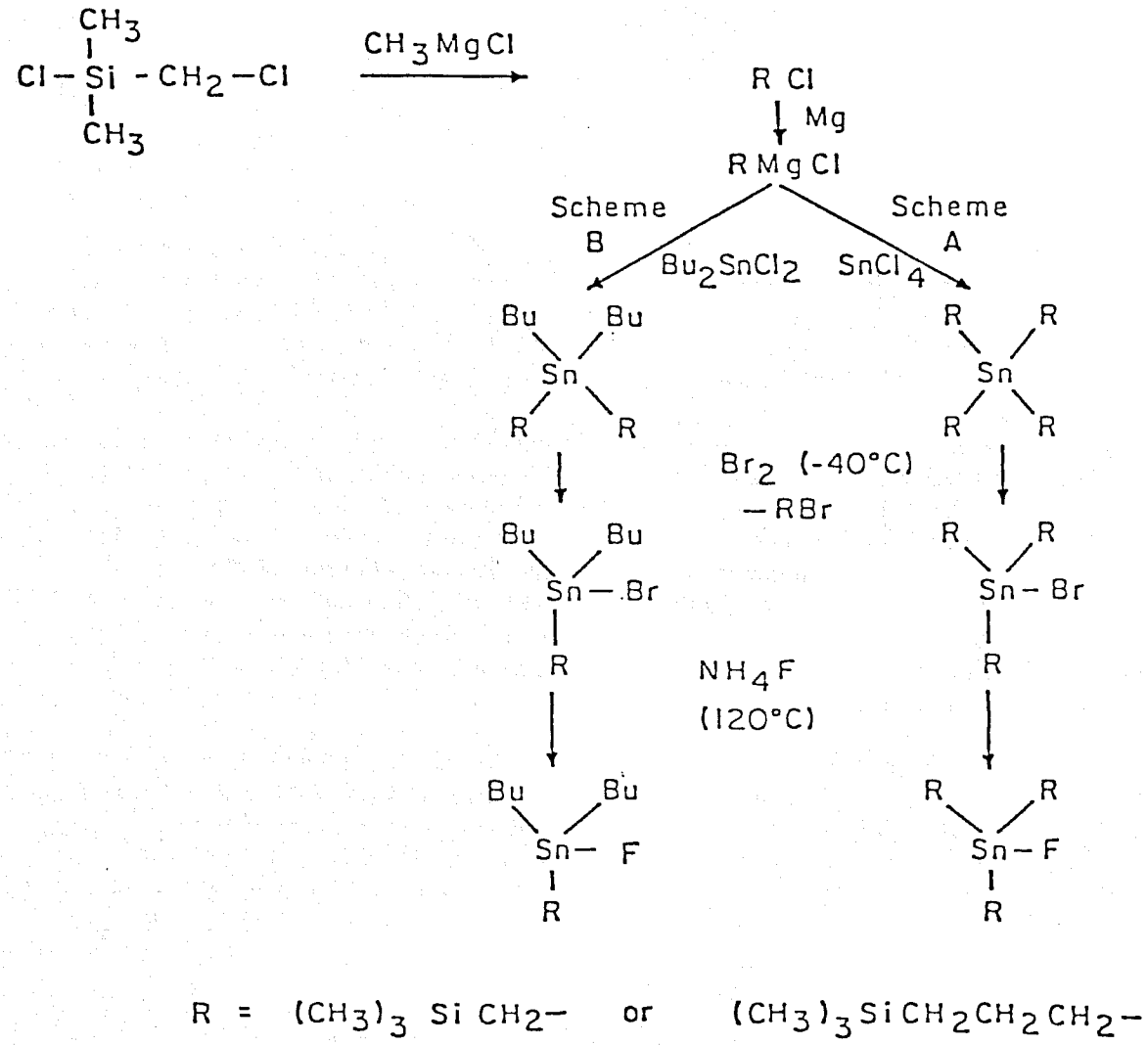

Figure 122. Synthesis of silylated organotin fluorides.

525 cm^{-1}	Sn-C Stretch
615 cm^{-1}	Sn-C Stretch
690 cm^{-1}	$-CH_2$ Stretch
712 cm^{-1}	$-CH_2$ Stretch
755 cm^{-1}	Nujol
840 cm^{-1}	Si-C Stretch
860 cm^{-1}	$(CH_3)_3$ Si Stretch
1250 cm^{-1}	Si - CH_3

Due to the unavailability of appropriate cells, the Sn-F absorptions in the far infrared region could not be studied.

The ^1H and ^{13}C nuclear magnetic resonance spectra of the three fluorides also were analyzed, and these spectra yielded confirmatory information as to the structure of the three compounds. The peak assignments for various groups in each compound match the chemical shifts characteristic of the different environments surrounding the protons or ^{13}C nuclei, and were verified by close correspondence of the calculated and observed peak ratio values. (See Dandge[105] for ^{13}C spectra of the fluorides.)

The solubilities of MTF, PTF, and BTF in various organic solvents including CO_2 are given in Table 18. The solvents are arranged in the order of increasing solubility parameters. It has been observed, after a comparative study with tri-n-alkyltin fluorides, that replacement of a methyl group by a trimethylsilyl group enhanced the solubility in nonpolar solvents, and this is well reflected in the markedly higher solubility of MTF, PTF, and BTF in CO_2. For example, tri-n-alkyltin fluorides dissolve to an extent of 1.26 gm/liter, whereas compounds having a trimethylsilyl group with the appropriate number of CH_2- groups dissolved to an extent of 4.5 gm/liter (see Table 18).

The rate of dissolution of PTF and BTF in nonpolar solvents is considerably higher than that of tri-n-alkyltin fluorides. The former dissolve instantly while the latter dissolve only by a slow swelling process. This indicates that the presence of the trimethylsilyl group, at the end of the chain and somewhat away from the Sn-F bond, imparts higher solubility as well as higher dissolution rates to triorganotin fluorides.

As a result of the transient polymer formation, the solutions of triorganotin fluorides in nonpolar solvents exhibit nonlinear concentration vs. viscosity curves. The concentration at which a steep rise in this curve begins has been termed as the critical or threshold concentration.[101,103,104] Figure 123 shows such typical curves for PTF and BTF in n-hexane. Despite the fact that different shear rates are involved in capillary viscometry, it can be said qualitatively that at a given concentration, PTF viscosified n-hexane better than BTF. It is clear from Fig. 123 that the critical concentration for these two compounds is above 0.7%, while analogous tri-n-alkyltin fluorides showed a critical concentration of less than 0.4%. This may be due to the presence of bulky Me_3Si-groups nearer to the Sn-F bond, which causes some steric hindrance to auto-association.

These results suggest that the solubility of trialkyltin fluorides in nonpolar solvents is increased considerably by the introduction of a trimethylsilyl group at the end of the chain. However, this increase in solubility decreases the ability of trialkyltin fluorides to viscosify these solvents.

Figure 124 shows the viscosity vs. concentration curves for PTF in various organic solvents. As would be expected, the viscosity was the lowest at any given concentration in toluene, the most polar among the four solvents. Figure 125 shows the effect of concentration on the viscosity in CO_2 at 25°C. The observed 50% increase in viscosity is not sufficient for enhanced oil recovery operations.

TABLE 18

SOLUBILITIES OF SILICON-CONTAINING TRIORGANOTIN FLUORIDES AT 25°C

Solvent	Solvent Solubility Parameter (cal/cm^3)[67,110]	Dipole Moment D[111]	Dielectric Constant (ϵ)[111]	Solvent Viscosity[111] CP	MTF[102]	PTF[102]	BTF[102]
carbon dioxide*	6.0	0	1.60	0.07		4.46§	4.14§
ethane*	6.0	0		0.16			
propane*	6.4	0.084	1.61	0.22 (25°C)			
butane	6.8	0.05		0.27	0	X+	X+
pentane	7.0	0	1.84	0.4	0	X+	X+
hexane	7.3	0.08	1.89 (25°C)	0.4	X	X+	X+
heptane	7.4	0	1.92 (20°C)	0.6	0	X+	X+
decane	8.0	0	1.99	1.26			
cyclohexane	8.2	0	2.02	1.3 (17°C)	X		
carbon tetrachloride	8.6	0	2.24	0.5	X	X+	X+
toluene	8.9	0.36	2.38	0.6 (30°C)	X+	X+	X+
benzene	9.2	0	2.275	0.7	X	X+	X+
chloroform	9.3	1.0	4.80	0.3	X	X+	X+

§ - in g/l
0 - insoluble
X - solubility at least 0.2 g/dl
X+ - solubility >> 0.4%

*Conditions used for solubility determinations

	Pressure PSI	Temp. °C
CO_2:	2500	25
ethane:	1200	25
propane:	1200	25

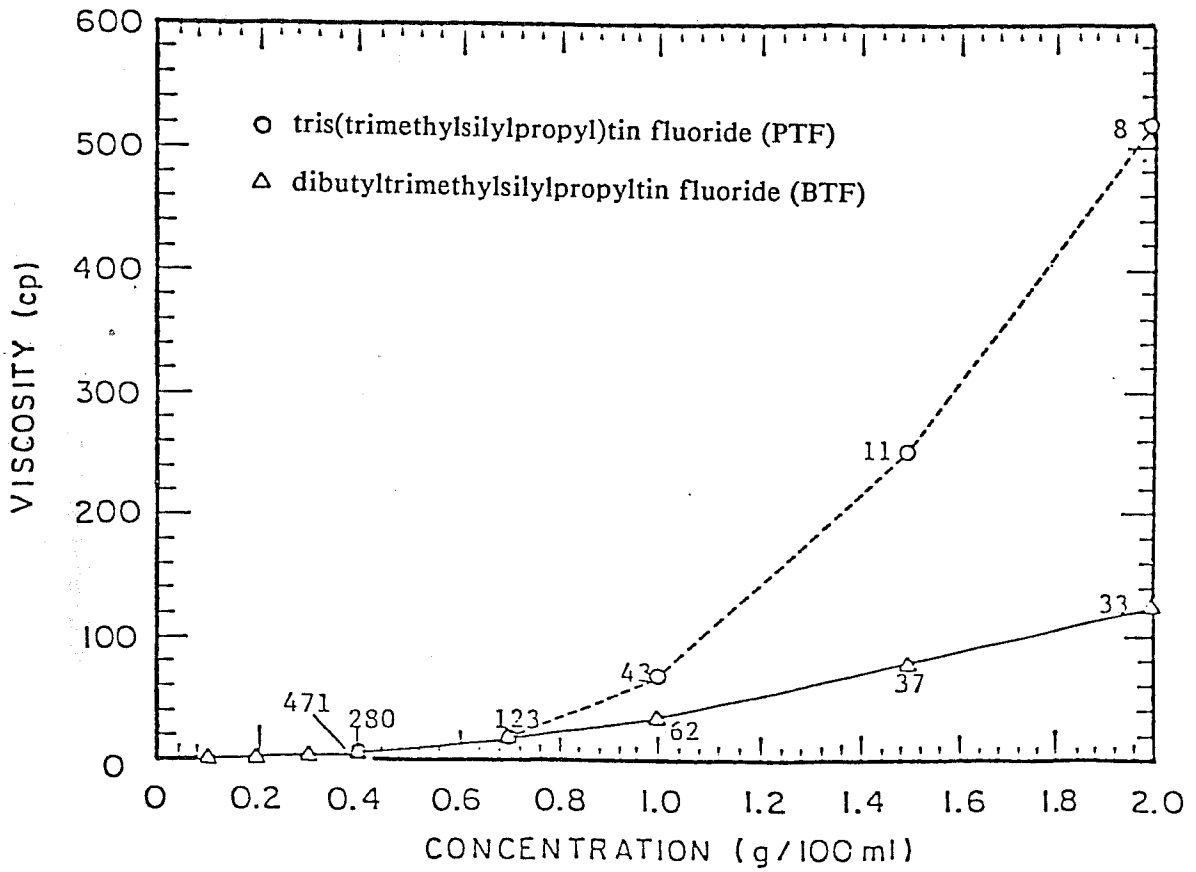

Figure 123. Viscosity as a function of concentration for tris(trimethylsilylpropyl)tin fluoride and dibutyltrimethylsilylpropyltin fluoride. Solvent—n-hexane, temperature—25°C. (Number near each data point indicates approximate shear rate at the wall.)

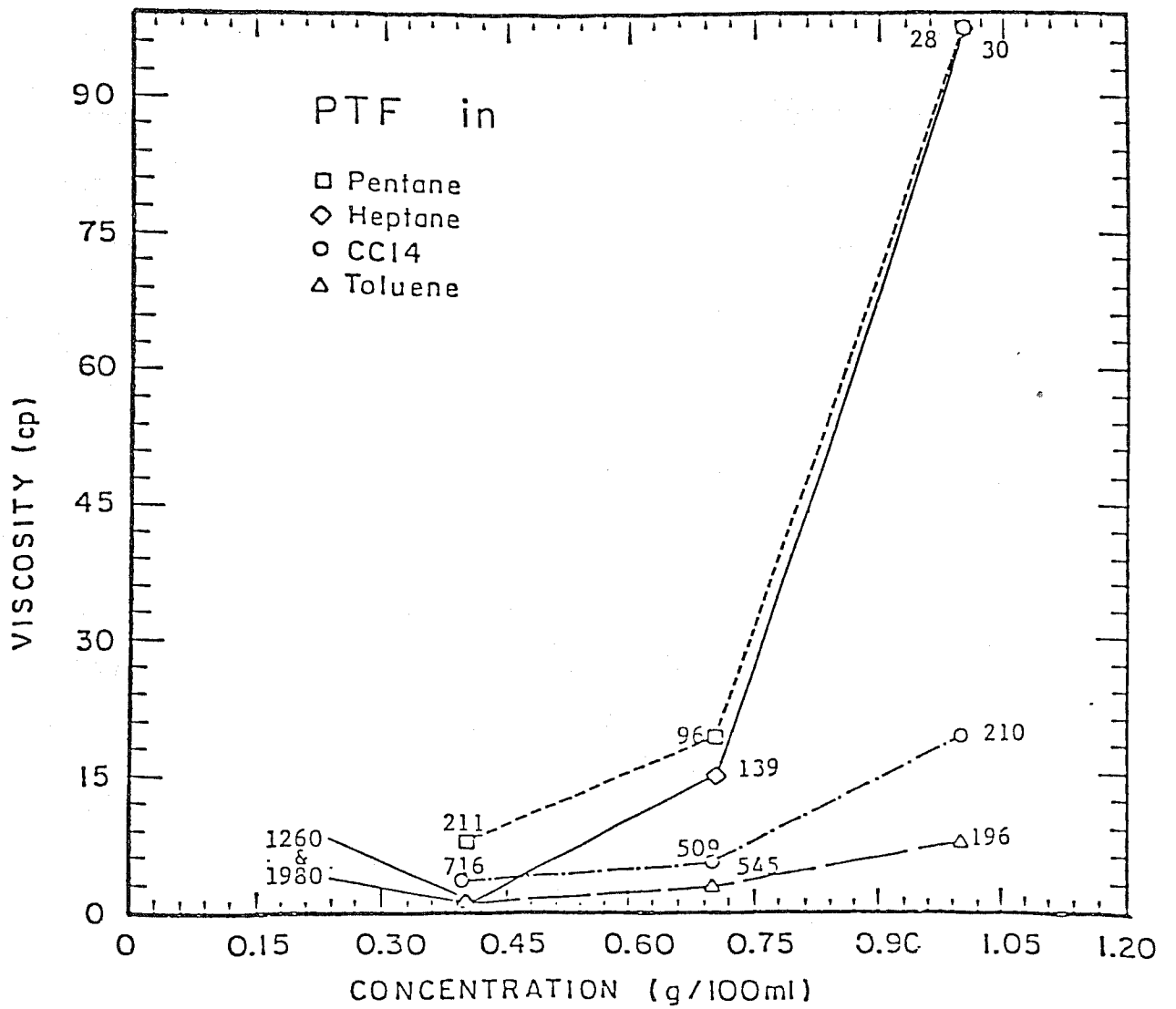

Figure 124. Viscosity vs. concentration curves for tris(trimethylsilylpropyl)tin fluoride in various solvents at 25°C. Number near each data point indicates approximate shear rate at the wall.

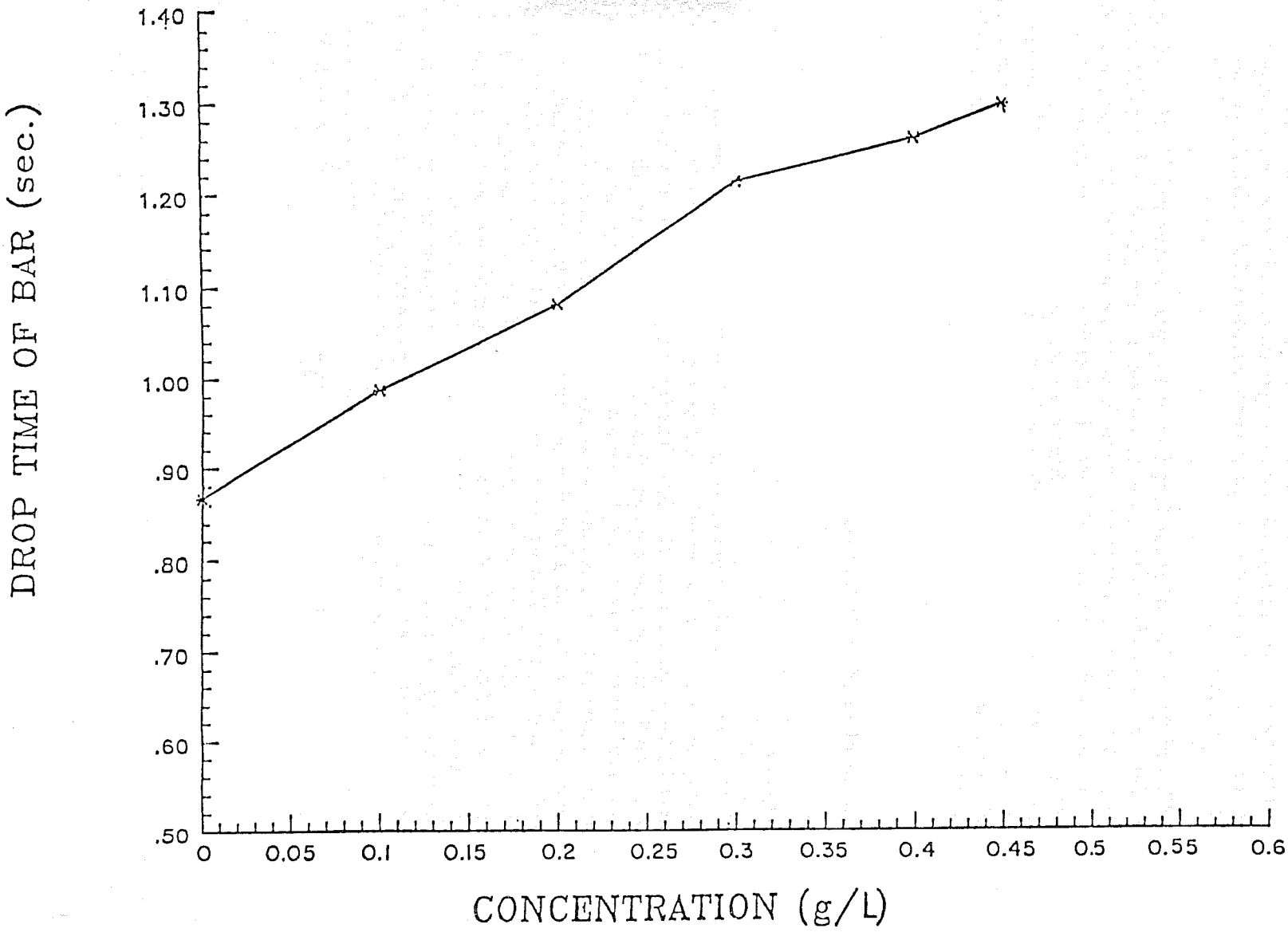

Figure 125. Viscosity of solutions of PTF in carbon dioxide.

The viscosity vs. shear rate data for PTF and BTF (Fig. 126a and Fig. 126b) were obtained in n-heptane solution at 25°C using a Contraves low-shear-rate instrument. n-Heptane was used as a nonpolar solvent because it has a high enough boiling point to avoid losses due to evaporation during the measurement period. The curves presented here are reproducible in both directions of shear and are thus time-independent.

In summary of the Method III research performed this year, synthesis of novel silicon-containing triorganotin fluorides was accomplished. It was shown that the introduction of a trimethylsilyl group on the alkyl chain considerably enhances the solubility of trialkyltin fluorides. However, if the bulky trimethylsilyl group is closer to the Sn-F bond, the effectiveness of such compounds in enhancing solvent viscosity is adversely affected. Higher solubilities in CO_2 were achieved, but the viscosification of CO_2 at the highest solubility (0.4%) was only 50%. Additional viscosity measurements will be made of the other two compounds described above. Further modifications in the molecular structure of these compounds might increase both their solubility and the viscosity of their CO_2 solutions as well.

D. CO_2-FOAM MOBILITY CONTROL

1. Overview

The CO_2-foam mobility control study encompasses CO_2-foam mobility measurements, dynamic surfactant adsorption experiments, and studies of physical properties of surface active agents, especially those used in foam flooding. The focus of these topics is a series of measurements of CO_2-foam mobility at high pressure and of dynamic surfactant adsorption using different rock types and permeabilities. The report is divided into four subsections. The first subsection summarizes the experimental results obtained in CO_2-foam mobility measurements. The mobility measurements are carried out as a function of Darcy's velocity. They include the effects of surfactant concentration, CO_2-flowing foam fraction, and rock sample permeability. The second subsection reports the data obtained in dynamic adsorption of surfactant through porous rocks. This experiment was carried out as a function of concentration at different flow rates. Berea and Rock Creek sandstones and Baker dolomite were employed to investigate the adsorption of surfactant within the porous rocks. The third subsection describes the high-temperature CO_2-foam mobility measurements. The design and construction of the experimental apparatus used to obtain these measurements will be discussed in detail along with some modification of the apparatus. The modification included a photosensor to distinguish between CO_2 and aqueous surfactant solution flows from the core sample. This additional means of observation will help to study the flow of foam through a porous medium, giving information especially on the population of the lamellae, which appear to be of primary importance in determining mobility reduction. The fourth and last subsection will discuss plans for future work in CO_2-foam mobility control. Future studies will involve more experiments in both CO_2-foam mobility and dynamic adsorption measurements using rocks from producing wells in actual oil reservoirs. In addition, CO_2-foam mobility measurements at high temperature will be performed. A further project being considered is the design and construction of a high-pressure foam height measurement device. The function of this device will be to assess directly the durability of foam lamellae between dense CO_2 and surfactant solution at room temperature and higher.

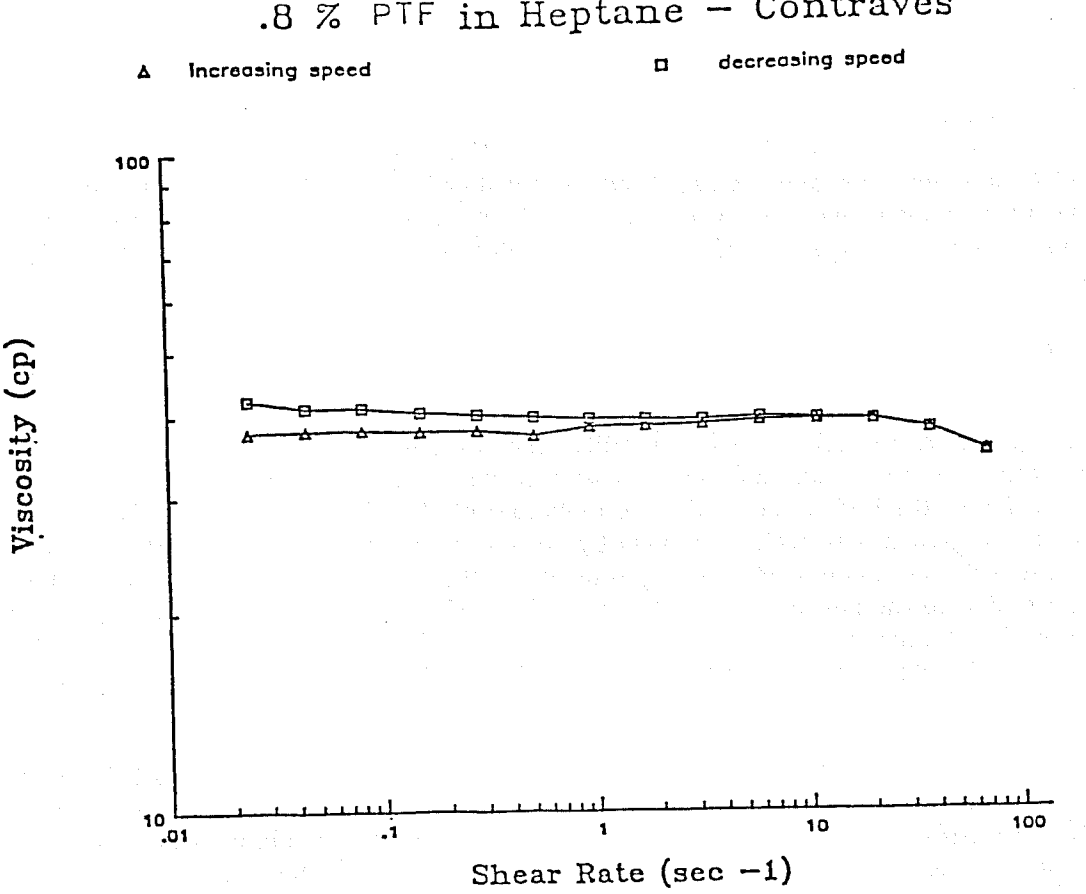

Figure 126a. Viscosity vs. shear rate plot of PTF.

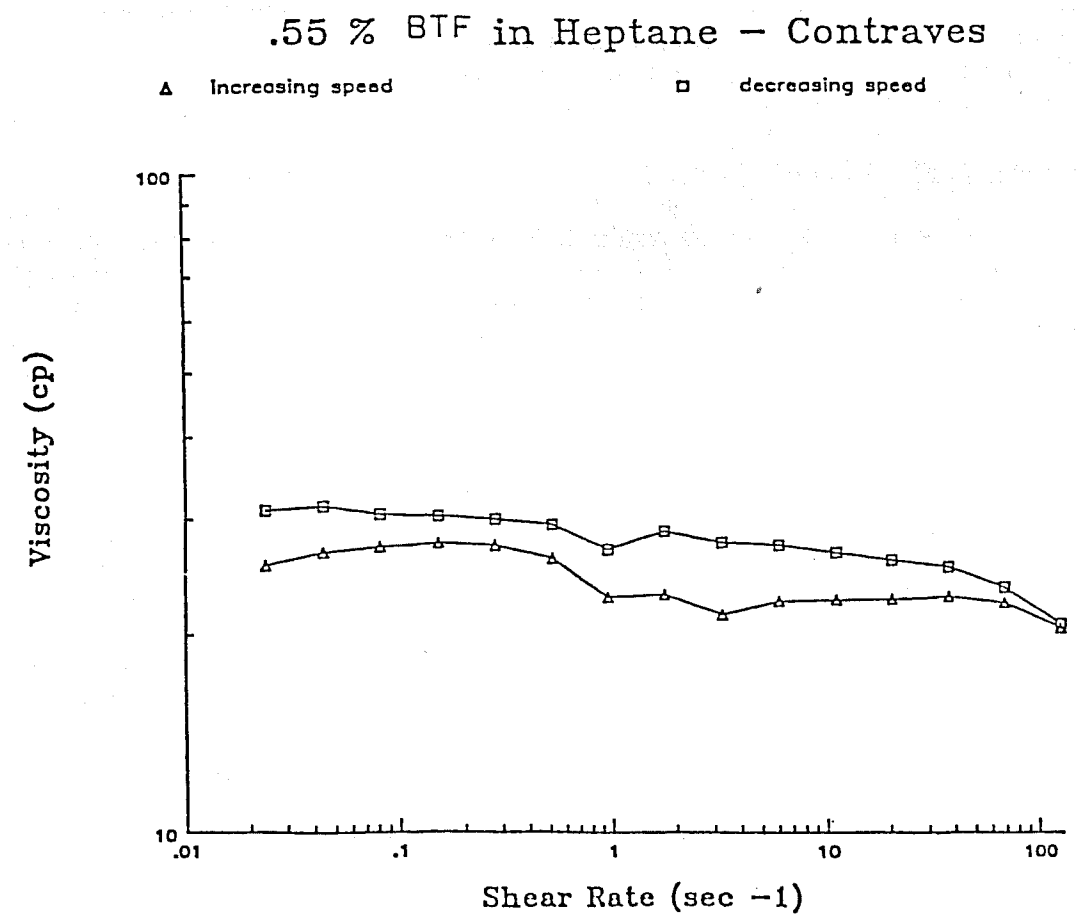

Figure 126b. Viscosity vs. shear rate plot of BTF.

2. Introduction

CO_2 flooding is a promising enhanced oil recovery technique with the capability of miscible displacement with many types of crude oil, if the CO_2 exists as a dense enough fluid at reservoir conditions. However, the use of dense CO_2 by itself as a displacing fluid may well be inadequate to meet this promise because of its low viscosity. The difference in viscosities between dense CO_2 and the crude oil enables the growth of viscous fingering, which causes early breakthrough and can result in inefficient oil displacement. In addition, this unfavorable mobility ratio accentuates flow non-uniformities due to permeability stratification or other heterogeneities. This crucial problem can be solved by injecting an aqueous solution of foaming agent with the dense CO_2 to produce lamellae within the pores. A reduction in CO_2 mobility results from the presence of these lamellae in the porous medium. Such a reduction in mobility leads to much more uniform displacement of the crude oil. In addition to the benefit derived from reduction of the displacement fluid mobility, another advantage of CO_2-foam has been confirmed by our experiments. This is the fact that, because the mobility reduction is greater in more permeable rock, one can expect that the non-uniform displacement due to the permeability heterogeneities will be lessened. Consequently, this process should result in a higher volumetric sweep efficiency. For the production of these lamellae, a much lower volume of surfactant solution than of dense CO_2 is required.

In addition to the need for a surfactant to form durable lamellae with dense CO_2 at reservoir conditions, and thus for it to be suitable for mobility control in this way, a successful foamant must not be adsorbed too strongly during flow of the foam through the reservoir rock. The major concern in this dynamic adsorption process is that the permanent adsorption should not be excessive. Because of its amphipatic nature, the surfactant has the property of adsorbing onto all of the surfaces or interfaces of the system. Hence, some losses onto the rock are inevitable. The magnitude of the adsorption is evaluated in dynamic adsorption experiments that are described below. In spite of these surfactant losses by adsorption, CO_2-foam flooding appears to be a promising method for improving oil recovery. In the work reported here, we believe we are taking the proper steps to solve and understand the nature of the existing problems.

3. CO_2-Foam Mobility Measurements

In this section are presented the results of laboratory measurements of CO_2-foam mobility at high pressure, along with descriptions of the experimental procedure, the apparatus, and the evaluation of the mobility. The order in which the mobility results are shown illustrates the effects of surfactant concentration, of CO_2-foam fraction, and of rock permeability. The preparation of the surfactant solution is briefly mentioned in the "Effect of Surfactant Concentrations" section. An anionic surfactant, Enordet X2001 from Shell, was used in these measurements.

a. Experimental

A simplified representation of the basic elements of the flow system is shown in Fig. 127. The CO_2 flows through the capillary tube, the pressure drop across which is measured by a Validyne differential pressure transducer. An Isco pump is used to pressurize the brine/surfactant solution which, along with the CO_2, flows through the foam generator and the core. The foams are generated inside the short core used as a foam generator, where the mixing between CO_2 and the surfactant solution occurs. The mixed CO_2-foam flows through the core. The pressure drop across the core is recorded by a second Validyne differential pressure transducer. Two fine, tapered needle valves in series are used to regulate the output flow rate of the mixture of the surfactant solution and dense CO_2. In addition to the digital readout of the values of the pressure drop across the capillary and

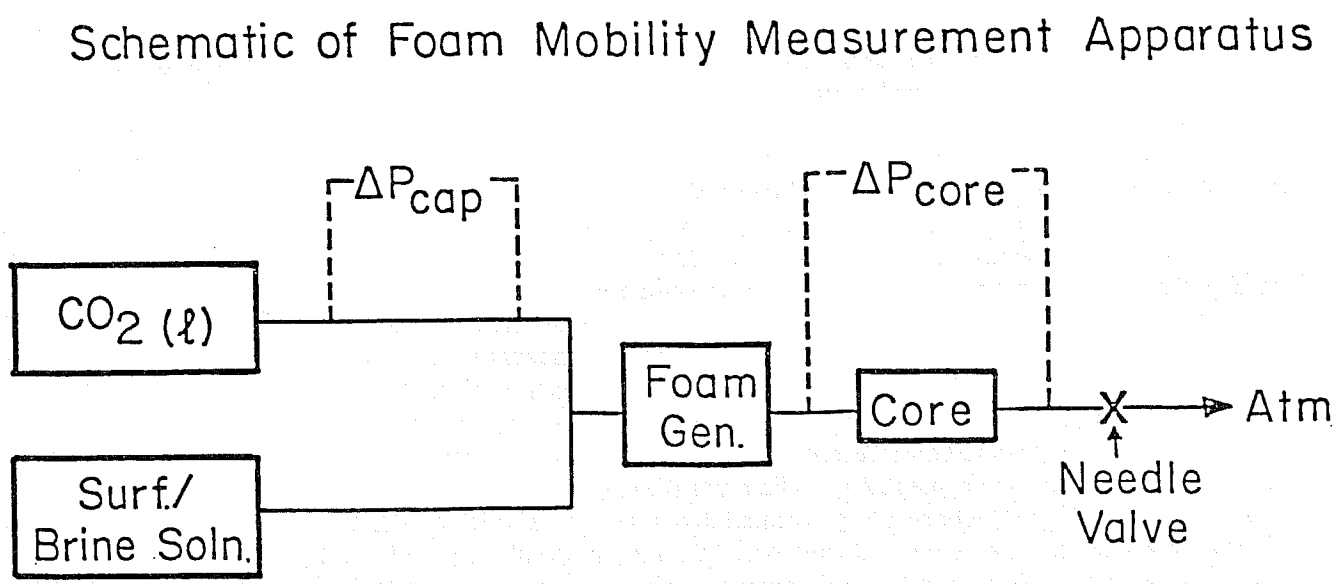

Figure 127. Schematic of foam mobility measurement apparatus.

across the core, a two-pen analog recorder is used to record these simultaneous measurements. Both of these measurements are subject to rapid short-term variations of fairly small magnitude that seem to be indicative of the mechanism of foam flow. All calculations were performed with steady-state values that were averaged over these short-term variations. In this experiment, the measured variables are ΔP_{cap} and ΔP_{core}. Knowing the ΔP_{cap}, the flow rate of pure CO_2 into the core is computed by using a calibration constant obtained by measuring the flow of dense CO_2 through the capillary tube. The setting of the Isco pump gives the flow rate of the aqueous surfactant solution, and the total flow rate is simply the sum of these two. From the total flow rate and the ΔP_{core}, the mobility, λ, can be evaluated from:

$$\lambda = \frac{Q/A}{\Delta P/L} \tag{70}$$

where

Q is the total flow rate in cc/sec,
A is the cross-sectional area of the rock sample in cm^2,
L is the length of the rock sample in cm,
ΔP_{core} is the pressure drop across the rock sample in standard atmospheres, and
λ is the mobility in cm^2/(atm-sec) or Darcy/cp.

b. The Effect of Surfactant Concentration

The effect of surfactant concentration on CO_2-foam mobility is plotted on a log-log scale in Fig. 128. The presented data points are the average mobility values obtained from a superficial velocity range of 1-10 ft/day, with the CO_2-foam fraction kept constant around 80%. This log-log plot is a direct comparison of the effect of surfactant concentrations among the three rocks. Baker dolomite is a quarried carbonate rock of uniform texture with microscopic vugs distributed throughout. Rock Creek and Berea are classified as sandstones, with different chemical compositions of the non-silica portion and different pore-size distributions. Among these rock samples, the Baker dolomite has the lowest permeability. The measured average permeability of the Baker dolomite with 1% brine was 6.09 md, whereas the permeabilities of the samples of the Rock Creek sandstone and of the Berea sandstone were 11.1 md and 302 md, respectively. The single-phase permeability measurements were obtained using 1% brine solution. The surfactant solution was prepared in 1% brine solution. For each mobility measurement with a sample rock, the initial surfactant concentration was determined on the basis of interfacial tension (IFT) measurements. The IFT's were measured with a Rosano surface tensiometer, which uses the Wihelmy plate method. The measurements of IFT were performed at laboratory temperature and atmospheric pressure against isooctane to simulate dense CO_2. The initial concentration was chosen to be near the CMC (critical micelle concentration), and the subsequent concentrations were increased from just above CMC to well above CMC.

The sequence of mobility measurements was conducted from low to high concentrations. Each time the concentration was increased in preparation for a new series of measurements, sufficient pore volume of new surfactant concentration was flowed through the rock to establish equilibrium conditions. The results in Fig. 128 show that the mobility is reduced nonlinearly as the surfactant concentration increases from the CMC to well above the CMC. Also, the magnitude of the mobility reduction decreased with the increase in concentration. It seems that as the surfactant concentration is increased from 10 to 20 times of the CMC of Enordet X2001, the mobility reduction is relatively small. Consequently, only an insignificant reduction in mobility is achieved by increasing the concentration from 0.5% to 1.0% for Rock Creek sandstone. A similar trend is anticipated to become evident with Berea sandstone and Baker dolomite after those sequences of measurements are completed. Hence, the overall outcome suggests that a plateau of lowered mobility can be reached

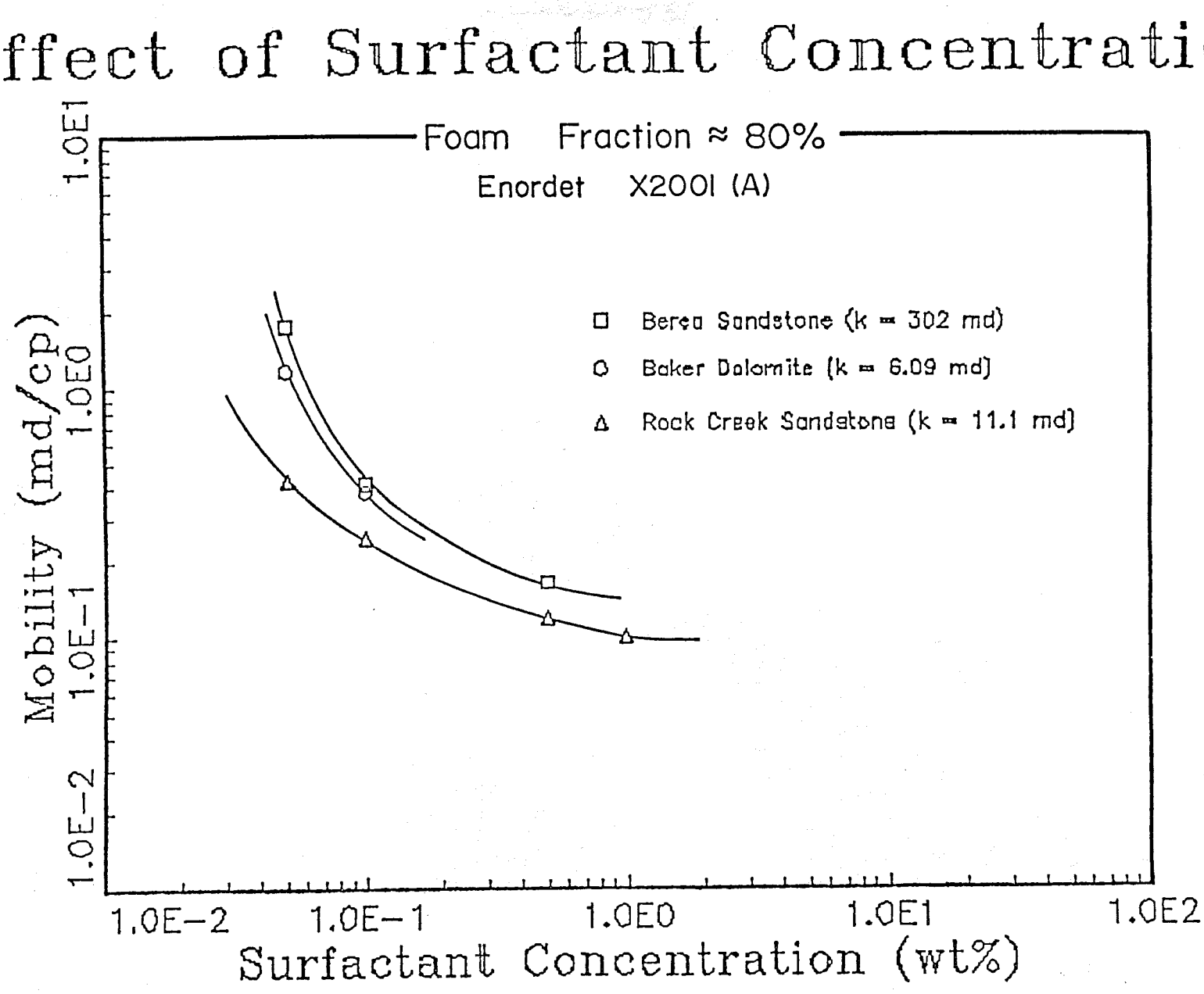

Figure 128. Effect of surfactant concentration on CO_2-foam mobility.

well above CMC regardless of either the surfactant type or the rock type. When no further reduction in mobility results from an increase in surfactant concentration, a surfactant-sufficient condition is indicated, in which there already exists the needed population of lamellae in the porous medium. An additional amount of surfactant beyond this concentration does not cause any noticeable mobility reduction. Besides its experimental implications, this fact also may have economic significance in the application of the process.

c. Effect of CO_2-Foam Fraction

The effect of CO_2-foam fraction on mobility also was studied with a brine containing 0.1% of Enordet X2001. CO_2-foam fraction is defined as the ratio of the flow rate of CO_2 to the total flow rate (of aqueous surfactant solution and CO_2) during the measurement. Four different CO_2-foam fractions were used to study the foam fraction effect at various flow rates. The results obtained with Baker dolomite are presented in Fig. 129 and with Berea sandstone in Fig. 130. Both figures clearly demonstrate that the mobility decreases with increase of surfactant fraction. These experimental results indicate that the volume fraction of the aqueous phase, which presumably drives the population of lamellae in the pore spaces, is responsible for reducing the foam mobility as well as for stabilizing the foam flow. The slopes of the fitted lines (that is, the derivatives of the mobility with flow velocity) in both figures suggest that more shear-thinning behavior is evident at 90% of CO_2-foam (which indicates a surfactant-deficient environment) than was observed at 60% or 70% of CO_2. Figure 131 also presents the CO_2-foam fraction effect measured with Baker dolomite and Berea sandstone. The data presented in Fig. 131 are the mobility measurements given as a function of foam fraction at an average velocity of 7.0 ft/day with 0.1% Enordet X2001. These fitted curves show the same trend noted in Figs. 129 and 130.

d. Effect of Rock Permeability

The differences between mobility measurements on the different kinds of rock are presented as the effect of rock permeability. This effect is illustrated in terms of relative mobility of the different samples. To emphasize the difference between the results in different kinds of rock, it is helpful to consider the relative mobility, λ_r, which is the ratio of the measured absolute mobility to the rock permeability. The dimension of relative mobility is reciprocal centipoise, whereas absolute mobility is measured in md/cp. Thus, in the very approximate sense in which "foam" can be considered to be a single-phase fluid that saturates the pore space (so that a single-phase permeability could be taken to characterize the rock), the "effective viscosity" of the foam is identified with the reciprocal of the relative mobility.

The comparisons of the relative mobility measurements made with Baker dolomite and Rock Creek and Berea sandstones are shown in Fig. 132 and Fig. 133. Figure 132 is a semi-log plot which graphically presents the relative mobility measurements made at different total flow rates (the latter are given as Darcy velocity in the rock) in the three kinds of rock. The CO_2-foam fraction was kept constant around 80% and a concentration of 0.1% Enordet X2001 was used. The Rock Creek sandstone is about twice as permeable as the Baker dolomite. However, the relative mobility in Baker dolomite is approximately three times less than it is in Rock Creek sandstone. Even between the sandstones, such as Rock Creek and Berea, the ratio of relative mobility reduction accompanying the flow of CO_2-foam depends on the rock type and its permeability. It is clear that mobility is greatly reduced in high-permeability rock. However, further experimental results are required with different rock samples in order to make a more general correlation between the reduction in relative mobility and rock permeability and to determine the extent of this effect.

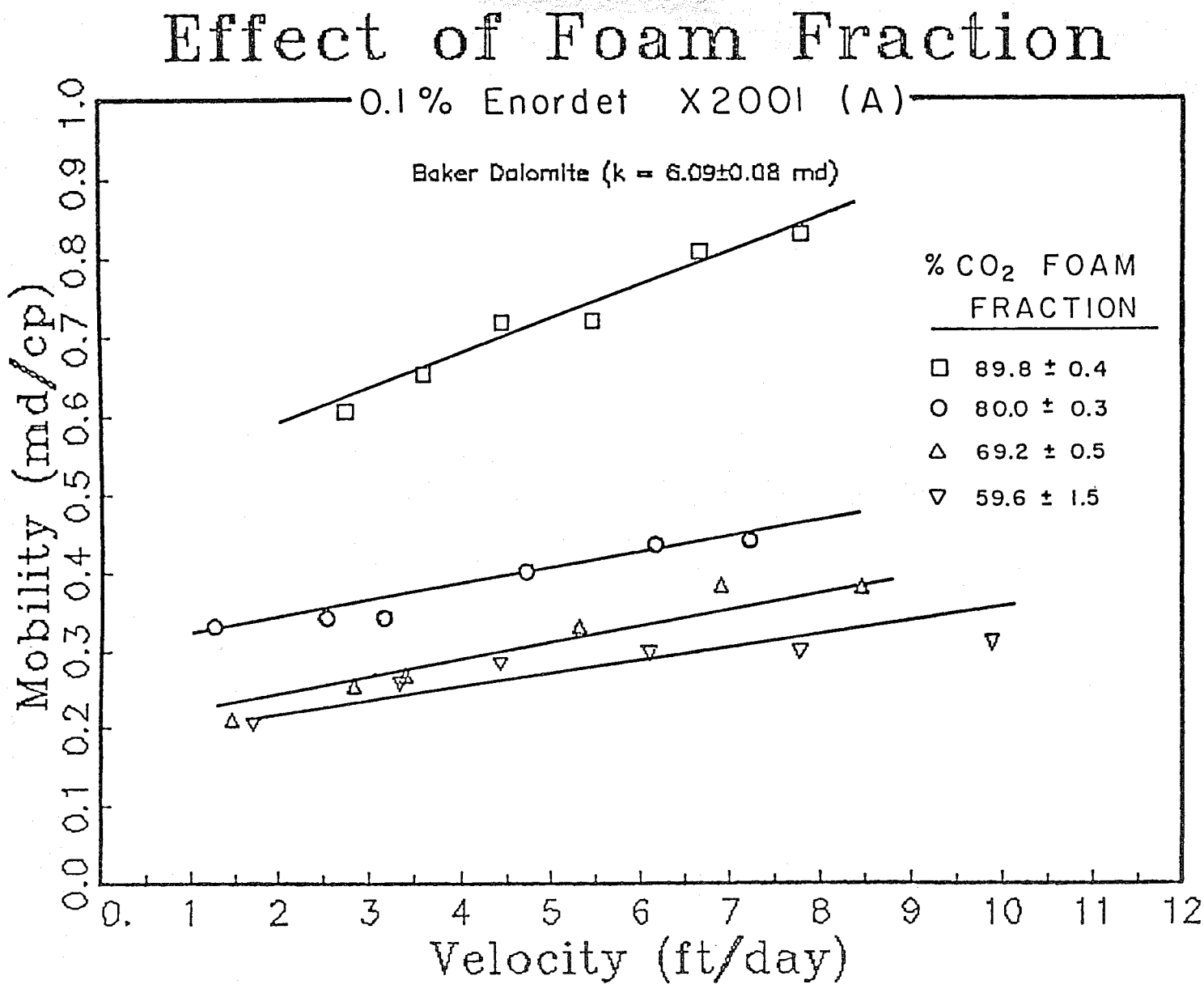

Figure 129. Effect of foam volume fraction on mobility - Baker Dolomite.

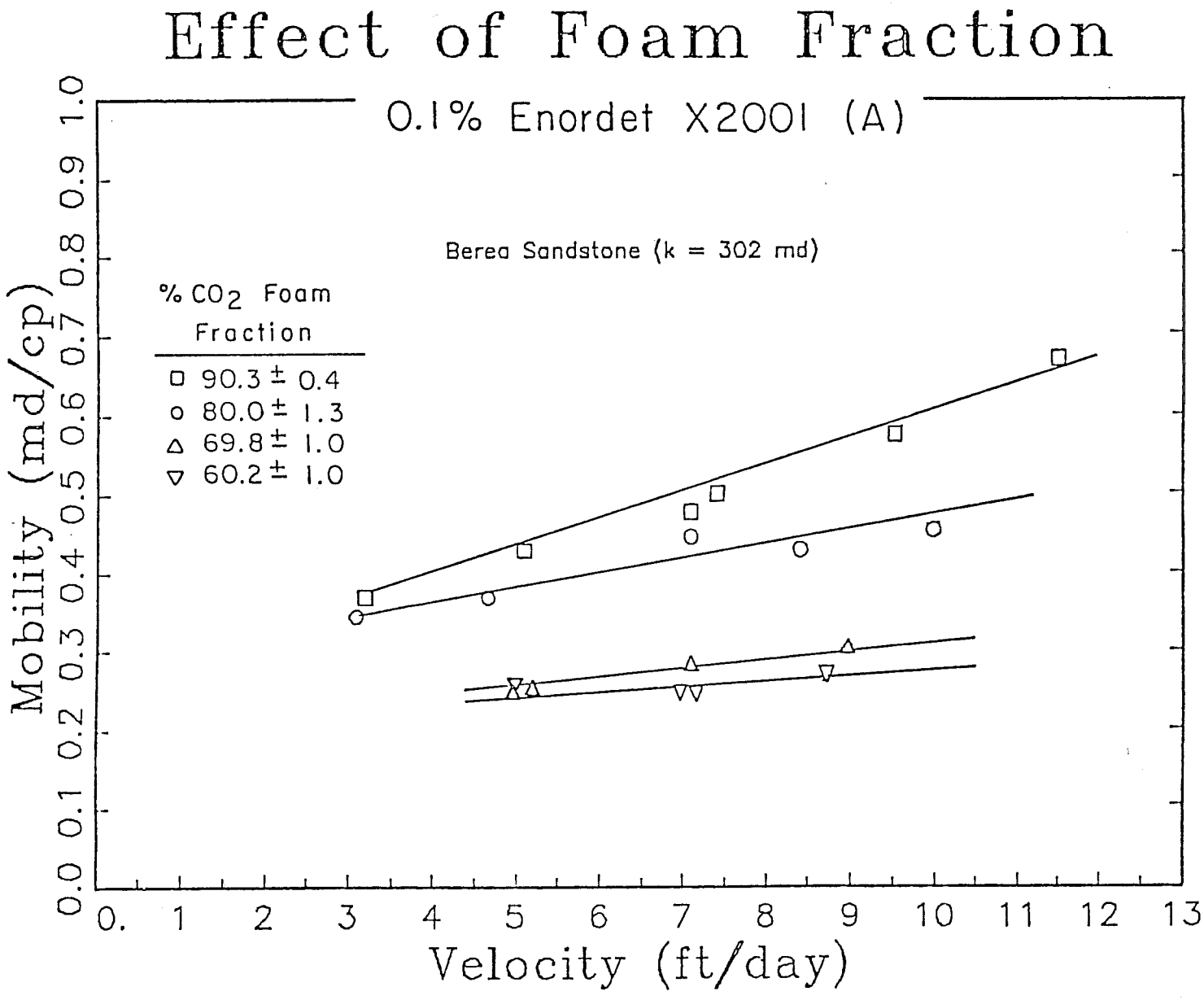

Figure 130. Effect of foam volume fraction on mobility - Berea sandstone.

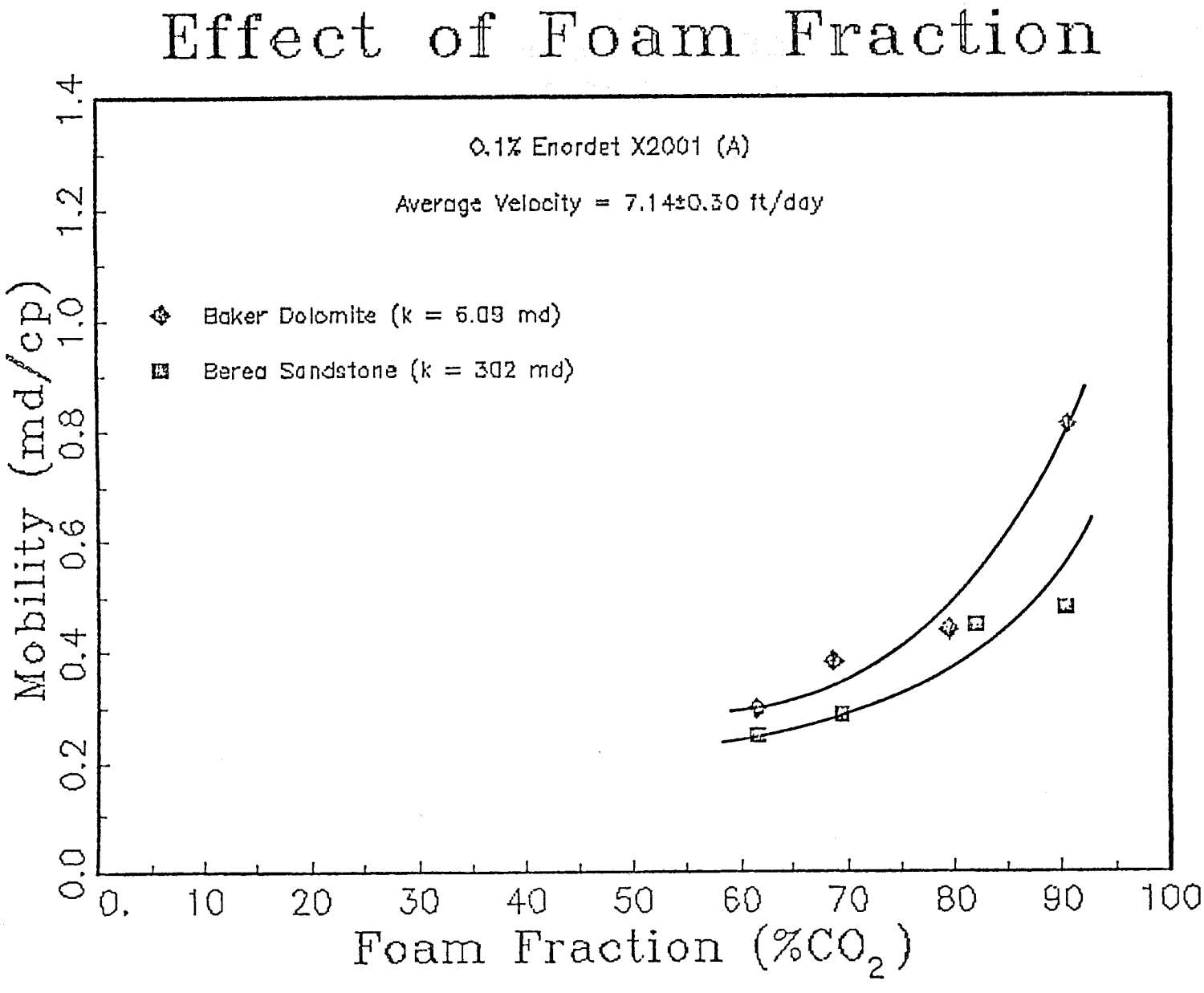

Figure 131. Foam Fraction effect at constant velocity.

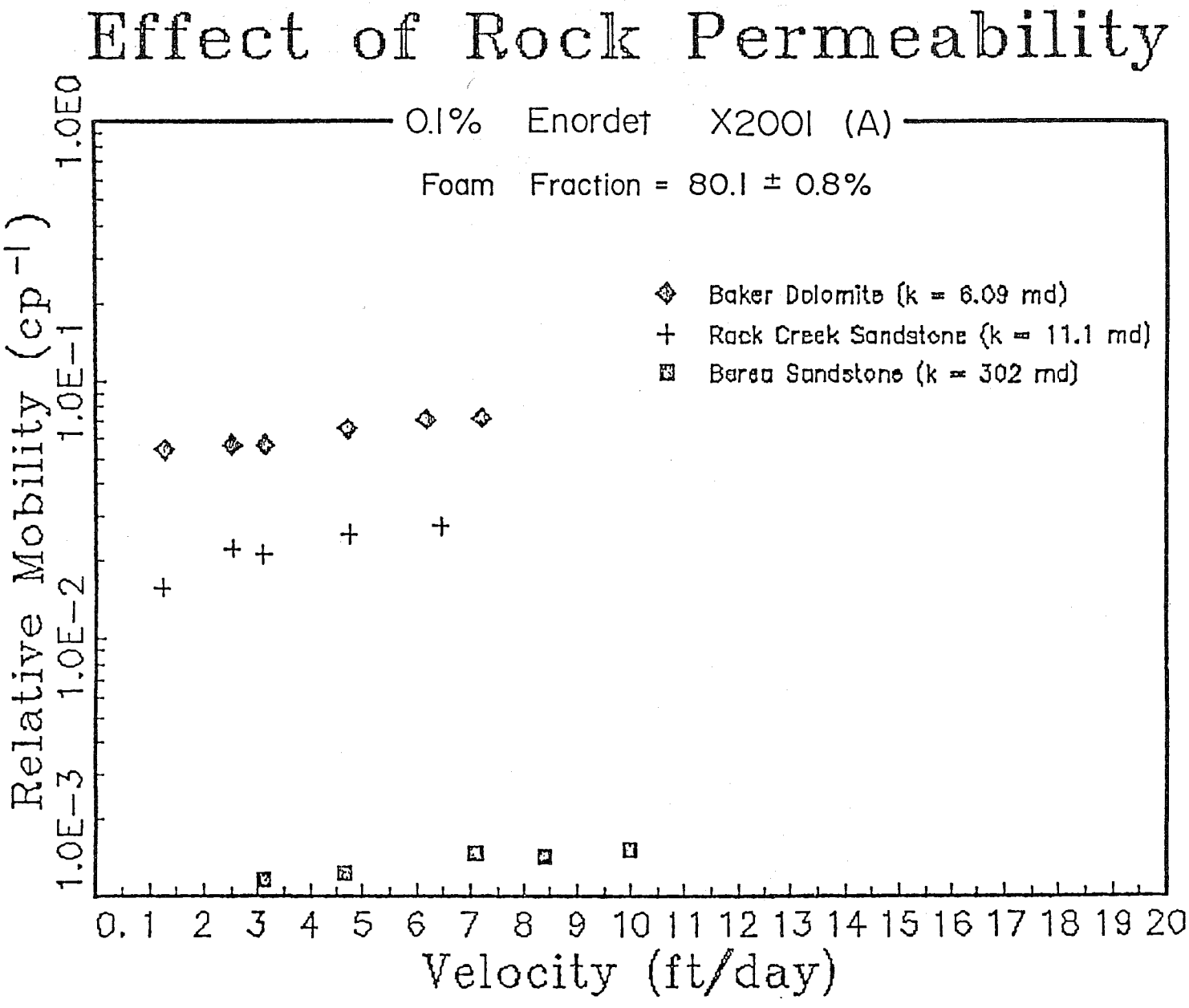

Figure 132. Relative mobility variations with velocity for different rocks.

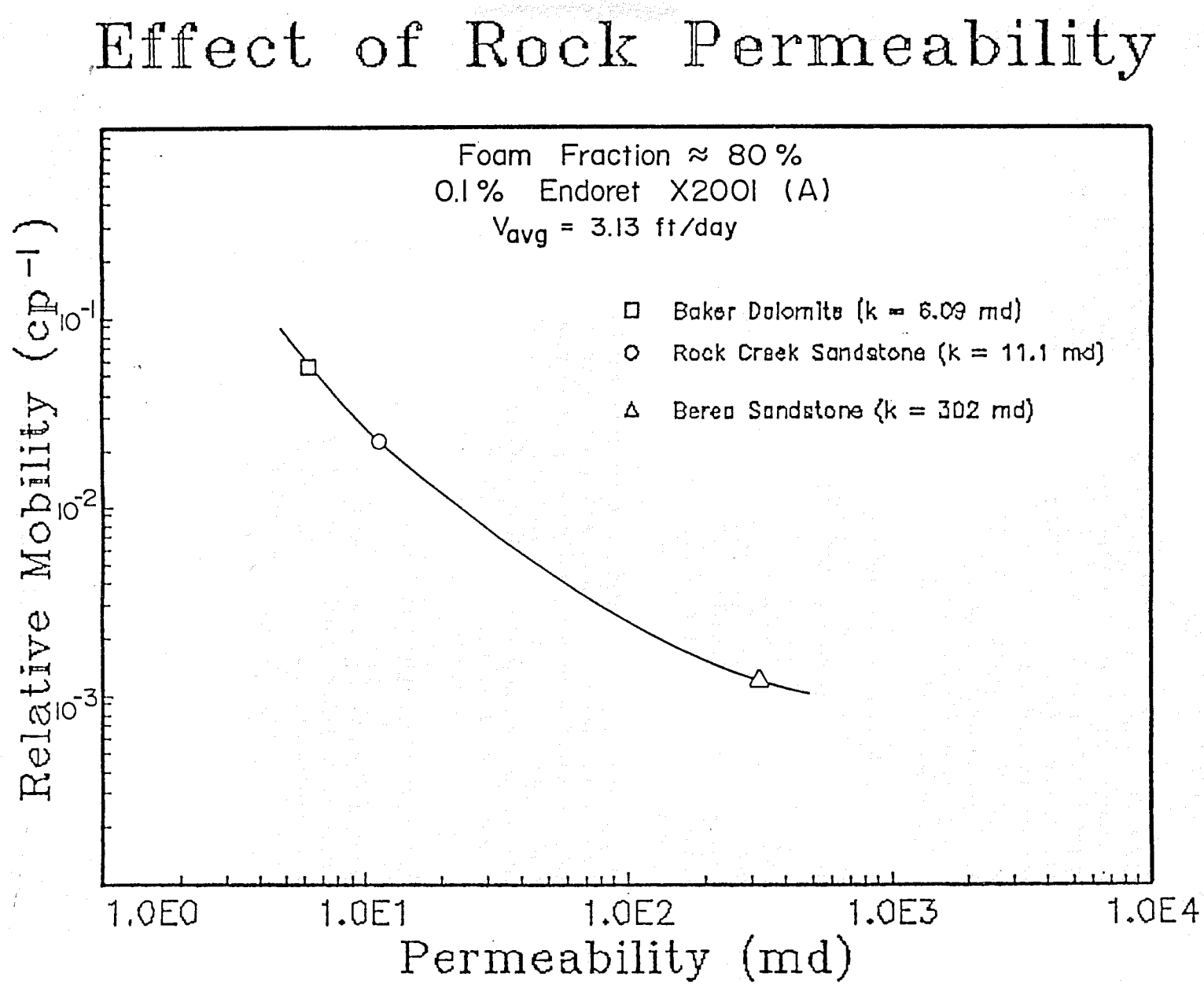

Figure 133. Effect of rock permeability or relative foam mobility.

Figure 133 is a log-log plot in which is presented a possible relationship between the relative mobility and permeability, based on the meager data we have. These data were collected at an average Darcy velocity of 3.13 ft/day. The foam fraction was kept constant around 80%, and 0.1% Enordet X2001 solution in standard brine was used throughout the experiments. As was illustrated in Fig. 132, the relative mobility was much lower in high-permeability rock like Berea sandstone than in Baker dolomite. The relative mobilities in the three rock samples lie on a smooth curve rather than a straight line. This indicates that the relative mobility reduction is nonlinear with respect to permeability. However, prior to any stronger conclusion, it will be necessary to carry out more experiments with different rock samples to see whether that data will fall onto this or other fitted curves under identical experimental conditions. It seems that in the more permeable sections of a heterogeneous rock, CO_2-foam will act like a more viscous liquid than in the less permeable sections. This behavior can render flow, and perhaps displacement, more uniform through such rock. To take advantage of this effect in the field will require a fuller understanding of its cause and of the permeability range over which it extends.

Figure 134 shows the effect of total velocity (or total flow rate) on CO_2-foam mobility at four different concentrations of surfactant solution. The experiment was carried out with Rock Creek sandstone and a CO_2-foam fraction of 80%. The results indicate that shear-thinning is more pronounced at lower surfactant concentrations. A similar phenomenon was observed during the study of the effect of CO_2-foam fraction. From the previous work, shear-thinning was quite evident in the presence of a high CO_2-foam fraction at a constant surfactant concentration. Physically, it seems that the shear-thinning behavior results from a surfactant-deficiency inside the porous medium. As the concentration is raised well above the CMC, the mobility reduction at higher flow rates becomes less noticeable.

In this report, we have not commented extensively on the mechanism by which mobility is more strongly reduced in high-permeability rock. However, we are planning to investigate this question along with other aspects of the mechanism of dense CO_2 and aqueous surfactant solution flows. For the purpose of this study, we are currently constructing a photosensor to distinguish between CO_2 and surfactant solution flows in the input and output tubing leading to the core. More details of this device are mentioned in the section titled "High Temperature CO_2-Foam Mobility Measurements."

4. Dynamic Surfactant Adsorption Experiment

Adsorption of the surfactant on porous media is an important variable in any enhanced oil recovery process that uses these chemicals. It is well understood that permanent adsorption does occur in the porous rock; this could increase drastically the cost of the process. To maintain the specific concentration that is required to achieve a desired mobility reduction, it is necessary to use an additional amount of surfactant in the injected aqueous phase. This extra amount corresponds to the quantity of surfactant adsorbed and retained on the rock within the time frame of the flood. The experiment described below is designed to enable calculation of this additional amount that is required to satisfy permanent or irreversible adsorption in the flood area of the reservoir.

In addition to the need for extra surfactant, the time required for a 'front' of the surfactant to flow through the core will be longer than that of the brine solution. This is an indication of chromatographic delay, a reversible adsorption of the surface active agents within the available times determined by the flow rates in the reservoir. The particular experiment described here will provide both the expected chromatographic delay factor of the surfactant front in the reservoir, and a measure of the quantity of surfactant that is (or might as well be) irreversibly adsorbed at the flow rates of the experiment.

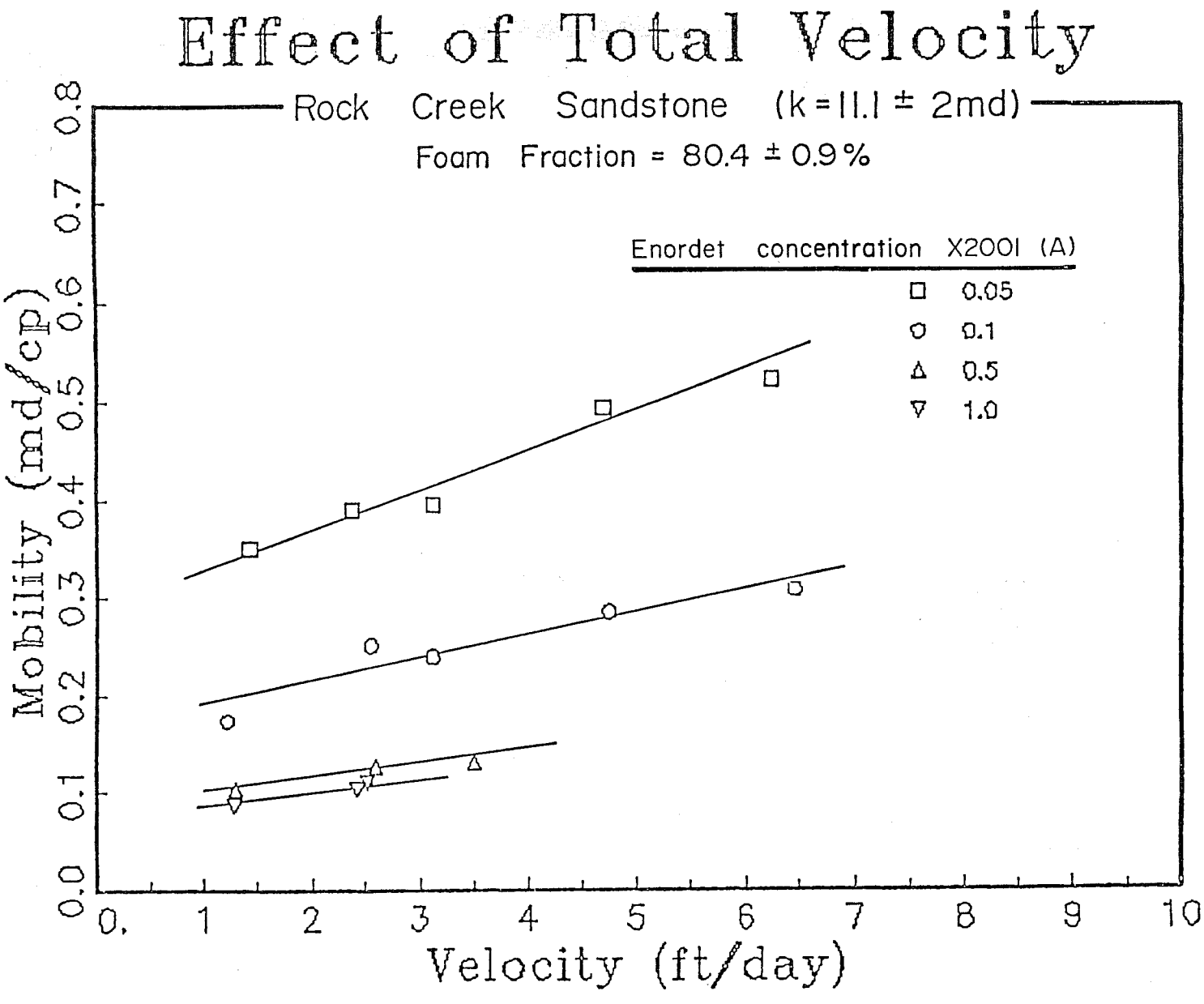

Figure 134. Effect of flow velocity at different surfactant concentrations.

In this section, the description of the experimental apparatus and the nature of the experiment are discussed. As noted, dual results of the adsorption measurements are presented. These are given as the amount of surfactant adsorbed per gram of rock and as the dimensionless chromatographic time delay factor.

a. Description of the Experiment and Apparatus

The apparatus for this experiment is shown in Fig. 135. The detailed description of the experiment was reported in the last annual report. In brief summary, three types of experiments are carried out for measurement of the adsorption parameters of a given rock sample. The response of the experiment is the measured difference between the refractive index of the fluid emerging from the core or capillary tube and that of the standard brine contained in the reference cell of the refractometer. This difference is registered on the chart recorder during operation. The descriptions of the three experiments are as follows.

Experiment A is a nonadsorption experiment through the core, performed to measure the time for emergence of a peak produced by a tracer which is not adsorbed. This is a sample of the standard brine at 1.3%—a concentration slightly higher than the standard. Because the experiment is performed at atmospheric pressure with no CO_2, the brines are acidified. The higher-concentration solution is loaded into the sample loop to be used as a sample medium for experiment A. This particular experiment is carried out to measure the travel time of a nonadsorbed slug by recording the time required before the peak is observed. This time also can be used to compute the exact porosity of the core, under the assumption of zero adsorption of salts from the brine.

Experiment B is also a nonadsorption experiment in which flow through the teflon capillary tube is used. The sample medium used in this case is the surfactant solution prepared in the 1% acidified brine. Results will be combined with those from Experiment C to compute the permanent or irreversible adsorption on the porous medium by measuring the peak areas in both experiments.

Experiment C is designed to yield information on the amount of the surfactant that is actually adsorbed on the rock. This experiment measures the variation of surfactant concentration at the outlet of the core, after injection of a "slug" of surfactant. During the experiment, the surfactant concentration in the brine flowing in the porespace depends on the position along the core and on time. The experiment is dynamic because the changing (but near equilibrium) level of the adsorbed surfactant at any point along the rock sample is a function of the concentration of the surfactant in the solution at that point. This is described by the adsorption isotherm: a plot of M, the mass of surfactant adsorbed per gram of rock vs. the concentration of surfactant in the solution at equilibrium with it.

The amount of permanent adsorption onto the rock can be computed from the type B and type C experiments. The mass of surfactant to which the rock is exposed is given by the volume of the sample loop and the initial surfactant concentration. The fraction adsorbed is given by the ratio of peak areas. The mass and bulk volume of the core plug are known, which enables the quantity adsorbed to be normalized to the size of the core. One can thus compute the additional amount of surfactant that will be required in a reservoir, over and above that which is required to provide the necessary surfactant concentration in the aqueous part of the CO_2-foam.

Combining the data from the type A and C experiments makes it possible to compute the factor by which the arrival of the surfactant peak is delayed. The chromatographic time delay factor is simply the ratio of the time before the arrival of the surfactant peak, in experiment C, to the time before the brine peak, in experiment A. The time for the surfactant slug to traverse the core is

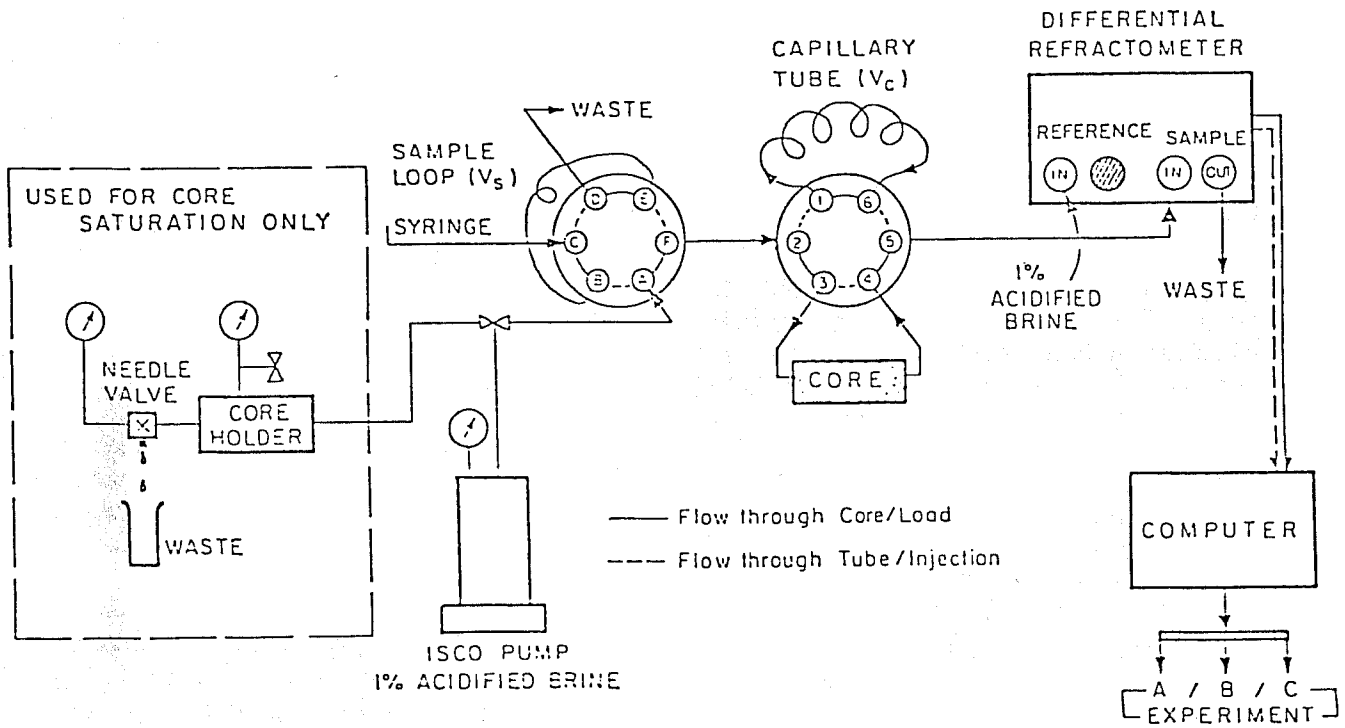

DYNAMIC ADSORPTION APPARATUS

Figure 135. Dynamic adsorption apparatus.

longer than that for the slug of changed brine concentration to traverse the same core. The chromatographic delay factor is due to reversible adsorption.

With knowledge of both the area ratio and the chromatographic delay factor from these experiments, and from the dimensions of the reservoir, the engineer will be able to decide the magnitude of two important quantities that dictate the proper use of foam in the reservoir. First, the peak area ratio gives data to calculate the additional amount of surfactant that will be required, to satisfy the reservoir rock's irreversible adsorption appetite. Second, from the time delay factor, the engineer can compute the volume of a "surfactant pad" or preflush. This is the amount of a first portion of surfactant solution that should precede the simultaneous injection of both surfactant and CO_2 so that the resulting bank of CO_2-foam will remain intact for the required distance.

b. Results and Discussion on Dynamic Adsorption Measurements

Dynamic adsorption was first studied during experiments using Baker dolomite. The computed porosity of the rock was 24%. One concentration below the CMC of Enordet X2001, one at CMC, and two concentrations above CMC were chosen to measure the adsorption of this surfactant with Baker dolomite. The mass of surfactant adsorbed per gram of rock is plotted as a function of flow rate in a semi-log plot in Fig. 136, at four different surfactant concentrations. The corresponding chromatographic time delay factors are presented in Table 19. The results displayed in Fig. 136 indicate that more adsorption of surfactant occurred at low flow rate. In the concentration range of this experiment, adsorption increased with increase of surfactant concentration. The shapes of the peaks from the flow through the core also are broader at low flow rate than at high flow rate. In addition, more antisymmetry, or deviations from the bell-shaped curve, was observed with an increase in concentration. Furthermore, more time was needed to reach baseline zero at high concentration. This last effect must be caused by the fact that since there is more adsorption, the time that molecules spend in the mobile phase decreases, resulting in a broad peak. Compared to the broad peak observed in core experiments, narrow and sharp peaks were observed with the tube flow.

Data presented in Table 19 show the chromatographic delay factor at the three flow rates. The results show that at the rate of 10 cc/hr, high concentration and strong adsorption are associated with a longer retention time. However, with flow rates of 20 cc/hr and 30 cc/hr, an expected trend similar to that at 10 cc/hr was not observed.

The results for Rock Creek sandstone are shown in Table 20. Column 3 depicts how much surfactant (in mg) is adsorbed per gram of rock in experiments at different concentrations and flow rates. It can be seen again quite clearly that more adsorption takes place as the concentration increases. The result with Baker dolomite showed that the amount of adsorption decreased as the flow rates were increased from 10 cc/hr to 30 cc/hr. The chromatographic time delay factor is close to 1.0, indicating that there is no significant time delay involved between the velocities of the brine and the surfactant solutions. A similar chromatographic time delay factor was obtained with Baker dolomite where the factor was close to unity. However, there was slightly more delay measurable in the Baker dolomite.

Table 21 compares the data obtained with Baker dolomite, Berea sandstone, and Rock Creek sandstone at 10 cc/hr. Three concentrations— 0.05%, 0.1%, and 0.5%—were studied. Since most of the surfactant will be used at concentrations well above the CMC, we omitted a measurement at 0.01% with Rock Creek sandstone. The results indicate that more surfactant was adsorbed with an increase in concentration. This trend was consistent among the three rocks. Also, a greater chromatographic time delay factor was observed as the concentration was increased. However, the

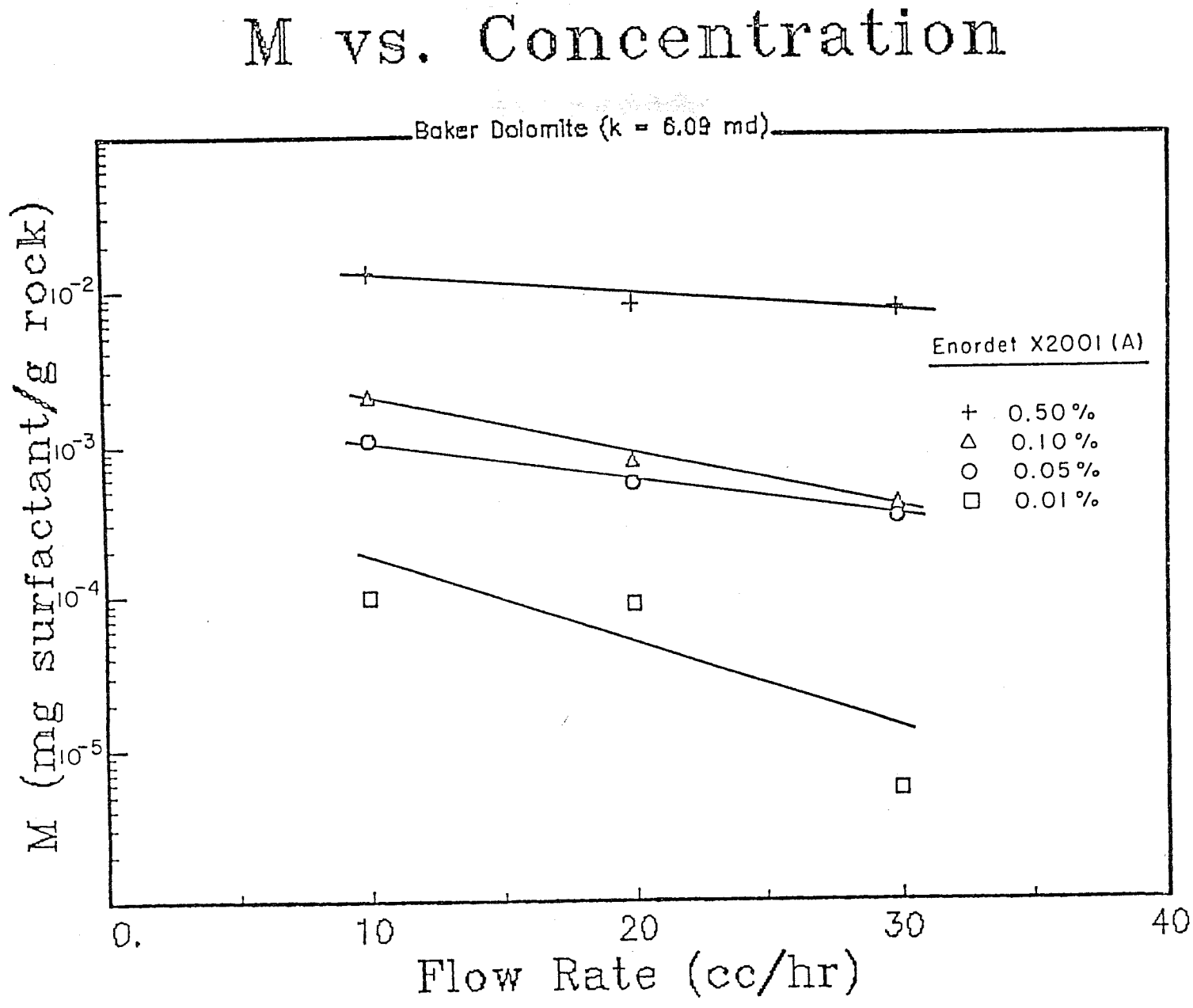

Figure 136 Irreversible adsorption, as function of flow rate.

TABLE 19

ADSORPTION MEASUREMENTS—BAKER DOLOMITE

Effects of Concentrations and Flow
Rates on Chromatographic Time Delay Factors

Q(cc/hr)	Conc. (wt%)	Time Delay Factor
10	0.01	1.15
	0.05	1.16
	0.1	1.21
	0.5	1.24
20	0.01	1.04
	0.05	1.05
	0.1	1.10
	0.5	1.05
30	0.01	1.10
	0.05	1.17
	0.1	1.06
	0.5	1.06

TABLE 20

ADSORPTION MEASUREMENTS—ROCK CREEK SANDSTONE

Effects of Concentrations and Flow Rates
on M and Chromatographic Time Delay Factors

Q(cc/hr)	Conc. (wt%)	M(mg Surfactant/g rock)	Time Delay Factor
10	0.01	2.69×10^{-4}	1.03
	0.05	1.19×10^{-3}	1.03
	0.1	1.98×10^{-3}	1.03
	0.5	2.30×10^{-2}	1.03
15	0.01	9.08×10^{-5}	0.98
	0.05	5.95×10^{-4}	0.97
	0.1	2.46×10^{-3}	0.98
	0.5	2.30×10^{-2}	0.97

TABLE 21

ADSORPTION MEASUREMENTS

Effects of Concentrations
on M and Chromatographic Time Delay Factor at 10cc/hr

Rock Type	Conc. (wt%)	M(mg Surfactant/g rock)	Time Delay Factor
Baker Dolomite	0.05	1.08×10^{-3}	1.16
	0.1	2.04×10^{-3}	1.21
	0.5	1.31×10^{-2}	1.24
Berea Sandstone	0.05	2.62×10^{-3}	1.03
	0.1	3.03×10^{-3}	1.06
	0.5	1.76×10^{-2}	1.10
Rock Creek Sandstone	0.05	1.19×10^{-3}	1.03
	0.1	2.98×10^{-3}	1.03
	0.5	2.30×10^{-2}	1.03

latter trend was not noted with Rock Creek sandstone. The data also show some similarity in adsorption behavior between the sandstones. The amount of surfactant adsorbed and the time delay factor seem very similar in magnitude for both of them, despite the difference between the types of clays in the two sandstones. Contrary to what one might expect, Baker dolomite showed less adsorption than the sandstones in these experiments. The dynamic surfactant adsorption experiment not only tells us about the permanent adsorption and time delay factor for the surfactant, but also is characteristic of the rock itself.

The widths of the peaks in the dynamic adsorption experiment are influenced by dispersion. Use of a core sample that is much longer than its diameter is intended to minimize the relative length of the transition zone produced by dispersion. Regarding these simply as miscible displacements, it can be seen that excessive peak width generated by a large amount of dispersion would make it more difficult to measure peak parameters accurately. Also, the underlying assumption of a simple theory is that adsorption occurs instantly on contact with the rock. The fraction that is classified as "permanent" in the above calculation depends on the flow rate of the experiment; it is the fraction that is not desorbed in the time available. The rest of the adsorption occurs reversibly, and equilibrium is effectively maintained between the surfactant in the solution and that adsorbed on the pore walls. The two parameters calculated from these experiments are expected to be those that would be operative in the field.

5. High Temperature CO_2-Foam Mobility Measurement

This subsection will describe the new CO_2-foam mobility measurement apparatus as well as a modification which was made on the core holder to eliminate the need to maintain a separate overburden pressure on the core. We also discuss briefly the future addition of a photosensor-based measurement of instantaneous fluid output.

a. Schematic of the Apparatus

The new high-temperature CO_2-foam mobility apparatus is depicted in Fig. 137. This apparatus employs two pumps: a Ruska Instruments Corporation #1448-803 m-278 pump, which contains dense CO_2, and an Isco LC-5000 syringe pump, which pressurizes the surfactant solution prepared in 1% brine. The surfactant solution then passes through a 0.45-micron millipore filter to remove any particulate matter or impurities that might clog the core and valve. The dense CO_2 is pumped into the system where it passes through a 40.5-in.-long capillary tube with a nominal ID of .006 in. and an OD of 1/16 in. The pressure drop across the capillary tube is measured using a Validyne differential pressure transducer with an 80-psi diaphragm. The transducer sends an AC signal to the respective CD-18, which converts the signal to a DC level. The output is displayed on the digital display of a #MC1-10 Validyne chassis, and it also is monitored by a linear chart recorder for convenience. The CO_2 and the surfactant solution are mixed by flow through a Swagelock 1/8-in. tee before entering the core. A differential pressure transducer with an 800-psi diaphragm measures the pressure drop across the core and sends a signal to its respective CD-18 in the #MC1-10. As in the previous case, this CD-18 also sends its signal both to the digital display and to a second pen on the linear chart recorder. The fluids exit the core and pass through a NUPRO dual needle valve (#SS-2SGD). A differential pressure transducer with a 3200-psi diaphragm measures the gauge pressure of the fluid emerging from the core prior to the major pressure drop which is developed across the regulating needle valves.

The high-temperature CO_2-foam mobility apparatus is inside a well-insulated box measuring about 4x4 ft. x 2-ft. deep. The box has doors made of 1/2-in.-thick Lexan. The Lexan provides

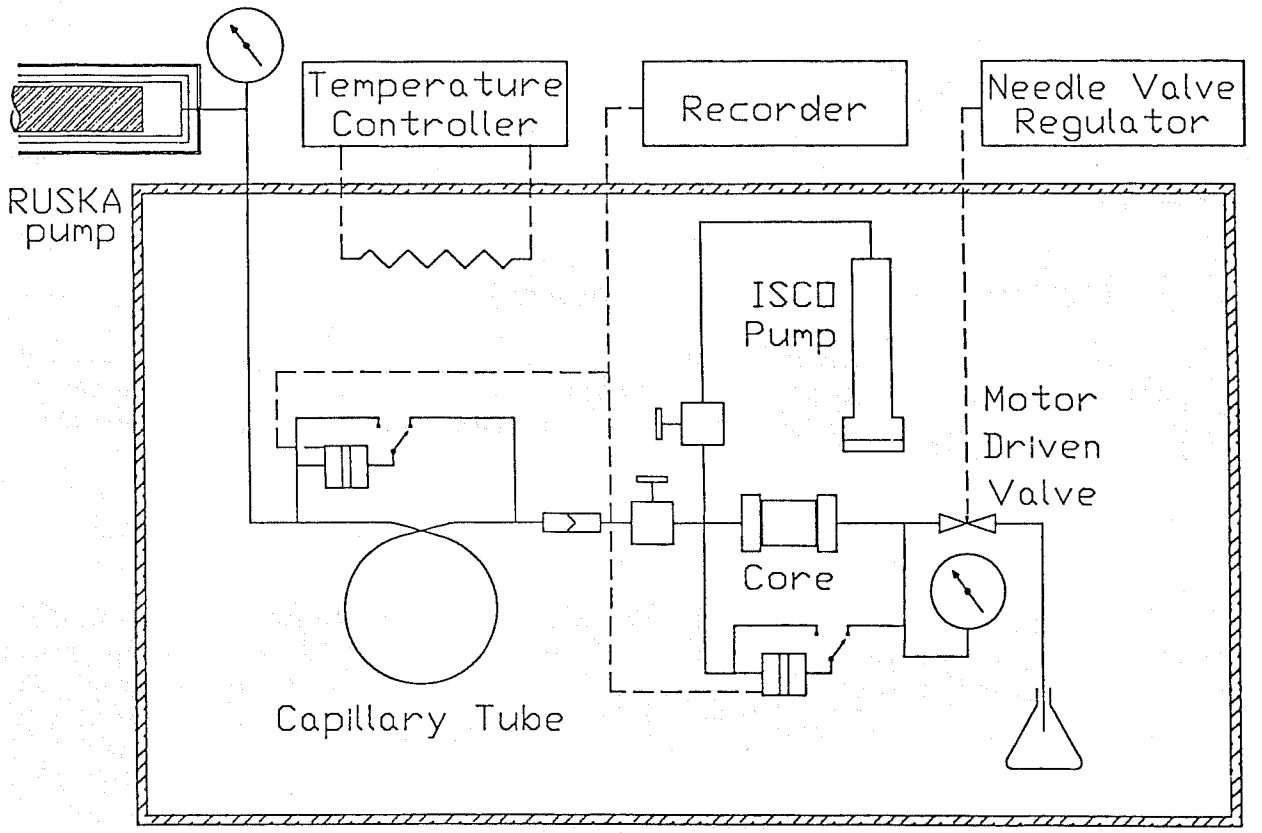

Figure 137. High temperature foam mobility apparatus.

insulation as well as protection from possible pressure failures. Inside, the box has a heater which can maintain the apparatus at temperatures up to 150°F and a fan to circulate the heated air. There are also two temperature sensors in the box. One sensor is centrally located to register the box temperature and to aid in the maintenance of the isothermal conditions inside, while the other sensor is attached to the outlet of the needle valve to monitor the effect of a valve heater designed to prevent the needle valve from freezing as CO_2 expands to the atmosphere.

b. Modification of the CO_2-Foam Mobility Apparatus

The initial testing of the apparatus, which was conducted at a temperature of 150°F, precipitated an unexpected problem. Specifically, the increase of temperature apparently caused the overburden pressure on the core to rise rapidly, consequently endangering the pressure seals and causing flow rates to become questionable. This problem has been resolved by the development of a new core preparation procedure and by the redesign of the endplates for the core holder.

The core preparation begins by first coating the core with a thin coat of epoxy. The epoxy used in this procedure is Armstrong C-7 resin and activator W. This mixture is prepared in a 1:1 weight ratio at room temperature. The epoxy is cured for 24 hours at room temperature, thus sealing the core from absorption of the epoxy in later stages of this procedure. The coated core is placed in a stainless steel core holder with teflon endcaps to secure it in a centered position. Another batch of the epoxy components at a 1:1 weight ratio is weighed in separate containers, and all three items are placed in a 180°C oven for 15 to 20 minutes. This heating decreases the viscosity of the resin and activator, allowing better mixing of the two components while avoiding air bubbles in the epoxy surrounding the core. The resin and activator are mixed and poured into the annulus of the core holder. The core/core holder assembly is replaced in the 180°C oven for a curing period of 24 hours. The cured core is removed and excess epoxy and rock core are machined off. This results in a modular system in which the core is mounted semipermanently and coaxially in a thick-walled stainless steel tube with a smooth epoxy surface in the exposed annular surfaces. These epoxy surfaces can seal against regular O-rings. The need for separate overburden pressure is eliminated by this modification.

The new mounting procedure for the core also includes a redesigned endplate (see Fig. 138). Since no separate overburden pressure is used with the core, the O-ring used to seal the overburden fluid from the atmosphere can be removed. This leaves only a single O-ring, at each end of the core, which seals between the epoxy annulus and the endplate. This seal is effective at pressures up to at least 1600 psi.

A further modification of the endplates, now in the construction phase, will enable the dense CO_2 or surfactant entering or leaving the core to pass through thick-walled glass capillary tubing. A photodetector will be used to determine at any instant whether CO_2 or surfactant solution is traversing the tubing. Photo input is provided by a bright light-emitting diode that is driven at a frequency of 10 KHz by a pulse generator. Light pulses passing through a slit that defines the bore of the tube are sensed by the photodetector. The refraction of light through the capillary tube depends strongly on the material it contains. Because the refractive indices of dense CO_2 and the surfactant solution are different (1.17 and 1.33), there will be a change in light intensity that the photodetector will monitor. The detector itself is a photodiode; its output current is amplified and fed through an active band pass filter to remove the noise. The clean signal then is converted to a DC level and compared to a fixed level by a comparator. The comparator provides a clean binary output indicating the presence of CO_2 or surfactant.

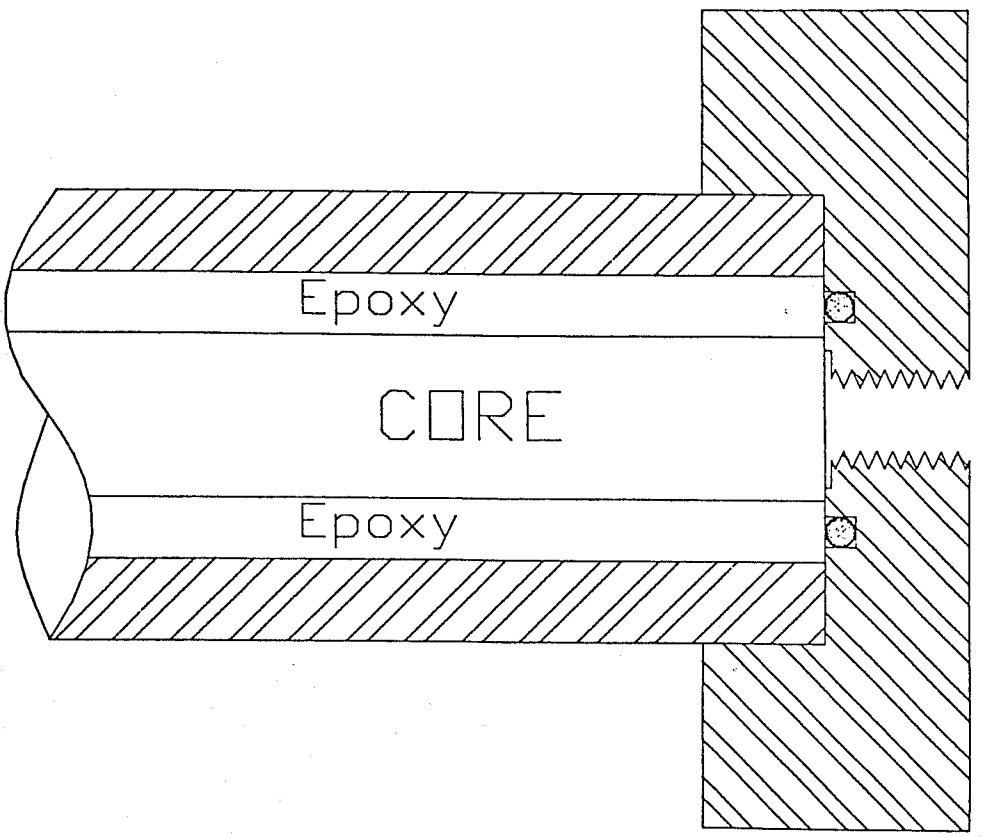

Figure 138. New endplate for high-pressure core holder.

c. Operating Procedure for the High Temperature CO_2-Foam Mobility Apparatus

Initially the heater is turned to 100% to heat the apparatus and the inside of the box to 65.6°C quickly. As this temperature is approached the heater controller is turned down to maintain the operating temperature. Before starting the flow of CO_2, the heater for the outlet needle valve must be turned on to prevent the formation of any solid CO_2 (dry ice) that would cause erratic operation of the outlet valve. The Ruska pump then is turned on and pressured up to 1600 psi at an operating temperature. After the apparatus has reached its operating temperature and the Ruska pump has come to pressure, the CO_2 needle valve at the Ruska pump CO_2 outlet is opened, as is the CO_2 needle valve inside the apparatus. This procedure is designed to prevent excess pressure build-up when CO_2 goes through the transition from 25°C to 65.6°C. The electronic servo system then is set at the desired ΔP_{cap}, keeping the CO_2 fraction and the surfactant fraction at the desired amount, e.g., CO_2 at 80% and surfactant at 20%. Since the electronic servo system is controlled electronically from outside of the box, the isothermal condition is maintained throughout the experiment. Finally the recorder is turned on, both pens are zeroed, and readings are taken from ΔP_{cap} and ΔP_{core}.

d. Calibration of the Capillary Tube Flowmeter

The capillary tube in the high-temperature CO_2-foam mobility apparatus was calibrated at room temperature. The pressure drop across the capillary tube was measured as a function of flow rate from 0 to 80 cc/hr, at an absolute pressure of 1590 psi ± 3 psi. Readings were taken every 3 cc/hr from 0 to 30 cc/hr and every 5 cc/hr from 35 to 80 cc/hr. Although a least squares fit of these points gave a reasonable calibration constant with a good correlation coefficient, the graph shows some systematic error. For this reason, we are planning to repeat the measurements. We will report the results of this work on the calibration constant in our next report.

6. Future Studies

The research under "CO_2 Mobility Control" will continue in all three subareas as described in previous pages. In the CO_2-foam mobility measurements, the acquisition of more data on the permeability dependence of the CO_2-foam will be the major emphasis. We plan to test as many rock samples as possible to investigate the effect of rock permeability. We want to test the permeability range, which will be of interest in the planning of actual field projects. Our plans are to perform these tests with rock samples from producing wells. Through the courtesy of Texaco and the cooperation of the Texas Bureau of Economic Geology in Austin, Texas, we have received some slabbed core from two interesting San Andres formations. These are a dolomite from the West Jordan Unit in Ector County, and the Queen sandstone from Magutex field in Andrews County in Texas. Core plugs are being taken from these samples for the CO_2-foam mobility tests, and we will be returning the unused portions of the slabs to Austin. We extend our appreciation to both organizations for allowing us to use this core material for further studies regarding the effect of rock permeability. Needless to say, we will be happy to accept core material from other operators as well. We also will continue to do the dynamic surfactant adsorption experiment using the available rock samples. It will facilitate the experiment if we have the right length for our experimental purpose. In order to perform the adsorption experiments, we need at least six inches of core. Shorter pieces can be used by stacking them together with minimum gap. Because the displacement tests used in these experiments are miscible, there will be no capillary effects at such boundaries.

We also will be testing some new surfactants in order to evaluate their effectiveness as CO_2-foamers, and will be keeping our sponsors informed of promising products. In addition to performing the experiments as described on CO_2-foam mobility and dynamic surfactant adsorption,

we are thinking of modifying the surfactant screening part of the work. In the past, we have used an atmospheric pressure measurement in which dense CO_2 is simulated with isooctane. Isooctane had been chosen because, like dense CO_2, it is nonpolar and a poor solvent. Its use permitted the foam height measurements to be done at ambient pressure. In the future, so that our surfactant screening will conform more closely to reservoir conditions, we plan to test the durability of lamellae between surfactant solutions and dense CO_2 itself. These tests will be performed at high pressure and temperature, and we are currently completing a design to enable them to be performed efficiently. We expect that this new experiment will benefit our supporters by providing more reliable and cost-effective assurance of surfactant suitability.

To summarize these paragraphs, we have expanded the work of the current "CO_2 Mobility Control" section in order to accomplish some new tasks in addition to the continuation of our previous work. We plan to perform some of our CO_2-foam mobility measurements at temperatures up to 150°F.

The main differences between the previous experiments and this new experiment will lie in the different physical property of the CO_2, and the further chemical interactions with rock and fluid that may become important. In addition, some new instrumentation is being designed, which we expect will prove useful in our program to supply more information for the field use of mobility control by CO_2-foams.

E. INTEGRATION WITH RESERVOIR SIMULATION

In the current practice of reservoir engineering, heavy reliance is placed on the computer simulation of recovery processes. The many programs that simulate flow in a reservoir differ widely in the complexity of the physical and chemical processes which are considered, and in the detailed computational methods utilized for solution of the equations. This is especially true for CO_2 or dense-gas floods. Nevertheless, there are certain common features of such simulators that are relevant here. The most important of these is that the procedures by which the equations are managed have by now become reasonably well established and that no major changes are desirable, even though some kind of modifications are necessary to improve their performance with respect to flow non-uniformity.

Most of the major reservoir simulators in use today are based on the so-called finite difference approximations of the flow equations. In these systems of solution, the calculations are based on a grid system which is drawn over the reservoir to be represented. These are used to determine the points at which approximate reservoir pressures are to be computed and the cells (or blocks) in which the average fluid contents and flow rates can be approximated. For each cell, a number of equations are written that involve the rock properties and deal with the pressure, the flow rates, and the compositions of the fluids in the block. All of these equations, for all of the cells, are to be solved simultaneously—a computational task performed by the computer in response to the simulator program. Only fairly large computer systems can accomplish the required work efficiently.

There are several reasons for this latter limitation, concerned both with the size of different types of memory available to the machine and with the computer's inherent speed in making the accurate calculations needed. All of the reasons, of course, are reducible to the simple economic limitation that more computation costs more money. The technical details of the limitations do not need to be discussed here, except to say that they are strongly influenced by the number of grid points utilized in the study. Thus the more numerous are the grid points—the higher the resolution with which the reservoir can be represented—the more costly is the study.

One can express one aspect of where the industry stands*** on the above economic terrain by evaluating the size of the "reservoir grid block," the actual piece of reservoir represented by the finite difference cell used in simulations. This number varies considerably with the complexity of the reservoir and the recovery process and with the importance placed on an accurate picture of the reservoir characteristics, as well as on the technical capabilities of the computer systems available. But given the current capabilities and costs of computer facilities, and considering only reservoirs in which there is considerable interest, one can say that it is rare to have the "reservoir grid block" smaller than twenty five feet on a side. Needless to say, major changes of reservoir properties and status can develop in much smaller distances.

Over the history of the last three or four decades, computers have become much faster and are able to communicate quickly with much larger memories. This progress has not been unpredictable, from one year to the next, but has resulted largely from comprehensive and fairly well documented engineering work on a multitude of problems. Given the capabilities and size of current computer systems and the status of current knowledge in the highly competitive computer industry, many new developments can be anticipated confidently. Nevertheless, it seems unlikely that the near future will bring such great improvements in performance that the reservoir grid block can be decreased by the factor of a thousand or more that would be needed to enable the representation of non-uniform flow on scales we can see in the laboratory.

It is a separate question, and a serious one, to ask whether the oil industry could pay for such increased resolution, or whether the benefits to be gained from it would be greater than the extra cost!

It is evident that conventional simulators can directly recognize only large-scale, frontal non-uniformities. The restriction applies whether the variability arises from viscous instability or from permeability heterogeneities. And yet it is already becoming evident, from studies such as those presented in this report, that such non-uniformities of displacement can lead to economically significant results, among which is the failure to obtain reliable predictions of reservoir performance. Thus, a more immediate and less hypothetical question than the one asked above is this: How can the results of research on flow non-uniformities be used to best advantage in the present environment of computer simulations?

This is the basic unanswered question that we wish to resolve in this part of the research. We wish to find computational methods that can indirectly take into account the variability of the reservoir and the flow within it. We also wish to supply the conventional simulation programs with modified parameters or procedures, such that proper representations can be attained even with large grid blocks. It will not be sufficient for the changes we propose to be based on a scientifically correct description of fluid displacement and on a statistically adequate view of the reservoir. To have a chance of being used, the proposed modifications must be economically practical and compatible with current practice.

Two examples can be given, at this time, of our approach to this problem. The first of these concerns the effect on displacement of permeability heterogeneity and deals with the set of results that are already partially available by virtue of the front-tracking simulation given above for a heterogeneous five-spot. If it can be shown that the geostatistical measures incorporated into the permeability variogram will alone be sufficient to describe the efficiency of floods in patterned arrangements, we shall perform more simulations of the type described. The object of these

---

***An entirely different consideration of the economics and technology of simulation is presented by Aronofsky et al.[112,113,114]

simulations will be to define, in more detail and over a greater range of conditions, the functional relationship. With these expanded conclusions, we can supply operators with information to correct their simulation results by a factor that depends on the size scale of their reservoir and the characteristics of the variogram they construct from log, core, production, and tracer data.

On the other hand, it seems quite possible that significant variation of the production curves may exist, depending on the particular orientation and arrangement of the wells with respect to the permeability extrema. In this case, our task also will include the estimation of the sensitivity of production efficiency to such local influences, under different circumstances.

A second example of this aspect of our work, the integration of our results into the current practice of simulation in reservoir engineering, concerns the severity of viscous fingering in miscible or developed miscibility floods. Because of the size scale of the reservoir grid block, as described above, the growth of frontal instability cannot be described directly by practical simulators. In those which do not simply ignore the effect of finger growth on recovery efficiency, empirical correction factors have been applied that do not attempt to take into account the physical and chemical mechanisms of the phenomena. As a result, the reliability of simulations performed at different scales is called into question.

Our work in this regard has been on a collaborative basis at the University of Texas, to assist in the testing and calibration of existing simulators under controlled circumstances in which the effects of known viscous and gravitational forces are calculable analytically. For instance, the computed growth predicted by a simulator, of sinusoidal perturbations on a front between miscible fluids, can be compared with that calculated from a perturbation analysis based on Darcy's equation. Such a comparison can be carried further into the very scale-sensitive domain in which transverse dispersion exerts a significant damping effect on finger growth.

As greater confidence is gained in the ability of a simulator to predict the response of the system to large-scale non-uniformities of the order of size of the grid blocks and larger, the program can be used to calibrate itself. By this approach, acceptable indirect procedures might be designed to estimate changes in amplitude of more closely spaced fingers, even in heterogeneous rock. These estimates could then be used to make the simulator more dependable in its predictions of displacement efficiency in dense-gas floods.

F. PROJECT PROSPECTS AND CONCLUSION

The first year of Task II of the continuation and extension of the PRRC research project, "Improvement of CO_2 Flood Performance," has been quite productive. We have directed our investigations toward the solution of important industry problems, and we expect our results to provide practical advantages to our supporters in their efforts to operate their reservoirs most profitably and efficiently. The following paragraphs summarize this work and point toward future research directions.

The three subareas that have been reported, and in which we have worked, are all concerned with what may be the most important reason for early breakthrough and low efficiency in EOR by CO_2 or dense-gas injection—the non-uniformity of displacement.

The first of these subareas is concerned with the heterogeneity of natural reservoirs and its effect on displacement. We have sought an orderly approach to this general problem, starting with an examination of the use of well-to-well tracers to evaluate the severity of heterogeneities in five-

spot patterns. This has resulted in definitive results giving the effect of longitudinal dispersion on the tracer production curves from an idealized homogeneous reservoir that consists of a single layer. The production behavior of a heterogeneous single-layer five-spot, with various random permeability fields, also has been reported, including successive front positions and production efficiencies at and beyond breakthrough.

Both of these computer studies are to be considered only beginnings in our program. The tracer study, from which we hope to see the development of techniques for the diagnosis of reservoir heterogeneity, next will be supplemented by the introduction of heterogeneities into the pattern. Our results on the displacement behavior from a heterogeneous five-spot have answered some questions and raised others concerning the relative importance of specific features of the reservoir to the statistical features. We expect to attack these questions by further simulations.

At the same time, we are engaged in experiments on the importance of heterogeneities in laboratory displacement experiments. This work is expected to yield information on the practical limits set by diffusion and dispersion to the non-uniform flow that is induced by rock variability.

The second and third subareas are both concerned with the development of mobility control additives by which CO_2 and other dense-gas floods can be rendered less liable to frontal instabilities. These two types of additives are direct thickeners and foam.

We have reported progress in the search for associative viscosifiers to make polymeric solutions in dense gases and other nonpolar solvents. We already have discovered a class of such thickeners that are quite effective in butane and propane, and we have been investigating several new classes of compounds that might be able to viscosify liquid or dense CO_2. Two of these classes are currently under investigation. Various organotin fluorides have been found to have a strong associative property when dissolved in nonpolar solvents. Due to a transitory association of the tin atom of one of these molecules with the fluorine atom from another, an effective polymer can be built up. If the concentration is higher than some critical value, the chains of this polymer become long enough to build a high viscosity in the solution. A second class of prospective direct thickeners also is associative in nature. Here, the individual links are themselves low-molecular-weight polymers that have sufficient solubility in CO_2. Through various manipulations of polymer chemistry, polar groups are appended onto each of these short-backbone polymers. If these polar groups are able to associate with each other strongly enough, it will become possible to build transitory viscosity in solutions of these compounds as well. We intend to continue our research into both of these classes of prospective direct thickeners.

The third subarea consists of the development of CO_2-foam, a dispersion of dense CO_2 in surfactant solution. The fine structure of the dispersion is larger than that of the rock, and it apparently achieves a lower mobility in porous media by creating stable lamellae that span the pores, restricting the fraction of the porespace through which the dense gas can flow freely. Our experiments have shown the effects on overall foam mobility of surfactant concentration, of the volumetric CO_2 fraction, and of the type of rock. The latter dependence in particular demonstrates that foam can be a very effective mobility control additive with an important supplementary feature. Within the range of applicability of the foam, it appears that the mobility is reduced much further in more permeable rock than in less permeable. We expect to find, then, that foam will be especially effective in heterogeneous rock, in which flow of the displacing fluid would be retarded more actively in the more permeable sections than in the tighter parts of the rock. Our foam experiments have been, and will continue to be, directed toward defining the range of values in which these properties can be relied upon, so as to obtain information of direct value in the design of field programs.

In all of the studies reported here, our goal is to provide reservoir engineers with tools to assist in the most efficient and profitable design and operation of EOR projects. A common feature of modern petroleum engineering is the use of computer modelling for this work, and we are therefore seeking ways in which to integrate our results into the practice of reservoir simulation.

REFERENCES

1. Ely, J.F. and Hanley, H.J.M.: "Transport Properties Prediction Program (TRAPP)," U.S. National Bureau of Standards, National Engineering Laboratory, Thermophysical Properties Division, Boulder, CO, 80303.

2. Stephan, K. and Lucas, K.: Viscosity of Dense Fluids, Plenum Press, New York (1979).

3. Lohrenz, J., Bray, B.G., and Clark, C.P.: "Calculating Viscosities of Reservoir Fluids from their Compositions," J. Pet. Tech. (Oct. 1964) 1171-1176.

4. Pedersen, K.S., Fredenslund, A., Christensen, P.L., and Thomassen, P.: "Viscosity of Crude Oils," Chem. Eng. Sci. (1984) 39, No. 6, 1011-1016.

5. Kovarik, F.S. and Taylor, M.A.: "Viscosity Measurements of High-Pressure CO_2/Hydrocarbon Mixtures," presented at the 1987 AIChE Annual Meeting, New York, Nov. 15-20.

6. Saeedi, J. and Rowe, A.M.: "Viscosity Correlations for Compositional Reservoir Simulator," paper SPE 9643 presented at the 1981 Middle East Technical Conference, Manama, Bahrain, March 9-12.

7. Lawal, A.S.L.: "Improved Fluid Property Predictions for Reservoir Compositional Simulation," Ph.D. dissertation, The University of Texas at Austin (1985).

8. Ely, J.F. and Hanley, J.M.: "Prediction of Transport Properties: 1. Viscosity of Fluids and Mixtures," Ind. Eng. Chem. Fund. (1981) **20**, 323-332.

9. Jossi, J.A., Stiel, L.I., and Thodos, G.: "The Viscosity of Pure Substances in the Dense Gaseous and Liquid Phases," AIChE J. (1962) **8**, No. 1, 59-63.

10. Pedersen, K.S. and Fredenslund, A.: "An Improved Corresponding States Model for the Prediction of Oil and Gas Viscosities and Thermal Conductivities," Chem. Eng. Sci. (1987) **42**, No. 11, 182-187.

11. Tham, M.J. and Gubbins, K.E.: "Correspondence Principle for Transport Properties of Dense Fluids. Nonpolar Polyatomic Fluids," Ind. Eng. Chem. Fundam. (1970), 9, No. 10, 63-70.

12. Mo, K.C. and Gubbins, K.E.: "Conformal Solution Theory for Viscosity and Thermal Conductivity of Mixtures," Mol. Phys. (1976) **31**, No. 3, 825-847.

13. Heller, J.P. and Kovarik, F.S., "Improvement of CO_2 Flood Performance," PRRC Report #87-8, Petroleum Recovery Research Center (1987).

14. Kovarik, F.S. and Heller, J.P.: "Improvement of CO_2 Flood Performance," PRRC Report 88-8, Petroleum Recovery Research Center (1988).

15. Lin, H.M. and Chao, K.C.: "Correlation of Critical Properties and Acentric Factor of Hydrocarbons and Derivatives," AIChE J. (1984) **30**, No. 6, 981-983.

16. Hankinson, R.W. and Thomson, G.H.: "A New Correlation for Saturated Densities of Liquids and Their Mixtures," AIChE J. (1979) **25**, No. 4, 653-663.

17. Thomson, G.H., Brobst, K.R., and Hankinson, R.W.: "An Improved Correlation for Densities of Compressed Liquids and Liquid Mixtures," AIChE J. (1982) **28**, No. 4, 671-676.

18. Tiffin, D.L., and Kremesee, V.J.: "Mechanistic Study of Gravity-Assisted CO_2 Flooding," SPE Reservoir Engineering (May 1988) 524-532.

19. Hill, S.: "Channelling in Packed Columns," Chem. Eng. Sci. (1952) **6**, No. 1, 247-253.

20. Larson, R.G., Davis, H.T., and Scriven, L.E.: "Elementary Mechanisms of Oil Recovery by Chemical Methods," paper SPE 8840 presented at the First Joint SPE/DOE Symposium on Enhanced Oil Recovery, Tulsa, April 20-23, 1980.

21. Mohanty, K.K., Davis, H.T., and Scriven, L.D.: "Physics of Oil Entrapment in Water-Wet Rock," paper SPE 9406 presented at the 55th SPE Annual Fall Technical Conference and Exhibition, Dallas, September 21-24, 1980.

22. Slattery, J.C.: "Interfacial Effects in the Entrapment and Displacement of Residual Oil," AIChE J. (November 1974) **20**, No. 6, 1145-1154.

23. Amaefule, J.O. and Handy, L.L.: "The Effect of Interfacial Tension on Relative Oil/Water Permeabilities of Consoldiated Porous Media," Soc. Pet. Eng. J. (June 1982) 371-381.

25. Huang, E.T.S. and Tracht, J.H.: "The Displacement of Residual Oil by Carbon Dioxide," paper SPE 4735 presented at the 1974 SPE Improved Oil Recovery Symposium, Tulsa, April 22-24.

24. Bardon, C. and Longeron, D.G.: "Influence of very Low Interfacial Tensions on Relative Permeability," Soc. Pet. Eng. J. (October 1980) 391-401.

25. Huang, E.T.S. and Tracht, J.H.: "The Displacement of Residual Oil by Carbon Dioxide," paper SPE 4735 presented at the 1974 SPE Improved Oil Recovery Symposium, Tulsa, April 22-24.

26. Metcalfe, R.S. and Yarborough, L.: "The Effect of Phase Equilibria on the CO_2 Displacement Mechanism," Soc. Pet. Eng. J. (Aug. 1979) 242.

27. Shelton, J.L. and Yarborough, L.: "Multiple Phase Behavior in Porous Media During CO_2 or Rich-Gas Flooding," J. Pet. Tech. (Sept. 1977) 1171.

28. Pontius, S.B. and Tham, M.J.: "North Cross (Devonian) Unit CO_2 Flood-Review of Flood Performance and Numerical Simulation Model," J. Pet. Tech. (Dec. 1978) 1706.

29. Henry, R.L. and Metcalfe, R.S.: "Multiple-Phase Generation During Carbon Dioxide Flooding," Soc. Pet. Eng. J. (Aug. 1983) 595.

30. Heller, J.P., Kovarik, F.S., and Taber, J.J. "Improvement of CO_2 Flood Performance," PRRC Report 87-9, Petroleum Recovery Research Center (October 1987).

31. Orr, F.M., Jr., "Displacement of Oil by Carbon Dioxide," PRRC Report 84-10, Petroleum Recovery Research center (March 1984).

32. Heller, J.P., Kovarik, F.S., and Taber, J.J.: "Improvement of CO_2 Flood Performance," PRRC Report 87-9, New Mexico Institute of Mining and Technology, Socorro (October 1987).

33. Bahralolom, I.M.: "Flow Visualization of CO_2-Crude Oil Mixtures: Solubility Versus Extraction and the Effect of Pore Structure," M.S. Thesis, New Mexico Institute of Mining and Technology, Socorro (May 1985).

34. Huh, D.G., Cochrane, T.D., and Kovarik, F.S.: "The Effect of Microscopic Heterogeneity on CO_2/Foam Mobility: A Mechanistic Study (part 1)," paper SPE 17359 presented at the 1988 SPE/DOE Sixth Joint Symposium on Enhanced Oil Recovery, Tulsa, April 17-20.

35. Roof, J.G.: "Snap-off of Oil Droplets in Water-Wet Pores," Soc. Pet. Eng. J. (March 1970) 85-90.

36. Mast, R.F.: "Microscopic Behavior of Foam in Porous Media," paper SPE 3997 presented at the 1972 SPE Annual Meeting, San Antonio, Oct. 8-11.

37. Radke, C.J. and Ransohoff, T.C.: "Mechanisms of Foam Generation in Glass Bead Packs," SPE Res. Eng. (May 1988) 573-585.

38. Lau, H.C. and O'Brien, S.M.: "Effects of Spreading and Nonspreading Oils on Foam Propagation Through Porous Media," SPE Res. Eng. (August 1988) 893-896.

39. Manlowe, D.J. and Radke, C.J.: "A Pore-Level Investigation of Foam/Oil Interactions in Porous Media," paper SPE 18069 presented at the 1988 SPE Annual Technical Conference and Exhibition, Houston, Oct. 2-5.

40. Chiang, J.C. et al.: "Foam as a Mobility Control Agent in Steam Injection Processes," paper SPE 8912 presented at the 1980 California Regional Meeting, Los Angeles, April 9-11.

41. Huh, D.G. and Handy, L.L.: "Comparison of Steady and Unsteady State Flow of Gas and Foaming Solution in Porous Media," paper SPE 15078 presented at the 1986 California Regional Meeting, Oakland, April 2-4.

42. Falls, A. H., Gauglitz, P. A., Hirasaki, G. J., Miller, D. D., Patzek, T. W., and Ratulowski, J.: "Development of a Mechanistic Foam Simulator: The Population Balance and Generation by Snap-Off," paper SPE/DOE 14961 presented at the 1986 SPE/DOE Fifth Symposium on Enhanced Oil Recovery, Tulsa, OK, April 20-23.

43. Friedmann, F., Chen, W. H., and Gauglitz, P. A.: "Experimental and Simulation Study of High-Temperature Foam Displacement in Porous Media," paper SPE/DOE 17357 presented at the 1988 SPE/DOE Enhanced Oil Recovery Symposium, Tulsa, OK, April 17-20.

44. Aronofsky, J.S.: "Mobility Ratio—Its Influence on Flood Patterns During Water Encroachment," Trans., AIME (1952) 195, 15.

45. Wagner, O.R.: "The Use of Tracers in Diagnosing Interwell Reservoir Heterogeneities—Field Results," J. Pet. Tech. (Nov. 1977), 1410-1416.

46. Carpenter, P.G., Morgan, T.D., and Parsons, E.D.: "Use of Boron Compounds as Water Flood Tracers," Prod. Monthly (1952) 16, No. 12, 12-19.

47. Strum, P.W. and Johnson, W.E.: "Field Experiments with Chemical Tracers in Flood Waters," Prod. Monthly (1951) 15, No. 2, 11-18.

48. deJong, G., Josselin: "Longitudinal and Transverse Diffusion in Granular Deposits," Trans., Am. Geophys. Union (1958) 39, 67-74.

49. Bear, J.: "On the Tensor Form of Dispersion in Porous Media," J. Geophys. Res. (1961) 66, No. 4, 1185-1198.

50. Blackwell, R.J.: "Laboratory Studies of Microscopic Dispersion Phenomena," Soc. Pet. Eng. J. (March, 1962) 1-8.

51. Perkins T.K. and Johnston O.C.: "A Review of Diffusion and Dispersion in Porous Media," Soc. Pet. Eng. J. (Mar. 1963).

52. Brigham, W.E. and Smith, D.H.: "Prediction of Tracer Behavior in Five Spots," paper SPE 1130 presented at the 1965 40th Annual Fall Meeting of SPE-AIME, Denver.

53. Baldwin, D.E., Jr.: "Prediction of Tracer Performance in a Five Spot Pattern," J. Pet. Tech. (April, 1966) 513-517.

54. Abbaszadeh-Dehghani M. and Brigham W.E.: "Analysis of Unit Mobility Ratio Well-to-Well Tracer Flow to Determine Reservoir Heterogeneity," DOE, DOE/SF/11564-1 (1983).

55. Lau, L.K., Daufman, W.J., and Todd, D.K.: "Dispersion of a Water Tracer in Radial Laminar Flow Through Homogeneous Porous Media," Sanitary Engineering Research Lab., U. of California at Berkeley (1959), Progress Report No. 5.

56. Brigham, W.E.: "Mixing Equations in Various Geometries," paper SPE 4585, SPE Res. Eng. (1986) 203-208.

57. Heller, J.P.: "Mobility Control For CO_2 Injection," DOE/MC/16426-19 (Aug. 1986) 111-136.

58. Prats, M. et al.: "Single Fluid Five-Spot Floods in Dipping Reservoirs," Trans., AIME (1955) 204, 160.

59. Morel-Seytoux, H.J.: "Unit Mobility Ratio Displacement Calculations for Pattern Floods in Homogeneous Medium," Trans., AIME (1966) 237, 217.

60. Ghori, S.G.: "Numerical Simulation of Miscible Displacement of a Tracer Slug in Homogeneous Five-Spot Pattern," MS thesis, New Mexico Inst. of Mining and Technology, Socorro (1988).

61. Muskat, M.: Flow of Homogeneous Fluids in Porous Media, J. Edwards, Inc., Ann Arbor, MI (1946).

62. Swearingen, J.S.: "Predicting Wet-Gas Recovery in Recycling Operations," The Oil Weekly (1939) 96, No. 3, 30.

63. Odeh, A.S., Bradley, H.B., and Heller, J.P.: "Scale Limitations in Potentiometric Model Construction," Trans., AIME (1956) **209**, 200.

64. Bradley, H.B., Heller, J.P., and Odeh, A.S.: "A Potentiometric Study of the Effects of Mobility Ratio on Reservoir Flow Patterns," Trans., AIME (1961) **222**, 125.

65. Wyckoff, R.D. et al.: "Mechanics of Porous Flow Applied to Water-flooding Problems," Trans., AIME (1933), **103**, 219.

66. Burton, M.B. and Crawford, P.B.: "Application of the Gelatin Model for Studying Mobility Ratio Effects," Trans., AIME (1956) **207**, 333.

67. Hurst, W.: "Determination of Performance Curve in Five-Spot Water Flood," Petr. Eng. (1953), **25**, B40-46.

68. Prats, M., Strickler, W.R., and Mathews, C.S.: "Single-Fluid Five-Spot Floods in Dipping Reservoirs," Trans., AIME (1956) **204**, 160.

69. McCarty, D.G. and Barfield, E.C.: "The Use of High-Speed Computers for Predicting Flood-Out Patterns," Trans., AIME (1958) **213**, 139.

70. Warren, J.E. and Price, H.S.: "An Evaluation of the Significance of Permeability Measurements," J. Pet. Tech. (1961) **13**, 739.

71. Law, J.: "A Statistical Approach to the Interstitial Heterogeneity of Sand Reservoirs," Trans., AIME (1944) **155**, 202.

72 Bulens, A.C.: "An Application of Statistical Methods to Core Analysis Data of Dolomitic Limestones," Trans., AIME, (1946) **165**, 297.

73. Warren, J.E. and Price H.S.: "Flow in Heterogeneous Porous Media," Soc. Pet. Eng. J. (Sept. 1961) 153.

74. Heller, J.P.: "Observations of Mixing and Diffusion in Porous Media," Proc., Second Symposium, Fundamentals of Transport Phenomena in Porous Media," IAHR-ISSS, Ontario (1972).

75. Smith, L. and Freeze, R.A.: "Stochastic Analysis of Steady State Groundwater Flow in a Bounded Domain, 1, One-Dimensional Simulations," Water Resour. Res. (1979) **15**, No. 3, 521.

76. Smith, L. and Freeze, R.A.: "Stochastic Analysis of Steady State Groundwater Flow in a Bounded Domain, 2, Two-Dimensional Simulations," Water Resour. Res. (1979) **15**, No. 6, 1543.

77. Gelhar, L.W.: "Effects of Hydraulic Conductivity Variations in Groundwater Flows," Second International IAHR Symposium on Stochastic Hydraulics, Lund, Sweden (1976).

78. Bakr, A.A.: "Stochastic Analysis of the Effect of Spatial Variations of Hydraulic Conductivity on Groundwater Flow," PhD dissertation, New Mexico Inst. of Mining and Technology, Socorro (1976).

79. Bakr, A.A., Gelhar, L.W., Gutjahr, A.L., and MacMillan J.R.: "Stochastic Analysis of Spatial Variability in Subsurface Flows, 1, Comparison of One- and Three-Dimensional Flows," Water Resour. Res. (1978), **14**, No. 2, 263.

80. McMillan, W.D.: "Theoretical Analysis of Groundwater Basin Operations," Hydraul. Lab., Univ. of Calif., Berkeley Tech. Rep., 6-25.

81. Freeze, R.A.: "A Stochastic-Conceptual Analysis of One-Dimensional Groundwater Flow in Nonuniform Homogeneous Media," Water Resour. Res. (1975) **11**, No. 5, 725.

82. Smith, L. and Schwartz, F.W.: "Mass Transport, 1, A Stochastic Analysis of Macroscopic Dispersion," Water Resour. Res. (1980) **16**, No. 2, 303.

83. Matheron, G.: "The Intrinsic Random Functions and Their Applications," Adv. Appl. Prob. (1973) **5**, 439.

84. Montoglou, A. and Wilson, J.L.: "The Turning Bands Method for Simulation of Random Fields Using Line Generation by a Spectral Method," Water Resour. Res. (1982) **18**, No. 5, 1379.

85. Bras, L.R. and Rodriguez-Iturbe, I.: Random Functions and Hydrology, Addison-Wesley Publishing Company, Massachusetts (1985).

86. Hewett, T.A.: "Fractal Distribution of Reservoir Heterogeneity and Their Influence on Fluid Transport," paper SPE 15386 presented at the 1986 SPE Annual Technical Conference and Exhibition, New Orleans, Oct. 5-8.

87. Mandelbrot, B.B.: The Fractal Geometry of Nature, Freeman, New York (1977, rev. 1983).

88. Burden, R.L. and Faires, J.D.: Numerical Analysis, Prindle, Weber & Schmidt, Boston (1981).

89. Dykstra, H. and Parsons, R.L.: "The Prediction of Oil Recovery by Waterflooding," Secondary Recovery of Oil in the United States, Second Edition, API, New York, NY (1950).

90. Willhite, G.P.: Waterflooding, Society of Petroleum Engineers, Richardson, TX (1986).

91. Heravi, N.E.: (1988) "Five-Spot Displacement at Unit Mobility Ratio in Reservoirs with Heterogeneous Permeability," MS thesis, New Mexico Inst. of Mining and Technology, Socorro (1988).

92. Morineau, Y., Simandoux, P., and Dupuy, M.: "Etude des hétérogénéités de perméabilités dans les milieux poreux." Compte rendu du IIème Colloque ARTFP (Rueil, May 31-June 4/1965) pp. 273-299.

93. Heller, J.P. "Interpretation of Model Experiments for Displacement of Fluids Through Porous Media," AIChE J. (July 1963) 456-459.

94. Withjack, E.M.: "Computed Tomography for Rock-Property Determination and Fluid-Flow Visualization," paper SPE 16951 presented at the 1987 SPE Annual Meeting, Dallas, Sept. 27-30.

95. Heller, J.P. and Kovarik, F.S.: "Improvement of CO_2 Flood Performance," Annual Report to DOE and NMRDI, PRRC #86-18, New Mexico Petroleum Recovery Research Center (1986).

96. Heller, J.P., Dandge, D.K., Donaruma, L.G., and Card, R.G.: "Direct Thickeners for Mobility Control of CO_2 Floods," Soc. Petr. Eng. J. (Oct. 1985) 679-686.

97. Dandge, D.K. and Heller, J.P.: "Polymers for Mobility Control in CO_2 Floods," paper SPE 16271 presented at the 1987 SPE International Symposium on Oilfield Chemistry, San Antonio, Texas, Feb 4-6.

98. Hildebrand, J.H. and Scott, R.L.: Solubility of Non-Electrolytes, 3rd Ed., Reinhold Publ. Corporation, New York (1950).

99. Barton, A.F.M: "Handbook of Solubility Parameters and Other Cohesion Parameters" CRC Press, Boca Raton, Florida (1983).

100. Makowski, H.S., Lundberg, R.D., Westerman, L., and Bock, J.: "Synthesis and Properties of Sulfonated EPDM," Ions in Polymers, American Chemical Society (1980) 3-19.

101. Taylor, C.: "Synthesis, Characterization, and Solution Properties of Trialkyltin Fluorides," MS thesis, New Mexico Inst. of Mining and Technology, Socorro (1987).

102. Singh, P. "Synthesis, Characterizaiton, and Solution Properties of 5 Triorganotin Fluorides," MS thesis, New Mexico Inst. of Mining and Technology, Socorro (1988).

103. Dandge, D.K., Taylor, C., and Heller, J.P.: "Associative Organotin Polymers: 1, Symmetric Trialkyltin Fluorides: Synthesis and Properties," accepted for publication in J. Appl Polymer Sci-Chemistry.

104. Dandge, D.K., Taylor, C., Heller, J.P., Wilson, K.V., and Brumley, N.: "Associative Organotin Polymers: 2. Solution Properties of Symmetric Trialkyltin Fluorides," accepted by J. Macromol. Science-Chem.

105. Dandge, D.K., Singh, P.K., and Heller, J.P.: "Associative Organotin Polymers: 5, Organotin Polymers in Miscible Gas Enhanced Oil Recovery," presented at the 1988 Symposium on Advances in Oilfield Chemistry, Division of Petr. Chem, Amer. Chem. Soc., Toronto, June 5-11. To be published in ACS Symposium Volume.

106. Dunn, P. and Oldfield, D.J.: Macromol. Sci. Chem. (1970) A4, 1157.

107. Reichle, W.T.: "Tetraneophyltin and Its Derivatives: The Effects of Steric Hindrance in Organotin Chemistry, J. Inorg. Chem. (1966), 5, 87.

108. Heller, J.P. and Dandge, D.K.: "Topical Viscosity Control for Light Hydrocarbon Displacing Fluids in Petroleum Recovery and in Fracturing Fluids for Well Stimulation," U.S. Patent 4,607,696 (1986).

109. Seyferth, D.J.: "Neopentyl Group Analog. I. The Preparation and Some Cleavage REactions of Trimethylsilyl Methyl-Substituted Tin Compounds," J. Am. Chem. Soc. (1957) 79, 5881.

110. Hildebrand, J.H.: Ind. Eng. Chem. Fundm. 1978, 17, 365-366.

111. Handbook of Chemistry and Physics (CRC Publ.)

112. Aronofsky, J.S., Cull, G.W.L., Cox, T.F., and Gaffney, P.D.: "Use and Abuse of Reservoir Simulation-1," Oil and Gas J. (Nov. 5, 1984) 79-82.

113. Aronofsky, J.S., Cull, G.W.L., Cox, T.F., and Gaffney, P.D.: "Use and Abuse of Reservoir Simulation-2," Oil and Gas J. (Nov.19, 1984) 109-110.

114. Aronofsky, J.S., Cull, G.W.L., Cox, T.F., and Gaffney, P.D.: "Use and Abuse of Reservoir Simulation-3," Oil and Gas J. (Dec. 3, 1984) 116-118.

APPENDIX A

Example of Detailed Compositional Analyses of Produced Fluid Samples from CPE 210 Used in the LBC Comparison

TABLE 1. COMPOSITIONS OF GAS AND LIQUIDS FOR UPPER PHASE SAMPLE 1

TOTAL WEIGHT OF OIL = 7.43 TOTAL VOLUME OF GAS = 0.00 TOTAL WEIGHT OF GAS = 0.00 MOLE WEIGHT OF C37+ =563.20

DENSITY = 0.8359 VISCOSITY = 4.3000

	GAS ANALYSIS				LIQUID ANALYSIS				RECOMBINED DATA				
C#	WT FR	CUM	MOL FR	CUM	WT FR	CUM	MOL FR	CUM	WT FR	CUM	MOL FR	CUM	MOLES
CO2	0.1427		0.2023		0.0000		0.0000		0.0000		0.0000		0.00000
1	0.0000	0.0000	0.0000	0.0000	0.0000	0.0000	0.0000	0.0000	0.0000	0.0000	0.0000	0.0000	0.00000
2	0.0000	0.0000	0.0000	0.0000	0.0000	0.0000	0.0000	0.0000	0.0000	0.0000	0.0000	0.0000	0.00000
3	0.0867	0.0867	0.1226	0.1226	0.0000	0.0000	0.0000	0.0000	0.0000	0.0000	0.0000	0.0000	0.00000
4	0.2527	0.3394	0.2714	0.3940	0.0000	0.0000	0.0000	0.0000	0.0000	0.0000	0.0000	0.0000	0.00000
5	0.2420	0.5814	0.2093	0.6033	0.0153	0.0153	0.0440	0.0440	0.0153	0.0153	0.0440	0.0440	0.00157
6	0.2216	0.8030	0.1605	0.7638	0.0296	0.0448	0.0713	0.1152	0.0296	0.0448	0.0713	0.1152	0.00255
7	0.0543	0.8573	0.0338	0.7977	0.0599	0.1047	0.1241	0.2394	0.0599	0.1047	0.1241	0.2394	0.00444
8	0.0000	0.8573	0.0000	0.7977	0.0640	0.1687	0.1164	0.3558	0.0640	0.1687	0.1164	0.3558	0.00416
9	0.0000	0.8573	0.0000	0.7977	0.0392	0.2078	0.0633	0.4191	0.0392	0.2078	0.0633	0.4191	0.00226
10	0.0000	0.8573	0.0000	0.7977	0.0376	0.2455	0.0550	0.4740	0.0376	0.2455	0.0550	0.4740	0.00196
11					0.0362	0.2817	0.0481	0.5222	0.0362	0.2817	0.0481	0.5222	0.00172
12					0.0361	0.3178	0.0441	0.5662	0.0361	0.3178	0.0441	0.5662	0.00157
13					0.0322	0.3500	0.0363	0.6025	0.0322	0.3500	0.0363	0.6025	0.00130
14					0.0409	0.3910	0.0429	0.6454	0.0409	0.3910	0.0429	0.6454	0.00153
15					0.0322	0.4232	0.0315	0.6769	0.0322	0.4232	0.0315	0.6769	0.00113
16					0.0318	0.4549	0.0291	0.7061	0.0318	0.4549	0.0291	0.7061	0.00104
17					0.0321	0.4871	0.0278	0.7339	0.0321	0.4871	0.0278	0.7339	0.00099
18					0.0245	0.5116	0.0200	0.7539	0.0245	0.5116	0.0200	0.7539	0.00072
19					0.0291	0.5407	0.0225	0.7764	0.0291	0.5407	0.0225	0.7764	0.00080
20					0.0223	0.5630	0.0164	0.7928	0.0223	0.5630	0.0164	0.7928	0.00059
21					0.0215	0.5845	0.0151	0.8079	0.0215	0.5845	0.0151	0.8079	0.00054
22					0.0221	0.6066	0.0148	0.8226	0.0221	0.6066	0.0148	0.8226	0.00053
23					0.0203	0.6269	0.0130	0.8356	0.0203	0.6269	0.0130	0.8356	0.00047
24					0.0139	0.6408	0.0086	0.8442	0.0139	0.6408	0.0086	0.8442	0.00031
25					0.0198	0.6607	0.0117	0.8559	0.0198	0.6607	0.0117	0.8559	0.00042
26					0.0205	0.6812	0.0116	0.8675	0.0205	0.6812	0.0116	0.8675	0.00041
27					0.0136	0.6947	0.0074	0.8749	0.0136	0.6947	0.0074	0.8749	0.00027
28					0.0140	0.7088	0.0074	0.8823	0.0140	0.7088	0.0074	0.8823	0.00026
29					0.0213	0.7301	0.0109	0.8931	0.0213	0.7301	0.0109	0.8931	0.00039
30					0.0139	0.7440	0.0068	0.9000	0.0139	0.7440	0.0068	0.9000	0.00024
31					0.0142	0.7582	0.0067	0.9067	0.0142	0.7582	0.0067	0.9067	0.00024
32					0.0126	0.7708	0.0058	0.9125	0.0126	0.7708	0.0058	0.9125	0.00021
33					0.0125	0.7832	0.0056	0.9181	0.0125	0.7832	0.0056	0.9181	0.00020
34					0.0122	0.7954	0.0053	0.9234	0.0122	0.7954	0.0053	0.9234	0.00019
35					0.0124	0.8078	0.0052	0.9286	0.0124	0.8078	0.0052	0.9286	0.00019
36					0.0123	0.8201	0.0051	0.9336	0.0123	0.8201	0.0051	0.9336	0.00018
37+					0.1799	1.0000	0.0664	1.0000	0.1799	1.0000	0.0664	1.0000	0.00237

AVERAGE MOLE WEIGHTS: OIL = 207.797 GAS = 62.410 HYDROCARBONS = 207.797 OVERALL = 207.797
C7+ MW= 224.333449867

TABLE 3. COMPOSITIONS OF GAS AND LIQUIDS FOR UPPER PHASE SAMPLE 2

TOTAL WEIGHT OF OIL = 5.16 TOTAL VOLUME OF GAS = 0.93 TOTAL WEIGHT OF GAS = 0.46 MOLE WEIGHT OF C37+ =563.20

DENSITY = 0.8416 VISCOSITY = 2.7800

	GAS ANALYSIS				LIQUID ANALYSIS				RECOMBINED DATA				
C#	WT FR	CUM	MOL FR	CUM	WT FR	CUM	MOL FR	CUM	WT FR	CUM	MOL FR	CUM	MOLES
CO2	0.7029		0.7836		0.0000		0.0000		0.0570		0.2279		0.00728
1	0.0000	0.0000	0.0000	0.0000	0.0000	0.0000	0.0000	0.0000	0.0000	0.0000	0.0000	0.0000	0.00000
2	0.0000	0.0000	0.0000	0.0000	0.0000	0.0000	0.0000	0.0000	0.0000	0.0000	0.0000	0.0000	0.00000
3	0.0214	0.0214	0.0238	0.0238	0.0000	0.0000	0.0000	0.0000	0.0017	0.0017	0.0069	0.0069	0.00022
4	0.0963	0.1176	0.0813	0.1050	0.0000	0.0000	0.0000	0.0000	0.0078	0.0095	0.0236	0.0306	0.00075
5	0.1002	0.2178	0.0681	0.1732	0.0109	0.0109	0.0344	0.0344	0.0181	0.0276	0.0442	0.0747	0.00141
6	0.0557	0.2735	0.0317	0.2049	0.0271	0.0379	0.0716	0.1060	0.0294	0.0570	0.0600	0.1347	0.00192
7	0.0236	0.2971	0.0116	0.2164	0.0445	0.0824	0.1012	0.2072	0.0428	0.0998	0.0752	0.2099	0.00240
8	0.0000	0.2971	0.0000	0.2164	0.0431	0.1255	0.0861	0.2933	0.0396	0.1394	0.0611	0.2709	0.00195
9	0.0000	0.2971	0.0000	0.2164	0.0304	0.1559	0.0538	0.3471	0.0279	0.1673	0.0382	0.3091	0.00122
10	0.0000	0.2971	0.0000	0.2164	0.0371	0.1929	0.0594	0.4065	0.0341	0.2014	0.0421	0.3512	0.00135
11					0.0357	0.2286	0.0521	0.4586	0.0328	0.2342	0.0369	0.3881	0.00118
12					0.0356	0.2643	0.0477	0.5063	0.0328	0.2669	0.0338	0.4220	0.00108
13					0.0317	0.2959	0.0392	0.5455	0.0291	0.2960	0.0278	0.4498	0.00089
14					0.0404	0.3364	0.0465	0.5920	0.0371	0.3332	0.0330	0.4827	0.00105
15					0.0316	0.3680	0.0340	0.6259	0.0291	0.3623	0.0241	0.5068	0.00077
16					0.0312	0.3992	0.0314	0.6574	0.0287	0.3909	0.0223	0.5291	0.00071
17					0.0316	0.4308	0.0300	0.6873	0.0290	0.4200	0.0213	0.5504	0.00068
18					0.0242	0.4550	0.0217	0.7090	0.0222	0.4422	0.0154	0.5657	0.00049
19					0.0286	0.4836	0.0243	0.7333	0.0263	0.4685	0.0172	0.5829	0.00055
20					0.0219	0.5054	0.0176	0.7509	0.0201	0.4885	0.0125	0.5955	0.00040
21					0.0211	0.5265	0.0162	0.7672	0.0194	0.5079	0.0115	0.6070	0.00037
22					0.0216	0.5481	0.0158	0.7830	0.0198	0.5277	0.0112	0.6182	0.00036
23					0.0199	0.5680	0.0140	0.7970	0.0183	0.5460	0.0099	0.6281	0.00032
24					0.0136	0.5815	0.0091	0.8061	0.0125	0.5585	0.0065	0.6346	0.00021
25					0.0193	0.6008	0.0124	0.8185	0.0177	0.5762	0.0088	0.6434	0.00028
26					0.0200	0.6208	0.0124	0.8310	0.0184	0.5945	0.0088	0.6522	0.00028
27					0.0129	0.6337	0.0077	0.8387	0.0119	0.6064	0.0055	0.6577	0.00018
28					0.0135	0.6472	0.0078	0.8465	0.0124	0.6188	0.0055	0.6632	0.00018
29					0.0205	0.6677	0.0114	0.8579	0.0188	0.6376	0.0081	0.6713	0.00026
30					0.0132	0.6808	0.0071	0.8650	0.0121	0.6497	0.0050	0.6764	0.00016
31					0.0133	0.6941	0.0069	0.8720	0.0122	0.6619	0.0049	0.6813	0.00016
32					0.0118	0.7059	0.0059	0.8779	0.0108	0.6727	0.0042	0.6855	0.00013
33					0.0116	0.7175	0.0057	0.8836	0.0107	0.6834	0.0040	0.6895	0.00013
34					0.0113	0.7288	0.0054	0.8890	0.0104	0.6938	0.0038	0.6934	0.00012
35					0.0114	0.7402	0.0053	0.8943	0.0104	0.7042	0.0037	0.6971	0.00012
36					0.0112	0.7514	0.0051	0.8993	0.0103	0.7145	0.0036	0.7007	0.00011
37+					0.2486	1.0000	0.1007	1.0000	0.2285	0.9430	0.0714	0.7721	0.00228

AVERAGE MOLE WEIGHTS: OIL = 228.079 GAS = 49.062 HYDROCARBONS = 214.974 OVERALL = 176.008
C7+ MW= 244.667361035

APPENDIX B

Example of Detailed Compositional Analyses of Produced Fluid Samples from CPE 234 Used in the LBC Comparison

TABLE 5. COMPOSITIONS OF GAS AND LIQUIDS FOR UPPER PHASE SAMPLE 3

TOTAL WEIGHT OF OIL = 6.09 TOTAL VOLUME OF GAS = 1.09 TOTAL WEIGHT OF GAS = 0.51 MOLE WEIGHT OF C37+ =563.20

DENSITY = 0.8590 VISCOSITY = 2.8690

	GAS ANALYSIS				LIQUID ANALYSIS				RECOMBINED DATA				
C#	WT FR	CUM	MOL FR	CUM	WT FR	CUM	MOL FR	CUM	WT FR	CUM	MOL FR	CUM	MOLES
CO2	0.8629		0.9128		0.0000		0.0000		0.0663		0.2650		0.00994
1	0.0000	0.0000	0.0000	0.0000	0.0000	0.0000	0.0000	0.0000	0.0000	0.0000	0.0000	0.0000	0.00000
2	0.0000	0.0000	0.0000	0.0000	0.0000	0.0000	0.0000	0.0000	0.0000	0.0000	0.0000	0.0000	0.00000
3	0.0000	0.0000	0.0000	0.0000	0.0000	0.0000	0.0000	0.0000	0.0000	0.0000	0.0000	0.0000	0.00000
4	0.0419	0.0419	0.0336	0.0336	0.0000	0.0000	0.0000	0.0000	0.0032	0.0032	0.0098	0.0098	0.00037
5	0.0358	0.0777	0.0231	0.0567	0.0151	0.0151	0.0480	0.0480	0.0167	0.0200	0.0408	0.0505	0.00153
6	0.0457	0.1234	0.0247	0.0813	0.0219	0.0370	0.0581	0.1061	0.0237	0.0437	0.0484	0.0989	0.00181
7	0.0039	0.1273	0.0018	0.0832	0.0491	0.0861	0.1121	0.2181	0.0456	0.0893	0.0801	0.1789	0.00300
8	0.0098	0.1371	0.0040	0.0872	0.0485	0.1346	0.0971	0.3153	0.0455	0.1348	0.0701	0.2490	0.00263
9	0.0000	0.1371	0.0000	0.0872	0.0459	0.1806	0.0817	0.3969	0.0424	0.1772	0.0580	0.3070	0.00217
10	0.0000	0.1371	0.0000	0.0872	0.0402	0.2208	0.0647	0.4616	0.0371	0.2144	0.0459	0.3529	0.00172
11					0.0291	0.2499	0.0426	0.5042	0.0269	0.2412	0.0302	0.3831	0.00113
12					0.0343	0.2842	0.0460	0.5502	0.0317	0.2729	0.0327	0.4158	0.00123
13					0.0257	0.3099	0.0319	0.5821	0.0238	0.2966	0.0227	0.4384	0.00085
14					0.0323	0.3422	0.0373	0.6194	0.0298	0.3265	0.0264	0.4649	0.00099
15					0.0255	0.3677	0.0274	0.6468	0.0235	0.3500	0.0195	0.4843	0.00073
16					0.0249	0.3926	0.0252	0.6720	0.0230	0.3730	0.0179	0.5022	0.00067
17					0.0198	0.4125	0.0189	0.6909	0.0183	0.3913	0.0134	0.5156	0.00050
18					0.0255	0.4380	0.0229	0.7138	0.0235	0.4148	0.0163	0.5318	0.00061
19					0.0187	0.4567	0.0159	0.7297	0.0173	0.4321	0.0113	0.5431	0.00042
20					0.0185	0.4752	0.0150	0.7447	0.0171	0.4492	0.0106	0.5538	0.00040
21					0.0179	0.4931	0.0138	0.7585	0.0165	0.4657	0.0098	0.5636	0.00037
22					0.0178	0.5109	0.0131	0.7716	0.0165	0.4822	0.0093	0.5729	0.00035
23					0.0170	0.5279	0.0120	0.7836	0.0157	0.4978	0.0085	0.5814	0.00032
24					0.0115	0.5394	0.0077	0.7913	0.0106	0.5084	0.0055	0.5869	0.00021
25					0.0215	0.5609	0.0140	0.8053	0.0199	0.5283	0.0099	0.5968	0.00037
26					0.0113	0.5722	0.0070	0.8123	0.0104	0.5387	0.0050	0.6018	0.00019
27					0.0114	0.5836	0.0068	0.8191	0.0105	0.5492	0.0048	0.6066	0.00018
28					0.0114	0.5949	0.0066	0.8257	0.0105	0.5597	0.0047	0.6113	0.00018
29					0.0115	0.6064	0.0064	0.8322	0.0106	0.5704	0.0046	0.6159	0.00017
30					0.0114	0.6179	0.0062	0.8383	0.0105	0.5809	0.0044	0.6203	0.00016
31					0.0171	0.6350	0.0090	0.8473	0.0158	0.5967	0.0064	0.6266	0.00024
32					0.0114	0.6464	0.0058	0.8531	0.0105	0.6072	0.0041	0.6307	0.00015
33					0.0173	0.6637	0.0085	0.8616	0.0160	0.6232	0.0060	0.6368	0.00023
34					0.0121	0.6758	0.0058	0.8674	0.0112	0.6344	0.0041	0.6409	0.00015
35					0.0064	0.6822	0.0030	0.8704	0.0059	0.6403	0.0021	0.6430	0.00008
36					0.0130	0.6952	0.0059	0.8762	0.0120	0.6523	0.0042	0.6471	0.00016
37+					0.3048	1.0000	0.1238	1.0000	0.2814	0.9337	0.0878	0.7350	0.00329

AVERAGE MOLE WEIGHTS: OIL = 228.698 GAS = 46.556 HYDROCARBONS = 223.345 OVERALL = 175.817
C7+ MW= 245.998770559

TABLE 7. COMPOSITIONS OF GAS AND LIQUIDS FOR UPPER PHASE SAMPLE 4

TOTAL WEIGHT OF OIL = 4.56 TOTAL VOLUME OF GAS = 2.27 TOTAL WEIGHT OF GAS = 1.05 MOLE WEIGHT OF C37+ =563.20

DENSITY = 0.8650 VISCOSITY = 1.4790

	GAS ANALYSIS				LIQUID ANALYSIS				RECOMBINED DATA				
C#	WT FR	CUM	MOL FR	CUM	WT FR	CUM	MOL FR	CUM	WT FR	CUM	MOL FR	CUM	MOLES
CO2	0.8845		0.9324		0.0000		0.0000		0.1659		0.4962		0.02114
1	0.0000	0.0000	0.0000	0.0000	0.0000	0.0000	0.0000	0.0000	0.0000	0.0000	0.0000	0.0000	0.00000
2	0.0000	0.0000	0.0000	0.0000	0.0000	0.0000	0.0000	0.0000	0.0000	0.0000	0.0000	0.0000	0.00000
3	0.0000	0.0000	0.0000	0.0000	0.0000	0.0000	0.0000	0.0000	0.0000	0.0000	0.0000	0.0000	0.00000
4	0.0198	0.0198	0.0158	0.0158	0.0000	0.0000	0.0000	0.0000	0.0037	0.0037	0.0084	0.0084	0.00036
5	0.0302	0.0500	0.0194	0.0352	0.0151	0.0151	0.0480	0.0480	0.0180	0.0217	0.0328	0.0412	0.00140
6	0.0404	0.0904	0.0217	0.0570	0.0219	0.0370	0.0581	0.1061	0.0253	0.0470	0.0387	0.0799	0.00165
7	0.0117	0.1021	0.0054	0.0624	0.0491	0.0861	0.1121	0.2181	0.0421	0.0891	0.0553	0.1352	0.00236
8	0.0083	0.1104	0.0034	0.0658	0.0485	0.1346	0.0971	0.3153	0.0410	0.1301	0.0472	0.1825	0.00201
9	0.0051	0.1155	0.0018	0.0676	0.0459	0.1806	0.0817	0.3969	0.0383	0.1684	0.0392	0.2217	0.00167
10	0.0000	0.1155	0.0000	0.0676	0.0402	0.2208	0.0647	0.4616	0.0327	0.2011	0.0302	0.2519	0.00129
11					0.0291	0.2499	0.0426	0.5042	0.0236	0.2247	0.0199	0.2718	0.00085
12					0.0343	0.2842	0.0460	0.5502	0.0279	0.2526	0.0215	0.2934	0.00092
13					0.0257	0.3099	0.0319	0.5821	0.0209	0.2735	0.0149	0.3083	0.00064
14					0.0323	0.3422	0.0373	0.6194	0.0263	0.2997	0.0174	0.3257	0.00074
15					0.0255	0.3677	0.0274	0.6468	0.0207	0.3204	0.0128	0.3385	0.00055
16					0.0249	0.3926	0.0252	0.6720	0.0203	0.3407	0.0118	0.3503	0.00050
17					0.0198	0.4125	0.0189	0.6909	0.0161	0.3568	0.0088	0.3592	0.00038
18					0.0255	0.4380	0.0229	0.7138	0.0207	0.3775	0.0107	0.3699	0.00046
19					0.0187	0.4567	0.0159	0.7297	0.0152	0.3927	0.0074	0.3773	0.00032
20					0.0185	0.4752	0.0150	0.7447	0.0150	0.4077	0.0070	0.3843	0.00030
21					0.0179	0.4931	0.0138	0.7585	0.0145	0.4223	0.0065	0.3908	0.00027
22					0.0178	0.5109	0.0131	0.7716	0.0145	0.4368	0.0061	0.3969	0.00026
23					0.0170	0.5279	0.0120	0.7836	0.0138	0.4506	0.0056	0.4025	0.00024
24					0.0115	0.5394	0.0077	0.7913	0.0093	0.4599	0.0036	0.4061	0.00015
25					0.0215	0.5609	0.0140	0.8053	0.0175	0.4774	0.0065	0.4127	0.00028
26					0.0113	0.5722	0.0070	0.8123	0.0092	0.4866	0.0033	0.4160	0.00014
27					0.0114	0.5836	0.0068	0.8191	0.0092	0.4958	0.0032	0.4192	0.00014
28					0.0114	0.5949	0.0066	0.8257	0.0092	0.5050	0.0031	0.4222	0.00013
29					0.0115	0.6064	0.0064	0.8322	0.0093	0.5144	0.0030	0.4253	0.00013
30					0.0114	0.6179	0.0062	0.8383	0.0093	0.5237	0.0029	0.4281	0.00012
31					0.0171	0.6350	0.0090	0.8473	0.0139	0.5376	0.0042	0.4323	0.00018
32					0.0114	0.6464	0.0058	0.8531	0.0093	0.5468	0.0027	0.4350	0.00012
33					0.0173	0.6637	0.0085	0.8616	0.0141	0.5609	0.0040	0.4390	0.00017
34					0.0121	0.6758	0.0058	0.8674	0.0099	0.5708	0.0027	0.4417	0.00012
35					0.0064	0.6822	0.0030	0.8704	0.0052	0.5759	0.0014	0.4431	0.00006
36					0.0130	0.6952	0.0059	0.8762	0.0105	0.5865	0.0027	0.4459	0.00012
37+					0.3048	1.0000	0.1238	1.0000	0.2477	0.8341	0.0579	0.5038	0.00247

AVERAGE MOLE WEIGHTS: OIL = 228.698 GAS = 46.393 HYDROCARBONS = 218.025 OVERALL = 131.673
C7+ MW= 244.535935355

APPENDIX C

Critical Temperatures and Pressures Using the Lin-Chao Correlations

```
1
2     Critical Properties Calculation for the CO2-
3        Maljamar Stock Tank Oil Run (CPE 210)
4
5  ***************************************************
6          Lin-Chao Critical Properties Correlation
7
8      mal_210.dat    (s1u.dat)
9
10     Avg. Molecular Weigth      =  224.3800048 g/gmol
11     Pseudocritical Temperature =  717.463807788318490 K
12     Pseudocritical Pressure    =  13.997111847353736 atm
13     Pseudocritical Molar Vol.  =  946.018933646002440 cc/mol
14     Pseudo Acentric Factor     =  .738756685853318
15
16 ***************************************************
17         Lin-Chao Critical Properties Correlation
18
19     mal_210.dat    (s2u.dat)
20
21     Avg. Molecular Weigth      =  244.6000061 g/gmol
22     Pseudocritical Temperature =  735.568742532681540 K
23     Pseudocritical Pressure    =  12.743864127831367 atm
24     Pseudocritical Molar Vol.  =  1032.944937344110900 cc/mol
25     Pseudo Acentric Factor     =  .789964640414737
26
27 ***************************************************
28         Lin-Chao Critical Properties Correlation
29
30     mal_210.dat    (s2l.dat)
31
32     Avg. Molecular Weigth      =  273.0719909 g/gmol
33     Pseudocritical Temperature =  759.828851796534420 K
34     Pseudocritical Pressure    =  11.130090325003165 atm
35     Pseudocritical Molar Vol.  =  1156.696299020385800 cc/mol
36     Pseudo Acentric Factor     =  .849792512947032
37
38 ***************************************************
39         Lin-Chao Critical Properties Correlation
40
41     mal_210.dat    (s3u.dat)
42
43     Avg. Molecular Weigth      =  225.4799957 g/gmol
44     Pseudocritical Temperature =  718.483008190876720 K
45     Pseudocritical Pressure    =  13.926033058600785 atm
46     Pseudocritical Molar Vol.  =  950.728289229859680 cc/mol
47     Pseudo Acentric Factor     =  .741698036856819
48
49 ***************************************************
50         Lin-Chao Critical Properties Correlation
51
52     mal_210.dat    (s3l.dat)
53
54     Avg. Molecular Weigth      =  238.2949981 g/gmol
55     Pseudocritical Temperature =  730.048634259375260 K
56     Pseudocritical Pressure    =  13.123332761428033 atm
57     Pseudocritical Molar Vol.  =  1005.757157927443250 cc/mol
58     Pseudo Acentric Factor     =  .774679462460278
59
60 ***************************************************
61         Lin-Chao Critical Properties Correlation
62
63     mal_210.dat    (s4u.dat)
64
65     Avg. Molecular Weigth      =  214.9900054 g/gmol
66     Pseudocritical Temperature =  708.557101375805700 K
67     Pseudocritical Pressure    =  14.619667917437676 atm
68     Pseudocritical Molar Vol.  =  905.906499478381310 cc/mol
69     Pseudo Acentric Factor     =  .713004034716855
70
71 ***************************************************
72         Lin-Chao Critical Properties Correlation
73
74     mal_210.dat    (s4l.dat)
75
76     Avg. Molecular Weigth      =  237.3070068 g/gmol
77     Pseudocritical Temperature =  729.174792401720650 K
78     Pseudocritical Pressure    =  13.183663122703958 atm
79     Pseudocritical Molar Vol.  =  1001.503710584872470 cc/mol
80     Pseudo Acentric Factor     =  .772225421812151
```

```
81
82  ***************************************************
83          Lin-Chao Critical Properties Correlation
84
85      mal_210.dat    (s61.dat)
86
87      Avg. Molecular Weigth       =  241.2720031 g/gmol
88      Pseudocritical Temperature =  732.666586494836340 K
89      Pseudocritical Pressure     =  12.942992030012933 atm
90      Pseudocritical Molar Vol.   =  1018.584805422550520 cc/mol
91      Pseudo Acentric Factor      =  .781978728912199
92
93  ***************************************************
94          Lin-Chao Critical Properties Correlation
95
96      mal_210.dat    (s71.dat)
97
98      Avg. Molecular Weigth       =  247.0379943 g/gmol
99      Pseudocritical Temperature =  737.680289717076330 K
100     Pseudocritical Pressure     =  12.599574388382440 atm
101     Pseudocritical Molar Vol.   =  1043.478271278890800 cc/mol
102     Pseudo Acentric Factor      =  .795694525578433
103
104 ***************************************************
105         Lin-Chao Critical Properties Correlation
106
107     mal_210.dat    (s81.dat)
108
109     Avg. Molecular Weigth       =  244.8739929 g/gmol
110     Pseudocritical Temperature =  735.806620723339390 K
111     Pseudocritical Pressure     =  12.727582903285427 atm
112     Pseudocritical Molar Vol.   =  1034.128123994552700 cc/mol
113     Pseudo Acentric Factor      =  .790613720105692
114
115 ***************************************************
116         Lin-Chao Critical Properties Correlation
117
118     mal_210.dat    (s91.dat)
119
120     Avg. Molecular Weigth       =  260.6069946 g/gmol
121     Pseudocritical Temperature =  749.273670293016270 K
122     Pseudocritical Pressure     =  11.818699712116508 atm
123     Pseudocritical Molar Vol.   =  1102.316785915555800 cc/mol
124     Pseudo Acentric Factor      =  .825594150567850
125
126 ***************************************************
127         Lin-Chao Critical Properties Correlation
128
129     mal_210.dat    (s101.dat)
130
131     Avg. Molecular Weigth       =  258.7900085 g/gmol
132     Pseudocritical Temperature =  747.732167560855490 K
133     Pseudocritical Pressure     =  11.921236744212059 atm
134     Pseudocritical Molar Vol.   =  1094.416590971080700 cc/mol
135     Pseudo Acentric Factor      =  .821795699237743
136
137 ***************************************************
138         Lin-Chao Critical Properties Correlation
139
140     mal_210.dat    (s111.dat)
141
142     Avg. Molecular Weigth       =  262.7919921 g/gmol
143     Pseudocritical Temperature =  751.125030617029670 K
144     Pseudocritical Pressure     =  11.696160454318139 atm
145     Pseudocritical Molar Vol.   =  1111.825939182441700 cc/mol
146     Pseudo Acentric Factor      =  .830073463645218
147
148 ***************************************************
149         Lin-Chao Critical Properties Correlation
150
151     mal_210.dat    (s121.dat)
152
153     Avg. Molecular Weigth       =  269.9830017 g/gmol
154     Pseudocritical Temperature =  757.211413279990440 K
155     Pseudocritical Pressure     =  11.298456527598498 atm
156     Pseudocritical Molar Vol.   =  1143.190393319280200 cc/mol
157     Pseudo Acentric Factor      =  .844108855112812
158
159 ***************************************************
160         Lin-Chao Critical Properties Correlation
```

```
161
162      mal_210.dat    (s13l.dat)
163
164      Avg. Molecular Weigth       =  285.3609924 g/gmol
165      Pseudocritical Temperature =  770.324631863854170 K
166      Pseudocritical Pressure     =  10.473493536171382 atm
167      Pseudocritical Molar Vol.   =  1210.627262036506900 cc/mol
168      Pseudo Acentric Factor      =  .870211449867093
169
170  ***************************************************
171           Lin-Chao Critical Properties Correlation
172
173      mal_210.dat    (s14l.dat)
174
175      Avg. Molecular Weigth       =  276.4859924 g/gmol
176      Pseudocritical Temperature =  762.728403620679610 K
177      Pseudocritical Pressure     =  10.945626421209685 atm
178      Pseudocritical Molar Vol.   =  1171.646556272674600 cc/mol
179      Pseudo Acentric Factor      =  .855822915457467
180
181  ***************************************************
182           Lin-Chao Critical Properties Correlation
183
184      mal_210.dat    (s15l.dat)
185
186      Avg. Molecular Weigth       =  274.7409973 g/gmol
187      Pseudocritical Temperature =  761.245265949595590 K
188      Pseudocritical Pressure     =  11.039703904164165 atm
189      Pseudocritical Molar Vol.   =  1164.001974784354600 cc/mol
190      Pseudo Acentric Factor      =  .852774008628238
191
```

```
1
2     Critical Properties Calculation for the CO2-
3         Wasson Stock Tank Oil Run (CPE 234)
4
5  ***************************************************
6          Lin-Chao Critical Properties Correlation
7
8      was_234.dat
9
10     Avg. Molecular Weigth       =  244.8999939 g/gmol
11     Pseudocritical Temperature  =  735.829187183537100 K
12     Pseudocritical Pressure     =  12.726038709858770 atm
13     Pseudocritical Molar Vol.   =  1034.240414319017900 cc/mol
14     Pseudo Acentric Factor      =  .790675249762199
15
16 ***************************************************
17         Lin-Chao Critical Properties Correlation
18
19     was_234.dat
20
21     Avg. Molecular Weigth       =  240.2810058 g/gmol
22     Pseudocritical Temperature  =  731.797538528183960 K
23     Pseudocritical Pressure     =  13.002787157029376 atm
24     Pseudocritical Molar Vol.   =  1014.312813051050970 cc/mol
25     Pseudo Acentric Factor      =  .779564975715764
26
27 ***************************************************
28         Lin-Chao Critical Properties Correlation
29
30     was_234.dat
31
32     Avg. Molecular Weigth       =  273.9370117 g/gmol
33     Pseudocritical Temperature  =  760.562723976351550 K
34     Pseudocritical Pressure     =  11.083194293432072 atm
35     Pseudocritical Molar Vol.   =  1160.481988599673100 cc/mol
36     Pseudo Acentric Factor      =  .851345697542316
37
38 ***************************************************
39         Lin-Chao Critical Properties Correlation
40
41     was_234.dat
42
43     Avg. Molecular Weigth       =  259.4100036 g/gmol
44     Pseudocritical Temperature  =  748.258400425384590 K
45     Pseudocritical Pressure     =  11.886182791240003 atm
46     Pseudocritical Molar Vol.   =  1097.111559793827200 cc/mol
47     Pseudo Acentric Factor      =  .823099241777478
48
49 ***************************************************
50         Lin-Chao Critical Properties Correlation
51
52     was_234.dat
53
54     Avg. Molecular Weigth       =  262.3930053 g/gmol
55     Pseudocritical Temperature  =  750.787119612986200 K
56     Pseudocritical Pressure     =  11.718475212273505 atm
57     Pseudocritical Molar Vol.   =  1110.088816247987800 cc/mol
58     Pseudo Acentric Factor      =  .829262820534207
59
60 ***************************************************
61         Lin-Chao Critical Properties Correlation
62
63     was_234.dat
64
65     Avg. Molecular Weigth       =  264.0039978 g/gmol
66     Pseudocritical Temperature  =  752.151189127198900 K
67     Pseudocritical Pressure     =  11.628539742827412 atm
68     Pseudocritical Molar Vol.   =  1117.104803372816600 cc/mol
69     Pseudo Acentric Factor      =  .832515767122002
70
71 ***************************************************
72         Lin-Chao Critical Properties Correlation
73
74     was_234.dat
75
76     Avg. Molecular Weigth       =  215.3840026 g/gmol
77     Pseudocritical Temperature  =  708.938812661267780 K
78     Pseudocritical Pressure     =  14.592947367964960 atm
79     Pseudocritical Molar Vol.   =  907.586428973125180 cc/mol
80     Pseudo Acentric Factor      =  .714106768734468
```

```
81
82  ****************************************************
83          Lin-Chao Critical Properties Correlation
84
85      was_234.dat
86
87      Avg. Molecular Weigth       =  221.9400024 g/gmol
88      Pseudocritical Temperature =  715.185867484054030 K
89      Pseudocritical Pressure     =  14.156114823491027 atm
90      Pseudocritical Molar Vol.   =  935.580460456589320 cc/mol
91      Pseudo Acentric Factor      =  .732174006605057
92
93  ****************************************************
94          Lin-Chao Critical Properties Correlation
95
96      was_234.dat
97
98      Avg. Molecular Weigth       =  225.7989959 g/gmol
99      Pseudocritical Temperature =  718.777707912957000 K
100     Pseudocritical Pressure     =  13.905488646549260 atm
101     Pseudocritical Molar Vol.   =  952.094426759332800 cc/mol
102     Pseudo Acentric Factor      =  .742547938107100
103
104 ****************************************************
105         Lin-Chao Critical Properties Correlation
106
107     was_234.dat
108
109     Avg. Molecular Weigth       =  232.6369934 g/gmol
110     Pseudocritical Temperature =  725.006983123334860 K
111     Pseudocritical Pressure     =  13.472216732077579 atm
112     Pseudocritical Molar Vol.   =  981.423483420549020 cc/mol
113     Pseudo Acentric Factor      =  .760419480235681
114
115 ****************************************************
116         Lin-Chao Critical Properties Correlation
117
118     was_234.dat
119
120     Avg. Molecular Weigth       =  233.8139953 g/gmol
121     Pseudocritical Temperature =  726.063512352329670 K
122     Pseudocritical Pressure     =  13.398952319048270 atm
123     Pseudocritical Molar Vol.   =  986.480531330047370 cc/mol
124     Pseudo Acentric Factor      =  .763426514145698
125
```

APPENDIX D

Specific Gravity Calculations of the C7+ Fractions

Using the Hankinson-Brobst-Thomson Correlation

```
 1
 2   Specific Gravity Calculations of the C7+ Fraction
 3       of the Maljamar Stock Tank Oil (CPE 210)
 4
 5  ****************************************************
 6      HBT Correlation for Saturated and Compressed
 7           Specific Liquid Mixture Volumes
 8
 9      s1u.dat
10
11    Avg. Molecular Weight =  224.3803863 g/gmol
12    Temperature           =  60.0 F
13    Pressure              =  14.696000000000000 psia
14    Satd. Spec. Volume    =  281.971912242441420 cc/gmol
15    Specific Molar Volume =  282.007476729334770 cc/gmol
16    Specific Volume       =  1.25682771 cc/g
17    Specific Gravity      =  .796974788500655
18
19  ****************************************************
20      HBT Correlation for Saturated and Compressed
21           Specific Liquid Mixture Volumes
22
23      s2u.dat
24
25    Avg. Molecular Weight =  244.6000366 g/gmol
26    Temperature           =  60.0 F
27    Pressure              =  14.696000000000000 psia
28    Satd. Spec. Volume    =  304.172181589157110 cc/gmol
29    Specific Molar Volume =  304.210159063016190 cc/gmol
30    Specific Volume       =  1.24370444 cc/g
31    Specific Gravity      =  .805384277185674
32
33  ****************************************************
34      HBT Correlation for Saturated and Compressed
35           Specific Liquid Mixture Volumes
36
37      s2l.dat
38
39    Avg. Molecular Weight =  273.0717163 g/gmol
40    Temperature           =  60.0 F
41    Pressure              =  14.696000000000000 psia
42    Satd. Spec. Volume    =  336.946935852401450 cc/gmol
43    Specific Molar Volume =  336.988112914831790 cc/gmol
44    Specific Volume       =  1.23406446 cc/g
45    Specific Gravity      =  .811675591210001
46
47  ****************************************************
48      HBT Correlation for Saturated and Compressed
49           Specific Liquid Mixture Volumes
50
51      s3u.dat
52
53    Avg. Molecular Weight =  225.4805145 g/gmol
54    Temperature           =  60.0 F
55    Pressure              =  14.696000000000000 psia
56    Satd. Spec. Volume    =  282.263881295974560 cc/gmol
57    Specific Molar Volume =  282.300331394989030 cc/gmol
58    Specific Volume       =  1.25199437 cc/g
59    Specific Gravity      =  .800051520094758
60
61  ****************************************************
62      HBT Correlation for Saturated and Compressed
63           Specific Liquid Mixture Volumes
64
65      s3l.dat
66
67    Avg. Molecular Weight =  238.2946929 g/gmol
68    Temperature           =  60.0 F
69    Pressure              =  14.696000000000000 psia
70    Satd. Spec. Volume    =  296.430349612642660 cc/gmol
71    Specific Molar Volume =  296.468317333071070 cc/gmol
72    Specific Volume       =  1.24412477 cc/g
73    Specific Gravity      =  .805112175258409
74
75  ****************************************************
76      HBT Correlation for Saturated and Compressed
77           Specific Liquid Mixture Volumes
78
79      s4u.dat
80
```

```
   Avg. Molecular Weight =  214.9902801 g/gmol
   Temperature           =  60.0 F
   Pressure              =  14.696000000000000 psia
   Satd. Spec. Volume    =  271.202955605952410 cc/gmol
   Specific Molar Volume =  271.237768012823320 cc/gmol
   Specific Volume       =  1.26162803 cc/g
   Specific Gravity      =  .793942409971632

*****************************************************
     HBT Correlation for Saturated and Compressed
           Specific Liquid Mixture Volumes

     s41.dat

   Avg. Molecular Weight =  237.3071289 g/gmol
   Temperature           =  60.0 F
   Pressure              =  14.696000000000000 psia
   Satd. Spec. Volume    =  295.292643387384370 cc/gmol
   Specific Molar Volume =  295.330528907472000 cc/gmol
   Specific Volume       =  1.24450767 cc/g
   Specific Gravity      =  .804864464737305

*****************************************************
     HBT Correlation for Saturated and Compressed
           Specific Liquid Mixture Volumes

     s61.dat

   Avg. Molecular Weight =  241.2724456 g/gmol
   Temperature           =  60.0 F
   Pressure              =  14.696000000000000 psia
   Satd. Spec. Volume    =  299.968433081770680 cc/gmol
   Specific Molar Volume =  300.006592819393970 cc/gmol
   Specific Volume       =  1.24343491 cc/g
   Specific Gravity      =  .805558855684304

*****************************************************
     HBT Correlation for Saturated and Compressed
           Specific Liquid Mixture Volumes

     s71.dat

   Avg. Molecular Weight =  247.0383453 g/gmol
   Temperature           =  60.0 F
   Pressure              =  14.696000000000000 psia
   Satd. Spec. Volume    =  306.592430936728420 cc/gmol
   Specific Molar Volume =  306.631158024358400 cc/gmol
   Specific Volume       =  1.24122906 cc/g
   Specific Gravity      =  .806990453614727

*****************************************************
     HBT Correlation for Saturated and Compressed
           Specific Liquid Mixture Volumes

     s81.dat

   Avg. Molecular Weight =  244.8742523 g/gmol
   Temperature           =  60.0 F
   Pressure              =  14.696000000000000 psia
   Satd. Spec. Volume    =  304.369354673058750 cc/gmol
   Specific Molar Volume =  304.407558317363680 cc/gmol
   Specific Volume       =  1.24311781 cc/g
   Specific Gravity      =  .805764339075423

*****************************************************
     HBT Correlation for Saturated and Compressed
           Specific Liquid Mixture Volumes

     s91.dat

   Avg. Molecular Weight =  260.6071167 g/gmol
   Temperature           =  60.0 F
   Pressure              =  14.696000000000000 psia
   Satd. Spec. Volume    =  321.898879774451760 cc/gmol
   Specific Molar Volume =  321.939506779678540 cc/gmol
   Specific Volume       =  1.23534429 cc/g
   Specific Gravity      =  .810834685936327

*****************************************************
     HBT Correlation for Saturated and Compressed
```

```
          Specific Liquid Mixture Volumes

     s101.dat

   Avg. Molecular Weight =  258.7904663 g/gmol
   Temperature           =  60.0 F
   Pressure              =  14.696000000000000 psia
   Satd. Spec. Volume    =  320.027340273648520 cc/gmol
   Specific Molar Volume =  320.067406039410570 cc/gmol
   Specific Volume       =  1.23678207 cc/g
   Specific Gravity      =  .809892074826890

*******************************************************
     HBT Correlation for Saturated and Compressed
          Specific Liquid Mixture Volumes

     s111.dat

   Avg. Molecular Weight =  262.7915954 g/gmol
   Temperature           =  60.0 F
   Pressure              =  14.696000000000000 psia
   Satd. Spec. Volume    =  324.563133180559590 cc/gmol
   Specific Molar Volume =  324.603796492942880 cc/gmol
   Specific Volume       =  1.23521376 cc/g
   Specific Gravity      =  .810920372833710

*******************************************************
     HBT Correlation for Saturated and Compressed
          Specific Liquid Mixture Volumes

     s121.dat

   Avg. Molecular Weight =  269.9832763 g/gmol
   Temperature           =  60.0 F
   Pressure              =  14.696000000000000 psia
   Satd. Spec. Volume    =  332.764424449486340 cc/gmol
   Specific Molar Volume =  332.806177012395320 cc/gmol
   Specific Volume       =  1.23269176 cc/g
   Specific Gravity      =  .812579453012639

*******************************************************
     HBT Correlation for Saturated and Compressed
          Specific Liquid Mixture Volumes

     s131.dat

   Avg. Molecular Weight =  285.3607482 g/gmol
   Temperature           =  60.0 F
   Pressure              =  14.696000000000000 psia
   Satd. Spec. Volume    =  350.317410926564720 cc/gmol
   Specific Molar Volume =  350.362204980945590 cc/gmol
   Specific Volume       =  1.22778690 cc/g
   Specific Gravity      =  .815825613656221

*******************************************************
     HBT Correlation for Saturated and Compressed
          Specific Liquid Mixture Volumes

     s141.dat

   Avg. Molecular Weight =  276.4862976 g/gmol
   Temperature           =  60.0 F
   Pressure              =  14.696000000000000 psia
   Satd. Spec. Volume    =  340.392306957003370 cc/gmol
   Specific Molar Volume =  340.434805771820380 cc/gmol
   Specific Volume       =  1.23128998 cc/g
   Specific Gravity      =  .813504547259999

*******************************************************
     HBT Correlation for Saturated and Compressed
          Specific Liquid Mixture Volumes

     s151.dat

   Avg. Molecular Weight =  274.7411499 g/gmol
   Temperature           =  60.0 F
   Pressure              =  14.696000000000000 psia
   Satd. Spec. Volume    =  338.578937186001840 cc/gmol
   Specific Molar Volume =  338.620774611177300 cc/gmol
   Specific Volume       =  1.23250842 cc/g
```

241 **Specific Gravity** = .812700329651814

Specific Gravity Calculations of the C7+ Fraction
of the Maljamar Stock Tank Oil (CPE 210)

****
Normalized Mole Fractions of C7+ Components
****

s1u.dat

Temperature = 60.00 F Pressure = 14.70 psia

7	.1402
8	.1315
9	.0715
10	.0622
11	.0544
12	.0498
13	.0410
14	.0485
15	.0356
16	.0329
17	.0314
18	.0226
19	.0254
20	.0185
21	.0171
22	.0167
23	.0147
24	.0097
25	.0132
26	.0131
27	.0084
28	.0084
29	.0123
30	.0077
31	.0076
32	.0066
33	.0063
34	.0060
35	.0059
36	.0058
37	.0750

****
Normalized Mole Fractions of C7+ Components
****

s2u.dat

Temperature = 60.00 F Pressure = 14.70 psia

7	.1180
8	.0959
9	.0599
10	.0661
11	.0579
12	.0530
13	.0436
14	.0518
15	.0378
16	.0350
17	.0334
18	.0242
19	.0270
20	.0196
21	.0180
22	.0176
23	.0155
24	.0102
25	.0138
26	.0138
27	.0086
28	.0086
29	.0127
30	.0078
31	.0077
32	.0066
33	.0063
34	.0060

```
                    35   .0058
                    36   .0056
                    37   .1120

*************************************************
    Normalized Mole Fractions of C7+ Components
*************************************************

    s21.dat

 Temperature =    60.00 F   Pressure =     14.70 psia

                     7   .0923
                     8   .0765
                     9   .0481
                    10   .0463
                    11   .0446
                    12   .0449
                    13   .0385
                    14   .0501
                    15   .0383
                    16   .0394
                    17   .0374
                    18   .0278
                    19   .0326
                    20   .0242
                    21   .0226
                    22   .0226
                    23   .0205
                    24   .0135
                    25   .0184
                    26   .0180
                    27   .0125
                    28   .0119
                    29   .0173
                    30   .0107
                    31   .0100
                    32   .0087
                    33   .0080
                    34   .0080
                    35   .0077
                    36   .0073
                    37   .1410

*************************************************
    Normalized Mole Fractions of C7+ Components
*************************************************

    s3u.dat

 Temperature =    60.00 F   Pressure =     14.70 psia

                     7   .1872
                     8   .1179
                     9   .0658
                    10   .0577
                    11   .0505
                    12   .0465
                    13   .0380
                    14   .0453
                    15   .0329
                    16   .0305
                    17   .0290
                    18   .0211
                    19   .0235
                    20   .0171
                    21   .0156
                    22   .0152
                    23   .0134
                    24   .0087
                    25   .0120
                    26   .0120
                    27   .0073
                    28   .0073
                    29   .0108
                    30   .0067
                    31   .0063
                    32   .0055
                    33   .0053
                    34   .0049
```

```
                    35   .0047
                    36   .0045
                    37   .0970

*****************************************************
    Normalized Mole Fractions of C7+ Components
*****************************************************

    s3l.dat

 Temperature =    60.00 F   Pressure =     14.70 psia

                     7   .1409
                     8   .1220
                     9   .0678
                    10   .0593
                    11   .0520
                    12   .0481
                    13   .0390
                    14   .0474
                    15   .0341
                    16   .0318
                    17   .0303
                    18   .0222
                    19   .0245
                    20   .0178
                    21   .0163
                    22   .0158
                    23   .0140
                    24   .0089
                    25   .0122
                    26   .0125
                    27   .0074
                    28   .0076
                    29   .0112
                    30   .0069
                    31   .0064
                    32   .0053
                    33   .0051
                    34   .0046
                    35   .0043
                    36   .0041
                    37   .1202

*****************************************************
    Normalized Mole Fractions of C7+ Components
*****************************************************

    s4u.dat

 Temperature =    60.00 F   Pressure =     14.70 psia

                     7   .1461
                     8   .1407
                     9   .0809
                    10   .0700
                    11   .0598
                    12   .0534
                    13   .0425
                    14   .0489
                    15   .0349
                    16   .0320
                    17   .0294
                    18   .0208
                    19   .0227
                    20   .0160
                    21   .0147
                    22   .0141
                    23   .0122
                    24   .0077
                    25   .0106
                    26   .0106
                    27   .0064
                    28   .0064
                    29   .0093
                    30   .0058
                    31   .0054
                    32   .0045
                    33   .0045
                    34   .0042
```

```
241                    35   .0042
242                    36   .0038
243                    37   .0777
244
245  ************************************************
246      Normalized Mole Fractions of C7+ Components
247  ************************************************
248
249      s41.dat
250
251   Temperature =    60.00 F   Pressure =     14.70 psia
252
253                     7   .1466
254                     8   .1213
255                     9   .0674
256                    10   .0589
257                    11   .0514
258                    12   .0477
259                    13   .0390
260                    14   .0471
261                    15   .0340
262                    16   .0318
263                    17   .0302
264                    18   .0218
265                    19   .0243
266                    20   .0178
267                    21   .0162
268                    22   .0156
269                    23   .0140
270                    24   .0087
271                    25   .0122
272                    26   .0125
273                    27   .0072
274                    28   .0075
275                    29   .0109
276                    30   .0069
277                    31   .0062
278                    32   .0053
279                    33   .0050
280                    34   .0047
281                    35   .0044
282                    36   .0041
283                    37   .1194
284
285  ************************************************
286      Normalized Mole Fractions of C7+ Components
287  ************************************************
288
289      s61.dat
290
291   Temperature =    60.00 F   Pressure =     14.70 psia
292
293                     7   .1403
294                     8   .1134
295                     9   .0646
296                    10   .0576
297                    11   .0510
298                    12   .0478
299                    13   .0391
300                    14   .0478
301                    15   .0349
302                    16   .0335
303                    17   .0311
304                    18   .0227
305                    19   .0255
306                    20   .0185
307                    21   .0171
308                    22   .0168
309                    23   .0150
310                    24   .0094
311                    25   .0133
312                    26   .0133
313                    27   .0080
314                    28   .0080
315                    29   .0119
316                    30   .0073
317                    31   .0070
318                    32   .0059
319                    33   .0056
320                    34   .0052
```

```
                    35   .0049
                    36   .0045
                    37   .1190

************************************************
    Normalized Mole Fractions of C7+ Components
************************************************

    s71.dat

 Temperature =    60.00 F   Pressure =     14.70 psia

                     7   .1288
                     8   .1084
                     9   .0625
                    10   .0559
                    11   .0501
                    12   .0474
                    13   .0393
                    14   .0486
                    15   .0355
                    16   .0339
                    17   .0324
                    18   .0235
                    19   .0266
                    20   .0197
                    21   .0181
                    22   .0177
                    23   .0158
                    24   .0100
                    25   .0139
                    26   .0143
                    27   .0085
                    28   .0089
                    29   .0127
                    30   .0077
                    31   .0073
                    32   .0066
                    33   .0062
                    34   .0058
                    35   .0054
                    36   .0050
                    37   .1234

************************************************
    Normalized Mole Fractions of C7+ Components
************************************************

    s81.dat

 Temperature =    60.00 F   Pressure =     14.70 psia

                     7   .1225
                     8   .1107
                     9   .0637
                    10   .0572
                    11   .0513
                    12   .0485
                    13   .0401
                    14   .0494
                    15   .0361
                    16   .0345
                    17   .0326
                    18   .0242
                    19   .0270
                    20   .0199
                    21   .0183
                    22   .0180
                    23   .0162
                    24   .0103
                    25   .0143
                    26   .0143
                    27   .0087
                    28   .0090
                    29   .0131
                    30   .0081
                    31   .0078
                    32   .0065
                    33   .0062
                    34   .0059
```

```
                    35   .0056
                    36   .0053
                    37   .1147

 ***************************************************
     Normalized Mole Fractions of C7+ Components
 ***************************************************

     s91.dat

  Temperature =    60.00 F   Pressure =     14.70 psia

                     7   .1115
                     8   .0996
                     9   .0587
                    10   .0532
                    11   .0482
                    12   .0460
                    13   .0384
                    14   .0478
                    15   .0355
                    16   .0340
                    17   .0329
                    18   .0246
                    19   .0279
                    20   .0206
                    21   .0192
                    22   .0188
                    23   .0167
                    24   .0109
                    25   .0148
                    26   .0152
                    27   .0091
                    28   .0094
                    29   .0138
                    30   .0083
                    31   .0080
                    32   .0069
                    33   .0065
                    34   .0062
                    35   .0058
                    36   .0058
                    37   .1459

 ***************************************************
     Normalized Mole Fractions of C7+ Components
 ***************************************************

     s101.dat

  Temperature =    60.00 F   Pressure =     14.70 psia

                     7   .1076
                     8   .0996
                     9   .0585
                    10   .0534
                    11   .0487
                    12   .0469
                    13   .0393
                    14   .0491
                    15   .0364
                    16   .0349
                    17   .0338
                    18   .0251
                    19   .0284
                    20   .0211
                    21   .0196
                    22   .0193
                    23   .0171
                    24   .0113
                    25   .0153
                    26   .0153
                    27   .0095
                    28   .0095
                    29   .0142
                    30   .0087
                    31   .0084
                    32   .0073
                    33   .0069
                    34   .0065
```

```
                    35   .0062
                    36   .0058
                    37   .1367

 ***************************************************
     Normalized Mole Fractions of C7+ Components
 ***************************************************

     s11l.dat

  Temperature =     60.00 F    Pressure =      14.70 psia

                     7   .1066
                     8   .0959
                     9   .0566
                    10   .0518
                    11   .0474
                    12   .0459
                    13   .0386
                    14   .0485
                    15   .0360
                    16   .0353
                    17   .0338
                    18   .0254
                    19   .0287
                    20   .0213
                    21   .0198
                    22   .0195
                    23   .0176
                    24   .0114
                    25   .0158
                    26   .0158
                    27   .0096
                    28   .0099
                    29   .0147
                    30   .0088
                    31   .0085
                    32   .0074
                    33   .0070
                    34   .0066
                    35   .0062
                    36   .0062
                    37   .1433

 ***************************************************
     Normalized Mole Fractions of C7+ Components
 ***************************************************

     s12l.dat

  Temperature =     60.00 F    Pressure =      14.70 psia

                     7   .0999
                     8   .0911
                     9   .0540
                    10   .0498
                    11   .0459
                    12   .0448
                    13   .0378
                    14   .0484
                    15   .0360
                    16   .0357
                    17   .0339
                    18   .0254
                    19   .0290
                    20   .0219
                    21   .0201
                    22   .0198
                    23   .0180
                    24   .0117
                    25   .0162
                    26   .0166
                    27   .0099
                    28   .0102
                    29   .0152
                    30   .0092
                    31   .0088
                    32   .0078
                    33   .0074
                    34   .0071
```

```
                    35   .0067
                    36   .0064
                    37   .1554

*************************************************
    Normalized Mole Fractions of C7+ Components
*************************************************

    s13l.dat

 Temperature =    60.00 F   Pressure =     14.70 psia

                     7   .0940
                     8   .0830
                     9   .0495
                    10   .0463
                    11   .0431
                    12   .0424
                    13   .0360
                    14   .0459
                    15   .0346
                    16   .0339
                    17   .0329
                    18   .0247
                    19   .0283
                    20   .0212
                    21   .0198
                    22   .0198
                    23   .0177
                    24   .0117
                    25   .0162
                    26   .0166
                    27   .0099
                    28   .0106
                    29   .0155
                    30   .0095
                    31   .0092
                    32   .0081
                    33   .0078
                    34   .0074
                    35   .0071
                    36   .0067
                    37   .1907

*************************************************
    Normalized Mole Fractions of C7+ Components
*************************************************

    s14l.dat

 Temperature =    60.00 F   Pressure =     14.70 psia

                     7   .0898
                     8   .0843
                     9   .0512
                    10   .0483
                    11   .0457
                    12   .0454
                    13   .0383
                    14   .0483
                    15   .0357
                    16   .0360
                    17   .0344
                    18   .0254
                    19   .0299
                    20   .0225
                    21   .0209
                    22   .0209
                    23   .0190
                    24   .0126
                    25   .0171
                    26   .0164
                    27   .0113
                    28   .0109
                    29   .0158
                    30   .0103
                    31   .0100
                    32   .0087
                    33   .0080
                    34   .0077
```

```
                    35   .0074
                    36   .0071
                    37   .1606

**************************************************
    Normalized Mole Fractions of C7+ Components
**************************************************

    s151.dat

 Temperature =    60.00 F   Pressure =     14.70 psia

                     7   .0876
                     8   .0831
                     9   .0507
                    10   .0481
                    11   .0456
                    12   .0449
                    13   .0385
                    14   .0488
                    15   .0372
                    16   .0372
                    17   .0359
                    18   .0266
                    19   .0311
                    20   .0234
                    21   .0218
                    22   .0218
                    23   .0196
                    24   .0128
                    25   .0176
                    26   .0170
                    27   .0115
                    28   .0112
                    29   .0164
                    30   .0106
                    31   .0103
                    32   .0087
                    33   .0083
                    34   .0080
                    35   .0074
                    36   .0071
                    37   .1511
```

```
 1
 2   Specific Gravity Calculations of the C7+ Fractions
 3       of the Wasson Stock Tank Oil Run (CPE 210)
 4
 5  ******************************************************
 6      HBT Correlation for Saturated and Compressed
 7            Specific Liquid Mixture Volumes
 8
 9      s2u.dat
10
11    Avg. Molecular Weight =  245.6690216 g/gmol
12    Temperature           =  60.0 F
13    Pressure              =  14.696000000000000 psia
14    Satd. Spec. Volume    =  304.037051257414080 cc/gmol
15    Specific Molar Volume =  304.076555574252210 cc/gmol
16    Specific Volume       =  1.23774886 cc/g
17    Specific Gravity      =  .809259480099663
18
19  ******************************************************
20      HBT Correlation for Saturated and Compressed
21            Specific Liquid Mixture Volumes
22
23      s3u.dat
24
25    Avg. Molecular Weight =  245.9614715 g/gmol
26    Temperature           =  60.0 F
27    Pressure              =  14.696000000000000 psia
28    Satd. Spec. Volume    =  304.370910480861600 cc/gmol
29    Specific Molar Volume =  304.410453721940030 cc/gmol
30    Specific Volume       =  1.23763466 cc/g
31    Specific Gravity      =  .809334154362075
32
33  ******************************************************
34      HBT Correlation for Saturated and Compressed
35            Specific Liquid Mixture Volumes
36
37      s3l.dat
38
39    Avg. Molecular Weight =  243.1735687 g/gmol
40    Temperature           =  60.0 F
41    Pressure              =  14.696000000000000 psia
42    Satd. Spec. Volume    =  301.295363140133190 cc/gmol
43    Specific Molar Volume =  301.334348101246290 cc/gmol
44    Specific Volume       =  1.23917389 cc/g
45    Specific Gravity      =  .808328846146742
46
47  ******************************************************
48      HBT Correlation for Saturated and Compressed
49            Specific Liquid Mixture Volumes
50
51      s4u.dat
52
53    Avg. Molecular Weight =  244.5459137 g/gmol
54    Temperature           =  60.0 F
55    Pressure              =  14.696000000000000 psia
56    Satd. Spec. Volume    =  302.727985755111210 cc/gmol
57    Specific Molar Volume =  302.767394225930670 cc/gmol
58    Specific Volume       =  1.23807991 cc/g
59    Specific Gravity      =  .809043096121837
60
61  ******************************************************
62      HBT Correlation for Saturated and Compressed
63            Specific Liquid Mixture Volumes
64
65      s4l.dat
66
67    Avg. Molecular Weight =  242.6511688 g/gmol
68    Temperature           =  60.0 F
69    Pressure              =  14.696000000000000 psia
70    Satd. Spec. Volume    =  300.704904488056170 cc/gmol
71    Specific Molar Volume =  300.743836372782710 cc/gmol
72    Specific Volume       =  1.23940814 cc/g
73    Specific Gravity      =  .808176073223301
74
75  ******************************************************
76      HBT Correlation for Saturated and Compressed
77            Specific Liquid Mixture Volumes
78
79      s5u.dat
80
```

```
Avg. Molecular Weight =  244.4274139 g/gmol
Temperature           =  60.0 F
Pressure              =  14.696000000000000 psia
Satd. Spec. Volume    =  302.587255966074340 cc/gmol
Specific Molar Volume =  302.626642552979210 cc/gmol
Specific Volume       =  1.23810434 cc/g
Specific Gravity      =  .809027127097974

*****************************************************
    HBT Correlation for Saturated and Compressed
         Specific Liquid Mixture Volumes

    s5l.dat

Avg. Molecular Weight =  241.1083374 g/gmol
Temperature           =  60.0 F
Pressure              =  14.696000000000000 psia
Satd. Spec. Volume    =  298.900385493797500 cc/gmol
Specific Molar Volume =  298.939176097438290 cc/gmol
Specific Volume       =  1.23985422 cc/g
Specific Gravity      =  .807885303456486

*****************************************************
    HBT Correlation for Saturated and Compressed
         Specific Liquid Mixture Volumes

    s6l.dat

Avg. Molecular Weight =  240.2980041 g/gmol
Temperature           =  60.0 F
Pressure              =  14.696000000000000 psia
Satd. Spec. Volume    =  297.990224055632780 cc/gmol
Specific Molar Volume =  298.028928052027420 cc/gmol
Specific Volume       =  1.24024725 cc/g
Specific Gravity      =  .807629285467401

*****************************************************
    HBT Correlation for Saturated and Compressed
         Specific Liquid Mixture Volumes

    s7l.dat

Avg. Molecular Weight =  273.8840026 g/gmol
Temperature           =  60.0 F
Pressure              =  14.696000000000000 psia
Satd. Spec. Volume    =  338.164784236865900 cc/gmol
Specific Molar Volume =  338.205080717332070 cc/gmol
Specific Volume       =  1.23484790 cc/g
Specific Gravity      =  .811160627444393

*****************************************************
    HBT Correlation for Saturated and Compressed
         Specific Liquid Mixture Volumes

    s8l.dat

Avg. Molecular Weight =  259.4868164 g/gmol
Temperature           =  60.0 F
Pressure              =  14.696000000000000 psia
Satd. Spec. Volume    =  320.073895819572560 cc/gmol
Specific Molar Volume =  320.114922836969920 cc/gmol
Specific Volume       =  1.23364615 cc/g
Specific Gravity      =  .811950814603055

*****************************************************
    HBT Correlation for Saturated and Compressed
         Specific Liquid Mixture Volumes

    s9l.dat

Avg. Molecular Weight =  262.3080749 g/gmol
Temperature           =  60.0 F
Pressure              =  14.696000000000000 psia
Satd. Spec. Volume    =  323.368700645390280 cc/gmol
Specific Molar Volume =  323.410060956622320 cc/gmol
Specific Volume       =  1.23293984 cc/g
Specific Gravity      =  .812415957389640

*****************************************************
    HBT Correlation for Saturated and Compressed
```

```
          Specific Liquid Mixture Volumes

    s10l.dat

  Avg. Molecular Weight =  264.1040039 g/gmol
  Temperature           =  60.0 F
  Pressure              =  14.696000000000000 psia
  Satd. Spec. Volume    =  325.546651495686260 cc/gmol
  Specific Molar Volume =  325.588086069753610 cc/gmol
  Specific Volume       =  1.23280251 cc/g
  Specific Gravity      =  .812506457167661

**************************************************
    HBT Correlation for Saturated and Compressed
          Specific Liquid Mixture Volumes

    s11l.dat

  Avg. Molecular Weight =  215.4256591 g/gmol
  Temperature           =  60.0 F
  Pressure              =  14.696000000000000 psia
  Satd. Spec. Volume    =  274.954937067567580 cc/gmol
  Specific Molar Volume =  274.988002884165670 cc/gmol
  Specific Volume       =  1.27648675 cc/g
  Specific Gravity      =  .784700661039880

**************************************************
    HBT Correlation for Saturated and Compressed
          Specific Liquid Mixture Volumes

    s12l.dat

  Avg. Molecular Weight =  221.8128814 g/gmol
  Temperature           =  60.0 F
  Pressure              =  14.696000000000000 psia
  Satd. Spec. Volume    =  281.850575074671950 cc/gmol
  Specific Molar Volume =  281.884125514396150 cc/gmol
  Specific Volume       =  1.27081943 cc/g
  Specific Gravity      =  .788200101316967

**************************************************
    HBT Correlation for Saturated and Compressed
          Specific Liquid Mixture Volumes

    s13l.dat

  Avg. Molecular Weight =  225.7000579 g/gmol
  Temperature           =  60.0 F
  Pressure              =  14.696000000000000 psia
  Satd. Spec. Volume    =  286.286819794106240 cc/gmol
  Specific Molar Volume =  286.320532157674850 cc/gmol
  Specific Volume       =  1.26858866 cc/g
  Specific Gravity      =  .789586120298716

**************************************************
    HBT Correlation for Saturated and Compressed
          Specific Liquid Mixture Volumes

    s14l.dat

  Avg. Molecular Weight =  232.6296844 g/gmol
  Temperature           =  60.0 F
  Pressure              =  14.696000000000000 psia
  Satd. Spec. Volume    =  293.613220944011970 cc/gmol
  Specific Molar Volume =  293.647623914048610 cc/gmol
  Specific Volume       =  1.26229644 cc/g
  Specific Gravity      =  .793522004557598

**************************************************
    HBT Correlation for Saturated and Compressed
          Specific Liquid Mixture Volumes

    s15l.dat

  Avg. Molecular Weight =  233.8092956 g/gmol
  Temperature           =  60.0 F
  Pressure              =  14.696000000000000 psia
  Satd. Spec. Volume    =  294.976347718277960 cc/gmol
  Specific Molar Volume =  295.010780735082850 cc/gmol
  Specific Volume       =  1.26175809 cc/g
```

241 **Specific Gravity** = .793860573338445

Specific Gravity Calculations of the C7+ Fractions
of the Wasson Stock Tank Oil Run (CPE 210)

****
Normalized Mole Fractions of C7+ Components
****

s2u.dat

Temperature = 60.00 F Pressure = 14.70 psia

7	.1246
8	.1079
9	.0968
10	.0719
11	.0474
12	.0511
13	.0355
14	.0415
15	.0305
16	.0280
17	.0210
18	.0255
19	.0177
20	.0167
21	.0153
22	.0146
23	.0133
24	.0086
25	.0156
26	.0078
27	.0076
28	.0073
29	.0071
30	.0069
31	.0100
32	.0064
33	.0094
34	.0064
35	.0033
36	.0066
37	.1376

****
Normalized Mole Fractions of C7+ Components
****

s3u.dat

Temperature = 60.00 F Pressure = 14.70 psia

7	.1259
8	.1102
9	.0912
10	.0721
11	.0475
12	.0514
13	.0357
14	.0415
15	.0306
16	.0281
17	.0211
18	.0256
19	.0178
20	.0167
21	.0154
22	.0146
23	.0134
24	.0086
25	.0156
26	.0079
27	.0075
28	.0074
29	.0072
30	.0069
31	.0101
32	.0064
33	.0094
34	.0064

```
                    35   .0033
                    36   .0066
                    37   .1380

*****************************************************
    Normalized Mole Fractions of C7+ Components
*****************************************************

    s3l.dat

 Temperature =    60.00 F   Pressure =     14.70 psia

                     7   .1238
                     8   .1125
                     9   .0950
                    10   .0723
                    11   .0481
                    12   .0514
                    13   .0359
                    14   .0408
                    15   .0310
                    16   .0283
                    17   .0212
                    18   .0255
                    19   .0179
                    20   .0166
                    21   .0155
                    22   .0145
                    23   .0135
                    24   .0086
                    25   .0156
                    26   .0079
                    27   .0076
                    28   .0074
                    29   .0071
                    30   .0071
                    31   .0109
                    32   .0071
                    33   .0109
                    34   .0077
                    35   .0041
                    36   .0084
                    37   .1258

*****************************************************
    Normalized Mole Fractions of C7+ Components
*****************************************************

    s4u.dat

 Temperature =    60.00 F   Pressure =     14.70 psia

                     7   .1306
                     8   .1115
                     9   .0926
                    10   .0713
                    11   .0470
                    12   .0508
                    13   .0352
                    14   .0411
                    15   .0302
                    16   .0279
                    17   .0208
                    18   .0253
                    19   .0175
                    20   .0165
                    21   .0153
                    22   .0144
                    23   .0132
                    24   .0085
                    25   .0153
                    26   .0078
                    27   .0076
                    28   .0073
                    29   .0071
                    30   .0068
                    31   .0099
                    32   .0064
                    33   .0094
                    34   .0064
```

```
                    35   .0033
                    36   .0064
                    37   .1367

 ************************************************
     Normalized Mole Fractions of C7+ Components
 ************************************************

     s4l.dat

  Temperature =    60.00 F   Pressure =     14.70 psia

                     7   .1247
                     8   .1140
                     9   .0947
                    10   .0723
                    11   .0480
                    12   .0511
                    13   .0360
                    14   .0407
                    15   .0308
                    16   .0282
                    17   .0211
                    18   .0256
                    19   .0177
                    20   .0167
                    21   .0154
                    22   .0146
                    23   .0133
                    24   .0086
                    25   .0157
                    26   .0078
                    27   .0076
                    28   .0073
                    29   .0070
                    30   .0070
                    31   .0107
                    32   .0070
                    33   .0107
                    34   .0076
                    35   .0042
                    36   .0083
                    37   .1255

 ************************************************
     Normalized Mole Fractions of C7+ Components
 ************************************************

     s5u.dat

  Temperature =    60.00 F   Pressure =     14.70 psia

                     7   .1313
                     8   .1107
                     9   .0925
                    10   .0713
                    11   .0469
                    12   .0510
                    13   .0353
                    14   .0413
                    15   .0303
                    16   .0278
                    17   .0209
                    18   .0253
                    19   .0175
                    20   .0166
                    21   .0153
                    22   .0144
                    23   .0131
                    24   .0084
                    25   .0153
                    26   .0078
                    27   .0075
                    28   .0072
                    29   .0072
                    30   .0069
                    31   .0100
                    32   .0063
                    33   .0094
                    34   .0063
```

```
                    35   .0031
                    36   .0066
                    37   .1366

****************************************************
    Normalized Mole Fractions of C7+ Components
****************************************************

    s51.dat

 Temperature =    60.00 F   Pressure =     14.70 psia

                     7   .1294
                     8   .1155
                     9   .0968
                    10   .0711
                    11   .0475
                    12   .0506
                    13   .0354
                    14   .0402
                    15   .0305
                    16   .0277
                    17   .0208
                    18   .0253
                    19   .0177
                    20   .0163
                    21   .0153
                    22   .0142
                    23   .0132
                    24   .0083
                    25   .0153
                    26   .0076
                    27   .0076
                    28   .0073
                    29   .0069
                    30   .0069
                    31   .0108
                    32   .0069
                    33   .0108
                    34   .0076
                    35   .0042
                    36   .0083
                    37   .1238

****************************************************
    Normalized Mole Fractions of C7+ Components
****************************************************

    s61.dat

 Temperature =    60.00 F   Pressure =     14.70 psia

                     7   .1305
                     8   .1191
                     9   .0958
                    10   .0710
                    11   .0473
                    12   .0502
                    13   .0351
                    14   .0400
                    15   .0302
                    16   .0277
                    17   .0208
                    18   .0249
                    19   .0175
                    20   .0163
                    21   .0151
                    22   .0143
                    23   .0131
                    24   .0086
                    25   .0155
                    26   .0077
                    27   .0073
                    28   .0073
                    29   .0069
                    30   .0069
                    31   .0106
                    32   .0069
                    33   .0106
                    34   .0073
```

```
                    35   .0041
                    36   .0082
                    37   .1232

*****************************************************
    Normalized Mole Fractions of C7+ Components
*****************************************************

    s71.dat

 Temperature =    60.00 F   Pressure =     14.70 psia

                     7   .0112
                     8   .0510
                     9   .0747
                    10   .0811
                    11   .0614
                    12   .0695
                    13   .0498
                    14   .0574
                    15   .0438
                    16   .0401
                    17   .0301
                    18   .0365
                    19   .0257
                    20   .0241
                    21   .0221
                    22   .0209
                    23   .0193
                    24   .0124
                    25   .0225
                    26   .0112
                    27   .0108
                    28   .0108
                    29   .0100
                    30   .0100
                    31   .0149
                    32   .0096
                    33   .0145
                    34   .0096
                    35   .0052
                    36   .0100
                    37   .1297

*****************************************************
    Normalized Mole Fractions of C7+ Components
*****************************************************

    s81.dat

 Temperature =    60.00 F   Pressure =     14.70 psia

                     7   .0939
                     8   .0973
                     9   .0882
                    10   .0701
                    11   .0479
                    12   .0524
                    13   .0373
                    14   .0434
                    15   .0328
                    16   .0302
                    17   .0230
                    18   .0279
                    19   .0196
                    20   .0185
                    21   .0170
                    22   .0162
                    23   .0151
                    24   .0098
                    25   .0177
                    26   .0090
                    27   .0087
                    28   .0083
                    29   .0079
                    30   .0079
                    31   .0117
                    32   .0075
                    33   .0109
                    34   .0075
```

```
                    35   .0038
                    36   .0079
                    37   .1505

 ***************************************************
     Normalized Mole Fractions of C7+ Components
 ***************************************************

     s91.dat

  Temperature =    60.00 F   Pressure =     14.70 psia

                     7   .0945
                     8   .0934
                     9   .0850
                    10   .0682
                    11   .0465
                    12   .0517
                    13   .0366
                    14   .0432
                    15   .0330
                    16   .0308
                    17   .0231
                    18   .0286
                    19   .0202
                    20   .0191
                    21   .0176
                    22   .0169
                    23   .0158
                    24   .0103
                    25   .0183
                    26   .0092
                    27   .0092
                    28   .0088
                    29   .0084
                    30   .0081
                    31   .0121
                    32   .0077
                    33   .0114
                    34   .0077
                    35   .0040
                    36   .0081
                    37   .1528

 ***************************************************
     Normalized Mole Fractions of C7+ Components
 ***************************************************

     s101.dat

  Temperature =    60.00 F   Pressure =     14.70 psia

                     7   .0923
                     8   .0920
                     9   .0823
                    10   .0658
                    11   .0458
                    12   .0510
                    13   .0369
                    14   .0437
                    15   .0334
                    16   .0310
                    17   .0238
                    18   .0293
                    19   .0207
                    20   .0196
                    21   .0183
                    22   .0176
                    23   .0162
                    24   .0107
                    25   .0193
                    26   .0096
                    27   .0093
                    28   .0093
                    29   .0090
                    30   .0086
                    31   .0127
                    32   .0083
                    33   .0117
                    34   .0083
```

```
                    35   .0041
                    36   .0083
                    37   .1512

 ************************************************
     Normalized Mole Fractions of C7+ Components
 ************************************************

     s11l.dat

  Temperature =    60.00 F   Pressure =     14.70 psia

                     7   .1147
                     8   .0927
                     9   .0924
                    10   .0764
                    11   .0529
                    12   .0615
                    13   .0423
                    14   .0529
                    15   .0398
                    16   .0369
                    17   .0288
                    18   .0352
                    19   .0249
                    20   .0238
                    21   .0224
                    22   .0213
                    23   .0195
                    24   .0128
                    25   .0234
                    26   .0117
                    27   .0114
                    28   .0110
                    29   .0110
                    30   .0103
                    31   .0149
                    32   .0096
                    33   .0142
                    34   .0092
                    35   .0046
                    36   .0092
                    37   .0082

 ************************************************
     Normalized Mole Fractions of C7+ Components
 ************************************************

     s12l.dat

  Temperature =    60.00 F   Pressure =     14.70 psia

                     7   .1080
                     8   .0884
                     9   .0871
                    10   .0727
                    11   .0512
                    12   .0604
                    13   .0420
                    14   .0531
                    15   .0402
                    16   .0377
                    17   .0295
                    18   .0362
                    19   .0258
                    20   .0249
                    21   .0233
                    22   .0224
                    23   .0206
                    24   .0135
                    25   .0249
                    26   .0123
                    27   .0120
                    28   .0117
                    29   .0117
                    30   .0110
                    31   .0156
                    32   .0101
                    33   .0150
                    34   .0098
```

```
                    35   .0049
                    36   .0098
                    37   .0141

*************************************************
    Normalized Mole Fractions of C7+ Components
*************************************************

    s13l.dat

 Temperature =    60.00 F   Pressure =     14.70 psia

                     7   .1086
                     8   .0777
                     9   .0807
                    10   .0706
                    11   .0506
                    12   .0602
                    13   .0421
                    14   .0539
                    15   .0413
                    16   .0388
                    17   .0306
                    18   .0375
                    19   .0268
                    20   .0260
                    21   .0243
                    22   .0235
                    23   .0216
                    24   .0142
                    25   .0263
                    26   .0129
                    27   .0129
                    28   .0126
                    29   .0123
                    30   .0118
                    31   .0167
                    32   .0107
                    33   .0159
                    34   .0104
                    35   .0049
                    36   .0104
                    37   .0134

*************************************************
    Normalized Mole Fractions of C7+ Components
*************************************************

    s14l.dat

 Temperature =    60.00 F   Pressure =     14.70 psia

                     7   .0986
                     8   .0774
                     9   .0788
                    10   .0677
                    11   .0490
                    12   .0591
                    13   .0412
                    14   .0532
                    15   .0412
                    16   .0387
                    17   .0306
                    18   .0379
                    19   .0273
                    20   .0262
                    21   .0248
                    22   .0242
                    23   .0223
                    24   .0148
                    25   .0273
                    26   .0131
                    27   .0131
                    28   .0128
                    29   .0125
                    30   .0120
                    31   .0173
                    32   .0111
                    33   .0164
                    34   .0106
```

```
                    35   .0053
                    36   .0106
                    37   .0248

*************************************************
    Normalized Mole Fractions of C7+ Components
*************************************************

    s15l.dat

 Temperature =    60.00 F   Pressure =     14.70 psia

                     7   .0928
                     8   .0769
                     9   .0781
                    10   .0683
                    11   .0493
                    12   .0594
                    13   .0417
                    14   .0539
                    15   .0415
                    16   .0392
                    17   .0311
                    18   .0382
                    19   .0276
                    20   .0266
                    21   .0250
                    22   .0243
                    23   .0225
                    24   .0149
                    25   .0276
                    26   .0134
                    27   .0134
                    28   .0129
                    29   .0126
                    30   .0121
                    31   .0172
                    32   .0111
                    33   .0164
                    34   .0109
                    35   .0053
                    36   .0106
                    37   .0250
```

APPENDIX E

Cubic Equations of State

Summary

When using an EOS for predicting the phase behavior of natural oils, it must be emphasized that the accuracy of the prediction depends on several factors:

1) The choice of the EOS

2) The correct description of the mixture in terms of pseudocomponents or, if the CT approach is used, the correct distribution of components

3) The assignment of the EOS parameters to each component, fraction or pseudocomponent used in the calculations

4) The tuning of the EOS parameters in order to optimize the predictions

For each aspect of the problem, several solutions have been proposed. In many cases the choice of a particular alternative implies a compromise between accuracy and simplicity, but the best results are not necessarily provided by the most complex technique. The search for new solutions which provide accurate predictions with reasonable complexity is ongoing. Included at the end of this appendix is an extensive bibliography for the use of consortium members; only a few of the papers are referenced in the text.

The Choice of Equation of State

The special problems that are associated with the use of EOS with crude oils do not arise in their ordinary application to pure components and to relatively simple mixtures of pure components. The questions range from the choice of the optimal EOS to use through the decisions on representative groups or pseudocomponents, selection of the proper choice of parameters based on measured physical properties, and the influence of different kinds of mixing rules. Finally, the use of an EOS calculation scheme usually must provide for the final "tuning" of the parameters, a set of small adjustments that must be made to secure peak performance.

For several reasons, cubic EOS are among the most popular expressions used in the industry for the representation of PVT data:

1) They are simple to handle and can be solved analytically. The proper choice of multiple solutions may be made unambiguously. More complicated expressions require prohibitively large amounts of computer time and data; however, less complicated expressions are unacceptably inaccurate.

2) Only one expression is used to predict the behavior of both the liquid and vapor phases.

3) Comparisons of EOS predictions with experimental results have shown an acceptable agreement, although there can be a large variation from equation to equation.

On the other hand, there are several limitations and problems with the cubic EOS that must be considered:

1) They are unable to correctly predict the critical point (and near critical region). Even though calculations are possible at any point and solutions are consistent, the predictions show an important inaccuracy in the critical region. This limitation is reportedly intrinsic to all cubic EOS.

2) Estimated liquid densities are subject to significant error. The situation is different for each equation, and a great effort to improve the predictions of liquid volumes is ongoing. These efforts seek new expressions that might be expected to yield better results.

The Peng-Robinson (PR) EOS (1976) is a good example of the capabilities and limitations of a cubic EOS. It has been extensively tested and it is widely used with petroleum fluids. The PR EOS does a very good job predicting phase compositions and vapor phase densities, but in predicting liquid phase densities, errors are often observed (regression techniques minimize these errors).

The PR EOS has the following expression:

$$P = \frac{RT}{v-b} - \frac{a(T)}{v(v+b) + b(v-b)} \qquad \text{(E-1)}$$

where:
P is the absolute pressure,
T is the absolute temperature,
v is the specific volume, and
R is the universal gas constant.

$$a(T) = a(Tc) \cdot \alpha$$

$$a(Tc) = \Omega_a \frac{R^2 Tc^2}{Pc}$$

$$\Omega_a = 0.45724$$

$$\alpha = \left[1+\beta\left(1-\left(\frac{T}{Tc}\right)^{1/2}\right)\right]^2$$

$$\beta = C_0 + C_1\omega + C_2\omega^2$$

$$b = \Omega_b \frac{RTc}{Pc}$$

$$\Omega_b = 0.07780$$

Pc and Tc are critical pressure and temperature; ω is the Pitzer acentric factor. These expressions can be rearranged in the equivalent cubic polynomial form:

$$Z^3 - (1-B)Z^2 + (A-3B^2-2B)Z - (AB-B^2-B^3) = 0$$

where:

$$A = \frac{aP}{R^2T^2}\ ;$$

$$B = \frac{bP}{RT}\ ; \qquad \text{(E-2)}$$

$$Z = \frac{Pv}{RT} \text{ is the compressibility factor.}$$

The above expressions hold for a pure compound; for mixtures, the parameters 'a' and 'b' become:

$$a = \sum_i \sum_j x_i\, x_j\, (1-\delta_{ij})\, \sqrt{a_i a_j} \qquad \text{(E-3)}$$

$$b = \sum_i x_i b_i \qquad \text{(E-4)}$$

where i and j denote pure components. The binary interaction parameter, δ_{ij}, is equal to 0 for pairs of identical molecules and, for any system, is estimated by fitting experimental data for the corresponding binary system. Since $\delta_{ii}=0$ and $\delta_{ij}=\delta_{ji}$, only n(n-1)/2 values of δ_{ij} need to be described in a system of n components.

In summary, to describe the thermodynamic state of a system of definite composition (x_i...) at a definite pressure and temperature using the PR EOS, the following data are required: Tc_i, Pc_i, ω_i, of each component; and δ_{ij} for each pair of components.

We, and others (Jhaveri, 1984) have seen that the Peng-Robinson EOS applied to reservoir fluids can have errors as high as 5% for gas-phase z-factors and 10% for liquid-phase densities. Peneloux et al. (1982) improved volumetric predictions by adding a third parameter to a two-parameter EOS. The third parameter does not change the VLE conditions generated by the unmodified, two-parameter EOS. It modifies phase volumes through translations along the volume axis. The Peneloux et al. (1982) method can be applied after the reservoir fluid has already been characterized by some two-parameter EOS. The applications of this method to the PR EOS (Jhaveri, 1984) can yield significant improvements in volumetric predictions.

The first concern when considering the use of an EOS is, of course, which equation is the most suitable in view of the available data and the goal of the calculations. To some extent there is a compromise between simplicity and accuracy. It is obvious that an eight-parameter EOS has the potential for providing a more accurate description of a system than a single two-parameter equation (like PR or SRK); however, the burden of finding the values of the parameters and the performance of calculation with a complicated expression is not justified for the usual margins of error required in the petroleum industry. Moreover, when using the EOS to describe petroleum fluids, the problem of how to characterize the complex mixture becomes relevant. The crude oil is described in terms of relatively few pseudocomponents, and the properties of each pseudocomponent must be assigned using some general correlation. This procedure produces an important uncertainty that is obviously reflected in the results. For that reason, when analyzing the results of any calculation using an EOS for a petroleum fluid, one must consider that these results are affected simultaneously by the validity of both the EOS and the characterization of the oil. Even the best EOS cannot be expected to yield a good result if the characterization of the oil is incorrect. Alternatively, a correct characterization of the oil will never overcome the limitations of the EOS used.

There are several EOS's published that, in principle, can be used in petroleum engineering. In many cases the results are comparable, but each EOS offers some advantages and some disadvantages (accuracy, simplicity, data required, etc). Several papers discuss and compare the different EOS's (Abbott, 1979; Martin, 1979; Adachi, 1984). It is common practice to evaluate an EOS by its predictions for pure components or very simple mixtures (containing only a few, well-known compounds). It is always expected that the EOS that does the best job with simple systems will also be the best for complex mixtures. This assumption is acceptable as long as the EOS has been checked against compounds similar to those forming the oil, i.e., hydrocarbons, CO_2, etc. Unfortunately, only a few of the EOS's have been developed considering heavier compounds; therefore, the empirical parameters of the EOS must be handled with care for heavy ends. The ranges for P and T used in the EOS are other obvious parameters to be considered.

Cubic EOS's can be classified according to the number of parameters they contain. The oldest is the van der Waals EOS, which contains two parameters. Also with two parameters are the PR (1976) and SRK (1972) versions. The versions by Patel-Teja (1982), Harmens-Knapp (1980), Martin (1967), and Schmidt-Wenzel (1980) are three-parameter equations. Lawal et al. (1985) presented a modification of the Lawal-Lake-Silberberg EOS, which is a four-parameter equation.

Abbott (1979) has shown that the most general expression for any cubic EOS contains five parameters. He also showed that all the cubic EOS's can be expressed in a VDW-like form, i.e., with a "repulsion" term, RT/(v-b), and an "attraction" term that is different in each EOS.

Of the two well known and proven EOS's (PR and SRK), the PR version produces somewhat better results than the SRK version when applied to most petroleum fluids. However, the deviation between predicted and measured liquid densities for both PR and SRK can be large enough sometimes to justify the use of an improved version (e.g., the Peneloux (1982) correction). In most cases the improved versions do not represent a significant increase in computer time. However, in some cases they require additional information not readily available, especially for crude oils. It is expected that the need for better predictions with EOS will make the use of newly developed versions more popular. These newer versions need to be adapted to and validated for use with crude oils.

Use of Cubic EOS with Crude Oils

Cubic equations of state (at least some of them) have proven to be accurate with simple systems composed of a few hydrocarbons and other pure compounds like CO_2 or N_2. In addition, as was mentioned earlier, they are even able to accurately predict complicated behavior like the liquid-liquid-vapor found in systems with crude oils. However, a crude oil contains many components, and it is impractical, if not impossible, to evaluate the concentration of each of the thousands of components in the mixture. A typical detailed analysis provides the composition of the light components up to C_6, and the description of the heavier components is given in terms of distillation or GC fractions or cuts, each one characterized by one or more properties such as molecular weight (MW), carbon number, specific gravity (Sg), normal boiling point (Tb), or paraffinic-naphthenic-aromatic (PNA) content.

In order to specify the EOS parameters, each of the "components" (actually a fraction) so defined by the chemical analysis must be characterized in terms of Tc, Pc, ω, and δ_{ij} to the directly measured values (MW, Sg, Tb, etc.).

A chemical analysis may provide too large a number of components (or fractions) from the point of view of the time required to perform EOS calculations. For instance, in the case of compositional simulators, numerous calculations of phase equilibria are performed with the EOS; if there are too many components considered for the calculations, the computer time required is prohibitive. For that reason, several of the components or fractions defined by the chemical analysis are lumped together to define a new pseudocomponent. The lumping scheme is far from arbitrary, it must produce an appreciable change in the required computer time with an acceptable level of accuracy of results.

In order to obtain the critical values and δ_{ij} for each pseudocomponent, some mixing rules must be applied. Each mixing rule can produce a different final result, so the choice of mixing rule must be considered with care.

In summary, in order to calculate the phase behavior of a crude oil with a cubic EOS, the following steps must be considered:

1) Chemical analysis of the oil;

2) Characterization of each fraction in terms of the values required by the EOS (normally Pc, Tc, ω, and δ_{ij});

3) Lumping components or fractions into a few pseudocomponents; and

4) Tuning the EOS parameters to obtain an optimal fit with PVT data.

The Lumping of Components

Many techniques have been proposed for the grouping of pseudocomponents (PSC) with the goal of maintaining the accuracy of calculations within acceptable limits. This problem is very complex and it is aggravated by the fact that the PSC's are made up not only of pure components but also of fractions that are defined by only a few properties. The central question is: To what extent is the lumping approximation an adequate representation of the actual mixture behavior? Several individual parts of this question can be distinguished:

A) How is the particular lumping scheme to be evaluated?

B) How many pseudocomponents should be used?

C) To which PSC should each compound (or fraction) be assigned?

D) How should properties be assigned to the PSC's from the properties of the pure components?

While no general answers to these questions are available, there have been many specific attempts to answer them that are recorded in the literature. In general, most people have their own consistent technique that is based upon their own experience with these calculations.

Conclusions

The errors in EOS calculations are caused by the limitations of the EOS used, by the limitations of the correlations to estimate parameters, and by uncertainty caused by the lumping of components. The presence of these errors leads to the conclusion that it is necessary to tune the EOS parameters to experimental data in order to attempt to overcome the limitations. This tuning consists of the systematic change of some parameters of the EOS in order to obtain an optimal match between the predicted and experimental values of some properties of the system. Normally the properties to be matched are the PVT values (such as bubble or dew point, densities, K values, etc.).

Because the quality of calculated results depends on the consistency and accuracy of the data used in the tuning process, an EOS can be considered, to some extent, as a sophisticated interpolative tool. In addition, because of its theoretical basis, the method has the capability of predicting the behavior of the system not far from the region for which experimental data is available.

REFERENCES

Abbott, M.A. (1979), "Cubic Equations of State: An Interpretative Review," Equations of State in Engineering and Research, K.C. Chao and R.L. Robinson (Eds), ACS, Advances in Chemistry Series, 182, Washington, Chapter 3, 47-70.

Adachi, Y., Suzie H., and Lu, B.C.Y. (1984), "Evolution of Cubic Equation of State," J. Chem. Eng. of Japan, 17 (6) 624-631.

Alexander, G.I., Creagh, A.L., and Prausnitz, J.M. (1985), "Phase Equilibria for High-Boiling Fossil-Fuel Distillates 1-Characterization," Ind. Eng. Chem. Fund., 24 (3) 301-310.

Alexander, G.L., Schwarz, B.J., and Prausnitz, J.M. (1985), "Phase Equilibria for the High-Boiling Fossil-Fuel Distillates 2 - Correlation of Equation-of-State Constants with Characterization Data for Phase-Equilibrium Calculations," Ind. Eng. Chem. Fund., 24 (3) 311-315.

Brule, M.R., Kumar, K.H., and Watanasiri, S. (1985), "Characterization Methods Improve Phase Behavior Predictions," Oil & Gas J., February 11, 87-93.

Brule, M.R., Lee, L.L., and Starling, K.E. (1979), "Predicting Thermodynamic Properties for Fossil-Fuel Chemicals," Chem. Eng., November 19, 155-164.

Cavett, R.H. (1962), "Physical Data for Distillation Calculations - Vapor-Liquid Equilibria," presented at the 27th Meeting API, May 15 (Pa: 2-5472).

Coats, K.H. (1985), "Simulation of Gas Condensate Reservoir Performance," J. Pet. Tech., 37 (11), October 1970-1986.

Coats, K.H. and Smart, G.T. (1986), "Application of a Regression-Based EOS PVT Program to Laboratory Data, SPE Reservoir Engineering, 1 (3) May, 277-299.

Colonomos, P., Gonzalez, E., and Rusinek, I. (1984), "A New Approach for Characterizing Oil Fractions and for Selecting Pseudocomponents of Hydrocarbons," paper CIM 84-35-27 presented at the 35th Annual Technical Meeting of the Petroleum Society of CIM, Calgary, June 10-13.

Conrad, P.G. and Gravier, J.F. (1980), "Peng-Robinson Equation of State Checks Validity of PVT Experiments," Oil & Gas J., April 21, 77-86.

Cotterman, R.L. and Prausnitz, J.M. (1985), "Flash Calculation for Continuous or Semicontinuous Mixtures Using an Equation of State," Ind. Eng. Chem., Process Des. Dev., 24, 434-443.

Cotterman, R.L., Bender, R., and Prausnitz, J.M. (1985), "Phase Equilibria for Mixtures Containing Very Many Components-Development and Application of Continuous Thermodynamics for Chemical Process Design," Ind. Eng. Chem., Process Des. Dev., 24, 194-203.

Dreisbach, R.R. (1955), "Physical Properties of Chemical Compounds I: Organic Cyclic Compounds," Advances in Chemistry Series 15, ACS, Washington.

Dreisbach, R.R. (1959), "Physical Properties of Chemical Compounds II: Organic Straight-Chain Compounds," Advances in Chemistry Series 22, ACS, Washington.

Dreisbach, R.R. (1961), "Physical Properties of Chemical Compounds III: Aliphatic and Miscellaneous Compounds," Advances in Chemistry Series 29, ACS, Washington.

Edmister, W.C. (1958), "Applied Hydrocarbon Thermodynamics Part 4: Compressibility Factors and Equations of State," Petrol. Refiner, 37 (4) 173-179.

Erbar, J.H. (1977), "Prediction of Absorber Oil K-Values and Euthalpies," GPA Research Report 13, Tulsa, OK, March.

Erbar, J.H. and Maddox, R.N. (1984), "C_6+ Fractions Need Special Attention," Oil & Gas J., February 16, 116-118.

Evelein, K.A., Moore, R.G., and Heidemann, R.A. (1976), "Correlation of the Phase Behavior in the Systems Hydrogen Sulfide-Water and Carbon Dioxide-Water," Ind. Eng. Chem., Proc. Des. Dev., 15 (3), 423-428.

Finatieri, J.D. and Fleming III, P.D. (1979), "The Use of Pseudocomponents in the Representation of Phase Behavior of Surfactant Systems," Soc. Pet. Eng. J., October, 289-300.

Fleming, P.D. and Vinatieri, J.E. (1977), "Phase Behavior of Multi-component Fluids," J. Chem. Phys., 66 (7) 3147-3154.

Garcia-Colin, L. (1977), "Ideas Modernas Sobre la Transicion Liquids-Gas," Memoria de El Colegio Nacional, Mexico, 8 (4).

Gibbons, R.M. and Laughton, A.P. (1984), "An Equation of State for Polar and Non-Polar Substances and Mixtures," J. Chem. Soc., Faraday Trans. 2, 80, 1019-1038.

Graboski, M.S. and Daubert, T.W. (1978), "A Modified Soave Equation of State for Phase Equilibrium Calculations," Ind. Eng. Chem., Prodess Des. Dev., 17 (4) 443-454.

Grigg, R.B. and Lingane, P.J. (1983), "Predicting Phase Behavior of Mixtures of Reservoir Fluids with Carbon Dioxide," SPE paper 11960, presented at the 58th Annaul Conference, San Francisco, October 5-8.

Hariv, O.H. and Sage, R.C. (1969), "Crude Split Figured by Computer," Hydrocarbon Processing, April, 143-148.

Harmens, A. and Knapp, H. (1980), "Three-Parameter Cubic Equation of State for Normal Substances," Ind. Eng. Chem., Fund., 19, 291-294.

Hong, K.C. (1982), "Lumped-Compnent Characterization of Crude Oils for Compositional Simulation," SPE/DOE Paper 10691, presented at the 3rd SPE/DOE Symposium on EOR, Tulsa, OK, April 4-7.

Hough, E.W. and Warren, H.G. (1966), "Correlation of Interfacial Tension of Hydrocarbons," Soc. Pet. Eng. J., December, 345-349.

Huron, M.J. and Vidal, J. (1979), "New Mixing Rules in Simple Equations of State for Representing Vapor-Liquid Equilibria of Strongly Non Ideal Mixtures," Fluid Phase Equilibria, 3, 255-271.

Jhaveri, B.S. and Youngren, G.K. (1984), "Three-Parameter Modification of the Peng-Robinson EOS to Improve Volumetric Predictions," SPE paper 13118, presented at the 59th Annual Conference, Houston, September 16-19.

Kato, K., Nagahama, K., and Hirata, M. (1981-a), "Generalized Interaction Parameters for the Peng-Robinson Equation of State: Carbon Dioxide-n-Paraffin Binary Systems," Fluid Phase Equilibria, 7, 219-231.

Kato, K. Nagahama, K., and Hirata, M. (1981-b), "Generalized Interaction Parameters Containing CO_2 and Normal Paraffins," IFA, Winfrith.

Katz, D.L. and Firoozabadi, A. (1978), "Predicting Phase Behavior of Condensate/Crude-Oil Systems Using Methane Interaction Coefficients," J. Pet. Tech., November, 1649-1655.

Katz, D.L., Monroe, R.R., and Trainer, R.P. (1943), "Surface Tension of Crude Oils Containing Dissolved Gases," Pet. Tech., September, TP 1624.

Kesler, M.G. and Lee, B.L. (1976), "Improve Predictions of Enthalpy of Fractions," Hydrocarbon Processing, March, 153-158.

Lawal, A.S., van der Laan, E.T., and Thambynayagam, R.K.M. (1985), "Four-Parameter Modification of the Lawal-Lake-Silberberg Equation of State for Calculating Gas-Condensate Phase Equilibria," paper SPE 14269 presented at the 1985 SPE Annual Meeting, Las Vegas, Sept. 22-25.

Lee, B.T. and Kesler, M.G. (1975), "A Generalized Thermodynamic Correlation Based on Three-Parameter Corresponding States," AIChE J., 21 (3), May, 510-527.

Lee, S.T., Jacoby, R.H., Chen, W.H., and Culham, W.E. (1981), "Experimental and Theoretical Studies on the Fluid Properties Required for Simulation of Thermal Processes," Soc. Pet. Eng. J., 21 (5) October, 535-550.

Li, Y.K., Nghiem, L.X., and Sayegh, S.G. (1982), "Phase Behavior Predictions of Oil-CO_2-SO_2 Mixtures Using the Peng-Robinson Equation of State," presented at the 1982 International Energy Agency Workshop of Enhanced Oil Recovery, Calgary, September.

Li, Y.K., Nghiem, L.X., and Siv, A. (1984), "Phase Behavior Computation for Reservoir Fluid: Effects of Pseudo Component on Phase Diagrams and Simulation Results," paper CIM 84-35-19 presented at the 35th Annual Technical Meeting of the Petroleum Society of CIM, Calgary, June 10-13 (PA: 375, 651).

Lielmezs, J., Howell, S.K., and Campbell, H.D. (1983), "Modified Redlich-Kwong Equation of State for Saturated Vapor-Liquid Equilibrium," Chem. Eng. Sci., 38 (8) 1293-1301.

Lin, Ho-Mu (1984), "Peng-Robinson EOS for Vapor-Liquid Equilibrium Calculations for CO_2 + Hydrocarbon Mixtures," Fluid Phase Equilibria, 16, 151-169.

Lin, Ho-Mu and Chao, K.C. (1984), "Correlation of Critical Properties and Acentric Factor of Hydrocarbons and Derivatives," AIChE J., 30 (6), November, 981-983.

Lorenz, J., Bray, B.G., and Clark, C.R. (1964), "Calculating Viscosities of Reservoir Fluids from Their Compositions," J. Pet. Tech., October, 1171-1176.

Lydersen, A.L. (1955), "Estimation of Critical Properties of Organic Compounds," Univ. of Wisconsin, Eng. Experimental Station Report 3, Madison, Wisconsin, April.

Maddox, R.N. and Erbar, J.H. (1984), "Improve P-V-T Predictions," Hydrocarbon Process., January, 119-121.

Martin, J.J. (1967), "Equations of State," Ind. Eng. Chem., 59 (12) 34-52.

Martin, J.J. (1979), "Cubic Equations of State - Which?," Ind. Eng. Chem., Fund., 18 (2) 81-97.

Mathis, P.M. and Copeman, T.W. (1983), "Extension of the Peng-Robinson Equation of State to Complex Mixtures: Evaluation of the Various Forms of the Local Composition Concept," Fluid Phase Equilibria, 13, 91-108.

Mehra, R.K., Heidemann, R.A., Aziz, K., and Donnelly, J.K. (1982), "A Statistical Approach for Combining Reservoir Fluids into Pseudocomponents for Compositional Model Studies," SPE Paper 11201, presented at the 57th Annual Conference, New Orleans, September 26-29.

Montel, F. and Gouel, P.L. (1984), "A New Lumping Scheme of Analytical Data for Compositional Studies," SPE Paper 13119, presented at the 59th Annual Conference, Houston, September 16-19.

Morii, S., Yazawa, N., Inoue, S., and Arihara, N. (1985), "Effects of Oil Composition on CO_2-Flood Displacement Performance," paper presented at the 1985 European Symposium on Enhanced Oil Recovery, Rome, April 16-19 (PA: 389-787).

Nath, J. (1983), "Empirical Equation for Estimation of Critical Pressures for Organic Compounds," Ind. Eng. Chem., Fund., 22 (3) 358-360.

Nokay, R. (1959), "Estimate Petrochemical Properties," Chemical Engineering, February 23, 147-148.

Passut, C.A. and Danner, R.P. (1972), "Correlation of Ideal Gas Enthalpy, Heat Capacity and Entropy," Ind. Eng. Chem., Process Des. Dev., 11 (4) 543-546.

Passut, C.A. and Danner, R.P. (1973), "Acentric Factor. A Valuable Correlating Parameter for the Properties of Hydrocarbons," Ind. Eng. Chem., Process Des. Dev., 12 (3) 365-368.

Patel, N.C. and Teja, A.S. (1982), "A New Cubic Equation of State for Fluids and Fluid Mixtures," Chem. Eng. Sci., 37 (3) 463-483.

Paunovic, R., Jovanovic, S., and Mihajlov, A. (1981), "Rapid Computation of Binary Interaction Coefficients of an Equation of State for Vapor-Liquid Equilibrium Calculations - Application to the Redlich-Kwong-Soave Equation of State," Fluid Phase Equilibria, 6, 141-168.

Pedersen, K.S., Thomassen, P., and Fredenslund, A. (1983), "SRK-EOS Calculation for Crude Oils," Fluid Phase Equilibria, 14, 209-218.

Pedersen, K.S., Thomassen, P., and Fredenslund, A. (1984-a), "Thermodynamics of Petroleum Mixtures Containing Heavy Hydrocarbons - 1. Phase Envelope Calculations by Use of the Soave-Redlich-Kwong Equation of State," Ind. Eng. Chem., Process Des. Dev., 23, 163-170.

Pedersen, K.S., Thomassen, P., and Fredenslund, A. (1984-b), "Thermodynamics of Petroleum Mixtures Containing Heavy Hydrocarbons - 2. Flash and PVT Calculations with the SRK Equation of State," Ind. Eng. Chem., Process Des. Dev., 23, 566-573

Pedersen, K.S., Thomassen, P., and Fredenslund, A. (1985), "Thermodynamics of Petroleum Mixtures Containing Heavy Hydrocarbons - 3. Efficient Flash Calculation Procedures Using the SRK Equation of State," Ind. Eng. Chem., Process Des. Dev., 24, 948-954.

Peneloux, A., Rauzy, E., and Freze, R. (1982), "A Consistent Correction for Redlich-Kwong-Soave Volumes," Fluid Phase Equilibria, 8, 7-23.

Peng, D.Y. and Robinson, D.B. (1976), "A New Two-Constant Equation of State," Ind. Eng. Chem., Fund., 15 (1) 59-64.

Prausnitz, J.M. (1983), "Phase Equilibria for Complex Fluid Mixtures," Fluid Phase Equilibria, 14, 1-18.

Redlich, O. and Kwong, J.N.S. (1949), "On the Thermodynamics of Solutions F: An Equation of State - Fugacities of Gaseous Solutions," Chem. Reviews, 44, 233-244.

Reid, R.C., Prausnitz, J.M., and Sherwood, T.K. (1977), "The Properties of Gases and Liquids," McGraw-Hill Book Company - 3rd Edition.

Riazi, W.R. and Daubert, T.E. (1980), "Simplify Property Predictions," Hydrocarbon Processing, March, 115-116.

Robinson, D.B. and Peng, D.Y. (1978), "The Characterization of the Heptanes and Heavier Fractions," Research Report 28, GPA, Tulsa, OK.

Schlijper, A.G. (1984), "Simulation of Compositional Processes: The Use of Pseudocomponents in Equation-of-State Calculations," SPE/DOE Paper 12633, presented at the 4th SPE/DOE Symposium on EOR, Tulsa, OK, April 15-18.

Schmidt, G. and Wenzel, H. (1980), "A Modified van der Waals Type Equation of State," Chem. Eng. Sci., 35 (7) 1503-1512.

Scott, R.L. and van Konynenburg, P.H. (1970), "Static Properties of Solutions - Van der Waals and Related Models for Hydrocarbon Mixtures," Disc. Faraday Soc., 49, 87-97.

Soave, G. (1972), "Equilibrium Constants from a Modified Redlich-Kwong Equation of State," Chem. Eng. Sci., 27 (6) 1197-1203.

Soave, G. (1984), "Improvement of the van der Waals Equation of State," Chem. Eng. Sci., 39 (2) 357-369.

Stewart, G., Todd, A.C., Stamaki, S., and Clancy, M. (1984), "PVT Behavior of Gas Condensate Systems," presented at a One-Day Seminar on Condensate Reservoir Studies at British Gas London Research Station, Oct. 17, (PA: 373-536)

Tsonopoulos, C. (1979), "Second Virial Cross-Coefficients: Correlations and Predictions of d_{ij}," Equations of State in Engineering and Research, K.C. Chao and R.L. Robinson (Eds), ACS, Advances in Chemistry Series, 182, Washington, Chapter 8, 143-162.

Tsonopoulos, C. and Heidman, J.L. (1985), "From Redlich-Kwong to the Present," Fluid Phase Equilibria, 24, 1-23.

Turek, E.A., Metcalfe, R.S., Yarborough, L., and Robinson, R.L., Jr. (1984), "Phase Equilibria in CO_2-Multicomponent Hydrocarbon Systems: Experimental Data and an Improved Prediction Technique," Soc. Pet. Eng. J., June, 308-324.

Varotsis, N., Steward, G., Todd, A.C., and Clancy, M. (1984), "The Phase Behavior of Systems Comprising North Sea Reservoir Fluids and Injection Gases," SPE/DOE Paper 12647, presented at the 4th SPE/DOE Symposium on EOR, Tulsa, OK, April 15-18.

Vasquez, M. and Beggs, H.D. (1980), "Correlations for Fluid Physical Properties Prediction," J. Pet. Eng., June, 968-970.

Vidal, J. (1983), "Equations of State - Reworking the Old Forms," Fluid Phase Equilibria, 13, 15-33.

Vogel, T.L., Turek, E.A., Metcalfe, R.S., Bergman, D.F., and Morris, R.W. (1983), "Applications of Equation of State to Calculate Reservoir Fluid Properties," Fluid Phase Equilibria, 14, 103-116.

Watanasiri, S., Owens, V.H., and Starling, K.E. (1985), "Correlations for Estimating Critical Constants, Acentric Factor and Dipole Moment for Undefined Coal-Fluid Fractions," Ind. Eng. Chem., Process Des. Dev., 24 (2) 294-296.

Whitson, C.H. (1983-a), "Practical Aspects of Characterizing Petroleum Fractions," OYEZ Science and Technical Service Ltd., North Sea Condensate Reservoirs and Their Development Conference, London, May 24-25 (PA: 348, 672).

Whitson, C.H. (1983-b), "Characterization of Hydrocarbon Plus Fraction," Soc. Pet. Eng. J., August, 683-694.

Whitson, C.H. (1984), "Effect of C_7+ Properties on Equation-of-State Predictions," Soc. Pet. Eng. J., December, 685-696.

Whitson, C.H. (1984-a), "Critical Properties Estimation from an Equation of State," SPE/DOE Paper 12634, presented at the 4th SPE/DOE Symposium on EOR, Tulsa, April 15-18.

Wilson, A., Maddox, R.N., and Erbar, J.H. (1978), "C_6+ Fractions Affect Phase Behavior," Oil & Gas J., August 21, 76-81.

Yarborough, L. (1979), "Application of a Generalized Equation of State to Petroleum Reservoir Fluids," Equations of State in Engineering and Research, K.C. Chao, R.L. Robinson (Eds), ACS, Advances in Chemistry Series, 182, Washington, Chapter 21, 385-439.

APPENDIX F

Modeling Multiphase Flow in Oil Reservoirs

MODELING MULTIPHASE FLOW IN OIL RESERVOIRS

Frank S. Kovarik and Dae G. Huh
New Mexico Petroleum Recovery Research Center
New Mexico Institute of Mining and Technology
Socorro, New Mexico 87801

ABSTRACT

This paper provides a brief description of the current level of development of the modeling of multiphase flow in oil reservoirs with emphasis on enhanced oil recovery (EOR) processes. The field of research is summarized, with emphasis on carbon dioxide miscible flooding. This paper is written for engineers and scientists who work in the area of simulation but are not familiar with the petroleum field.

Enhanced oil recovery (EOR) is frequently separated into three research areas (Taber 1985): high-pressure gas flooding, chemical flooding, and thermal recovery methods. Between 1973 and 1980, thermal methods accounted for the steady growth in enhanced oil recovery in the U.S. Since 1980, the growth in thermal recovery projects has stabilized; chemical EOR and gas injection (primarily miscible) methods are responsible for the recent increases in enhanced recovery. The growth in the chemical flooding area has been provided by polymer-augmented waterflooding. CO_2 flooding has been the fastest growing gas injection process; however, hydrocarbon miscible gas projects have been expanding. In recent years, three large pipelines, which deliver CO_2 to the west Texas Permian Basin and also eastern New Mexico, have been completed, and CO_2 flooding projects have almost tripled from 1982 to 1986. CO_2 flooding is expected to increase at a fairly rapid rate (if the oil price is above $20/barrel) in the U.S.

The EOR perspective throughout the world is similar, but with much less emphasis on CO_2 and polymer flooding methods. Most of the EOR activity in the world is accounted for by thermal recovery. However, miscible gas projects have been increasing rapidly. Both miscible and immiscible nitrogen injection has become more popular recently because of favorable cost and availability in more remote areas. A majority of planned EOR projects outside the U.S. have been scheduled to use the hydrocarbon miscible gas process (based on 1984 data).

A brief history of reservoir simulation is given in this paper, then a short introduction to the field of enhanced oil recovery. Next, the simulation of miscible gas flooding is discussed in more detail, followed by brief, general descriptions of various reservoir models. Current model formulations and equation solving methods are presented. Examples are given of the new mechanistic models that are being developed and are now starting to be used in conjunction with the large, three dimensional, field-scale reservoir simulators in order to enable improved prediction of the performance of oil recovery projects. Indeed, these mechanistic models, based on engineering fundamentals, can help predict performance at the laboratory-scale and are being used to define new mechanisms that effect reservoir-scale displacements.

We will examine some of the reasons why simulation models are used, i.e., what questions need to be answered regarding projected reservoir performance, and then conclude with our view of the future of the simulation of multiple phase flow in oil reservoirs.

INTRODUCTION

As in all papers of this sort, we make no claims at universality, but hope the reader's interest will be held by what is included and his/her curiosity piqued by what is left out or partially described. For those of you who have not already done so, a brief tour of a prior review (Coats 1982), which this introduction is, in part, based upon, would be worthwhile. We have categorized the contents here primarily on the basis of what we consider to be the important new frontiers in reservoir simulation. A brief look at the history of reservoir simulation follows.

Reservoir simulation is the utilization of mathematics to predict oil recovery (reservoir performance) and also to compare the economics of alternate recovery methods. Before 1960, Buckley-Leverett calculations, analytical methods, and zero-dimensional material balances, were the state of the art.

The 1960's brought forth the development of sophisticated computer programs which could solve large sets of finite difference equations describing three-dimensional, transient, multiphase flow in porous media. Reservoir simulation was primarily concerned with two-phase gas/water and three-phase, three-component (oil, water, gas) problems, and the recovery methods modeled were usually pressure maintenance or depletion. The main concern was the matching of production history not the correct representation of recovery process physics.

During the 1970's, simulation methods spread to enhanced recovery processes such as miscible flooding, especially CO_2 flooding, as well as chemical flooding, steam flooding, and in-situ combustion. Individual models were assembled for each complex recovery scheme. Difficult problems addressing the physics of oil displacement needed to be tackled, such as the influence of chemical agents (e.g., interfacial tension reduction and emulsification), reaction kinetics, and complex multicomponent phase behavior on oil recovery.

A reservoir simulation model can be described in the simplest manner as a set of material balance

equations which are combined with Darcy's Law (modified to include relative permeability) and subjected to a number of constraints, capillary pressure relations, and equilibrium conditions. Reservoir properties and fluid properties are generally considered uniform throughout a grid block, but can vary from one block to another. Fluid properties can also vary with time. Some causes of the complexity of the model are (1) reservoir heterogeneity, (2) the nonlinearity of relative permeability and capillary pressure as a function of saturation, and (3) the nonlinearity of fluid PVT properties.

Types of input required for the model include reservoir description data and fluid PVT properties, as well as well locations, perforated intervals, rate schedules, and productivity indices. Output includes spatial fluid pressures and saturation distributions, injection/production rate for each well, and producing GOR (gas-oil ratios) and WOR (water-oil ratios).

ENHANCED OIL RECOVERY (Baily 1984)

Enhanced oil recovery, defined by the National Petroleum Council (Baily 1984), is the "incremental ultimate oil that can be economically produced from a petroleum reservoir over that which can be economically recovered by conventional primary and secondary methods." Primary recovery relies upon natural reservoir energy to drive the oil out of the reservoir through the production well. As this natural energy dissipates over a period of time, additional energy is needed in order to continue to produce oil; and so, water or gas are added, under pressure, to the reservoir in secondary recovery processes. Waterflooding is a very successful method for improving oil recovery.

The EOR processes, commonly known as tertiary recovery methods are broadly classified into three areas: (1) miscible flooding, (2) chemical flooding, and (3) thermal recovery. Conventional primary and secondary recovery methods are expected to recovery only about one-third of the original oil that is in the reservoir. Thus, the potential impact of EOR processes on domestic oil production is significant.

Miscible EOR methods (Taber 1985) include the use of nitrogen, CO_2, and hydrocarbon gases as miscible solvents and have the ability to recover lower viscosity oils. Carbon dioxide flooding should make the largest contribution to oil recovery by miscible enhanced methods in the future. And indeed, CO_2 flooding has been the fastest growing gas injection method in recent years, with around 70 active projects in the United States. CO_2 flooding projects almost tripled between 1982 to 1986, and recent surveys indicated a continued rapid growth in the United States (provided the oil price is above $20/barrel).

Chemical EOR includes surfactant (micellar-polymer or microemulsion) flooding, alkaline flooding, and polymer flooding methods. Surfactant flooding has received the greatest attention in recent years in research centers because of the excellent potential for improving low-to-moderate viscosity oil recovery. However, it is a complex process where a significant (and detailed) laboratory effort is necessary for field project design.

Thermal EOR includes in-situ combustion, cyclic steam injection, and steam flooding. Steam processes have been used the most in the field (the most advanced EOR method) and, thus, have the least uncertainty in predicting field performance. Steam floods are frequently applied in reservoirs, in place of primary or secondary methods, to recover viscous oils or tars. In-situ combustion has not proved economically successful to date.

RESERVOIR SIMULATION OF MISCIBLE FLOODING PROCESSES

The reader is referred to Stalkup (1983), Katz and Stalkup (1982), Coats (1982), and Stalkup (1982) upon which most of this section is based.

One of the key weaknesses in reservoir simulation is in the area of reservoir description. Spatial macroscopic permeability and continuity within the oil zone, as well as locations of faults, fractures, and shale barriers, initial fluid saturations, well productivity and injectivity, and other rock properties need to be described in the model. History matching, whereby the reservoir description is consistent with past performance can also be of help, but only gives a gross picture and is, in our opinion, used far too much in reservoir studies.

The reservoir pressure must be above the minimum miscibility pressure (MMP) in order to achieve miscible displacement. Besides pressure distribution, an efficient miscible gas sweep of the oil zone is affected by the size and type of miscible solvent slug as well as the drive fluid used to displace the solvent slug, the mobilities of the reservoir fluids, and reservoir heterogeneity. Volumetric sweepout can be influenced by gravity tonguing, viscous fingering, and channeling. Multiphase flow effects on sweep efficiency, the residual oil to a miscible flood, and solid phase precipitation should all be evaluated. Other important considerations tied to miscible sweepout are the optimal WAG (water-alternate-gas) injection system which is believed to reduce solvent mobility over continuous gas injection, the effects of gravity segregation, and the extent of oil trapping.

Not all oil displaced in a miscible flood is recovered, and the residual oil saturation left after contact by a miscible solvent (unit displacement efficiency) depends on complex phase behavior, rock properties, and the degree of dispersion. As an oil bank is displaced some of the oil is lost to crossflow into stagnant zones, and production wells should be positioned such as to capture and produce the maximum amount of contacted and displaced oil. Immiscible displacement mechanisms (oil swelling and viscosity reduction, vaporization of hydrocarbons, etc.) must be accounted for when the reservoir pressure drops below the miscibility pressure.

The relative permeability of fluids in a reservoir can be reduced by bypassed oil behind a solvent front as well as by immobile phases caused by complex system phase behavior (e.g. CO_2/oil systems). Accurate relative permeability and capillary pressure functions are necessary for any predictive technique.

A general finite difference simulator that represents all the important process physics in miscible and near-miscible displacements, has not been developed; however, the main ones currently applicable to miscible flooding include the modified black oil simulators (Todd and Longstaff 1972) and compositional simulators (Coats 1980). Several types

of modified black oil simulators and compositional simulators have been proposed. In general, neither type of simulator accurately predicts the effect of physical dispersion on oil displacement and recovery.

Large grid blocks average-out the fine structure of a viscous finger-dominated displacement front. The initial displacement front perturbation and nonlinear growth cycles should be described in detail by a predictive model. The relative velocity that exists between the solvent and oil fingers is neglected in the diffusion-convection simulator (Peaceman and Rachford 1962) and other modified black oil simulators; the solvent and oil are assumed to be well-mixed in the grid block and to flow at a uniform velocity, which causes optimistic sweepout calculations.

A mixing parameter model (Todd and Longstaff 1972) was developed in order to improve the predicted sweepout and oil recovery in viscous finger-dominated floods where omega, the mixing parameter, is used to calculate solvent and oil component viscosities. Omega equalling one corresponds to complete mixing, and omega equalling zero corresponds to negligible mixing within the grid block. The model is critically limited, however, because omega is effectively only a fitting parameter.

Compositional models describe the hydrocarbon content of a reservoir as an N-component mixture. Equilibrium K-values and gas/oil phase behavior are determined from correlations or from equations of state (usually cubic). Physical dispersion terms are generally not included in the mass balance equations.

Some advantages of compositional simulation over black oil include: (1) predicting near-miscible displacement performance where compositionally-dependent condensation, vaporization, and swelling are important, (2) including the effect of composition on interfacial tension which in turn helps determine residual oil saturation, (3) considering the effects of complex phase behavior, dynamic (multiple contact) miscibility, and composition dependent viscosity and density on reservoir fluid recovery efficiency. Calculation of phase behavior can be extremely difficult in near-to-fully miscible displacements because phase composition paths travel through the critical point region. Compositional simulators should be tuned against continuous phase equilibrium data and also one-dimensional, slim tube data in the range of interest.

Numerical dispersion (spatial truncation error) in finite difference simulations, in physical terms, is exhibited through smeared solvent fronts in miscible flooding, and usually results in early gas breakthrough. Smaller, and greater numbers of, grid blocks reduce numerical dispersion, however, computing time and storage constraints are generally exceeded before the dispersion is eliminated. An unreasonable number of grid blocks is usually necessary to achieve dynamic miscibility over a few feet in the reservoir (scaled to match the laboratory data). Numerical dispersion also affects the (1) mixing of transition zone fluids resulting in erroneously predicted multiple phases and (2) the dilution of solvent slugs which causes errors in optimum slug size calculations.

Computational speed, storage, and vectorization have improved dramatically over the last decade (Coats 1982). Vector processing capabilities enable the coding of more efficient simulators, e.g., vectorization of code can reduce computing time by one to two orders of magnitude. So, larger, fully compositional, reservoir studies are becoming more feasible. However, three-dimensional, field simulations have been infrequent because of cost and complexity. Two-dimensional areal and vertical cross section schemes frequently are used to study sensitivity to reservoir and process variables and also to predict final performance.

MODEL TYPES

A mathematical model of a petroleum reservoir is an expression of the physical system translated into mathematical equations, a set of partial differential equations (PDE). Mathematical models of petroleum reservoirs can be divided into four different groups according to the mechanisms associated with recovery methods: the black oil (or β) model, the compositional (or miscible) model, the chemical, and the thermal model. In this section, basic governing equations are introduced for each mathematical model.

Black oil model (Aziz and Settari 1979)

The black oil model is the simplest model, in which only two hydrocarbon components are considered in addition to the water component: a non-volatile component (=black oil) and a volatile component (=gas). The basic flow equation in a black oil model is a diffusivity equation. This is a combination of the mass continuity equation for each phase for each grid block and the Darcy's equation representing the phase flow rate between each grid block. As an example, consider a control volume in a one-dimensional multi-phase fluid flow. The continuity equations for the three phases (water, oil, and gas) are:

$$-\nabla\cdot\left(\frac{U_w}{B_w}\right)=\frac{\partial}{\partial t}\left(\frac{\phi S_w}{B_w}\right)+q_w \tag{1}$$

$$-\nabla\cdot\left(\frac{U_o}{B_o}\right)=\frac{\partial}{\partial t}\left(\frac{\phi S_o}{B_o}\right)+q_o \tag{2}$$

$$-\nabla\cdot\left(\frac{R_{sw}U_w}{B_w}+\frac{R_{so}U_o}{B_o}+\frac{U_g}{B_g}\right)=\frac{\partial}{\partial t}\left[\phi\left(\frac{R_{sw}S_w}{B_w}+\frac{R_{so}S_o}{B_o}+\frac{S_g}{B_g}\right)\right]+R_{sw}q_w+R_{so}q_o+q_g \tag{3}$$

And the Darcy's equations are:

$$U_w=-\frac{kk_{rw}}{\mu_w}(\nabla p_w-\gamma_w\nabla z) \tag{4}$$

$$U_o=-\frac{kk_{ro}}{\mu_o}(\nabla p_o-\gamma_o\nabla z) \tag{5}$$

$$U_g=-\frac{kk_{rg}}{\mu_g}(\nabla p_g-\gamma_g\nabla z) \tag{6}$$

Combining these equations, the final forms are:

$$\nabla \cdot [\lambda_w(\nabla p_w - \gamma_w \nabla z)] = \frac{\partial}{\partial t}\left(\frac{\phi S_w}{B_w}\right) + q_w \qquad (7)$$

$$\nabla \cdot [\lambda_o(\nabla p_o - \gamma_o \nabla z)] = \frac{\partial}{\partial t}\left(\frac{\phi S_o}{B_o}\right) + q_o \qquad (8)$$

$$\nabla \cdot [R_{sw}\lambda_w(\nabla p_w - \gamma_w \nabla z) + R_{so}\lambda_o(\nabla p_o - \gamma_o \nabla z) + \lambda_g(\nabla p_g - \gamma_g \nabla z)]$$
$$= \frac{\partial}{\partial t}\left[\phi\left(\frac{R_{sw}S_w}{B_w} + \frac{R_{so}S_o}{B_o} + \frac{S_g}{B_g}\right)\right] + R_{sw}q_w + R_{so}q_o + q_g \qquad (9)$$

with the transmissibility $\lambda_j = \frac{kk_{rj}}{\mu_j B_j}$

In order to solve the above three PDEs, the following constraint equations are needed:

$$S_w + S_o + S_g = 1 \qquad (10)$$

$$Pc_{ow} = P_o - P_w \qquad (11)$$

$$Pc_{go} = P_g - P_o \qquad (12)$$

In the black oil model, there are basically three diffusivity equations and three constraint equations with six unknowns (P_o, P_w, P_g, S_o, S_w, S_g). Three PDEs are discretized into finite difference equations (FDE) and solved by the finite differences method or the finite element method. These discretized methods are explained in the next section, Model Formulation.

Compositional Model (Coats 1980, Nghiem et al. 1981)

The compositional model differs from the black oil model in that the oil and gas phases are represented by multicomponent mixtures, rather than two components. This model contains N_c hydrocarbon components in addition to the water phase.

A compositional simulator has significant advantages over a black oil model when the situation involves compositional-dependent mechanisms such as vaporization, condensation, and oil swelling. The diffusivity equations for the compositional model are:

$$\nabla \cdot [T_w(\nabla p_o - \nabla p_{cow} - \gamma_w \nabla z)] = \frac{\partial}{\partial t}[\rho_w \phi S_w] + q_w \qquad (13)$$

$$\nabla \cdot [T_g y_i(\nabla p_o + \nabla p_{cgo} - \gamma_g \nabla z)] + \nabla \cdot [T_o x_i(\nabla p_o - \gamma_o \nabla z)]$$
$$= \frac{\partial}{\partial t}[\phi Z_i(\rho_o S_o + \rho_g S_g)] + q_i \qquad \text{for} \quad i = 1...N_c \qquad (14)$$

where $T_j = \frac{kk_{rj}\rho_j}{\mu_j}$

Besides these equations, there are thermodynamic equilibrium equations:

$$fu_i^g = fu_i^l \qquad \text{for} \quad i = 1...N_c \qquad (15)$$

$$Z_i = Lx_i + Vy_i \qquad \text{for} \quad i = 1...N_c \qquad (16)$$

$$V = \frac{\rho_g S_g}{\rho_g S_g + \rho_o S_o} \qquad (17)$$

$$L = \frac{\rho_o S_o}{\rho_g S_g + \rho_o S_o} \qquad (18)$$

Also, the constraint equations are:

$$\sum_{i=1}^{N_c} x_i = \sum_{i=1}^{N_c} y_i = 1 \qquad (19)$$

$$S_w + S_o + S_g = 1 \qquad (20)$$

In a compositional model, there are $3N_c+6$ equations with $3N_c+6$ unknowns (x_i, y_i, Z_i, P_o, S_o, S_g, S_w, L, and V).

Equilibrium compositions of the phases co-existing in each grid block are determined from flash calculations using K-value correlations or from solving equations of state at the thermodynamic equilibrium condition of equal fugacity of a given component in each phase.

Thermal Recovery Model (Coats 1980)

The thermal recovery methods are used mainly in heavy and/or high viscosity oil reservoirs. In these reservoirs, generation of heat reduces the reservoir flow resistance by reducing the viscosity of the crude oil. Thermal recovery methods include hot water flooding, steam drive, cyclic steam injection, and in-situ combustion (wet or dry, and forward or backward).

In this model, there is one more constituent equation in addition to the mass balance equations. This is the energy balance equation. Coats developed a simulator which models four phases (j=1 for water, j=2 for oil, j=3 for gas, and j=4 for solid coke) and N_c components. The N_c components are as follows:

N_c	
1	- water
2	- oil (heavy oil)
3	- gas
4	- coke
5 to N_c	- gas or oil components

The constituent equations are:

a) Mass Balance equations

$$\frac{\partial}{\partial t}(\phi \sum_{j=1}^{N_p} \rho_j S_j x_{ij}) = \sum_{j=1}^{3} \nabla \cdot [T_j x_{ij}(\nabla p + \nabla p_{cj} - \gamma_j \nabla z)] - q_i + \sum_{r=1}^{N_R} q_{ir} \quad (21)$$

for $i = \ldots N_c$

where $T_j = \frac{k k_{rj} \rho_j}{\mu_j}$

b) Energy Balance

$$\frac{\partial}{\partial t}[\phi \sum_{j=1}^{N_p} \rho_j S_j E_j + (1-\phi) M_f (T - T_{in})]$$

$$= \sum_{j=1}^{3} \nabla \cdot [T_j H_j (\nabla p + \nabla p_{cj} - \gamma_j \nabla z)] + \nabla \cdot (k_t \nabla T) \quad (22)$$

$$+ \nabla \cdot (k_t \alpha_3 \nabla T^4) - Q_H - Q_{HL} + \sum_{r=1}^{N_R} H_r$$

And the constraint equations are:

c) Saturation constraint

$$\sum_{j=1}^{N_p} S_j = 1 \quad (23)$$

d) Mole fraction constraints

$$\sum_{i=1}^{N_c} x_{ij} = 1 \qquad \text{for} \quad j = 1 \ldots N_p \quad (24)$$

Chemical Model (Pope & Nelson 1978)

Chemical flooding can be broadly classified as any EOR process which uses chemicals in order to reduce the mobility of the displacing fluid, or to lower the interfacial tension between oil and water. These include low and high tension flooding, polymer flooding, and alkaline flooding.

A chemical model, in general, uses N_c material balance equations. For example, a one-dimensional compositional chemical simulator used N_c continuity equations to model several major processes such as phase behavior, interfacial tension effect on residual saturation, and increased polymer viscosity with concentration. This model included three phases (water, oil, and microemulsion) and six components (water, oil, surfactant, polymer, total anion, and Ca^{++}ion).

The continuity equations for the component i and the Np phases are:

$$\frac{\partial}{\partial t}(C_i + \hat{C}_i) + \frac{q}{A\phi} \frac{\partial}{\partial x} \sum_{j=1}^{N_p} f_j C_{ij} = 0$$

$$\text{for} \quad i = 1 \ldots N_c \quad (25)$$

$$\text{where} \quad f_j = \frac{k_j/\mu_j}{\sum_{j=1}^{N_p}(k_j/\mu_j)}$$

This can be discretized by the explicit finite difference method. Using dimensionless terms, this equation becomes:

$$(C_i + \hat{C}_i)_{\Delta Q_D + Q_D} = (C_i + \hat{C}_i)_{Q_D}$$

$$+ \frac{\Delta Q_D}{\Delta X_D} \sum_{j=1}^{N_p} [(f_j C_{ij})_{X_D - \Delta X_D} - (f_j C_{ij})_{X_D}]_{Q_D} \quad (26)$$

with $X_D = \frac{x}{l}$ and $\partial Q_D = \frac{q}{lA\phi} \partial t$

constraint equations are:

$$C_i = \sum_{j=1}^{N_p} S_j C_{ij} \quad (27)$$

and

$$\sum_{j=1}^{N_p} S_j = 1 \quad (28)$$

In this model, the "Hand" plot (Treybal 1963) is used for the numerical representation of the phase diagram of the binodal curve and the distribution curve.

MODEL FORMULATION (COATS 1982)

The general simulation model is a set of partial differential equations. These partial differential equations are discretized into finite difference equations implicitly or explicitly. The most frequently used formulation (numerical model) in multiphase flow is the IMPES™ method. This method denotes implicit pressure and explicit saturation. IMPES uses old time level values of relative permeabilities in the interblock flow terms. Solution of a single pressure equation is followed by an explicit updating of fluid saturations and compositions in each grid block (Coats 1982). This formulation becomes unstable if the volumetric flow through a grid block in a time step exceeds a small fraction of the block pore volume. A more stable formulation than IMPES is the sequential method, in which solution of fluid saturation equations using implicit values of relative permeabilities follows the pressure equation solution. However, the implicit method is the most stable method. The implicit formulation (or SS formulation) solves the N_c equations simultaneously.

Computer time per time step increases from the IMPES to the sequential to the implicit formulation when the time step size is constant. However, the overall computing time depends upon the time step size for each formulation.

Most of the petroleum reservoir simulators have been written in a finite difference formulation which utilizes a semi-regular distribution of grid points. The finite element method is also used, but results in increased computer time. Advantages of the finite element method over the finite differences method are the relative ease with which the boundary conditions

of the problem are handled and the variational treatment of grid blocks. For the discretization from PDE to the finite difference equation, the Taylor series expansion is usually used. There are two ways to discretize equations in 2-dimensional space. One is the five-point finite difference method, and the other is the nine-point finite difference method. Nine-point finite difference schemes have four more diagonal points than the ordinary five-point. Using the nine-point scheme, the grid-orientation effect can be reduced (Coats 1982).

SOLUTION TECHNIQUES

After the PDEs are discretized, the resulting finite difference equations are linearized. These linear equations should then be solved either by the direct method (Gaussian elimination or Gauss-Jordan) or the iteration method.

In the direct method, LU factorization and Gaussian elimination are used. The form of the resulting matrix depends on the ordering of equations. In order to reduce the computer time and storage, a D4 ordering scheme is often used. D4 matrix-banding is an alternating diagonal ordering scheme and is explained in detail by Price and Coats (1973). It is more economical to use the iteration method in a multidimensional simulation. The most frequently used iteration methods are:

SIP (strongly implicit)
SOR (successive over relaxation)
ADIP (Alternating direction iteration).

Other iteration methods are Jacobi and Gauss-Seidel methods.

The finite difference equation in the single phase 2-D case with a regular ordering scheme can be written as:

$$a_{ij}U_{i,j} + b_{ij}U_{i-1,j} + c_{ij}U_{i+1,j} + d_{ij}U_{i,j-1} + e_{ij}U_{i,j+1} = f_{ij} \quad (29)$$

where a, b, c, d, e, f are coefficients and U is a dependent variable.

Using the Jacobi method, this becomes:

$$U_{ij}^{(k+1)} = -\frac{1}{a_{ij}}[b_{ij}U_{i-1,j}^{(k)} + c_{ij}U_{i+1,j}^{(k)} + d_{ij}U_{i,j-1}^{(k)} + e_{ij}U_{i,j+1}^{(k)} - f_{ij}] \quad (30)$$

Using the Gauss-Seidel method:

$$U_{ij}^{(k+1)} = -\frac{1}{a_{ij}}[b_{ij}U_{i-1,j}^{(k+1)} + c_{ij}U_{i+1,j}^{(k)} + d_{ij}U_{i,j-1}^{(k+1)} + e_{ij}U_{i,j+1}^{(k)} - f_{ij}] \quad (31)$$

The SOR method is a modified Gauss-Seidel method:

$$U_{ij}^{(k+1)} = (1-\omega)U_{ij}^{(k)} - \frac{\omega}{a_{ij}}[b_{ij}U_{i-1,j}^{(k+1)} + c_{ij}U_{i+1,j}^{(k)} + d_{ij}U_{i,j-1}^{(k+1)} + e_{ij}U_{i,j+1}^{(k)} - f_{ij}] \quad (32)$$

When $0 < \omega < 1$, this method is called under-relaxation and when $\omega > 1$, it is called over-relaxation or SOR (successive over relaxation). The SOR method accelerates the speed of convergence. If the optimum relaxation factor (ω) is obtained, the rate of convergence is accelerated.

In order to explain the ADIP method (Aziz and Settari 1979), Eq. 29 is rewritten in the following form by grouping it into three terms:

$$(a_1x_{ij}U_{i,j} + b_{ij}U_{i-1,j} + c_{ij}U_{i+1,j}) + (a_2y_{ij}U_{i,j} + d_{ij}U_{i,j-1} + e_{ij}U_{i,j+1}) + (g_{ij}U_{i,j}) = f_{ij} \quad (33)$$

If this equation is written in a matrix form:

$$(H + V + \Sigma)u = d \quad (34)$$

$$(H + \tfrac{1}{2}\Sigma + rI)u = (rI - V - \tfrac{1}{2}\Sigma)u + d \quad (35a)$$

$$(V + \tfrac{1}{2}\Sigma + rI)u = (rI - H - \tfrac{1}{2}\Sigma)u + d \quad (35b)$$

$$\{(H + \tfrac{1}{2}\Sigma) + r^{(k+1)}I\}u^* = \{r^{(k+1)}I - (V + \tfrac{1}{2}\Sigma)\}u^{(k)} + d \quad (36a)$$

$$\{(V + \tfrac{1}{2}\Sigma) + r^{(k+1)}I\}u^{(k+1)} = \{r^{(k+1)}I - (H + \tfrac{1}{2}\Sigma)\}u^* + d \quad (36b)$$

where H = matrix of horizontal direction derivative
V = matrix of vertical direction derivative
Σ = matrix of time derivative
r = iteration parameter chosen to accelerate convergence of the iterative process.

First Eq. 36a is solved for u^*, then Eq. 36b is solved for $u^{(k+1)}$. This process is continued until convergence is obtained.

In the SIP method (Aziz and Settari 1979), the general matrix form of Au = d can be rewritten as:

$$(A + N)u = (A + N)u - (Au - d) \quad (37)$$

so that A + N is easily factored into L and U matrices which are sparse. Hence the equation becomes:

$$(LU)u^{(k+1)} = (LU)u^{(k)} - (Au^{(k)} - d) \quad (38)$$

or $(LU)\delta^{(k+1)} = -R^{(k)}$ where $\delta^{(k+1)} = u^{(k+1)} - u^{(k)}$ and $R^{(k)} = Au^{(k)} - d$. After the elements of LU are computed, $U\delta^{(k+1)}$ is calculated and then $\delta^{(k+1)}$ is solved.

MECHANISTIC MODELING

Fractured Reservoirs

Petroleum reservoirs are often fractured, either naturally, or by artificial stimulation, or even by having excessive pressure applied during injection of fluids in EOR flooding operations. Large fractures provide conduits through which flow readily occurs, but the majority of the reservoir fluid is generally stored in the pore space of the intact matrix. Thus,

in the extreme case of a highly fractured reservoir, a gas or waterflooding operation may effectively sweep only the fractures and leave much of the oil bypassed. Therefore simulation of fluid flow in fractured reservoirs is of great interest to the petroleum industry.

Most of the fractured reservoir simulations have been based on a dual porosity concept, in which a reservoir is represented by homogeneous matrix blocks separated by continuous fractures. Thomas et al. (1983) described the dual porosity, fractured reservoir model. The flow equations in this model are essentially the same as those in the conventional black oil model except for the matrix/fracture transfer terms.

The flow equations in fracture are

$$\nabla\cdot[\lambda_i(\nabla p_i-\gamma_i\nabla z)]-q_i+\lambda_i^{mf}(p_{im}-p_i)=\frac{\partial}{\partial t}(\phi S_w/B_w)$$
for i = oil &water, and (39)

$$\nabla\cdot[\lambda_g(\nabla p_g-\gamma_g\nabla z)]+\nabla\cdot[\lambda_o R_{so}(\nabla p_o-\gamma_o\nabla z)]-q_g-R_{so}q_o$$
$$+\lambda_g^{mf}(p_{gm}-p_g)+\lambda_o^{mf}R_{so}(p_{om}-p_o)=\frac{\partial}{\partial t}(\phi S_g/B_g+\phi R_{so}S_o/B_o) \quad (40)$$

for gas phase

The matrix/fracture flow equations for three phases are

$$-\lambda_w^{mf}(p_{wm}-p_w)=\frac{\partial}{\partial t}(\phi S_w/B_w)_{matrix} \quad (41)$$

$$-\lambda_o^{mf}(p_{om}-p_o)=\frac{\partial}{\partial t}(\phi S_o/B_o)_{matrix} \quad (42)$$

$$-\lambda_g^{mf}(p_{gm}-p_g)-\lambda_o^{mf}R_{so}(p_{om}-p_o)=\frac{\partial}{\partial t}(\phi S_g/B_g+\phi R_{so}S_o/B_o)_{matrix} \quad (43)$$

where $$\lambda_w^{mf}=\sigma\left(\frac{kk_{rw}}{B_w\mu_w}\right)_{matrix} \quad (44)$$

$$\lambda_o^{mf}=\sigma\left(\frac{kk_{ro}}{B_o\mu_o}\right)_{matrix} \quad (45)$$

$$\lambda_g^{mf}=\sigma\left(\frac{kk_{rg}}{B_g\mu_g}\right)_{matrix} \quad (46)$$

σ is the geometric factor that accounts for the surface area of the matrix blocks per unit volume and a characteristic length associated with matrix/fracture flow.

Also the constraint equations are:

$$S_w+S_o+S_g=1 \quad (47)$$

$$p_{cow}=p_o-p_w \quad (48)$$

$$p_{cgo}=p_g-p_o \quad (49)$$

for both fracture and matrix.

Viscous Fingering in Porous Media

Viscous fingering, the frontal instability of a displacement, occurs when the mobility of a displacing fluid is greater than the mobility of the displaced fluids. Viscous fingering is very common, both in immiscible displacement of water flooding of high viscosity oils and in miscible displacement due to the low viscosity of solvents (gases). There have been many mathematical treatments of unstable miscible displacements with unfavorable mobility ratios. Some of these are listed below.

Peaceman & Rachford (1962) developed a system which takes into account the influence of gravity, the spatial distribution of permeability, diffusion, and fluid viscosities and densities. A small random variation of permeability using the following equation was used to initiate the finger growth.

$$k_{ij}=k_{av}(1+k_s\beta_{ij})Z \quad (50)$$

where β_{ij} is a random number,
Z is a correction factor, and
k_s is a specified standard deviation

For the effect of viscous fingering on displacement efficiency, Koval (1963) developed the K-factor method similar to the Buckley-Leverett calculations.

In his K-factor method, the oil recovery and solvent cut are easily calculated by the following equations with K as the parameter:

$$N_{pv}=\frac{2(KV_{pi})^{1/2}-1-V_{pi}}{K-1} \quad (51)$$

$$f_s=\frac{K-(K/V_{pi})^{1/2}}{K-1} \quad (52)$$

where K represents the multiplication of the heterogeneity factory H and the effective viscosity ratio E.

In this calculation, he assumed the fractional flow equation describing miscible displacement as the following equation:

$$f_s=\frac{1}{1+\frac{1-S_s}{S_s}(1/H)(1/E)}=\frac{KS}{1+S(K-1)} \quad (53)$$

where $$E=\frac{\mu_{oe}}{\mu_{se}}=[0.78+0.22(\mu_o/\mu_s)^{1/4}]^4 \quad (54)$$

Vossoughi et al. (1984) used a method similar to Koval's whereby they modified the convection-dispersion equation to reflect viscous fingering:

$$D\frac{\partial^2 S_1}{\partial x^2}-U\frac{\partial f_1}{\partial x}=\frac{\partial S_1}{\partial t} \quad (55)$$

Converting into dimensionless terms, this equation becomes:

$$\frac{\partial^2 C_D}{\partial x_D^2}-N_{pe}\left(\frac{\partial f_1}{\partial S_1}\right)\left(\frac{\partial C_D}{\partial x_D}\right)=\frac{\partial C_D}{\partial t_D} \quad (56)$$

with $$f_1 = \frac{(\mu_2/\mu_1) - [S_1 + (1 - S_1)(\mu_2/\mu_1)^{1/\gamma}]^\gamma}{(\mu_2/\mu_1) - 1} \quad (57)$$

$$C_D = \frac{C}{C_{in}}$$

$$x_D = \frac{x}{l}$$

$$t_D = \frac{tD}{l^2}$$

$$N_{pe} = \frac{Ul}{D}$$

and γ is an empirical parameter

Todd and Longstaff (1972) developed a miscible displacement model using the gas and oil relative permeabilities under the assumption of complete miscibility between oil and gas (= solvent). Therefore, $P_{cgo} = 0$.

Considering the reduction of area available for one component by the presence of another component, the relative permeabilities are

$$k_{ro} = \frac{S_o}{S_n}(k_{rn})$$

and $$k_{rg} = \frac{S_g}{S_n}(k_{rn}) \quad (58)$$

where $S_n = S_o + S_g$

A mixing parameter (ω) is used to determine the effective viscosities of the miscible components. The two limiting viscosities are the pure component viscosity (μ_o, μ_g) and the viscosity when the entire block is occupied by the dispersed zone (μ_m),

where $$\mu_m = \frac{\mu_o \mu_g}{\left(\frac{S_o}{S_n}\mu_o^{1/4} + \frac{S_g}{S_n}\mu_g^{1/4}\right)^4} \quad (59)$$

Then the effective viscosities are expressed by following equations after the mixing parameter model proposed by Lee and Claridge (1964).

$$\mu_{oe} = \mu_o^{1-\omega}\mu_m^{\omega}$$

with $0 < \omega < 1$ (60)

$$\mu_{ge} = \mu_g^{1-\omega}\mu_m^{\omega}$$

Todd and Langstaff applied the same concept to the density calculation

$$\rho_{oe} = \rho_o\left(\frac{S_o}{S_n}\right)_{oe} + \rho_g\left[1 - \left(\frac{S_o}{S_n}\right)_{oe}\right] \quad (61)$$

$$\rho_{ge} = \rho_o\left(\frac{S_o}{S_n}\right)_{ge} + \rho_g\left[1 - \left(\frac{S_o}{S_n}\right)_{ge}\right] \quad (62)$$

Here the effective fractional saturations are obtained by rearranging the equation (59):

$$\frac{S_o}{S_n} = \frac{M^{1/4} - \left(\frac{\mu_e}{\mu_m}\right)^{1/4}}{M^{1/4} - 1} \quad (63)$$

$$\left(\frac{S_o}{S_n}\right)_{ge} = \frac{M^{1/4} - \left(\frac{\mu_e}{\mu_{ge}}\right)^{1/4}}{M^{1/4} - 1} \quad (64)$$

$$\left(\frac{S_o}{S_n}\right)_{oe} = \frac{M^{1/4} - \left(\frac{\mu_e}{\mu_{oe}}\right)^{1/4}}{M^{1/4} - 1} \quad (65)$$

with $M = \frac{\mu_o}{\mu_g}$ and $\frac{S_g}{S_n} = 1 - \frac{S_o}{S_n}$

When M = 1, they use the following simple equations

$$\rho_{oe} = (1 - \omega)\rho_o + \omega\rho_m \quad (66)$$

$$\rho_{ge} = (1 - \omega)\rho_g + \omega\rho_m \quad (67)$$

where $\rho_m = \rho_o\left(\frac{S_o}{S_n}\right) + \rho_g\left(\frac{S_g}{S_n}\right)$

The value of $\omega = 1$ corresponds to complete mixing of oil and solvent, while $\omega = 0$ corresponds to no mixing. A value in the range of 0.5 - 0.7 is frequently used. In this model, the wetting phase is water and oil, and the gas phases are non-wetting phases.

In Homsy's (1987) review of viscous fingering, he concluded that the viscous fingering experienced a cyclic process: shielding, spreading, and splitting. At the beginning of fingering initiation, a single finger is dominant because it runs slightly ahead of the other fingers and shields them from further growth. This dominant single finger spreads while advancing due to surface tension (immiscible case) and dispersion (miscible case). When fingering width exceeds a critical value (the accurate value of this critical finger width is not known, but is considered to happen at $[(12\mu U/\sigma)(\ell/b)^2 \approx 10^3]$), the tip of the finger becomes unstable and splits into two or more fingers.

In order to study the initiation and development of viscous fingers and gravity tongues, Chang (1988) has performed three-dimensional numerical simulations for horizontal displacements. The system is a bed of unconsolidated sand having a uniform porosity and a uniform permeability. The mass density of the fluid phase is a weak linear function of the concentration of the displacing fluid.

The dimensionless governing equations are written as:

$$\nabla \cdot \bar{v} = 0 \quad (68)$$

$$\nabla \bar{p} - Gw\bar{b} + \frac{\hat{\mu}}{k}\bar{v} = 0 \quad (69)$$

$$\phi\frac{\partial w}{\partial t}+\vec{v}\cdot\nabla w+\nabla\cdot\vec{j}=0 \qquad (70)$$

where $$\vec{j}=-\phi(D_d+a_t\mid\vec{v}\mid)\nabla w-\phi(a_l-a_t)\frac{\vec{v}\cdot\nabla w}{\mid\vec{v}\mid}\vec{v}$$

In order to reduce the numerical diffusion and to obtain a high degree of accuracy, the flux-corrected transport method is used to find the concentration field. The pressure field is obtained by using the alternating direction implicit procedure with successive over-relaxation.

For N ≠ 1 and M = 1, the calculations do not show any instabilities even with macroscopic perturbations to the system at the injection face. For M ≠ 1 and N = 1, fingers appear when the system has been perturbed macroscopically at the injection face. Numerical errors are not sufficient to trigger the fingers. For N ≠ 1 and M ≠ 1, instabilities can be triggered both by numerical errors and by macroscopic perturbations to the system at the injection face.

Two different seeds of the random number generator are used for macroscopic perturbations to the system. When the seed of the random number generator is changed, the manner in which the fingers grow changes, with the larger finger sometimes developing off-center. The results of the simulations clearly are dependent on the form of the perturbations used to trigger the instabilities.

Front Tracking

The major problems in a miscible flood simulation include: numerical dispersion in the finite difference method, oscillating solutions for convection-dominated flow, and the grid orientation effect. As mentioned in a previous section, the grid orientation effect can be minimized by using a nine-point finite difference scheme. Numerical dispersion is usually used to model physical dispersion, and it is a major source of error in an unstable miscible flood.

In order to suppress numerical dispersion and include physical dispersion explicitly, Hatziavramidis (1987) introduced the psuedospectral method. He used Chebyshev polynomial expansions to approximate the spatial derivatives. The direction of the displacement is divided into elements whose boundaries and size change as the approximate location of the front evolves in time. The method of collocation is used to project the equations from physical into spectral space. This results in finer resolution of the areas of interest.

First, the approximate position of the displacement front is calculated at every time step by

$$X_f^k=X_f^{k-1}+U_f^{k-1}\Delta t \qquad (71))$$

where

X_f = dimensionless front position

U_f = dimensionless front velocity

Then, the regions in front of and behind the interface are divided into subdomains, and local Chebyshev polynomials are used to approximate the derivations of the functions in the axial direction to suppress the oscillating solution.

When the points at which the solution is calculated are chosen as the extrema of the Nth order Chebyshev polynomial, a denser distribution of points close to the boundaries are obtained, and the approximation of the derivatives is carried out according to the method of collocation points.

The procedures of the psuedospectral method are as follows:

When the collocation points are $x_j = \cos[\pi(j-1)/N]$, for j = 1 . . . N+1, the first two derivatives of the function to be estimated, F (x), can be approximated by

$$F'(x_j)=\sum_{l=1}^{N+1}\hat{G}^{(1)}_{j,l}F(X_l) \qquad (72)$$

$$F''(x_j)=\sum_{l=1}^{N+1}\hat{G}^{(2)}_{j,l}F(X_l) \qquad (73)$$

with $$\hat{G}^{(k)}=TG^{(k)}\hat{T} \quad \text{for} \quad k=1,2 \qquad (74)$$

and $$G^{(2)}=G^{(1)}G^{(1)} \qquad (75)$$

Here, T, $\hat{T}$ and $G^{(1)}$ are matrices with the following elements:

$$T_{ij}=\cos\left[\frac{\pi(i-1)(j-1)}{N}\right] \qquad (76)$$

$$\hat{T}_{ij}=\frac{2}{NC_iC_j}\cos\left[\frac{\pi(i-1)(j-1)}{N}\right] \qquad (77)$$

with $$C_1=C_{N+1}=2, \quad C_i=1 \quad \text{for} \quad 1<i<N+1$$

$$G^{(1)}_{ij}=\begin{cases}0 & \text{, if } i\geq j \text{ or } i+j \text{ even}\\ \dfrac{2(j-1)}{\overline{C}_i} & \text{, } (\overline{C}_1=2,\overline{C}_2=\overline{C}_3=\ldots=1) \text{ otherwise}\end{cases} \qquad (78)$$

Foam Flow in Porous Media

Due to the poor sweep efficiency of the enhanced oil recovery methods using gas injection, the use of a foaming agent for profile modification becomes increasingly important. It is not an easy task to simulate the flow of foam through porous media because the flow behavior of gas and the foaming solution may be a combination of continuous gas flow, continuous liquid flow, and breaking/reforming foam

continuous liquid flow, and breaking/reforming foam flow. The effect of trapped gas saturation also should be included.

A mathematical model of foam viscosity in smooth capillaries was developed by Hirasaki and Lawson (1985). They modeled the foam flow through smooth capillaries, accounting for three dynamic changes at gas-liquid interfaces. These changes are 1) resistance caused by liquid slugs between gas bubbles, 2) interface deformation due to the viscous and capillary force against the restoring force of surface tension, and 3) the surface tension gradient. This model should be expanded further, before being applied to flow in a porous media because the authors assumed that the foam exists either as bulk foam or as a chain of bubbles, which may be true only in smooth capillaries.

The apparent viscosity contribution of the three dynamic changes are:

$$\frac{\mu_{app}}{\mu} = L_s n_L + 0.85\frac{n_L R}{r_c/R}(3\mu U/\sigma)^{-1/3}[(r_c/R)^2+1] + (n_L R)(3\mu U/\sigma)^{-1/3}\sqrt{N_s}\frac{(1-e^{-N_L})}{(1+e^{-N_L})} \quad (79)$$

where L_s = length of liquid slug
n_L = number of equivalent lamellae/unit length
R = capillary radius
r_c = radius of curvature of gas-liquid interface

U = velocity of bubble
σ = surface tension
μ = viscosity of water

$$N_s = -\frac{1}{(p)_c\mu}\frac{d\sigma}{d\Gamma}\frac{\Gamma_o}{\alpha}\frac{1}{r_c} = \frac{\beta}{r_c} \quad (80)$$

$$N_L = \frac{[2/(p)_c][L_B/r_c][3\mu U/\sigma]^{-1/3}}{([1/(p)_c][1/\mu][d\sigma/d\Gamma][\Gamma_o/\alpha][1/r_c])^{1/2}} \quad (81)$$

where L_B = length of thin film portion of bubble
$(P)_c$ = coefficient from constant integration
Γ = surface excess concentration
Γ_o = equilibrium concentration
α = mass transfer rate constant
β and $2/(P)_c$ should be determined from the experiment

The first term of the right-hand side is due to the liquid slug, the second term is due to the shape deformation, and last term is due to the surface tension gradient.

The population balance approach was used to model foam flow by Fall et al. (1986). The usual conservation equations are coupled with balances on the densities of flowing and stationary bubbles in the foam. Mass conservation equations for one-dimensional, two-phase, incompressible flow are:

$$\phi\frac{\partial S_w}{\partial t} + U_t\frac{\partial f_w}{\partial x} = 0 \qquad \text{for water phase} \quad (82)$$

where $f_w = \dfrac{1+\frac{k}{U_T}\lambda_{rg}[\partial p_c/\partial x + g(\rho_w-\rho_g)\sin\alpha]}{1+\lambda_{rg}/\lambda_{rw}}$

and λ_r is relative mobility

and

$$\phi\frac{\partial(S_g X_f n_f)}{\partial t} = -\nabla\cdot(U_g n_f) + G_f \quad (83)$$

for gas phase

where $U_g = -\lambda_{rg}\,(n_f, X_f \ldots)\, k\nabla\Phi_g$

and $G_f = \begin{cases} \dfrac{N_n}{\dfrac{a_1}{P_c^* - P_c} + \dfrac{b_1}{v_g}} & \text{, if } P_c < P_c^* \text{ and } t_{form} < t_{conv} \\ 0 & \text{, otherwise} \end{cases}$

This approach takes into account the number and size distribution of the foam bubbles (foam texture). It was assumed that capillary snap-off was the only mechanism changing bubble density.

SUMMARY

Reservoir simulation (Coats 1982) estimates recovery for a given producing operation, evaluates the differences in oil recovery from altered operating methods (e.g., alternative enhanced oil recovery processes), and compares the economics inherent to different recovery programs. The main types of simulators used for miscible displacement, modified black oil and compositional, have been considered along with other specialized models. Methods of prediction were shown to be influenced by many factors, including reservoir description, nonlinear relative permeability and capillary pressure functions, nonlinear fluid PVT properties, well injectivity and productivity, numerical dispersion, pressure distribution, crossflow of displaced oil, etc.

Errors inherent to finite difference approximations and cell size, i.e., numerical dispersion and grid orientation, were discussed. Some of the other causes of calculation uncertainty in miscible and immiscible performance predictions include the poor representation of displacement front instabilities, crossflow-and-dispersion/phase behavior interactions, transition zone (dynamic) miscibility, diffusional-mass-transfer recovery of oil trapped by water, and in general, a less than satisfactory representation of the physical mechanisms by which oil is mobilized and recovered.

The degree of error that remains under the most optimistic conditions is estimated to be around ± 25

percent for ultimate recovery predictions and much greater for producing rate predictions. Predicting future performance and developing methods which increase the ultimate oil recovered are the primary concerns for reservoir simulation study. Some examples of the types of questions that we can attempt to answer through a reservoir simulation study are (Aziz and Settari 1979):

> How should a field be developed and produced (for example, well pattern and spacing, producing rate, etc.) in order to maximize profit?
>
> How and when should the best enhanced recovery method be implemented at the field?
>
> What laboratory data are necessary and what is the sensitivity of the model to process parameters? What are the most important parameters to follow in the field application of an enhanced recovery process?
>
> How can laboratory results be scaled up for field application?
>
> What part of the reservoir is being depleted of oil?

Some Thoughts on the Future of Reservoir Simulation

We have been moving toward larger and larger field studies, i.e., using more grid blocks for better reservoir definition or characterization, with the advent of increased computer speeds, storage capabilities, and vectorized codes (Coats 1982). There will be a continued development of hardware and improved user interface (Aziz 1987). Research is continuing on the development of single, generalized simulators capable of modeling most recovery methods of interest (Coats 1982). Different types of specialized, "limited" compositional simulators are also being developed. Front-tracking models, important in EOR processes, are being actively researched.

The complicated physical processes present in the EOR methods are poorly understood and not adequately represented in reservoir simulators. Laboratory-scale mechanistic models which characterize pore-level process mechanisms present in EOR systems, and also in fluid diversion treatments for improved sweep efficiency, are continuing to be developed, probably more so on the academic side. These mechanistic models enable prediction of oil recovery performance at the laboratory-scale and are being used to define the critical parameters that affect reservoir-scale displacements.

Modeling physical processes as the system is scaled up from the laboratory to the field, i.e., representing scale-up parameters, is another challenge for reservoir simulation developers. Reservoir description, which is poorly accounted for in current models, can influence predictions at each scale, especially in EOR processes. Techniques need to be developed which incorporate reservoir information at scales above and below the scale of the grid block (Aziz 1987). Detailed field studies also need to be conducted with unusually well-characterized reservoirs to enable the coupling of complex physics to various length scales of heterogeneity.

NOMENCLATURE

a_1	constant
A	cross sectional area
a_ℓ	dimensionless longitudinal dispersivity
a_t	dimensionless transverse dispersivity
B	formation volume factor
b_1	constant
b	thickness of porous medium or Hele-shaw model
b	unit vector in the direction of gravity
C_i	total concentration of component i in mobile phase
$\hat{C}_i$	total concentration of component i in rock (= adsorption)
D	dispersion coefficient
D_d	dimensionless effective diffusion coefficient
E	internal energy
f	fractional flow
fu	fugacity
g	gravitational acceleration
G	dimensionless quantity characterizing the ratio of the excess gravitational forces attributable to the density difference between the displacing fluid and the displaced fluid to the viscous forces
H	enthalpy
H_r	heat of reaction r
$\bar{j}$	dimensionless effective mass flux vector
$\bar{J}_D$	flux of bubble due to hydrodynamic dispersion
k	permeability
$\hat{k}$	dimensionless permeability
k_{av}	average permeability
k_{ij}	permeability in 2-D space
k_r	relative permeability
k_s	standard deviation in permeability
k_t	thermal conductivity
ℓ	length (of system)
L	mole fraction of liquid phase
M	the ratio of the viscosity of the displaced fluid to the viscosity of the displacing fluid
M_f	reservoir rock heat capacity
n	density of bubbles in the gas phase
N	the ratio of the density of the displacing fluid to the density of the displaced fluid
N_c	number of components
N_p	number of phases
N_R	number of chemical reactions
P	pressure
$\hat{P}$	dimensionless modified pressure
P_c	capillary pressure
P_{cj}	phase j capillary pressure, Pj - P
q	sink or production (negative for source or injection)
Q_H	production rate of enthalpy

Q_{HL} heat loss rate to overburden

q_{ir} rate of creation of component i due to reaction r

R_s solution gas-oil (water) ratio

S saturation

t time

T temperature

T_{in} initial temperature

T_j transmissibility

U Darcy or superficial velocity vector

v interstitial velocity

V mole fraction of vapor phase

$\tilde{v}$ dimensionless velocity of the fluid

w normalized mass fraction

x distance

X_f fraction of gas phase flowing

x_i mole fraction of component i in oil phase

x_{ij} mole fraction of component i in phase j

y_i mole fraction of component i in vapor phase

z depth (vertical downward direction)

Z_i overall mole fraction of component i

α dip angle

α_3 ratio of radiation to heat conduction

β_{ij} constant from random number

γ specific weight

λ_r relative mobility

λ transmissibility

μ viscosity

$\hat{\mu}$ dimensionless viscosity

ρ molar density

σ interfacial tension

ϕ porosity

ω relaxation factor

Φ flow potential

Differential operator

$$\nabla = i\frac{\partial}{\partial x} + j\frac{\partial}{\partial y} + k\frac{\partial}{\partial z}$$

SUBSCRIPT

app apparent
e effective
f flowing gas phase
g gas
i component
in initial
j phase
m mixture
n non wetting phase
o oil
s solvent
t total
w water
1 displacing fluid
2 displaced fluid

SUPERSCRIPT

o oil
g gas
k iteration number
mf matrix/fracture

ACKNOWLEDGEMENTS

The authors wish to thank Joe Taber for his help on the introduction, Eric S.H. Chang for his contribution to the viscous fingering section and for his assistance in proofreading the manuscript, Phil Johnson for insights into fractured reservoir modeling, and Carol Dotson for typing this manuscript.

This work was supported, in part, by the U.S. Department of Energy, the New Mexico Research and Development Institute, and a consortium of major oil companies including the Abu Dhabi National Reservoir Research Foundation, Amoco, ARCO, Cities Service, Conoco, Chevron, Marathon, Sohio, Petro-Canada, JNOC, and Texaco.

REFERENCES

Aziz, K. and Settari, A.: Petroleum Reservoir Simulation, Applied Science Publishers, London, 1979.

Aziz, K.: "From the CMG Panel on the Future of Reservoir Simulation," GMG Advances, June, 1987.

Baily, R.E. et al.: Enhanced Oil Recovery, National Petroleum Council, June, 1984.

Chang, Shih-Hsien: "Stability of Miscible Displacements in Porous Media,": PhD dissertation, Northwestern University, Evanston, IL (1988)

Coats, K.H.: "In-Situ Combustion Model," SPEJ (December, 1980) 533-554.

Coats, K.H.: "An Equation of State Compositional Model," SPEJ (October, 1980) 363-376.

Coats, K.H.: "Reservoir Simulation: State of the Art," JPT (August, 1982) 1633-1642.

Falls, A.H. et al.: "Development of a Mechanistic Foam Simulator: The Population Balance and Generation by Snap-Off," paper SPE/DOE 14961 presented at the SPE/DOE 5th Symposium on EOR, Tulsa, April 20-23, 1986.

Gardner, A.O., Peaceman, D.W., and Pozzi, A.L. (1964) Soc. Pet. Eng. J., March.

Hatziavramidis, D.T.: "A New Computational Approach to the Miscible Displacement Problem," paper SPE 16004 presented at the 9th SPE Symposium on Reservoir Simulation, San Antonio, February 1-4, 1987.

Hirasaki, G.J. and Lawson, J.B.: "Mechanisms of Foam Flow in Porous Media: Apparent Viscosity in Smooth Capillaries," SPEJ (April, 1985) 176-190.

Homsy, G.M.: "Viscous Fingering in Porous Media," Ann. Rev. Fluid Mech., 19, (1987) 271-311.

Katz, M.L. and Stalkup, F.I.: "Oil Recovery by Miscible Displacement," 11th World Petroleum Conference, London, July, 1983.

Koval, E.J.: "A Method for Predicting the Performance of Unstable Miscible Displacement in Heterogeneous Media," SPEJ (June, 1963) 145-154.

Nghiem, L.S. et al.: "Compositional Modeling with an Equation of State," SPEJ (December, 1981) 687-698.

Peaceman, D.W. and Rachford, Jr., H.H.: "Numerical

Calculation of Multidimensional Miscible Displacement," SPEJ (December, 1962) 327-339.

Pope, G.A. and Nelson, R.C.: "A Chemical Flooding Compositional Simulator," SPEJ (October, 1978) 339-354.

Price, H.S. and Coats, K.H.: "Direct Methods in Reservoir Simulation," paper 4278 presented at the 3rd Numerical Simulation Symposium, Houston, January 11-12, 1973.

Stalkup, F.I., "Status of Miscible Displacement," presented at the International Petroleum Exhibition and Technical Symposium of the SPE, Bejing, China, March, 1982.

Stalkup, F.I., Miscible Displacement, Monograph 8, SPE of AIME, New York, 1983.

Taber, J.J.: "Enhanced Oil Recovery by Gas Miscible Flooding," presented at the EOR Symposium of the International Energy Agency Collaborative Research Program, Tokyo, Japan, October, 1985.

Thomas, L.K. et al.: "Fractured Reservoir Simulations," SPEJ (February, 1983) 42-45.

Todd, M.R. and Longstaff, W.J.: "The Development, Testing and Application of a Numerical Simulator for Predicting Miscible Flood Performance," J. Pet. Tech., July, 1972.

Treybal, R.E.,: Liquid Extraction, 2nd Ed., McGraw Hill Book Co., Inc., New York, (1963) 37.

Vossoughi, S. et al.: "A New Method to Simulate the Effect of Viscous Fingering on Miscible Displacement Processes in Porous Media," SPEJ (February, 1984) 56-64.

APPENDIX G

Nuclear Magnetic Resonance Imaging Study on Fluid Flow Through Fractured Reservoirs

Experiments have been conducted in order to determine the feasibility of applying nuclear magnetic resonance imaging (NMRI) to the study of fluid flow through fractured porous material. The NMRI instrument used in these studies is a Questa 4300 NMRI spectrometer equipped with a two-Tesla, wide-bore, Oxford Magnet providing about 80 MHz resonance frequency for protons. To date, feasibility studies have consisted of the following:

1. Determination of spin-lattice (T_1) and spin-spin (T_2) relaxation times of water and various oils, pure and in the presence of two different size distributions of glass beads (210-420 microns and 10-53 microns).

2. Screening of porous materials (glass beads, Berea sandstone, Baker dolomite, and polyethylene beads) to find an optimum system for NMRI studies.

3. NMRI experiments to distinguish between water and oil in porous material.

4. NMRI experiments involving flow of water/oil through glass-bead-packed columns.

The T_1 and T_2 relaxation times provide criteria for selection of suitable fluids and porous materials for NMRI studies and are related to motional properties of proton- containing molecules through rotational correlation times. Such motional properties are dependent on the immediate environments experienced by these molecules. Water and several oils have been evaluated in a pure state and in the presence of a glass-beads matrix.

The first porous materials considered for NMRI studies were glass beads and Berea sandstone. Both were found to provide unacceptable line widths (about 2000-3000 Hz) for proton resonances of fluids incorporated into them. On the other hand, a Baker dolomite and polyethylene beads show substantially narrower proton linewidths (less than 200 Hz). We plan to carry out further NMRI studies with the later two porous materials.

The first experiments to distinguish between water and oil in porous material involved either glass beads or Berea sandstone incorporated with water and Soltrol 220. Although we were able to distinguish between water and oil, resolution was seriously reduced because of the large linewidths characteristic of fluids in these porous materials. Results with polyethylene beads and Baker dolomite exhibit substantial enhanced resolution of images. A two-dimensional imaging experiment of a bottle containing the two immiscible fluids (water and oil) and polyethylene beads was performed. Water and oil were well resolved based on differences in spectral position. For a spectrum of water and Soltrol 220 in a Baker dolomite core sample, linewidths were about 186 Hz (water) and 156 Hz (oil). Future NMRI experiments will be conducted with Baker dolomite or polyethylene beads as the porous material.

We have conducted one simulated waterflood experiment. A 3.8-cm diameter (i.d.) polyethylene column was constructed and was packed with a slurry of Soltrol 220 and glass beads (210-420 microns). Water was then forced into the column to displace the oil. Despite extensive broadening of the proton resonances caused by the glass beads, we were able to resolve oil and water in the column. We anticipate substantially improved resolution when Baker dolomite or polyethylene beads are used as the porous materials.

During the past four months we have experimented with various porous materials and a variety of NMRI methodologies. We are now better prepared to pursue one of our principal objectives—to simulate fractured flow in a porous material and employ NMRI methods to distinguish fractured flow of CO_2, oil, and water. A one-inch by five-inch cylindrical core will be cut into two equal halves along the cylindrical axis. The halves will be placed together, and the outside surfaces of the cylinder will be sealed with epoxy resin. It is anticipated that the centrally cut plane will simulate a fracture in the core. We also plan to perform similar experiments using two immiscible fluids.

APPENDIX H

Summary of Ongoing Reservoir Simulator Development

The Gas Flooding Processes and Reservoir Simulation group is actively studying the mechanisms associated with how oil is trapped during a gas flood (including residual oil and bypassed oil). Our work is geared toward predicting, with much greater accuracy than is now available, the expected efficiency of an enhanced oil recovery process. Interactions existing among (1) displacement fronts, (2) length-scale of rock heterogeneity, and (3) complex process chemistry are of special interest to us.

We are developing a two-dimensional foam flood simulator (FFS) which focuses on zone blockage and fluid diversion in fractured (high-permeability zone) reservoirs. This model is currently being made compositional. This "first generation" model is being used to predict the conditions necessary for increased gas flood sweep efficiency and improved oil recovery. We expect that this model will be made available to consortium members by the summer of 1989. We will continue to develop the FFS over the next two years, and we expect that it will provide a reasonable estimate of the effectiveness of selected gas-foam surfactants in increasing oil recovery. The FFS could be used as a supplement to commercial reservoir simulators when making field-specific predictions.

We also have been actively formulating a three-dimensional, displacement-front instability model--a nonlinear analysis of both miscible and "near miscible" displacements. This past summer an NMR Imaging study commenced for the purpose of (1) determining velocity profiles and tracking displacement fronts in both fractured and homogeneous systems, and (2) deriving matrix-fracture, fluid transport functions for the numerical simulator.

Eventually both mechanistic models, i.e., unstable front tracking through heterogeneous systems, and zone blockage and fluid diversion with gas-foams, are expected to converge into a new type of reservoir simulator. This simulator will represent the chemical and physical processes by which high pressure gas-foam (CO_2, hydrocarbon, N_2) dampens displacement-front instabilities in heterogeneous rock, increases gas flood sweep efficiency, and enables the recovery of bypassed oil.

We also are continuing our investigations into determining the "pressure for optimal oil recovery" which targets immiscible CO_2 flooding. We are specifically interested in, at this time, characterizing and mathematically modeling the effect that multiple phases have on CO_2 sweep efficiency. Lab results suggest that higher recoveries could be obtained, under certain conditions, below the slim tube MMP.

☆U.S. GOVERNMENT PRINTING OFFICE: 1989-661-023/00031